Image-based data assimilation methods for the personalization of mechanical models - Application to cardiac mechanics and tagged-MRI

Alexandre Imperiale

To cite this version:

Alexandre Imperiale. Image-based data assimilation methods for the personalization of mechanical models - Application to cardiac mechanics and tagged-MRI. Numerical Analysis [math.NA]. Université Pierre et Marie Curie - Paris VI, 2013. English. NNT : . tel-00936027

HAL Id: tel-00936027
https://theses.hal.science/tel-00936027

Submitted on 24 Jan 2014

L'UNIVERSITÉ PIERRE ET MARIE CURIE - PARIS VI

Ecole doctorale de Paris Centre - UFR 929
Thèse présentée en vue de l'obtention du grade de Docteur de l'Université de Pierre et Marie Curie,
spécialité Mathématiques Appliquées.

Méthodes d'assimilation de la donnée image pour la personnalisation de modèles mécaniques

Application à la mécanique cardiaque et aux images de marquage tissulaire

Thèse présentée par
Alexandre IMPERIALE

Soutenue le 11/12/13 devant le jury formé de

Dominique CHAPELLE	Directeur de thèse
Stanley DURRLEMAN	Examinateur
Pascal FREY	Examinateur
Carole LE GUYADER	Rapporteur
Jean-Frédéric GERBEAU	Examinateur
Philippe MOIREAU	Directeur de thèse
Karim RAMDANI	Examinateur
Alain TROUVÉ	Examinateur
Arthur VIDARD	Rapporteur

Remerciements

C’est un exercice bien difficile de chercher à remercier ceux qui m’ont permis, au cours de ces trois ans de thèse, d’aboutir à ce manuscrit, car aucune entreprise de cette difficulté ne peut se faire seul. Cependant, je peux arriver, il me semble, à extraire de l’ensemble des personnes que j’ai cotoyé pendant cette période celles qui ont eu une influence majeure.

Dans cet ensemble, la première et principale personne qui apparait naturellement est Philippe Moireau. Je tiens à le remercier, profondément et avec sincérité. Il m’a tant appris et m’a permis d’évoluer d’un point de vue scientifique, professionnel et personnel. Par nature, les travaux reportés dans ce manuscrit sont intensément multidisciplinaires et j’ai eu la chance de pouvoir observer l’étendue de ses connaissances scientifiques, qui fut pour moi une source d’étonnement quotidienne. Par ailleurs, j’ai pu bénéficier de son incroyable dynamisme et de sa force de caractère qui ont été, sans aucun doute possible, un soutien solide à ma motivation. Je me considère donc chanceux d’avoir pu travailler avec lui pendant ces trois ans. Je tiens aussi à remercier Dominique Chapelle qui m’a énormement apporté scientifiquement et dont la patience et la sagesse ont été incroyablement rassurantes pendant les moments complexes de la thèse. Je tiens particulièrement à lui montrer ma reconnaissance pour m’avoir si bien épaulé pendant le grand sprint final de la préparation (administrative et pratique) de la soutenance.

Un grand merci aussi à mes deux rapporteurs de thèse Carole Le Guyader, que j’ai déjà eu la chance de connaître sur les bancs de l’école et dont je garde un excellent souvenir, et Arthur Vidard. Je les remercie tous les deux pour leur disponibilité et pour avoir accepté de faire un travail de synthèse et de critique de grande qualité avec des délais extraordinairement courts. Je remercie aussi les autres membres du jury Stanley Durrleman, Pascal Frey, Jean-Frédéric Gerbeau, Karim Ramdani et Alain Trouvé pour le temps et l’intérêt qu’ils ont pu déployer donnant ainsi lieu à une soutenance de thèse dont je suis extrêmement fier.

Il me semble que lorsqu’on décide, après une période de réflexion longue ou courte, de commencer une thèse on arrive facilement à identifier *a priori* les personnes avec lesquelles on va intéragir. Cependant, on oublie généralement qu’on peut aussi faire de surprenantes rencontres. Je tiens donc à adresser mes remerciements à Annabelle Collin qui par son intelligence, sa sensibilité ou sa simple présence a su m’aider dans toutes les situations, aussi catastrophiques qu’elles pouvaient paraitre. Je ne suis pas certain de pouvoir mesurer encore aujourd’hui l’ensemble des choses que cette rencontre inattendue m’a apporté sur le plan humain. Un immense merci à Saverio Smaldone qui fut un complice hors pair pendant ces trois ans et ce dès notre arrivée simultanée au sein de l'Inria. Son humour et sa générosité avec lesquels il m'a accompagné m'ont permis de vivre de fabuleuses expériences dont je garderai, le plus longtemps possible, de merveilleux souvenirs. Je pense aussi à Karine Mauffrey qui a su me guider à travers ses conseils toujours animés par une infinie tendresse ainsi qu'à Matthieu Caruel pour sa bonne humeur inébranlable. Je tiens également à remercier Nicolae Cîndea et Radomir Chabiniok avec qui j'ai pu partager des moments de collaboration agréables et fructueux.

J'ai été chanceux parce qu'ils étaient là, invariablement. Ils étaient là, ces amis. Ces amis qui ne comprennent pas ce que vous faites. Ces amis qui ne comprennent pas pourquoi, après tous vos efforts, vous n'avez pas encore fini. Ces amis qui, au final, n'ont pas besoin de comprendre pour vous soutenir et vous faire confiance. Ils sont là, généreux, et vous donnent un peu d'air en vous parlant d'autre chose. Merci Vincent, Cerise, Chloé et Benjamin.

À Anita, Michel et Sébastien,
peu de mots, mais des mots justes,
des mots vivants,
pour remercier ceux qui m'ont toujours fait confiance.

Contents

Communications

Pre-prints articles

- Data assimilation of time under-sampled measurements using observers, application to wave-like equations. *Cîndea, N., Imperiale, A. and Moireau, P.*
- Cardiac estimation from tagged-MR images. *Chapelle, D., Imperiale, A. and Moireau, P.*
- State estimation of distributed mechanical systems using domain information from current based discrepancy measurement. *Imperiale, A., Routier, A. and Moireau, P.*

Conference Proceedings

- Constitutive parameter estimation methodology using tagged-MRI data. *A. Imperiale, R. Chabiniok, P. Moireau and D. Chapelle* – FIMH 2011
- Improving efficiency of data assimilation procedure for a biomechanical heart model by representing surfaces as currents. *Imperiale, A., Routier, A., Durrleman, S. and Moireau, P.* – FIMH 2013

Conferences

- Functional Imaging and Modelling of the Heart (FIMH) N.Y.C., U.S.A., 2011 – *oral presentation*.
- Congrès d'analyse numérique (CANUM) Superbesse, France, 2012 – *oral presentation*.
- Cardiac Imaging & Modelling, Mayneord Phillips Summer School, Oxford, U.K. 2012 – *poster presentation*.
- Mathematical and Numerical Modelling of Physiological Flows (MPF), Chia, Italy, 2013 – *oral presentation*.
- Functional Imaging and Modelling of the Heart (FIMH) London, U.K., 2013 – *poster presentation*.

Introduction

Cette thèse a été effectuée au sein de l'équipe Inria MΞDISIM – qui fait suite à l'équipe-projet MACS – sous la direction de Philippe Moireau et Dominique Chapelle.

Contexte général de la thèse

Les Maladies Cardio-Vasculaires (MCV) représentent la cause principale de mortalité en Europe mais aussi, à travers le monde, dans les pays en voie de développement. À titre d'illustration de l'amplitude de ces maladies il s'avère [Nichols et al., 2012] que les MCV sont à l'origine de 47% des décès en Europe. La Figure 1 regroupe l'ensemble des principales causes de décès chez les Femmes et les Hommes d'Europe âgés de moins de 65 ans et on peut clairement observer que ces maladies y prennent une place dominante. Même si la tendance est à la baisse dans la plupart des pays européens, certains facteurs favorisant ces maladies comme le tabagisme, les régimes alimentaires déséquilibrés ou le manque d'activité sportive deviennent de plus en plus important [Nichols et al., 2012].

Pour permettre l'identification et la prévention de ces maladies, les cardiologues ont à leur disposition tout un ensemble d'outils qui permettent d'obtenir des informations sur le fonctionnement du système cardiovasculaire d'un patient. Parmi ces observations on distinguera les données dites invasives, c'est-à-dire qui nécessitent au préalable l'installation *in-vivo* d'instruments de mesures, et les données non-invasives qui sont obtenues sans perturbation éventuelle de l'intégrité physique du patient. Bien que ces dernières soient généralement plus complexes à interpréter (car moins directes) elles sont celles qui intéressent le plus les cardiologues car elles affectent le mois possible l'état de santé du patient. Un exemple est l'électrocardiogramme qui permet de mesurer, à l'aide de capteurs disposés sur la peau du patient, l'évolution dans le temps des variations du potentiel électrique nécessaire à la rythmique cardiaque. Un autre exemple est l'imagerie cardiaque et on peut citer l'Imagerie par Résonance Magnétique (IRM) – parmi toute une gamme de modalité d'imagerie comme les CT-scan ou l'échographie. Ces images captent le champ magnétique émis lors de la relaxation du spin des protons constituant la matière, préalablement excitée. Un exemple typique est le cine-IRM qui permet d'évaluer à partir du niveau de gris de l'image la zone correspondant au *myocarde*, le muscle cardiaque. Ces images donnent d'importantes informations sur les déformations au cours du cycle cardiaque de la surface interne et externe du cœur (appelées endo- et épicarde). Cependant elles ne peuvent pas fournir d'information sur les déformations dites *intra-myocardiques*. Pour cela un autre type d'imagerie est envisageable, l'IRM de marquage tissulaire [Zerhouni et al., 1988, Axel and Dougherty, 1989]. Ces modalités d'imageries visent à permettre l'évaluation des déplacements du muscle cardiaque au sein du myocarde en implantant dans l'image (par modulation spécifique de la magnétisation du tissu) un motif régulier. Ce motif régulier, prenant généralement l'aspect

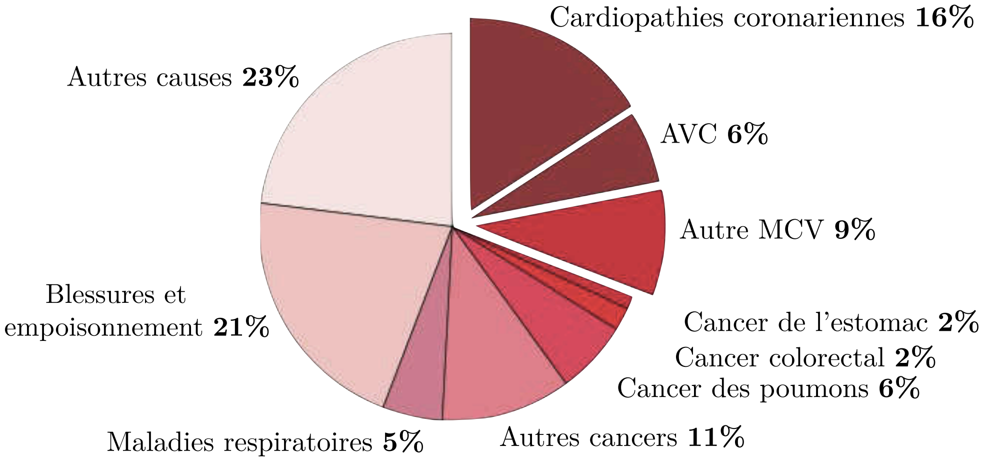

(a) Chez l'Homme de moins de 65 ans

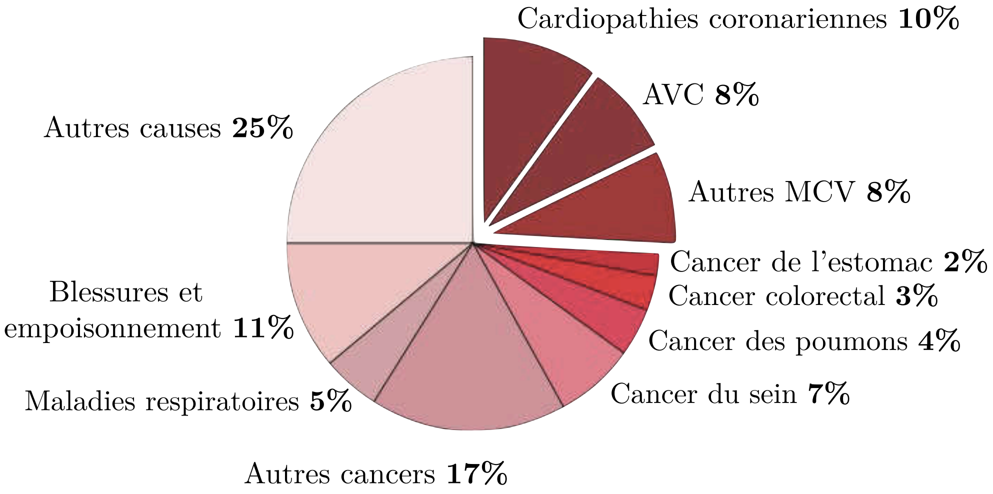

(b) Chez la Femme de moins de 65 ans

FIGURE 1 – Les différentes causes de décès en Europe. Données Extraites de *European Cardiovascular Disease Statistics, 2012 Edition*.

d'une grille, est assujetti aux déformations du muscle cardiaque pendant le temps d'acquisition. La Figure 2 nous permet d'illustrer ces différents types d'imagerie durant la systole, la contraction cardiaque, d'un cœur.

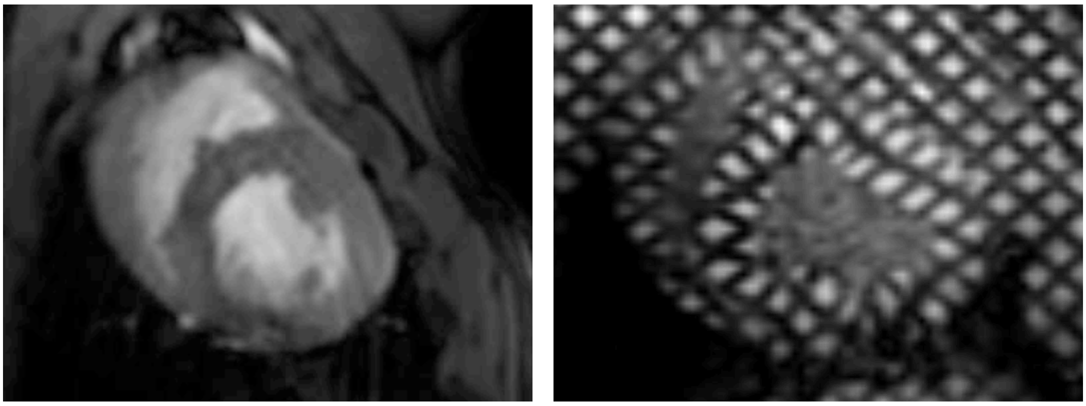

(a) cine-IRM (coupe petit axe) (b) IRM de marquage tissulaire (coupe petit axe)

FIGURE 2 – Exemple de données non-invasives d'imagerie.

Bien que l'ensemble des ces données suffisent, dans la plupart des cas, à l'expert pour permettre un disagnostic elles sont généralement incomplètes et bruitées. En effet, si on reprend l'exemple de la donnée image, il est commun d'imaginer qu'on possède seulement une vingtaine d'images sur tout un cycle cardiaque. En plus de ce sous-échantillonnage temporel, les images sont généralement bi-dimensionelles avec une faible résolution spatiale.

Au vu des enjeux et des difficultés que concentrent la prévention, le disagnostic et le traitement des maladies cardio-vasculaires on comprend la nécessité de proposer des solutions innovantes dans ce domaine. Les projets européens tels que le projet *euHeart*[1], qui a permis le financement de cette thèse, cherchent notamment à proposer au corps médical un ensemble de nouveaux outils numériques et de modélisation. Ces outils proposent des nouvelles solutions dans un large spectre d'application dont on peut citer l'aide à la planification pré-opératoire, le conseil et l'optimisation des programmes de traitement ainsi que l'assistance au disagnostic.

Historiquement, l'utilisation de méthodes mathématiques appliquées à la médecine est relativement ancienne et on peut par exemple citer les travaux du français P. C. A. Louis qui fut l'un des premiers à démontrer mathématiquement, dans les années 1830, l'inefficacité de traitement par saignée des maladies infectieuses telles que la pneumonie [Louis, 1835]. Pour appuyer cette conclusion l'auteur utilisait principalement des outils statistiques (simples) pour pouvoir comparer l'évolution de deux groupes de patients malades, un premier groupe auquel on fait subir des saignées et un autre non. Dans un des articles [Louis, 1834], traduit à l'époque en anglais et dont les propos sont aussi rapportés dans [Shimkin, 1964], P.C.A. Louis a appelé cette méthode "The Numerical Method" et a commenté

> *"The only reproach that can be made to the Numerical Method [...] is that it offers real difficulties in its execution [...] but [...] research of truth requires much labor, and is beset with difficulty."*

---

[1] `http://www.euheart.eu`

Ces mots de P.C.A. Louis, datant de près de 200 ans, apparaissent comme étant d'une étonnante actualité. Plus récemment, un exemple bien connu d'implication des sciences numériques en routine clinique est la chirurgie robotique. Elle a pour objectif de permettre, grâce à l'utilisation de robots adaptés à l'environnement médical, l'aide à l'intervention chirurgicale en augmentant la précision et l'efficacité des gestes du médecin tout en restant le moins invasif possible. Pour se donner un repère chronologique l'une des premières opérations assistées fut en 1985 par Kwoh *et. al.* lors d'une biopsie du cerveau. On pourra notamment se référer à [Lanfranco et al., 2004] pour quelques informations sur le paysage actuel de la robotique chirurgicale. Les deux exemples que nous avons cités cherchent à innover et à proposer de nouvelles solutions et ceci ce fait notamment par le mélange et l'interaction entre plusieurs disciplines et communautés scientifiques. Ces interactions permettent notamment de bâtir une relation de confiance avec le corps médical, une confiance qui s'acquiert avec le temps comme signalé dans [Lanfranco et al., 2004]

"Robotics [...] has been slow to enter the field of medicine".

Tout comme l'analyse statistique de données ou la robotique, l'analyse numérique de modèles biophysiques pourrait être un nouvel outil mis à disposition de la médecine. Cet outil est basé sur le regroupement de considérations physiques, concernant le phénomène observé, encapsulées dans un formalisme mathématique. De nos jours, il existe déjà un grand nombre de modèles décrivant des phénomènes intervenant dans les sciences du vivant. En ce qui concerne le corps humain il existe déjà tout un ensemble d'outils de modélisation concernant un large spectre de phénomènes, par exemples les modèles de croissance de tumeurs, l'analyse mécanique des os et des tendons ou encore l'étude de type interaction fluide-structure pour la pression intracrânienne. Dans ce même registre, on peut aussi donner l'exemple du flux sanguin dans les grandes artères dont la modélisation se fait par l'utilisation de techniques avancées d'interaction fluide-structure [Fernández et al., 2007] qui correspondent à un couplage de l'équation de Navier-Stokes pour un fluide incompressible, le sang, avec les équations de la mécanique régissant la dynamique de la structure, ici l'artère. Un autre exemple important est la modélisation dans le domaine de l'électrophysiologie [Sachse, 2004, Pullan et al., 2005]. Cette modélisation cherche à représenter les phénomènes chimiques et électriques se produisant se produisant au niveau du tissu cardiaque et conduisant à son excitation électrique qui est responsable de la contraction des cellules constituant le myocarde. En ce qui concerne la mécanique du muscle cardiaque on peut citer les travaux de [Hunter, 1975] ou [Peskin, 1982]. Plus récemment les travaux de [Sainte-Marie et al., 2006] ont conduit à un modèle complet du cœur où la loi de comportement du matériau est décomposée (de façon additive) en une partie passive, correspondant aux propriétés visco-élastiques sous-jacentes du myocarde, et une partie active, sensible à l'activation électrique. Ces trois derniers éléments de modélisation (flux sanguin, électrophysiologie et mécanique cardiaque) dépendent l'un de l'autre. Cependant, en pratique, le curseur de précision est ajusté en fonction des besoins. Dans la perspective de proposer un outil supplémentaire au médecin, les besoins du "modélisateur" sont évidemment imposés par le type de pathologie que l'on cherche à traiter. Dans cette thèse nous sommes particulièrement intéressés aux MCV conduisant à une altération des propriétés mécaniques du tissu, et on peut penser par exemple aux maladies de type *cardiopathie coronarienne* pouvant notamment conduire à la nécrose (mort tissulaire) d'une partie du muscle cardiaque.

Comme nous l'avons mentionné plus haut, les médecins ont déjà à leur disposition tout un ensemble de moyens d'observation sur l'état d'un patient. Nous avons notamment donné l'exemple des données d'IRM de marquage tissulaire qui est une donnée extrêmement riche permettant d'observer les déformations du cœur pendant sa contraction. Ces données souffrent des défauts inhérents à tout processus de mesure mais sont en contrepartie spécifiques au patient que l'on cherche à traiter. À l'extrême opposé, sur une ligne conceptuelle modulant spécificité et précision, nous trouvons le modèle. En effet, un modèle par nature nous donne des informations complètes (en temps et en espace) mais n'est *a priori* pas disposé à représenter une situation bien précise. Pour cela, il est nécessaire de faire appel aux méthodes d'*assimilation de données* pour permettre la *personnalisation* du modèle.

La discipline de l'assimilation de données est historiquement apparue dans le contexte de la météorologie ou de l'océanographie, et on pourra se référer notamment à [Corpetti et al., 2009, Blum et al., 2008] pour avoir un échantillon des différentes avancées récentes dans ce domaine. Dans la communauté de l'assimilation de données, il est commun de considérer que les données, aussi appelées *observations* et notées z dans l'ensemble de la présentation de ces travaux de thèse, sont obtenues à partir d'une trajectoire cible $x_\bullet$ par

$$z(t) = H(x_\bullet(t)) + \chi(t),$$

où H est appelé l'*opérateur d'observation* et χ est un potentiel bruit (additif) de mesure. Le modèle est quant à lui représenté par une dynamique généralement écrite sous la forme

$$\begin{cases} \dot{x}_\bullet(t) = A(x_\bullet(t), \theta_\bullet, t) \\ \\ x_\bullet(0) = x_\diamond + \zeta_\bullet^x, \quad \theta_\bullet = \theta_\diamond + \zeta_\bullet^\theta, \end{cases}$$

où $(x_\diamond, \theta_\diamond)$ sont des connaissances *a priori* sur la condition initiale et les paramètres de la trajectoire cible et $(\zeta_\bullet^x, \zeta_\bullet^\theta)$ sont des incertitudes potentielles. L'assimilation de données cherche donc à coupler les deux sources d'informations pour permettre de gommer ces incertitudes sur le système, et ainsi reconstruire une trajectoire dite *estimée* fidèle aux données. Les méthodes d'assimilation de données rentrent dans le cadre (plus général) des *problèmes inverses*, dans le sens où elles permettent de proposer un inverse généralisé de l'opérateur d'observation. Il existe diverses méthodes d'assimilation de données que l'on peut séparer en deux catégories. Une catégorie de méthodes dites *variationnelles* visent à minimiser un critère cherchant à équilibrer la confiance que l'on donne aux observations et aux a priori [Blum et al., 2008, Papadakis and Mémin, 2008, Navon, 2008, Titaud et al., 2010] c'est-à-dire

$$\min_{\zeta_x, \zeta_\theta} J(\zeta_x, \zeta_\theta) = \frac{1}{2}\|\zeta_x\|^2_{\mathcal{N}_x} + \frac{1}{2}\|\zeta_\theta\|^2_{\mathcal{N}_\theta} + \frac{1}{2}\int_0^T \|z(t) - H(x(t))\|^2_{\mathcal{N}_z} \mathrm{d}t,$$

où x est solution de

$$\begin{cases} \dot{x}(t) = A(x(t), \theta, t) \\ x(0) = x_\diamond + \zeta_x, \quad \theta = \theta_\diamond + \zeta_\theta. \end{cases}$$

La deuxième famille de méthodes d'assimilation de données est la classe des méthodes dites *séquentielles* qui cherchent à *filtrer* pendant la simulation les différences entre les observations et l'estimation courante de la trajectoire. Cette classe de méthode construit ce qu'on appelle des *observateurs* que l'on note $(\widehat{x}, \widehat{\theta})$ et dont la dynamique s'écrit sous la forme générale [Bensoussan, 1971, Simon, 2006]

$$\begin{cases} \dot{\widehat{x}} = A(\widehat{x}, \widehat{\theta}, t) + G_x\big(z - H(\widehat{x})\big) \\ \dot{\widehat{\theta}} = G_\theta\big(z - H(\widehat{x})\big) \\ \widehat{x}(0) = x_\diamond, \quad \widehat{\theta}(0) = \theta_\diamond, \end{cases}$$

où G_x et G_θ sont les opérateurs de gain construits dans le but d'obtenir le comportement asymptotique suivant

$$(\widehat{x}, \widehat{\theta}) \underset{t\to\infty}{\to} (x_\bullet, \theta_\bullet).$$

Au-delà des différentes possibilités de modélisation (en terme de formalisme et de précision) il est clair que, pour avoir un impact dans le domaine d'application visé,

le travail de modélisation ne peut être complètement mis à profit que s'il s'inscrit dans une stratégie d'assimilation de données.

En effet, par nature l'assimilation de données cherche à combiner les deux protagonistes, modèle & données, pour créer une entité profitant des avantages des deux parties, c'est-à-dire spécificité et précision. Cependant, comme a pu le signaler avant nous P.C.A. Louis, la mise en oeuvre de ces méthodes (numériques) reste une tâche complexe. La raison principale étant qu'elles appartiennent à une discipline, par définition, extrêmement transverse mélangeant modélisation, analyse mathématique et numérique et interprétation des données. Ces méthodes d'assimilation de données prennent une place de plus en plus importante dans le domaine de la modélisation pour les Sciences du Vivant. Dans le cas de la mécanique cardiaque on peut notamment citer les travaux de [Moireau et al., 2009, Moireau et al., 2008] qui proposent une méthodologie séquentielle d'assimilation de données pour permettre l'estimation conjointe d'état et de paramètres. D'incroyables progrès se font dans ces différentes disciplines (de façon plus ou moins indépendante) et l'assimilation de données cherche alors à combiner des sources d'informations de plus en plus complexes et précises. Cependant,

indépendamment du type de méthode d'assimilation de données, il est nécessaire de savoir mesurer les dissimilarités entre le modèle et les observations.

Autrement dit, la difficulté inhérente à ces méthodes de couplage est qu'elles nécessitent de savoir mesurer les différences du type $z - H(x)$. La complexité de cette opération est bien sûr liée au fait qu'en pratique le modèle et les observations sont de nature extrêmement différente. Dans le cas simplifié d'observations dites directes, c'est-à-dire dans le cas où l'opérateur d'observation est linéaire, on cherche à s'appuyer sur la structure algébrique de l'espace d'observation qui généralement permet le calcul de ces dissimilarités. Dans le cas plus réaliste d'observations indirectes cette différence n'a pas de sens direct. Si on reprend l'exemple de la modélisation cardiaque, le modèle considère comme inconnue le déplacement depuis une configuration de référence alors que les observations réalistes, par exemple les données d'IRM, se déclinent sous la forme d'une fonction de niveau de gris affichant les variations dans le temps de la surface externe de l'objet. Un cas moins complexe mais toujours très illustratif est celui où les observations se déclinent comme un ensemble de surfaces typiquement obtenues après la segmentation de la séquence IRM. Dans cet exemple, il faut être capable de donner du sens à l'opération "une surface moins une autre". C'est dans ce contexte que vient s'inscrire les travaux de cette thèse. Plus précisément,

nous proposons dans cette thèse un ensemble d'outils méthodologiques pour mesurer des différences entre un modèle mécanique et des données complexes (objets géométriques ou même images) pour permettre l'utilisation de méthodes d'assimilation de données dans des cas réalistes.

Pour illustrer ces moyens de comparaison nous utiliserons un modèle biomécanique du cœur décrit dans [Bestel et al., 2001, Sainte-Marie et al., 2006, Moireau et al., 2009, Chapelle et al., 2012b] et déjà utilisé dans un contexte d'assimilation de données dans [Moireau et al., 2009, Chabiniok et al., 2012]. Cette modélisation s'inscrit dans une description Lagrangienne du déplacement $\underline{y}$ du matériau depuis une configuration de référence Ω_0. Cette inconnue (le déplacement) vérifie le principe fondamental de la dynamique. Dans ce cadre, les conditions aux limites représentent les interactions entre le cœur et son entourage, alors que les efforts extérieurs correspondent typiquement à la pression sanguine intra-ventriculaire et sont les points d'entrée d'un possible couplage avec un modèle fluide. À ces efforts extérieurs viennent s'équilibrer les contraintes internes, représentées par le tenseur de Cauchy $\underline{\underline{\sigma}}$. Ces contraintes se décomposent en une partie dite passive, prenant en compte le comportement visco-élastique sous-jacent du matériau cardiaque, et une partie active, sensible à l'excitation électrique du cœur. Ce modèle se base sur une composition additive de ces deux composantes

$$\underline{\underline{\sigma}} = \underline{\underline{\sigma}}_{\mathrm{passif}} + \underline{\underline{\sigma}}_{\mathrm{actif}}.$$

Le premier terme de cette loi additive est communément obtenu à partir de la dérivation d'un potentiel hyperélastique W^{e}. La modélisation des contraintes actives est quant à elle basée sur le modèle de création et destruction des ponts d'actine-myosine de Huxley [Huxley, 1957] et permet (entre autre) de prendre en compte le fameux effet Frank-Starling [Chapelle et al., 2012b]. Cet effet est fondamental pour la capacité d'adaptation à l'effort du cœur. Nous noterons par ailleurs que cette contrainte active est le point d'entrée d'un potentiel couplage avec un modèle électro-physiologique.

Par ailleurs, la stratégie d'assimilation de données que nous avons choisi de suivre tout au long de ces travaux s'appuie sur une méthode séquentielle, décrite en détails dans [Moireau et al., 2008], permettant l'estimation conjointe état-paramètres. Cette méthode de filtrage cherche à construire la dynamique de l'estimateur $(\widehat{x}, \widehat{\theta})$ (aussi appelé observateur) de telle sorte que celui-ci converge vers la trajectoire exacte du système. Cette dynamique est bâtie en filtrant les différences entre les observations réelles et celles reconstruites par application de l'opérateur d'observation sur l'estimateur,

$$\begin{cases} \dot{\widehat{x}}(t) = A(\widehat{x}, \widehat{\theta}, t) + G_x(t)\big(z(t) - H(\widehat{x}(t))\big), \\ \dot{\widehat{\theta}}(t) = G_\theta(t)\big(z(t) - H(\widehat{x}(t))\big). \end{cases}$$

Plusieurs définitions des opérateurs de gains G_x et G_θ sont possibles. On citera notamment le gain de Kalman [Kalman and Bucy, 1961, Bensoussan, 1971] qui, au moins en linéaire, est directement lié à une approche dite variationelle visant à minimiser un critère d'optimalité construit sur les conditions initiales (état et paramètres) de l'estimateur. Ce type de filtre conduit cependant à une expression du gain qui, après discrétisation, apparaît comme une matrice pleine de dimension égale à celle de la variable augmentée $\begin{pmatrix}\widehat{x} & \widehat{\theta}\end{pmatrix}^{\intercal}$. Cette particularité du filtre de Kalman, appelée "curse of dimensionality" dans la littérature, le rend inabordable dans la perspective de manipuler des vecteurs de degrés de libertés issus d'une discrétisation éléments finis. Pour cette raison nous détaillons une autre alternative, le filtre de Luenberger [Luenberger, 1971, Auroux and Blum, 2007, Ramdani et al., 2012], qui n'est cette fois pas construit grâce à un critère optimal mais qui vise uniquement à stabiliser le système de l'erreur d'estimation. À partir de là, l'assemblage de ces deux méthodes, initialement proposé par [Moireau et al., 2009], permet de construire une stratégie complète d'estimation état-paramètre. Le filtre de Luenberger pour l'état et un filtre de Kalman réduit à l'espace des paramètres sont les deux composantes de cette stratégie.

Dans ce cadre les objectifs et problématiques de cette thèse peuvent se décrire de la façon suivante. Nous cherchons à appliquer ce couple modèle & données dans un contexte qui se rapproche des cas réalistes d'applications. Notamment, nous considérerons principalement des données de type image. Comme nous l'avons détaillé précédemment ceci implique de savoir mesurer les dissimilarités entre le modèle mécanique et les observations extraites du système cible, cette tâche étant d'autant plus complexe que ces deux entités sont de nature sensiblement différente. Pour faciliter cette procédure nous pourrons tout d'abord supposer une étape préalable de traitement de l'image permettant d'obtenir des observations plus simple à manipuler. Par exemple, dans le cas de la données d'IRM de marquage tissulaire nous pourrons imaginer successivement qu'on a réussit à obtenir des surfaces de tags, se déformant avec le motif de l'image, ou encore des grilles de tags ou finalement des champs de déplacement apparent dans l'image. Cependant, en réduisant au minimum nos exigences sur cette étape de traitement des observations, le but est de tendre vers une méthode d'assimilation directement bâtie sur l'image brute.

Dans le but de mieux appréhender les travaux novateurs effectués pendant cette thèse nous proposons d'achever cette introduction par un récapitulatif des cinq chapitres accompagnés de leurs principales contributions correspondantes.

Chapitre 1 - Le cœur numérique

Contributions principales (mots-clés)
Péricarde et surface de contact, loi passive exponentielle, implémentation d'un schéma en temps conservatif, modélisation en boucle fermée du système cardiovasculaire.

Les contributions principales de ce chapitre de thèse peuvent se résumer de la façon suivante. Nous avons participé à l'amélioration du modèle bio-mécanique du cœur décrit dans [Sainte-Marie et al., 2006] et ce de la façon suivante. Nous avons implémenté le schéma en temps conservatif proposé dans [Chapelle et al., 2012b] assurant ainsi une meilleure stabilité lors des simulations directes du modèle. De plus nous avons mis en place une loi passive de type exponentielle plus adaptée à la représentation des nonlinéarités du matériau [Nash and Hunter, 2000, Costa et al., 2001, Dokos et al., 2002] s'exprimant de la façon suivante

$$W^{\mathrm{e}} = C_0 \exp\left(C_1(J_1 - 3)^2\right) + C_2 \exp\left(C_3(J_4 - 1)^2\right),$$

où J_1 est le premier invariant réduit et J_4 l'invariant réduit dans la direction de la fibre cardiaque, représente fidèlement les nonlinéarités (passives) du matériau. En ce qui concerne les conditions limites, nous proposons de représenter l'interaction du cœur avec le sac péricardique en utilisant une surface de contact entourant la géométrie de calcul. Ce type de condition limite est pris en compte grâce à un opérateur distance entre l'épicarde du modèle et la surface de contact, introduisant donc une autre nonlinéarité dans le modèle.

Dans la perspective d'appliquer une méthode d'assimilation de donnée basée sur ce modèle, le coût d'une modélisation complète du problème d'interaction fluide-structure semble prohibitif. Pour cette raison nous considérons une pression homogène à l'intérieur de la cavité qui est, par ailleurs, liée à un modèle réduit du système cardiovasculaire – un modèle de *Windkessel* – par l'intermédiaire d'une fonction de valve. On présente plusieurs types de Windkessel, un modèle dit *one-way* et un modèle en boucle fermée.

Après avoir présenté le schéma en temps permettant la conservation au niveau discret de l'énergie du système [Chapelle et al., 2012b] nous donnons des résultats numériques modélisant un cœur sain et un cœur admettant un infarctus du myocarde localisé dans le septum.

Chapitre 2 - Filtrage des données à faible résolution temporelle

Contributions principales (mots-clés)

Analyse théorique et numérique d'un observateur d'état On/Off, comparaison de la stratégie On/Off avec la stratégie d'interpolation des données.

Dans ce chapitre nous rappelons, et illustrons par plusieurs exemples, la méthode d'assimilation de données présentée dans [Moireau et al., 2008]. Par ailleurs nous présenterons nos travaux autour de l'influence de la distribution temporelle des données sur l'estimateur d'état de type Luenberger. En effet, une des particularités des données extraites d'imagerie médicale type IRM est qu'elles ne sont disponibles qu'à une faible fréquence d'échantillonnage. Par exemple, on peut espérer obtenir environ une vingtaine de cine-IRM dans un battement cardiaque. Ceci empêche d'appliquer directement les algorithmes d'assimilation de données qui supposent généralement que les données sont disponibles à chaque pas de temps. Une solution naturelle dans ce genre de situation est d'utiliser un schéma d'interpolation en temps, une stratégie adoptée par [Moireau et al., 2009]. Cependant ce type de schéma introduit directement, dans la dynamique de l'estimateur, l'erreur d'interpolation qui agit de la même façon qu'un bruit de mesure. Pour cette raison nous avons étudié la discrétisation en temps d'un observateur de Luenberger de type prédiction-correction qui s'exprime sous la forme suivante

$$\begin{cases} \widehat{x}_-^{n+1} = A_{n+1|n}(\widehat{x}_+^n) \\ \widehat{x}_+^{n+1} = \widehat{x}_-^{n+1} + \delta^{n+1} G_x \left(z^{n+1} - H\widehat{x}_+^{n+1} \right), \end{cases}$$

où δ^n vaut 1 si la donnée est disponible ou 0 sinon. L'analyse complète de cet observateur d'un point de vue théorique et numérique ainsi que la comparaison avec l'estimateur utilisant un schéma d'interpolation en temps sont regroupées en fin de chapitre sous la forme d'un article pre-print.

Communications correspondantes :

- Article pre-print, *Data assimilation of time under-sampled measurements using observers, application to wave-like equations – Cîndea, N., Imperiale, A. and Moireau, P.* .
- Conférence (communication orale), Congrès d'analyse numérique (CANUM) Super-Besse, France, 2012.

Chapitre 3 - Assimilation des images de marquage tissulaire

Contributions principales (mots-clés)
Filtrage des plans de tags, grilles de tag et déplacements apparents. Analyse théorique et numérique du filtre d'état. Schéma en temps pour l'estimateur d'état de type prédiction-correction. Gestion d'opérateurs d'observation de grande dimension.

Dans ce chapitre nous proposons de construire des observateurs à partir d'un ensemble relativement complet de potentielles données obtenues après une phase de traitement de l'IRM de marquage tissulaire. Ce qui a motivé ce travail est la richesse apparente de images marquées qui permettent d'évaluer (au moins de façon qualitative) les déformations intra-myocardiques. Ainsi dans nos travaux nous supposons qu'un traitement de ce type d'images a permis l'obtention des déplacements des points de la grille de tag – on parle d'un "feed-back" direct des déplacements – mais aussi des données moins riches comme les plans de tag ou les grilles de tag suivant les déformations du motif. Nous proposons par ailleurs un moyen de filtrer les déplacements apparents calculés directement à partir de l'image bi-dimensionelle.

Un des aspects les plus intéressants de ces travaux est que nous arrivons à montrer, numériquement et théoriquement (après linéarisation des opérateurs), que lorsque le motif de tag se raffine l'opérateur de stabilisation dans le filtre de Luenberger se comporte de la même façon qu'un opérateur donnant le déplacement du solide dans un sous-domaine comprenant l'ensemble des images taggées. Ceci conforte notre intuition sur le fait que ce type de modalité d'imagerie détient une richesse d'information incomparable à celle des techniques d'imageries plus classique comme les cine-IRM.

Une autre contribution apportée par ces travaux est de permettre, grâce à un schéma de type prédiction-correction pour l'observateur de Luenberger, la manipulation d'opérateurs d'observation à grande largeur de bande. En effet, en voulant traiter ces types de données (particulièrement pour le cas des déplacements apparents) nous nous sommes confrontés au problème de manipulation d'un espace d'observation de grande dimension, proportionnelle à la résolution des plans de l'image. Un schéma prédiction-correction permet d'utiliser des méthodes de résolution des systèmes linéaires différentes pour ces deux étapes. Les problèmes en mécanique du solide peuvent alors être résolus par un solveur direct (ce qui est fait traditionnellement à cause du mauvais conditionnement des matrices éléments finis sous-jacentes) alors qu'on peut utiliser un algorithme itératif pour la résolution de l'étape correction, permettant ainsi de ne pas stocker les matrices intervenant dans le système linéaire correspondant. Il a l'autre avantage de permettre d'utiliser deux codes de calcul différents et indépendants pour la mise en place de cette stratégie d'assimilation de donnée : un gérant le modèle et un autre les données, comme imaginé dans la bibliothèque d'assimilation *Verdandi* [Chapelle et al., 2012a].

Communications correspondantes :

- Article pre-print, *Cardiac estimation from tagged-MR images – Chapelle, D., Imperiale, A. and Moireau, P.* .
- Acte de conférence, *Constitutive parameter estimation methodology using tagged-MRI data – A. Imperiale, R. Chabiniok, P. Moireau and D. Chapelle* – FIMH 2011.
- Conférence (communication orale), Functional Imaging and Modelling of the Heart (FIMH) N.Y.C., U.S.A., 2011.
- Conférence (poster), Cardiac Imaging & Modelling, Mayneord Phillips Summer School, Oxford, U.K. 2012.
- Conférence (communication orale), Mathematical and Numerical Modelling of Physiological Flows (MPF), Chia, Italy, 2013.

Chapitre 4 - Les *courants* et l'assimilation de données

Contributions principales (mots-clés)

Lien entre les mesures de similarités proposées en traitement d'image et le filtrage d'état. Adaptation du formalisme des courants à l'assimilation de données. Proposition d'une méthode d'assimilation de la donnée image brute.

Ce chapitre est dédié à la formulation plus générale de la méthode de filtrage qu'on utilise dans les chapitres précédents. Plus générale dans le sens où on inscrit la méthode de filtrage dans une méthodologie qui permet de prendre en compte tout type de mesure de similarité construit *a priori* dans un cadre statique, ce qui est typiquement le cas dans la communauté du traitement d'image. Ainsi nous autorisons la méthode d'assimilation de données à se nourrir de l'ensemble des efforts considérables [Le Guyader and Vese, 2009, Arrate et al., 2010, Derfoul et al., 2013, Le Guyader et al., 2013] faits au sein de cette communauté pour proposer des mesures de similarité de plus en plus sophistiquées.

Comme exemple d'application, nous proposons d'adapter le formalisme des courants [Glaunès et al., 2008, Chou and Younes, 2008, Arrate et al., 2010, Younes, 2010, Durrleman et al., 2011]. Ce formalisme considère les surfaces comme des formes linéaires sur un espace de fonctions régulières. Plus précisément, en considérant S une surface admettant $\underline{n}$ comme vecteur normal, on définit un courant (aussi noté S) à partir de cette surface par son application sur les éléments $\underline{w} \in \mathcal{W}$ tel que

$$\langle S, \underline{w} \rangle_{\mathcal{W}'\mathcal{W}} = \int_S \underline{n} \cdot \underline{w} \, \mathrm{d}S.$$

Par ailleurs, on peut montrer [Glaunès et al., 2008, Arrate et al., 2010, Younes, 2010, Durrleman et al., 2011] qu'en choisissant comme espace de fonctions tests un espace de Hilbert à noyau reproduisant (RKHS) on peut définir le représentant de Riesz $\underline{s}$ d'une surface S tel que $\langle S, \underline{w} \rangle_{\mathcal{W}'\mathcal{W}} = (\underline{s}, \underline{w})_{\mathcal{W}}$ et

$$\underline{s}(\underline{x}) = \int_S K(\underline{x}, \underline{\widetilde{x}}) \underline{n}(\underline{\widetilde{x}}) \, \mathrm{d}S.$$

De cette façon on a construit $\mathcal{W}'$ un espace de Hilbert dans lequel les surfaces sont définies et telle que la différence entre deux surfaces $S_1 - S_2$ a du sens et peut être évaluée en utilisant la norme sur $\mathcal{W}'$. Pour adapter ce formalisme il faut ensuite comprendre comment un courant dépend du déplacement mécanique pour pouvoir établir la sensibilité de ce courant par rapport à une variation de déplacement, un outil nécessaire à la construction de l'opérateur de gain dans notre méthode de filtrage. De plus, nous proposons une méthode permettant de construire à partir du niveau de gris d'une image de type cine-MRI une estimation du représentant d'une surface, permettant ainsi de réduire le nombre d'étapes nécessaires de traitement de données avant d'appliquer une stratégie d'assimilation de données.

Communications correspondantes :

- Article pre-print, *State estimation of distributed mechanical systems using domain information from current based discrepancy measurement – Imperiale, A., Routier R. and Moireau, P.*.
- Acte de conférence, *Improving efficiency of data assimilation procedure for a biomechanical heart model by representing surfaces as currents – Imperiale, A., Routier, A., Durrleman, S. and Moireau, P.* – FIMH 2013.
- Conférence (poster), Functional Imaging and Modelling of the Heart (FIMH) London, U.K., 2013.

Chapitre 5 - Perspectives d'applications sur données réelles

Contributions principales (mots-clés)
Mise en place d'une méthodologie permettant l'application de la méthode de filtrage sur un cas réel. Méthode automatique d'adaptation de géométries de calculs et de construction des surfaces de contact. Construction des grilles de tags à partir des déplacements apparents.

Dans ce dernier chapitre nous proposons de remettre l'ensemble des travaux et des contributions présentés dans cette thèse dans un cadre d'application sur un cas réel. L'objectif principal est de comprendre tout d'abord que, d'un point de vue méthodologique, nous pouvons appliquer ces méthodes sur un cas réaliste. Deuxièmement, nous mettons en valeur le fait que, même si les aspects méthodologiques sont présents, certaines difficultés subsistent qui placent l'utilisation de données réelles un cran au dessus en terme de difficulté de mise en oeuvre. Nous proposons, pour l'ensemble de ces problèmes supplémentaires, diverses solutions envisageables.

Plus précisément nous discutons l'obtention des données brutes de types champs de déplacements ou grilles de tags à partir de l'IRM de marquage tissulaire ainsi que les surfaces internes et externes du ventricules gauche, obtenues à partir de l'IRM-cine. Ensuite, d'un point de vue modèle, nous proposons un ensemble d'outils permettant la construction de l'ensemble des géométries nécessaires (maillage de calcul et surface de contact) ainsi que l'estimation d'une condition initiale pour le système dynamique. En ce qui concerne les difficultés pouvant apparaître en voulant appliquer la méthode d'assimilation de données nous proposons une façon de gérer la surface de contact, qui apparaît comme une contrainte ainsi qu'une façon d'estimer le déplacement du matériau au temps de marquage du motif de tag (nécessaire au filtrage des images de marquage tissulaire, comme précisé dans le Chapitre 3).

Bibliographie de l'introduction

[Arrate et al., 2010] Arrate, F., Tilak Ratnanather, J., and Younes, L. (2010). Diffeomorphic active contours. *SIAM Journal of Imaging Sciences*, 3(2) :176–198.

[Auroux and Blum, 2007] Auroux, D. and Blum, J. (2007). A nudging-based data assimilation method : the back and forth nudging (bfn) algorithm. *Nonlin. Processes Geophys.*

[Axel and Dougherty, 1989] Axel, L. and Dougherty, L. (1989). Mr imaging of motion with spatial modulation of magnetization. *Radiology*, pages 841–845.

[Bensoussan, 1971] Bensoussan, A. (1971). *Filtrage optimal des systèmes linéaires*. Dunod.

[Bestel et al., 2001] Bestel, J., Clément, F., and Sorine, M. (2001). A biomechanical model of muscle contraction. In Niessen, W. and Viergever, M., editors, *Medical Image Computing and Computer-Assisted Intervention – MICCAI 2001*, volume 2208 of *Lecture Notes in Computer Science*, pages 1159–1161. Springer Berlin Heidelberg.

[Blum et al., 2008] Blum, J., LeDimet, F. X., and Navon, I. N. (2008). Data assimilation for geophysical fluids. *Computational Methods for the Atmosphere and the Oceans*, 14 :377–434.

[Chabiniok et al., 2012] Chabiniok, R., Moireau, P., Lesault, P.-F., Rahmouni, A., Deux, J.-F., and Chapelle, D. (2012). Estimation of tissue contractility from cardiac cine-mri using a biomechanical heart model. *Biomech. Model. Mechanobiol.*, 11(609-630).

[Chapelle et al., 2012a] Chapelle, D., Fragu, M., Mallet, V., and Moireau, P. (2012a). Fundamental principles of data assimilation underlying the verdandi library : applications to biophysical model personalization within euheart. *Medical & Biological Eng & Computing*, pages 1–13.

[Chapelle et al., 2012b] Chapelle, D., Le Tallec, P., Moireau, P., and Sorine, M. (2012b). Energy-preserving muscle tissue model : formulation and compatible discretizations. *Journal For Multiscale Computational Engineering*, 10(2) :189–211.

[Chou and Younes, 2008] Chou, H.-F. and Younes, L. (2008). Smoothing directional vector fields using dual norms. *SIAM Journal of Imaging Sciences*, 2(1) :41–63.

[Corpetti et al., 2009] Corpetti, T., Héas, P., Mémin, E., and Papadakis, N. (2009). Pressure image assimilation for atmospheric motion estimation. *Tellus A.*, 61(1) :160–178.

[Costa et al., 2001] Costa, K. D., Holmes, J. W., and McCulloch, A. D. (2001). Modelling cardiac mechanical properties in three dimensions. *Phil. Trans. R. Soc.*, 359 :1233–1250.

[Derfoul et al., 2013] Derfoul, R., Veiga, S. D., Gout, C., Guyader, C. L., and Tillier, E. (2013). Image processing tools for better incorporation of 4d seismic data into reservoir models. *Journal of Computational and Applied Mathematics*, 240(0) :111 – 122. <ce :title>MATA 2012</ce :title>.

[Dokos et al., 2002] Dokos, S., Smaill, B. H., Young, A. A., and LeGrice, I. J. (2002). Shear properties of passive ventricular myocardium. *Am. J. Physio. Circ. Physiol.*, 283 :2650–2659.

[Durrleman et al., 2011] Durrleman, S., Fillard, P., Pennec, X., Trouvé, A., and Ayache, A. (2011). Registration, atlas estimation and variability analysis of white matter fiber boundles modeled as currents. *NeuroImage*, 55(3) :1073.

[Fernández et al., 2007] Fernández, M. A., Gerbeau, J.-F., and Grandmont, C. (2007). A projection semi-implicit scheme for the coupling of an elastic structure with an incompressible fluid. *Int. J. Numer. Meth. Engng*, 69 :794–821.

[Glaunès et al., 2008] Glaunès, J., Qui, J., M., I., M., and Younes, L. (2008). Large deformation diffeomorhpic metric curve mapping. *International Journal of Computer Vision*, 80(3) :317–336.

[Hunter, 1975] Hunter, P. J. (1975). *Finite element analysis of cardiac muscle mechanics*. PhD thesis, University of Oxford.

[Huxley, 1957] Huxley, A. F. (1957). Muscle structure and theories of contraction. *Prog. Biophys. Mol. Bio.*, 7 :258–318.

[Kalman and Bucy, 1961] Kalman, R. E. and Bucy, R. S. (1961). New results in linear filtering and prediction theory. *Journal of Basic Engineering*, 83(3) :95–108.

[Lanfranco et al., 2004] Lanfranco, A. R., Castellanos, A. E., Desai, J. P., and Meyers, W. C. (2004). Robotic surgery, a current perspective. *Ann. Surg.*, pages 14–21.

[Le Guyader et al., 2013] Le Guyader, C., Gout, C., Macé, A.-S., and Apprato, D. (2013). Gradient field approximation : Application to registration in image processing. *J. Comput. Appl. Math.*, 240 :135–147.

[Le Guyader and Vese, 2009] Le Guyader, C. and Vese, L. A. (2009). A combined segmentation and registration framework with a nonlinear elasticity smoother. In *Scale Space and Variational Methods in Computer Vision*, pages 600–611. Springer.

[Louis, 1834] Louis, P. C. A. (1834). Essay on clinical instruction.

[Louis, 1835] Louis, P. C. A. (1835). Recherchers sur les effets de la saignée.

[Luenberger, 1971] Luenberger, D. G. (1971). An introduction to observers. *IEEE T. Automat. Contr.*

[Moireau et al., 2008] Moireau, P., Chapelle, D., and Le Tallec, P. (2008). Joint state and parameter estimation for distributed mechanical systems. *Computer Methods in Applied Mechanics and Engineering*, 197 :659–677.

[Moireau et al., 2009] Moireau, P., Chapelle, D., and LeTallec, P. (2009). Filtering for distributed mechanical systems using position measurements : Perspectives in medical imaging. *Inverse Problems*, 25.

[Nash and Hunter, 2000] Nash, M. P. and Hunter, P. J. (2000). Computational mechanics of the heart. *J. Elasticity*, 61 :113–141.

[Navon, 2008] Navon, I. N. (2008). *Data assimilation for numerical weather prediction : a review*. Springer.

[Nichols et al., 2012] Nichols, M., Townsend, N., Luengo-Fernandez, R., Leal, J., Gray, A., Scarborough, P., and Rayner, M. (2012). European cardiovascular disease statistics. *European Heart Neatwork, Brussels, European Sociaty of Cardiology, Sophia Antipolis*.

[Papadakis and Mémin, 2008] Papadakis, N. and Mémin, E. (2008). Variational assimilation of fluid motion from image sequence. *SIAM J. Imaging Sciences*, 1(4) :343–363.

[Peskin, 1982] Peskin, C. S. (1982). The fluid dynamics of heart valves : experimental, theoritical, and computational methods. *Annual Review of Fluid Mechanics*, 14 :235–259.

[Pullan et al., 2005] Pullan, A., Buist, M., and Cheng, L. (2005). Mathematically modeling the electrical activity of the heart. *World Scientific*.

[Ramdani et al., 2012] Ramdani, K., Tucsnak, M., and Weiss, G. (2012). Recovering the initial state of an infinite-dimensional system using observers. *Automatica*, pages 1616–1625.

[Sachse, 2004] Sachse, F. (2004). *Computational cardiology : modeling of anatomy, electrophysiology and mechanics*. Springer-Verlag.

[Sainte-Marie et al., 2006] Sainte-Marie, J., Chapelle, D., Cimrman, R., and Sorine, M. (2006). Modeling and estimation of the cardiac electromechanical activity. *Comput. Struct.*, 84 :1743–1759.

[Shimkin, 1964] Shimkin, M. S. (1964). The numerical method in therapeutic medicine. *43d Jams M. Anders Lecture*, 79(1).

[Simon, 2006] Simon, D. (2006). *Optimal state estimation : Kalman, H_∞ and nonlinear approaches*. Wiley-Interscience.

[Titaud et al., 2010] Titaud, O., Vidard, A., Souopgui, I., and LeDimet, F. X. (2010). Assimilation of image sequences in numerical models. *Tellus A*, 62(1) :30–47.

[Younes, 2010] Younes, L. (2010). *Shapes and diffeomorphisms*. Springer.

[Zerhouni et al., 1988] Zerhouni, E. A., Parish, D., Rogers, W., Yang, A., and Shapiro, E. (1988). Human heart : tagging with mr imaging - a method for noninvasive assessment of myocardial motion. *Radiology*, pages 59–63.

CHAPTER 1

From physiology to mechanical modeling for a numerical heart

Even though this thesis is focused on performing *inverse problems*, a wide topic that will be treated later on, it is of major importance to have a precise understanding of the *direct problem*. In this chapter we focus our attention on presenting a complete biomechanical model of the heart behavior. This model inspired from physiological observations and physical modeling gives a description of the complex heart material, from its underlying visco-elasticity to its contractile function. It also takes into account the interactions between the heart and the cardiovascular system. In order to provide numerical solutions, we carry out the non-trivial task of discretizing the obtained dynamical system. This procedure enables us to extract distributed quantitive mechanical indicators during the simulation time window – *e.g.* stress within the cardiac fiber or pressure inside the heart cavities – that are of major interest in the perspective of diagnosis assistance. This first chapter is divided as follows: to start with we consider the physiological and modeling aspects of the passive behavior of the heart tissue followed by its active counter-part. Next, we present how the heart biomechanical model is linked with the rest of the cardiovascular system through a reduced modeling approach. During this third part we also deal with the interactions between the heart and its surroundings by detailing the boundary conditions appearing in the model. We finish by providing some numerical results aiming at describing a healthy and an infarcted heart.

As it is not the goal of this Chapter to provide extensive physiological details but rather to understand the conception of the biomechanical model that we will use, we have opted to give an original presentation. The different *physiological key points* will be spread out in Section 1.1, 1.2 and 1.3 (text in frame) wherever they may enlighten or justify the modeling aspect under discussion. Here follows a small example:

Physiological key point

An active & passive material

The heart evolves during the cardiac cycle between two main operating modes: an *active* mode – where the electrical activation triggers the heart contraction – and a *passive* mode – where the heart is subject to what we call the passive filling due to the inflow of blood.

For this reason we separate the presentation of the heart model into two main parts corresponding to the passive and active behavior. Most of these key points are well-known aspects concerning the heart and the cardiovascular system and can be found in any reference literature on the matter, see [Tortora and Derrickson, 2009] for example.

1.1 The passive behavior of the heart material

1.1.1 Mechanical model of the heart passive material

Physiological key point

The heart function

The heart is a muscle responsible for the blood circulation in the organism. It is a pump whose impulse comes from electrical signals and it is made of four chambers – see Figure 1.1 for an illustration of the anatomy of the heart. These four chambers are decomposed into two types: the two superior receiving chambers are the *atria* and the two inferior pumping chambers are the *ventricles*. The right ventricle is responsible for the blood circulation towards the lungs where the blood can be re-oxygenated whereas the left ventricle ejects the blood to the rest of the body through the *aorta*. Filling and ejection of blood in each ventricle is made possible by a system of valves. The two *atrioventricular* valves, connecting the atria with their respective ventricles, allow the blood flows coming from the circulation system to fill the ventricles and prevent back flow from ventricles to atria during the heart contraction. Additionally, the *aortic valve* and the *pulmonary valve* controls the blood ejection from the left and the right ventricle respectively.

As any muscle the heart needs oxygen and nutrients. To obtain these necessary elements from the blood, the heart has its own network of blood vessels constituting the *coronary circulation*. The *coronary arteries* branch from the aorta and pervade the heart. The blood is traveling from the arteries, into capillaries (where exchange between the blood and the cells are made) and then into the *coronary veins*. Because of this particular network we say that the heart runs under *blood perfusion*.

During a normal beat, the heart cells change length by over 20%.

Deformations in a total Lagrangian formalism To describe the kinematics of the heart we use the Lagrangian formalism. In general, at any time t the region occupied by the deformed solid under consideration is denoted by $\Omega(t)$ with boundary $\partial\Omega(t)$. In a Lagrangian formulation we use a reference configuration Ω_0 to describe the deformations of the solid. If $\underline{\xi}$ is the spatial variable defining Ω_0, we assume that the deformation $\underline{\varphi}(\underline{\xi},t)$ leading to the deformed configuration $\Omega(t)$ is a bijective mapping – see Figure 1.2. We can define the displacement $\underline{y}(\underline{\xi})$ of a material point $\underline{\xi}$ in the reference configuration by

$$\underline{\varphi} \left| \begin{array}{l} \Omega_0 \times [0,T] \longrightarrow \Omega(t) \\ \qquad (\underline{\xi},t) \longmapsto \underline{x} = \underline{\varphi}(\underline{\xi},t) = \underline{\xi} + \underline{y}(\underline{\xi},t). \end{array}\right.$$

To describe the changes affecting the material at a local scale we will extensively use the deformation gradient $\underline{\underline{F}}$ with respect to the spatial variables,

$$\underline{\underline{F}}(\underline{\xi},t) = \underline{\underline{\nabla}}_{\underline{\xi}}\,\underline{\varphi}(\underline{\xi},t) = \underline{\underline{\mathbb{1}}} + \underline{\underline{\nabla}}_{\underline{\xi}}\,\underline{y}(\underline{\xi},t).$$

From this tensor we classically define the Cauchy-Green strain tensor by

$$\underline{\underline{C}} = \underline{\underline{F}}^{\mathsf{T}} \cdot \underline{\underline{F}},$$

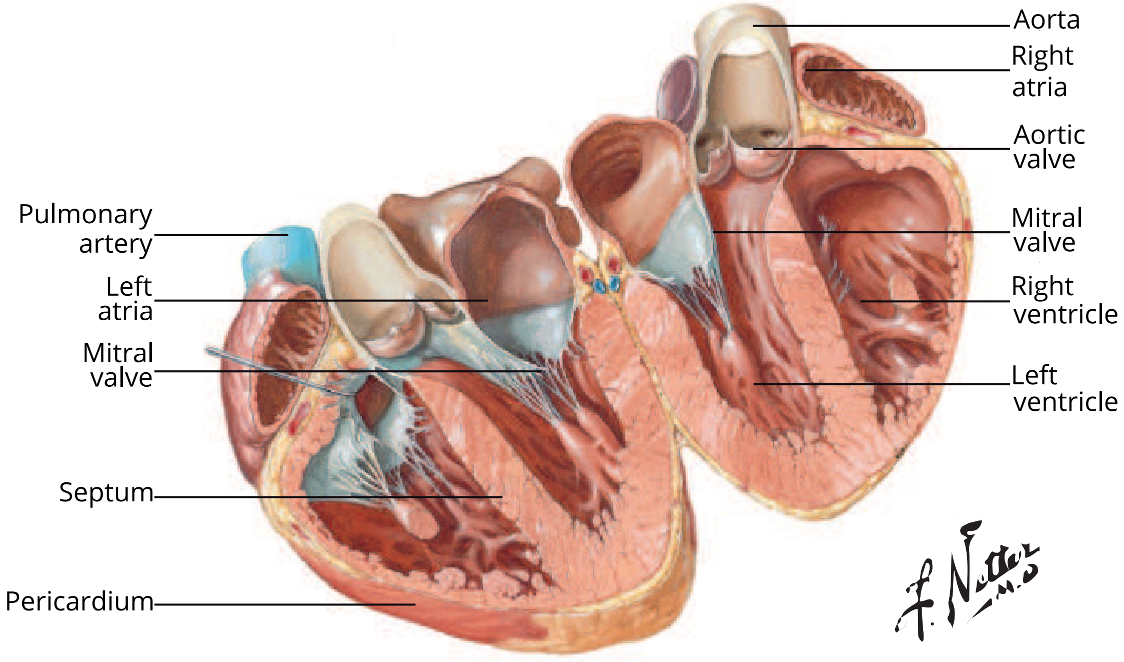

Figure 1.1: Representation of the heart anatomy (from [Netter, 1994]).

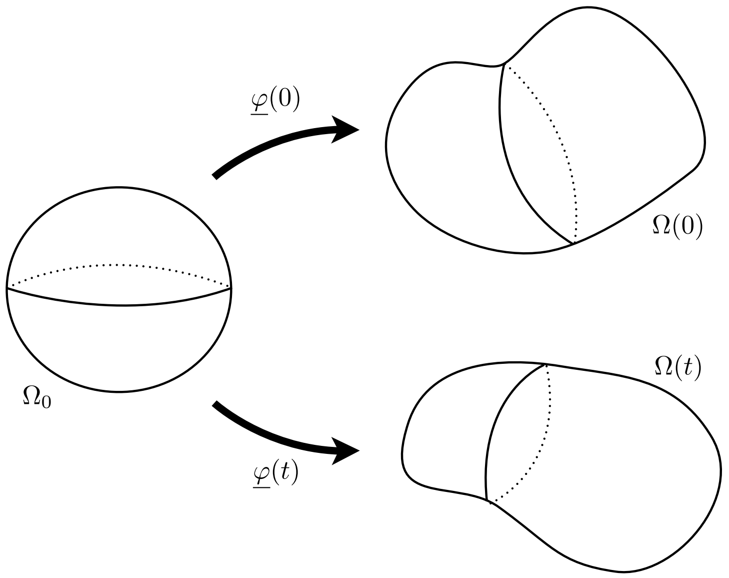

Figure 1.2: Reference configuration, initial configuration and deformed configuration.

and the Green-Lagrange strain tensor

$$\underline{\underline{e}} = \frac{1}{2}\left(\underline{\underline{C}} - \underline{\underline{\mathbb{1}}}\right) = \frac{1}{2}(\underline{\underline{\nabla_{\xi}y}} + \underline{\underline{\nabla_{\xi}y}}^{\mathsf{T}} + \underline{\underline{\nabla_{\xi}y}}^{\mathsf{T}} \cdot \underline{\underline{\nabla_{\xi}y}}).$$

These tensors have a natural geometrical interpretation. For instance, considering two material fibers $\underline{\mathrm{d}\xi}_1$ and $\underline{\mathrm{d}\xi}_2$ in the reference configuration deformed into $\underline{\mathrm{d}x}_1$ and $\underline{\mathrm{d}x}_2$, the Cauchy-Green tensor defines the metrics in the reference configuration since

$$\underline{\mathrm{d}x}_1 \cdot \underline{\mathrm{d}x}_2 = \left(\underline{\underline{F}} \cdot \underline{\mathrm{d}\xi}_1\right) \cdot \left(\underline{\underline{F}} \cdot \underline{\mathrm{d}\xi}_2\right) = \underline{\mathrm{d}\xi}_1 \cdot \underline{\underline{C}} \cdot \underline{\mathrm{d}\xi}_2.$$

On the other hand the Green-Lagrange tensor measure the variations in length of material fibers

$$\underline{\mathrm{d}x}_1 \cdot \underline{\mathrm{d}x}_2 - \underline{\mathrm{d}\xi}_1 \cdot \underline{\mathrm{d}\xi}_2 = \underline{\mathrm{d}\xi}_1 \cdot \left(\underline{\underline{C}} - \underline{\underline{\mathbb{1}}}\right) \cdot \underline{\mathrm{d}\xi}_2.$$

Transportation of volume and surface element It is quite common to define from the deformation gradient how the volume and surface elements change as the solid is deforming. Considering three material fibers $\underline{\mathrm{d}\xi}_1$, $\underline{\mathrm{d}\xi}_2$ and $\underline{\mathrm{d}\xi}_3$ a volume element

$$\mathrm{d}\Omega_0 = \underline{\mathrm{d}\xi}_3 \cdot (\underline{\mathrm{d}\xi}_2 \wedge \underline{\mathrm{d}\xi}_1),$$

is transported into

$$\mathrm{d}\Omega = \underline{\mathrm{d}x}_3 \cdot (\underline{\mathrm{d}x}_2 \wedge \underline{\mathrm{d}x}_1) = \det(\underline{\underline{F}})\ \underline{\mathrm{d}\xi}_3 \cdot (\underline{\mathrm{d}\xi}_2 \wedge \underline{\mathrm{d}\xi}_1) = J\ \mathrm{d}\Omega_0.$$

A surface element $\underline{\mathrm{d}\sigma}_0 = \underline{\mathrm{d}\xi}_1 \wedge \underline{\mathrm{d}\xi}_2$ is transported into $\underline{\mathrm{d}\sigma}$, such that for any vector field $\underline{u}$ we have

$$\underline{\mathrm{d}\sigma} \cdot \underline{u} = J\ (\underline{\mathrm{d}\xi}_1 \wedge \underline{\mathrm{d}\xi}_2) \cdot \left(\underline{\underline{F}}^{-1} \cdot \underline{u}\right) = \left(J\underline{\underline{F}}^{-\mathsf{T}} \cdot \underline{\mathrm{d}\sigma}_0\right) \cdot \underline{u},$$

that is to say,

$$\underline{\mathrm{d}\sigma} = J\underline{\underline{F}}^{-\mathsf{T}} \cdot \underline{\mathrm{d}\sigma}_0.$$

The fundamental law of dynamics In this paragraph we rapidly recall the general weak form of the fundamental principal of the dynamics. This presentation is largely inspired from [Chapelle et al., 2012]. Denoting by $\underline{\underline{\sigma}}$ the symmetric Cauchy stress tensor, describing the internal stress of the solid in the deformed configuration, the fundamental law of dynamics reads

$$\rho\underline{\ddot{y}} - \mathrm{div}(\underline{\underline{\sigma}}) = \rho\underline{f}, \quad \text{in } \Omega,$$

where ρ is the volumic mass density of the solid and $\underline{f}$ represents the external force density. Assuming free surface boundary conditions, for a test displacement $\underline{v}^{\flat}$ belonging to the space of admissible displacements $\mathcal{X}^{y}(\Omega)$, the corresponding weak formulation reads

$$\int_{\Omega} \rho\underline{\ddot{y}} \cdot \underline{v}^{\flat}\ \mathrm{d}\Omega + \int_{\Omega} \underline{\underline{\sigma}} : \underline{\underline{\nabla_{x}v}}^{\flat}\ \mathrm{d}\Omega = \int_{\Omega} \rho\underline{f} \cdot \underline{v}^{\flat}\ \mathrm{d}\Omega.$$

In a total Lagrangian formulation, we perform a change of variables to write this equation in the reference configuration. The main reason for this operation is that the constitutive law, binding stress and strain together, is, in most practical cases, known on this configuration. Recalling the standard identity

$$\underline{\underline{\nabla_{x}v}}^{\flat} = \underline{\underline{\nabla_{\xi}v}}^{\flat} \cdot \underline{\underline{\nabla_{\xi}x}}^{-1} = \underline{\underline{\nabla_{\xi}v}}^{\flat} \cdot \underline{\underline{F}}^{-1},$$

we obtain

$$\forall \underline{v}^\flat \in \mathcal{X}^y(\Omega_0) \quad \int_{\Omega_0} \rho_0 \underline{\ddot{y}} \cdot \underline{v}^\flat \,\mathrm{d}\Omega_0 + \int_{\Omega_0} \underline{\underline{\sigma}} : \underline{\underline{\nabla}}_{\underline{\xi}} \underline{v}^\flat \cdot \underline{\underline{F}}^{-1}\, J \,\mathrm{d}\Omega_0 = \int_{\Omega_0} \rho_0 \underline{f} \cdot \underline{v}^\flat \,\mathrm{d}\Omega_0.$$

In this expression we implicitly assume that the external forces are independent of the configuration, which might not be the case in practice. We are now able to introduce the so-called first Piola-Kirchhoff tensor $\underline{\underline{T}} = J\underline{\underline{\sigma}} \cdot \underline{\underline{F}}^{-\intercal}$ appearing in

$$\int_{\Omega_0} \rho_0 \underline{\ddot{y}} \cdot \underline{v}^\flat \,\mathrm{d}\Omega_0 + \int_{\Omega_0} \underline{\underline{T}} : \underline{\underline{\nabla}}_{\underline{\xi}} \underline{v}^\flat \,\mathrm{d}\Omega_0 = \int_{\Omega_0} \rho_0 \underline{f} \cdot \underline{v}^\flat \,\mathrm{d}\Omega_0.$$

Defining $\underline{\underline{\Sigma}} = J\underline{\underline{F}}^{-1} \cdot \underline{\underline{\sigma}} \cdot \underline{\underline{F}}^{-\intercal}$ the so-called second Piola-Kirchhoff tensor we obtain

$$\int_{\Omega_0} \rho_0 \underline{\ddot{y}} \cdot \underline{v}^\flat \,\mathrm{d}\Omega_0 + \int_{\Omega_0} \underline{\underline{\Sigma}} : \underline{\underline{F}}^\intercal \cdot \underline{\underline{\nabla}}_{\underline{\xi}} \underline{v}^\flat \,\mathrm{d}\Omega_0 = \int_{\Omega_0} \rho_0 \underline{f} \cdot \underline{v}^\flat \,\mathrm{d}\Omega_0.$$

Since $\underline{\underline{\Sigma}}$ is a symmetric tensor, this expression is equivalent to

$$\int_{\Omega_0} \rho_0 \underline{\ddot{y}} \cdot \underline{v}^\flat \,\mathrm{d}\Omega_0 + \int_{\Omega_0} \underline{\underline{\Sigma}} : \frac{1}{2}\left(\underline{\underline{F}}^\intercal \cdot \underline{\underline{\nabla}}_{\underline{\xi}} \underline{v}^\flat + \underline{\underline{\nabla}}_{\underline{\xi}} \underline{v}^{\flat\,\intercal} \cdot \underline{\underline{F}}\right) \mathrm{d}\Omega_0 = \int_{\Omega_0} \rho_0 \underline{f} \cdot \underline{v}^\flat \,\mathrm{d}\Omega_0.$$

Remarking that the differential of the Green-Lagrange tensor with respect to a test displacement is expressed as

$$\mathrm{d}_y \underline{\underline{e}} \cdot \underline{v}^\flat = \frac{1}{2}\left(\mathrm{d}_y \underline{\underline{F}}^\intercal \ \cdot \underline{v}^\flat + \underline{\underline{F}} \cdot \ \mathrm{d}_y \underline{\underline{F}} \cdot \underline{v}^\flat\right) = \frac{1}{2}\left(\underline{\underline{F}}^\intercal \cdot \underline{\underline{\nabla}}_{\underline{\xi}} \underline{v}^\flat + \underline{\underline{\nabla}}_{\underline{\xi}} \underline{v}^{\flat\,\intercal} \cdot \underline{\underline{F}}\right),$$

we finally obtain a fully symmetric weak form of the fundamental principal of the dynamics

$$\int_{\Omega_0} \rho_0 \underline{\ddot{y}} \cdot \underline{v}^\flat \,\mathrm{d}\Omega_0 + \int_{\Omega_0} \underline{\underline{\Sigma}} : \mathrm{d}_y \underline{\underline{e}} \cdot \underline{v}^\flat \,\mathrm{d}\Omega_0 = \int_{\Omega_0} \rho_0 \underline{f} \cdot \underline{v}^\flat \,\mathrm{d}\Omega_0. \tag{1.1}$$

Even though this expression is a fundamental starting point to model the mechanical behavior of the heart, the most important task is to give a relevant stress-strain law for both active and passive operating modes of the heart.

Linearized mechanics and linear stress-strain law Previously we have rapidly described the general form of the mechanical formulation which depends nonlinearly on the displacement of the solid through the Cauchy stress tensor but also through the strain tensor $\underline{\underline{e}}$. A very popular case is when relatively small displacements around the reference configuration occur so that $\underline{\underline{e}}$ is approximated by

$$\underline{\underline{\varepsilon}} = \frac{1}{2}(\underline{\underline{\nabla}}_{\underline{\xi}} \underline{y} + \underline{\underline{\nabla}}_{\underline{\xi}} \underline{y}^\intercal).$$

If this assumption goes so far as neglecting terms of order two in both the displacement and its spatial derivative (to favor intuition let us say that the displacement is small enough in $\mathcal{H}^1$-norm) then the fundamental principle is directly written on the reference configuration

$$\int_{\Omega_0} \rho_0 \underline{\ddot{y}} \cdot \underline{v}^\flat \,\mathrm{d}\Omega_0 + \int_{\Omega_0} \underline{\underline{\sigma}} : \underline{\underline{\varepsilon}}(\underline{v}^\flat) \,\mathrm{d}\Omega_0 = \int_{\Omega_0} \rho_0 \underline{f} \cdot \underline{v}^\flat \,\mathrm{d}\Omega_0.$$

The remaining nonlinearity comes from the constitutive law. Assuming a linear elastic model, that is to say there exists a fourth order tensor $\underline{\underline{\underline{\underline{A}}}}$ such that

$$\underline{\underline{\sigma}} = \underline{\underline{\underline{\underline{A}}}} : \underline{\underline{\varepsilon}},$$

then the fully linear dynamical weak form of the mechanical model becomes

$$\int_{\Omega_0} \rho_0 \underline{\ddot{y}} \cdot \underline{v}^\flat \, \mathrm{d}\Omega_0 + \int_{\Omega_0} \underline{\underline{\varepsilon}}(\underline{v}^\flat) : \underline{\underline{\underline{\underline{A}}}} : \underline{\underline{\varepsilon}}(\underline{y}) \, \mathrm{d}\Omega_0 = \int_{\Omega_0} \rho_0 \underline{f} \cdot \underline{v}^\flat \, \mathrm{d}\Omega_0. \tag{1.2}$$

Remark 1. *We recognize here an instance of the abstract linear second order hyperbolic equation of the form:*

$$\textit{find} \quad u \in \mathcal{H} \quad \textit{such that} \quad \forall v \in \mathcal{H} \quad (\ddot{u}, v)_{\mathcal{H}} + a(u, v) = l(v).$$

In our case we enter this particular mathematical setting only after some possibly restrictive linearization assumptions and after considering a linear constitutive law. An important example is the well-known Hooke law where

$$\underline{\underline{\sigma}}(\underline{\underline{\varepsilon}}) = \lambda \mathrm{tr}(\underline{\underline{\varepsilon}}) \underline{\underline{\mathbb{1}}} + 2\mu \underline{\underline{\varepsilon}},$$

λ *and* μ *being the so-called Lamé coefficients. Readers may refer to [Ciarlet, 1988] or [Le Dret, 2004] for a complete mathematical study of this class of problems. The two previous assumptions, different in nature, are independent. As an example the Saint-Venant-Kirchhoff's material is a material where the assumption of small displacement is not verified but the stress-strain law is linear and is defined by*

$$\underline{\underline{\Sigma}}(\underline{\underline{e}}) = \lambda \mathrm{tr}(\underline{\underline{e}}) \mathbb{1} + 2\mu \underline{\underline{e}}. \tag{1.3}$$

Remark 2. *In practice equation* (1.2) *is completed with some viscous component that may take different forms, depending on the regularity of the solution,* e.g.

$$\int_{\Omega_0} \underline{\underline{\underline{\underline{A}}}} \, \underline{\underline{\varepsilon}}(\underline{\dot{y}}) : \underline{\underline{\varepsilon}}(\underline{v}^\flat) \, \mathrm{d}\Omega_0 \quad \textit{or} \quad \int_{\Omega_0} \rho_0 \underline{\dot{y}} \cdot \underline{v}^\flat \, \mathrm{d}\Omega_0.$$

Hyperelastic isotropic material In the previous physiological key point we gave an approximation of the deformation rate during the heart contraction (around 20%). This physiological fact clearly rules out the small displacement assumption. As far as the constitutive law is concerned, a linear relation between strain and stress is not sufficient in order to provide a biomechanical model that meets our expectations in terms of precision. Therefore we have to consider the more general theory of hyperelasticity. Since it is not the purpose of this thesis, we will restrict ourselves to only cite the main notions behind it in order to help the understanding of the necessary modeling aspects. Readers can refer to *e.g.* [Ciarlet, 1988, Le Tallec, 2000, Temam and Miranville, 2005, Forest et al., 2008] for a more precise description of this theory.

In this context, a material is said to be elastic if the stress tensor in the current deformed configuration only depends on the spatial variable $\underline{x}$ and on the deformation gradient $\underline{\underline{F}}$, namely

$$\underline{\underline{\sigma}}(\underline{x}, t) = \mathcal{F}(\underline{x}(t), \underline{\underline{F}}(\xi, t)).$$

Here $\mathcal{F}$ represents the constitutive law that we want to characterize for the particular case of the heart tissue. Applying the second principle of thermodynamics in its local form –

namely the Clausius-Duhem inequality – and assuming, in a first step, that no dissipation occurs during any admissible deformations of the material, one can state that there exists an elastic potential W^{e} such that

$$\underline{\underline{T}}(\underline{\underline{F}}) = \frac{\partial W^{\mathrm{e}}}{\partial \underline{\underline{F}}}.$$

It is possible to characterize the dependencies of W^{e} by choosing adequate admissible transformations. As a first step let $\underline{\underline{Q}}$ be any rigid rotation, this type of deformation does not alter the amount of energy stored in the mechanical system, that is to say

$$W^{\mathrm{e}}(\underline{\underline{F}}) = W^{\mathrm{e}}(\underline{\underline{Q}} \cdot \underline{\underline{F}}).$$

Choosing $\underline{\underline{Q}} = \sqrt{\underline{\underline{C}}} \cdot \underline{\underline{F}}^{-1}$ we see that W^{e} is a function of $\underline{\underline{C}}$. Using the fact that, for now, we restrict ourselves to isotropic materials we have

$$W^{\mathrm{e}}(\underline{\underline{C}}) = W^{\mathrm{e}}(\underline{\underline{Q}} \cdot \underline{\underline{C}} \cdot \underline{\underline{Q}}^{\intercal}).$$

Choosing $\underline{\underline{Q}}$ as the matrix of the eigenvectors of the $\underline{\underline{C}}$ tensor we can conclude that the elastic potential for isotropic elastic material depends only of the eigenvalues of the tensor which can be uniquely expressed with its invariants

$$I_1 = \mathrm{tr}(\underline{\underline{C}}), \quad I_2 = \frac{1}{2}\left((\mathrm{tr}(\underline{\underline{C}}))^2 - \mathrm{tr}(\underline{\underline{C}}^2)\right), \quad I_3 = \det(\underline{\underline{C}}).$$

The stress-strain law is then obtained from the differentiation of the elastic potential with respect to its invariant

$$\underline{\underline{\Sigma}}(\underline{\underline{e}}) = \frac{\partial W^{\mathrm{e}}}{\partial \underline{\underline{e}}}(I_1, I_2, I_3) = 2\frac{\partial W^{\mathrm{e}}}{\partial \underline{\underline{C}}}(I_1, I_2, I_3) = 2\sum_{i=1}^{3} \frac{\partial W^{\mathrm{e}}}{\partial I_i}\frac{\partial I_i}{\partial \underline{\underline{C}}}. \tag{1.4}$$

Hence, the construction of a constitutive law is reduced to defining the expression of the elastic potential in terms of invariants. One classical example is the Mooney-Rivlin law where

$$W^{\mathrm{e}} = \kappa_1(I_1 - 3) + \kappa_2(I_2 - 3).$$

In our case, we will see that the elastic potential modeling the passive behavior is more complex, mainly due to the presence of fibers in the tissue that favors particular directions.

Remark 3. *The linearization around the reference configuration of the stress tensor with respect to* $\underline{\underline{e}}$ *leads to an expression of the form* (1.3) *(assuming the reference configuration is stress-free), where the Lamé coefficients are expressed by differentiation of the elastic potential. We will see later an example of this linearization procedure.*

Pressure-deviatoric decomposition We recall a useful decomposition of the stress tensor with respect to the work produced in contraction or dilatation that will be of major importance when modeling incompressible materials. To start with, we define

$$p = -\frac{1}{3J}\underline{\underline{\Sigma}} : \underline{\underline{C}} \quad \text{and} \quad \underline{\underline{\Sigma}}_d = \underline{\underline{\Sigma}} + pJ\underline{\underline{C}}^{-1}.$$

Considering a test displacement $\underline{v}^\flat = \lambda \underline{x}$, the differential of the Green-Lagrange tensor with respect to this type of deformation is easily obtained by

$$\mathrm{d}_y \underline{\underline{e}} \cdot \underline{v}^\flat = \frac{1}{2} \mathrm{d}_y \underline{\underline{C}} \cdot \underline{v}^\flat = \frac{1}{2} \left(\mathrm{d}_y \underline{\underline{F}}^\top \cdot \underline{v}^\flat \cdot \underline{\underline{F}} + \underline{\underline{F}} \cdot \mathrm{d}_y \underline{\underline{F}} \cdot \underline{v}^\flat \right) = \lambda \underline{\underline{C}}.$$

We finally obtain that $\underline{\underline{\Sigma}}_d$, called the deviatoric part of the stress tensor, does not produce work on this type of deformation

$$\underline{\underline{\Sigma}}_d : \mathrm{d}_y \underline{\underline{e}} \cdot \underline{v}^\flat = \lambda \underline{\underline{\Sigma}} : \underline{\underline{C}} + \lambda p J \underline{\underline{C}}^{-1} : \underline{\underline{C}} = \lambda \underline{\underline{\Sigma}} : \underline{\underline{C}} \left(1 - \frac{1}{3} \underline{\underline{C}}^{-1} : \underline{\underline{C}} \right) = 0.$$

Therefore, in the sequel we may use the following decomposition of the stress tensor

$$\underline{\underline{\Sigma}} = \underline{\underline{\Sigma}}_d - pJ \underline{\underline{C}}^{-1}, \tag{1.5}$$

where p will be referred to as the hydrostatic pressure.

Reduced invariants We now define the reduced invariants which are more adapted to the pressure-deviatoric decomposition of the stress tensor in the sense that they remarkably simplify the expression – with respect to the invariants – of both terms appearing in the decomposition. The idea is to rewrite the elastic potential as

$$W^{\mathrm{e}}(I_1, I_2, I_3) = W^{\mathrm{e}}(J_1, J_2, J_3),$$

where $\{J_i\}_{i=1}^3$ are functions of $\{I_i\}_{i=1}^3$. To find the proper modification, once again we use the contraction-dilatation transformation $\underline{v}^\flat = \underline{x}$. Remarking that

$$\frac{\partial I_1}{\partial \underline{\underline{C}}} : \underline{\underline{C}} = I_1, \quad \frac{\partial I_2}{\partial \underline{\underline{C}}} : \underline{\underline{C}} = 2I_2, \quad \frac{\partial I_3}{\partial \underline{\underline{C}}} : \underline{\underline{C}} = 3I_3,$$

we can choose

$$J_1 = I_1 I_3^{-\frac{1}{3}}, \quad J_2 = I_2 I_3^{-\frac{2}{3}}, \quad J_3 = I_3^{\frac{1}{2}} = J, \tag{1.6}$$

so that

$$\frac{\partial J_1}{\partial \underline{\underline{C}}} : \underline{\underline{C}} = 0, \quad \frac{\partial J_2}{\partial \underline{\underline{C}}} : \underline{\underline{C}} = 0, \quad \frac{\partial J_3}{\partial \underline{\underline{C}}} : \underline{\underline{C}} = \frac{3}{2} J.$$

For the particular case of transformations that we are considering we can obtain another useful decomposition result. As a matter of fact,

$$\underline{\underline{\Sigma}} : \mathrm{d}_y \underline{\underline{e}} \cdot \underline{v}^\flat = -pJ \underline{\underline{C}}^{-1} : \underline{\underline{C}} = -3pJ,$$

combined with

$$\underline{\underline{\Sigma}} : \mathrm{d}_y \underline{\underline{e}} \cdot \underline{v}^\flat = 2 \sum_{i=1}^{3} \frac{\partial W^{\mathrm{e}}}{\partial J_i} \frac{\partial J_i}{\partial \underline{\underline{C}}} : \underline{\underline{C}} = 3 \frac{\partial W^{\mathrm{e}}}{\partial J} J,$$

we obtain

$$\underline{\underline{\Sigma}}_d = 2 \sum_{i=1}^{2} \frac{\partial W^{\mathrm{e}}}{\partial J_i} \frac{\partial J_i}{\partial \underline{\underline{C}}}, \quad p = -\frac{\partial W^{\mathrm{e}}}{\partial J}. \tag{1.7}$$

Incompressibility

Physiological key point

Nearly incompressible material

The question of the heart tissue compressibility is a rather complex one and its consequences in terms of modeling and numerical aspects are of significant importance. One argument for assuming the heart material to be incompressible is that its various structural components along with the blood perfusing the tissue are mainly composed of compartmentalized water, an incompressible fluid. On the other hand, the contraction of the tissue induces a decrease of vascular volume of the perfused blood introducing an effective compressibility – see [Yin et al., 1996] for further insight on the matter. In the sequel we will consider the heart to be a nearly incompressible material.

To build a good intuition on how the incompressibility can be handled let us consider a static problem of hyperelasticity. We recall that the elastic energy of the mechanical system at hand is given by

$$\mathcal{E}_{\mathrm{e}} = \int_{\Omega_0} W^{\mathrm{e}}(\underline{\underline{e}}) \, \mathrm{d}\Omega_0.$$

If the solid is subject to external forces represented by the work $\mathcal{W}^{\mathrm{ext}}$, the resulting deformation $\underline{y}$ satisfies

$$\underline{y} = \arg\min_{\underline{y}} (\mathcal{E}_{\mathrm{e}} - \mathcal{W}^{\mathrm{ext}}).$$

For incompressible materials, every deformations preserve the volume at all points, which means that a deformation is said to be admissible if it satisfies

$$J = \det(\underline{\underline{F}}) = 1.$$

This enters in the previously stated minimization problem as a constraint. It should be noted that it also entails $W^{\mathrm{e}} = W^{\mathrm{e}}(J_1, J_2)$. Finally the resulting deformation is the solution of the minimization problem

$$\min_{\underline{y} \text{ s.t. } J=1} (\mathcal{E}_{\mathrm{e}} - \mathcal{W}^{\mathrm{ext}}) = \min_{\underline{y}} \max_{q} \left(\int_{\Omega_0} W^{\mathrm{e}}(\underline{\underline{e}}) + q(1-J) \, \mathrm{d}\Omega_0 \; - \; \mathcal{W}^{\mathrm{ext}} \right),$$

where q is the Lagrangian multiplier introduced to solve the constraint. Applying the optimality condition of order one for a test displacement $\underline{v}^\flat$ we obtain

$$\int_{\Omega_0} \left(\frac{\partial W^{\mathrm{e}}}{\partial \underline{\underline{e}}} - q \frac{\partial J}{\partial \underline{\underline{e}}} \right) : \mathrm{d}_y \underline{\underline{e}} \cdot \underline{v}^\flat \, \mathrm{d}\Omega_0 - \mathrm{d}_y \mathcal{W}^{\mathrm{ext}} \cdot \underline{v}^\flat = 0,$$

where we can identify the stress tensor

$$\underline{\underline{\Sigma}} = \frac{\partial W^{\mathrm{e}}}{\partial \underline{\underline{e}}} - q \frac{\partial J}{\partial \underline{\underline{e}}} = \frac{\partial W^{\mathrm{e}}}{\partial \underline{\underline{e}}} - q J \underline{\underline{C}}^{-1},$$

and – as $W^{\mathrm{e}} = W^{\mathrm{e}}(J_1, J_2)$ – we recognize the pressure-deviatoric decomposition of the stress tensor, which means that the Lagrangian multiplier q is in fact the hydrostatic pressure p. Therefore, for an incompressible material, we obtain the following so-called mixed formulation, $\forall(\underline{v}^\flat, q) \in \mathcal{X}^y \times \mathcal{X}^p$:

$$\left\{\begin{aligned} &\int_{\Omega_0} \rho_0 \underline{\ddot{y}} \cdot \underline{v}^\flat \,\mathrm{d}\Omega_0 + \int_{\Omega_0} \underline{\underline{\Sigma}}(\underline{y}, p) : \mathrm{d}_y \underline{\underline{e}} \cdot \underline{v}^\flat \,\mathrm{d}\Omega_0 = \int_{\Omega_0} \rho_0 \underline{f} \cdot \underline{v}^\flat \,\mathrm{d}\Omega_0, \\ &\int_{\Omega_0} \rho_0 (\det \underline{\underline{F}}(\underline{y}) - 1) q \,\mathrm{d}\Omega_0 = 0, \end{aligned}\right. \tag{1.8}$$

where $\mathcal{X}^p$ is the functional space of admissible pressures.

Nearly incompressible materials To model nearly incompressible material one can add a penalization terms in the elastic potential, for example

$$W^{\mathrm{e}}_\kappa(\underline{\underline{e}}) = W^{\mathrm{e}}(J_1, J_2) + \frac{\kappa}{2}(1 - J)^2,$$

where κ is the penalization parameter that tends to reach large values in order to penalize the variations of J from the value 1. Other penalization schemes can be imagined, one important example being the Ciarlet-Geymonat elastic potential

$$W^{\mathrm{e}}(\underline{\underline{e}}) = \kappa_1(J_1 - 3) + \kappa_2(J_2 - 3) + \kappa(J - 1) - \kappa \ln(J), \tag{1.9}$$

which provides an efficient way to model nearly incompressible material whose deformation gives J close to one and $J > 0$. It is important to notice that this penalization procedure allows to clear the system of actual constraints, therefore no mixed formulation is needed in theory.

Modeling viscous material

Physiological key point

Viscosity of soft biological material

The mechanical behavior of soft biological tissues is known to be viscoelastic – see [Pioletti et al., 1998]. One way, for example, to observe such viscous behavior is to perform traction tests on the material at hand and to observe that the shape of the stress-strain curve depends on the strain rate at which the experiment is performed.

To model viscous materials we invoke once again the Clausius-Duhem inequality that states that during a thermomechanical process the dissipation is necessarily positive, which is written, in the case of isothermal deformations, as

$$\forall \underline{\underline{e}}, \underline{\underline{\dot{e}}}, \quad \left(\underline{\underline{\Sigma}} - \frac{\partial W^{\mathrm{e}}}{\partial \underline{\underline{e}}}\right) : \underline{\underline{\dot{e}}} \;\geq\; 0.$$

One way to verify this inequality is to introduce a functional $W^{\mathrm{v}}(\underline{\underline{e}}, \underline{\underline{\dot{e}}})$, convex in $\underline{\underline{\dot{e}}}$, such that

$$\underline{\underline{\Sigma}} = \frac{\partial W^{\mathrm{e}}}{\partial \underline{\underline{e}}} + \frac{\partial W^{\mathrm{v}}}{\partial \underline{\underline{\dot{e}}}}. \tag{1.10}$$

A simple example being $W^{\mathrm{v}} = \dfrac{\eta}{2}\mathrm{tr}(\underline{\underline{\dot{e}}}^2)$ leading to $\dfrac{\partial W^{\mathrm{v}}}{\partial \underline{\underline{\dot{e}}}} = \eta \underline{\underline{\dot{e}}}$.

1.1.2 Formulating cardiac passive model

Physiological key point

Structure of the heart tissue

In this keypoint we give further insight on the composition of the heart tissue and more specifically of the ventricles. Each ventricle consists of three distinct layers : the inner layer is called the *endocardium* which encloses the internal blood compartments, the middle layer constituting most of the wall thickness is referred to as the *myocardium* and the outer layer is the *epicardium*, constituting the exterior boundary. The ventricles have a typical thickness of 0.5 cm on the right and 1.5 cm on the left.

Concerning the orientation of the heart, we can define the long axis as the main principal axis of inertia. The inferior part of the ventricles is called *apex* and the upper part – where the atria and the blood vessels are connected – is the *base*. The American Heart Association (AHA) has proposed a subdivision of the left ventricle into seventeen regions – see Figure 1.3. These regions roughly correspond to the main coronary territories.

The ventricular wall is made of layers of parallel muscular fibers called *myocytes*, occupying approximately 70% of the volume – the remaining 30% consists of various interstitial components. The fibers are wound as in a coil and laid out on parallel layers extending from the endocardium to the epicardium with connections across layers occurring in the apical region. The muscle fibers orientation changes with the position through the wall. In the *sub-epicardial* region (a superficial layer) the direction rotates from -60 to -80 degrees to nearly orthoradial orientation in the mid-wall regions whereas in the *sub-endocardial* region the fibers rotate from +60 to +80 degrees. Several works – see [Holzapfel and Ogden, 2009, Dokos et al., 2002] – have also shown that there exists another privileged component in the radial direction, hence orthogonal to the fiber direction, called *sheets*.

Transverse isotropy From a modeling standpoint this arrangement of cardiac cells in the myocardium clearly states that the heart wall is an anisotropic material. Consequently, so should be the mechanical model. It is possible to show – see [Raoult, 2009] – that other invariants are necessary to define the elastic potential. The type of anisotropy that we consider is the transverse isotropy where we can find a particular direction $\underline{n}_0$ so that any rotation around this axis does not change the local behavior of the material. The elastic potential can be expressed as a function of five invariants

$$W^{\mathrm{e}} = W^{\mathrm{e}}(I_1, I_2, I_3, I_4, I_5),$$

where

$$I_4 = \underline{n}_0 \cdot \underline{\underline{C}} \cdot \underline{n}_0, \quad I_5 = \underline{n}_0 \cdot \underline{\underline{C}}^2 \cdot \underline{n}_0. \tag{1.11}$$

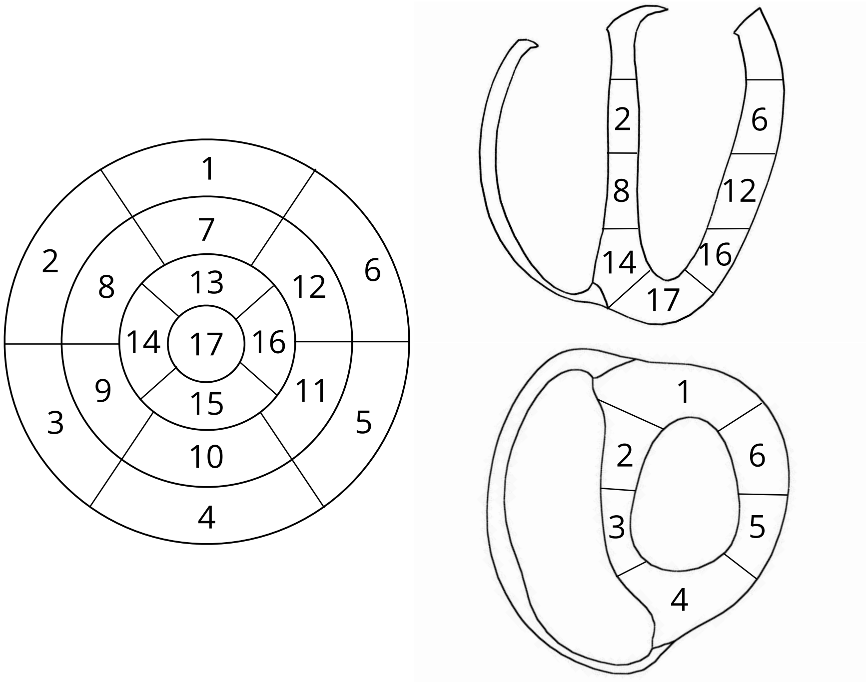

Figure 1.3: Representation of the AHA regions of the left ventricle.

The expression (1.4) of the stress tensor can also be formulated in this case to obtain

$$\underline{\underline{\Sigma}}(\underline{\underline{e}}) = 2\sum_{i=1}^{3} \frac{\partial W^{\mathrm{e}}}{\partial I_i}\frac{\partial I_i}{\partial \underline{\underline{C}}} + \frac{\partial W^{\mathrm{e}}}{\partial I_4}\underline{n}_0 \otimes \underline{n}_0 + \frac{\partial W^{\mathrm{e}}}{\partial I_5}\big((\underline{\underline{C}}\cdot\underline{n}_0)\otimes\underline{n}_0 + \underline{n}_0\otimes(\underline{\underline{C}}\cdot\underline{n}_0)\big). \tag{1.12}$$

Remark 4. *It is possible to also use the pressure-deviatoric decomposition with reduced invariants in the case of transverse isotropic hyperelastic law. In the case where one can characterize a particular behavior for the three directions, the material is said to be orthotropic and the elastic potential can be expressed with up to 8 invariants.*

Passive constitutive law of the heart From the previously described composition of the heart tissue, two main directions can be extracted : the direction given by the fibers and the one representing the sheets direction. As far as the mechanical model is concerned, most of the recent developments, see [Holzapfel and Ogden, 2009, Dokos et al., 2002, Göktepe et al., 2011] for example, tend to consider the passive myocardium to be orthotropic. In [Dokos et al., 2002] this statement is based on observing the heart wall response to simple shear experiments on three orthogonal planes, an argument followed by [Holzapfel and Ogden, 2009]. Moreover several experiments – see [Holzapfel and Ogden, 2009, Humphrey and Yin, 1989, Guccione et al., 1995, Costa et al., 2001, Nash and Hunter, 2000, Dokos et al., 2002, Göktepe et al., 2011] – aiming at fitting strain measurements showed that an exponential constitutive law is well-suited to represent the heart material nonlinearities. In our case we choose to define the passive elastic potential as transverse isotropic of exponential type. We justify our approach in two manners. The first one being that, even though we do not consider a complete orthotropic model, studies in [Guccione et al., 1995] or in [Vetter and McCulloch, 2000] have shown that a transverse isotropic constitutive law based only on the fiber direction adequately reproduces measured epicardial strain. The second one is that in practice, the characterization of sheets direction can become really complex since very little physiological data are available.

At the reference configuration we consider the fiber direction $\underline{n}_0$. Defining the fourth reduced invariant as

$$J_4 = I_4 I_3^{-\frac{1}{3}}, \tag{1.13}$$

we express the passive elastic potential of the myocardium as a combination of a Ciarlet-Geymonat isotropic law with penalized incompressibility terms and of a transverse isotropic exponential law:

$$W^{\mathrm{e}} = \mu_1(J_1-3)+\mu_2(J_2-3)+C_0\exp\big(C_1(J_1-3)^2\big)+C_2\exp\big(C_3(J_4-1)^2\big)+\kappa(J-1)-\kappa\ln(J). \tag{1.14}$$

The linear terms – with respect to the invariants J_1 and J_2 – of the Ciarlet-Gaymonat law are added to mainly give a better control on the stiffness around the reference configuration and to insure an overall numerical stability of the system while the exponential part prevails in larger deformations. From this expression, using (1.12) we obtain the stress tensor by differentiating the elastic potential with respect to the invariants, namely,

$$\left|\begin{aligned}
\frac{\partial W^{\mathrm{e}}}{\partial I_1} &= 2C_0C_1 I_3^{-\frac{2}{3}}(I_1 - 3I_3^{\frac{1}{3}})\exp\big(C_1(I_1 I_3^{\frac{1}{3}} - 3)^2\big) + \mu_1 I_3^{-\frac{1}{3}},\\[2ex]
\frac{\partial W^{\mathrm{e}}}{\partial I_2} &= \mu_2 I_3^{-\frac{2}{3}},\\[2ex]
\frac{\partial W^{\mathrm{e}}}{\partial I_3} &= -\frac{2}{3}C_0C_1 I_3^{-\frac{5}{3}} I_1(I_1 - 3I_3^{\frac{1}{3}})\exp\big(C_1(I_1 I_3^{\frac{1}{3}} - 3)^2\big),\\
&\quad + \frac{2}{3}C_2C_3 I_3^{-\frac{5}{3}} I_4(I_3^{\frac{1}{3}} - I_4)\exp\big(C_3(I_4 I_3^{-\frac{1}{3}} - 1)^2\big),\\
&\quad - \mu_1\frac{1}{3}I_1 I_3^{-\frac{4}{3}} - \mu_2\frac{2}{3}I_2 I_3^{-\frac{5}{3}} + \kappa\frac{1}{2}\big(I_3^{-\frac{1}{2}} - I_3^{-1}\big),\\[2ex]
\frac{\partial W^{\mathrm{e}}}{\partial I_4} &= -2C_2C_3 I_3^{-\frac{2}{3}}(I_3^{\frac{1}{3}} - I_4)\exp\big(C_1(I_1 I_3^{\frac{1}{3}} - 3)^2\big).
\end{aligned}\right. \tag{1.15}$$

As a direct consequence of the nonlinearities of the passive elastic potential, the weak formulation of the fundamental principle of the dynamics (1.1) that will be discretized – in a manner that will be described in following sections – is nonlinear. Therefore in order to obtain a numerical solution we will use Newton's method which requires the expression of the tangent of the operator appearing in the nonlinear system, that is to say the derivative of the stress tensor or equivalently the second derivative of the elastic potential. Here follows the desired expressions:

$$\left|\begin{aligned}
\frac{\partial^2 W^{\mathrm{e}}}{\partial I_1^2} =& 2C_0C_1I_3^{-\frac{4}{3}}\left(2C_1(I_1-3I_3^{\frac{1}{3}})^2+I_3^{\frac{2}{3}}\right)\exp\left(C_1(I_1I_3^{\frac{1}{3}}-3)^2\right),\\
\frac{\partial^2 W^{\mathrm{e}}}{\partial I_2\partial I_1} =& 0,\\
\frac{\partial^2 W^{\mathrm{e}}}{\partial I_3\partial I_1} =& -\frac{2}{3}C_0C_1I_3^{-\frac{7}{3}}(2C_1I_1(I_1-3I_3^{\frac{1}{3}})^2+2I_1I_3^{\frac{2}{3}}-3I_3)\exp\left(C_1(I_1I_3^{\frac{1}{3}}-3)^2\right)-\mu_1\frac{1}{3}I_3^{-\frac{4}{3}},\\
\frac{\partial^2 W^{\mathrm{e}}}{\partial I_4\partial I_1} =& 0, \quad \frac{\partial^2 W^{\mathrm{e}}}{\partial I_1 I_2} = \frac{\partial^2 W^{\mathrm{e}}}{\partial I_2\partial I_1}, \quad \frac{\partial^2 W^{\mathrm{e}}}{\partial I_2^2} = 0, \quad \frac{\partial^2 W^{\mathrm{e}}}{\partial I_3 I_2} = -\mu_2\frac{2}{3}I_3^{-\frac{5}{3}}, \quad \frac{\partial^2 W^{\mathrm{e}}}{\partial I_4 I_2} = 0,\\
\frac{\partial^2 W^{\mathrm{e}}}{\partial I_1 I_3} =& \frac{\partial^2 W^{\mathrm{e}}}{\partial I_3 I_1}, \quad \frac{\partial^2 W^{\mathrm{e}}}{\partial I_2 I_3} = \frac{\partial^2 W^{\mathrm{e}}}{\partial I_3 I_2},\\
\frac{\partial^2 W^{\mathrm{e}}}{\partial I_3^2} =& \frac{2}{9}I_3^{-\frac{10}{3}}\Big[C_0C_1I_1\big(2C_1I_1(I_1-3I_3^{\frac{1}{3}})^2+5I_1I_3^{\frac{2}{3}}-12I_3\big)\exp\left(C_1(I_1I_3^{\frac{1}{3}}-3)^2\right)\\
&+C_2C_3I_4\big(-4I_3+(5+2C_3)I_4I_3^{\frac{2}{3}}-4C_3I_3^{\frac{1}{3}}I_4^2+2C_3I_4^3\big)\exp\left(C_3(I_4I_3^{-\frac{1}{3}}-1)^2\right)\Big]\\
&+\mu_1\frac{4}{9}I_1I_3^{-\frac{7}{3}}+\mu_2\frac{10}{9}I_2I_3^{-\frac{8}{3}}+\frac{1}{2}\kappa(I_3^{-2}-\frac{1}{2}I_3^{-\frac{3}{2}}),\\
\frac{\partial^2 W^{\mathrm{e}}}{\partial I_4 I_3} =& -\frac{2}{3}C_2C_3I_3^{-\frac{7}{3}}(-I_3+2(1+C_3)I_3^{\frac{2}{3}}I_4-4C_3I_3^{\frac{1}{3}}I_4^2+2C_3I_4^3)\exp\left(C_3(I_4I_3^{-\frac{1}{3}}-1)^2\right),\\
\frac{\partial^2 W^{\mathrm{e}}}{\partial I_1 I_4} =& \frac{\partial^2 W^{\mathrm{e}}}{\partial I_4 I_1}, \quad \frac{\partial^2 W^{\mathrm{e}}}{\partial I_2 I_4} = \frac{\partial^2 W^{\mathrm{e}}}{\partial I_4 I_2}, \quad \frac{\partial^2 W^{\mathrm{e}}}{\partial I_3 I_4} = \frac{\partial^2 W^{\mathrm{e}}}{\partial I_4 I_3},\\
\frac{\partial^2 W^{\mathrm{e}}}{\partial I_4^2} =& 2C_2C_3I_3^{-\frac{4}{3}}((1+2C_3)I_3^{\frac{2}{3}}-4C_3I_3^{\frac{1}{3}}I_4+2C_3I_4^2)\exp\left(C_3(I_4I_3^{-\frac{1}{3}}-1)^2\right).
\end{aligned}\right.$$

Passive filling of the heart At this point we have all the elements to consider the static problem of passive heart filling. To this goal, we denote by $\mathcal{E}n_{\mathrm{L}}$ and $\mathcal{E}n_{\mathrm{R}}$ the left and right endocardium of a model geometry. Each ventricle is subject to a uniform pressure $P_{\mathrm{L}}^{\mathrm{v}}$ and $P_{\mathrm{R}}^{\mathrm{v}}$. The loading terms induced by such loading is therefore

$$\forall \underline{v}^\flat \in \mathcal{X}^y \quad \mathcal{P}^{\mathrm{ext}}(\underline{v}^\flat) = -P_{\mathrm{L}}^{\mathrm{v}}\int_{\mathcal{E}n_{\mathrm{L}}} \underline{n}_{\mathrm{L}}\cdot\underline{v}^\flat \mathrm{d}\sigma - P_{\mathrm{R}}^{\mathrm{v}}\int_{\mathcal{E}n_{\mathrm{R}}} \underline{n}_{\mathrm{R}}\cdot\underline{v}^\flat \mathrm{d}\sigma,$$

where $\underline{n}_{L,R}$ are the outer normals of the endocardium of the left and right ventricle. Assuming free surface boundary conditions on the rest of the geometry – that is to say of Neumann homogenous type – then the static problem of passive filling consists in finding the displacement $\underline{y}$ from a reference configuration Ω_0 that satisfies $\forall \underline{v}^\flat \in \mathcal{X}^y(\Omega_0)$

$$\int_{\Omega_0} \underline{\underline{\Sigma}}(\underline{y}) : \mathrm{d}_y \underline{\underline{e}} \cdot \underline{v}^\flat \, \mathrm{d}\Omega_0 = \mathcal{P}^{\mathrm{ext}}(\underline{v}^\flat). \tag{1.16}$$

1.1.3 Numerical passive filling of the heart

To finish the description of the passive behavior we give some key points of how spatial discretization can be performed to provide numerical solutions of problems such as the static load problem (1.16). By doing so we will observe that the assumption of nearly incompressible material significantly increases the difficulty of providing an accurate numerical solution.

Finite element spatial discretization Let us consider for now a standard Galerkin $\mathcal{P}_1$ finite element discretization providing the finite dimensional space $\mathcal{X}_h^y \subset \mathcal{X}^y$ and built using a tetrahedral mesh of the reference configuration. The discrete static load problem reads

$$\text{find} \quad \underline{y}_h \in \mathcal{X}_h^y \quad \text{such that} \quad \int_{\Omega_0} \underline{\underline{\Sigma}}(\underline{y}_h) : \mathrm{d}_y \underline{\underline{e}} \cdot \underline{v}_h^\flat \, \mathrm{d}\Omega_0 = \mathcal{P}^{\mathrm{ext}}(\underline{v}_h^\flat), \quad \forall \underline{v}_h^\flat \in \mathcal{X}_h^y.$$

As the loading terms are written in the deformed configuration, they depend nonlinearly on the displacement through the deformed normal surface $\underline{n}$ and the deformed surface element $\mathrm{d}\sigma$. For this reason, the construction of a numerical solution of this problem will also require the differentiation of $\mathcal{P}^{\mathrm{ext}}$ with respect to the displacement in order to apply Newton's method. More precisely, writing the equation (1.16) as

$$\forall \underline{v}^\flat \in \mathcal{X}^y \quad \mathcal{F}(\underline{y}_h, \underline{v}^\flat) = 0,$$

and denoting by $\underline{y}_h^{(k)}$ the k^{th} iteration with a given first guess $\underline{y}_h^{(0)}$, Newton's algorithm reads

$$\mathrm{d}_y \mathcal{F}(\underline{y}_h^{(k)}, \underline{v}^\flat) \cdot (\underline{y}_h^{(k+1)} - \underline{y}_h^{(k)}) = -\mathcal{F}(\underline{y}_h^{(k)}, \underline{v}^\flat). \tag{1.17}$$

Considering only the left ventricle for the sake of simplicity, the tangent operator appearing in (1.17) is decomposed as follows, $\forall \underline{w}^\flat \in \mathcal{X}^y$

$$\begin{aligned} \mathrm{d}_y \mathcal{F}(\underline{y}_h^{(k)}, \underline{v}^\flat) \cdot \underline{w}^\flat = & \int_{\Omega_0} \mathrm{d}_y \underline{\underline{\Sigma}}(\underline{y}_h^{(k)}) \cdot \underline{w}^\flat : \mathrm{d}_y \underline{\underline{e}}^{(k)} \cdot \underline{v}^\flat \, \mathrm{d}\Omega_0 + \int_{\Omega_0} \underline{\underline{\Sigma}}(\underline{y}_h^{(k)}) : \mathrm{d}_y^2 \underline{\underline{e}}(\underline{v}^\flat, \underline{w}^\flat) \, \mathrm{d}\Omega_0 \\ & + P_{\mathrm{L}}^{\mathrm{V}} \int_{\mathcal{E}n_{\mathrm{L}}^{(k)}} \underline{v}^\flat \cdot \mathrm{d}_y \big(\underline{n}_{\mathrm{L}}^{(k)} \mathrm{d}\sigma \big) \cdot \underline{w}^\flat, \end{aligned}$$

where $\mathcal{E}n_{\mathrm{L}}^{(k)}$ is the endocardium deformed y the displacement $\underline{y}_h^{(k)}$ admitting $\underline{n}_L^{(k)}$ as its outer normal vector field. In this expression we have used the notation

$$\mathrm{d}_y^2 \underline{\underline{e}}(\underline{v}^\flat, \underline{w}^\flat) = \mathrm{d}_y(\mathrm{d}_y \underline{\underline{e}} \cdot \underline{v}^\flat) \cdot \underline{w}^\flat = \frac{1}{2} \left(\underline{\underline{\nabla}}_{\underline{\xi}} \underline{v}^{\flat\,\top} \cdot \underline{\underline{\nabla}}_{\underline{\xi}} \underline{w}^\flat + \underline{\underline{\nabla}}_{\underline{\xi}} \underline{w}^{\flat\,\top} \cdot \underline{\underline{\nabla}}_{\underline{\xi}} \underline{v}^\flat \right),$$

which is independent of the current deformation. If we denote by $\{\underline{\varphi}_i\}_{i=1}^{\mathrm{N}_h}$ the set of basis functions of $\mathcal{X}_h^y$, the matrices appearing in the algorithm are

$$\left|\begin{aligned} &\mathbb{K}(\underline{y}_h^{(k)}) = \left(\int_{\Omega_0} \mathrm{d}_y\underline{\underline{\Sigma}}(\underline{y}_h^{(k)})\cdot\underline{\varphi}_j : \mathrm{d}_y\underline{\underline{e}}^{(k)}\cdot\underline{\varphi}_i \;+\; \underline{\underline{\Sigma}}(\underline{y}_h^{(k)}) : \mathrm{d}_y^2\underline{\underline{e}}(\underline{\varphi}_i,\underline{\varphi}_j)\mathrm{d}\Omega_0\right)_{i,j=1}^{\mathrm{N}_h}, \\ \\ &\mathbb{P}(\underline{y}_h^{(k)}) = \left(P_{\mathrm{L}}^{\mathrm{v}}\int_{\mathcal{E}n_{\mathrm{L}}^{(k)}} \underline{\varphi}_i\cdot\mathrm{d}_y\underline{n}_{\mathrm{L}}^{(k)}\mathrm{d}\sigma\cdot\underline{\varphi}_j\right)_{i,j=1}^{\mathrm{N}_h}. \end{aligned}\right. \tag{1.18}$$

Let $\overrightarrow{V^\flat} \in \mathbb{R}^{\mathrm{N}_h}$ be the vector regrouping the degrees of freedom of a test function $\underline{v}_h^\flat \in \mathcal{X}^y$, Newton's method – described in (1.17) – reads

$$\left(\mathbb{K}(\underline{y}_h^{(k)}) + \mathbb{P}(\underline{y}_h^{(k)})\right)(\overrightarrow{Y}^{(k+1)} - \overrightarrow{Y}^{(k)}) = -\overrightarrow{R}(\underline{y}_h^{(k)}), \tag{1.19}$$

where $\overrightarrow{R}$ is the residual obtained from

$$\overrightarrow{R}(\underline{y}_h^{(k)}) = \left(\int_{\Omega_0} \underline{\underline{\Sigma}}(\underline{y}_h^{(k)}) : \mathrm{d}_y\underline{\underline{e}}^{(k)}\cdot\underline{\varphi}_i\,\mathrm{d}\Omega_0 + P_{\mathrm{L}}^{\mathrm{v}}\int_{\mathcal{E}n_{\mathrm{L}}^{(k)}} \underline{n}_{\mathrm{L}}^{(k)}\cdot\underline{\varphi}_i\mathrm{d}\sigma\right)_{i=1}^{\mathrm{N}_h}. \tag{1.20}$$

Tangent stiffness In the sequel we give some complementary details on the first operator appearing in (1.20) referred to as *tangent stiffness*. Using the expression of the stress tensor with respect to the invariant we have, for a test function $\underline{v}^\flat \in \mathcal{X}^y$,

$$\begin{aligned} \mathrm{d}_y\underline{\underline{\Sigma}}(\underline{y}_h^{(k)})\cdot\underline{v}^\flat &= 2\sum_{i=1}^{4}\Big(\mathrm{d}_y\frac{\partial W^{\mathrm{e}}}{\partial I_i}\cdot\underline{v}^\flat\frac{\partial I_i}{\partial\underline{\underline{C}}} + \frac{\partial W^{\mathrm{e}}}{\partial I_i}\mathrm{d}_y\frac{\partial I_i}{\partial\underline{\underline{C}}}\cdot\underline{v}^\flat\Big) \\ &= 2\sum_{i=1}^{4}\sum_{j=1}^{4}\frac{\partial^2 W^{\mathrm{e}}}{\partial I_j\partial I_i}\Big(\frac{\partial I_j}{\partial\underline{\underline{C}}} : \big(\mathrm{d}_y\underline{\underline{C}}^{(k)}\cdot\underline{v}^\flat\big)\Big)\frac{\partial I_i}{\partial\underline{\underline{C}}} + 2\sum_{i=1}^{4}\frac{\partial W^{\mathrm{e}}}{\partial I_i}\frac{\partial^2 I_i}{\partial\underline{\underline{C}}^2} : \big(\mathrm{d}_y\underline{\underline{C}}^{(k)}\cdot\underline{v}^\flat\big) \\ &= 4\sum_{i=1}^{4}\sum_{j=1}^{4}\frac{\partial^2 W^{\mathrm{e}}}{\partial I_j\partial I_i}\frac{\partial I_j}{\partial\underline{\underline{e}}} : \mathrm{d}_y\underline{\underline{e}}^{(k)}\cdot\underline{v}^\flat\,\frac{\partial I_i}{\partial\underline{\underline{e}}} + 4\sum_{i=1}^{4}\frac{\partial W^{\mathrm{e}}}{\partial I_i}\frac{\partial^2 I_i}{\partial\underline{\underline{e}}^2}\,\mathrm{d}_y\underline{\underline{e}}^{(k)}\cdot\underline{v}^\flat, \end{aligned}$$

where the expressions of the energy derivative – and its second derivative – are given in (1.19). For the second part of the tangent stiffness operator we just recall that

$$\mathrm{d}_y\underline{\underline{e}}^{(k)}\cdot\underline{v}^\flat = \frac{1}{2}\left(\underline{\underline{F}}^{\top}(\underline{y}_h^{(k)})\cdot\underline{\underline{\nabla}}_{\xi}\underline{v}^\flat + \underline{\underline{\nabla}}_{\xi}\underline{v}^{\flat\top}\cdot\underline{\underline{F}}(\underline{y}_h^{(k)})\right).$$

Remark 5. *Traditionally the two terms of operator* $\mathbb{K}(\underline{y}_h^{(k)})$ *appearing in* (1.18) *are written as*

$$\mathbb{K}(\underline{y}_h^{(k)}) = (\mathbb{K}_{\mathrm{L}} + \mathbb{K}_{\mathrm{NL}})(\underline{y}_h^{(k)}),$$

the first term is called the linear stiffness since it is based on the derivative of the stress tensor whereas the second term is called the nonlinear stiffness.

Tangent following pressure Concerning the second part of the tangent operator where the cavity pressure appears. If we take two finite element test functions $\underline{v}_h^\flat, \underline{w}_h^\flat \in \mathcal{X}_h^y$, this operator reads

$$\mathrm{d}_y \mathcal{P}^{\mathrm{ext}}(\underline{y}_h^{(k)}, \underline{v}_h^\flat) \cdot \underline{w}_h^\flat = P_{\mathrm{L}}^{\mathrm{v}} \int_{\mathcal{E}n_{\mathrm{L}}^{(k)}} \underline{v}_h^\flat \cdot \big(\mathrm{d}_y \underline{n}_{\mathrm{L}}^{(k)} \mathrm{d}\sigma\big) \cdot \underline{w}_h^\flat. \tag{1.21}$$

In order to give a computational expression of this operator we will use the fact that we consider a $\mathcal{P}_1$ finite element space and we start by decomposing the integral on each triangle of the considered surface (in our case the endo- or epicardium of the ventricles). On each triangle, the spatial coordinate in the deformed configuration can be uniquely expressed using a local barycentric coordinate system

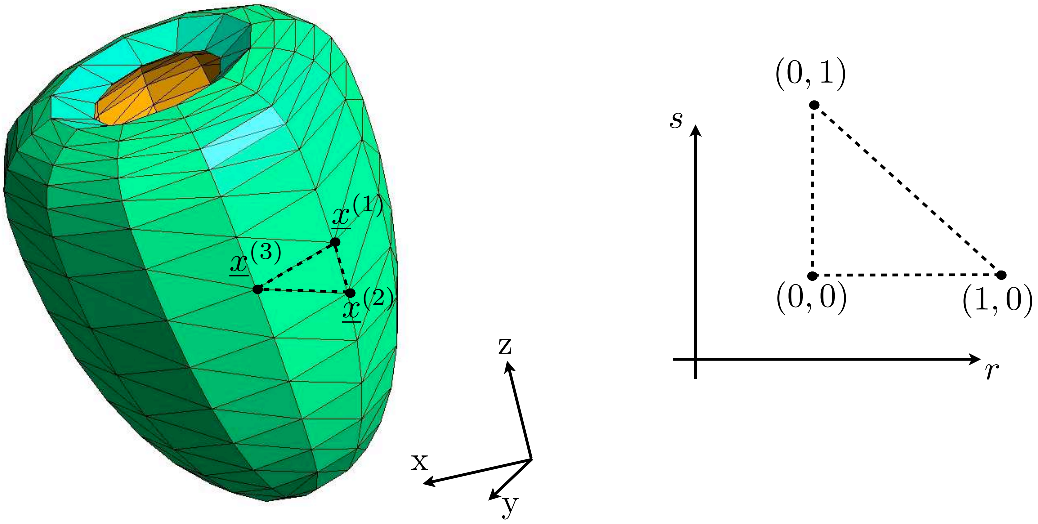

Figure 1.4: Local coordinate system to compute following pressure tangent operator.

$$\underline{x} = \underline{x}(r,s) = \sum_{i=1}^{3} \lambda_i(r,s)\underline{x}^{(i)},$$

where $\{\lambda_i(r,s)\}_{i=1}^3$ are the two dimensional linear shape functions

$$\begin{cases} \lambda_1(r,s) = r, \\ \lambda_2(r,s) = s, \\ \lambda_3(r,s) = 1 - r - s, \end{cases}$$

and $\{\underline{x}^{(i)}\}_{i=1}^3$ are the vertices of a deformed triangle, see Figure 1.4. With these notations, the surface differential of the triangles of the deformed surface are given by

$$\underline{n}\,\mathrm{d}\sigma = \frac{\partial \underline{x}}{\partial r} \wedge \frac{\partial \underline{x}}{\partial s}\,\mathrm{d}r\mathrm{d}s.$$

One can easily verify that

$$\begin{cases} \dfrac{\partial \lambda_1}{\partial r}(r,s) = 1, \quad \dfrac{\partial \lambda_1}{\partial s}(r,s) = 0, \\[2ex] \dfrac{\partial \lambda_2}{\partial r}(r,s) = 0, \quad \dfrac{\partial \lambda_2}{\partial s}(r,s) = 1, \\[2ex] \dfrac{\partial \lambda_3}{\partial r}(r,s) = -1, \quad \dfrac{\partial \lambda_3}{\partial s}(r,s) = -1, \end{cases}$$

entailing

$$\frac{\partial \underline{x}}{\partial r} = \underline{x}^{(1)} - \underline{x}^{(3)} = \underline{e}^{(2)}, \quad \frac{\partial \underline{x}}{\partial s} = \underline{x}^{(2)} - \underline{x}^{(3)} = \underline{e}^{(1)}.$$

Moreover, any restriction of a function in $\mathcal{X}_h^y$ to a triangle can also be expressed using the local map, namely

$$\underline{w}_h^\flat(r,s) = \sum_{i=1}^{3} \lambda_i(r,s)\underline{w}^{\flat(i)},$$

where $\{\underline{w}^{\flat(i)}\}_{i=1}^3$ are the nodal values of the finite element function $\underline{w}_h^\flat$. Using this representation we obtain, at a local scale, the following expression

$$\mathrm{d}_y\underline{n}\,\mathrm{d}\sigma \cdot \underline{w}_h^\flat = \frac{\partial \underline{w}_h^\flat}{\partial r} \wedge \frac{\partial \underline{x}}{\partial s} + \frac{\partial \underline{x}}{\partial r} \wedge \frac{\partial \underline{w}_h^\flat}{\partial s} = (\underline{w}^{\flat(1)} - \underline{w}^{\flat(3)}) \wedge \underline{e}^{(1)} + \underline{e}^{(2)} \wedge (\underline{w}^{\flat(2)} - \underline{w}^{\flat(3)}).$$

Introducing the compact notation

$$\Big[\frac{\partial \underline{x}}{\partial s} \wedge\ \Big] = \begin{pmatrix} 0 & -e_3^{(1)} & e_2^{(1)} \\ e_3^{(1)} & 0 & -e_1^{(1)} \\ -e_2^{(1)} & e_1^{(1)} & 0 \end{pmatrix} \quad \text{and} \quad \Big[\frac{\partial \underline{x}}{\partial r} \wedge\ \Big] = \begin{pmatrix} 0 & -e_3^{(2)} & e_2^{(2)} \\ e_3^{(2)} & 0 & -e_1^{(2)} \\ -e_2^{(2)} & e_1^{(2)} & 0 \end{pmatrix},$$

along with the 3×9 local matrix $\mathbb{Q}$ defined by

$$\mathbb{Q} = \begin{pmatrix} \mathbb{O}_{3\times3} & \Big[\dfrac{\partial \underline{x}}{\partial r} \wedge\ \Big] & -\Big[\dfrac{\partial \underline{x}}{\partial r} \wedge\ \Big] \end{pmatrix} + \begin{pmatrix} -\Big[\dfrac{\partial \underline{x}}{\partial s} \wedge\ \Big] & \mathbb{O}_{3\times3} & \Big[\dfrac{\partial \underline{x}}{\partial s} \wedge\ \Big] \end{pmatrix},$$

then

$$\frac{\partial \underline{w}_h^\flat}{\partial r} \wedge \frac{\partial \underline{x}}{\partial s} + \frac{\partial \underline{x}}{\partial r} \wedge \frac{\partial \underline{w}_h^\flat}{\partial s} = \mathbb{Q}\begin{pmatrix} \underline{w}^{\flat(1)} \\ \underline{w}^{\flat(2)} \\ \underline{w}^{\flat(3)} \end{pmatrix}.$$

Finally, defining $\mathbb{I}$ the 3×9 local matrix responsible for the numerical integration of a finite element function on a triangle, that is to say

$$\mathbb{I} = \begin{pmatrix} 1/6 & & & 1/6 & & & 1/6 & & \\ & 1/6 & & & 1/6 & & & 1/6 & \\ & & 1/6 & & & 1/6 & & & 1/6 \end{pmatrix},$$

then the local tangent operator of the following pressure operator is decomposed into

$$P_{\mathrm{L}}^{\mathrm{v}} \int_{r,s} \underline{v}_h^{\flat} \cdot \frac{\partial \underline{w}_h^{\flat}}{\partial r} \wedge \frac{\partial \underline{x}}{\partial s} + \frac{\partial \underline{x}}{\partial r} \wedge \frac{\partial \underline{w}_h^{\flat}}{\partial s} \, \mathrm{d}r\mathrm{d}s = P_{\mathrm{L}}^{\mathrm{v}} \begin{pmatrix} \underline{v}^{\flat(1)} \\ \underline{v}^{\flat(2)} \\ \underline{v}^{\flat(3)} \end{pmatrix}^{\mathsf{T}} \mathbb{I}^{\mathsf{T}} \mathbb{Q} \begin{pmatrix} \underline{w}^{\flat(1)} \\ \underline{w}^{\flat(2)} \\ \underline{w}^{\flat(3)} \end{pmatrix}. \tag{1.22}$$

Linearized passive law for studying incompressibility We have considered so far that the heart tissue is a nearly incompressible material. As we will see, this modeling aspect may introduce some difficulties when carrying out the numerical discretization of the model. In this section we give some insights on why the standard finite element space may fail to provide reasonable solutions in that case – see [Bathe, 1996] for an extensive description of the subject. To do so we will consider the linearized stress tensor around the reference configuration, which is obtained by conserving only the linear terms with respect to $\underline{\underline{e}}$ when expanding the expression (1.12). To start with, we give the extension of the invariants

$$\left| \begin{aligned} & I_1 = \mathrm{tr}(\underline{\underline{C}}) = 3 + 2\mathrm{tr}(\underline{\underline{e}}), \\ & I_2 = \frac{1}{2}\big((\mathrm{tr}(\underline{\underline{C}}))^2 - \mathrm{tr}(\underline{\underline{C}}^2)\big) = 3 + 4\mathrm{tr}(\underline{\underline{e}}) + O(\|\underline{\underline{e}}\|^2), \\ & I_3 = \det(\underline{\underline{C}}) = 1 + 2\mathrm{tr}(\underline{\underline{e}}) + O(\|\underline{\underline{e}}\|^2), \\ & I_4 = \underline{n}_0 \cdot \underline{\underline{C}} \cdot \underline{n}_0 = 1 + 2\underline{n}_0 \cdot \underline{\underline{e}} \cdot \underline{n}_0. \end{aligned} \right. \tag{1.23}$$

To linearize (1.12) we start by giving the extension of the first term, that is to say the derivative of the elastic energy, namely

$$\frac{\partial W^{\mathrm{e}}}{\partial I_i} = \frac{\partial W^{\mathrm{e}}}{\partial I_i}\Big|_{\underline{\underline{e}}=0} + \sum_{j=1}^{4} \frac{\partial^2 W^{\mathrm{e}}}{\partial I_i \partial I_j}\Big|_{\underline{\underline{e}}=0} \frac{\partial I_j}{\partial \underline{\underline{e}}}\Big|_{\underline{\underline{e}}=0} (\underline{\underline{e}}) + O(\|\underline{\underline{e}}\|^2).$$

From (1.25) we obtain

$$\left| \begin{aligned} & \frac{\partial I_1}{\partial \underline{\underline{e}}}\Big|_{\underline{\underline{e}}=0} (\underline{\underline{e}}) = 2\mathrm{tr}(\underline{\underline{e}}), \quad \frac{\partial I_2}{\partial \underline{\underline{e}}}\Big|_{\underline{\underline{e}}=0} (\underline{\underline{e}}) = 4\mathrm{tr}(\underline{\underline{e}}), \\ & \frac{\partial I_3}{\partial \underline{\underline{e}}}\Big|_{\underline{\underline{e}}=0} (\underline{\underline{e}}) = 2\mathrm{tr}(\underline{\underline{e}}), \quad \frac{\partial I_4}{\partial \underline{\underline{e}}}\Big|_{\underline{\underline{e}}=0} (\underline{\underline{e}}) = 2\underline{n}_0 \cdot \underline{\underline{e}} \cdot \underline{n}_0, \end{aligned} \right.$$

which gives us

$$\begin{aligned} \frac{\partial W^{\mathrm{e}}}{\partial I_i} = \frac{\partial W^{\mathrm{e}}}{\partial I_i}\Big|_{\underline{\underline{e}}=0} + 2\left(\frac{\partial^2 W^{\mathrm{e}}}{\partial I_i \partial I_1} + 2\frac{\partial^2 W^{\mathrm{e}}}{\partial I_i \partial I_2} + \frac{\partial^2 W^{\mathrm{e}}}{\partial I_i \partial I_3}\right)\Big|_{\underline{\underline{e}}=0} \mathrm{tr}(\underline{\underline{e}}) \\ + 2\frac{\partial^2 W^{\mathrm{e}}}{\partial I_i \partial I_4}\Big|_{\underline{\underline{e}}=0} \underline{n}_0 \cdot \underline{\underline{e}} \cdot \underline{n}_0 + O(\|\underline{\underline{e}}\|^2). \end{aligned} \tag{1.24}$$

We continue our linearization procedure by treating the derivatives of the invariants with respect to the Cauchy-Green tensor appearing in (1.12),

$$\left|\begin{aligned}
&\frac{\partial I_1}{\partial \underline{\underline{C}}} = \underline{\underline{\mathbb{1}}},\\
&\frac{\partial I_2}{\partial \underline{\underline{C}}} = I_1\underline{\underline{\mathbb{1}}} - \underline{\underline{C}} = 2\underline{\underline{\mathbb{1}}} + 2\mathrm{tr}(\underline{\underline{e}})\underline{\underline{\mathbb{1}}} - 2\underline{\underline{e}} + O(\|\underline{\underline{e}}\|^2),\\
&\frac{\partial I_3}{\partial \underline{\underline{C}}} = I_3\underline{\underline{C}}^{-1} = \underline{\underline{\mathbb{1}}} + 2\mathrm{tr}(\underline{\underline{e}})\underline{\underline{\mathbb{1}}} - 2\underline{\underline{e}} + O(\|\underline{\underline{e}}\|^2),\\
&\frac{\partial I_4}{\partial \underline{\underline{C}}} = \underline{n}_0 \otimes \underline{n}_0.
\end{aligned}\right. \tag{1.25}$$

Finally, from (1.25) and (1.12), we obtain

$$\underline{\underline{\Sigma}} = 2\frac{\partial W^{\mathrm{e}}}{\partial I_1}\underline{\underline{\mathbb{1}}} + 2\frac{\partial W^{\mathrm{e}}}{\partial I_2}\big(2\underline{\underline{\mathbb{1}}} + 2\mathrm{tr}(\underline{\underline{e}})\underline{\underline{\mathbb{1}}} - 2\underline{\underline{e}}\big) + 2\frac{\partial W^{\mathrm{e}}}{\partial I_3}\big(\underline{\underline{\mathbb{1}}} + 2\mathrm{tr}(\underline{\underline{e}})\underline{\underline{\mathbb{1}}} - 2\underline{\underline{e}}\big) + 2\frac{\partial W^{\mathrm{e}}}{\partial I_4}\underline{n}_0 \otimes \underline{n}_0 + O(\|\underline{\underline{e}}\|^2),$$

which, using (1.24), leads to

$$\underline{\underline{\Sigma}} = \underline{\underline{\Sigma}}_0 \; + \; \lambda\mathrm{tr}(\underline{\underline{e}})\underline{\underline{\mathbb{1}}} \; + \; 2\mu\underline{\underline{e}} \; + \; \underline{n}_0 \cdot \underline{\underline{e}} \cdot \underline{n}_0 \left(\alpha\underline{\underline{\mathbb{1}}} + \beta\underline{n}_0 \otimes \underline{n}_0\right) \; + \; \gamma\mathrm{tr}(\underline{\underline{e}})\underline{n}_0 \otimes \underline{n}_0 + O(\|\underline{\underline{e}}\|^2), \tag{1.26}$$

with the following detailed expressions of the coefficients with respect to the derivative of the elastic potential

$$\left|\begin{aligned}
&\underline{\underline{\Sigma}}_0 = 2\left(\frac{\partial W^{\mathrm{e}}}{\partial I_1} + 2\frac{\partial W^{\mathrm{e}}}{\partial I_2} + \frac{\partial W^{\mathrm{e}}}{\partial I_3}\right)\Big|_{\underline{\underline{e}}=0}\underline{\underline{\mathbb{1}}} + 2\frac{\partial W^{\mathrm{e}}}{\partial I_4}\Big|_{\underline{\underline{e}}=0}\underline{n}_0 \otimes \underline{n}_0,\\
&\lambda = 4\left(\frac{\partial^2 W^{\mathrm{e}}}{\partial I_1^2} + 4\frac{\partial^2 W^{\mathrm{e}}}{\partial I_2^2} + \frac{\partial^2 W^{\mathrm{e}}}{\partial I_3^2} + 4\frac{\partial^2 W^{\mathrm{e}}}{\partial I_1 \partial I_2} + 2\frac{\partial^2 W^{\mathrm{e}}}{\partial I_1 \partial I_3} + 4\frac{\partial^2 W^{\mathrm{e}}}{\partial I_2 \partial I_3} + \frac{\partial W^{\mathrm{e}}}{\partial I_2} + \frac{\partial W^{\mathrm{e}}}{\partial I_3}\right)\Big|_{\underline{\underline{e}}=0},\\
&\mu = -2\left(\frac{\partial W^{\mathrm{e}}}{\partial I_2} + \frac{\partial W^{\mathrm{e}}}{\partial I_3}\right)\Big|_{\underline{\underline{e}}=0},\\
&\alpha = 2\left(\frac{\partial^2 W^{\mathrm{e}}}{\partial I_1 \partial I_4} + 4\frac{\partial^2 W^{\mathrm{e}}}{\partial I_2 \partial I_4} + 2\frac{\partial^2 W^{\mathrm{e}}}{\partial I_4^2}\right)\Big|_{\underline{\underline{e}}=0},\\
&\beta = 4\frac{\partial^2 W^{\mathrm{e}}}{\partial I_4^2}\Big|_{\underline{\underline{e}}=0},\\
&\gamma = 4\left(\frac{\partial^2 W^{\mathrm{e}}}{\partial I_1 \partial I_4} + 2\frac{\partial^2 W^{\mathrm{e}}}{\partial I_2 \partial I_4} + \frac{\partial^2 W^{\mathrm{e}}}{\partial I_3 \partial I_4}\right)\Big|_{\underline{\underline{e}}=0}.
\end{aligned}\right. \tag{1.27}$$

Remark 6. *If the reference configuration is chosen to be at rest, that is to say stress-free, then the prestress field* $\underline{\underline{\Sigma}}_0$ *is necessarily equals to zero. If the elastic potential does not depend on the* *fourth invariant, as the Ciarlet-Gaymonat law for example (see* (1.9)*) then the linearized constitutive equation is in fact the Hooke law (as mentioned previously) where the expressions of the Lamé coefficients are given by the second and third equality in* (1.27)*.*

From the expression (1.15) we can derive the expression of the linearized constitutive law depending on the different parameters of the passive law. Namely, using the fact that

$$I_1\Big|_{\underline{\underline{e}}=0} = 3, \quad I_2\Big|_{\underline{\underline{e}}=0} = 3, \quad I_3\Big|_{\underline{\underline{e}}=0} = 1, \quad I_4\Big|_{\underline{\underline{e}}=0} = 1,$$

we obtain

$$\frac{\partial W^{\mathrm{e}}}{\partial I_1}\Big|_{\underline{\underline{e}}=0} = \mu_1, \quad \frac{\partial W^{\mathrm{e}}}{\partial I_2}\Big|_{\underline{\underline{e}}=0} = \mu_2, \quad \frac{\partial W^{\mathrm{e}}}{\partial I_3}\Big|_{\underline{\underline{e}}=0} = -\mu_1 - 2\mu_2, \quad \frac{\partial W^{\mathrm{e}}}{\partial I_4}\Big|_{\underline{\underline{e}}=0} = 0,$$

which directly implies that

$$\underline{\underline{\Sigma}}_0 = 0 \quad \text{and} \quad \mu = 2(\mu_1 + \mu_2). \tag{1.28}$$

The symmetric second derivative of the elastic potential evaluated at zero reads

$$\left(\frac{\partial^2 W^{\mathrm{e}}}{\partial I_i \partial I_j}\right)_{i,j=1}^{4}\Bigg|_{\underline{\underline{e}}=0} = \begin{pmatrix} 2C_0C_1 & 0 & -2C_0C_1 - \frac{1}{3}\mu_1 & 0 \\ \cdot & 0 & -\frac{2}{3}\mu_2 & 0 \\ \cdot & \cdot & 2C_0C_1 + \frac{2}{9}C_2C_3 + \frac{4}{3}\mu_1 + \frac{10}{3}\mu_2 + \frac{1}{4}\kappa & -\frac{2}{3}C_2C_3 \\ \cdot & \cdot & \cdot & 2C_2C_3 \end{pmatrix},$$

leading to

$$\lambda = -\frac{4}{3}(\mu_1 + \mu_2) + \kappa + \frac{8}{9}C_2C_3, \quad \alpha = 4C_2C_3, \quad \beta = 8C_2C_3 \quad \text{and} \quad \gamma = -\frac{8}{3}C_2C_3. \tag{1.29}$$

Regrouping (1.28) and (1.29) and assuming that only small displacements occur, we finally obtain the desired expression of the linearized stress tensor

$$\begin{aligned} \underline{\underline{\sigma}} = \left(-\frac{4}{3}(\mu_1 + \mu_2) + \kappa + \frac{8}{9}C_2C_3\right)\mathrm{tr}(\underline{\underline{\varepsilon}})\underline{\underline{\mathbb{1}}} + 4(\mu_1 + \mu_2)\underline{\underline{\varepsilon}} \\ + 4C_2C_3\left(\underline{n}_0 \cdot \underline{\underline{\varepsilon}} \cdot \underline{n}_0(\underline{\underline{\mathbb{1}}} + 2\underline{n}_0 \otimes \underline{n}_0) - \frac{2}{3}\mathrm{tr}(\underline{\underline{\varepsilon}})\underline{n}_0 \otimes \underline{n}_0\right). \end{aligned} \tag{1.30}$$

Incompressibility and numerical locking For the sake of simplicity, as the goal of this section is to provide the main components to understand the difficulty lying behind incompressible material, we assume that we have an isotropic passive law – obtained by setting, for example, $C_2C_3 = 0$. The linearized constitutive law is equivalent to the one obtained after linearization of the Ciarley-Gaymonat stress-strain law and reduces

$$\underline{\underline{\sigma}} = \left(-\frac{4}{3}(\mu_1 + \mu_2) + \kappa\right)\mathrm{tr}(\underline{\underline{\varepsilon}})\underline{\underline{\mathbb{1}}} + 4(\mu_1 + \mu_2)\underline{\underline{\varepsilon}} = \lambda\mathrm{tr}(\underline{\underline{\varepsilon}})\underline{\underline{\mathbb{1}}} + 2\mu\underline{\underline{\varepsilon}}.$$

Remark 7. *In this particular case of linear isotropic constitutive law we can see that the Lamé coefficients necessarily verify two constrains. The first one being that*

$$\mu > 0, \tag{1.31}$$

and is obtained by considering pure deviatoric deformation characterised by $\mathrm{tr}(\underline{\underline{\varepsilon}}) = 0$. *More precisely, let* $\underline{y}_d$ *be a displacement of the solid corresponding to a deviatoric deformation, the mechanical energy needed to perform this deformation is obtained by*

$$\int_{\Omega_0} \underline{\underline{\sigma}}(\underline{\underline{\varepsilon}}(\underline{y}_d)) : \underline{\underline{\varepsilon}}(\underline{y}_d)\, \mathrm{d}\Omega_0 = 2\mu \int_{\Omega_0} \underline{\underline{\varepsilon}}(\underline{y}_d) : \underline{\underline{\varepsilon}}(\underline{y}_d)\, \mathrm{d}\Omega_0 \ > 0,$$

justifying the positivity of μ. *The second one is obtained by considering contraction-extension deformation of the form* $\underline{\underline{\varepsilon}} = \alpha\underline{\underline{\mathbb{1}}}$. *For this type of deformation the obtained stress is*

$$\underline{\underline{\sigma}} = (3\lambda + 2\mu)\alpha\underline{\underline{\mathbb{1}}},$$

as expected from standard linear isotropic material, the adequate stress response to contraction-extension deformation is compression or tension respectively, hence $(3\lambda + 2\mu)\alpha$ *is of the same sign as* α *or equivalently*

$$3\lambda + 2\mu > 0. \tag{1.32}$$

The assumption of small displacements implies that the pressure terms in the static load problem does not depend of the deformation. Therefore the problem (1.16) takes the following fully linear form : find $\underline{y} \in \mathcal{X}^y$, such that $\forall \underline{v}^\flat \in \mathcal{X}^y$

$$a(\underline{y}, \underline{v}^\flat) = l(\underline{v}^\flat),$$

where,

$$a(\underline{y}, \underline{v}^\flat) = \int_{\Omega_0} \underline{\underline{\sigma}}(\underline{y}) : \underline{\underline{\varepsilon}}(\underline{v}^\flat)\, \mathrm{d}\Omega_0 \quad \text{and} \quad l(\underline{v}^\flat) = -P_L \int_{\mathcal{E}n_{\mathrm{L}0}} \underline{v}^\flat \cdot \underline{n}\, \mathrm{d}\sigma_0. \tag{1.33}$$

As we have done in the case of hyperelasticity we can provide a linearized pressure-deviatoric decomposition

$$\underline{\underline{\varepsilon}}_d = \underline{\underline{\varepsilon}} - \frac{1}{3}\mathrm{tr}(\underline{\underline{\varepsilon}})\underline{\underline{\mathbb{1}}},$$

leading to the following expression of the bilinear form

$$a(\underline{y}, \underline{v}^\flat) = \int_{\Omega_0} \frac{3\lambda + 2\mu}{3}\mathrm{tr}(\underline{\underline{\varepsilon}}(\underline{y}))\mathrm{tr}(\underline{\underline{\varepsilon}}(\underline{v}^\flat)) + 2\mu\underline{\underline{\varepsilon}}_d(\underline{y}) : \underline{\underline{\varepsilon}}_d(\underline{v}^\flat)\, \mathrm{d}\Omega_0.$$

For this type of problem, the adequate functional space is $\mathcal{X}^y = \mathcal{H}^1(\Omega_0)^3$. As a remark we can verify that this problem is well-posed. Indeed we note that the inequalities (1.31) and (1.32) imply

$$\exists C > 0, \quad \text{such that} \quad \forall \underline{v}^\flat \in \mathcal{H}^1(\Omega_0)^3 \quad a(\underline{v}^\flat, \underline{v}^\flat) \ \geq \ C\|\underline{\underline{\varepsilon}}(\underline{v}^\flat)\|^2_{\mathcal{L}^2(\Omega_0)^3}.$$

The Korn inequality [Le Dret, 2004, Ciarlet, 1988] insures the control of the $\mathcal{H}^1(\Omega_0)^3$ norm by the right hand-side of the previous estimate so that we can apply the Lax-Milgram theorem to prove the well-posedness of the problem.

Remark 8. *This problem favours solutions that satisfy the nearly incompressibility property of the material. To see this it is sufficient to recall that the static load problem* (1.33) *is in fact the optimality condition of order one of the following minimisation problem*

$$\min_{\underline{v}^\flat \in \mathcal{X}^y} \frac{1}{2}a(\underline{v}^\flat, \underline{v}^\flat) - l(\underline{v}^\flat).$$

Hence, considering all other parameters fixed, λ *grows as* κ, *therefore the solution of this minimisation problem will tend to verify* $\mathrm{tr}(\underline{\underline{\varepsilon}}) = 0$, *which is the linearized version of the incompressibility constrain* $J = 1$.

Defining

$$\varepsilon = \sqrt{\frac{2\mu}{\lambda}},$$

we recast the bilinear form in (1.33) as

$$a(\underline{y}, \underline{v}^\flat) = 2\mu \int_{\Omega_0} \underline{\underline{\varepsilon}}(\underline{y}) : \underline{\underline{\varepsilon}}(\underline{v}^\flat)\, \mathrm{d}\Omega_0 + \varepsilon^{-2} 2\mu \int_{\Omega_0} \mathrm{tr}(\underline{\underline{\varepsilon}}(\underline{y}))\mathrm{tr}(\underline{\underline{\varepsilon}}(\underline{v}^\flat))\, \mathrm{d}\Omega_0 = a_1(\underline{y}, \underline{v}^\flat) + \varepsilon^{-2} a_2(\underline{y}, \underline{v}^\flat).$$

The spatial discrete static load problem then reads: find $\underline{y}_h \in \mathcal{X}_h^y$ such that $\forall \underline{v}_h^\flat \in \mathcal{X}_h^y$

$$a_1(\underline{y}_h, \underline{v}_h^\flat) + \varepsilon^{-2} a_2(\underline{y}_h, \underline{v}_h^\flat) = l(\underline{v}_h^\flat).$$

Classical a priori estimates for standard Galerkin approximation gives us

$$\|\underline{y} - \underline{y}_h\|_{\mathcal{H}^1(\Omega_0)^3} \le \sqrt{\frac{C}{\alpha}} \inf_{\underline{w}_h^\flat \in \mathcal{X}_h^y} \|\underline{y} - \underline{w}_h^\flat\|_{\mathcal{H}^1(\Omega_0)^3},$$

with C the continuity constant of $a_1 + \varepsilon^{-2} a_2$, which is clearly in $O(\varepsilon^{-2}\mu)$ and α the coercivity constant in $O(\mu)$. Therefore the accuracy of the numerical solution may decrease in $O(\varepsilon^{-1})$, that is to say in $O(\kappa^{\frac{1}{2}})$. In practice numerical experiments show that the discrete system behaves as an overly stiff material, the discrete solution tends to zero as κ grows. This phenomenon is called *numerical locking*.

Remark 9. *Taking into account this numerical artefact, two possible approaches can be considered. The first one is to use specific finite element spaces that verify the so-called inf-sup condition (verified by the continuous system), which leads to a locking free numerical solution but naturally increases the complexity of the implementation and the cost of the finite element procedure. The second approach – followed in our work – is to assume that the material is compressible enough so that the numerical locking is sufficiently small to be neglected with respect to other sources of error (modeling errors for instance).*

Numerical results of passive filling In the sequel we provide several numerical solutions of the static load problem expressed in (1.19) for various values of the loading and of the penalisation parameter κ. In order to have a better understanding of the numerical locking phenomenon we use different toy geometries that represent the left ventricle. These geometries differ by their number of vertices as Figures 1.5(a), 1.5(b), 1.5(c) and 1.5(d) show and are referred to by their number of tetrahedra in their thickness. For these simulations we have chosen the following set of parameters

$$\mu_1 = 0.0, \quad \mu_2 = 0.0, \quad C_0 = 1.9 \cdot 10^3, \quad C_1 = 1.1 \cdot 10^{-1}, \quad C_2 = 1.9 \cdot 10^3, \quad C_3 = 1.1 \cdot 10^{-1}.$$

As far as the boundary conditions are concerned, to block rigid modes we impose homogeneous Dirichlet boundary conditions on the base of the geometry. We plot in Figures 1.6(a), 1.6(b), 1.6(c) and 1.6(d) the evolution of the volume for various values of

$$\kappa = \{10^3, 10^4, 10^5, 5 \cdot 10^5\}.$$

For higher values of κ the continuation process used to solve the static load did not converge – mainly due to the highly nonlinear profile of the elastic potential. However, with this results, we can remark is that the *1-Tetra* clearly acts as an over-stiff material and cannot be used to obtain an accurate numerical solution. Secondly, even though the convergence process slightly deteriorates we obtain a reasonable overall behaviour. This will justify our choice when choosing the various parameters for the complete heart model.

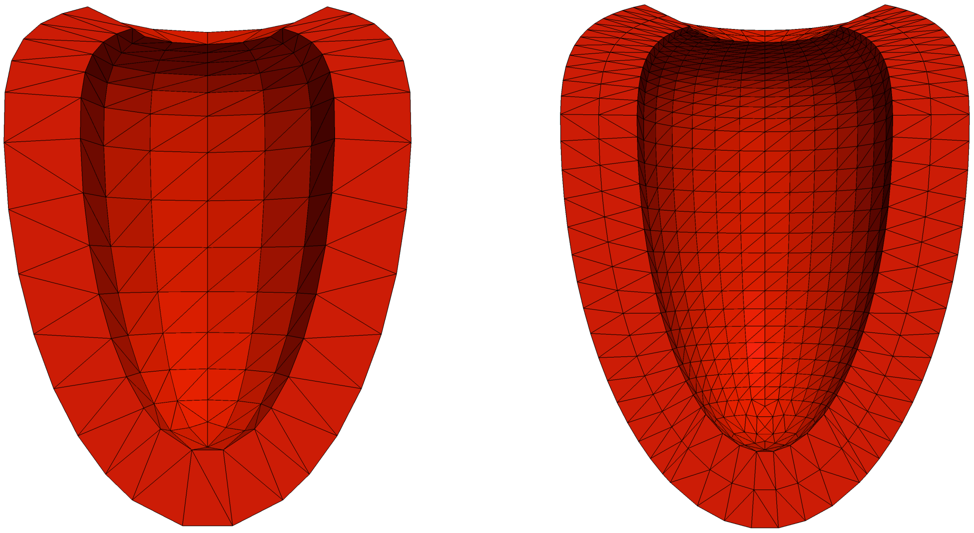

(a) *1-Tetra* mesh, 344 vertices. (b) *2-Tetra* mesh, 2628 vertices.

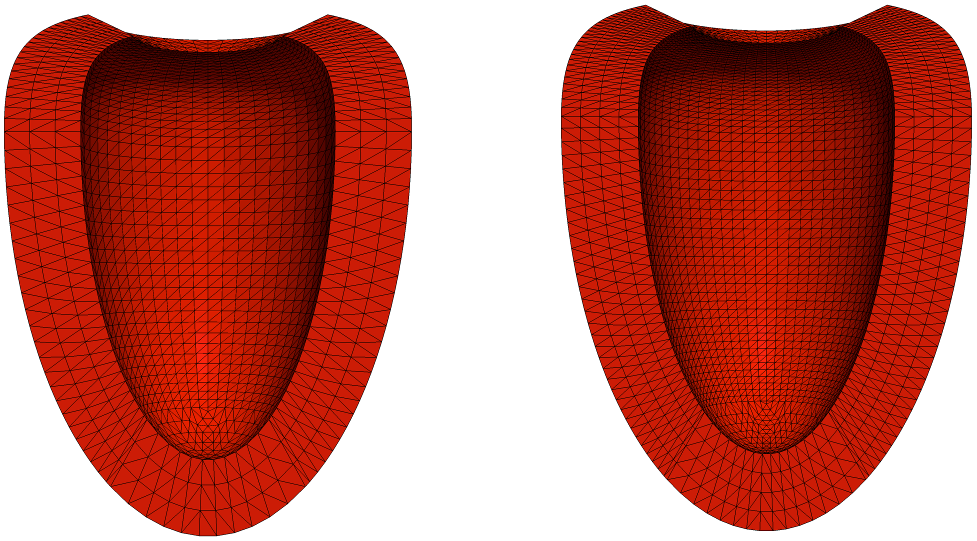

(c) *3-Tetra* mesh, 8496 vertices. (d) *4-Tetra* mesh, 19580 vertices.

Figure 1.5: Long axis view of the toy geometries, distinguished by their number of tetrahedra in their thickness.

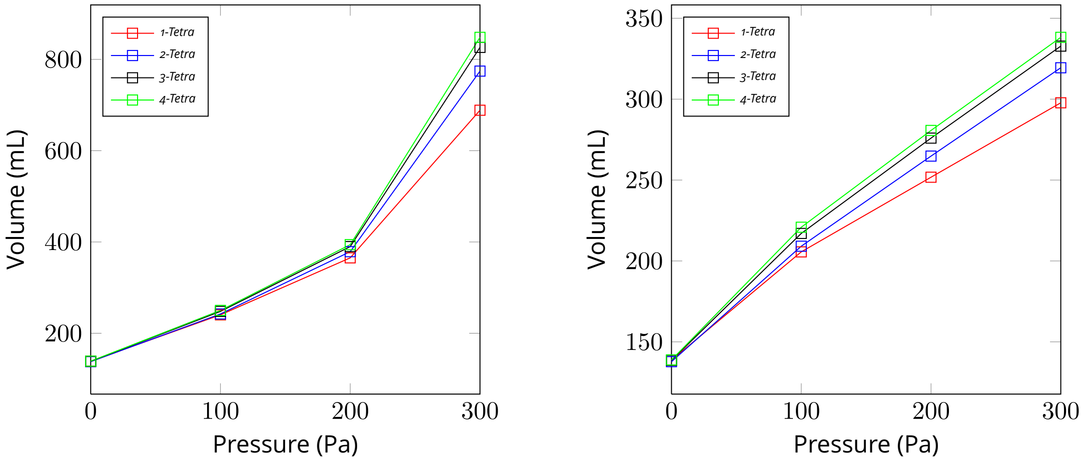

(a) Penalization parameter $\kappa = 10^3$ (b) Penalization parameter $\kappa = 10^4$

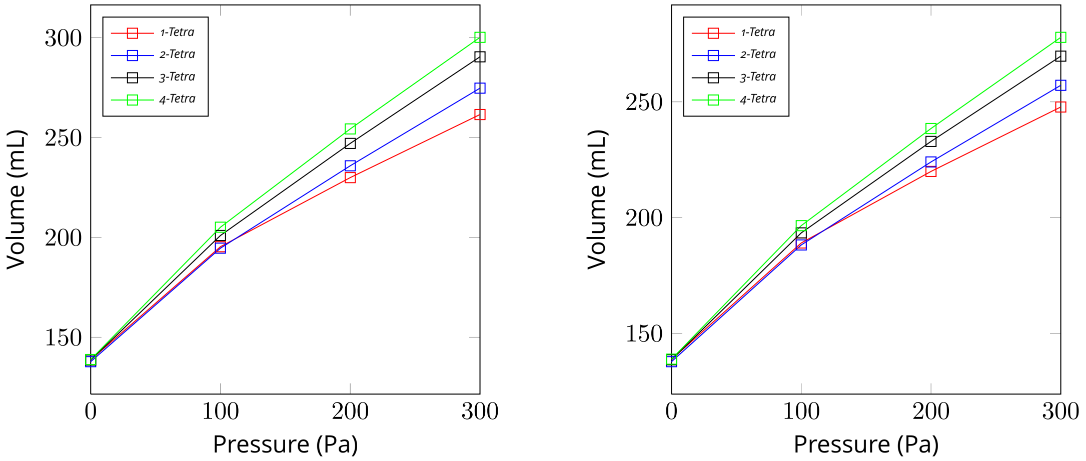

(c) Penalization parameter $\kappa = 10^5$ (d) Penalization parameter $\kappa = 5 \cdot 10^5$

Figure 1.6: Evolution of the volume for various values of the penalization parameter.

1.2 The active behavior of the heart material

In the following we will give a rapid description of the multi-scale model of the active behavior of the heart material. Readers may refer to [Sainte-Marie et al., 2006] or [Chapelle et al., 2012] for more details. Even though our work provides little improvement on this modeling part per say, we have carried out the non trivial task of implementing the algorithm obtained after discretization and presented in [Chapelle et al., 2012].

1.2.1 Active stress of the heart material

Physiological key point

Contraction of a cardiac cell

As we have already mentioned, the heart material is mostly composed of muscular cells called myocytes. At a microscale, each fiber contains a succession of *sarcomeres*, responsible for the contraction of the cell, separated by the *Z disks*. This contraction is enabled by the *myosin* – gathered in so-called *thick filaments* to form molecular motors – that can attach to the surrounding *thin filaments* made of *actin*. The structure of a myosin head attached to an actin site forms a so-called *cross-bridge*. The formations of these cross-bridges induce the sliding of the interdigitated thin and thick filaments, hence the shortening of the sarcomere, leading to a macroscopic contraction. The initial (relatively to a contraction phase and corresponding to the *prelaod* of the heart) number of cross-bridges in a sarcomere dictates the force that a single sarcomere can produce during its contraction. Naturally, as the length of the sarcomere increases the number of possible actin-myosin connections decreases leading to a loss of potential contraction. Similarly, too small values of the length of a sarcomere reduce the number of cross-bridges creations. Between these extreme situations, the sarcomere length reaches an optimum value and this particularity of the cardiac cells will be referred to as the *Frank-Starling mechanism*. In a normal state, the heart is known to be below the optimal value of the sarcomere length so that an increase of the preload leads to an increase of the active force. This feature is of utmost importance in a cardiac cycle since it enables the heart to be synchronized with the venous return.

One-dimensional active stress in the constitutive law To take into account the active properties of the heart we define a one-dimensional stress $\sigma_{1\mathrm{D}}$ in the fiber direction and we choose an additive composition law. In a general way, the stress-strain becomes

$$\underline{\underline{\Sigma}} = \underline{\underline{\Sigma}}_{\mathrm{p}} + \sigma_{1\mathrm{D}}\, \underline{n}_0 \otimes \underline{n}_0, \tag{1.34}$$

where $\underline{\underline{\Sigma}}_{\mathrm{p}}$ regroups all the passive modeling components described previously, namely,

$$\underline{\underline{\Sigma}}_{\mathrm{p}} = \frac{\partial W^{\mathrm{e}}}{\partial \underline{\underline{e}}} + \frac{\partial W^{\mathrm{v}}}{\partial \underline{\underline{\dot{e}}}}.$$

One convenient way to represent complex mechanical behaviors is to use rheological models.

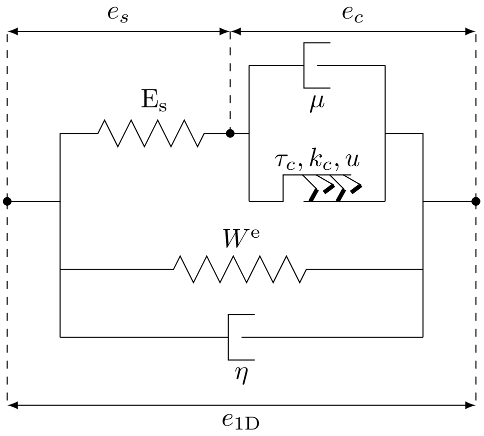

Figure 1.7: Combination of passive constitutive law (including elastic and viscous terms) with an active one-dimensional component.

Decomposition of the active stress Following [Chapelle et al., 2012] we decompose σ_{1D} into a first elastic part describing the stiffness of the Z disks and a second active component corresponding to a contraction model of the sarcomeres. The former is assumed to be a simple linear spring constitutive law, namely

$$\sigma_{\mathrm{s}} = \mathrm{E_s} e_{\mathrm{s}}, \tag{1.35}$$

and a remaining active part $(\sigma_{\mathrm{c}}, e_{\mathrm{c}})$ describing the mechanical motors in the sarcomeres. Because of large deformations, the individual strains in the active branch compose according to a multiplicative law, namely

$$1 + 2e_{\mathrm{1D}} = (1 + 2e_{\mathrm{s}})(1 + 2e_{\mathrm{c}}), \tag{1.36}$$

where we denote by $e_{\mathrm{1D}} = \underline{n}_0 \cdot \underline{\underline{e}} \cdot \underline{n}_0$ the strain along the fiber direction. The generated stresses satisfy (see [Chapelle et al., 2012])

$$\sigma_{\mathrm{1D}} = \frac{\sigma_{\mathrm{c}}}{1 + 2e_{\mathrm{s}}} = \frac{\sigma_{\mathrm{s}}}{1 + 2e_{\mathrm{c}}}. \tag{1.37}$$

Equation (1.36) enables us to build a relation between the one-dimensional strain e_{1D} and the strain in the sarcomere e_{c}. Combining (1.36), (1.37) and (1.35) we obtain

$$\sigma_{\mathrm{c}} = \frac{\mathrm{E_s}}{(1 + 2e_{\mathrm{c}})} \left(\frac{1}{2} \frac{1 + 2e_{\mathrm{1D}}}{1 + 2e_{\mathrm{c}}} - \frac{1}{2} \right) \frac{1 + 2e_{\mathrm{1D}}}{1 + 2e_{\mathrm{c}}} = \mathrm{E_s} \frac{e_{\mathrm{1D}} - e_{\mathrm{c}}}{(1 + 2e_{\mathrm{c}})^3} (1 + 2e_{\mathrm{1D}}).$$

1.2.2 Constitutive law in the sarcomere

In order to provide the complete stress-strain law of the heart we follow [Chapelle et al., 2012] and propose a definition of the relation between the strain and the stress in the sarcomere, that is to say e_{c} and σ_{c} respectively. This modeling aspect starts from the Huxley's representation of binding and unbinding of a myosin head [Huxley, 1957] – the microscopic scale – and is lifted to a mesoscopic scale by averaging the quantities considered in the previous lower scale.

On a microscopic scale, the binding of a myosin head occurs within a certain range $[0,h]$ for the displacement of the tip of the head with respect to a reference position on the actin filament. When dividing the tip displacement by h, we obtain a dimensionless strain quantity s. Defining by $n(t,s)$ the normalized density of existing bridges at time t and strain s, the derivative of n is written as

$$\frac{\mathrm{d}n(t,s)}{\mathrm{d}t} = \frac{\partial n}{\partial t} + \dot{s}\frac{\partial n}{\partial s}.$$

Making the assumption of an infinitely stiff actin and myosin filaments we can state that the microscopic strain $\dot{s}$ is equivalent to the mesoscopic strain in the sarcomere $\dot{e}_\mathrm{c}$. Denoting by f and g the binding and unbinding rate of bridges, the variation in time of the number of bridge reads

$$\frac{\partial n}{\partial t} + \dot{e}_\mathrm{c}\frac{\partial n}{\partial s} = (n_0(e_\mathrm{c}) - n)f - ng. \tag{1.38}$$

In (1.38) the strain dependent function n_0 accounts for the Frank-Starling effect described in the corresponding physiological key points. The different rates f and g are modelled by

$$\left| \begin{aligned} & f(s,t) = |u|_+ \mathbb{1}_{s\in[0;1]}, \\ & \\ & g(s,t) = |u| + \alpha|\dot{e}_\mathrm{c}| - f(s,t) = |u|_+ \mathbb{1}_{s\notin[0;1]} + |u|_- + \alpha|\dot{e}_\mathrm{c}|, \end{aligned} \right. \tag{1.39}$$

where u denotes a variable reaction rate summarizing chemical activation, inducing contraction or relaxation depending on whether u is positive or negative. In (1.39) the term $\alpha|\dot{e}_\mathrm{c}|$ appearing in the destruction rate g represents the fact that the destruction of bridges may occur when the relative speed between myosin and actin is too high. One way to pass to an upper scale is to consider the sarcomere as a collection of springs – the myosin heads – attached in parallel so that the global stiffness of the sarcomere k_c and the global associated stress τ_c are

$$\left| \begin{aligned} & k_c(t) = k_0 \int_{\mathbb{R}} n(t,s)\mathrm{d}s, \\ & \\ & \tau_c(t) = \int_{\mathbb{R}} \frac{\partial \mathrm{W}^b}{\partial s}(t,s) n(t,s)\mathrm{d}s. \end{aligned} \right. \tag{1.40}$$

In (1.40), k_0 is the stiffness of the bridges. We choose W^b as

$$\mathrm{W}^b(t,s) = \frac{k_0}{2}(s+s_0)^2, \tag{1.41}$$

s_0 being a possible prestrain. The stress in the sarcomere then reads

$$\tau_c(t) = k_0 \int_{\mathbb{R}} (s+s_0)n(t,s)\mathrm{d}s. \tag{1.42}$$

From (1.38) we obtain the variations in time of the global stiffness of the sarcomere

$$\dot{k}_c(t) = k_0 \int_{\mathbb{R}} (n_0(e_\mathrm{c}) - n(t,s))f(t) - n(t,s)g(t)\mathrm{d}s = -(|u| + \alpha|\dot{e}_\mathrm{c}|)k_c(t) + k_0 n_0 |u|_+,$$

and the variation of the stress

$$\dot{\tau}_c(t) = k_0 \int_{\mathbb{R}} (s+s_0)\big((n_0(e_{\mathrm{c}}) - n(t,s))f(t) - n(t,s)g(t)\big)\mathrm{d}s + \dot{e}_{\mathrm{c}} k_c$$

$$= -(|u| + \alpha|\dot{e}_{\mathrm{c}}|)\tau_c(t) + \dot{e}_{\mathrm{c}} k_c + k_0 n_0 \int_{\mathbb{R}} (s+s_0) f(s)\mathrm{d}s.$$

Denoting by

$$\sigma_0 = (\frac{1}{2} + s_0)k_0, \tag{1.43}$$

and adding one contribution to account for the fact that the creation or destruction of bridges dissipates energy through viscous effects. We finally obtain the following constitutive law

$$\begin{cases} \dot{k}_c(t) = -(|u| + \alpha|\dot{e}_{\mathrm{c}}|)k_c(t) + k_0 n_0 |u|_+, \\ \\ \dot{\tau}_c(t) = -(|u| + \alpha|\dot{e}_{\mathrm{c}}|)\tau_c(t) + \dot{e}_{\mathrm{c}} k_c + n_0 \sigma_0 |u|_+, \\ \\ \sigma_{\mathrm{c}} = \tau_c + \mu \dot{e}_{\mathrm{c}}. \end{cases} \tag{1.44}$$

1.3 The complete biomechanical model of the heart

So far we have proposed to gather a set of modeling ingredients to represent the heart material during both active and passive regimes. Moreover, the heart is situated within the body and in interaction with numerous other components. Therefore, prior to giving the complete biomechanical model of the heart we present how its relationship with the rest of the cardiovascular system and with its surroundings can be taken into account. Let us say that this section is dedicated to boundary conditions in a wide sense. In this matter the contribution of our work is twofold: first we propose a model of the complete cardiovascular system leading to a fully coupled system and secondly we propose a mean of describing the contact between the outer surface of the ventricle and the pericardium.

1.3.1 Valve model and *Windkessel* systems

Physiological key point

A cardiac cycle

A cardiac cycle is made of four phases ruled by the various pressures in the structure atrium-ventricle-artery and guided by a valve system.

1- Systole, isovolumetric phase: The ventricle is contracting in reaction to the electrical activation of the cardiac cells. The valves between the atrium and the artery is closed so that the contraction is isovolumetric. Therefore, the pressure inside the cavity rapidly increases until it reaches the aortic pressure leading to the opening of the aortic valve.

2- Ejection phase: As the aortic valve is open, the ventricle – still contracting – ejects the blood through the artery. The ejection occurs until the excitation of the ventricle stops. At this point the pressure in the cavity decreases until it reaches a lower value than the aortic pressure. The aortic valve closes.

3- Isovolumetric relaxation: Once again the cavity is in an isovolumetric phase, both valves are closed. The cavity pressure drops rapidly until it reaches the atrium pressure. At the end of this phase the atrioventricular valve opens.

4- Diastole, filling phase: As the valve is open, the blood runs from the atrium to the ventricle leading to most of the passive filling of the ventricle. The contraction of the atrium finishes the filling of the ventricle.

For the left ventricle, the volume reaches a peak at approximately $120\ \mathrm{mL}$ after the left atrium contraction and its lower value is about $40 - 50\ \mathrm{mL}$ after ejection of the aorta. Its maximum pressure during ejection reaches $1.6 \cdot 10^4\ \mathrm{Pa}$.

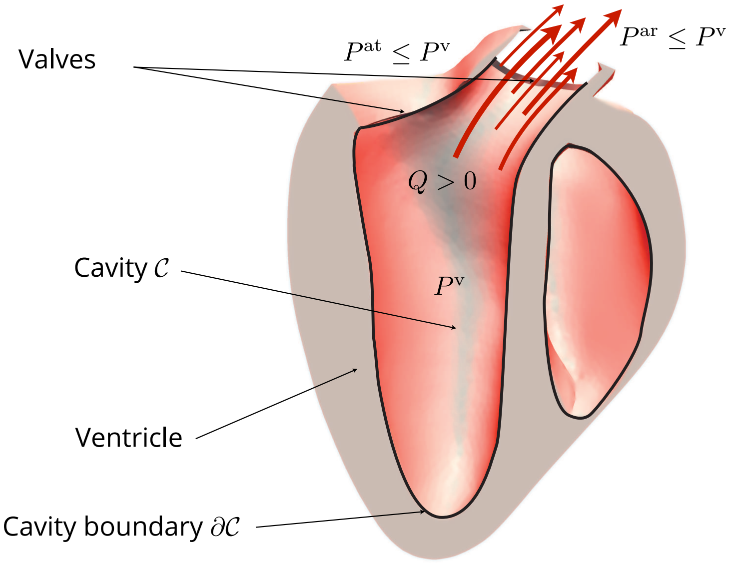

Figure 1.8: Representation of a cavity within the structure atrium-ventricle-artery.

A valve model As we understood from the previous physiological key point, the valves play a fundamental role – within the structure atrium-ventricle-artery – since they regulate inflow and outflow of the blood. If we consider a cavity $\mathcal{C}$ delimited by the closure of the endocardium with the two valve rings, its volume is

$$\mathcal{V}(t) = \int_{\mathcal{C}} \mathrm{d}\Omega,$$

and the flow of ejected blood Q^- is obtained from

$$Q^-(t) = -\dot{\mathcal{V}}(t).$$

From a numerical standpoint, the complete fluid-structure interaction problem – see [Fernández et al., 2007, Formaggia et al., 2009] as an example of references on the matter – is out of reach in the perspective of performing *inverse problems*. Hence we follow [Sainte-Marie et al., 2006] and model the valve system by a relationship between the ejected blood flow and the pressures in the atrium P^{at}, the ventricle P^{v} and the artery P^{ar}, namely

$$-\dot{\mathcal{V}}(t) = f(P^{\mathrm{at}}, P^{\mathrm{v}}, P^{\mathrm{ar}}). \tag{1.45}$$

These scalar values represent an uniform pressure inside the cavity. Before giving an expression of the valve function f, we recall how the flow Q^{-} is derived from the velocity of the solid. To start with, let us notice that

$$\frac{\mathrm{d}}{\mathrm{d}t}\mathcal{V}(t) = \frac{\mathrm{d}}{\mathrm{d}t}\mathcal{V}(\underline{y}(t)) = \mathrm{d}_y\mathcal{V}(t)\cdot\underline{\dot{y}}.$$

Additionally, the differential of the volume with respect to the displacement comes by

$$\forall \underline{v}^{\flat} \in \mathcal{X}^y \quad \mathrm{d}_y\mathcal{V}(t)\cdot\underline{v}^{\flat} = \int_{\mathcal{C}_0} \mathrm{d}_y J\cdot\underline{v}^{\flat}\mathrm{d}\Omega_0 = \int_{\mathcal{C}_0} \frac{\partial J}{\partial \underline{\underline{F}}} : \mathrm{d}_y\underline{\underline{F}}\cdot\underline{v}^{\flat}\mathrm{d}\Omega_0,$$

where $\mathcal{C}_0$ is the cavity geometry in the reference configuration. To give an expression of the integrand we consider two tensors $\underline{\underline{A}}$ – assumed invertible – and $\underline{\underline{B}}$, we have

$$\begin{aligned}
\det(\underline{\underline{A}} + h\underline{\underline{B}}) - \det(\underline{\underline{A}}) &= \det(\underline{\underline{A}})\big(\det(\underline{\underline{\mathbb{1}}} + h\underline{\underline{A}}^{-1}\underline{\underline{B}}) - 1\big)\\
&= h\det(\underline{\underline{A}})\mathrm{tr}(\underline{\underline{A}}^{-1}\underline{\underline{B}}) + O(h^2)\\
&= h\det(\underline{\underline{A}})\underline{\underline{A}}^{-1} : \underline{\underline{B}} + O(h^2).
\end{aligned} \tag{1.46}$$

Hence, the volume differential becomes

$$\begin{aligned}
\mathrm{d}_y\mathcal{V}(t)\cdot\underline{v}^{\flat} &= \int_{\mathcal{C}_0} J\underline{\underline{F}}^{-1} : \mathrm{d}_y\underline{\underline{F}}\cdot\underline{v}^{\flat}\mathrm{d}\Omega_0\\
&= \int_{\mathcal{C}} \underline{\underline{\mathbb{1}}} : \underline{\underline{\nabla}}_x\underline{v}^{\flat}\mathrm{d}\Omega = \int_{\mathcal{C}} \mathrm{div}_x(\underline{v}^{\flat})\mathrm{d}\Omega.
\end{aligned}$$

Applying the Stokes theorem, the valve function is in relation with the velocity of the solid through

$$Q^{-}(t) = -\int_{\partial\mathcal{C}} \underline{\dot{y}}\cdot\underline{n_{\mathcal{C}}}\,\mathrm{d}\sigma = f(P^{\mathrm{at}}, P^{\mathrm{v}}, P^{\mathrm{ar}}). \tag{1.47}$$

In (1.47) we denoted by $\partial\mathcal{C}$ the surface of the cavity with normal vector field $\underline{n_{\mathcal{C}}}$. Concerning the valve function we follow [Sainte-Marie et al., 2006] and define

$$f(P^{\mathrm{at}}, P^{\mathrm{v}}, P^{\mathrm{at}}) = \begin{cases} K^{\mathrm{ar}}(P^{\mathrm{ar}} - P^{\mathrm{v}}) + K^{\mathrm{iso}}(P^{\mathrm{at}} - P^{\mathrm{ar}}) & \text{if} \quad P^{\mathrm{v}} \geq P^{\mathrm{ar}},\\ K^{\mathrm{iso}}(P^{\mathrm{at}} - P^{\mathrm{v}}) & \text{if} \quad P^{\mathrm{at}} \leq P^{\mathrm{v}} \leq P^{\mathrm{ar}},\\ K^{\mathrm{at}}(P^{\mathrm{at}} - P^{\mathrm{v}}) & \text{if} \quad P^{\mathrm{v}} \leq P^{\mathrm{at}}, \end{cases} \tag{1.48}$$

where the constants K^{ar} and K^{at} represent the loss induced by the passage of the blood through the different valves. They are proportional to $\frac{\pi R^2}{\rho c}$, with R the radius of the valve

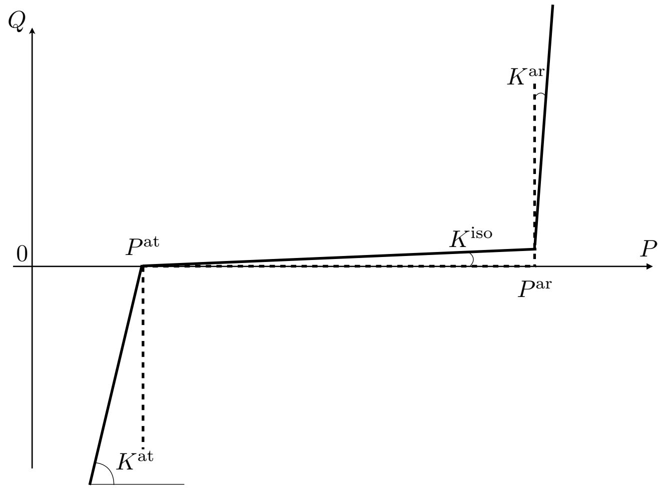

Figure 1.9: The valve function.

under consideration, ρ the volumic mass of the blood and c its velocity. K^{iso} is used to relax the isovolumic constrain and can be seen as a penalization strategy.

Hence, we add in the model three pressure variables per cavity corresponding to

$$\left(P_{\square}^{\mathrm{at}},\ P_{\square}^{\mathrm{v}},\ P_{\square}^{\mathrm{at}}\right),\quad \text{with}\quad \square = \mathrm{L},\mathrm{R},$$

along with two valve relations

$$Q_{\square}^{-}(t) = -\dot{\mathcal{V}}_{\square}(t) = f(P_{\square}^{\mathrm{at}}, P_{\square}^{\mathrm{v}}, P_{\square}^{\mathrm{ar}}),\quad \text{with}\quad \square = \mathrm{L},\mathrm{R}.$$

***Windkessel* models** During non isovolumetric phases, the heart interacts with the rest of the cardiovascular system. A complementary model of this system should be provided in order to represent these interactions. As we cannot afford a complex and detailed modeling of the cardiovascular system and following [Sainte-Marie et al., 2006], we opt for a *Windkessel* model [Wetserhof et al., 2008] – which is based on an analogy with electrical systems. The intensity represents the blood flow in the part of the cardiovascular system under study and the potential represents the blood pressure. As the blood runs through an organ to provide necessary nutrients the blood pressure decreases, therefore organs can be represented as resistances. Moreover, the elasticity of large arteries subject to high pressure gives birth to spaces that can store blood. This particularity – called the *Windkessel effect* – is taken into account using capacitances.

A *one way* model. For a given cavity $\mathcal{C}$, Figure 1.10 describes a possible Windkessel system. This model is made of two R-C blocks, the first one corresponding to the arterial pressure and the second one to a further *distal* pressure. The prescribed pressure $P_{\square}^{\mathrm{e}}$ at the end of the circuit can represent – in the case of the systemic circulation for example – the pressure in the veins after a passage through the organs.

From the classical laws ruling electrical circuits we obtain the following relations (where

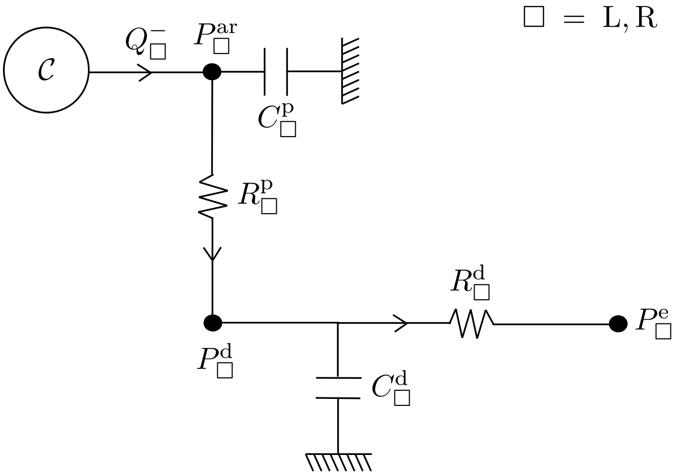

Figure 1.10: Sketch of the *one way* Windkessel model.

we omitted the □ symbol for the sake of clarity)

$$\begin{cases} \dfrac{1}{R^{\mathrm{p}}}\big(P^{\mathrm{ar}} - P^{\mathrm{d}}\big) + C^{\mathrm{p}}\dot{P}^{\mathrm{ar}} = |Q^-|_+, \\[2ex] \dfrac{1}{R^{\mathrm{d}}}\big(P^{\mathrm{d}} - P^{\mathrm{e}}\big) + C^{\mathrm{d}}\dot{P}^{\mathrm{d}} = \dfrac{1}{R^{\mathrm{p}}}\big(P^{\mathrm{ar}} - P^{\mathrm{d}}\big). \end{cases} \tag{1.49}$$

In (1.49), the input

$$|Q^-|_+ = Q^- \mathbb{1}_{Q^->0},$$

corresponds to the ejected blood flow from the cavity when the valve is open. In practice we give a closure to the complete system (biomechanical model of the heart wall and the pressure variables) by prescribing the final pressure point $P_\square^{\mathrm{e}}$ and the atrial pressure as well.

A *closed loop* model. The system of relations (1.49) is written for both ventricles. It should be noted that both the atrial pressures and the ending pressures are prescribed. To provide a more realistic model one can consider a closed loop system (as shown in Figure 1.11) where the ending pressure of the Windkessel system of the left ventricle would be the right atrial pressure – thus forming a model of the systemic circulation. Reciprocally the left atrial pressure would be connected to the right ventricle – that is to say the pulmonary circulation. In this configuration the atrium and the ventricle (of a same side) are connected by a natural conservation of the blood flow.

To start with, Figure 1.12(a) shows in details the Windkessel model for the sytemic circulation. As for the *one way* model, it is made of two R-C blocks except that we added a resistance

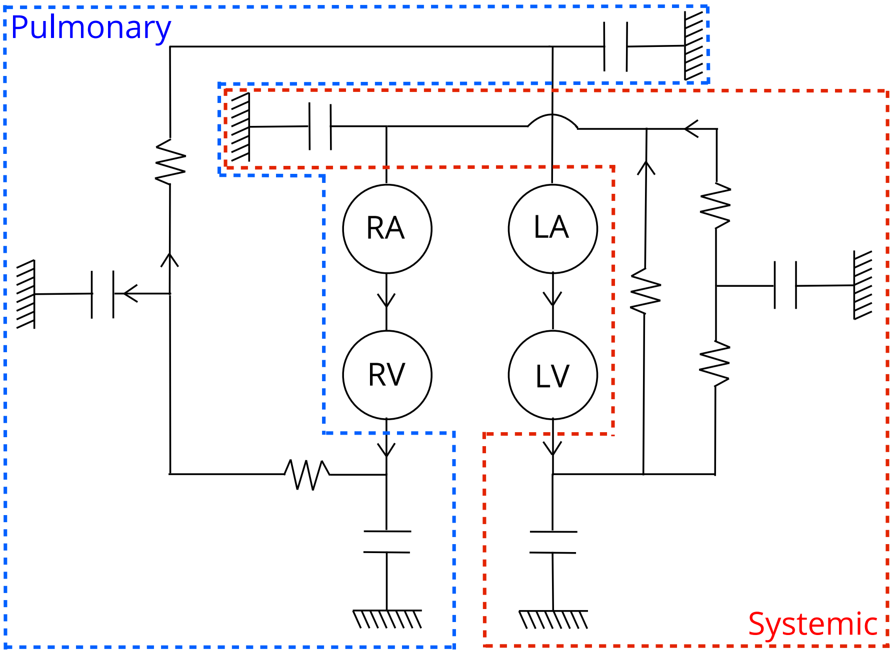

Figure 1.11: Complete modeling of the cardiovascular system using Windkessel models.

R^{co} to model the coronary system. We derive the following expressions

$$\begin{cases} C_{\mathrm{L}}^{\mathrm{p}} \dot{P}_{\mathrm{L}}^{\mathrm{ar}} + \dfrac{1}{R^{\mathrm{co}}} \left(P_{\mathrm{L}}^{\mathrm{ar}} - P_{\mathrm{R}}^{\mathrm{at}} \right) + \dfrac{1}{R_{\mathrm{L}}^{\mathrm{p}}} \left(P_{\mathrm{L}}^{\mathrm{ar}} - P_{\mathrm{L}}^{\mathrm{d}} \right) = |Q_{\mathrm{L}}^{-}|_{+}, \\[2ex] C_{\mathrm{L}}^{\mathrm{d}} \dot{P}_{\mathrm{L}}^{\mathrm{d}} + \dfrac{1}{R_{\mathrm{L}}^{\mathrm{d}}} \left(P_{\mathrm{L}}^{\mathrm{d}} - P_{\mathrm{R}}^{\mathrm{at}} \right) = \dfrac{1}{R_{\mathrm{L}}^{\mathrm{p}}} \left(P_{\mathrm{L}}^{\mathrm{ar}} - P_{\mathrm{L}}^{\mathrm{d}} \right), \\[2ex] Q_{\mathrm{R}}^{+} + C_{\mathrm{R}}^{\mathrm{at}} \dot{P}_{\mathrm{R}}^{\mathrm{at}} = \dfrac{1}{R_{\mathrm{L}}^{\mathrm{d}}} \left(P_{\mathrm{L}}^{\mathrm{d}} - P_{\mathrm{R}}^{\mathrm{at}} \right) + \dfrac{1}{R^{\mathrm{co}}} \left(P_{\mathrm{L}}^{\mathrm{at}} - P_{\mathrm{R}}^{\mathrm{at}} \right). \end{cases} \tag{1.50}$$

As far as the pulmonary circulation is concerned – see Figure 1.12(b) – the Windkessel model is exactly as the *one way* model except that the ending pressure point is the left atrial pressure. The arising relations are

$$\begin{cases} C_{\mathrm{R}}^{\mathrm{p}} \dot{P}_{\mathrm{R}}^{\mathrm{ar}} + \dfrac{1}{R_{\mathrm{R}}^{\mathrm{p}}} \left(P_{\mathrm{R}}^{\mathrm{ar}} - P_{\mathrm{R}}^{\mathrm{d}} \right) = |Q_{\mathrm{R}}^{-}|_{+}, \\[2ex] C_{\mathrm{R}}^{\mathrm{d}} \dot{P}_{\mathrm{R}}^{\mathrm{d}} + \dfrac{1}{R_{\mathrm{R}}^{\mathrm{d}}} \left(P_{\mathrm{R}}^{\mathrm{d}} - P_{\mathrm{L}}^{\mathrm{at}} \right) = \dfrac{1}{R_{\mathrm{R}}^{\mathrm{p}}} \left(P_{\mathrm{R}}^{\mathrm{ar}} - P_{\mathrm{R}}^{\mathrm{d}} \right), \\[2ex] Q_{\mathrm{L}}^{+} + C_{\mathrm{L}}^{\mathrm{at}} \dot{P}_{\mathrm{L}}^{\mathrm{at}} = \dfrac{1}{R_{\mathrm{R}}^{\mathrm{d}}} \left(P_{\mathrm{R}}^{\mathrm{d}} - P_{\mathrm{L}}^{\mathrm{at}} \right). \end{cases} \tag{1.51}$$

Finally the atria and the ventricles are connected by the conservation of the blood flow, namely

$$\begin{cases} Q_{\mathrm{L}}^{\mathrm{at}} = Q_{\mathrm{L}}^{+} - |Q_{\mathrm{L}}^{-}|_{-}. \\ \\ Q_{\mathrm{R}}^{\mathrm{at}} = Q_{\mathrm{R}}^{+} - |Q_{\mathrm{R}}^{-}|_{-}, \end{cases} \tag{1.52}$$

with

$$|Q_{\square}^{-}|_{-} = Q_{\square}^{-} \mathbb{1}_{Q_{\square}^{-} < 0}, \quad \square = \mathrm{L}, \mathrm{R}.$$

In (1.52) we denoted by $Q_{\mathrm{L}}^{\mathrm{at}}$ and $Q_{\mathrm{R}}^{\mathrm{at}}$ the flows of blood through the left and the right atrium respectively. Assuming that a mechanical model is available on the atria, these quantities take the form of (1.47).

1.3.2 The heart and its surrounding

Physiological key point

Location of the heart

The heart has the same size as a closed fist, about 12 cm long, 9 cm wide at its broadest point and 6 cm thick. It rests on the diaphragm and lies in a region called the *mediastinum* that extends from the sternum to the vertebral column and from the first rib to the diaphragm. Situated around the heart, the *pericardium* protects the organ while enabling rapid displacement during contraction.

In this section we focus our attention on modeling the interaction between the pericardium and the outer surface of the heart. Since the endocardium is supposed to be able to slide onto the inner pericardium, standard viscoelastic boundary condition may not be suitable. Therefore we opt for a contact boundary condition that aims at penalizing the material point outside a given geometry $\mathcal{P}$ representing the pericardium. We denote by $\mathcal{E}p\iota_{\mathrm{L}}$ and $\mathcal{E}p\iota_{\mathrm{R}}$ the part of the left and right epicardium such that

$$\mathcal{A} \cup \mathcal{E}p\iota_{\mathrm{L}} \cup \mathcal{E}p\iota_{\mathrm{R}} \cup \mathcal{B}$$

form the complete outer surface of a heart geometry – see Figure 1.13. Let $\mathcal{E}p\iota = \mathcal{E}p\iota_{\mathrm{L}} \cup \mathcal{E}p\iota_{\mathrm{R}}$ be the gathering of the two surfaces, the penalization term takes the following form

$$\mathrm{W}^{\mathrm{c}}(\underline{y}) = \frac{\kappa_{\mathrm{c}}}{2} \int_{\mathcal{E}p\iota} |\mathrm{dist}(\underline{x}, \mathcal{P})|_{-}^{2} \, \mathrm{d}\sigma, \tag{1.53}$$

where $\kappa_{\mathrm{c}} > 0$ is a penalization parameter and dist is the signed distance operator. As in [Moireau et al., 2009] we can express the derivative of this operator with respect to a test displacement $\underline{v}^{\flat} \in \mathcal{X}^{y}$. Namely, let M be a point on the heart model, P be the projection point of M onto $\mathcal{P}$ and $\underline{n}_{\mathcal{P}}$ be the normal of the pericardium surface at P, we have

$$\mathrm{d}_{y}\mathrm{dist}(\underline{x}, \mathcal{P}) \cdot \underline{v}^{\flat} = \mathrm{d}_{y} \left(\underline{PM} \cdot \underline{n}_{\mathcal{P}} \right) \cdot \underline{v}^{\flat} = \underline{n}_{\mathcal{P}} \cdot \underline{v}^{\flat}.$$

Hence, the variational form of the boundary condition is

$$\mathcal{P}^{\mathrm{c}}(\underline{v}^{\flat}) = \kappa_{\mathrm{c}} \int_{\mathcal{E}p\iota} |\mathrm{dist}(\underline{x}, \mathcal{P})|_{-} \, \underline{n}_{\mathcal{P}} \cdot \underline{v}^{\flat} \, \mathrm{d}\sigma. \tag{1.54}$$

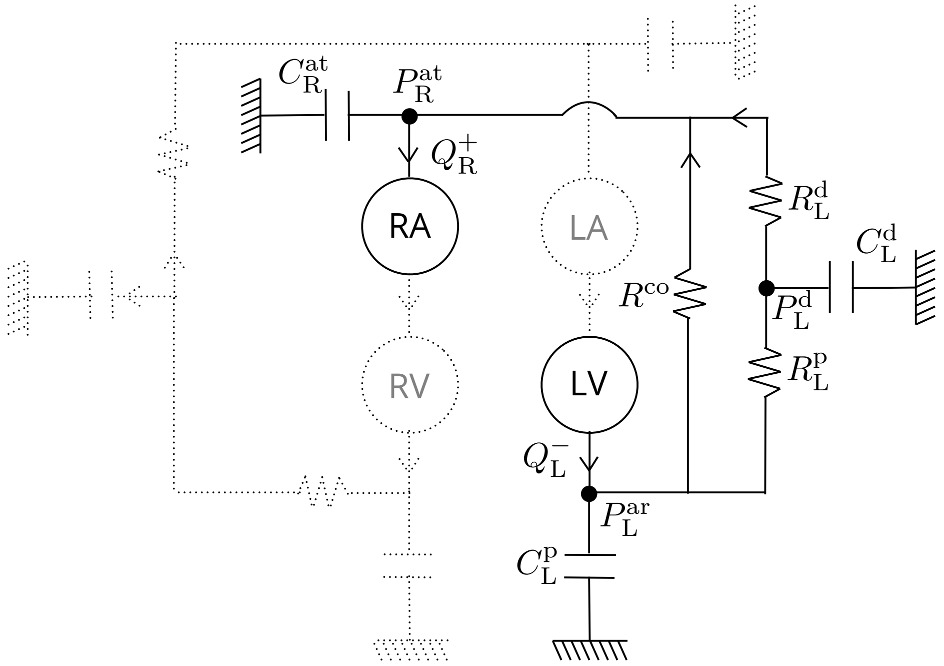

(a) The systemic circulation.

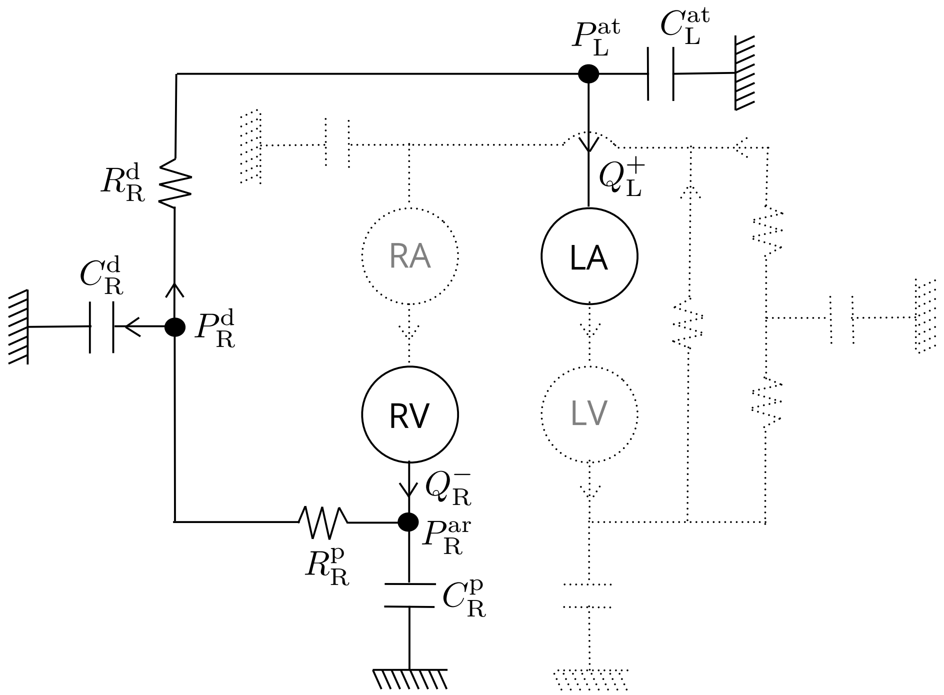

(b) The pulmonary circulation.

Figure 1.12: The Closed loop Windkessel model.

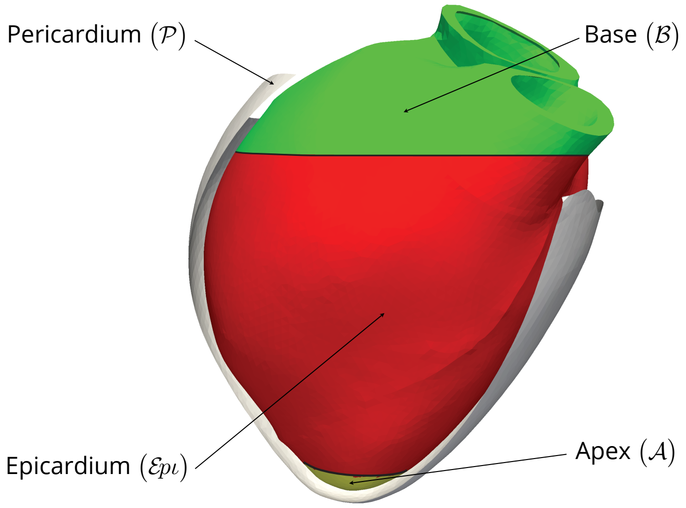

Figure 1.13: Representation of the various areas of the heart model subject to boundary conditions.

Concerning the apex and the base of the heart geometry we prescribed viscoelastic boundary conditions, that is to say variational terms of the form

$$\alpha_{\mathcal{A},\mathcal{B}} \int_{\mathcal{A},\mathcal{B}} \underline{y} \cdot \underline{v}^\flat \, \mathrm{d}\sigma + \beta_{\mathcal{A},\mathcal{B}} \int_{\mathcal{A},\mathcal{B}} \underline{\dot{y}} \cdot \underline{v}^\flat \, \mathrm{d}\sigma, \tag{1.55}$$

to represent the fact that the veins and arteries connected to the base resist to the heart displacement.

1.3.3 Complete discretization of the model

At this stage we have gathered all the necessary elements to constitute a biomechanical heart model. Prior to giving some details on the numerical approximation procedure that we carried out to provide a numerical solution, we recall that the complete model in its variational form reads $\forall \underline{v}^\flat \in \mathcal{X}^y$,

$$
\left\{
\begin{array}{l}
\displaystyle \int_{\Omega_0} \rho_0 \underline{\ddot{y}} \cdot \underline{v}^\flat \, \mathrm{d}\Omega_0 + \int_{\Omega_0} \underline{\underline{\Sigma}} : \mathrm{d}_y \underline{\underline{e}} \cdot \underline{v}^\flat \, \mathrm{d}\Omega_0 = \\
\begin{array}{r|l}
\textit{(following pressure)} & \displaystyle - \int_{\mathcal{E}n_{\mathrm{L}}} P_{\mathrm{L}}^{\mathrm{v}} \, \underline{n}_{\mathrm{L}} \cdot \underline{v}^\flat \mathrm{d}\sigma \; - \int_{\mathcal{E}n_{\mathrm{R}}} P_{\mathrm{R}}^{\mathrm{v}} \, \underline{n}_{\mathrm{R}} \cdot \underline{v}^\flat \mathrm{d}\sigma \\[2ex]
\textit{(contact boundary condition)} & \displaystyle - \kappa_{\mathrm{c}} \int_{\mathcal{E}p\iota} |\mathrm{dist}(\underline{x}, \mathcal{P})|_{-} \, \underline{n}_{\mathcal{P}} \cdot \underline{v}^\flat \, \mathrm{d}\sigma \\[2ex]
\textit{(viscoelastic boundary condition)} & \displaystyle - \alpha_{\mathcal{A},\mathcal{B}} \int_{\mathcal{A},\mathcal{B}} \underline{y} \cdot \underline{v}^\flat \, \mathrm{d}\sigma - \beta_{\mathcal{A},\mathcal{B}} \int_{\mathcal{A},\mathcal{B}} \underline{\dot{y}} \cdot \underline{v}^\flat \, \mathrm{d}\sigma,
\end{array} \\[6ex]
\text{with} \quad \displaystyle \underline{\underline{\Sigma}} = \frac{\partial W^{\mathrm{e}}}{\partial \underline{\underline{e}}} + \frac{\partial W^{\mathrm{v}}}{\partial \underline{\underline{\dot{e}}}} + \sigma_{1\mathrm{D}} \, \underline{n}_0 \otimes \underline{n}_0 \quad \text{, where} \\
\begin{array}{r|l}
\textit{(rheological model)} & \displaystyle \sigma_{1\mathrm{D}} = \frac{1 + 2e_{1\mathrm{D}}}{1 + 2e_{\mathrm{c}}} \sigma_{\mathrm{c}}, \\[3ex]
 & \displaystyle \sigma_{\mathrm{c}} = \tau_c + \mu \dot{e}_{\mathrm{c}} = \mathrm{E}_{\mathrm{s}} \frac{e_{1\mathrm{D}} - e_{\mathrm{c}}}{(1 + 2e_{\mathrm{c}})^3} (1 + 2e_{1\mathrm{D}}), \\[3ex]
\textit{(mean stiffness of sarcomeres)} & \dot{k}_c = -(|u| + \alpha |\dot{e}_{\mathrm{c}}|) k_c + k_0 n_0 |u|_{+}, \\[2ex]
\textit{(mean stress of sarcomeres)} & \dot{\tau}_c = -(|u| + \alpha |\dot{e}_{\mathrm{c}}|) \tau_c + \dot{e}_{\mathrm{c}} k_c + n_0 \sigma_0 |u|_{+},
\end{array} \\[10ex]
\text{and} \\
\begin{array}{r|l}
\textit{(valve model)} & \displaystyle Q_{\Box}^{-} = - \int_{\mathcal{E}n_{\Box}} \underline{\dot{y}} \cdot \underline{n}_{\Box} \, \mathrm{d}\sigma = f(P_{\Box}^{\mathrm{at}}, P_{\Box}^{\mathrm{v}}, P_{\Box}^{\mathrm{ar}}), \\[3ex]
\textit{(proximal R-C block of Winkdessel model)} & \displaystyle \frac{1}{R_{\Box}^{\mathrm{p}}} \big(P_{\Box}^{\mathrm{ar}} - P_{\Box}^{\mathrm{d}} \big) + C^{\mathrm{d}} \dot{P}_{\Box}^{\mathrm{ar}} = |Q_{\Box}^{-}|_{+}, \\[3ex]
\textit{(distal R-C block of Winkdessel model)} & \displaystyle \frac{1}{R_{\Box}^{\mathrm{d}}} \big(P_{\Box}^{\mathrm{d}} - P_{\Box}^{\mathrm{e}} \big) + C^{\mathrm{d}} \dot{P}_{\Box}^{\mathrm{d}} = \frac{1}{R^{\mathrm{p}}} \big(P_{\Box}^{\mathrm{ar}} - P_{\Box}^{\mathrm{d}} \big),
\end{array} \\[6ex]
\text{for } \Box = \mathrm{L}, \mathrm{R}.
\end{array}
\right.
\tag{1.56}
$$

In this model, the variables are the collection of the displacement, the velocity, the *internal* variables describing the active part and the pressures of the Windkessel models, namely

$$\big(\underline{y}, \underline{v}, e_{\mathrm{c}}, \tau_c, k_c, P_{\Box}^{\mathrm{v}}, P_{\Box}^{\mathrm{ar}} \big), \quad \Box = \mathrm{L}, \mathrm{R}.$$

It should be noted that, as previously mentioned and following [Chapelle et al., 2012, Sainte-Marie et al., 2006], we choose two decoupled *one way* Windkessel models where the atrial and ending pressures are prescribed. The distal pressures can be directly derived from (1.49). The electrical potential u is an input of this model.

Continuous energy balance Prior to give the time discretization of (1.56) we provide the total energy balance of the system – as in [Chapelle et al., 2012] – which we will transfer at a discrete level in order to insure the numerical stability of the time scheme. To start with let us remark that, for a test displacement $\underline{v}^\flat \in \mathcal{X}^y$, we have

$$\underline{\underline{\Sigma}} : \mathrm{d}_y \underline{\underline{e}} \cdot \underline{v}^\flat = \big(\frac{\partial W^{\mathrm{e}}}{\partial \underline{\underline{e}}} + \frac{\partial W^{\mathrm{v}}}{\partial \underline{\underline{\dot{e}}}}\big) : \mathrm{d}_y \underline{\underline{e}} \cdot \underline{v}^\flat + \sigma_{1\mathrm{D}}\, \underline{n}_0 \otimes \underline{n}_0 : \mathrm{d}_y \underline{\underline{e}} \cdot \underline{v}^\flat$$

$$= \big(\frac{\partial W^{\mathrm{e}}}{\partial \underline{\underline{e}}} + \frac{\partial W^{\mathrm{v}}}{\partial \underline{\underline{\dot{e}}}}\big) : \mathrm{d}_y \underline{\underline{e}} \cdot \underline{v}^\flat + \sigma_{1\mathrm{D}}\, \mathrm{d}_y e_{1\mathrm{D}} \cdot \underline{v}^\flat.$$

Relation (1.36) gives us

$$\mathrm{d}_y e_{1\mathrm{D}} \cdot \underline{v}^\flat = \mathrm{d}e_{\mathrm{s}} \cdot \underline{v}^\flat\ (1 + 2e_{\mathrm{c}}) + \mathrm{d}e_{\mathrm{c}} \cdot \underline{v}^\flat\ (1 + 2e_{\mathrm{s}}),$$

hence, using (1.37) we obtain

$$\underline{\underline{\Sigma}} : \mathrm{d}_y \underline{\underline{e}} \cdot \underline{v}^\flat = \big(\frac{\partial W^{\mathrm{e}}}{\partial \underline{\underline{e}}} + \frac{\partial W^{\mathrm{v}}}{\partial \underline{\underline{\dot{e}}}}\big) : \mathrm{d}_y \underline{\underline{e}} \cdot \underline{v}^\flat + \sigma_{\mathrm{c}} \mathrm{d}e_{\mathrm{c}} \cdot \underline{v}^\flat + \sigma_{\mathrm{s}} \mathrm{d}e_{\mathrm{s}} \cdot \underline{v}^\flat.$$

Therefore using the velocity as a test function in the variational formulation (1.56) we obtain

$$\frac{\mathrm{d}}{\mathrm{d}t}\big(\mathcal{E}_{\mathrm{k}} + \mathcal{E}_{\mathrm{e}} + \frac{1}{2}\int_{\Omega_0} \mathrm{E}_{\mathrm{s}} e_{\mathrm{s}}^2\, \mathrm{d}\Omega_0 + \alpha_{\mathcal{A},\mathcal{B}} \int_{\mathcal{A},\mathcal{B}} \|\underline{y}\|^2 \mathrm{d}\sigma\big) + \int_{\Omega_0} \tau_c \dot{e}_{\mathrm{c}}\, \mathrm{d}\Omega_0 =$$
$$- \int_{\Omega_0} \eta\, \frac{\partial W^{\mathrm{v}}}{\partial \underline{\underline{\dot{e}}}} : \underline{\underline{\dot{e}}} \mathrm{d}\Omega_0 - \int_{\Omega_0} \mu \dot{e}_{\mathrm{c}}^2\, \mathrm{d}\Omega_0 - \beta_{\mathcal{A},\mathcal{B}} \int_{\mathcal{A},\mathcal{B}} \|\underline{\dot{y}}\|^2\, \mathrm{d}\sigma + P_{\square}^{\mathrm{v}} Q_{\square}^{-} + \mathcal{P}^{\mathrm{c}}(\underline{\dot{y}}).$$

Following [Chapelle et al., 2012], we introduce the averaged elastic energy stored in a sarcomere as

$$\mathcal{E}_{\mathrm{c}} = \frac{k_0}{2} \int (s + s_0)^2 n(t,s)\, \mathrm{d}s,$$

verifying

$$\dot{\mathcal{E}}_{\mathrm{c}} = k_0 \int \dot{e}_{\mathrm{c}} (s + s_0) n(t,s) \mathrm{d}s + \frac{k_0}{2} \int (s + s_0)^2 \big((n_0 - n(t,s)) f(t) - n(t,s) g(t)\big)\, \mathrm{d}s$$

$$= \tau_c \dot{e}_{\mathrm{c}} - (|u| + \alpha |\dot{e}_{\mathrm{c}}|) \mathcal{E}_{\mathrm{c}} + n_0 |u|_+ \mathcal{E}_0,$$

with $\mathcal{E}_0 = \frac{k_0}{2}\left(\frac{1}{3} + s_0 + s_0^2\right)$. Finally we obtain the following energy estimate

$$\frac{\mathrm{d}}{\mathrm{d}t}\big(\mathcal{E}_{\mathrm{k}} + \mathcal{E}_{\mathrm{e}} + \frac{1}{2}\int_{\Omega_0} \mathrm{E}_{\mathrm{s}} e_{\mathrm{s}}^2\, \mathrm{d}\Omega_0 + \alpha_{\mathcal{A},\mathcal{B}} \int_{\mathcal{A},\mathcal{B}} \|\underline{y}\|^2 \mathrm{d}\sigma + \int_{\Omega_0} \mathcal{E}_{\mathrm{c}}\, \mathrm{d}\Omega_0\big) =$$

$$- \int_{\Omega_0} \big(\eta\, \frac{\partial W^{\mathrm{v}}}{\partial \underline{\underline{\dot{e}}}} : \underline{\underline{\dot{e}}}\ +\ \mu \dot{e}_{\mathrm{c}}^2\ +\ (|u| + \alpha |\dot{e}_{\mathrm{c}}|) \mathcal{E}_{\mathrm{c}}\big)\, \mathrm{d}\Omega_0 - \beta_{\mathcal{A},\mathcal{B}} \int_{\mathcal{A},\mathcal{B}} \|\underline{\dot{y}}\|^2\, \mathrm{d}\sigma \tag{1.57}$$

$$+ P_{\square}^{\mathrm{v}} Q_{\square}^{-} + \int_{\Omega_0} n_0 |u|_+ \mathcal{E}_0\, \mathrm{d}\Omega_0 + \mathcal{P}^{\mathrm{c}}(\underline{\dot{y}}).$$

In (1.57) we denoted by $\mathcal{E}_{\mathrm{k}}$ the kinetic energy and

$$\mathcal{E}_{\mathrm{e}} = \int_{\Omega_0} W^{\mathrm{e}}\, \mathrm{d}\Omega_0,$$

the passive three-dimensional elastic energy. The dissipative terms are of three types:

- $\displaystyle\int_{\Omega_0} \eta \, \frac{\partial W^{\mathrm{v}}}{\partial \underline{\underline{\dot{e}}}} : \underline{\underline{\dot{e}}} \; + \; \mu \dot{e}_{\mathrm{c}}^2 \mathrm{d}\Omega_0$, the three-dimensional viscosity and the passive viscosity in the sarcomere,

- $\displaystyle\int_{\Omega_0} (|u| + \alpha |\dot{e}_{\mathrm{c}}|) \mathcal{E}_{\mathrm{c}} \, \mathrm{d}\Omega_0$, the dissipation during destruction or construction of bridges in the sarcomere, *i.e.* during activation,

- $\displaystyle\beta_{\mathcal{A},\mathcal{B}} \int_{\mathcal{A},\mathcal{B}} \|\underline{\dot{y}}\|^2 \, \mathrm{d}\sigma$, the dissipation due to possible frictions with surrounding of the heart.

On the other hand, the source terms are

- $\int_{\Omega_0} n_0 |u|_+ \mathcal{E}_0 \, \mathrm{d}\Omega_0$, the contraction power,

- $\mathcal{P}^{\mathrm{c}}(\underline{\dot{y}})$, possible contact reaction with the epicardium.

The last term $P^{\mathrm{v}}_{\square} Q^{-}_{\square}$ is quite particular since it can be either an input in the energy balance or a dissipative term depending on the state of the valves :

- Atrioventricular valve open, $P^{\mathrm{v}}_{\square} \leq P^{\mathrm{at}}_{\square}$, it is a source term since

  $$P^{\mathrm{v}}_{\square} Q^{-}_{\square} = K^{\mathrm{at}} P^{\mathrm{v}}_{\square} (P^{\mathrm{at}}_{\square} - P^{\mathrm{v}}_{\square}) \; \geq \; 0.$$

  The input comes from the pressure imposed by the atria.

- Isovolumetric phase, $P^{\mathrm{at}}_{\square} \leq P^{\mathrm{v}}_{\square} \leq P^{\mathrm{ar}}_{\square}$, due to the penalization strategy, we also obtain a source term

  $$P^{\mathrm{v}}_{\square} Q^{-}_{\square} = K^{\mathrm{iso}} P^{\mathrm{v}}_{\square} (P^{\mathrm{at}}_{\square} - P^{\mathrm{v}}_{\square}) \; \geq \; 0 \; ,$$

  but of significantly lower magnitude since the scalar value K^{iso} is small in practice.

- Aortic valve open, $P^{\mathrm{v}}_{\square} \geq P^{\mathrm{ar}}_{\square} \geq P^{\mathrm{at}}_{\square}$, in this case it turns out to be a dissipative term

  $$P^{\mathrm{v}}_{\square} Q^{-}_{\square} = K^{\mathrm{ar}} P^{\mathrm{v}}_{\square} (P^{\mathrm{ar}}_{\square} - P^{\mathrm{v}}_{\square}) + K^{\mathrm{iso}} P^{\mathrm{v}}_{\square} (P^{\mathrm{at}}_{\square} - P^{\mathrm{ar}}_{\square}) \leq 0,$$

  which represents the fact that the cavities are delivering blood into the Windkessel models.

Time discretization of the heart model In order to ensure its stability, the numerical algorithm is built so that the energy balance of the continuous problem is transmitted at the time-discrete level. As far as the heart model is concerned, the particularity of the internal variables makes the task more complex compared with standard nonlinear elasticity problems. In our work, we implemented the conservative time scheme proposed in [Chapelle et al., 2012].

Prior to give the expression of the time scheme, let us gather some standard assertions concerning the time discretization of nonlinear elastic problem – see [Gonzalez, 2000,Hauret and Le Tallec, 2006] and reference therein for further details. From a general standpoint, we look at the family of midpoint scheme of the form

$$\begin{cases} \dfrac{\underline{v}^{n+1} + \underline{v}^{n}}{2} = \dfrac{\underline{y}^{n+1} - \underline{y}^{n}}{\Delta \mathrm{t}}, \\[2ex] \displaystyle\int_{\Omega_0} \rho_0 \frac{\underline{v}^{n+1} - \underline{v}^{n}}{\Delta \mathrm{t}} \cdot \underline{v}^{\flat} \, \mathrm{d}\Omega_0 + \int_{\Omega_0} \underline{\underline{\Sigma}}^{n+\frac{1}{2}\sharp} : \mathrm{d}_y \underline{\underline{e}}^{n+\frac{1}{2}\sharp} \cdot \underline{v}^{\flat} \, \mathrm{d}\Omega_0 = 0. \end{cases} \tag{1.58}$$

In (1.58) we denoted by $(\cdot)^n$ the approximation of an unknown at time $n\Delta\mathrm{t}$ and by $(\cdot)^{n+\frac{1}{2}}$ the standard midpoint value. The problem of finding an appropriate time scheme is then reduced to giving the expression of the *algorithmic* tensors $\underline{\underline{\Sigma}}^{n+\frac{1}{2}\sharp}$ and $\mathrm{d}_y \underline{\underline{e}}^{n+\frac{1}{2}\sharp} \cdot \underline{v}^{\flat}$.

For the sake of simplicity we assumed in (1.58) that the no external forces are applied on the system. Several possibilities are available, the first one that we introduce is the so-called trapezoidal rule

$$\underline{\underline{G}}^{n+\frac{1}{2}\sharp} = \frac{\underline{\underline{G}}(\underline{y}^{n+1}) + \underline{\underline{G}}(\underline{y}^{n})}{2}, \tag{1.59}$$

where $\underline{\underline{G}}$ is any tensor depending on the displacement field. The second possibility, that we will use in the sequel, is the midpoint rule where

$$\underline{\underline{G}}^{n+\frac{1}{2}\sharp} = \underline{\underline{G}}(\underline{y}^{n+\frac{1}{2}}). \tag{1.60}$$

In both cases, as the derivative of the Green-Lagrange tensor is linear with respect to the displacement, its expression is

$$\mathrm{d}_y \underline{\underline{e}}^{n+\frac{1}{2}\sharp} \cdot \underline{v}^{\flat} = \frac{1}{2}\left(\underline{\underline{F}}^{\top}(\underline{y}^{n+\frac{1}{2}}) \cdot \underline{\underline{\nabla}}_{\underline{\xi}} \underline{v}^{\flat} + \underline{\underline{\nabla}}_{\underline{\xi}} \underline{v}^{\flat\top} \cdot \underline{\underline{F}}(\underline{y}^{n+\frac{1}{2}}) \right).$$

Both (1.59) and (1.60) lead to conservative time schemes of order two – see [Gonzalez, 2000, Hauret and Le Tallec, 2006]. That is to say, in both cases we have the following relation between discrete energies

$$\frac{\mathcal{E}_{\mathrm{k}}^{n+1} - \mathcal{E}_{\mathrm{k}}^{n}}{\Delta \mathrm{t}} + \frac{\mathcal{E}_{\mathrm{e}}^{n+1} - \mathcal{E}_{\mathrm{e}}^{n}}{\Delta \mathrm{t}} = O(\Delta \mathrm{t}^2). \tag{1.61}$$

In [Chapelle et al., 2012] another type of possible midpoint expression of the algorithmic tensor is used – originally proposed in [Gonzalez, 2000] – leading to a fully conservative time scheme. However this expression leads to a significant increase of complexity, in terms of implementation. Therefore we will restrict ourselves to a time discretization of type (1.60). However, concerning the internal variables, we directly follow [Chapelle et al., 2012] to finally obtain the following time scheme:

$$\left\{\begin{array}{l}
\dfrac{\underline{v}^{n+1}+\underline{v}^{n}}{2}=\dfrac{\underline{y}^{n+1}-\underline{y}^{n}}{\Delta\mathrm{t}}, \\[4ex]
\displaystyle\int_{\Omega_0}\rho_0\frac{\underline{v}^{n+1}-\underline{v}^{n}}{\Delta\mathrm{t}}\cdot\underline{v}^{\flat}\,\mathrm{d}\Omega_0+\int_{\Omega_0}\underline{\underline{\Sigma}}^{n+\frac{1}{2}\sharp}:\mathrm{d}_{y}\underline{\underline{e}}^{n+\frac{1}{2}\sharp}\cdot\underline{v}^{\flat}\,\mathrm{d}\Omega_0= \\
\qquad\qquad\left|\begin{array}{l}
\displaystyle -\int_{\mathcal{E}n_{\mathrm{L}}}P_{\mathrm{L}}^{\mathrm{v}}\,\underline{n}_{\mathrm{L}}^{n+\frac{1}{2}\sharp}\cdot\underline{v}^{\flat}\mathrm{d}\sigma\;-\int_{\mathcal{E}n_{\mathrm{R}}}P_{\mathrm{R}}^{\mathrm{v}}\,\underline{n}_{\mathrm{R}}^{n+\frac{1}{2}\sharp}\cdot\underline{v}^{\flat}\mathrm{d}\sigma \\[3ex]
\displaystyle -\kappa_{\mathrm{c}}\int_{\mathcal{E}p\iota}|\mathrm{dist}(\underline{x}^{n+\frac{1}{2}},\mathcal{P})|_{-}\,\underline{n}_{\mathcal{P}}^{n+\frac{1}{2}\sharp}\cdot\underline{v}^{\flat}\,\mathrm{d}\sigma \\[3ex]
\displaystyle -\alpha_{\mathcal{A},\mathcal{B}}\int_{\mathcal{A},\mathcal{B}}\underline{y}^{n+\frac{1}{2}}\cdot\underline{v}^{\flat}\,\mathrm{d}\sigma-\beta_{\mathcal{A},\mathcal{B}}\int_{\mathcal{A},\mathcal{B}}\underline{v}^{n+\frac{1}{2}}\cdot\underline{v}^{\flat}\,\mathrm{d}\sigma,
\end{array}\right. \\[8ex]
\text{with } \underline{\underline{\Sigma}}^{n+\frac{1}{2}\sharp}=\dfrac{\partial W^{\mathrm{e}}}{\partial\underline{\underline{e}}}^{n+\frac{1}{2}\sharp}+\dfrac{\partial W^{\mathrm{v}}}{\partial\underline{\underline{\dot{e}}}}^{n+\frac{1}{2}\sharp}+\sigma_{\mathrm{1D}}^{n+\frac{1}{2}\sharp}\,\underline{n}_0\otimes\underline{n}_0\quad\text{and} \\[6ex]
\qquad\qquad\left|\begin{array}{l}
\sigma_{\mathrm{1D}}^{n+\frac{1}{2}\sharp}=\dfrac{1+2e_{\mathrm{1D}}^{n+\frac{1}{2}\sharp}}{1+2e_{\mathrm{c}}^{n+\frac{1}{2}}}\sigma_{\mathrm{c}}^{n+\frac{1}{2}}, \\[5ex]
\sigma_{\mathrm{c}}^{n+\frac{1}{2}}=\sqrt{k_c^{n+1}}\Big(\dfrac{\tau_c}{\sqrt{k_c}}\Big)^{n+1}+\mu\dfrac{e_{\mathrm{c}}^{n+1}-e_{\mathrm{c}}^{n}}{\Delta\mathrm{t}}=\mathrm{E_s}\dfrac{e_{\mathrm{1D}}^{n+\frac{1}{2}\sharp}-e_{\mathrm{c}}^{n+\frac{1}{2}}}{(1+2e_{\mathrm{c}}^{n+\frac{1}{2}})^3}(1+2e_{\mathrm{1D}}^{n+\frac{1}{2}\sharp}), \\[5ex]
\dfrac{k_c^{n+1}-k_c^{n}}{\Delta\mathrm{t}}=-(|u^{n+1}|+\alpha|\dfrac{e_{\mathrm{c}}^{n+1}-e_{\mathrm{c}}^{n}}{\Delta\mathrm{t}}|)k_c^{n+1}+k_0n_0|u^{n+1}|_{+}, \\[4ex]
\dfrac{1}{\Delta\mathrm{t}}\Big(\Big(\dfrac{\tau_c}{\sqrt{k_c}}\Big)^{n+1}-\Big(\dfrac{\tau_c}{\sqrt{k_c}}\Big)^{n}\Big)=\sqrt{k_c^{n+1}}\dfrac{e_{\mathrm{c}}^{n+1}-e_{\mathrm{c}}^{n}}{\Delta\mathrm{t}} \\
+n_0\sigma_0\dfrac{|u^{n+1}|_{+}}{\sqrt{k_c^{n+1}}}\left(1-\dfrac{k_0}{2\sigma_0\sqrt{k_c^{n+1}}}\Big(\dfrac{\tau_c}{\sqrt{k_c}}\Big)^{n+1}\right)-\dfrac{1}{2}(|u^{n+1}|+\alpha|\dfrac{e_{\mathrm{c}}^{n+1}-e_{\mathrm{c}}^{n}}{\Delta\mathrm{t}}|)\Big(\dfrac{\tau_c}{\sqrt{k_c}}\Big)^{n+1}.
\end{array}\right.
\end{array}\right. \tag{1.62}$$

Hence, The set of unknowns becomes

$$\big(\underline{y}^{n+1},\underline{v}^{n+1},e_{\mathrm{c}}^{n+1},\Big(\frac{\tau_c}{\sqrt{k_c}}\Big)^{n+1},k_c^{n+1},P_{\square}^{\mathrm{v},n+1},P_{\square}^{\mathrm{ar},n+1}\big),\quad\square=\mathrm{L},\mathrm{R}.$$

It can be proved that this time scheme, along with a Gonzalez algorithmic stress tensor [Gonzalez, 2000], leads to an exactly conservative time scheme with respect to the continuous energy balance stated in (1.57).

Concerning the contact boundary condition, the term appearing in the algorithm is

$$\mathcal{P}^{\mathrm{c}}(\underline{v}^{\flat})^{n+\frac{1}{2}\sharp}=-\kappa_{\mathrm{c}}\int_{\mathcal{E}p\iota}|\mathrm{dist}(\underline{x}^{n+\frac{1}{2}},\mathcal{P})|_{-}\,\underline{n}_{\mathcal{P}}^{n+\frac{1}{2}\sharp}\cdot\underline{v}^{\flat}\,\mathrm{d}\sigma.$$

In the perspective of performing a Newton's method to solve this problem, one has to differentiate $\mathcal{P}^{\mathrm{c}}(\underline{v}^{\flat})^{n+\frac{1}{2}\sharp}$ with respect to the displacement. This leads to the derivative of the normal vector field of the surface representing the epicardium, *i.e.* its curvature. Besides increasing the complexity of the terms involved in the Newton's method, the curvature might be irregular in practice when surfaces are represented by triangulated meshes. Thus, we overcome this difficulty by proposing a linearized version of the contact boundary condition. Namely we introduce the following linear operator

$$\widetilde{\mathcal{P}}^{c}(\underline{v}^{\flat})^{n+\frac{1}{2}} = -\kappa_{\mathrm{c}} \int_{\mathcal{E}p\iota} |\mathrm{dist}(\underline{x}^{e}, \mathcal{P})|_{-}\, \underline{n}^{e}_{\mathcal{P}} \cdot \underline{v}^{\flat}\, \mathrm{d}\sigma - \kappa_{\mathrm{c}} \int_{\mathcal{E}p\iota} \mathbb{1}_{\mathrm{dist}(\underline{x}^{e}, \mathcal{P})<0}\, \underline{n}^{e}_{\mathcal{P}} \cdot (\underline{y}^{n+\frac{1}{2}} - \underline{y}^{\mathrm{e}})\, \underline{n}^{e}_{\mathcal{P}} \cdot \underline{v}^{\flat}, \tag{1.63}$$

In (1.63) $\underline{y}^{e}$ is an adequate extrapolated displacement, chosen so that this linearization procedure respect the order of consistence of the time scheme. More precisely we have

$$\mathcal{P}^{\mathrm{c}}(\underline{v}^{\flat})^{n+\frac{1}{2}\sharp} - \widetilde{\mathcal{P}}^{c}(\underline{v}^{\flat})^{n+\frac{1}{2}} = -\kappa_{\mathrm{c}} \int_{\mathcal{E}p\iota} |\mathrm{dist}(\underline{x}^{e}, \mathcal{P})|_{-} \left(\mathrm{d}_{y}\underline{n}^{e}_{\mathcal{P}} \cdot (\underline{y}^{n+\frac{1}{2}} - \underline{y}^{\mathrm{e}})\right) \cdot \underline{v}^{\flat}\, \mathrm{d}\sigma + O(\kappa_{\mathrm{c}} \|\underline{y}^{n+\frac{1}{2}} - \underline{y}^{e}\|^{2}).$$

The key argument to justify this approach is that, as any penalization strategy, the coefficient κ_{c} is meant to reach large values whereas the product $\kappa_{\mathrm{c}}|\mathrm{dist}(\underline{x}^{e}, \mathcal{P})|_{-}$ remains finite. Hence we can state that

$$\mathcal{P}^{\mathrm{c}}(\underline{v}^{\flat})^{n+\frac{1}{2}\sharp} - \widetilde{\mathcal{P}}^{c}(\underline{v}^{\flat})^{n+\frac{1}{2}} = O(\|\underline{y}^{n+\frac{1}{2}} - \underline{y}^{e}\|)\, O(1 + \kappa_{\mathrm{c}} \|\underline{y}^{n+\frac{1}{2}} - \underline{y}^{e}\|).$$

By choosing an extrapolation point of order two, for example $\underline{y}^{e} = \frac{3}{2}\underline{y}^{n} - \frac{1}{2}\underline{y}^{n-1}$, we obtain

$$\mathcal{P}^{\mathrm{c}}(\underline{v}^{\flat})^{n+\frac{1}{2}\sharp} - \widetilde{\mathcal{P}}^{c}(\underline{v}^{\flat})^{n+\frac{1}{2}} = O(\Delta \mathrm{t}^{2} + \kappa_{\mathrm{c}} \Delta \mathrm{t}^{4}).$$

Hence, there exists for any large values of the penalization parameter a sufficiently small time step such that the linearization procedure explained above does not alter the order two consistency of the time scheme.

1.4 Simulation results

Prior to comment the numerical results that we have obtained, it seems important to summarize the context of the experiment by gathering the various parameters used in our simulations. These are extracted from the calibration strategy proposed in [Caruel et al., 2013] – based on a reduced modeling approach.

- **Passive parameters:** As shown in Figure 1.18(b) and 1.19(b) we decompose the volume of the geometry into four regions: the valve, the base and the left and right ventricles. In these different regions we provide the following set of parameters to specify the passive law (1.14)

	Valve	Base	Left Vent.	Right Vent.
μ_1	0	0	0	0
μ_2	0	0	0	0
C_0	$85.5 \cdot 10^3$	$28.5 \cdot 10^3$	$5.7 \cdot 10^3$	$5.7 \cdot 10^3$
C_1	$1.1 \cdot 10^{-1}$	$1.1 \cdot 10^{-1}$	$1.1 \cdot 10^{-1}$	$1.1 \cdot 10^{-1}$
C_2	$57 \cdot 10^3$	$28.5 \cdot 10^3$	$5.7 \cdot 10^3$	$5.7 \cdot 10^3$
C_3	$1.1 \cdot 10^{-1}$	$1.1 \cdot 10^{-1}$	$1.1 \cdot 10^{-1}$	$1.1 \cdot 10^{-1}$
η	$7 \cdot 10^1$	$7 \cdot 10^1$	$7 \cdot 10^1$	$7 \cdot 10^1$
κ	$2 \cdot 10^5$	$2 \cdot 10^5$	$2 \cdot 10^5$	$2 \cdot 10^5$

The first remark is that we did not use the quadratic part – or Ciarlet-Geymonat part – appearing in (1.14), but define the hyperelastic potential as a pure exponential function of the invariants. Secondly we see that this decomposition of the geometry enables us to stiffen the base and the valves in order to take into account the fact that they are connected to the atria, the veins and the arteries. Finally, concerning the incompressibility we are led to using a rather large value of κ since it needs to balance with the active stress during contraction.

- **Boundary conditions:** The left endocardium and right endocardium of the geometry are subject to a contact boundary condition as explained in the previous section. As far as the visco-elastic boundary conditions are concerned – see (1.55) – we prescribe

$$\alpha_{\mathcal{A}} = 9.5 \cdot 10^6 \quad , \ \alpha_{\mathcal{B}} = 1.0 \cdot 10^6 \quad , \ \beta_{\mathcal{A}} = 3.0 \cdot 10^4 \quad , \ \beta_{\mathcal{B}} = 1.0 \cdot 10^4 .$$

We note that, in order to avoid large displacements at the apex, we tend to give large values of the stiffness in the corresponding region.

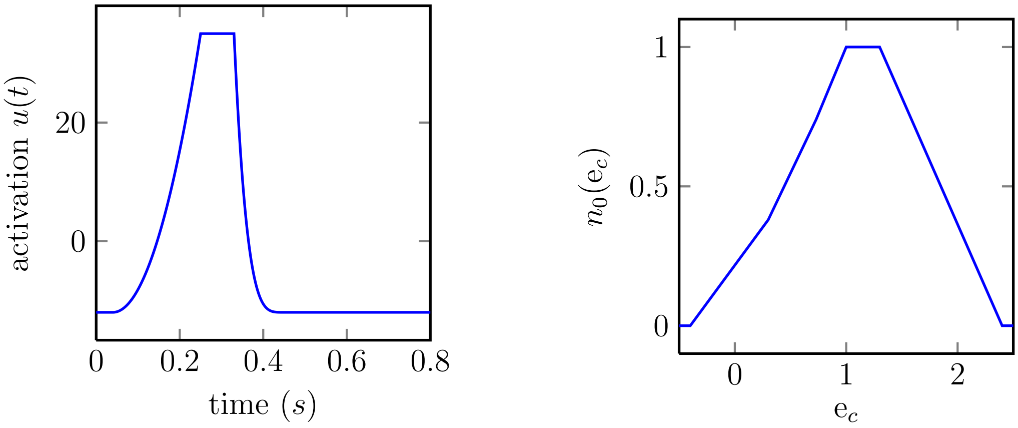

(a) Electrical activation

(b) Starling function

Figure 1.14: Electrical activation and starling function used in practice during a direct simulation.

- **Active parameters:** For the active part of the heart model we provide the following parameters

	Valve	Base	Left Vent.	Right Vent.
α	1.5	1.5	1.5	1.5
σ_0	$6.2 \cdot 10^5$	$6.2 \cdot 10^5$	$6.2 \cdot 10^5$	$7.44 \cdot 10^5$
$\mathrm{E_s}$	$3.0 \cdot 10^7$	$3.0 \cdot 10^7$	$3.0 \cdot 10^7$	$3.0 \cdot 10^7$
k_0	$1.0 \cdot 10^5$	$1.0 \cdot 10^5$	$1.0 \cdot 10^5$	$1.0 \cdot 10^5$
μ	$7 \cdot 10^1$	$7 \cdot 10^1$	$7 \cdot 10^1$	$7 \cdot 10^1$

The parameters are identical in the different regions except that we slightly increase the contractility in the right ventricle in order to make up for the fact that the thickness of the heart wall in this part of the geometry is significantly reduced. Concerning the Starling function n_0 we prescribe a piecewise-linear function of e_c – see Figure 1.14(b). The activation potential is represented in Figure (1.14(b)).

- **Windkessel models:** As we have already mentioned we choose to link both left and right cavities with a one-way model. The corresponding parameters are

	Left Cavity	Right Cavity
C^{p}	$2.0 \cdot 10^{-9}$	$2.0 \cdot 10^{-10}$
R^{p}	$2.0 \cdot 10^7$	$1.0 \cdot 10^7$
C^{d}	$0.505 \cdot 10^{-8}$	$1.0 \cdot 10^{-8}$
R^{d}	$2.0 \cdot 10^8$	$3.0 \cdot 10^7$
P^{e}	$1.0 \cdot 10^3$	$1.0 \cdot 10^3$

Simulating a healthy heart These parameters where calibrated to represent a healthy heart, in the sense that the principal physiological indicators follow standard known values. For instance, Figures 1.16(a) and 1.17(a) shows the evolution of the pressures for the both left and right cavity – more precisely both left and right atrium-cavity-aorta structure. Generally, very little physiological information on the right ventricle is available, however for the left ventricle we see that the ventricle and aortic pressure during systole reach a peak at approximately $1.55 \cdot 10^4$ Pa which is relevant, having in mind the target of $1.6 \cdot 10^4$ Pa. Focusing on the left cavity, we can see that, during the cycle the previously presented calibration of the Windkessel model leads to a almost perfectly cycling aortic pressure – with an initial pressure of $1.1 \cdot 10^4$ Pa.

As far as the cavity volumes are concerned, Figures 1.16(b) and 1.17(b) show their evolution during a simulation run. Even though both cavity volumes reach after the atrial contraction a rather smaller value than general physiological indicator (100 mL instead of 120 mL) the overall evolution of the volumes are quite satisfactory, the volume after contraction is quite good and we also observe that the atrial loading represents approximately a fifth of the ejected volume (another physiological feature). Combining the cavity pressures and their corresponding values enables us to obtain satisfactory *PV-loop* diagrams, as shown in Figures 1.16(c) and 1.17(c).

Figures 1.16(d) and 1.17(d) show the evolution of $\overline{J}$ used in the first part of this Chapter to measure the incompressibility of the material. As expected, during contraction, the volume decreases due to the dramatic increase of internal stresses. However, the large prescribed bulk value enables us to keep its value above 0.9 in both cavities which is consistent with our assumption of a nearly incompressible material.

Figures 1.18 and 1.19 show snapshots of the deforming heart model (the steady light blue line represents the reference configuration) in both short axis view (SAX) and long axis view (LAX). This representation enables us to measure the apparent thickening of the heart wall during contraction.

Simulating an infarct in the septum In the perspective of diagnosis assistance it is important to evaluate if the model of the heart behavior is able to capture the physiological changing that may appear when a part of the heart wall is altered. To do so we set another volume region in the septum of our geometry (the red part in Figure 1.15). We recall that, when a part of a heart has suffered an infarct tissue, the part of the tissue that is damaged tends to stiffen and to lack in contractility. To represent both effects we define two parameters (that are constant per volume regions) θ_{K} and θ such that the hyperelastic potential and the contractility of the tissue are transformed into

$$W^{\mathrm{e}} \to 2^{\theta_{\mathrm{K}}} W^{\mathrm{e}} \quad , \; \sigma_0 \to 2^{\theta} \sigma_0 .$$

To start with, Figure 1.20 compares the previously simulated healthy heart with a modelled infarcted heart where only the contractility is decreased (more precisely we set $\theta = -1$ in the septum). Apart from the diminished stroke volume, we observe that the thickening of the septum during contraction has clearly decreased. Figure 1.21 shows a modelled infarcted heart where both the stiffness and the contractility are altered ($\theta = -1$ and $\theta_{\mathrm{K}} = 1$ in the septum), we see here the combination of two effects: the stiffening induces a loss of preload after atrial contraction and the loss of contractility decreases the stroke volume. It is interesting to see that these parameters affect the heart in two separate ways, it will have its importance when we will perform inverse problems.

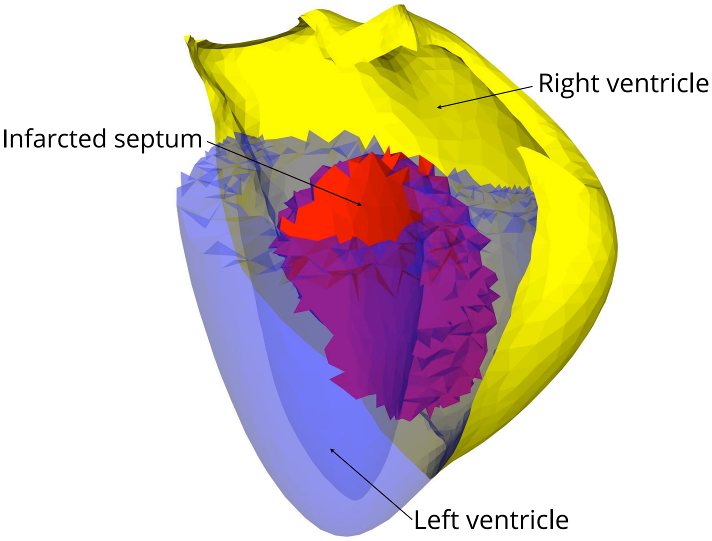

Figure 1.15: Example of an infarcted septum, in (red), in the heart geometry.

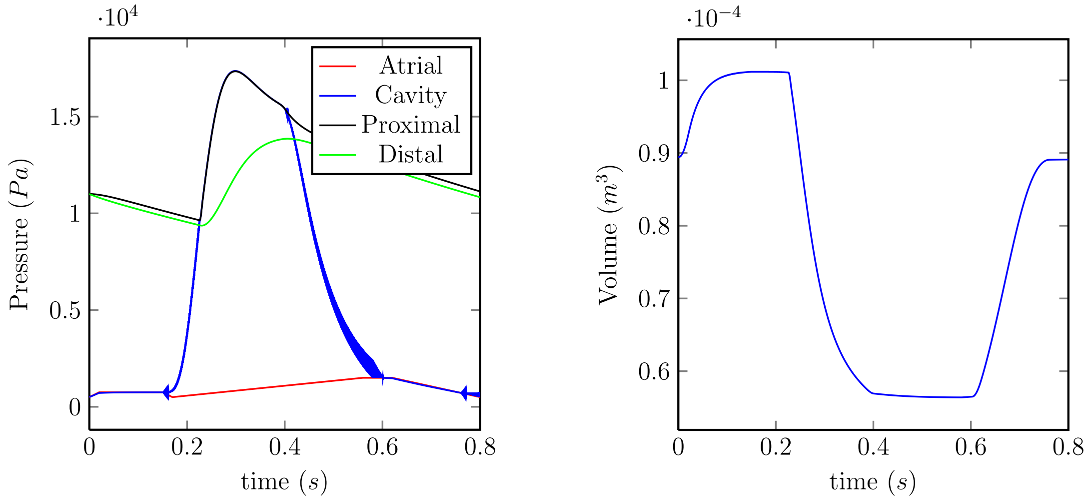

(a) Pressures of the left cavity

(b) Volume of the left cavity

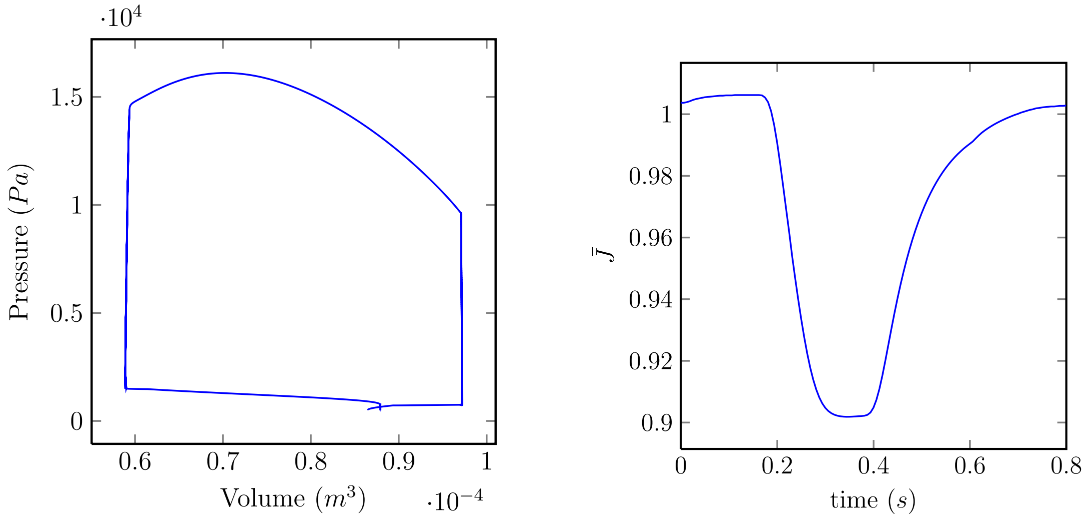

(c) PV loop of the left cavity

(d) Incompressibility in the left cavity

Figure 1.16: Evolution of various indicators of the left ventricle during one cardiac cycle.

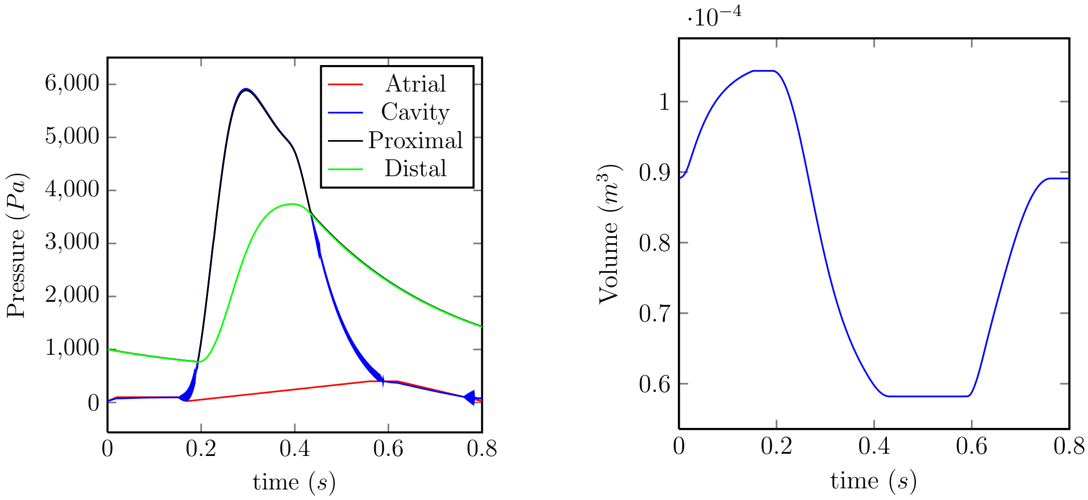

(a) Pressures of the right cavity

(b) Volume of the right cavity

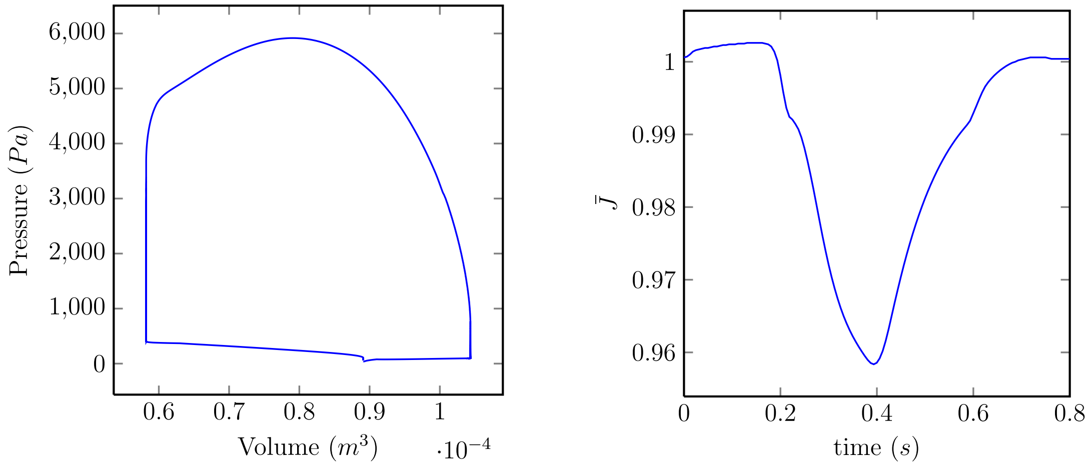

(c) P-V loop of the right cavity

(d) Incompressibility in the right cavity

Figure 1.17: Evolution of various indicators of the right ventricle during one cardiac cycle.

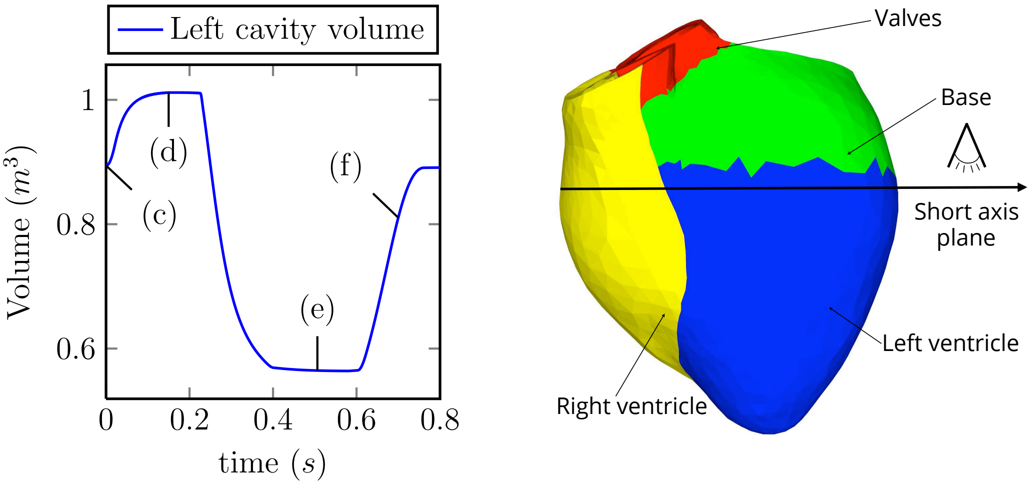

(a) Position of the snapshots in the heart cycle

(b) Representation of the short axis (SAX) view

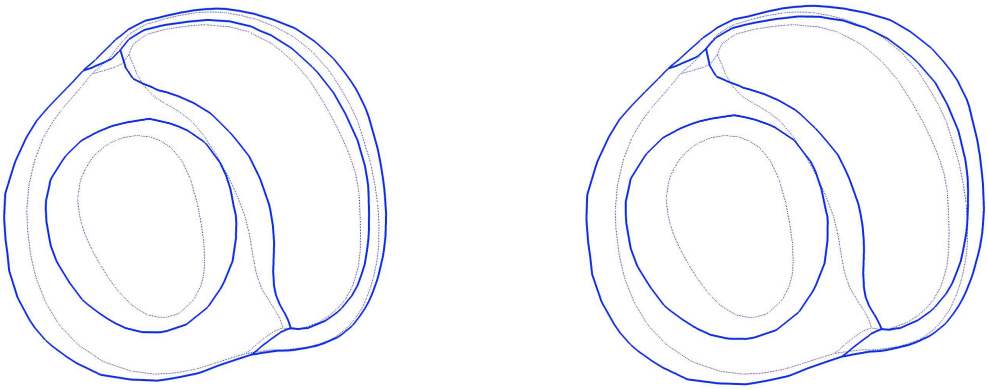

(c) SAX view in diastole

(d) SAX view in tele-diastole

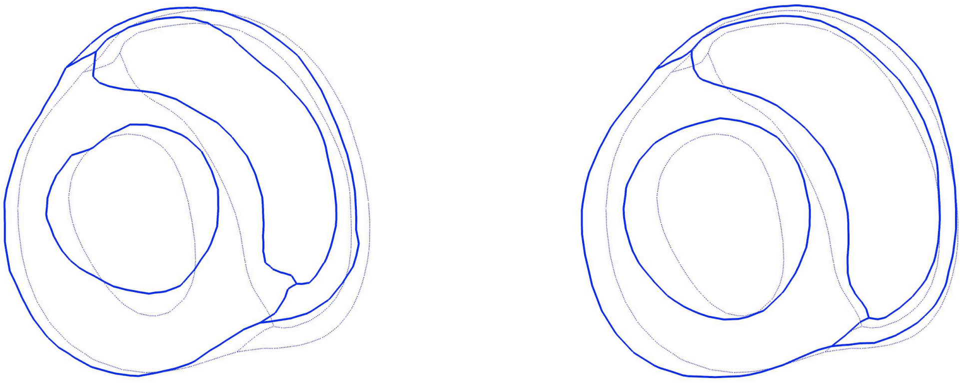

(e) SAX view in tele-systole

(f) SAX view in diastole

Figure 1.18: Snapshots of the numerical solution of the heart model in short axis view.

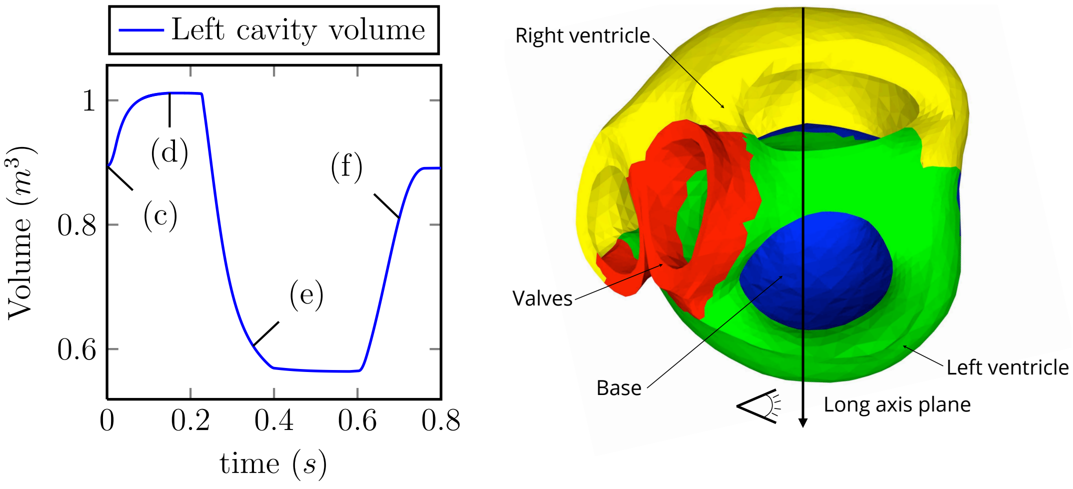

(a) Position of the snapshots in the heart cycle

(b) Representation of the long axis (LAX) view

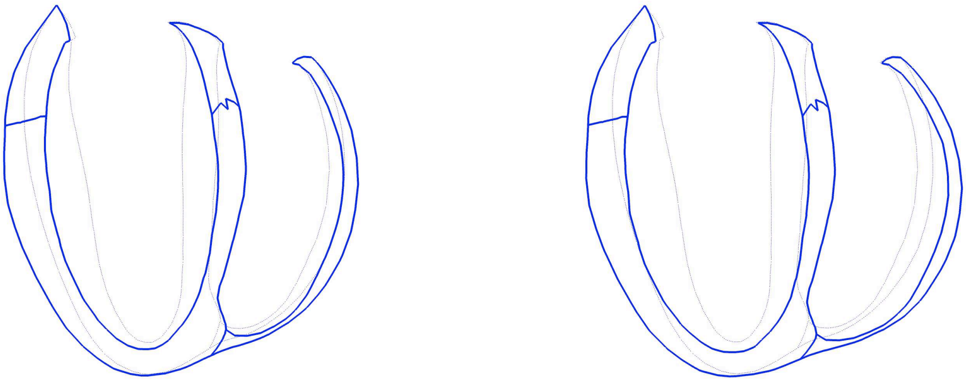

(c) LAX view in diastole

(d) LAX view in tele-diastole

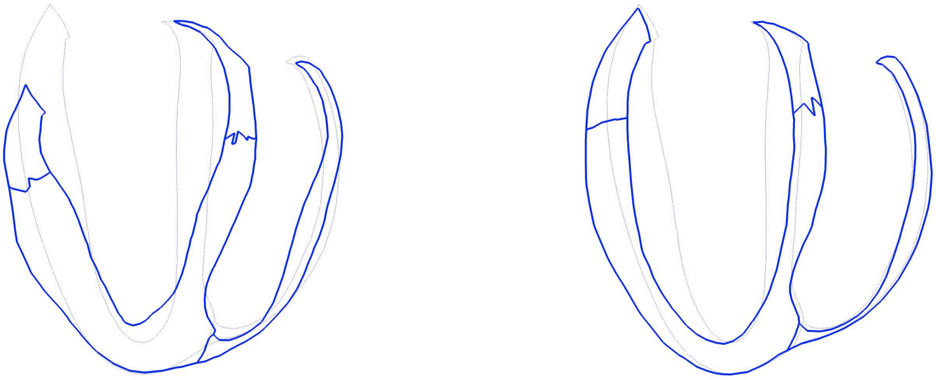

(e) LAX view in systole

(f) LAX view in diastole

Figure 1.19: Snapshots of the numerical solution of the heart model in long axis view.

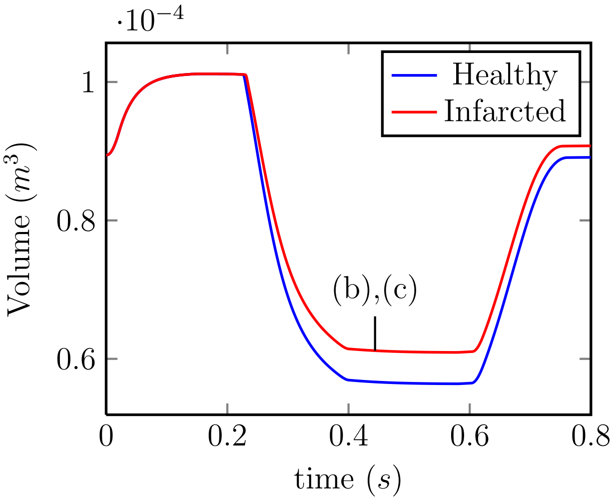

(a) Evolution of the volume of the left cavity in a cardiac cycle.

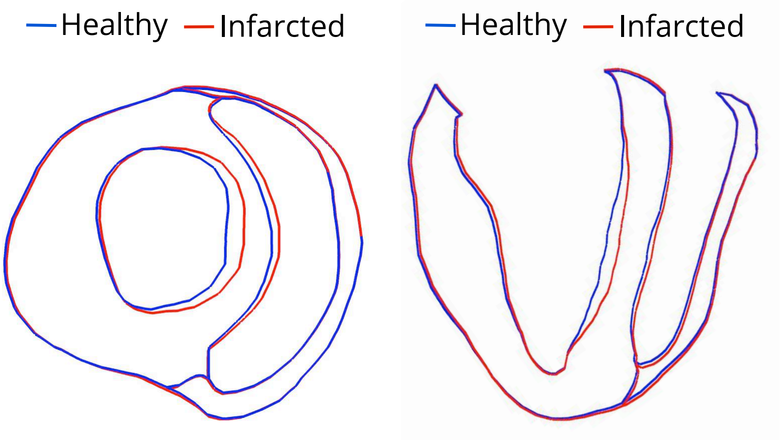

(b) SAX view in late systole.

(c) LAX view in late systole.

Figure 1.20: Simulation results with an infarcted heart modelled using a decrease of contractility: $\theta = -1.0$ in the septum and $\theta = 0.0$ in the remaining part of the heart.

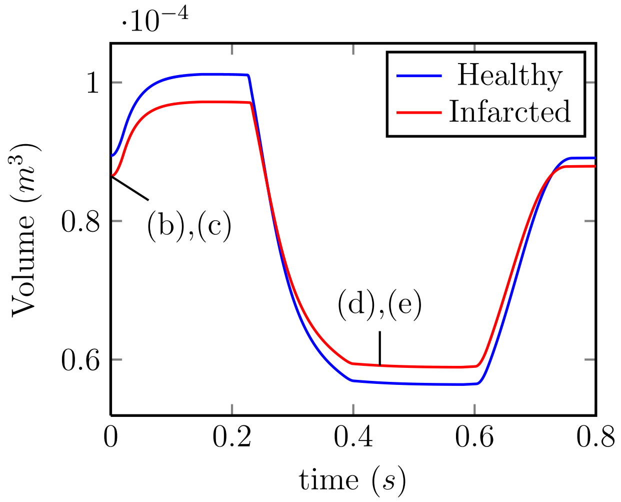

(a) Evolution of the volume of the left cavity in a cardiac cycle.

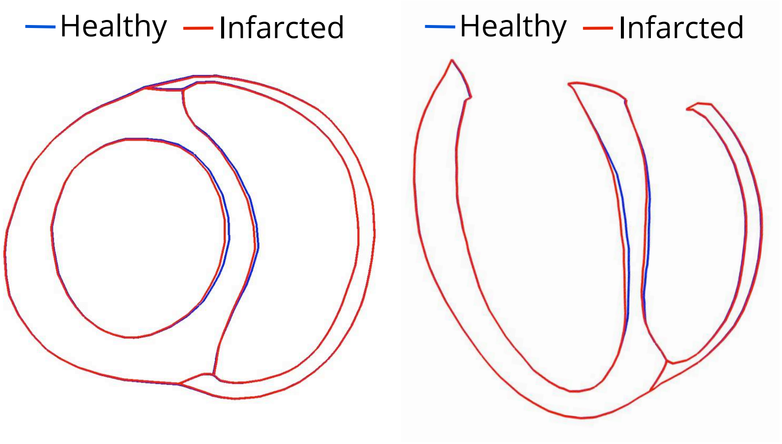

(b) SAX view in diastole.

(c) LAX view in diastole.

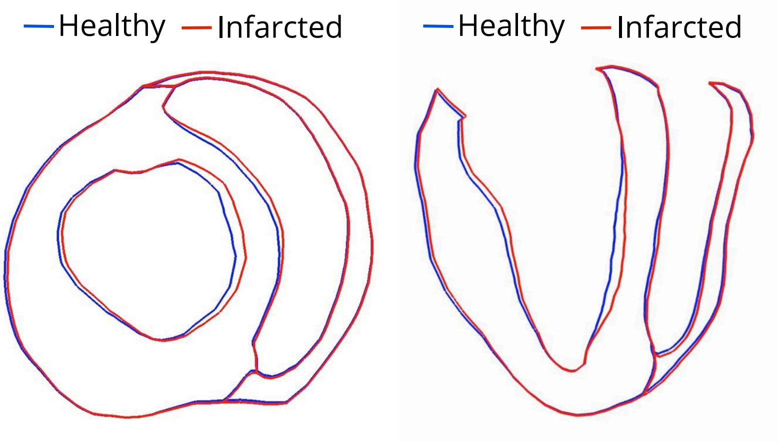

(d) SAX view in late systole.

(e) LAX view in late systole.

Figure 1.21: Simulation results with an infarcted heart modelled using a decrease of contractility and an increase of passive stiffness: $\theta = -1.0$, $\theta_{\mathrm{K}} = 1.0$ in the septum and $\theta = \theta_{\mathrm{K}} = 0.0$ in the remaining part of the heart.

1.5 Conclusion

In this Chapter we have presented a complete biomechanical model of the heart. This description was divided into two main components corresponding to the modeling of the passive and the active behavior of the heart.

The passive part is associated with an hyperelastic potential of exponential type – up to some terms accounting for the incompressibility of the material. This type of hyperelastic law arises in the literature of cardiac tissue modeling as a standard to faithfully represents the stress-strain relation of the material.

The active part is a multi-scale modeling inspired from Huxley's model of creation and destruction of cross-bridges. These cross-bridges are constituted whenever the electrical signal is triggered, thus leading to a stiffening at the upper scale of the myocardial fiber.

Additionally we have detailed a model of the interactions between the heart and its surroundings using a *contact surface*. Moreover, we have seen how the ventricles can be linked with the rest of the cardiovascular system with a – possibly fully coupled – Windkessel model.

We have also provided extensive details on the discretization algorithm – as their implementation was a (non-visible) contribution of this thesis. As we have seen, this discretization task induces some significant difficulties. More precisely, concerning the spatial discretization, the fact that the heart material is a nearly incompressible material potentially induces numerical locking. Hence, the choice of the bulk coefficient is crucial. Concerning the time discretization, the active part of the constitutive law clearly increases the complexity of the conservative time scheme.

Finally, we were able to provide numerical results that faithfully respect some standard physiological characteristics in both healthy and infarcted situations. It is now nothing but natural to aim at performing inverse problems using this model in order to potentially capture detailed physiological features of a particular case under observation.

Bibliography of the first Chapter

[Bathe, 1996] Bathe, K.-J. (1996). *Finite element procedures*.

[Caruel et al., 2013] Caruel, M., Chabiniok, R., Moireau, P., Lecarpentier, Y., and Chapelle, D. (2013). Dimensional reduction of cardiac models for effective validation and calibration. In *7th International Conference on Functional Imaging and Modeling of the Heart, FIMH 2013*, pages 259–267.

[Chapelle et al., 2012] Chapelle, D., Le Tallec, P., Moireau, P., and Sorine, M. (2012). Energy-preserving muscle tissue model: formulation and compatible discretizations. *Journal For Multiscale Computational Engineering*, 10(2):189–211.

[Ciarlet, 1988] Ciarlet, P. G. (1988). *Mathematical elasticity, Volume I: Three-dimensional elasticity*. Elsevier Science Publishers.

[Costa et al., 2001] Costa, K. D., Holmes, J. W., and McCulloch, A. D. (2001). Modelling cardiac mechanical properties in three dimensions. *Phil. Trans. R. Soc.*, 359:1233–1250.

[Dokos et al., 2002] Dokos, S., Smaill, B. H., Young, A. A., and LeGrice, I. J. (2002). Shear properties of passive ventricular myocardium. *Am. J. Physio. Circ. Physiol.*, 283:2650–2659.

[Fernández et al., 2007] Fernández, M. A., Gerbeau, J.-F., and Grandmont, C. (2007). A projection semi-implicit scheme for the coupling of an elastic structure with an incompressible fluid. *Int. J. Numer. Meth. Engng*, 69:794–821.

[Forest et al., 2008] Forest, S., Amestoy, M., Cantournet, S., Damamme, G., Kruch, S., and Maurel, V. (2008). *Mécanique des milieux continus*. École des Mines de Paris.

[Formaggia et al., 2009] Formaggia, L., Quarteroni, A., and Veneziani, A. (2009). *Cardiovascular mathematics, modeling and simulation of the circulatory system*. Springer.

[Göktepe et al., 2011] Göktepe, S., Acharya, S., Wong, J., and Kuhl, E. (2011). Computational modeling of passive myocardium. *Int. J. Numer. Meth. Biomed. Engng.*, 27:1–12.

[Gonzalez, 2000] Gonzalez, O. (2000). Exact energy and momentum conserving algorithms for general models in nonlinear elasticity. *Comput. Methods Appl. Mech. Engrg.*, 190:1763–1783.

[Guccione et al., 1995] Guccione, J. M., Costa, K. D., and McCulloch, A. D. (1995). Finite element stress analysis of left ventricular mechanics in the beating dog heart. *J. Biomech.*, 28(10):1167–1177.

[Hauret and Le Tallec, 2006] Hauret, P. and Le Tallec, P. (2006). Energy-controlling time integration methods for nonlinear elastodynamics and low-velocity impact. *Comput. Methods Appl. Mech. Engrg.*, 195:4890–4916.

[Holzapfel and Ogden, 2009] Holzapfel, G. A. and Ogden, R. W. (2009). Constitutive modelling of passive myocardium: a structurally based framework for material charcterization. *Phil. Trans. R. Soc*, 367:3445–3475.

[Humphrey and Yin, 1989] Humphrey, J. D. and Yin, F. C. P. (1989). Constitutive relations and finite deformations of passive cardiac tissue ii: stress analysis in the left ventricle. *Circ. Res.*, 65:805–817.

[Huxley, 1957] Huxley, A. F. (1957). Muscle structure and theories of contraction. *Prog. Biophys. Mol. Bio.*, 7:258–318.

[Le Dret, 2004] Le Dret, H. (2004). *Méthodes mathématiques en élasticité*. Université Pierre Marie Curie.

[Le Tallec, 2000] Le Tallec, P. (2000). *Introduction à la dynamique des structures*. Editions Ellipses.

[Moireau et al., 2009] Moireau, P., Chapelle, D., and LeTallec, P. (2009). Filtering for distributed mechanical systems using position measurements: Perspectives in medical imaging. *Inverse Problems*, 25.

[Nash and Hunter, 2000] Nash, M. P. and Hunter, P. J. (2000). Computational mechanics of the heart. *J. Elasticity*, 61:113–141.

[Netter, 1994] Netter, F. H. (1994). *The Netter collection of medical illustrations*, volume 4. Saunders.

[Pioletti et al., 1998] Pioletti, D. P., Rakotomanana, L. R., Benvenuti, J.-F., and Leyvraz, P.-F. (1998). Viscoelastic constitutive law in large deformations: application to humane knee ligaments and tendons. *J. Biomech.*, 31:753–757.

[Raoult, 2009] Raoult, A. (2009). Symmetry groups in nonlinear elasticity: an exercise in vintage mathematics. *Comm. Pure Appl. Math.*, 8:435–456.

[Sainte-Marie et al., 2006] Sainte-Marie, J., Chapelle, D., Cimrman, R., and Sorine, M. (2006). Modeling and estimation of the cardiac electromechanical activity. *Comput. Struct.*, 84:1743–1759.

[Temam and Miranville, 2005] Temam, R. and Miranville, A. (2005). *Mathematical modeling in continuum mechanics*. Cambridge University Press.

[Tortora and Derrickson, 2009] Tortora, G. J. and Derrickson, B. (2009). *Principles of anatomy and physiology*. Wiley.

[Vetter and McCulloch, 2000] Vetter, F. J. and McCulloch, A. D. (2000). Three-dimensional stress and strain in passive rabbit left ventricl: a model study. *Ann. Biomed. Eng.*, 28:781–792.

[Wetserhof et al., 2008] Wetserhof, N., Lankhaar, J.-W., and E., W. B. (2008). The arterial windkessel. *Med. Biol. Eng. Comput.*

[Yin et al., 1996] Yin, F. C. P., Chan, C. C. H., and Judd, R. M. R. (1996). Compressibility of perfused passive myocardium. *Am. J. Physio.*, 271:1864–1870.

CHAPTER 2

Data assimilation strategy to perform joint state-parameter estimation

In Chapter 1 we have provided a complete description of a biomechanical model of the heart behavior. A calibration strategy can be applied – using real data set or physiological standard values – in order to obtain a numerical model of the heart that meets some important physiological indicators. However, in the perspective of patient specific simulations or diagnosis assistance, the need for means of coupling data (or observations, medical images of a patient for example) with the biomechanical model at hand naturally appears. This coupling is, in essence, the definition of data assimilation. This Chapter is decomposed as follows. First, we start by giving an overview of the different classes of data assimilations methods one could consider to perform this coupling. In the second section we provide some details and examples of a particular type of sequential filter called nudging. In a third part we gather the key components of the method explained in [Chapelle et al., 2009, Moireau et al., 2009, Moireau and Chapelle, 2011] in order to perform joint state-parameter estimation. In particular we will see that this procedure is a hybrid data assimilation method made of a nudging strategy for the state space and of a reduceed-order Kalman filter for the parameter space. This method is then numerically illustrated in the last Section where we retrieve some constitutive parameters of the biomechanical model of the heart described in Chapter 1 using synthetic data.

Most of the contributions are gathered at the very end of this Chapter in the form of an included pre-printed article:

Data assimilation of time under-sampled measurements using observers, application to wave-like equations. – *Cîndea, N., Imperiale, A. and Moireau, P.*

2.1 Introducing sequential data assimilation methodology

The discipline of data assimilation historically appeared in the context of meteorology and oceanography, see [Navon, 2008, Papadakis and Mémin, 2008, Blum et al., 2008, Corpetti et al., 2009, Titaud et al., 2010] as an example of reference on the subject. It has grown very popular in the context of life sciences, more particularly in cardiology – see [Sainte-Marie et al., 2006, Sermesant et al., 2006, Moireau et al., 2009, Chabiniok et al., 2012, Delingette et al., 2012]. The two main actors in a data assimilation context are the model and the data. The former regroups physical informations on the system under consideration encapsulated in a mathematical formalism and is, in most practical cases, subject to numerical discretization. Traditionally, a model takes the form of a set of coupled partial differential equations, potentially nonlinear. Apart from its ability to simulate any configuration, a model also contains a large range of potential errors: on the operator governing the dynamical system, on the boundary conditions, on the initial conditions, or even errors on the geometry (which can be complex in the case of the heart biomechanical model) used to support the model. On the other hand, the data provide specific and valuable informations on a real system but are partial (in time and space), incomplete and are likely to be corrupted by the noise inherent of any measurement process. A data assimilation procedure tries to cumulate the complementary sources of information to build an estimation of the real system under study.

To start with, let us introduce some standard notations that will help us to understand most of the concepts lying behind data assimilation. Let x be the so-called state of the system, for instance the solution of a partial differential equation – in that case the state space is an infinite dimensional space – or a finite element solution of a discretized dynamical system. In the following , the state space will be denoted by $\mathcal{X}$. As an example, for the cardiac biomechanical model described in the first Chapter, the state variable are

$$\left(\underline{y}, \underline{v}, e_{\mathrm{c}}, \tau_c, k_c, P_{\square}^{\mathrm{v}}, P_{\square}^{\mathrm{ar}}\right), \quad \square = \mathrm{L}, \mathrm{R},$$

that is to say the displacement and the velocity, the internal variables used in the contraction model and the pressures of both left and right cavities appearing in the Windkessel models. From a general point of view, we assume that x satisfies the following dynamical system

$$\dot{x}(t) = A(x(t), \theta, t), \tag{2.1}$$

where A is the potentially nonlinear *dynamical operator* and θ represents the set of parameters characterizing the model. While the state space may be of infinite or very large dimension (e.g. the dimension of a finite element space), the set of parameters is generally far smaller. More importantly, keeping in mind the example of a finite element procedure, the dimension of the parameter space remains bounded whereas the dimension of the state space tends, by nature, to reach large values. Moreover, even in the case of spatially distributed parameters we assume that their variations are sufficiently small to be represented with a restricted number of degrees of freedom.

To fix the ideas let us give a relevant example in the case of the biomechanical model of the heart described in Chapter 1. In the case of an infarct the damaged region of the myocardium tends to stiffen. Hence, to take into account this particularity, one can consider a positive spatial evolution law $\theta_{\mathrm{K}}(\underline{\xi})$ such that the passive elastic potential becomes

$$W^{\mathrm{e}} = 2^{\theta_{\mathrm{K}}}\Big(\mu_1(J_1 - 3) + \mu_2(J_2 - 3) + C_0 \exp\left(C_1(J_1 - 3)^2\right) + C_2 \exp\left(C_3(J_4 - 1)^2\right)\Big) \\ + \kappa(J - 1) - \kappa \ln(J). \tag{2.2}$$

The healthy case will then be represented by $\forall \underline{\xi},\ \theta_{\mathrm{K}}(\underline{\xi}) = 0$. In an infarcted region the value of θ_{K} increases depending on the severeness of the condition. As far as the spatial discretization of this distributed parameter is concerned, one can use for example the AHA regions to define a piecewise constant representation of θ_{K} leading to a set of 17 parameters for the left ventricle.

Assuming that the problem (2.1) is well-posed, only the initial condition $x(0)$ and θ need to be prescribed. However, in most practical cases these quantities are not perfectly known and we decompose the initial condition into a known part $x_\diamond$, the so-called *a priori*, and an uncertainty ζ_x. We also decompose the parameters into their a priori $\theta_\diamond$ and their corresponding uncertainty ζ_θ so that the dynamical system (2.1) finally reads,

$$\begin{cases} \dot{x}(t) = A(x(t), \theta, t), \\ x(0) = x_\diamond + \zeta_x, \\ \theta = \theta_\diamond + \zeta_\theta, \end{cases} \tag{2.3}$$

We could also consider possible modelling errors, a typical example being when one considers some additive noise ω in the dynamical system:

$$\dot{x}(t) = A(x(t), \theta, t) + B\omega(t),$$

but, for the applications contained within the scope of our work, we will restrict ourselves to errors on initial conditions and on the parameters. In the context of cardiac modelling and patient specific simulation these errors have natural interpretations. The main source of error for the initial condition comes from the fact that the reference configuration of the heart is never observed in practice and is, in most cases, only estimated. Concerning the parameters, as the set of parameter represents the physiological condition of a patient (for example the location and severeness of possible damaged parts of the tissue) it is hardly known a priori – the contrary would dramatically diminish the interest of a diagnosis.

In this formalism, let us consider a target system, formally represented by the combination of state and parameter $(x_\bullet, \theta_\bullet)$, that we aim at estimating – for example the heart condition of a patient. To help us reconstructing the target trajectory and additionally to the a priori $x_\diamond$ and $\theta_\diamond$ we assume that some observations z are available on the target system. Classically, the process of extracting the measurements from the system is represented through the action of the so-called *observation* operator H,

$$z(t) = H(x_\bullet(t), t) + \chi(t). \tag{2.4}$$

In (2.4) we denoted by χ some possible additive noise appearing during the measurement procedure. It should be noted that the parameters are not directly observed, which is relevant with practical cases. This observation operator is of major importance since it enables to map the state space to the *observation* space $\mathcal{Z}$. In the most simple case of *direct* measurements – where the observation space is reduced to a subspace of $\mathcal{X}$ – H takes the form of a projection operator. In most practical cases we are facing indirect observations obtained through a complex measurement process, and most likely leading to a nonlinear observation operator.

As an illustration of observations, Figure 2.1 shows two snapshots of cine-MR images. In this case, we understand that a complete definition of the observation operator, that is to say the operator that from the tissue extracts the grey level image, is a difficult task since it should incorporate the reaction of the tissue material points to the magnetic excitation along with the measurement of tissue magnetic relaxation leading to the observed images. To avoid this difficulty we will assume that a prior step a data processing is carried out in order to obtain a simpler form of the observations. A classical example in the case of the cine MR images is the segmentation of the endo- and epicardium of the left ventricle – see [Chabiniok et al., 2012, Chabiniok et al., 2011] and references therein for an example of data assimilation using this type of data. Moreover, during all the presentation of our work, we will suppose that the time sampling of the data is coarse – which is, once again, relevant with practical cases – prohibiting in particular a time differentiation of the data. This implies that all the considered observations are obtained from the displacement of the material and not the velocity.

As we will understand in the following section, most of the data assimilation procedures are based from a capacity to *compare* the data with the model. Assuming that one can define

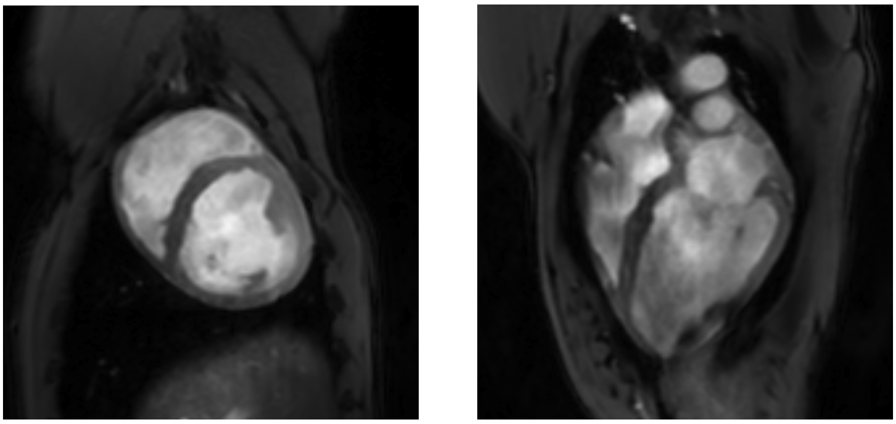

(a) Example of Short Axis (SAX) View of a heart

(b) Example of Long Axis (LAX) View of a heart

Figure 2.1: Example of realistic observations (cine-MR images).

a proper observation operator, corresponding to the data at hand, and assuming that the observation space $\mathcal{Z}$ is equipped with standard algebraic operations, then one can feed a data assimilation by computing the difference

$$z(t) - H(x(t), t).$$

The assumption of that algebraic operations make sense in the observation space is in fact not so trivial. For instance, having in mind the case of endo- and epicardium segmentations, the difference between two surfaces has no simple definition. Therefore, in some practical cases, we need to consider a more general relationship between the observations and the exact trajectory, taking the form of the implicit relation

$$D(z(t), x_\bullet(t)) = \chi(t). \tag{2.5}$$

A typical example, for the case of surfaces, is to use the signed distance function – see [Chabiniok et al., 2011, Chabiniok et al., 2012] as an example of application.

The goal of data assimilation is to reconstruct an estimator $(\widehat{x}(t), \widehat{\theta}(t))$ of the exact trajectory $(x_\bullet(t), \theta_\bullet)$ by coupling the model and the observations. In the following, the estimation $(\widehat{x}(t), \widehat{\theta}(t))$ may also be referred to as the observer. To reach this goal several strategies may be considered. These strategies are traditionally decomposed into two main families: the first one being the family of variational methods – built around the idea of minimizing a given functional – and the second one is the family of sequential methods where the discrepancies between the observer and the data are filtered during the simulation – hence their name. To start with and to fix the ideas we give a quick overview of these two types of data assimilation procedures in a linear setting.

2.1.1 Overview of variational methods

In the following we suppose that both the dynamical operator A and the observation operator H are linear. Moreover we assume, for simplicity, that the state space $\mathcal{X}$ and the observation space $\mathcal{Z}$ are finite dimensional spaces. Variational methods have been widely used in the context of geophysical flows, see [Navon, 2008] or [Blum et al., 2008], and more recently in the context of cardiac function estimation, see [Perego et al., 2011,Sermesant et al., 2006,Sainte-Marie et al., 2006]. In essence, variational methods seek to minimize a functional that balances the confidence one has in the a priori values and the confidence in the data. An illuminating example is when, for simplicity, we consider only some state measurements with some initial errors. The functional to be minimized reads:

$$J(\zeta_x) = \frac{1}{2}\int_0^T \|z(t) - Hx(t)\|^2_{M_z}\mathrm{d}t + \frac{1}{2}\|\zeta_x\|^2_{P_{xx}^{-1}}. \tag{2.6}$$

This minimization is performed with respect to the unknown ζ_x. In (2.6), we denoted by M_z the norm on the observation space and by P_{xx}^{-1} the norm on the initial conditions. These norms play a fundamental role in the data assimilation method since they represent how much importance one gives to the data or to the model. In a way variational methods can be understood as a minimization problem under the constraint imposed by the model dynamical system. In a fully linear and autonomous setting the optimality condition of order one fully characterizes the optimal value, hence we seek the error $\overline{\zeta_x}$ verifying

$$\mathrm{d}_{\zeta_x} J|_{\overline{\zeta_x}} = 0.$$

Let ζ_x^* be a test error, we differentiate the functional as follows:

$$\mathrm{d}_{\zeta_x} J \cdot \zeta_x^* = -\int_0^T (z - Hx)^\intercal \, M_z \, H\mathrm{d}_{\zeta_x} x \cdot \zeta_x^* \mathrm{d}t \; + \; \zeta_x^\intercal P_{xx}^{-1}\zeta_x^*.$$

Now remarking that

$$\begin{cases} \dot{\widehat{\mathrm{d}_{\zeta_x} x}} = A\mathrm{d}_{\zeta_x} x, \\ \mathrm{d}_{\zeta_x} x|_{t=0} = \mathbb{1}, \end{cases}$$

we define the so-called adjoint variable p verifying

$$\begin{cases} \dot{p}(t) + A^\intercal p(t) = -H^\intercal M_z(z - Hx), \\ p(T) = 0, \end{cases}$$

so that the gradient of the functional J reads

$$\mathrm{d}_{\zeta_x} J \cdot \zeta_x^* = -p(0)^\intercal \zeta_x^* + \; \zeta_x^\intercal P_{xx}^{-1}\zeta_x^*.$$

The optimal value derives from this expression

$$\overline{\zeta_x} = P_{xx}p(0) \quad \Longrightarrow \quad \forall \zeta_x^* \quad \mathrm{d}_{\zeta_x} J|_{\overline{\zeta_x}} \cdot \zeta_x^* = 0.$$

In a nutshell, variational data assimilation procedures seek the minimum of the functional J obtained by solving the following two ends problem:

$$\begin{cases} \dot{\overline{x}}(t) = A\overline{x}(t) + R \\ \dot{p}(t) + A^\intercal p(t) = -H^\intercal M_z(z(t) - H\overline{x}(t)), \\ \overline{x}(0) = x_\diamond + P_{xx}p(0), \\ p(T) = 0. \end{cases} \tag{2.7}$$

In practice, one has to consider an iterative process, in order to solve this problem: starting from the a priori $x_\diamond$ one solve the direct problem verified by $\overline{x}$ followed by the resolution of the adjoint problem verified by p to obtain another estimation of the initial condition for the direct problem. This iterative process continues until convergence. This formalism can be directly extended to perform state and parameter estimation. In this case, the cost functional becomes

$$J(\zeta_x, \zeta_\theta) = \frac{1}{2}\int_0^T \|z(t) - Hx(t)\|^2_{M_z} \mathrm{d}t + \frac{1}{2}\|\zeta\|^2_{P^{-1}},$$

with,

$$\zeta = \begin{pmatrix} \zeta_x \\ \zeta_\theta \end{pmatrix}, \quad \text{and} \quad P = \begin{pmatrix} P_{xx} & P_{x\theta} \\ P_{\theta x} & P_{\theta\theta} \end{pmatrix}.$$

To conclude this rapid overview, variational methods provide a mean for estimation regardless of the model – or dynamical system – at hand. However, in order to numerically compute the optimal solution one needs to solve several times the direct and adjoint problems.

2.1.2 Overview of sequential methods

As we mentioned in the introduction of this section, sequential data assimilation methods aim at reconstructing the exact trajectory by filtering the discrepancy between the observation and the data during a simulation run. This type of method is particularly useful when we are more interested in providing an estimation of the actual trajectory at some particular moment in the time window than retrieving the exact initial condition of the target system. Obviously, in the case of constant (in time) parameters, retrieving the initial condition or providing an estimation at a given time is equivalent. In a formal way this general type of method tends to define a modified dynamical system called *observer* by incorporating to the model dynamical system a *correction* term. More precisely, let us define $(\widehat{x}(t), \widehat{\theta}(t))$ the sequential estimator of the target trajectory $(x_\bullet(t), \theta_\bullet)$, the new system reads:

$$\begin{cases} \dot{\widehat{x}}(t) = A\widehat{x}(t) + R + G_x(z(t) - H\widehat{x}(t)), \\ \dot{\widehat{\theta}}(t) = G_\theta(z(t) - H\widehat{x}(t)), \\ \widehat{x}(0) = x_\diamond, \\ \widehat{\theta}(0) = \theta_\diamond. \end{cases} \tag{2.8}$$

Where in (2.8) we denoted by G_x and G_θ the gain operators for the state and the parameters respectively. The main goal of this estimator is to converge, in time, towards the exact trajectory $(x_\bullet(t), \theta_\bullet)$.

In order to provide an example of a sequential estimator we consider for now and for the sake of simplicity only some state measurements with some initial errors. A very popular example is the so-called *optimal filter* verifying

$$\widehat{x}(T) = \overline{x}(T), \tag{2.9}$$

where T is the time window upper bound. In a linear framework the problem of characterizing this sequential estimator has been solved – see for example [Simon, 2006, Bensoussan, 1971] among others – and it leads to the famous *Kalman filter*. The expression of the gain operator is obtained by reformulating the problem (2.7) into a sequential formulation. More precisely, and following the presentation made in [Moireau, 2008], we start by considering $\mathcal{R}(t)$ the operator that for any initial condition $(\overline{x}(0), p(0))$ gives the solution $(\overline{x}(t), p(t))$. This operator is well defined since, in a linear framework, one can prove the existence and uniqueness of the minimizer of the functional J. Decomposing this (linear) operator into

$$\mathcal{R} = \begin{pmatrix} \mathcal{R}_{\overline{x}\overline{x}} & \mathcal{R}_{\overline{x}p} \\ \mathcal{R}_{p\overline{x}} & \mathcal{R}_{pp} \end{pmatrix},$$

the solution at time $(\overline{x}(t), p(t))$ is given by

$$\begin{cases} \overline{x}(t) = \mathcal{R}_{\overline{x}\overline{x}}\overline{x}(0) + \mathcal{R}_{\overline{x}p}p(0) + K_{\overline{x}}(t), \\ \\ p(t) = \mathcal{R}_{p\overline{x}}\overline{x}(0) + \mathcal{R}_{pp}p(0) + K_p(t). \end{cases}$$

These equations are typically obtained applying Duhamel's formula. Using the fact that

$$p(0) = P_{xx}^{-1}(\overline{x}(0) - x_\diamond),$$

we obtain that

$$\begin{cases} \overline{x}(t) = \big(\mathcal{R}_{\overline{x}\overline{x}} + \mathcal{R}_{\overline{x}p}P_{xx}^{-1}\big)\overline{x}(0) - \mathcal{R}_{\overline{x}p}P_{xx}^{-1}x_\diamond + K_{\overline{x}}(t), \\ \\ p(t) = \big(\mathcal{R}_{p\overline{x}} + \mathcal{R}_{pp}P_{xx}^{-1}\big)\overline{x}(0) - \mathcal{R}_{pp}P_{xx}^{-1}x_\diamond + K_p(t). \end{cases} \tag{2.10}$$

The fact that there exists a unique solution of the problem (2.7) insures the inversibility of the operator $\big(\mathcal{R}_{p\overline{x}} + \mathcal{R}_{pp}P_{xx}^{-1}\big)$. Thus, the expression of the initial state reads

$$\overline{x}(0) = \big(\mathcal{R}_{p\overline{x}} + \mathcal{R}_{pp}P_{xx}^{-1}\big)^{-1}\big(p(t) + \mathcal{R}_{pp}P_{xx}^{-1}x_\diamond - K_p(t)\big).$$

Introducing this expression in (2.10) leads to

$$\begin{aligned} \overline{x}(t) = \Big(\big(\mathcal{R}_{\overline{x}\overline{x}} + \mathcal{R}_{\overline{x}p}P_{xx}^{-1}\big)\big(\mathcal{R}_{p\overline{x}} + \mathcal{R}_{pp}P_{xx}^{-1}\big)^{-1} - \mathcal{R}_{\overline{x}p}P_{xx}^{-1}\Big)x_\diamond \\ + \Big(K_{\overline{x}}(t) - \big(\mathcal{R}_{\overline{x}\overline{x}} + \mathcal{R}_{\overline{x}p}P_{xx}^{-1}\big)\big(\mathcal{R}_{p\overline{x}} + \mathcal{R}_{pp}P_{xx}^{-1}\big)^{-1}K_p(t)\Big) \\ + \big(\mathcal{R}_{\overline{x}\overline{x}} + \mathcal{R}_{\overline{x}p}P_{xx}^{-1}\big)\big(\mathcal{R}_{p\overline{x}} + \mathcal{R}_{pp}P_{xx}^{-1}\big)^{-1}p(t). \end{aligned}$$

Denoting this expression by

$$\overline{x}(t) = \widehat{x}(t) + P(t)p(t), \tag{2.11}$$

with $\widehat{x}(t)$ independent of $p(t)$ and differentiating with respect to the time variable we obtain

$$\dot{\widehat{x}} + \Big(\dot{P} - AP - PA^\intercal + PH^\intercal M_z HP\Big)p = A\widehat{x} + R + PH^\intercal M_z(z - H\widehat{x}).$$

As $\widehat{x}(t)$ is independent of p the matrix P necessarily follows the so-called Riccati equation, namely

$$\begin{cases} \dot{P} - PA^\intercal - AP + PH^\intercal M_z HP = 0, \\ P(0) = P_{xx}, \end{cases} \tag{2.12}$$

and we deduce the expression of the *Kalman gain*

$$G_x = PH^\intercal M_z. \tag{2.13}$$

The matrix P following the differential equation (2.12) can be interpreted, from a probabilistic standpoint, as the covariance matrix of the estimation error. Moreover we can easily check that (2.11) combined with the fact that $p(T) = 0$ necessarily entails the desired link with the optimal solution defined in (2.9). This construction of the observer dynamical system directly extends in the case of joint state-parameter estimation

Another example of sequential filtering is the so-called Luenberger filter or nudging – see [Auroux and Blum, 2007, Luenberger, 1971, Ramdani et al., 2012, Bertoglio et al., 2013]. Focusing on state estimation, this procedure tries to stabilize the dynamical system verified by the estimation error

$$\widetilde{x}(t) = x_\bullet(t) - \widehat{x}(t).$$

That is to say, from (2.8), (2.3) and (2.4)

$$\begin{cases} \dot{\widetilde{x}}(t) = (A - G_x H)\widetilde{x}(t) - G_x \chi, \\ \widetilde{x}(0) = \zeta_x. \end{cases} \tag{2.14}$$

This filter – in this general form – is not necessarily optimal since it only aims at controlling the estimation error dynamical system towards zero. For this method to be reasonable, we understand that the gain operator needs to be defined so that $A - G_x H$ is a dissipative operator.

To conclude this prompt description of some methods to perform the reconstruction of an estimation of a target trajectory from the data, let us summarize some drawbacks and advantages. To start with, the variational method has the advantages to be available for any type of model dynamical system. On the other hand it requires to perform an iterative process to obtain a numerical solution and, for this particular reason, this type of method is likely to be more efficient for situations where the cost of solving a direct problem is relatively small. Secondly, Kalman filtering also provides an observer for any type of model and is, on top of that, a sequential method, but it requires to solve the Riccati equation for the full matrix P. This drawback turns out to be a major obstacle when facing large systems obtained after finite element discretization of partial differential equations. Finally, comparing to the first two data assimilation methods, the nudging procedure is not optimal, however it benefits from a greater flexibility. As a matter of fact we will see in the next section that with the simplest choice of the gain operator one can obtain – still in the linear case – an exponential convergence of the observer towards the target trajectory. The major difficulty of this strategy is that it requires a precise understanding of the operator governing the dynamical system (2.3) in order to insure that $A - G_x H$ is dissipative. Additionally to the fact that this method is model dependent and since, by nature, the parameters are constant in time, it is not directly suitable for parameter identification.

2.2 Nudging, a state estimation procedure

In this section we focus our attention on providing some theoretical components around the nudging procedure that we will use in the context of a joint state-parameter estimation for the cardiac model presented in Chapter 1.

2.2.1 From state estimation to control theory

To start with, let us recall the weak formulation of the fundamental principle of dynamics (without the source term for simplicity and with homogeneous Dirichlet boundary conditions),

$$\begin{cases} \displaystyle\int_{\Omega_0} \rho_0 \underline{\ddot{y}} \cdot \underline{v}^\flat \,\mathrm{d}\Omega_0 + \int_{\Omega_0} \underline{\underline{\Sigma}} : \mathrm{d}_y \underline{\underline{e}} \cdot \underline{v}^\flat \,\mathrm{d}\Omega_0 = 0, \\ \\ \underline{y}(0) = \underline{y}_0 + \underline{\zeta}_0, \quad \underline{\dot{y}}(0) = \underline{y}_1 + \underline{\zeta}_1, \end{cases}$$

where $\underline{\zeta}_0$ and $\underline{\zeta}_1$ are possible uncertainties on the initial condition. For the sake of simplicity we make the assumption of small displacements so that the strong formulation of this problem reads

$$\begin{cases} \rho_0 \underline{\ddot{y}} - \mathrm{div}(\underline{\underline{\sigma}}(\underline{y})) = 0, & \text{in} \quad \Omega_0 \\ \\ \underline{y} = 0, & \text{on} \quad \partial\Omega_0 \\ \\ \underline{y}(0) = \underline{y}_0 + \underline{\zeta}_0, \quad \underline{\dot{y}}(0) = \underline{y}_1 + \underline{\zeta}_1. \end{cases} \tag{2.15}$$

Moreover, we make the assumption, once again for simplicity reasons, of an isotropic material admitting a Hooke's law as its constitutive law

$$\underline{\underline{\sigma}}(\underline{y}) = \lambda \mathrm{tr}(\underline{\underline{\varepsilon}}(\underline{y}))\underline{\underline{\mathbb{1}}} + 2\mu \underline{\underline{\varepsilon}}(\underline{y}).$$

With these assumptions, this type of problem fits into the general family of abstract problems of the form

$$\begin{cases} \ddot{w}(t) + A_0 w(t) = 0, \\ w(0) = w_0 + \zeta_0, \quad \dot{w}(0) = w_1 + \zeta_1. \end{cases} \tag{2.16}$$

In (2.16), $A_0 : \mathcal{D}(A_0) \to \mathcal{H}$ is a self adjoint, positive-definite operator with compact resolvent – where $\mathcal{H}$ is a Hilbert space endowed with an inner product $(\cdot, \cdot)$ and the associated norm $\|\cdot\|$. In our case we have

$$\mathcal{H} = \mathcal{L}^2(\Omega_0)^3, \quad \mathcal{D}(A_0) = \left\{ \underline{w}^* \in \mathcal{H}_0^1(\Omega_0)^3 \mid \mathrm{div}(\underline{\underline{\sigma}}(\underline{w}^*)) \in \mathcal{L}^2(\Omega_0)^3 \right\},$$

and

$$\forall w^* \in \mathcal{D}(A_0) \quad A_0 w^* = -\frac{1}{\rho_0} \mathrm{div}(\underline{\underline{\sigma}}(\underline{w}^*)).$$

Denoting by

$$x(t) = \begin{pmatrix} w(t) \\ \dot{w}(t) \end{pmatrix} \in \mathcal{X} = \mathcal{D}(A_0^{\frac{1}{2}}) \times \mathcal{H} = \mathcal{H}_0^1(\Omega_0)^3 \times \mathcal{L}^2(\Omega_0)^3,$$

the system (2.16) can be rewritten as a first order dynamical system

$$\begin{cases} \dot{x}(t) = Ax(t), \\ \\ x(0) = \begin{pmatrix} w_0 + \zeta_0 \\ w_1 + \zeta_1 \end{pmatrix}, \end{cases} \tag{2.17}$$

where $A : \mathcal{D}(A) \to \mathcal{X}$ is a skew-adjoint operator with compact resolvent defined by

$$A = \begin{pmatrix} 0 & \mathbb{1} \\ -A_0 & 0 \end{pmatrix}, \quad \mathcal{D}(A) = \mathcal{D}(A_0) \times \mathcal{D}(A_0^{\frac{1}{2}}).$$

To start with, we consider that the observations take the form

$$z(t) = Hx(t) + \chi(t),$$

where the observation operator $H \in \mathcal{L}(\mathcal{X}, \mathcal{Z})$ is linear and bounded operator and $\mathcal{Z}$ is another Hilbert space equipped with the norm $\| \cdot \|_{\mathcal{Z}}$. In this context, the nudging procedure – used in [Moireau et al., 2009] and [Chabiniok et al., 2011, Bertoglio et al., 2012, Moireau et al., 2013, **?**, Chabiniok et al., 2012, Bertoglio et al., 2013] – proposes to build an estimation $\widehat{x}(t)$ of the exact trajectory $x(t)$ through the following dynamical system

$$\begin{cases} \dot{\widehat{x}}(t) = A\widehat{x}(t) + \gamma H^*(z(t) - H\widehat{x}(t)), \\ \\ \widehat{x}(0) = \begin{pmatrix} w_0 \\ w_1 \end{pmatrix}, \end{cases} \tag{2.18}$$

that is to say the nudging gain operator takes the most simplest form of

$$G = \gamma H^*,$$

where H^* is the adjoint operator of the observation operator (for the corresponding metrics in the state space and in the observation space) and $\gamma > 0$ is a scalar value. Therefore, the dynamical system verified by the estimation error is

$$\begin{cases} \dot{\widetilde{x}}(t) = (A - \gamma H^* H)\widetilde{x}(t) + \gamma H^* \chi(t), \\ \\ \widetilde{x}(0) = \begin{pmatrix} \zeta_0 \\ \zeta_1 \end{pmatrix}. \end{cases} \tag{2.19}$$

Neglecting the observation noise – appearing as a source term in the estimation error dynamical system – for a moment so that we can favour our intuition, we can see that, since A is a skew-adjoint operator, the nudging procedure is a modification of the (conservative) model dynamical system entailing a damped dynamical system of the estimation error. More precisely one can directly derive the following energy estimate

$$\frac{1}{2}\frac{\mathrm{d}}{\mathrm{d}t}\|\widetilde{x}(t)\|_{\mathcal{X}}^2 = -\gamma \|H\widetilde{x}\|_{\mathcal{Z}}^2.$$

Another equivalent interpretation is that the nudging procedure aims at stabilizing the estimation error dynamical system through a feedback control. The simple form of the gain operator, compared to other data assimilation procedure, is the most attractive asset of this nudging procedure.

2.2.2 Examples of applications

The efficiency of the nudging procedure is appreciated by considering the speed of convergence towards zero of the estimation error. In some (ideal) cases this speed can be theoretically estimated but in practical cases, as we will encounter later, the quality of the filter will be estimated by considering the poles of the stabilized operator $A - \gamma H^* H$.

In the linear case with a bounded and linear observation operator, it is a well-known result – see [Liu, 1997] – that the exponential stabilization of the system (2.19) (where the source term induced from the observation noise is omitted), namely

$$\exists M > 0 \text{ and } \mu > 0 \quad \|\widetilde{x}(t)\|_{\mathcal{X}} \leq M \exp(-\mu t)\|\widetilde{x}(0)\|_{\mathcal{X}} \quad \forall t > 0, \tag{2.20}$$

is equivalent to the so-called *observability inequality* verified by any solution of the system (2.17). The inequality takes the following form. $\exists T > 0$ and $C_T > 0$ such that any solution of $\dot{x} = Ax$ satisfies

$$\int_0^T \|Hx(t)\|_{\mathcal{Z}}^2 \,\mathrm{d}t \geq C_T \|x(0)\|_{\mathcal{X}}^2. \tag{2.21}$$

The inequality (2.21) is a condition on the observation operator which – simply stated – describes the fact that, over time, the observation operator gathers enough coercivity to be able to control the energy initially introduced in the system.

In this section we provide some classical examples of application of the nudging procedure for various types of data and observation operators. These examples will enable us to understand the main features of the nudging procedure.

Example of velocity feedback in a subdomain. To illustrate this filtering procedure we suppose that we directly observe the velocity of the solution in a subdomain ω_0 of the reference configuration Ω_0, that is to say:

$$H = \begin{pmatrix} 0 & H_0 \end{pmatrix} : \left| \begin{array}{ccc} \mathcal{H}_0^1(\Omega_0)^3 \times \mathcal{L}^2(\Omega_0)^3 & \longrightarrow & \mathcal{L}^2(\omega_0)^3 \\ \begin{pmatrix} \underline{y} \\ \underline{\dot{y}} \end{pmatrix} & \longmapsto & \underline{\dot{y}}|_{\omega_0}. \end{array} \right.$$

In this particular case, the observation space is $\mathcal{Z} = \mathcal{L}^2(\omega_0)^3$ equipped with the classical $\mathcal{L}^2$-norm on the domain of observation. Since the functional space of velocities is $\mathcal{L}^2(\Omega_0)^3$, the adjoint operator of H is easily defined as the characteristic function of the subdomain

$$\forall z \in \mathcal{L}^2(\omega_0)^3, \quad H^* z = \mathbb{1}_{\omega_0} z \in \mathcal{L}^2(\Omega_0)^3.$$

Hence, the dynamical system verified by the observer is

$$\begin{cases} \underline{\ddot{\widehat{y}}} - \mathrm{div}(\underline{\underline{\sigma}}(\underline{\widehat{y}})) = \gamma \mathbb{1}_{\omega_0}\Big(z - \underline{\dot{\widehat{y}}}|_{\omega_0}\Big), & \text{in } \Omega_0, \\ \underline{\widehat{y}} = 0, & \text{on } \partial\Omega_0, \\ \underline{\widehat{y}}(0) = \underline{y}_0, \quad \underline{\dot{\widehat{y}}}(0) = \underline{y}_1. & \end{cases} \tag{2.22}$$

From an energy standpoint we clearly see that this procedure adds a classical dissipative term in the estimation error dynamical system

$$\ddot{\underline{\widetilde{y}}} - \gamma \mathbb{1}_{\omega_0}\big(\dot{\underline{\widetilde{y}}}|_{\omega_0}\big) - \operatorname{div}(\underline{\underline{\sigma}}(\underline{\widetilde{y}})) = 0,$$

entailing the following energy estimate

$$\frac{\mathrm{d}}{\mathrm{d}t}\Big(\mathcal{E}_{\mathrm{e}}(\underline{\widetilde{y}}(t)) + \mathcal{E}_{\mathrm{k}}(\dot{\underline{\widetilde{y}}}(t))\Big) = -\gamma \|\dot{\underline{\widetilde{y}}}\|^2_{\mathcal{L}^2(\omega_0)^3}, \tag{2.23}$$

where in (2.23) we denote the elastic energy and the kinetic energy as

$$\forall \underline{v}^\flat \in \mathcal{H}^1_0(\Omega_0)^3 \quad \mathcal{E}_{\mathrm{e}}(\underline{v}^\flat) = \frac{1}{2}\int_{\Omega_0} \underline{\underline{\sigma}}(\underline{v}^\flat) : \underline{\underline{\varepsilon}}(\underline{v}^\flat)\, \mathrm{d}\Omega_0 \quad \text{and} \quad \mathcal{E}_{\mathrm{k}}(\underline{v}^\flat) = \frac{1}{2}\int_{\Omega_0} \|\dot{\underline{v}}^\flat\|^2 \rho_0\, \mathrm{d}\Omega_0.$$

The convergence of this observer towards the exact trajectory clearly depends on the observation domain ω_0. As a matter of fact, if ω_0 satisfies the geometric control condition of Bardos, Lebeau and Rauch [Bardos et al., 1992] then the observability inequality (2.21) is satisfied. This leads to the exponential decrease of the estimation error energy, thus the exponential convergence of the estimator towards the exact trajectory.

Remark 10. *The weak formulation of the system* (2.22) *reads,* $\forall \underline{v}^\flat \in \mathcal{H}^1_0(\Omega_0)^3$*,*

$$\big(\ddot{\underline{\widehat{y}}}, \underline{v}^\flat\big)_{\mathcal{E}_{\mathrm{k}}} + \big(\underline{\widehat{y}}, \underline{v}^\flat\big)_{\mathcal{E}_{\mathrm{e}}} = \gamma\left(\mathbb{1}_{\omega_0}\Big(z - \dot{\underline{\widehat{y}}}|_{\omega_0}\Big), \underline{v}^\flat\right)_{\mathcal{L}^2(\Omega_0)^3} = \gamma\left(z - \dot{\underline{\widehat{y}}}|_{\omega_0}, \underline{v}^\flat|_{\omega_0}\right)_{\mathcal{L}^2(\omega_0)^3},$$

where we implicitly define the inner product, $\forall \underline{v}^\flat, \underline{w}^\flat \in \mathcal{H}^1_0(\Omega_0)^3$*,*

$$\big(\underline{w}^\flat, \underline{v}^\flat\big)_{\mathcal{E}_{\mathrm{e}}} = \int_{\Omega_0} \underline{\underline{\sigma}}(\underline{w}^\flat) : \underline{\underline{\varepsilon}}(\underline{v}^\flat)\, \mathrm{d}\Omega_0 \quad \textit{and} \quad \big(\underline{w}^\flat, \underline{v}^\flat\big)_{\mathcal{E}_{\mathrm{k}}} = \int_{\Omega_0} \underline{v}^\flat \cdot \underline{w}^\flat \rho_0\, \mathrm{d}\Omega_0.$$

It is interesting to note that, considering the discrepancy measure

$$\forall \underline{v}^\flat \in \mathcal{L}^2(\Omega_0)^3, \quad E_D(z, \underline{v}^\flat) = \frac{1}{2}\|z - \underline{v}^\flat|_{\omega_0}\|^2_{\mathcal{L}^2(\omega_0)^3},$$

the previously stated weak formulation is reduced to

$$\big(\ddot{\underline{\widehat{y}}}, \underline{v}^\flat\big)_{\mathcal{E}_{\mathrm{k}}} + \big(\underline{\widehat{y}}, \underline{v}^\flat\big)_{\mathcal{E}_{\mathrm{e}}} = -\gamma \left\langle \mathrm{d}E_D(z, \dot{\underline{\widehat{y}}}), \underline{v}^\flat \right\rangle_{\mathcal{L}^2(\Omega_0)'\mathcal{L}^2(\Omega_0)},$$

where $\mathrm{d}E_D$ *is the Gâteaux derivative of the discrepancy measure, here represented as a linear form on the velocity space. This form of the observer may inspire a similar filtering procedure with a more general type of discrepancy measure.*

Example of displacement feedback in a subdomain. This time we consider partial displacement measurement, a case that is closer to the type of information that we will obtain in the context of cardiac estimation, see [Chapelle et al., 2012] for more details on this particular case. The design of sequential observer in this context was originally introduced by authors in [Moireau et al., 2009]. We suppose that

$$H = \begin{pmatrix} H_0 & 0 \end{pmatrix} : \left| \begin{array}{ll} \mathcal{H}^1_0(\Omega_0)^3 \times \mathcal{L}^2(\Omega_0)^3 & \longrightarrow \mathcal{H}^1(\omega_0)^3 \\ \begin{pmatrix} \underline{y} \\ \dot{\underline{y}} \end{pmatrix} & \longmapsto \underline{y}|_{\omega_0}. \end{array} \right.$$

In this case, the observation space is $\mathcal{Z} = \mathcal{H}^1(\omega_0)^3$. To define the adjoint operator we can introduce the so-called lifting or extension operator Ext_{ω_0} defined by

$$\mathrm{Ext}_{\omega_0} \; : \left| \begin{array}{rl} \mathcal{H}^1(\omega_0)^3 & \longrightarrow \mathcal{H}^1_0(\Omega_0)^3 \\ \underline{\varphi} & \longmapsto \underline{u} = \mathrm{Ext}_{\omega_0}(\underline{\varphi}), \end{array} \right.$$

where $\underline{u}$ is solution of

$$\begin{cases} -\mathrm{div}(\underline{\underline{\sigma}}(\underline{u})) = 0, & \text{in } \Omega_0 \backslash \omega_0, \\ \underline{u} = 0, & \text{on } \partial\Omega_0, \\ \underline{u} = \underline{\varphi}, & \text{in } \overline{\omega_0}. \end{cases} \tag{2.24}$$

We denote by $\mathcal{H}^1_{\omega_0}$ the space $\mathcal{H}^1(\omega_0)^3$ equipped with the norm

$$\forall\ \underline{\varphi} \in \mathcal{H}^1_{\omega_0}, \quad \|\underline{\varphi}\|^2_{\mathcal{H}^1_{\omega_0}} = \|\mathrm{Ext}_{\omega_0}(\underline{\varphi})\|^2_{\mathcal{E}_\mathrm{e}}.$$

Remarking that the extension operator verifies an *orthogonality property*, namely

$$\forall \underline{\varphi} \in \mathcal{H}^1(\omega_0)^3, \quad \forall \underline{v}^\flat \in \mathcal{H}^1_0(\Omega_0)^3, \quad \underline{v}^\flat|_{\omega_0} = 0, \quad \left(\mathrm{Ext}_{\omega_0}(\underline{\varphi}), \underline{v}^\flat\right)_{\mathcal{E}_\mathrm{e}} = 0.$$

We can verify that $\mathrm{Ext}_{\omega_0}(\cdot)$ is the adjoint operator of H_0 for the metrics $(\cdot,\cdot)_{\mathcal{H}^1_{\omega_0}}$ and $(\cdot,\cdot)_{\mathcal{E}_\mathrm{e}}$ since $\forall \underline{\varphi} \in \mathcal{H}^1_{\omega_0}$ and $\forall \underline{v}^\flat \in \mathcal{H}^1_0(\Omega_0)^3$,

$$\begin{aligned} \left(\underline{\varphi}, \underline{v}^\flat|_{\omega_0}\right)_{\mathcal{H}^1_{\omega_0}} &= \left(\mathrm{Ext}_{\omega_0}(\underline{\varphi}), \mathrm{Ext}_{\omega_0}(\underline{v}^\flat|_{\omega_0})\right)_{\mathcal{E}_\mathrm{e}} \\ &= \left(\mathrm{Ext}_{\omega_0}(\underline{\varphi}), \underline{v}^\flat\right)_{\mathcal{E}_\mathrm{e}} + \left(\mathrm{Ext}_{\omega_0}(\underline{\varphi}), \mathrm{Ext}_{\omega_0}(\underline{v}^\flat|_{\omega_0}) - \underline{v}^\flat\right)_{\mathcal{E}_\mathrm{e}} \\ &= \left(\mathrm{Ext}_{\omega_0}(\underline{\varphi}), \underline{v}^\flat\right)_{\mathcal{E}_\mathrm{e}}. \end{aligned}$$

Hence the dynamical system verified by the estimator is

$$\begin{cases} \dot{\underline{\widehat{y}}} = \underline{\widehat{v}} + \gamma \mathrm{Ext}_{\omega_0}(z - \underline{\widehat{y}}|_{\omega_0}), & \text{in } \Omega_0, \\ \dot{\underline{\widehat{v}}} - \mathrm{div}(\underline{\underline{\sigma}}(\underline{\widehat{y}})) = 0\ , & \text{in } \Omega_0, \\ \underline{\widehat{y}} = 0, & \text{on } \partial\Omega_0, \\ \underline{\widehat{y}}(0) = \underline{y}_0, \quad \underline{\widehat{v}}(0) = \underline{y}_1. \end{cases} \tag{2.25}$$

Concerning the convergence of this observer, authors in [Chapelle et al., 2012] have shown, in the case of the scalar wave equation, that, if ω_0 verifies the same geometric control condition of Bardos, Lebeau and Rauch [Bardos et al., 1992], then the observability inequality (2.21) is verified.

Remark 11. *It is important to remark that, in the case of displacement observations, the natural equation $\underline{v} = \dot{\underline{y}}$ is modified and no longer true. This is a direct consequence of the definition of the observer* (2.18). *Moreover, concerning the weak form of this dynamical system, both equations should be considered in $\mathcal{H}_0^1(\Omega_0)^3$, that is to say: $\forall (\underline{v}^\flat, \underline{w}^\flat) \in \mathcal{H}_0^1(\Omega_0)^3 \times \mathcal{H}_0^1(\Omega_0)^3$ we have*

$$\begin{cases} \left(\dot{\widehat{\underline{y}}}, \underline{v}^\flat\right)_{\mathcal{E}_\mathrm{e}} = \left(\widehat{\underline{v}}, \underline{v}^\flat\right)_{\mathcal{E}_\mathrm{e}} + \gamma \left(\mathrm{Ext}_{\omega_0}(z - \widehat{\underline{y}}|_{\omega_0}), \underline{v}^\flat\right)_{\mathcal{E}_\mathrm{e}}, \\ \\ \left(\dot{\widehat{\underline{v}}}, \underline{w}^\flat\right)_{\mathcal{E}_\mathrm{k}} + \left(\widehat{\underline{y}}, \underline{w}^\flat\right)_{\mathcal{E}_\mathrm{e}} = 0, \\ \\ \widehat{\underline{y}}(0) = \underline{y}_0, \quad \widehat{\underline{v}}(0) = \underline{y}_1. \end{cases} \tag{2.26}$$

This weak form is non-standard since it requires more regularity of the weak functional spaces than the standard weak formulation of the linear elastodynamic problem since both $\widehat{\underline{y}}$ and $\widehat{\underline{v}}$ belongs to $\mathcal{H}_0^1(\Omega_0)^3$. As far as the energy of the estimation error is concerned, we see that the weak form of the estimation error dynamical system is

$$\begin{cases} \left(\dot{\widetilde{\underline{y}}}, \underline{v}^\flat\right)_{\mathcal{E}_\mathrm{e}} = \left(\widetilde{\underline{v}}, \underline{v}^\flat\right)_{\mathcal{E}_\mathrm{e}} - \gamma \left(\mathrm{Ext}_{\omega_0}(\widetilde{\underline{y}}|_{\omega_0}), \underline{v}^\flat\right)_{\mathcal{E}_\mathrm{e}}, \\ \\ \left(\dot{\widetilde{\underline{v}}}, \underline{w}^\flat\right)_{\mathcal{E}_\mathrm{k}} + \left(\widetilde{\underline{y}}, \underline{w}^\flat\right)_{\mathcal{E}_\mathrm{e}} = 0, \\ \\ \widetilde{\underline{y}}(0) = \underline{\zeta}_0, \quad \widetilde{\underline{v}}(0) = \underline{\zeta}_1. \end{cases} \tag{2.27}$$

Substituting $(\underline{v}^\flat, \underline{w}^\flat)$ by $(\widetilde{\underline{y}}, \widetilde{\underline{v}})$, this system leads to

$$\begin{cases} \left(\widetilde{\underline{v}}, \widetilde{\underline{y}}\right)_{\mathcal{E}_\mathrm{e}} = \left(\dot{\widetilde{\underline{y}}}, \widetilde{\underline{y}}\right)_{\mathcal{E}_\mathrm{e}} + \gamma \left(\mathrm{Ext}_{\omega_0}(\widetilde{\underline{y}}|_{\omega_0}), \widetilde{\underline{y}}\right)_{\mathcal{E}_\mathrm{e}}, \\ \\ \left(\dot{\widetilde{\underline{v}}}, \widetilde{\underline{v}}\right)_{\mathcal{E}_\mathrm{k}} + \left(\widetilde{\underline{y}}, \widetilde{\underline{v}}\right)_{\mathcal{E}_\mathrm{e}} = 0, \\ \\ \widetilde{\underline{y}}(0) = \underline{\zeta}_0, \quad \widetilde{\underline{v}}(0) = \underline{\zeta}_1. \end{cases} \tag{2.28}$$

In (2.28) *we emphasized the coupling terms in (cyan). These coupling terms are a direct effect of considering the first equation in $\mathcal{H}_0^1(\Omega_0)^3$. Substituting in the second equation we obtain the following energy estimate*

$$\frac{\mathrm{d}}{\mathrm{dt}}\Big(\mathcal{E}_\mathrm{e}(\widetilde{\underline{y}}(t)) + \mathcal{E}_\mathrm{k}(\widetilde{\underline{v}}(t))\Big) = -\gamma \|\widetilde{\underline{y}}\|^2_{\mathcal{H}^1_{\omega_0}}. \tag{2.29}$$

Having in mind that the regularity of solutions of the linear elastodynamic problem is entirely defined by the regularity of the initial conditions we can summarize the different situations. Assuming that

$$(\underline{y}_0 + \underline{\zeta}_0, \underline{y}_1 + \underline{\zeta}_1) \in \mathcal{D}(A_0) \times \mathcal{D}(A_0^{\frac{1}{2}}),$$

then a strong solution of (2.25) *exists and estimate* (2.29) *is verified. However, if one seeks a weaker solution, it appears that the best functional spaces are*

$$(\underline{y}_0 + \underline{\zeta}_0, \underline{y}_1 + \underline{\zeta}_1) \in \mathcal{D}(A_0^{\frac{1}{2}}) \times \mathcal{D}(A_0^{\frac{1}{2}}),$$

so that the formulation (2.26) *makes sense and the estimate* (2.29) *is verified.*

Remark 12. *Considering the discrepancy measure*

$$\forall \underline{v}^\flat \in \mathcal{H}^1_0(\Omega_0)^3, \quad E_D(z,\underline{v}^\flat) = \frac{1}{2}\|z - \underline{v}^\flat|_{\omega_0}\|^2_{\mathcal{H}^1_{\omega_0}},$$

and remarking that, $\forall \underline{v}^\flat \in \mathcal{H}^1(\Omega_0)^3$

$$\begin{aligned}
-\left\langle \mathrm{d}E_D(z,\widehat{\underline{y}}), \underline{v}^\flat \right\rangle_{\mathcal{H}^1_0(\Omega_0)'\mathcal{H}^1_0(\Omega_0)} &= \left(z - \widehat{\underline{y}}|_{\omega_0}, \underline{v}^\flat|_{\omega_0}\right)_{\mathcal{H}^1_{\omega_0}} \\
&= \left(\mathrm{Ext}_{\omega_0}(z - \widehat{\underline{y}}|_{\omega_0}), \mathrm{Ext}_{\omega_0}(\underline{v}^\flat|_{\omega_0})\right)_{\mathcal{E}_\mathrm{e}} \\
&= \left(\mathrm{Ext}_{\omega_0}(z - \widehat{\underline{y}}|_{\omega_0})), \underline{v}^\flat\right)_{\mathcal{E}_\mathrm{e}},
\end{aligned}$$

we can rewrite, as previously done in the case of velocity observations, the weak formulation of the observer as

$$\begin{cases}
\left(\dot{\widehat{\underline{y}}}, \underline{v}^\flat\right)_{\mathcal{E}_\mathrm{e}} = \left(\widehat{\underline{v}}, \underline{v}^\flat\right)_{\mathcal{E}_\mathrm{e}} - \gamma\left\langle \mathrm{d}E_D(z,\widehat{\underline{y}}), \underline{v}^\flat \right\rangle_{\mathcal{H}^1_0(\Omega_0)'\mathcal{H}^1_0(\Omega_0)}, \\
\left(\dot{\widehat{\underline{v}}}, \underline{w}^\flat\right)_{\mathcal{E}_\mathrm{k}} + \left(\widehat{\underline{y}}, \underline{w}^\flat\right)_{\mathcal{E}_\mathrm{e}} = 0, \\
\widehat{\underline{y}}(0) = \underline{y}_0, \quad \widehat{\underline{v}}(0) = \underline{y}_1.
\end{cases} \tag{2.30}$$

System (2.30) *may inspire a nudging procedure for general – possibly non linear – discrepancy measures.*

Example of partial displacement feedback in a subdomain In this third example we consider the case where only a part of the displacement is given in the subdomain. More precisely let us define a particular direction $\underline{\mathrm{e}}$ (that we assume invariant in space and time for now) along with two orthogonal directions $(\underline{\mathrm{e}}_1^\perp, \underline{\mathrm{e}}_2^\perp)$. The observation operator reads

$$H = \begin{pmatrix} H_0 & 0 \end{pmatrix} : \left| \begin{array}{ccc} \mathcal{H}^1_0(\Omega_0)^3 \times \mathcal{L}^2(\Omega_0)^3 & \longrightarrow & \mathcal{H}^1(\omega_0) \\ \begin{pmatrix} \underline{y} \\ \dot{\underline{y}} \end{pmatrix} & \longmapsto & \underline{y}|_{\omega_0} \cdot \underline{\mathrm{e}}. \end{array} \right.$$

Following the case of complete displacement feedback in a subdomain we use an extension operator to define the adjoint of the observation operator. More precisely we introduce the lifting operator $\mathrm{Ext}_{\omega_0}(\cdot\,;\,\underline{\mathrm{e}})$ defined by

$$\mathrm{Ext}_{\omega_0}(\cdot\,;\,\underline{\mathrm{e}}) : \left| \begin{array}{ccc} \mathcal{H}^1(\omega_0) & \longrightarrow & \mathcal{H}^1_0(\Omega_0)^3 \\ \varphi & \longmapsto & \underline{u} = \mathrm{Ext}_{\omega_0}(\varphi\,;\,\underline{\mathrm{e}}), \end{array} \right.$$

where $\underline{u}$ is the unique solution of

$$\begin{cases}
-\mathrm{div}(\underline{\underline{\sigma}}(\underline{u})) = 0, & \text{in } \Omega_0\backslash\omega_0, \\
\underline{u} = 0, & \text{on } \partial\Omega_0, \\
\underline{u}\cdot\underline{\mathrm{e}} = \varphi, & \text{in } \overline{\omega_0}, \\
\mathrm{div}(\underline{\underline{\sigma}}(\underline{u}))\cdot\underline{\mathrm{e}}_1^\perp = \mathrm{div}(\underline{\underline{\sigma}}(\underline{u}))\cdot\underline{\mathrm{e}}_2^\perp = 0, & \text{in } \overline{\omega_0}.
\end{cases} \tag{2.31}$$

One can also verify the following orthogonal property

$$\forall \varphi \in \mathcal{H}^1(\omega_0), \quad \forall \underline{v}^\flat \in \mathcal{H}^1_0(\Omega_0)^3, \quad \underline{v}^\flat|_{\omega_0} \cdot \underline{\mathrm{e}} = 0, \quad \big(\mathrm{Ext}_{\omega_0}(\varphi\ ;\ \underline{\mathrm{e}}), \underline{v}^\flat\big)_{\mathcal{E}_\mathrm{e}} = 0,$$

since, by standard computation, we have

$$\begin{aligned}
\big(\mathrm{Ext}_{\omega_0}(\varphi\ ;\ \underline{\mathrm{e}}), \underline{v}^\flat\big)_{\mathcal{E}_\mathrm{e}} &= -\int_{\omega_0} \mathrm{div}\big(\underline{\underline{\sigma}}(\mathrm{Ext}_{\omega_0}(\varphi\ ;\ \underline{\mathrm{e}}))\big) \cdot \underline{v}^\flat \,\mathrm{d}\Omega_0 \\
&= -\int_{\omega_0} \mathrm{div}\big(\underline{\underline{\sigma}}(\mathrm{Ext}_{\omega_0}(\varphi\ ;\ \underline{\mathrm{e}}))\big) \cdot \Big(\big(\underline{v}^\flat \cdot \underline{\mathrm{e}}_1^\perp\big)\underline{\mathrm{e}}_1^\perp + \big(\underline{v}^\flat \cdot \underline{\mathrm{e}}_2^\perp\big)\underline{\mathrm{e}}_2^\perp \Big) \,\mathrm{d}\Omega_0 \\
&= 0.
\end{aligned}$$

Denoting by $\mathcal{H}^{1,\underline{\mathrm{e}}}_{\omega_0}$ the space $\mathcal{H}^1(\omega_0)$ equipped with the norm

$$\forall\ \varphi \in \mathcal{H}^{1,\underline{\mathrm{e}}}_{\omega_0}, \quad \|\varphi\|^2_{\mathcal{H}^{1,\underline{\mathrm{e}}}_{\omega_0}} = \|\mathrm{Ext}_{\omega_0}(\varphi\ ;\ \underline{\mathrm{e}})\|^2_{\mathcal{E}_\mathrm{e}}.$$

one can verify that $\mathrm{Ext}_{\omega_0}(\cdot\ ;\ \underline{\mathrm{e}})$ is the adjoint operator of H_0 for the corresponding metrics since $\forall \varphi \in \mathcal{H}^{1,\underline{\mathrm{e}}}_{\omega_0}$ and $\forall \underline{v}^\flat \in \mathcal{H}^1_0(\Omega_0)^3$

$$\begin{aligned}
\big(\varphi, \underline{v}^\flat|_{\omega_0} \cdot \underline{\mathrm{e}}\big)_{\mathcal{H}^{1,\underline{\mathrm{e}}}_{\omega_0}} &= \big(\mathrm{Ext}_{\omega_0}(\varphi\ ;\ \underline{\mathrm{e}}), \mathrm{Ext}_{\omega_0}(\underline{v}^\flat|_{\omega_0} \cdot \underline{\mathrm{e}}\ ;\ \underline{\mathrm{e}})\big)_{\mathcal{E}_\mathrm{e}} \\
&= \big(\mathrm{Ext}_{\omega_0}(\varphi\ ;\ \underline{\mathrm{e}}), \underline{v}^\flat\big)_{\mathcal{E}_\mathrm{e}} + \big(\mathrm{Ext}_{\omega_0}(\varphi\ ;\ e), \mathrm{Ext}_{\omega_0}(\underline{v}^\flat|_{\omega_0} \cdot \underline{\mathrm{e}}\ ;\ \underline{\mathrm{e}}) - \underline{v}^\flat\big)_{\mathcal{E}_\mathrm{e}} \\
&= \big(\mathrm{Ext}_{\omega_0}(\underline{\varphi}), \underline{v}^\flat\big)_{\mathcal{E}_\mathrm{e}}.
\end{aligned}$$

The last assertion comes from the orthogonality property and the fact that

$$\Big(\mathrm{Ext}_{\omega_0}(\underline{v}^\flat|_{\omega_0} \cdot \underline{\mathrm{e}}\ ;\ \underline{\mathrm{e}}) - \underline{v}^\flat\Big)|_{\omega_0} \cdot \underline{\mathrm{e}} = 0.$$

Hence the dynamical system verified by the estimator is

$$\begin{cases}
\dot{\widehat{\underline{y}}} = \widehat{\underline{v}} + \gamma \mathrm{Ext}_{\omega_0}(z - \widehat{\underline{y}}|_{\omega_0} \cdot \underline{\mathrm{e}}\ ;\ \underline{\mathrm{e}}), & \text{in } \Omega_0, \\
\dot{\widehat{\underline{v}}} - \mathrm{div}(\underline{\underline{\sigma}}(\widehat{\underline{y}})) = 0\ , & \text{in } \Omega_0, \\
\widehat{\underline{y}} = 0, & \text{on } \partial\Omega_0, \\
\widehat{\underline{y}}(0) = \underline{y}_0, \quad \widehat{\underline{v}}(0) = \underline{y}_1.
\end{cases} \tag{2.32}$$

We can also demonstrate the same type of energy estimate as in (2.29) for the estimation error. The corresponding discrepancy measure in this case reads

$$\forall \underline{v}^\flat \in \mathcal{H}^1_0(\Omega_0)^3, \quad E_D(z, \underline{v}^\flat) = \frac{1}{2}\|z - \underline{v}^\flat|_{\omega_0} \cdot \underline{\mathrm{e}}\|^2_{\mathcal{H}^{1,\underline{\mathrm{e}}}_{\omega_0}}.$$

Remark 13. *Concerning the observability of this configuration it seems rather complicated for this particular observation operator to be able to completely stabilize the estimation error dynamical system since it is blind to displacements in the orthogonal plane. The question is however still valid in the case of anisotropic material or in the case of spatially and/or time varying observation direction* $\underline{\mathrm{e}}$*. Once again, we recall that the important aspect lying behind the concept of observability is that it is sufficient to gather enough coercivity over time.*

Example of displacement feedback on the boundary In this paragraph we give an example of major importance where the displacement information is available at the boundary of the reference configuration. We will understand at the end of this Chapter that this is the linear counter-part of practical cases arising when assimilating discrepancies between endo- and epicardium surfaces of the heart. In this configuration the observation operator is defined as

$$H = \begin{pmatrix} H_0 & 0 \end{pmatrix} \; : \left| \begin{array}{ll} \mathcal{H}^1(\Omega_0)^3 \times \mathcal{L}^2(\Omega_0)^3 & \longrightarrow \mathcal{H}^{\frac{1}{2}}(\partial\Omega_0)^3 \\ \begin{pmatrix} \underline{y} \\ \dot{\underline{y}} \end{pmatrix} & \longmapsto \underline{y}|_{\partial\Omega_0}. \end{array} \right.$$

For this example to have any interest we assume that problem (2.15) admits homogeneous Neumann boundary conditions. We introduce the lifting operator $\mathrm{Ext}_{\partial\Omega_0}$ defined as

$$\mathrm{Ext}_{\partial\Omega_0} \; : \left| \begin{array}{rl} \mathcal{H}^{\frac{1}{2}}(\partial\Omega_0)^3 & \longrightarrow \mathcal{H}^1(\Omega_0)^3 \\ \underline{\varphi} & \longmapsto \underline{u} = \mathrm{Ext}_{\partial\Omega_0}(\varphi), \end{array} \right.$$

where $\underline{u}$ is solution of

$$\begin{cases} -\mathrm{div}(\underline{\underline{\sigma}}(\underline{u})) = 0, & \text{in } \Omega_0, \\ \underline{u} = \underline{\varphi}, & \text{on } \partial\Omega_0. \end{cases} \tag{2.33}$$

Once again we can also prove the orthogonal property

$$\forall \underline{\varphi} \in \mathcal{H}^{\frac{1}{2}}(\partial\Omega_0)^3, \quad \forall \underline{v}^\flat \in \mathcal{H}^1(\Omega_0)^3, \quad \underline{v}^\flat|_{\partial\Omega_0} = 0, \quad \left(\mathrm{Ext}_{\partial\Omega_0}(\underline{\varphi}), \underline{v}^\flat\right)_{\mathcal{E}_\mathrm{e}} = 0.$$

This property and the fact that

$$\forall \underline{v}^\flat \in \mathcal{H}^1(\Omega_0)^3 \quad \left(\mathrm{Ext}_{\partial\Omega_0}(\underline{v}^\flat|_{\partial\Omega_0}) - \underline{v}^\flat\right)|_{\partial\Omega_0} = 0$$

insure that $\mathrm{Ext}_{\partial\Omega_0}$ is the adjoint operator of the trace operator for the $\mathcal{H}^{\frac{1}{2}}$-norm. Therefore, the observer is

$$\begin{cases} \dot{\widehat{\underline{y}}} = \widehat{\underline{v}} + \gamma \mathrm{Ext}_{\partial\Omega_0}(z - \widehat{\underline{y}}|_{\partial\Omega_0}), & \text{in } \Omega_0, \\ \dot{\widehat{\underline{v}}} - \mathrm{div}(\underline{\underline{\sigma}}(\widehat{\underline{y}})) = 0\ , & \text{in } \Omega_0, \\ \underline{\underline{\sigma}}(\widehat{\underline{y}}) \cdot \underline{n} = 0, & \text{on } \partial\Omega_0, \\ \widehat{\underline{y}}(0) = \underline{y}_0, \quad \widehat{\underline{v}}(0) = \underline{y}_1. \end{cases} \tag{2.34}$$

Remark 14. *Observer* (2.34) *is a specification of the general dynamical system* (2.30) *with the discrepancy measure*

$$\forall \underline{v}^\flat \in \mathcal{H}^1_0(\Omega_0)^3, \quad E_D(z, \underline{v}^\flat) = \frac{1}{2} \|\mathrm{Ext}_{\partial\Omega_0}(z - \underline{v}^\flat|_{\partial\Omega_0})\|^2_{\mathcal{E}_\mathrm{e}}.$$

This particular choice of the norm, resulting from the particular choice of the observation space, has been proven by authors in [Moireau et al., 2009] to be crucial in terms of efficiency. As a *matter of fact another possible choice to assimilate boundary observations would be to consider the observation operator as*

$$H = \begin{pmatrix} H_0 & 0 \end{pmatrix} \ : \ \left| \begin{array}{ll} \mathcal{H}^1(\omega_0)^3 \times \mathcal{L}^2(\omega_0)^3 & \longrightarrow \mathcal{L}^2(\partial\Omega_0)^3 \\ \qquad\quad \begin{pmatrix} \underline{y} \\ \underline{\dot{y}} \end{pmatrix} & \longmapsto \underline{y}|_{\partial\Omega_0}, \end{array} \right.$$

or equivalently

$$\forall \underline{v}^\flat \in \mathcal{H}^1_0(\Omega_0)^3, \quad E_D(z, \underline{v}^\flat) = \frac{1}{2} \| z - \underline{v}^\flat|_{\omega_0} \|^2_{\mathcal{L}^2(\partial\Omega_0)^3}.$$

In this case, defining the extension operator as

$$\mathrm{Ext}^{\mathrm{N}}_{\partial\Omega_0} \ : \ \left| \begin{array}{ll} \mathcal{L}^2(\partial\Omega_0)^3 & \longrightarrow \mathcal{H}^1(\Omega_0)^3 \\ \qquad\quad \underline{\varphi} & \longmapsto \underline{u} = \mathrm{Ext}^{\mathrm{N}}_{\partial\Omega_0}(\varphi), \end{array} \right.$$

where $\underline{u}$ is solution of

$$\begin{cases} -\mathrm{div}(\underline{\underline{\sigma}}(\underline{u})) = 0, & \textit{in } \Omega_0, \\ \underline{\underline{\sigma}}(\underline{u}) \cdot \underline{n} = \underline{\varphi}, & \textit{on } \partial\Omega_0, \end{cases}$$

directly gives the adjoint operator for the considered metrics since, using Green's formula, we obtain

$$\forall \underline{\varphi} \in \mathcal{L}^2(\partial\Omega_0)^3, \quad \forall \underline{v}^\flat \in \mathcal{H}^1(\Omega_0)^3, \quad \big(\mathrm{Ext}_{\partial\Omega_0}(\underline{\varphi}), \underline{v}^\flat\big)_{\mathcal{E}_{\mathrm{e}}} = \big(\underline{\varphi}, \underline{v}^\flat|_{\partial\Omega_0}\big)_{\mathcal{L}^2(\partial\Omega_0)^3}.$$

However, by a spectral analysis of the stabilized operator appearing in the dynamical system verified by the estimation error, authors in [Moireau et al., 2009] have shown that choosing $\mathcal{L}^2(\partial\Omega_0)^3$ as the observation space is much less efficient than $\mathcal{H}^{\frac{1}{2}}(\partial\Omega_0)^3$, emphazising the importance of the construction of the adjoint operator which is of course closely related to one's understanding of the observations at hand.

Example of partial displacement feedback on the boundary From definitions (2.33) and (2.31) of the lifting operators in the case of boundary observations and partial observations in a subdomain we can easily infer the nudging strategy in the case of partial displacement at the boundary. More precisely, let $\underline{\mathrm{e}}$ be a particular direction defined at the boundary and $(\underline{\mathrm{e}}_1^\perp, \underline{\mathrm{e}}_2^\perp)$ two orthogonal directions, we consider the observation operator

$$H = \begin{pmatrix} H_0 & 0 \end{pmatrix} \ : \ \left| \begin{array}{ll} \mathcal{H}^1(\Omega_0)^3 \times \mathcal{L}^2(\Omega_0)^3 & \longrightarrow \mathcal{H}^{\frac{1}{2}}(\partial\Omega_0) \\ \qquad\quad \begin{pmatrix} \underline{y} \\ \underline{\dot{y}} \end{pmatrix} & \longmapsto \underline{y}|_{\partial\Omega_0} \cdot \underline{\mathrm{e}}. \end{array} \right.$$

As in (2.31) we introduce the lifting operator $\mathrm{Ext}_{\partial\Omega_0}(\cdot\,;\,\underline{\mathrm{e}})$ defined by

$$\mathrm{Ext}_{\partial\Omega_0}(\cdot\,;\,\underline{\mathrm{e}}) \ : \ \left| \begin{array}{ll} \mathcal{H}^{\frac{1}{2}}(\partial\Omega_0) & \longrightarrow \mathcal{H}^1(\Omega_0)^3 \\ \qquad\quad \varphi & \longmapsto \underline{u} = \mathrm{Ext}_{\partial\Omega_0}(\varphi\,;\,\underline{\mathrm{e}}), \end{array} \right.$$

where $\underline{u}$ is solution of

$$\begin{cases} -\mathrm{div}(\underline{\underline{\sigma}}(\underline{u})) = 0, & \text{in } \Omega_0, \\ \underline{u} \cdot \underline{\mathrm{e}} = \varphi, & \text{on } \partial\Omega_0, \\ \big(\underline{\underline{\sigma}}(\underline{u}) \cdot \underline{n}\big) \cdot \underline{\mathrm{e}}_1^\perp = \big(\underline{\underline{\sigma}}(\underline{u}) \cdot \underline{n}\big) \cdot \underline{\mathrm{e}}_2^\perp = 0, & \text{on } \partial\Omega_0. \end{cases} \tag{2.35}$$

As previously, we can verify the orthogonal property

$$\forall \varphi \in \mathcal{H}^{\frac{1}{2}}(\partial\Omega_0), \quad \forall \underline{v}^\flat \in \mathcal{H}^1(\Omega_0)^3, \quad \underline{v}^\flat|_{\partial\Omega_0} \cdot \underline{\mathrm{e}} = 0, \quad \big(\mathrm{Ext}_{\partial\Omega_0}(\varphi\,;\,\underline{\mathrm{e}}), \underline{v}^\flat\big)_{\mathcal{E}_\mathrm{e}} = 0,$$

since

$$\big(\mathrm{Ext}_{\partial\Omega_0}(\varphi\,;\,\underline{\mathrm{e}}), \underline{v}^\flat\big)_{\mathcal{E}_\mathrm{e}} = \int_{\partial\Omega_0} \Big(\underline{\underline{\sigma}}(\mathrm{Ext}_{\partial\Omega_0}(\varphi\,;\,\underline{\mathrm{e}})) \cdot \underline{n}\Big) \cdot \Big(\big(\underline{v}^\flat \cdot \underline{\mathrm{e}}_1^\perp\big)\underline{\mathrm{e}}_1^\perp + \big(\underline{v}^\flat \cdot \underline{\mathrm{e}}_2^\perp\big)\underline{\mathrm{e}}_2^\perp\Big)\,\mathrm{d}\sigma = 0.$$

Therefore, denoting by $\mathcal{H}^{\frac{1}{2},\underline{\mathrm{e}}}$ the space $\mathcal{H}^{\frac{1}{2}}(\partial\Omega_0)$ equipped with the norm

$$\forall \varphi \in \mathcal{H}^{\frac{1}{2},\underline{\mathrm{e}}}, \ \|\varphi\|_{\mathcal{H}^{\frac{1}{2},\underline{\mathrm{e}}}} = \|\mathrm{Ext}_{\partial\Omega_0}(\varphi\,;\,\underline{\mathrm{e}})\|_{\mathcal{E}_\mathrm{e}},$$

we verify that $\mathrm{Ext}_{\partial\Omega_0}(\cdot\,;\,\underline{\mathrm{e}})$ is the adjoint operator of H_0 and that the observer reads

$$\begin{cases} \dot{\underline{\widehat{y}}} = \underline{\widehat{v}} + \gamma \mathrm{Ext}_{\partial\Omega_0}(z - \underline{\widehat{y}}|_{\partial\Omega_0} \cdot \underline{\mathrm{e}}\,;\,\underline{\mathrm{e}}), & \text{in } \Omega_0, \\ \dot{\underline{\widehat{v}}} - \mathrm{div}(\underline{\underline{\sigma}}(\underline{\widehat{y}})) = 0\,, & \text{in } \Omega_0, \\ \underline{\underline{\sigma}}(\underline{\widehat{y}}) \cdot \underline{n} = 0, & \text{on } \partial\Omega_0, \\ \underline{\widehat{y}}(0) = \underline{y}_0, \quad \underline{\widehat{v}}(0) = \underline{y}_1. \end{cases} \tag{2.36}$$

Remark 15. *The discrepancy measure corresponding to the observer* (2.36) *is*

$$\forall \underline{v}^\flat \in \mathcal{H}_0^1(\Omega_0)^3, \quad E_D(z, \underline{v}^\flat) = \frac{1}{2}\|\mathrm{Ext}_{\partial\Omega_0}(z - \underline{v}^\flat|_{\partial\Omega_0} \cdot \underline{\mathrm{e}}\,;\,\underline{\mathrm{e}})\|^2_{\mathcal{E}_\mathrm{e}}.$$

Application in a nonlinear setting As we have mentioned in the introduction of this Chapter, in most practical cases the observations are obtained from the real trajectory from a complex and therefore nonlinear process. Hence we need to be able to give a filtering procedure that considers a nonlinear observation process. On top of that, as we are interested in the particular cases of assimilating medical imaging (with low temporal resolution) we assume displacement-based measurements, namely

$$z = H(\underline{y}) + \chi.$$

The nudging strategy in this case can be inferred from the general weak formulation (2.30) of the filter. More precisely, considering the discrepancy measure

$$\forall \underline{v}^\flat \in \mathcal{X}^y, \quad E_D(z, \underline{v}^\flat) = \frac{1}{2}\|z - H(\underline{v}^\flat)\|^2_{\mathcal{Z}}, \tag{2.37}$$

we define the observer as

$$\begin{cases} \big(\dot{\underline{\widehat{y}}}, \underline{v}^\flat\big)_{\mathcal{E}_\mathrm{e}} = \big(\underline{\widehat{v}}, \underline{v}^\flat\big)_{\mathcal{E}_\mathrm{e}} + \gamma\left(z - H(\underline{\widehat{y}}), \mathrm{d}H(\underline{\widehat{y}})\underline{v}^\flat\right)_{\mathcal{Z}}, \\ \big(\dot{\underline{\widehat{v}}}, \underline{w}^\flat\big)_{\mathcal{E}_\mathrm{k}} + \big(\underline{\widehat{y}}, \underline{w}^\flat\big)_{\mathcal{E}_\mathrm{e}} = 0, \\ \underline{\widehat{y}}(0) = \underline{y}_0, \quad \underline{\widehat{v}}(0) = \underline{y}_1. \end{cases} \tag{2.38}$$

Where $\mathrm{d}H(\widehat{\underline{y}})$ is the tangent operator of the observation operator evaluated at $\widehat{\underline{y}}$. The corresponding strong formulation of (2.38) reads

$$\begin{cases} \dot{\widehat{\underline{y}}} = \widehat{\underline{v}} + \gamma \mathrm{d}H(\widehat{\underline{y}})^* \big(z - H(\widehat{\underline{y}})\big), \\ \dot{\widehat{\underline{v}}} - \mathrm{div}(\underline{\sigma}(\widehat{\underline{y}})) = 0, \\ \widehat{\underline{y}}(0) = \underline{y}_0, \quad \widehat{\underline{v}}(0) = \underline{y}_1. \end{cases} \tag{2.39}$$

We justify our approach by remarking that, locally, we introduce some dissipation in the estimation error dynamical system. More precisely, from (2.38) we observe that the estimation error verifies

$$\begin{cases} \big(\dot{\widetilde{\underline{y}}}, \underline{v}^\flat\big)_{\mathcal{E}_\mathrm{e}} = \big(\widetilde{\underline{v}}, \underline{v}^\flat\big)_{\mathcal{E}_\mathrm{e}} - \gamma \left(z - H(\widehat{\underline{y}}), \mathrm{d}H(\widehat{\underline{y}})\underline{v}^\flat\right)_{\mathcal{Z}}, \\ \big(\dot{\widetilde{\underline{v}}}, \underline{w}^\flat\big)_{\mathcal{E}_\mathrm{k}} + \big(\widetilde{\underline{y}}, \underline{w}^\flat\big)_{\mathcal{E}_\mathrm{e}} = 0, \\ \widetilde{\underline{y}}(0) = \underline{\zeta}_0, \quad \widetilde{\underline{v}}(0) = \underline{\zeta}_1. \end{cases} \tag{2.40}$$

Therefore the energy associated with (2.38) verifies

$$\frac{\mathrm{d}}{\mathrm{d}t}\Big(\mathcal{E}_\mathrm{e}(\widetilde{\underline{y}}(t)) + \mathcal{E}_\mathrm{k}(\widetilde{\underline{v}}(t))\Big) = -\gamma \left(z - H(\widehat{\underline{y}}), \mathrm{d}H(\widehat{\underline{y}})\widetilde{\underline{y}}\right)_{\mathcal{Z}}.$$

Remarking that, using standard linearization arguments we have

$$\left|\begin{array}{l} z - H(\widehat{\underline{y}}) = z - H(\underline{y}) + \mathrm{d}H(\underline{y})\widetilde{\underline{y}} + O(\|\widetilde{\underline{y}}\|^2_{\mathcal{X}^y}) = \mathrm{d}H(\underline{y})\widetilde{\underline{y}} + \chi + O(\|\widetilde{\underline{y}}\|^2_{\mathcal{X}^y}), \\ \mathrm{d}H(\underline{y})\widetilde{\underline{y}} = \mathrm{d}H(\widehat{\underline{y}})\widetilde{\underline{y}} + O(\|\widetilde{\underline{y}}\|^2_{\mathcal{X}^y}), \end{array}\right.$$

we obtain

$$\frac{\mathrm{d}}{\mathrm{d}t}\Big(\mathcal{E}_\mathrm{e}(\widetilde{\underline{y}}(t)) + \mathcal{E}_\mathrm{k}(\widetilde{\underline{v}}(t))\Big) = -\gamma \|\mathrm{d}H(\underline{y})\widetilde{\underline{y}}\|^2_{\mathcal{Z}} - \gamma \left(\chi, \mathrm{d}H(\underline{y})\widetilde{\underline{y}}\right)_{\mathcal{Z}} + O(\|\widetilde{\underline{y}}\|^2_{\mathcal{X}^y}). \tag{2.41}$$

Assuming that the observation noise is somehow limited, we observe that the dynamical system (2.38) insures a locally dissipative behavior of the estimation error dynamical system. The data assimilation procedure described by (2.38) directly extends in the case of implicit relation between the observation and the target trajectory, namely

$$D(z, \underline{y}) = \chi,$$

by considering the following discrepancy measure

$$\forall \underline{v}^\flat \in \mathcal{X}^y, \quad E_D(z, \underline{v}^\flat) = \frac{1}{2}\|D(z, \underline{v}^\flat)\|^2_{\mathcal{Z}}. \tag{2.42}$$

This leads to the following definition of the observer

$$\begin{cases} \dot{\widehat{\underline{y}}} = \widehat{\underline{v}} - \gamma \mathrm{d}D(z, \widehat{\underline{y}})^* D(z, \underline{v}^\flat), \\ \dot{\widehat{\underline{v}}} - \mathrm{div}(\underline{\sigma}(\widehat{\underline{y}})) = 0, \\ \widehat{\underline{y}}(0) = \underline{y}_0, \quad \widehat{\underline{v}}(0) = \underline{y}_1. \end{cases} \tag{2.43}$$

Following the same arguments as previously the estimation errors dynamical system is also locally dissipative, in the sense that

$$\frac{\mathrm{d}}{\mathrm{d}t}\Big(\mathcal{E}_{\mathrm{e}}(\underline{\widetilde{y}}(t)) + \mathcal{E}_{\mathrm{k}}(\underline{\widetilde{v}}(t))\Big) = -\gamma\|\mathrm{d}D(z,\underline{y})\underline{\widetilde{y}}\|^2_{\mathcal{Z}} - \gamma\left(\chi, \mathrm{d}D(z,\underline{y})\underline{\widetilde{y}}\right)_{\mathcal{Z}} + O(\|\underline{\widetilde{y}}\|^2_{\mathcal{X}^y}). \tag{2.44}$$

Adjoint operators in a penalization strategy In the previous examples of application of the nudging procedure we have seen that most of the presented adjoint operators are given using an extension operator. As a matter of fact, the extension operator can be expressed – in the case of displacement feedback – as

$$\forall \varphi \in \mathcal{Z}, \quad \underline{u} = \mathrm{Ext}(\varphi) \in \mathcal{X}^y \text{ is solution of } \min_{\underline{u}\in\mathcal{X}^y \,\big|\, H_0\underline{u}=\varphi} \frac{1}{2}\|\underline{u}\|^2_{\mathcal{E}_{\mathrm{e}}}.$$

Solving this minimization under constraint naturally leads to a mixed problem with an additional distributed (in the observation space) variable which entails substantial numerical cost in practice. To circumvent this difficulty authors in [Moireau et al., 2009] have proposed a penalization strategy which reads, for a (small) penalization parameter $\varepsilon > 0$,

$$\forall \varphi \in \mathcal{Z}, \quad \underline{u}^{\varepsilon} = \mathrm{Ext}^{\varepsilon}(\varphi) \in \mathcal{X}^y \text{ is solution of } \min_{\underline{u}\in\mathcal{X}^y} \frac{\varepsilon}{2}\|\underline{u}\|^2_{\mathcal{E}_{\mathrm{e}}} + \frac{1}{2}\|\varphi - H_0\underline{u}\|^2_{\mathcal{Z}}.$$

This penalization strategy, which is in fact a Tikhonov regularization of φ, is, numerically speaking, much lighter than the previous one. It gives birth however to some natural questions that we will expose taking the example of boundary measurements.

From the necessary and sufficient order one optimality condition we can ensure that the previous definition is equivalent to defining the lifting operator $\mathrm{Ext}^{\varepsilon}_{\partial\Omega_0}$ as

$$\mathrm{Ext}^{\varepsilon}_{\partial\Omega_0} : \left|\begin{array}{rl} \mathcal{H}^{\frac{1}{2}}(\partial\Omega_0)^3 & \longrightarrow \mathcal{H}^1(\Omega_0)^3 \\ \underline{\varphi} & \longmapsto \underline{u}^{\varepsilon} = \mathrm{Ext}^{\varepsilon}_{\partial\Omega_0}(\underline{\varphi}), \end{array}\right.$$

where $\underline{u}^{\varepsilon}$ is solution of

$$\begin{cases} -\mathrm{div}(\underline{\underline{\sigma}}(\underline{u}^{\varepsilon})) = 0, & \text{in } \Omega_0, \\ \varepsilon\underline{\underline{\sigma}}(\underline{u}^{\varepsilon})\cdot\underline{n} + \underline{u}^{\varepsilon} = \underline{\varphi}, & \text{in } \partial\Omega_0. \end{cases}$$

Hence, the observer would read

$$\begin{cases} \dot{\underline{\widehat{y}}} = \underline{\widehat{v}} + \gamma\mathrm{Ext}^{\varepsilon}_{\partial\Omega_0}(z - \underline{\widehat{y}}|_{\partial\Omega_0}), & \text{in } \Omega_0, \\ \dot{\underline{\widehat{v}}} - \mathrm{div}(\underline{\underline{\sigma}}(\underline{\widehat{y}})) = 0\ , & \text{in } \Omega_0, \\ \underline{\underline{\sigma}}(\underline{\widehat{y}})\cdot\underline{n} = 0, & \text{on } \partial\Omega_0, \\ \underline{\widehat{y}}(0) = \underline{y}_0, \quad \underline{\widehat{v}}(0) = \underline{y}_1. \end{cases} \tag{2.45}$$

Denoting by $\mathcal{H}^{\frac{1}{2},\varepsilon}$ the space $\mathcal{H}^{\frac{1}{2}}(\partial\Omega_0)$ equipped with the norm

$$\forall \underline{\varphi} \in \mathcal{H}^{\frac{1}{2},\varepsilon} \quad \|\underline{\varphi}\|_{\mathcal{H}^{\frac{1}{2},\varepsilon}} = \|\mathrm{Ext}^{\varepsilon}_{\partial\Omega_0}(\underline{\varphi})\|_{\mathcal{E}_{\mathrm{e}}},$$

we have $\forall \underline{\varphi} \in \mathcal{H}^{\frac{1}{2}}(\partial\Omega_0)^3$ and $\forall \underline{v}^\flat \in \mathcal{H}^1(\Omega_0)^3$,

$$\left(\underline{\varphi}, \underline{v}^\flat|_{\partial\Omega_0}\right)_{\mathcal{H}^{\frac{1}{2}},\varepsilon} = \left(\mathrm{Ext}^{\varepsilon}_{\partial\Omega_0}(\underline{\varphi}), \underline{v}^\flat\right)_{\mathcal{E}_\mathrm{e}} + \left(\mathrm{Ext}^{\varepsilon}_{\partial\Omega_0}(\underline{\varphi}), \mathrm{Ext}^{\varepsilon}_{\partial\Omega_0}(\underline{v}^\flat|_{\partial\Omega_0}) - \underline{v}^\flat\right)_{\mathcal{E}_\mathrm{e}}.$$

We see here that $\mathrm{Ext}^{\varepsilon}_{\partial\Omega_0}$ is not the adjoint operator of the trace operator since

$$\Big(\mathrm{Ext}^{\varepsilon}_{\partial\Omega_0}(\underline{v}^\flat|_{\partial\Omega_0}) - \underline{v}^\flat\Big)|_{\partial\Omega_0} = -\varepsilon\Big(\underline{\underline{\sigma}}(\mathrm{Ext}^{\varepsilon}_{\partial\Omega_0}(\underline{v}^\flat|_{\partial\Omega_0})) \cdot \underline{n}\Big).$$

However, remarking that, by construction, we have

$$\Big(\underline{\varphi} - \mathrm{Ext}^{\varepsilon}_{\partial\Omega_0}(\underline{\varphi})\Big)|_{\partial\Omega_0} = O(\varepsilon),$$

we can comfort our intuition concerning the asymptotic behavior by noting that

$$\left(\mathrm{Ext}^{\varepsilon}_{\partial\Omega_0}(\underline{\varphi}), \mathrm{Ext}^{\varepsilon}_{\partial\Omega_0}(\underline{v}^\flat|_{\partial\Omega_0}) - \underline{v}^\flat\right)_{\mathcal{E}_\mathrm{e}} = -\int_{\partial\Omega_0} \Big(\underline{\varphi} - \mathrm{Ext}^{\varepsilon}_{\partial\Omega_0}(\underline{\varphi})\Big) \cdot \Big(\underline{\underline{\sigma}}(\mathrm{Ext}^{\varepsilon}_{\partial\Omega_0}(\underline{v}^\flat|_{\partial\Omega_0})) \cdot \underline{n}\Big)\,\mathrm{d}\sigma = O(\varepsilon).$$

To conclude, even though this is not a complete demonstration, it seems that the penalized extension operator is in fact an approximation of the adjoint operator in the sense that

$$\left(\underline{\varphi}, \underline{v}^\flat|_{\partial\Omega_0}\right)_{\mathcal{H}^{\frac{1}{2}},\varepsilon} = \left(\mathrm{Ext}^{\varepsilon}_{\partial\Omega_0}(\underline{\varphi}), \underline{v}^\flat\right)_{\mathcal{E}_\mathrm{e}} + O(\varepsilon).$$

2.3 Joint state-parameter estimation

So far we have rapidly seen the main types of data assimilation procedure that may provide a solution to perform the reconstruction of a *real trajectory* being observed. We have particularly detailed the nudging procedure that provides a cheap and efficient way to perform state estimation, assuming one can have a keen understanding of the underlying physical dynamical system. In this section we give further details on how the joint state-parameter estimator is built – readers may refer to [Moireau et al., 2007, Moireau et al., 2009, Chapelle et al., 2009, Moireau and Chapelle, 2011] for extensive details. More precisely we will use the nudging filter to reduce the uncertainty on the state space in order to justify a reduced-order Kalman filtering procedure on the remaining parameter space. This combination has the advantage to circumvent the difficulty of managing the state large dimension – which is managed by a numerically tractable nudging procedure – and it uses the generality of Kalman filters to correct the parameters sequentially. To start with we rapidly recall some classical constructions of Kalman filtering in a non linear setting – see [Tuan Pham et al., 1997, Tuan Pham, 2000, Simon, 2006] – to finally give the complete state-parameter estimation algorithm. We illustrate this procedure by estimating parameters in the cardiac model described in the first Chapter.

2.3.1 Kalman filtering in a nonlinear setting

Time discrete optimal filtering. In the context of state and parameter estimation, the Kalman filter, (2.8), (2.12) and (2.13) reads

$$\begin{cases} \dot{\widehat{x}}(t) = A\widehat{x}(t) + R + P_{xx}H^\intercal M_z(z(t) - H\widehat{x}(t)), \\ \dot{\widehat{\theta}}(t) = P_{\theta x}H^\intercal M_z(z(t) - H\widehat{x}(t)), \\ \widehat{x}(0) = x_\diamond, \\ \widehat{\theta}(0) = \theta_\diamond. \end{cases} \tag{2.46}$$

We recall that the augmented covariance matrix P verifies the Riccati equation leading to the following dynamical system

$$\begin{cases} \dot{P}_{xx} = AP_{xx} + P_{xx}A^\intercal - P_{xx}H^\intercal M_z H^T P_{xx}, \\ \dot{P}_{x\theta} = AP_{x\theta} + P_{x\theta}A^\intercal - P_{xx}H^\intercal M_z H^T P_{x\theta}, \\ \dot{P}_{\theta\theta} = -P_{x\theta}H^\intercal M_z H^T P_{x\theta}, \end{cases} \tag{2.47}$$

with the initial conditions

$$P_{xx}(0) = P_{xx,0}, \quad P_{\theta\theta}(0) = P_{\theta\theta,0}, \quad P_{x\theta}(0) = 0. \tag{2.48}$$

As we have seen in the first part of this Chapter, this filter is linked with the optimal solution (2.7). In a time discrete setting, the corresponding functional to be minimized reads

$$J(\zeta_x, \zeta_\theta) = \frac{1}{2}\|\zeta_\theta\|^2_{P^{-1}_{\theta\theta,0}} + \frac{1}{2}\|\zeta_x\|^2_{P^{-1}_{xx,0}} + \frac{1}{2}\sum_{k=1}^{n} \|z^k - Hx^k\|^2_{M_z^k}, \tag{2.49}$$

where $M_z^k = \Delta\mathrm{t}M_z$ comes from the natural numerical integration of the time integral and $[0\ ;\ n\Delta\mathrm{t}]$ represents the simulation time window. To simplify the presentation we only consider the state estimation problem – the discrete Kalman filter formulation for state and parameter estimation will be directly derived afterwards. Hence we consider the following functional

$$J(\zeta_x) = \frac{1}{2}\|\zeta_x\|^2_{P^{-1}_{xx,0}} + \frac{1}{2}\sum_{k=1}^{\mathrm{N}} \|z^k - Hx^k\|^2_{M_z^k}. \tag{2.50}$$

As previously observed in a time continuous context, this minimization is performed under the constraint

$$\begin{cases} x^k = A_{k|k-1}x^{k-1} + R, \\ x^0 = x_\diamond + \zeta_x. \end{cases} \tag{2.51}$$

In (2.51), $A_{k|k-1}$ is the so-called *transition* operator. Therefore the functional (2.50) can be reformulated as

$$J(x^0) = \frac{1}{2}\|x^0 - x_\diamond\|^2_{P^{-1}_{xx,0}} + \frac{1}{2}\sum_{k=1}^{n} \|z^k - H\sum_{j=0}^{k-1} A_{k|j+1}R - HA_{k|0}x\|^2_{M_z^k}.$$

In order to characterize the optimal solution – more precisely the optimal initial condition – we start by gathering all the informations that we possess on the system and we define

$$\mathbf{z} = \begin{pmatrix} z^1 \\ \vdots \\ z^n - H\sum\limits_{j=0}^{n-1} A_{n|j+1}R \end{pmatrix} = \begin{pmatrix} \widetilde{z}^1 \\ \vdots \\ \widetilde{z}^n \end{pmatrix},$$

where we use, for clarity, the compact notation

$$\forall k = 1, \cdots, n \quad \overline{z}^k = z^k - H \sum_{j=0}^{k-1} A_{k|j+1} R.$$

We also define the observation norm and operator consistent with these observations, namely

$$\mathbf{M_z} = \begin{pmatrix} M_z^0 & & \\ & \ddots & \\ & & M_z^n \end{pmatrix} \quad \text{and} \quad \mathbf{H} = \begin{pmatrix} HA_{0|0} \\ \vdots \\ HA_{n|0} \end{pmatrix},$$

where, by convention, we set $A_{0|0} = \mathbb{1}$. With these notations the optimal solution of (2.50)-(2.51) is in fact the minimizer of the functional

$$\mathbf{J}(x^0) = \frac{1}{2} \|x - x_\diamond\|^2_{P^{-1}_{xx,0}} + \frac{1}{2} \|\mathbf{z} - \mathbf{H} x^0\|^2_{\mathbf{M_z}}.$$

Hence, the optimal solution verifying the optimality condition of order one is given by

$$\overline{x}^0 = \Big(P^{-1}_{xx,0} + \mathbf{H}^\top \mathbf{M_z} \mathbf{H} \Big)^{-1} \Big(x_\diamond + \mathbf{H}^\top \mathbf{M_z} \mathbf{z} \Big).$$

As the number of observations increases one can hope to build a better estimation of the exact trajectory. To represent the dependency of the optimal solution with respect to the number of observations we denote

$$\overline{x}^0 = \overline{x}^0_n.$$

In the following this type of dependencies will be indicated by subscripts whereas actual time iterations will be represented in superscript. The next step is to provide a recursive construction of this optimal solution that will be used to obtain a time discrete version of the (sequential) Kalmn filter. To start with let us consider the following sequence of operators

$$\left| \begin{aligned} &\overline{P}_0^{-1} = H^\top M_z H + P^{-1}_{xx,0}, \\ &\overline{P}_n^{-1} = \sum_{k=0}^{n} A^\top_{k|0} H^\top M_z^k H A_{k|0} = A^\top_{n|0} H^\top M_z^n H A_{n|0} + \overline{P}^{-1}_{n-1}. \end{aligned} \right.$$

For completeness purposes we give – without demonstration – the following inversion Lemma,

Lemma. *Let M_1, M_{12}, M_{21} and M_2 four matrices. If M_1, M_2 and $M_2 - M_{21} M_1^{-1} M_{12}$ are invertible, then $M_1 - M_{12} M_2^{-1} M_{21}$ is invertible and*

$$\big(M_1 - M_{12} M_2^{-1} M_{21} \big)^{-1} = M_1^{-1} + M_1^{-1} M_{12} \big(M_2 - M_{21} M_1^{-1} M_{12} \big)^{-1} M_{21} M_1^{-1}.$$

With this relation we can give the explicit recurrence relation

$$\overline{P}_n = \overline{P}_{n-1} - \overline{P}_{n-1} A^\top_{n|0} H^\top \big((M_z^n)^{-1} + H A_{n|0} \overline{P}_{n-1} A^\top_{n|0} H^\top \big)^{-1} H A_{n|0} \overline{P}_{n-1}. \tag{2.52}$$

The optimal initial condition hence satisfies the following recursive scheme,

$$\begin{aligned} \overline{x}^0_n &= \overline{P}_n \Big(x_\diamond + \sum_{k=0}^{n} A^\top_{k|0} H^\top M_z^k \overline{z}^k \Big) \\ &= \overline{P}_n \Big(\overline{P}^{-1}_{n-1} \overline{x}^0_{n-1} + A^\top_{n|0} H^\top M_z^n \overline{z}^n \Big). \end{aligned}$$

Replacing $\overline{P}_n$ by its expression in (2.52) we obtain

$$\overline{x}_n^0 = \overline{x}_{n-1}^0 + \overline{P}_n A_{n|0}^\top H^\top M_z^n \widetilde{z}^n - \overline{G}_n H A_{n|0} \overline{x}_{n-1}^0,$$

with

$$\begin{aligned}
\overline{G}_n &= \overline{P}_{n-1} A_{n|0}^\top H^\top \big((M_z^n)^{-1} + H A_{n|0} \overline{P}_{n-1} A_{n|0}^\top H^\top \big)^{-1} \\
&= \overline{P}_n \overline{P}_n^{-1} \overline{P}_{n-1} A_{n|0}^\top H^\top \big((M_z^n)^{-1} + H A_{n|0} \overline{P}_{n-1} A_{n|0}^\top H^\top \big)^{-1} \\
&= \overline{P}_n \big(A_{n|0}^\top H^\top M_z^n H A_{n|0} + \overline{P}_{n-1}^{-1} \big) \overline{P}_{n-1} A_{n|0}^\top H^\top \big((M_z^n)^{-1} + H A_{n|0} \overline{P}_{n-1} A_{n|0}^\top H^\top \big)^{-1} \\
&= \overline{P}_n \big(A_{n|0}^\top H^\top M_z^n H A_{n|0} \overline{P}_{n-1} A_{n|0}^\top H^\top + A_{n|0}^\top H^\top \big) \big((M_z^n)^{-1} + H A_{n|0} \overline{P}_{n-1} A_{n|0}^\top H^\top \big)^{-1} \\
&= \overline{P}_n A_{n|0}^\top H^\top M_z^n \big(H A_{n|0} \overline{P}_{n-1} A_{n|0}^\top H^\top + (M_z^n)^{-1} \big) \big((M_z^n)^{-1} + H A_{n|0} \overline{P}_{n-1} A_{n|0}^\top H^\top \big)^{-1} \\
&= \overline{P}_n A_{n|0}^\top H^\top M_z^n.
\end{aligned}$$

The optimal solution finally satisfies

$$\overline{x}_n^0 = \overline{x}_{n-1}^0 + \overline{G}_n \big(\widetilde{z}^n - H A_{n|0} \overline{x}_{n-1}^0 \big). \tag{2.53}$$

The expression of the sequential filter directly follows from this relationship. Let us define $\widehat{x}_n^+$ the solution of (2.51) at iteration n and with initial condition $\overline{x}_n^0$, namely

$$\widehat{x}_+^n = A_{n|0} \overline{x}_n^0 + \sum_{k=0}^{n-1} A_{n|k+1} R.$$

Defining

$$\widehat{x}_-^n = A_{n|n-1} \widehat{x}_+^{n-1} + R, \tag{2.54}$$

and using (2.53) we remark that

$$\widehat{x}_+^n = \widehat{x}_-^n + A_{n|0} \overline{G}_n \big(z^n - H \widehat{x}_-^n \big), \tag{2.55}$$

Similarly we consider the propagated covariance

$$P_+^n = A_{n|0} \overline{P}_n A_{n|0}^\top.$$

Defining

$$P_-^n = A_{n|n-1} P_+^{n-1} A_{n|n-1}^\top, \tag{2.56}$$

we observe the following relation

$$\begin{aligned}
(P_+^n)^{-1} &= A_{n|0}^{-\top} \big(A_{n|0}^\top H^\top M_z^n H A_{n|0} + \overline{P}_{n-1}^{-1} \big) A_{n|0}^{-1} \\
&= H^\top M_z^n H + (P_-^n)^{-1}.
\end{aligned} \tag{2.57}$$

Using once again the inversion Lemma, we obtain

$$\begin{aligned}
P_+^n &= P_-^n - P_-^n H^\top \big((M_z^n)^{-1} + H P_-^n H^\top \big)^{-1} H P_-^n, \\
&= P_-^n - \big(P_z^n \big) \big(P_{zz}^n \big)^{-1} \big(P_z^n \big)^\top,
\end{aligned} \tag{2.58}$$

where in (2.58) we use the notations

$$\left|\begin{array}{l} P_z^n = P_-^n H^\top, \\ \\ P_{zz}^n = (M_z^n)^{-1} + H P_-^n H^\top. \end{array}\right. \tag{2.59}$$

The discrete gain operator G_x^n hence reads

$$G_x^n = A_{n|0}\overline{G}_n = A_{n|0}\overline{P}_n A_{n|0}^\top H^\top M_z^n = P_+^n H^\top M_z^n.$$

Following the same arguments (but backwards) used to give a simpler expression of $\overline{G}_n$, the gain operator is equivalently represented by

$$G_x^n = P_z^n \big(P_{zz}^n\big)^{-1}.$$

Regrouping (2.54), (2.55), (2.56) and (2.58) we obtain the so-called *Kalman-Bucy* algorithm [Bensoussan, 1971, Simon, 2006] written here as a predication-correction scheme:

$$\text{(Initialization)} \quad \begin{cases} P_z^0 = P_{xx,0} H^\top, \\ P_{zz}^0 = (M_z^0)^{-1} + H P_{xx,0} H^\top, \\ P_+^0 = P_{xx,0} - \big(P_z^0\big)\big(P_{zz}^0\big)^{-1}\big(P_z^0\big)^\top, \\ G_x^0 = P_+^0 H^\top M_z^0 = P_z^0\big(P_{zz}^0\big)^{-1}, \\ \widehat{x}_+^0 = x_\diamond + G_x^0\big(z^0 - Hx_\diamond\big), \end{cases} \tag{2.60}$$

$$\text{(Prediction)} \quad \begin{cases} \widehat{x}_-^n = A_{n|n-1}\widehat{x}_+^{n-1} + R, \\ \\ P_-^n = A_{n|n-1} P_+^{n-1} A_{n|n-1}^\top, \end{cases} \tag{2.61}$$

$$\text{(Correction)} \quad \begin{cases} P_z^n = P_-^n H^\top, \\ P_{zz}^n = (M_z^n)^{-1} + H P_-^n H^\top, \\ P_+^n = P_-^n - \big(P_z^n\big)\big(P_{zz}^n\big)^{-1}\big(P_z^n\big)^\top, \\ G_x^n = P_+^n H^\top M_z^n = P_z^n\big(P_{zz}^n\big)^{-1}, \\ \widehat{x}_+^n = \widehat{x}_-^n + G_x^n\big(z^n - H\widehat{x}_-^n\big). \end{cases} \tag{2.62}$$

Remark 16. *As we have mentioned, the algorithm* (2.60), (2.61) *and* (2.62) *directly extends in the case of state-parameter estimation where we aim at minimizing the functional* (2.49) *under the constraint*

$$\begin{cases} x^n = A_{n|n-1}x^{n-1} + B_{n|n-1}\theta^{n-1} + R, \\ \theta^n = \theta^{n-1}, \\ x^0 = x_\diamond + \zeta_x, \\ \theta^0 = \theta_\diamond + \zeta_\theta, \end{cases}$$

where $B_{n|n-1}$ *is a linear operator acting on the parameter space into the state space – typically a rectangular matrix. We decompose the covariance matrix into*

$$P^n_- = \begin{pmatrix} P^n_{xx-} & P^n_{x\theta-} \\ (P^n_{x\theta-})^\top & P^n_{\theta\theta-} \end{pmatrix} = \begin{pmatrix} A_{n|n-1} & B_{n|n-1} \\ 0 & \mathbb{1} \end{pmatrix} P^{n-1}_+ \begin{pmatrix} A^\top_{n|n-1} & 0 \\ B^\top_{n|n-1} & \mathbb{1} \end{pmatrix}$$

$$= \begin{pmatrix} A_{n|n-1} & B_{n|n-1} \\ 0 & \mathbb{1} \end{pmatrix} \begin{pmatrix} P^{n-1}_{xx+} A^\top_{n|n-1} + P^{n-1}_{x\theta+} B^\top_{n|n-1} & P^{n-1}_{x\theta+} \\ (P^{n-1}_{x\theta+})^\top A^\top_{n|n-1} + P^{n-1}_{\theta\theta+} B^\top_{n|n-1} & P^{n-1}_{\theta\theta+} \end{pmatrix}$$

$$= \begin{pmatrix} \begin{matrix} A_{n|n-1} P^{n-1}_{xx+} A^\top_{n|n-1} + A_{n|n-1} P^{n-1}_{x\theta+} B_{n|n-1} \\ \quad + B_{n|n-1} (P^{n-1}_{x\theta+})^\top B^\top_{n|n-1} + B_{n|n-1} P^{n-1}_{\theta\theta+} B^\top_{n|n-1} \end{matrix} & A_{n|n-1} P^{n-1}_{x\theta+} + B_{n|n-1} P^{n-1}_{\theta\theta+} \\ \\ (P^{n-1}_{x\theta+})^\top A^\top_{n|n-1} + P^{n-1}_{\theta\theta+} B^\top_{n|n-1} & P^{n-1}_{\theta\theta+} \end{pmatrix}.$$

Similarly, the gain operator is written as

$$G^n = \begin{pmatrix} G^n_x \\ G^n_\theta \end{pmatrix} = \begin{pmatrix} P^n_{xx+} & P^n_{x\theta+} \\ (P^n_{x\theta+})^\top & P^n_{\theta\theta+} \end{pmatrix} \begin{pmatrix} H^\top \\ 0 \end{pmatrix} = \begin{pmatrix} P^n_{xx+} H^\top \\ (P^n_{x\theta+})^\top H^\top \end{pmatrix}.$$

Finally, using the notation

$$\mathbf{H}^n = \Big((M^n_z)^{\frac{1}{2}} H \quad 0 \Big),$$

we obtain the following algorithm

$$\text{(Initialization)} \quad \begin{cases} P^0_+ = \big((\mathbf{H}^0)^\top \mathbf{H}^0 + (P_0)^{-1} \big)^{-1}, \\ G^0_x = P^0_{xx+} H^\top M^0_z, \\ G^0_\theta = (P^0_{x\theta+})^\top H^\top M^0_z, \\ \widehat{x}^0_+ = x_\diamond + G^0_x \big(z^0 - H x_\diamond \big), \\ \widehat{\theta}^0_+ = \theta_\diamond + G^0_\theta \big(z^0 - H x_\diamond \big), \end{cases} \tag{2.63}$$

$$\text{(Prediction)} \quad \begin{cases} \widehat{x}^n_- = A_{n|n-1} \widehat{x}^{n-1}_+ + B_{n|n-1} \widehat{\theta}^{n-1}_+ + R, \\ \widehat{\theta}^n_- = \widehat{\theta}^{n-1}_+, \\ P^n_{xx-} = A_{n|n-1} P^{n-1}_{xx+} A^\top_{n|n-1} + A_{n|n-1} P^{n-1}_{x\theta+} B^\top_{n|n-1} \\ \qquad\quad + B_{n|n-1} (P^{n-1}_{x\theta+})^\top B^\top_{n|n-1} + B_{n|n-1} P^{n-1}_{\theta\theta+} B^\top_{n|n-1}, \\ P^n_{x\theta-} = A_{n|n-1} P^{n-1}_{x\theta+} + B_{n|n-1} P^{n-1}_{\theta\theta+}, \\ P^n_{\theta\theta-} = P^{n-1}_{\theta\theta+}, \end{cases} \tag{2.64}$$

$$\text{(Correction)} \quad \begin{cases} P^n_+ = \big((\mathbf{H}^n)^\top \mathbf{H}^n + (P^n_-)^{-1} \big)^{-1}, \\ G^n_x = P^n_{xx+} H^\top M^n_z, \\ G^n_\theta = (P^n_{x\theta+})^\top H^\top, \\ \widehat{x}^n_+ = \widehat{x}^n_- + G^n_x \big(z^n - H \widehat{x}^n_- \big), \\ \widehat{\theta}^n_+ = \widehat{\theta}^n_- + G^n_\theta \big(z^n - H \widehat{x}^n_- \big). \end{cases} \tag{2.65}$$

Extended Kalman filtering for nonlinear systems. For applications purposes, we are interested in finding the corresponding Kalman filtering in a nonlinear setting. More precisely we consider a consistent and stable time approximation of the target system (2.3) taking the form of

$$\begin{cases} x^n = A_{n|n-1}(x^{n-1}, \theta^{n-1}), \\ x^0 = x_\diamond + \zeta_x, \\ \theta^0 = \theta_\diamond + \zeta_\theta. \end{cases} \tag{2.66}$$

In (2.66) the transition operator $A_{n|n-1}$ is nonlinear. In a complete nonlinear framework, the observation operator is also nonlinear and the functional to be minimized in a variational procedure is defined by

$$J(\zeta_x, \zeta_\theta) = \frac{1}{2}\|\zeta_\theta\|^2_{P^{-1}_{\theta\theta,0}} + \frac{1}{2}\|\zeta_x\|^2_{P^{-1}_{xx,0}} + \frac{1}{2}\sum_{k=1}^{n} \|z^k - H(x^k)\|^2_{M^k_z}. \tag{2.67}$$

The Extended Kalman filtering (EKF) – see [Simon, 2006, Tuan Pham et al., 1997, Tuan Pham, 2000] – is a linearization scheme based on the pattern described in (2.63), (2.60) and (2.60). More precisely, defining

$$\mathrm{d}A_{n|n-1} = \begin{pmatrix} \mathrm{d}_x A_{n|n-1} & \mathrm{d}_\theta A_{n|n-1} \end{pmatrix}$$

the tangent operator of the transition operator and

$$\mathrm{d}_x H^n = \mathrm{d}_x H|_{\widehat{x}^n_-}, \quad \text{and} \quad \mathrm{d}\mathbf{H}^n = \begin{pmatrix} \mathrm{d}_x H^n (M^n_z)^{\frac{1}{2}} & 0 \end{pmatrix}$$

the tangent operator of the observation operator, the EKF algorithm reads

$$\text{(Initialization)} \quad \begin{cases} P^0_+ = \left((\mathrm{d}\mathbf{H}^0)^\intercal \mathrm{d}\mathbf{H}^0 + (P_0)^{-1}\right)^{-1}, \\ G^0_x = P^0_{xx+}(\mathrm{d}_x H^0)^\intercal M^0_z, \\ G^0_\theta = (P^0_{x\theta+})^\intercal (\mathrm{d}_x H^0)^\intercal M^0_z, \\ \widehat{x}^0_+ = x_\diamond + G^0_x\big(z^0 - H(x_\diamond)\big), \\ \widehat{\theta}^0_+ = \theta_\diamond + G^0_\theta\big(z^0 - H(x_\diamond)\big), \end{cases} \tag{2.68}$$

$$\text{(Prediction)} \quad \begin{cases} \widehat{x}^n_- = A_{n|n-1}(\widehat{x}^{n-1}_+, \widehat{\theta}^{n-1}_+), \\ \widehat{\theta}^n_- = \widehat{\theta}^{n-1}_+, \\ P^n_{xx-} = (\mathrm{d}_x A_{n|n-1}) P^{n-1}_{xx+} (\mathrm{d}_x A_{n|n-1})^\intercal + (\mathrm{d}_x A_{n|n-1}) P^{n-1}_{x\theta+} (\mathrm{d}_\theta A_{n|n-1})^\intercal \\ \qquad + (\mathrm{d}_\theta A_{n|n-1}) (P^{n-1}_{x\theta+})^\intercal (\mathrm{d}_\theta A_{n|n-1})^\intercal + (\mathrm{d}_\theta A_{n|n-1}) P^{n-1}_{\theta\theta+} (\mathrm{d}_\theta A_{n|n-1})^\intercal, \\ P^n_{x\theta-} = (\mathrm{d}_x A_{n|n-1}) P^{n-1}_{x\theta+} + (\mathrm{d}_\theta A_{n|n-1}) P^{n-1}_{\theta\theta+}, \\ P^n_{\theta\theta-} = P^{n-1}_{\theta\theta+}, \end{cases} \tag{2.69}$$

$$\text{(Correction)} \quad \begin{cases} P^n_+ = \left((\mathrm{d}\mathbf{H}^n)^\intercal \mathrm{d}\mathbf{H}^n + (P^n_-)^{-1}\right)^{-1}, \\ G^n_x = P^n_{xx+}(\mathrm{d}_x H^n)^\intercal M^n_z, \\ G^n_\theta = (P^n_{x\theta+})^\intercal (\mathrm{d}_x H^n)^\intercal M^n_z, \\ \widehat{x}^n_+ = \widehat{x}^n_- + G^n_x\big(z^n - H(\widehat{x}^n_-)\big), \\ \widehat{\theta}^n_+ = \widehat{\theta}^n_- + G^n_\theta\big(z^n - H(\widehat{x}^n_-)\big). \end{cases} \tag{2.70}$$

Unscented Kalman filtering. The Unscented Kalam Filter (UKF) – see [Julier et al., 1995, Julier et al., 2000, Julier, 2002, Julier and Uhlmann, 2002, Julier and Uhlmann, 2004, Romanenko and Castro, 2008, Särkkä, 2007, Moireau and Chapelle, 2011] – is another alternative for performing state estimation in a nonlinear framework. This new method was initially proposed to circumvent some classical drawbacks of the EK filter. The first one being that the EKF requires the computation of the tangent operators of the model and the observation operator, namely $\mathrm{d}A$ and $\mathrm{d}_x H$ in our formalism. In practical cases, these computations may become significantly complex. The second disadvantage is that this linearization scheme may become extremely inaccurate and potentially leading to the algorithm divergence.

The UK filter is historically embedded in a stochastic framework where P_-^n, P_+^n and $\widehat{x}_-^n$, $\widehat{x}_+^n$ are interpreted as covariances and means (*a posteriori* and *a priori*). In a Kalman filter, the means and covariances are propagated by the model operator during the prediction phase and by the observation operator during the correction phase. The idea of the UKF is to use a particular choice of sampling points which are propagated by the nonlinear operators themselves (instead of their linearizations) in order to estimate the means and the covariances.

In this section we propose to summarize the construction of this filter. Readers may refer to [Julier and Uhlmann, 2004, Moireau and Chapelle, 2011] for more details. To start with let us consider a finite dimensional random variable x of mean $E(x)$ and covariance $P(x)$. As we are interested in the propagation of these probabilistics moments, we consider a nonlinear transformation A and the corresponding propagated random variable $x_A = A(x)$.

As we have mentioned, the unscented filter uses well-chosen sampling points denoted by x^i and transformed into

$$\forall i = 1, \cdots, n_{\mathrm{P}} \quad x_A^i = A(x^i),$$

where n_{P} represents the number of sampling points. Each sampling point deviates from the mean by a distance-to-mean value that we represent by $\widetilde{x}^i$ so that

$$\forall i = 1, \cdots, n_{\mathrm{P}} \quad x^i = E(x) + \widetilde{x}^i.$$

We associate to the sampling points n_{P} interpolation coefficients α_i so that the gathering $\{(x^i, \alpha_i)\}_{i=1}^{n_{\mathrm{P}}}$ satisfies by construction

$$\left|\begin{aligned}
&\sum_{i=1}^{n_{\mathrm{P}}} \alpha_i = 1,\\[2ex]
&E_\alpha(x) = \sum_{i=1}^{n_{\mathrm{P}}} \alpha_i x^i = E(x),\\[2ex]
&P_\alpha(x) = \sum_{i=1}^{n_{\mathrm{P}}} \alpha_i \big(x^i - E_\alpha(x)\big) \cdot \big(x^i - E_\alpha(x)\big)^{\intercal} = P(x).
\end{aligned}\right. \tag{2.71}$$

It is in the sense of (2.71) that the sampling points are said to be *well-chosen*. It implies that

$$\left|\begin{array}{l}\displaystyle\sum_{i=1}^{n_{\mathrm{P}}} \alpha_i \widetilde{x}^i = 0,\\ \\ \displaystyle\sum_{i=1}^{n_{\mathrm{P}}} \alpha_i \big(\widetilde{x}^i\big) \cdot \big(\widetilde{x}^i\big)^{\top} = P(x).\end{array}\right. \tag{2.72}$$

Assuming (2.72) is verified, classical arguments of linearization around the mean of the random variable – see [Moireau and Chapelle, 2011] for detailed computations – leads to the following estimates

$$\left|\begin{array}{l}E_{\alpha}(x_A) = E(x_A) + o(E(\|x - E(x)\|^2)),\\ \\ P_{\alpha}(x_A) = P(x_A) + o(E(\|x - E(x)\|^2)).\end{array}\right. \tag{2.73}$$

Sampling points satisfiying (2.72) are referred to as *sigma-points*. In practice such sigma-points can be constructed from *unitary* sampling points $I^{[i]}$ – with zero mean and unit covariance – by

$$x^i = E(x) + P(x)^{\frac{1}{2}} I^{[i]}.$$

See [Moireau and Chapelle, 2011] for numerous examples of sampling procedure. Casting aside, for clarity reasons, the initialization step, the UKF filter reads

$$\text{(Sampling)} \qquad \widehat{x}_+^{[i]n-1} = \widehat{x}_+^{n-1} + (P_+^{n-1})^{\frac{1}{2}} I^{[i]}, \quad \forall i = 1, \cdots, n_{\mathrm{P}}, \tag{2.74}$$

$$\text{(Prediction)} \quad \begin{cases}\widehat{x}_-^n = \sum_{i=1}^{n_{\mathrm{P}}} \alpha_i A_{n|n-1}(\widehat{x}_+^{[i]n-1}),\\ \\ P_-^n = \sum_{i=1}^{n_{\mathrm{P}}} \alpha_i \big(A_{n|n-1}(\widehat{x}_+^{[i]n-1}) - \widehat{x}_-^n\big) \cdot \big(A_{n|n-1}(\widehat{x}_+^{[i]n-1}) - \widehat{x}_-^n\big)^{\top},\end{cases} \tag{2.75}$$

$$\text{(Resampling)} \quad \begin{cases}\widehat{x}_-^{[i]n} = \widehat{x}_-^n + (P_-^n)^{\frac{1}{2}} I^{[i]}, \quad \forall i = 1, \cdots, n_{\mathrm{P}},\\ \\ z^{[i]n} = H(\widehat{x}_-^{[i]n}), \quad \forall i = 1, \cdots, n_{\mathrm{P}},\end{cases} \tag{2.76}$$

$$\text{(Correction)} \quad \begin{cases}z_-^n = \sum_{i=1}^{n_{\mathrm{P}}} \alpha_i z^{[i]n},\\ P_z^n = \sum_{i=1}^{n_{\mathrm{P}}} \alpha_i \big(\widehat{x}_-^{[i]n} - \widehat{x}_-^n\big) \cdot \big(z^{[i]n} - z_-^n\big)^{\top},\\ P_{zz}^n = (M_z^n)^{-1} + \sum_{i=1}^{n_{\mathrm{P}}} \alpha_i \big(z^{[i]n} - z_-^n\big) \cdot \big(z^{[i]n} - z_-^n\big)^{\top},\\ P_+^n = P_-^n - \big(P_z^n\big)\big(P_{zz}^n\big)^{-1}\big(P_z^n\big)^{\top},\\ G_x^n = P_z^n\big(P_{zz}^n\big)^{-1},\\ \widehat{x}_+^n = \widehat{x}_-^n + G_x^n\big(z^n - z_-^n\big).\end{cases} \tag{2.77}$$

Remark 17. *Estimates* (2.73) *shows that the order of approximation proposed by the UK filter is similar to that provided by a second order extended Kalman filter – see [Simon, 2006]. On top of that, as the computation of the estimator only requires the computation of independent sampling trajectories – also referred to as particle. This algorithm is, by construction, naturally performed in parallel.*

2.3.2 Combination of nudging and reduced-order Kalman filtering

As their time continuous counter-part, the various algorithms that we have exhibited so far remain – in the perspective of finite element discretization of a partial differential equation – numerically intractable since they require to manage a full covariance matrix of size equal to the state space dimension. This so-called *curse of dimensionality* is a well-known limitation of the standard Kalman filters and one way to circumvent this difficulty is to consider a *singular value decomposition* of the covariance matrix in order to manage only matrices of reduced size. This approach has been historically used in the context of data assimilation for oceanography in [Tuan Pham et al., 1997] where authors extend this approach in a nonlinear setting. In this section we start by recalling the main principle of reduced-order Kalman filtering. This approach will be used in the second section where we present the complete joint state-parameter filter using a nudging method to control the uncertainty on the state space, hence justifying a reduced-order Kalman filter on the remaining parameter space.

Linear reduced-order filtering To start with let us replace in (2.56) the expression (2.58) of the covariance a posteriori in order to obtain the recurrence relation for the a priori covariance

$$P_-^n = A_{n|n-1} P_-^{n-1} A_{n|n-1}^\intercal - A_{n|n-1} P_-^{n-1} H^\intercal \big((M_z^n)^{-1} + H P_-^n H^\intercal \big)^{-1} H P_-^{n-1} A_{n|n-1}.$$

Assuming that P_-^n and P_-^{n-1} are of rank p so that both matrices can be decomposed into

$$P_-^k = L^k (U^{k-1})^{-1} (L^k)^\intercal,$$

for $k = n, n-1$ with U an invertible $p \times p$ matrix and L is rectangular $d \times p$ (d being the state space dimension) then the matrices appearing in the decomposition necessarily verify

$$\left| \begin{aligned} & L^n = A_{n|n-1} L^{n-1}, \\ & U^n = U^{n-1} + (L^n)^\intercal H^\intercal M_z^n H L^n. \end{aligned} \right. \tag{2.78}$$

From (2.78) and (2.58) we note that the a posteriori covariance directly derives as

$$P_n^+ = L^n (U^n)^{-1} (L^n)^\intercal. \tag{2.79}$$

Therefore, the reduced-order Kalman filter, in the linear case, reads

$$\text{(Initilaization)}\quad \begin{cases} P_0 = L_0 U_0^{-1} L_0^\top, \\ L^0 = L_0, \\ U^0 = U_0 + (L^0)^\top H^\top M_z^0 H L^0, \\ G_x^0 = L^0 (U^0)^{-1} (L^0)^\top H^\top M_z^n, \\ \widehat{x}_+^0 = x_\diamond + G_x^0 \big(z^0 - H x_\diamond\big), \end{cases} \tag{2.80}$$

$$\text{(Prediction)}\quad \begin{cases} \widehat{x}_-^n = A_{n|n-1} \widehat{x}_+^{n-1} + R, \\ L^n = A_{n|n-1} L^{n-1}, \\ U^n = U^{n-1} + (L^n)^\top H^\top M_z^n H L^n, \end{cases} \tag{2.81}$$

$$\text{(Correction)}\quad \begin{cases} G_x^n = L^n (U^n)^{-1} (L^n)^\top H^\top M_z^n, \\ \\ \widehat{x}_+^n = \widehat{x}_-^n + G_x^n \big(z^n - H \widehat{x}_-^n\big). \end{cases} \tag{2.82}$$

We remark that in the algorithm (2.81) and (2.82) the previously stated difficulty of managing a full covariance matrix is reduced to managing the matrix U (of small size) at each time step since the matrix L is by nature a sparse matrix. A typical example is when we consider state-parameter estimation where the uncertainties are reduced to the parameter space, namely

$$P_0 = \begin{pmatrix} 0 & 0 \\ 0 & P_{\theta\theta,0} \end{pmatrix}. \tag{2.83}$$

In this case the decomposition of the covariance matrix simply reads

$$L_0 = \begin{pmatrix} L_{x,0} \\ L_{\theta,0} \end{pmatrix} = \begin{pmatrix} 0 \\ \mathbb{1} \end{pmatrix} \quad \text{and} \quad U_0^{-1} = P_{\theta\theta,0}^{-1}.$$

Hence, omitting the initialization phase for the sake of clarity, the Kalman filter reduced to the parameter space can be stated as

$$\text{(Prediction)}\quad \begin{cases} \widehat{x}_-^n = A_{n|n-1} \widehat{x}_+^{n-1} + B_{n|n-1} \widehat{\theta}_+^{n-1} + R, \\ \widehat{\theta}_-^n = \widehat{\theta}_+^{n-1}, \\ L_x^n = A_{n|n-1} L_x^{n-1} + B_{n|n-1}, \\ L_\theta^n = L_\theta^{n-1} = \mathbb{1}, \\ U^n = U^{n-1} + (L_x^n)^\top H^\top M_z^n H L_x^n, \end{cases} \tag{2.84}$$

$$\text{(Correction)}\quad \begin{cases} \widehat{x}_+^n = \widehat{x}_-^n + L_x^n (U^n)^{-1} (L_x^n)^\top H^\top M_z^n \big(z^n - H \widehat{x}_-^n\big), \\ \\ \widehat{\theta}_+^n = \widehat{\theta}_-^n + (U^n)^{-1} (L_x^n)^\top H^\top M_z^n \big(z^n - H \widehat{x}_-^n\big). \end{cases} \tag{2.85}$$

Complete joint state-parameter methodology The approach that we will use in the context of parameter identification for the cardiac biomechanical model presented in Chapter 1 is two fold. First we use a modified dynamical system aiming at stabilizing the state estimation error – a modification described and illustrated in Section 2.2. Second, as the state estimation error is stabilizing we use the decomposition (2.83) to perform the parameter identification of the model.

In a complete linear context, using a prediction-correction algorithm for the time discrete state estimation (detailed in Chapter 3) the complete joint state-parameter estimation methodology reads.

$$\text{(State Prediction)} \quad \frac{\widehat{x}^n_{--} - \widehat{x}^{n-1}_{+}}{\Delta \mathrm{t}} = \big(A + \eta V\big)\frac{\widehat{x}^n_{--} + \widehat{x}^{n-1}_{+}}{2} + B_{n|n-1}\widehat{\theta}^{n-1}_{+} + R, \tag{2.86}$$

$$\text{(State Correction)} \quad \frac{\widehat{x}^n_{-} - \widehat{x}^n_{--}}{\Delta \mathrm{t}} = \gamma H^*\Big(z^n - H\frac{\widehat{x}^n_{-} - \widehat{x}^n_{--}}{2}\Big), \tag{2.87}$$

$$\text{(Joint Prediction)} \quad \begin{cases} \widehat{\theta}^n_{-} = \widehat{\theta}^{n-1}_{+}, \\ L^n_x = A_{n|n-1}L^n_{x-} + B_{n|n-1}, \\ U^n = U^{n-1} + (L^n_x)^\top H^\top M^n_z H L^n_x, \end{cases} \tag{2.88}$$

$$\text{(Joint Correction)} \quad \begin{cases} \widehat{x}^n_{+} = \widehat{x}^n_{-} + L^n_x (U^n)^{-1}(L^n_x)^\top H^\top M^n_z\big(z^n - H\widehat{x}^n_{-}\big), \\ \widehat{\theta}^n_{+} = \widehat{\theta}^n_{-} + (U^n)^{-1}(L^n_x)^\top H^\top M^n_z\big(z^n - H\widehat{x}^n_{-}\big). \end{cases} \tag{2.89}$$

Using the arguments presented in [Chapelle et al., 2009, Moireau and Chapelle, 2011, Moireau et al., 2007] this methodology can be used in a nonlinear setting using a reduced-order Unscented Kalman filter.

2.4 Example of application using cine-MR images

In this section we propose an example of application using cine-MR images. More precisely, we assume that a prior step of image processing led to the construction of the endo- and epicardium surfaces of the left ventricle. To simulate this processing step we extract from an infarcted direct simulation the parts of the model geometry corresponding to the external surface of the left ventricle.

2.4.1 Available informations and discrepancy measure

Obviously, in practical cases, no one-to-one mapping from the model left ventricle surface and the data surfaces are available. Therefore, following [Moireau et al., 2009, Chabiniok et al., 2011], we compare the estimated surfaces and the data using a signed distance function. This example directly enters in the case of implicit discrepancy measure. More precisely, defining S_0 as the model left ventricle surface in the reference configuration and in light of (2.36) – where we have detailed a nudging procedure for direct partial displacement feedback on the boundary – we aim at feeding the data assimilation procedure with the following fidelity-to-data term:

$$E_D(\widehat{\underline{x}}, S) = \frac{1}{2}\left\|\mathrm{Ext}_{S_0}(\mathrm{dist}(\widehat{\underline{x}}, S)\ ;\ \underline{n}_S)\right\|^2_{\mathcal{E}_\mathrm{e}}. \tag{2.90}$$

In (2.90) we denoted by S the data surface and $\mathrm{dist}(\widehat{\underline{x}}, S)$ the signed distance between an estimated position $\widehat{\underline{x}}$ and the data surface S, typically defined by

$$\mathrm{dist}(\widehat{\underline{x}}, S) = \left(\widehat{\underline{x}} - \Pi_S \widehat{\underline{x}}\right) \cdot \underline{n}_S. \tag{2.91}$$

In (2.90) and (2.91) we have defined $\underline{n}_S$ the normal of the data surface S at the projection of the estimation point on S, namely $\Pi_S \widehat{\underline{x}}$. It should be noted that $\underline{n}_S$ clearly depends on the estimated position $\widehat{\underline{x}}$.

Once the fidelity-to-data is defined, the next step – in order to build the dynamical system verified by the state observer – is to differentiate this term with respect to a test displacement. In this case, the dependancies of $E_D(\widehat{\underline{x}}, S)$ are twofold: the first one is in the distance operator and the second one is in the vector field used to define the extension operator. More precisely, as explained at the end of Section 2.2.2, if we define the vector field $\underline{u} \in \mathcal{X}^y$ as

$$\underline{u} = \mathrm{Ext}_{S_0}(\mathrm{dist}(\widehat{\underline{x}}, S)\ ;\ \underline{n}_S),$$

then $\underline{u}$ is equivalently represented as the solution of the optimization problem

$$\min_{\underline{u} \cdot \underline{n}_S = \mathrm{dist}(\widehat{\underline{x}}, S)} \frac{1}{2}\|\underline{u}\|^2_{\mathcal{E}_\mathrm{e}}. \tag{2.92}$$

Introducing λ as the Lagrangian multiplier, this optimization problem is equivalent to

$$\min_{\underline{u} \in \mathcal{X}^y} \max_{\lambda \in \mathcal{L}^2(S_0)} \frac{1}{2}\|\underline{u}\|^2_{\mathcal{E}_\mathrm{e}} + (\lambda, \underline{u} \cdot \underline{n}_S - \mathrm{dist}(\widehat{\underline{x}}, S))_{\mathcal{L}^2(S_0)},$$

thus, leading to the mixed formulation, $\forall (\underline{v}^\flat, \mu^*) \in \mathcal{X}^y \times \mathcal{L}^2(S_0)$,

$$\begin{cases} \left(\underline{u}, \underline{v}^\flat\right)_{\mathcal{E}_\mathrm{e}} + \left(\lambda, \underline{v}^\flat \cdot \underline{n}_S\right)_{\mathcal{L}^2(S_0)} = 0, \\ \\ (\underline{u} \cdot \underline{n}_S, \mu^*)_{\mathcal{L}^2(S_0)} = (\mathrm{dist}(\widehat{\underline{x}}, S), \mu^*)_{\mathcal{L}^2(S_0)}. \end{cases}$$

Therefore, differentiating this formulation with respect to a test displacement $\underline{\delta y} \in \mathcal{X}^y$ leads to

$$\begin{cases} \left(\mathrm{d}_y \underline{u} \cdot \underline{\delta y}, \underline{v}^\flat\right)_{\mathcal{E}_\mathrm{e}} + \left(\mathrm{d}_y \lambda \cdot \underline{\delta y}, \underline{v}^\flat \cdot \underline{n}_S\right)_{\mathcal{L}^2(S_0)} = -\left(\lambda, \underline{v}^\flat \cdot \left(\mathrm{d}_y \underline{n}_S \cdot \underline{\delta y}\right)\right)_{\mathcal{L}^2(S_0)}, \\ \\ (\mathrm{d}_y \underline{u} \cdot \underline{\delta y}) \cdot \underline{n}_S = \underline{\delta y} \cdot \underline{n}_S - \underline{u} \cdot (\mathrm{d}_y \underline{n}_S \cdot \underline{\delta y}). \end{cases}$$

We note that the derivative of the normal appears in these two equations. These terms lead to further complications that we do not intend to manage. Instead we propose to define an approximation of the differentiation of the extension, so that the strong formulation of the state observer becomes

$$\begin{cases} \dot{\widehat{\underline{y}}} = \widehat{\underline{v}} + \gamma \mathrm{Ext}_{S_0}(\mathrm{dist}(\widehat{\underline{x}}, S)\ ;\ \underline{n}_S), & \text{in } \Omega_0, \\ \dot{\widehat{\underline{v}}} - \mathrm{div}(\underline{\underline{\sigma}}(\widehat{\underline{y}})) = 0\ , & \text{in } \Omega_0, \\ \underline{\underline{\sigma}}(\widehat{\underline{y}}) \cdot \underline{n} = 0, & \text{on } \partial\Omega_0, \\ \widehat{\underline{y}}(0) = \underline{y}_0, \quad \widehat{\underline{v}}(0) = \underline{y}_1. & \end{cases} \tag{2.93}$$

2.4.2 Applications using synthetic data

In these examples of applications we extract from the direct simulations of Figure 1.20 (infarcted represented with a lower contractility) and Figure 1.21 (infarcted represented with a lower contractility and a higher stiffness) the external surface of the left ventricle. In both cases we try to retrieve in one run of the sequential data assimilation method the values of the parameter. In a first case we have the exact location of the infarcted region (but not the values of the parameter) – this case will be referred to as the 2-Regions case – and in a second case we use the AHA-Regions to retrieve both the location and the intensity of the infarct.

Estimation of contractility, 2-Regions case. This case is the simplest case that we consider. The infarct location is give and we propose to estimate only 2 active parameters in the two regions (one region to account for the infarct and another one for the rest of the heart). In figure 2.2 we plot the evolution during the one simulation run of the data assimilation method with a large confidence in the data represented by a large weight on the observation norm, namely $M_z = 10^7 \times \mathbb{M}_{S_0}$ (where $\mathbb{M}_{S_0}$ is the mass norm on the external surface of the ventricle). We see that the mean value of the parameters (the cyan solid line) and the standard deviations of the parameters (the cyan dashed lines) converge towards the correct values (the **black** solid line).

When we decrease the weight on the observation norm – as an example, Figure 2.3 shows the evolution of the parameters with $M_z = 10^5 \times \mathbb{M}_{S_0}$ – we observe that the parameters converge slowly towards the exact value and the trust region, delimited by the standard deviation, becomes naturally wider.

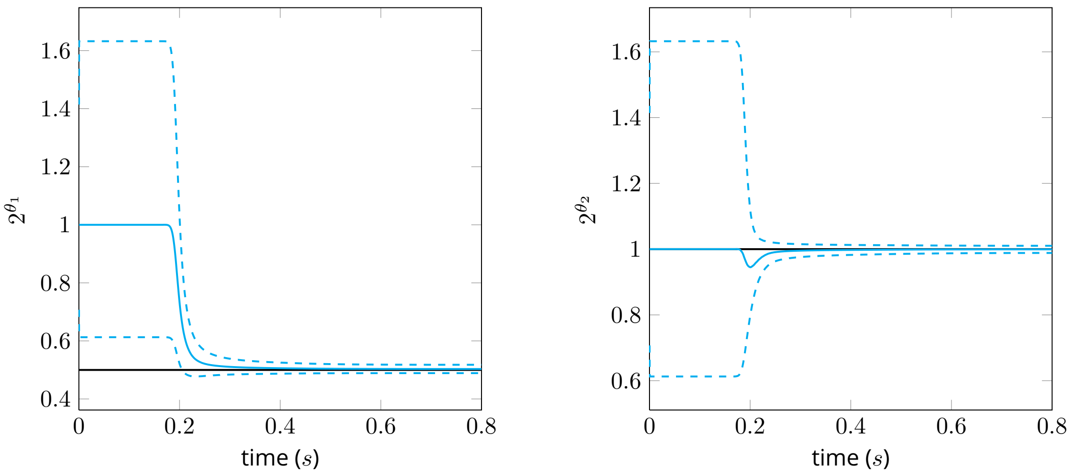

Figure 2.2: Estimation of active parameters using endo- and epicardium synthetic segmentation, $M_z = 10^7 \times \mathbb{M}_{S_0}$.

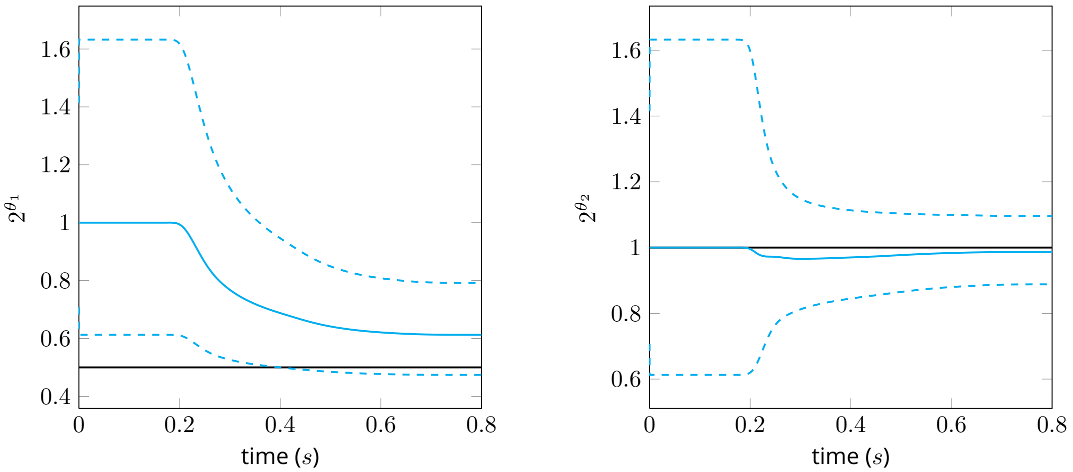

Figure 2.3: Estimation of active parameters using endo- and epicardium synthetic segmentation, $M_z = 10^5 \times \mathbb{M}_{S_0}$.

Estimation of contractility, AHA-Regions case. In this case we perform parameter identification without any prior an the infarct location. In order to retrieve the location and the intensity of the infarct, we use the AHA decomposition of the myocardium (See Figure 1.3 of Chapter 1) and we propose a piece-wise constant representation of the (spatially varying) active parameter. Figure 2.4 shows the obtained parameter at the end of the simulation run. The target parameters are obtained by interpolating the 2-Region mesh used in the (infarcted) direct simulation (and presented in Figure 1.15 of Chapter 1) into the AHA-Region mesh.

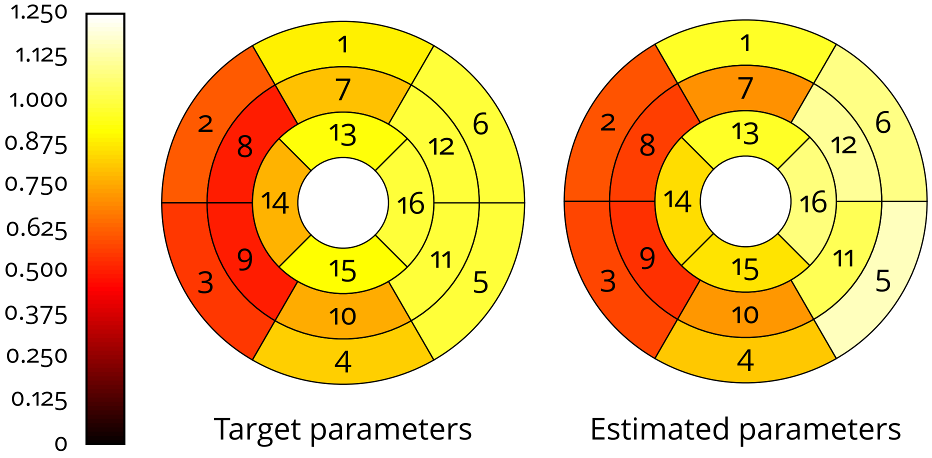

Figure 2.4: Estimation of active parameters using endo- and epicardium synthetic segmentation, $M_z = 10^7 \times \mathbb{M}$.

We clearly see from Figure 2.4 a good reconstruction of the infarct location and also a correct estimation of the parameters.

Estimation of stiffening and contractility, 2-Regions case. In this case, we propose to perform the identification of the active and passive parameters used in the direct simulation presented in the Figure 1.21 of the Chapter 1. The difficulty in this exercise is that during the heart cycle the *purely passive* behavior of the heart is *visible* only during a short time at the end of the ventricular diastole. Hence, it is during this time window that the estimation of passive parameters can be performed.

In Figure 2.5 we show the evolution of the four parameters (two passives and two actives) during one simulation run with a high confidence in the data, i.e. $M_z = 10^7 \times \mathbb{M}_{S_0}$. Even though the reconstruction of the passive parameters is remarkably good, it is striking to see that as soon as the contraction starts the estimation of the passive parameters stops. The estimation of the active parameters is slightly deteriorated but, over all, it provides a correct estimation.

When setting $M_z = 10^5 \times \mathbb{M}_{S_0}$, we see in Figure 2.6 that the estimation of the passive parameters dramatically deteriorates. This is another illustration of the fact that the visibility of the passive parameters in the cardiac cycle is very limited.

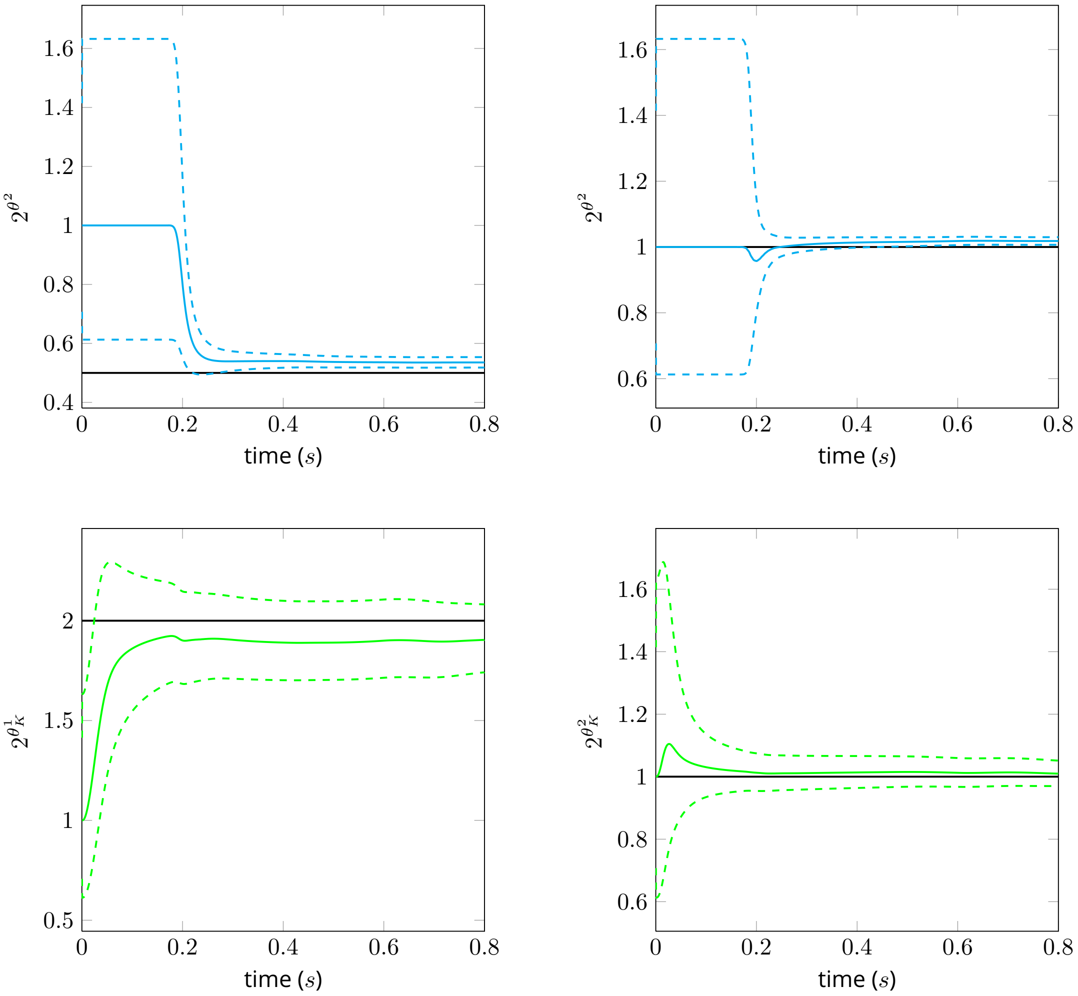

Figure 2.5: Estimation of passive and active parameters using endo- and epicardium synthetic segmentation, $M_z = 10^7 \times \mathbb{M}_{S_0}$.

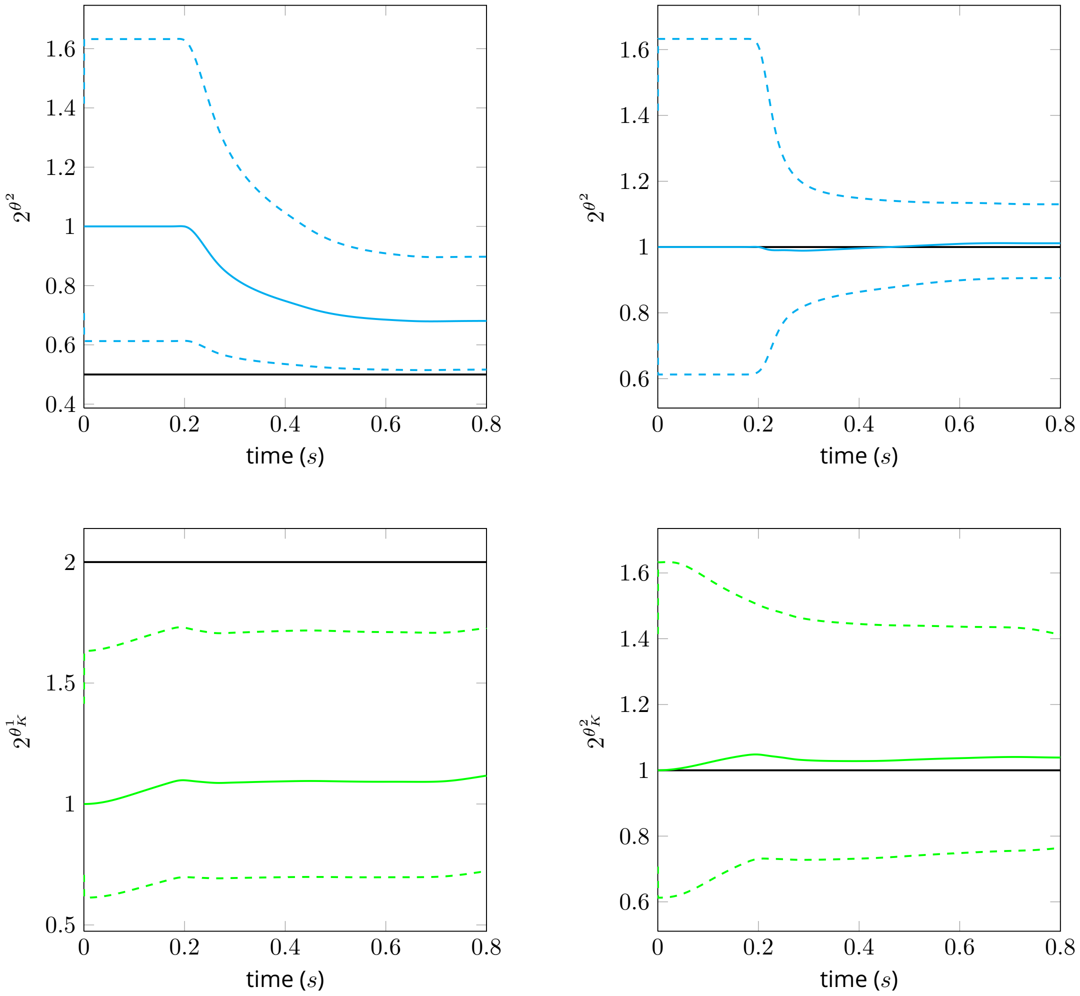

Figure 2.6: Estimation of passive and active parameters using endo- and epicardium synthetic segmentation, $M_z = 10^5 \times \mathbb{M}_{S_0}$.

Estimation of stiffening and contractility, AHA-Regions case. We finally provide a passive and active parameter estimation, without a priori on the infarct location, and using the AHA regions as a spatial discretization of the parameters.

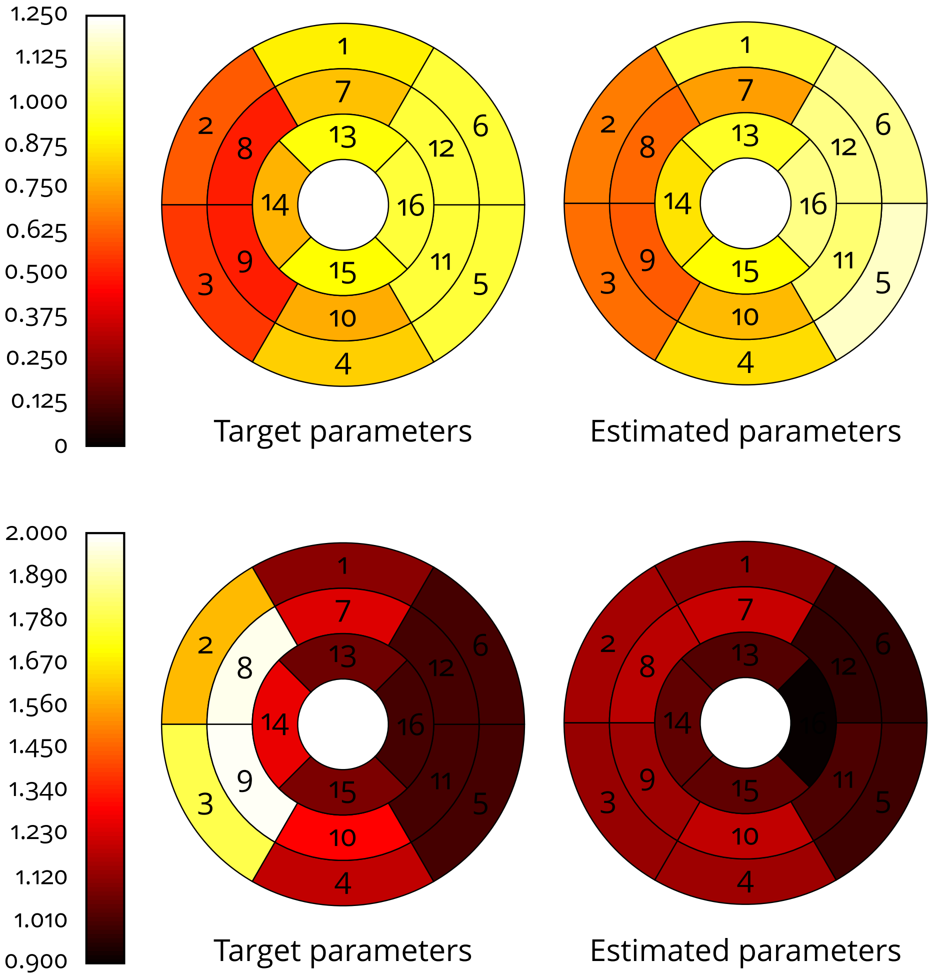

Figure 2.7: Estimation of passive and active parameters using endo- and epicardium synthetic segmentation, $M_z = 10^7 \times \mathbb{M}$.

Figure 2.7 shows the set of parameters (active parameters in the row and passive parameters in the second row). While the estimation of active parameters is quite good, the passive parameters are not well estimated nor can we even extract from this estimation – when looking only at the passive estimation – the location of the infarct. Moreover in Figure 2.8 we show the evolution in time of these parameters and we clearly observe that the passive parameters are totally hidden by the active parts.

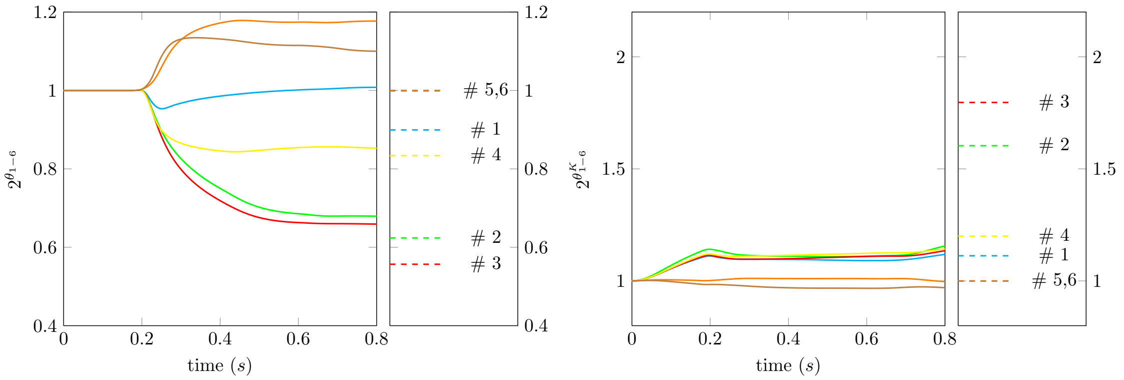

(a) Active #1 - #6

(b) Passive #1 - #6

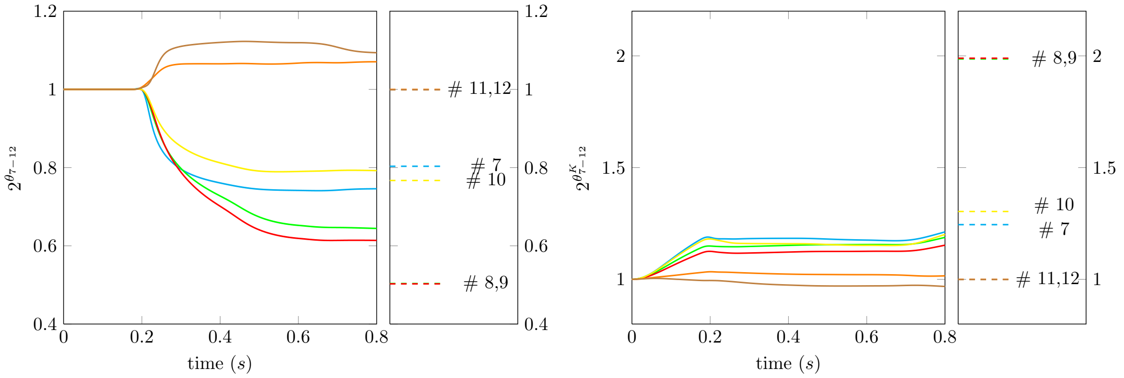

(c) Active #7 - #12

(d) Passive #7 - #12

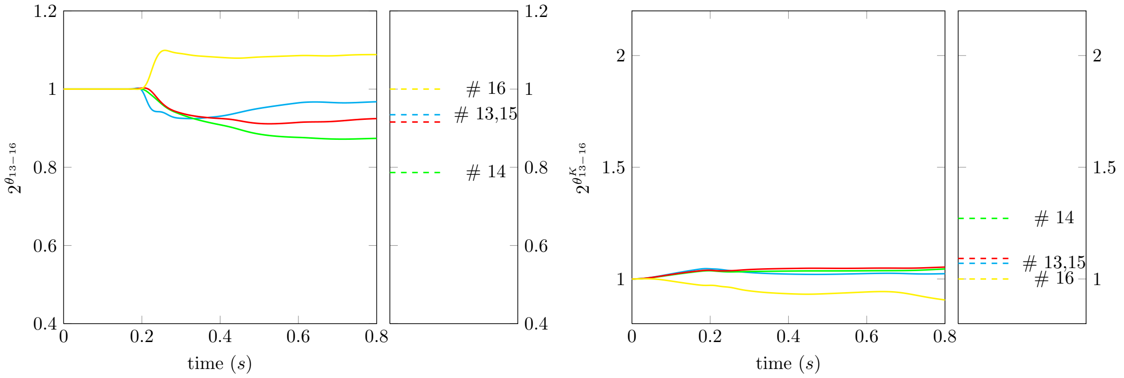

(e) Active #13 - #16

(f) Passive #13 - #16

Figure 2.8: Time evolution of active (left column) and passive (right column) estimated parameters using endo- and epicardium synthetic segmentation, $M_z = 10^7 \times \mathbb{M}$.

Bibliography of the second Chapter

[Auroux and Blum, 2007] Auroux, D. and Blum, J. (2007). A nudging-based data assimilation method: the back and forth nudging (bfn) algorithm. *Nonlin. Processes Geophys.*

[Bardos et al., 1992] Bardos, C., Lebeau, G., and Rauch, J. (1992). Sharp sufficient conditions for the observation, control, and stabilization of waves from the boundary. *SIAM J. Control Optim.*, 30(5):1024–1065.

[Bensoussan, 1971] Bensoussan, A. (1971). *Filtrage optimal des systèmes linéaires*. Dunod.

[Bertoglio et al., 2013] Bertoglio, C., Chapelle, D., Fernández, M. A., Gerbeau, J. F., and Moireau, P. (2013). State observers of a vascular fluid–structure interaction model through measurements in the solid. *Comput. Methods Appl. Mech. Engrg.*, 256:149–168.

[Bertoglio et al., 2012] Bertoglio, C., Moireau, P., and Gerbeau, J. F. (2012). Sequential parameter estimation for fluid-structure problems: Application to hemodynamics. *Int. J. Numer. Meth. Biomed. Engng.*, 28(434-455).

[Blum et al., 2008] Blum, J., LeDimet, F. X., and Navon, I. N. (2008). Data assimilation for geophysical fluids. *Computational Methods for the Atmosphere and the Oceans*, 14:377–434.

[Chabiniok et al., 2011] Chabiniok, R., Moireau, P., Lesault, P.-F., Rahmouni, A., Deux, J.-F., and Chapelle, D. (2011). Trials on tissue contractility estimation from cardiac cine mri using a biomechanical heart model. In *Proceedings of FIMH'11, LNCS 6666*, pages 304–313. Springer.

[Chabiniok et al., 2012] Chabiniok, R., Moireau, P., Lesault, P.-F., Rahmouni, A., Deux, J.-F., and Chapelle, D. (2012). Estimation of tissue contractility from cardiac cine-mri using a biomechanical heart model. *Biomech. Model. Mechanobiol.*, 11(609-630).

[Chapelle et al., 2012] Chapelle, D., Cîndea, N., De Buhan, M., and Moireau, P. (2012). Exponential convergence of an observer based on partial field measurements for the wave equation. *Mathematical Problems in Engineering*, 2012:12.

[Chapelle et al., 2009] Chapelle, D., Moireau, P., and LeTallec, P. (2009). Robust filtering for joint state-parameter estimation in distributed mechanical systems. *Discret. Contin. Dyn. S.*, pages 65–84.

[Corpetti et al., 2009] Corpetti, T., Héas, P., Mémin, E., and Papadakis, N. (2009). Pressure image assimilation for atmospheric motion estimation. *Tellus A.*, 61(1):160–178.

[Delingette et al., 2012] Delingette, H., Billet, F. Wong, K. C. L. S. M., Rhode, K., Ginks, M., Aldo Rinaldi, C., Razavi, R., and Ayache, N. (2012). Personalization of cardiac motion and contractility from images using variational data assimilation. *IEEE Trans. Biomed. Eng.*, 59(1):20–24.

[Julier, 2002] Julier, S. J. (2002). The scaled unscented transformation. *Proceedings of the American Control Conference*.

[Julier and Uhlmann, 2002] Julier, S. J. and Uhlmann, J. K. (2002). Reduced sigma point filters for the propagation of means and covariances through nonlinear transformations. *Proceedings of the American Control Conference*.

[Julier and Uhlmann, 2004] Julier, S. J. and Uhlmann, J. K. (2004). Unscented filtering and nonlinear estimation. *Proceedings of the IEEE*, 92(3):401–422.

[Julier et al., 1995] Julier, S. J., Uhlmann, J. K., and Durrant-Whyte, H. F. (1995). A new approach for filtering non linear systems. *Proceedings of the American Control Conference*, pages 1628–1632.

[Julier et al., 2000] Julier, S. J., Uhlmann, J. K., and Durrant-Whyte, H. F. (2000). A new method for the nonlinear transformation of means and covariances in filter and estimators. *IEEE T. Automat. Contr.*, 45(3):477–482.

[Liu, 1997] Liu, K. (1997). Locally distributed control and damping for the conservative systems. *SIAM J. Control Optim.*, 35(5):1574–1590.

[Luenberger, 1971] Luenberger, D. G. (1971). An introduction to observers. *IEEE T. Automat. Contr.*

[Moireau, 2008] Moireau, P. (2008). *Assimilation de données par filtrage pour les systèmes hyperboliques du second order. Applications à la mécanique cardiaque.* PhD thesis, École Polytechnique.

[Moireau et al., 2013] Moireau, P., Bertoglio, C., Xiao, N., Figueroa, C. A., Taylor, C. A., Chapelle, D., and Gerbeau, J. F. (2013). Sequential identification of boundary support parameters in a fluid-structure vascular model using patient image data. *Biomech. Model. Mechanobiol.*, 12:475–496.

[Moireau and Chapelle, 2011] Moireau, P. and Chapelle, D. (2011). Reduced-order unscented kalman filtering with application to parameter identification in large-dimensional systems. *ESAIM: COCV*, 17:380–405.

[Moireau et al., 2007] Moireau, P., Chapelle, D., and LeTallec, P. (2007). Joint state and parameter estimation for distributed mechanical systems. *Comput. Methods Appl. Mech. Engrg.*, 197:659–677.

[Moireau et al., 2009] Moireau, P., Chapelle, D., and LeTallec, P. (2009). Filtering for distributed mechanical systems using position measurements: Perspectives in medical imaging. *Inverse Problems*, 25.

[Navon, 2008] Navon, I. N. (2008). *Data assimilation for numerical weather prediction: a review*. Springer.

[Papadakis and Mémin, 2008] Papadakis, N. and Mémin, E. (2008). Variational assimilation of fluid motion from image sequence. *SIAM J. Imaging Sciences*, 1(4):343–363.

[Perego et al., 2011] Perego, M., Veneriani, A., and Vergara, C. (2011). A variational approach for estimating the compliance of the cardiovascular tissue: an inverse fluid-structure interaction problem. *SIAM J. Sci. Comput.*, 33(3):1181–1211.

[Ramdani et al., 2012] Ramdani, K., Tucsnak, M., and Weiss, G. (2012). Recovering the initial state of an infinite-dimensional system using observers. *Automatica*, pages 1616–1625.

[Romanenko and Castro, 2008] Romanenko, A. and Castro, J. A. A. M. (2008). The unscented filter as an alternative to the ekf for nonlinear state estimation: a simulation case study. *Comput. Chem. Eng.*, 28:347–355.

[Sainte-Marie et al., 2006] Sainte-Marie, J., Chapelle, D., Cimrman, R., and Sorine, M. (2006). Modeling and estimation of the cardiac electromechanical activity. *Comput. Struct.*, 84:1743–1759.

[Särkkä, 2007] Särkkä, S. (2007). On unscented kalman filtering for state estimation of continuous-time nonlinear systems. *IEEE T. Automat. Contr.*

[Sermesant et al., 2006] Sermesant, M., Moireau, P., Camara, P., Sainte-Marie, J., Andriantsimiavona, R., Cimrman, R., Hill, D., Chapelle, D., and Razavi, R. (2006). Cardiac function estimation from mri using a heart model and data assimilation: Advances and difficulties. *Med. Image. Anal.*, 10(642-656).

[Simon, 2006] Simon, D. (2006). *Optimal state estimation: Kalman, H_∞ and nonlinear approaches*. Wiley-Interscience.

[Titaud et al., 2010] Titaud, O., Vidard, A., Souopgui, I., and LeDimet, F. X. (2010). Assimilation of image sequences in numerical models. *Tellus A*, 62(1):30–47.

[Tuan Pham, 2000] Tuan Pham, D. (2000). Stochastic methods for data assimilation in strongly nonlinear systems. *Mon. Weather. Rev.*, 129:1194–1207.

[Tuan Pham et al., 1997] Tuan Pham, D., Verron, J., and Gourdeau, L. (1997). Singular evolutive kalman filters for data assimilation in oceanography. *C. R. Acad. Sci. Paris*, pages 255–260.

Data assimilation of time under-sampled measurements using observers, application to wave-like equations.

The main motivation of this work comes from the simple fact that, in a clinical routine, the MR images are most likely to have a coarse distribution in time compared with the time line of the numerical procedure. For example, the cine-MR images usually represents a sequence of ~20 images in a cardiac cycle.

This clearly discards any hope of proposing a data assimilation method that use velocity informations obtained by differentiating the observations with respect to the time variable but more importantly it addresses the issue of manipulating – in a data assimilation procedure – these highly coarse data. To circumvent this difficulty, it is common to use a time interpolation scheme to reconstruct a continuous distribution of the data. For instance – in the context of cardiac modelling – authors in [Moireau et al., 2009, Chabiniok et al., 2011, Bertoglio et al., 2012, Chabiniok et al., 2012, Moireau et al., 2013] provide some estimation results obtained using the filtering procedure described in this Chapter with a linear time interpolation of the discrepancy measure. In this work in collaboration with N. Cîndea and P. Moireau, we propose to study an observer built for vibrating systems – typically used for state estimation – and that assimilates observations only when they are available. We also propose to compare this strategy with the observer using an interpolation scheme – typically linear. The comparison is carried out both theoretically – since we provide convergence estimates in both cases – and numerically.The numerical assessment of these approaches is first performed from a spectral analysis in the particular example of the (1D) wave equation. This enables us to choose an optimal gain for the two observers and to infer an empirical law linking these gain values and the ratio between the sampling and the numerical time step. Secondly we compare the efficiency of the two observers in different cases by varying the initial noise in the system and the sampling period.

The conclusions are twofold. First we observe that the interpolation remains valid in the case of reasonable repartition (in time) of the data with potentially high levels of noise. This particularity comes from the presence, at each time step, of the stabilized operator. Secondly, in the case of poor data availability the on/off switch appears to be quite robust since no interpolation error – otherwise entering as a source term in the estimation error dynamical system – are introduced.

Data assimilation of time under-sampled measurements using observers, application to wave-like equations

N. Cîndea*, A. Imperiale†, P. Moireau†,
†Project-Team MΞDISIM, Inria Saclay-Île de France, France
* Laboratoire de Mathématiques, Université Blaise Pascal (Clermont-Ferrand 2)

Abstract

We propose a sequential data assimilation scheme using Luenberger type observers when only some measurements, that are partial in space and under-sampled in time, are available. More precisely, we consider a wave-like equation for which we assume known the restriction of the solution to an open non-empty subset of the spatial domain and for some time samples (typically the sampling step in time is much larger than the time discretization step). To assimilate the available data, two strategies are proposed and analyzed. The first strategy consists in assimilating data only if they are available and the second one in assimilating interpolation of the available data at all the discretization times. In order to tackle the spurious high frequencies which appear when we discretize the wave equation, for both strategies, we introduce a numerical viscous term and. In this case, we prove some error estimates between the exact solution and our observers. Numerical simulations illustrate the theoretical results in the case of the one dimensional wave equation.

AMSC : 35L05; 35L20; 65D05; 65M12; 93B07; 93B70; 93D15.
Keywords : Data assimilation; time under-sampled measurements; Luenberger observers; numerical analysis; interpolation.

Contents

1 Introduction

The discipline of data assimilation historically appeared in the context of meteorology and oceanography – see for example the recent surveys [Blum et al., 2008, Corpetti et al., 2009] – but has also reached new fields of research for instance in life sciences [Chapelle et al., 2013]. The two main ingredients in a data assimilation formulation are the model and the data. On the one hand, the model regroups physical information on the system under consideration encapsulated in a mathematical dynamical system – mostly based on (nonlinear) evolution partial differential equations in the data assimilation community – and allows after discretization to simulate various configurations of interest. However, the model contains a various range of potential errors, for example: on the operator driving the dynamical system, on the boundary conditions or on the initial conditions. On the other hand, the data bring complementary and valuable information on the studied system but they are often partial – in space and time – and are likely to be corrupted by the noise inherent to any measurement process. Data assimilation aims at providing a reconstruction of the (observed) real trajectory by coupling the information contained in the model and in the data, hence filtering their respective uncertainties.

To reach this goal several strategies have been considered which are traditionally classified into two main families. The two approaches can be considered in a stochastic or deterministic formalism but we will focus here on the deterministic one. The first family of methods is called the variational approach [Papadakis and Mémin, 2008, Navon, 2008] which, in essence, seeks to minimize a functional that balances the various uncertainties present in the model and the data. The second one – of interest in our work – is the family of sequential methods where the discrepancy between the simulated system and the data at hand is filtered in time in order to adjust to the pursued trajectory. More precisely, a sequential data assimilation procedure provides an observer $\widehat{x}$ of the exact trajectory $x_\bullet$ – more often referred to as an estimator in the stochastic context. The evolution satisfied by this observer is written in a general form of a dynamical system with a feedback law based on the discrepancy between the model and the data. The most popular observer is the Kalman filter formulated by equivalence with an optimal criterion minimization [Bensoussan, 1971, Simon, 2006], hence applicable to any model. However it ultimately leads to operators which are after discretization numerically intractable. As an alternative for this "curse of dimensionality" – in the context of the wave-like systems considered in the present article – several works [Ramdani et al., 2012, Moireau et al., 2009, Li and Xu, 2011, Bertoglio et al., 2013] have proposed simplified but effective feedback laws directly based on the physical properties of the system at hand. This strategy was originally introduced by Luenberger [Luenberger, 1971] in a general context and is also denominated *nudging* in the data assimilation community [Hoke and Anthes, 1976, Auroux and Blum, 2007]. In essence, this procedure only seeks to stabilize the dynamical system satisfied by the estimation error $\widetilde{x} = x_\bullet - \widehat{x}$ without relying on any optimality condition.

In general, these observers are defined in an abstract time continuous framework assuming that the model and the data are available at any time. This clearly represents the asymptotic of any real configuration where in general the data are time-sampled. Eventually the model should be considered with its time-discretization which has no reason to be dependent of the time-sampling of the data. Therefore, we must analyze the impact of the data discretization in the observer definition. In particular, we are concerned by coarse data in time with respect to the model discretization. As an illustration, we can cite the case of image sequences assimilation for cardiovascular systems – described *e.g.* in [Chabiniok et al., 2011, Imperiale et al., 2011, Moireau et al., 2013] – where the time-sampling of the data is of one or two orders of magnitude larger than the model time-step discretization. Facing this situation, there exist two alternatives. The first one – considered for example in [Moireau et al., 2009] – consists in interpolating the data in time in order to regenerate a time-continuous sequence which can then be compatible with any time discretization of the model. This approach is very attractive from an abstract standpoint but at the price of an additional time-interpolation error perturbing the observer dynamics as any other measurement noise. Moreover, this perturbation has the consistency of the data sampling period. A second approach – often used in practice without even mentioning it – is to compute the discrepancy only when the data are available. This intermittent correction is potentially error free but may induce correction shocks which limit the stabilization of the error between the observer trajectory and the pursued trajectory.

In this paper, we address the issue of analyzing a data assimilation procedure where an intermittent feedback law is defined and compared to a procedure where a time interpolation of the data is considered. The comparison is carried out both theoretically – since convergence estimates are provided in both cases – and numerically – using a simple one-dimensional wave equation model. Indeed, we restrict our analysis to the specific case of a wave-like system and the Luenberger associated observer proposed in [Moireau et al., 2009]. However, this work is intended to illustrate how the data time-sampling influences the definition of any data assimilation sequential strategy.

The outline of the paper is as follows. In Section 2 we introduce the observer methodology in the case of wave-like systems and we propose two types of time discretization presented in a general form. In Section 3 we provide convergence estimates of both observers. Section 4 and Section 5 are then devoted to numerical illustrations where (1) we analyse the spectra of the stabilized operators appearing in the dynamical systems satisfied by the estimation error in order to provide an optimal gain for both observers and (2) we provide time simulations which illustrate the robustness of the on/off switch strategy with respect to the strategy where the data are (poorly) interpolated.

2 Time discrete observer design

2.1 Nudging for wave-like systems

We consider in this work a general class of second order hyperbolic systems in bounded domain characteristic of wave equations or elasticity systems. These models typically correspond to simplified situations of those encountered in the cardiac modeling context where a heart mechanical model is registered on coarse data obtained from a sequence of few medical images [Sainte-Marie et al., 2006, Moireau et al., 2009]. Formally we introduce a Hilbert space $\mathcal{H}$ endowed with the inner product $(\cdot,\cdot)$ and we denote by $\|\cdot\|$ the associated norm. Then, we define a self adjoint operator $A_0 : \mathcal{D}(A_0) \to \mathcal{H}$, positive-definite with compact resolvent and we consider the general class of systems

$$\begin{cases} \ddot{w}(t) + A_0 w(t) = 0, \\ \\ w(0) = w_0 + \zeta_0, \quad \dot{w}(0) = w_1 + \zeta_1, \end{cases} \tag{1}$$

where $\dot{x}$ denotes the time derivative of any variable x, (ζ_0, ζ_1) represent some potential errors on the initial conditions and (w_0, w_1) are some known *a priori*. We point out that (1) represents a conservative system and, therefore, any errors on the initial conditions are conserved in time. Denoting by

$$x(t) = \begin{pmatrix} w(t) \\ \dot{w}(t) \end{pmatrix} \in \mathcal{X} = \mathcal{D}(A_0^{\frac{1}{2}}) \times \mathcal{H},$$

we can rewrite (1) as a first-order system

$$\begin{cases} \dot{x}(t) = Ax(t), & t > 0 \\ x(0) = x_0 + \zeta, \end{cases} \tag{2}$$

where $x_0 = \begin{pmatrix} w_0 & w_1 \end{pmatrix}^\intercal$, $\zeta = \begin{pmatrix} \zeta_0 & \zeta_1 \end{pmatrix}^\intercal$ and $A : \mathcal{D}(A) \to \mathcal{X}$ is defined by

$$\mathcal{D}(A) = \mathcal{D}(A_0) \times \mathcal{D}(A_0^{\frac{1}{2}}), \qquad A = \begin{pmatrix} 0 & \mathbb{1} \\ -A_0 & 0 \end{pmatrix}.$$

On this system we consider a particular target system $x_\bullet$ associated with a specific unknown $\zeta_\bullet$. Moreover, we assume that measurements z – also called observations – are available and defined by

$$z(t) = Hx_\bullet(t), \qquad t > 0, \tag{3}$$

where $H \in \mathcal{L}(\mathcal{X}, \mathcal{Z})$ is the so-called *observation operator* and $\mathcal{Z}$ is the Hilbert space associated with the observations endowed with its norm $\| \cdot \|_{\mathcal{Z}}$. For the sake of simplicity we restrict ourselves to bounded observation operators but a more general class of admissible observation operators can also be considered [Tucsnak and Weiss, 2009]. The observation operator can be applied to any solution of (2) and we assume that the pair (A, H) is exactly observable in a time T_{obs}, *i.e.* there exists a constant $C_{\text{obs}} > 0$ such that every solution of (2) satisfies

$$\int_0^{T_{\text{obs}}} \|Hx(t)\|_{\mathcal{Z}}^2 \, \mathrm{d}t \geq C_{\text{obs}} \|x(0)\|_{\mathcal{X}}^2, \qquad x(0) \in \mathcal{X}. \tag{4}$$

In order to benefit from the available data $z(t)$ and considering only the available *a priori* x_0 that we have on the initial condition, we consider the Luenberger observer $\widehat{x}(t)$ [Chapelle et al., 2012a] – see also similar formulations in [Ervedoza and Zuazua, 2009, Ramdani et al., 2012] – estimating $x_\bullet(t)$ from the dynamics

$$\begin{cases} \dot{\widehat{x}}(t) = A\widehat{x}(t) + \gamma H^* \left(z(t) - H\widehat{x}(t) \right), & t > 0 \\ \widehat{x}(0) = x_0, \end{cases} \tag{5}$$

where $H^* \in \mathcal{L}(\mathcal{Z}, \mathcal{X})$ is the adjoint of the observation operator and $\gamma > 0$ is a gain parameter. We justify the use of this observer by noticing that the estimation error $\widetilde{x}(t) = x_\bullet(t) - \widehat{x}(t)$ satisfies the – damped – dynamics

$$\begin{cases} \dot{\widetilde{x}}(t) = \big(A - \gamma H^* H \big) \widetilde{x}(t), & t > 0 \\ \widetilde{x}(0) = \zeta_\bullet. \end{cases} \tag{6}$$

Provided that H satisfies (4) it is well known – see *e.g.* [Liu, 1997] – that the error is exponentially stable, namely there exist two constants $M > 0$ and $\mu > 0$ such that

$$\|\widetilde{x}(t)\|_{\mathcal{X}} \leq M \exp(-\mu t) \|\widetilde{x}(0)\|_{\mathcal{X}}, \qquad t > 0. \tag{7}$$

Remark 1
In the filtering strategy described by (5) *we see that the initial dynamics* (2) *is modified by a feedback law where the so-called gain operator is, here, simply given by* $G = \gamma H^*$. *In comparison,*

in the context of Kalman filtering [Bensoussan, 1971, Simon, 2006], the gain is given by $G = P(t)H^*$*, where* $P \in \mathcal{L}(\mathcal{X},\mathcal{X})$ *satisfies the Riccati equation*

$$\dot{P} = AP + PA^* + PH^*HP, \quad P(0) = P_0,$$

in the mild sense.

Remark 2
We may distinguish in the wave-like equation context two classes of observation operators. The one corresponding to velocity observations, namely $H = \begin{pmatrix} 0 & H_0 \end{pmatrix}$*, and the one corresponding to the direct observation of the field, i.e.* $H = \begin{pmatrix} H_0 & 0 \end{pmatrix}$*. It should be noted that in the context of poor time resolution of the data the two cases are indeed two independent situations since the data cannot be differentiated with respect to time without dramatically amplifying the measurement noise. We point out that the exponential convergence of these two classes of observers have been demonstrated. The first one is standard see [Haraux and Zuazua, 1988, Cox and Zuazua, 1994, Moireau et al., 2007]. The second one is less classical since the adjoint* H^* *induces a modification of the identity between the time-derivation of the field and the velocity. This observer can therefore only be considered as a virtual system and has been demonstrated to converge in [Chapelle et al., 2012a, Chapelle et al., 2012b]. Ultimately the exponential convergence of both observer systems requires the geometric control conditions to be satisfied – see [Bardos et al., 1992] for the wave equation and [Daoulatli et al., 2010] for the elasticity system.*

2.2 Time discrete observer

In the first section, we have introduced an abstract observer which assumes that the data at hand are available at any time. However in practice, they are time-sampled and we want to study the influence of their discretization in the definition of the observer. In this respect, we decide to directly introduce the time-discretization avoiding the technicalities induced by potential Dirac distributions associated with the data time-sampling. However, we should consider an observer time-discretization which conserves at the time-discrete level – and uniformly with respect to the time-discretization – the stability properties of the estimation error. Unfortunately, when discretizing in time systems such as (6) spurious high-frequency modes may arise provoking the loss of the uniform decay rate of the error – see *e.g.* [Zhang et al., 2007, Zuazua, 2005, Ervedoza and Zuazua, 2009]. These modes cannot be captured by the localized observation operator, thus leading to a loss of uniform observability. In other words, a direct discretization of the observer (5) for example using conservative mid-point rules

$$\frac{\widehat{x}^{n+1} - \widehat{x}^n}{\Delta \mathrm{t}} = A\frac{\widehat{x}^{n+1} + \widehat{x}^n}{2} + \gamma H^*\Big(\frac{z^{n+1} + z^n}{2} - H\frac{\widehat{x}^{n+1} + \widehat{x}^n}{2}\Big) \tag{8}$$

may not satisfy at the discrete-level a time-discrete counterpart of the observation inequality (4) of the form

$$\sum_{n=0}^{N_{\mathrm{obs}}} \|Hx(n\Delta \mathrm{t})\|_{\mathcal{Z}}^2 \geq C_{\mathrm{obs}}\left(\|w_0\|^2_{\mathcal{D}(A_0^{\frac{1}{2}})} + \|w_1\|^2\right). \tag{9}$$

Note that in (8) we still avoid to consider the time sampling of the data and denote by

$$z^n = Hx_{\bullet}(n\Delta \mathrm{t}), \tag{10}$$

a discrete (in time) observation potentially available at any model time-step.

Remark 3
We should point out that the observation inequality (9) *can be expected to be obtained from its continuous counterpart* (4) *only with a time discretization small enough so that there is several time steps included in the characteristic time associated with the smallest frequency of the system. Otherwise, we could imagine a degenerate situation where the measurements are considered at the exact same frequency than a system mode making it unobservable. This condition on the data sampling will be assumed to be satisfied in the rest of the article.*

To circumvent this difficulty, authors in [Ervedoza and Zuazua, 2009] propose two main options. The first possibility is to impose a (restrictive) CFL condition that discards these undesired high frequency modes. The second option consists in adding an artificial viscous term consistent with the order of the numerical scheme and responsible for the dissipation of the spurious modes. Among various possibilities detailed in [Ervedoza and Zuazua, 2009], we retain for instance the discretization

$$\begin{cases} \dfrac{\widehat{x}_-^{n+1} - \widehat{x}_+^n}{\Delta \mathrm{t}} = A \dfrac{\widehat{x}_-^{n+1} + \widehat{x}_+^n}{2}, \qquad n > 0 \\[2ex] \dfrac{\widehat{x}_+^{n+1} - \widehat{x}_-^{n+1}}{\Delta \mathrm{t}} = \gamma_{n+1} H^* \Big(z^{n+1} - H \widehat{x}_+^{n+1} \Big) + \nu_{\Delta \mathrm{t}} A^2 \widehat{x}_+^{n+1}, \qquad n > 0 \\[2ex] \widehat{x}_+^0 = \begin{pmatrix} w_0 \\ w_1 \end{pmatrix}, \end{cases} \tag{11}$$

where some numerical viscosity is introduced with the specific viscous operator (suggested by [Ervedoza and Zuazua, 2009])

$$A^2 = \begin{pmatrix} -A_0 & 0 \\ 0 & -A_0 \end{pmatrix}, \tag{12}$$

and $\nu_{\Delta \mathrm{t}}$ controls the amount of this numerical viscosity. In order to respect the order of consistency of this time scheme – and as advised in [Ervedoza and Zuazua, 2009] – we ought to set $\nu_{\Delta \mathrm{t}} = O(\Delta \mathrm{t}^2)$. This time discretization can be understood as a prediction-correction scheme where the dynamics of the model leading to $\widehat{x}_-^n$ is then corrected by computing a model-data interaction to produce $\widehat{x}_+^n$.

Once the time discretization of the observer is chosen, we can go back to our considerations on the data time-sampling. We define $(j_r)_{r \in \mathbb{N}} \subset \mathbb{N}$ as a strictly increasing sequence of natural numbers so that the available measurements are

$$z^r = z(j_r \Delta \mathrm{t}), \qquad r \in \mathbb{N}. \tag{13}$$

We then consider two strategies to introduce these time-sampled data in (11). The first one is to consider the data only when they are available, hence in essence $\gamma_n = 0$ when the data z^n is not available. The second one consists in interpolating the data to generate an approximated

z^n for all n. We summarize these two strategies by

$$\begin{cases} \dfrac{\widehat{x}_-^{n+1} - \widehat{x}_+^n}{\Delta \mathrm{t}} = A \dfrac{\widehat{x}_-^{n+1} + \widehat{x}_+^n}{2}, & n > 0 \\[2ex] \dfrac{\widehat{x}_+^{n+1} - \widehat{x}_-^{n+1}}{\Delta \mathrm{t}} = \delta^{n+1} \gamma H^* \left(d^{n+1} - H \widehat{x}_+^{n+1} \right) + \nu_{\Delta \mathrm{t}} A^2 \widehat{x}_+^{n+1}, & n > 0 \\[2ex] \widehat{x}_+^0 = \begin{pmatrix} w_0 \\ w_1 \end{pmatrix} = \widehat{x}_0, \end{cases} \tag{14}$$

where $(\delta^n)_{n \in \mathbb{N}}$ and $(d^n)_{n \in \mathbb{N}}$ will be referred to as the switching coefficients and the interpolated data respectively. For the first idea – named *on/off switch* and where the correction term only appears when measurements are available – we have

$$\delta^n = \begin{cases} 1 \\ 0 \end{cases} \qquad d^n = \begin{cases} z^r & \text{if } \exists r \in \mathbb{N} \ : \ n = j_r \\ 0 & \text{otherwise.} \end{cases} \tag{15}$$

The second choice where we interpolate in time the data reads, in the particular case of linear interpolation,

$$\delta^n = 1 \qquad \forall n, \qquad d^n = \frac{n - j_r}{j_{r+1} - j_r} z^{r+1} + \left(1 - \frac{n - j_r}{j_{r+1} - j_r} \right) z^r \qquad j_r \leq n \leq j_{r+1}. \tag{16}$$

Then in the next sections, we propose to study the convergence of the time-discrete observer given by (14)-(15) – see Theorem 1 – and given by (14)-(16) – see Theorem 2.

Remark 4
There is also an exact counterpart at the time-discrete level of the popular Kalman observer mentioned in Remark 1. The resulting time-discrete observer for the system (2)-(3) *– called Kalman-Bucy estimator [Kalman and Bucy, 1961] – is also based on a prediction-correction paradigm reading*

$$\text{(Prediction)} \quad \begin{cases} \widehat{x}_-^{n+1} = A_{n+1|n} \widehat{x}_+^n, \\ P_-^{n+1} = A_{n+1|n} P_+^n A_{n+1|n}^*, \end{cases} \tag{17}$$

$$\text{(Correction)} \quad \begin{cases} \widehat{x}_+^{n+1} = \widehat{x}_-^{n+1} + \Delta \mathrm{t} P_+^{n+1} H^* \big(z^{n+1} - H \widehat{x}_-^{n+1} \big), \\ P_+^{n+1} = ((P_-^{n+1})^{-1} + H^* H)^{-1}, \end{cases} \tag{18}$$

where we denoted by $A_{n+1|n}$ *the state transition operator corresponding to a stable and consistent discretization of the dynamical system* (2) *for instance in the case of a mid-point discretization*

$$A_{n+1|n} = \big(\mathbb{1} - \frac{\Delta \mathrm{t}}{2} A \big)^{-1} \big(\mathbb{1} + \frac{\Delta \mathrm{t}}{2} A \big).$$

One can prove – see e.g. [Nichols, 2010] – that the time-discrete observer derives from seeking the minimum value of the functional

$$J(\widetilde{x}_0) = \frac{1}{2} \| \widetilde{x}_0 \|^2_{P_0^{-1}} + \frac{1}{2} \sum_{k=1}^{n} \| z^k - H x^k \|^2_{M_z} \Delta \mathrm{t}, \tag{19}$$

with x^k *subject to* $x^k = A_{k|k-1} x^{k-1}$ *and* $x^0 = x_0 + \widetilde{x}_0$. *Hence, an on/off version of the Kalman-Bucy observer corresponds to the minimum of the adequately adjusted functional*

$$J(\widetilde{x}_0) = \frac{1}{2} \| \widetilde{x}_0 \|^2_{P_0^{-1}} + \frac{1}{2} \sum_{r=1}^{c_n} \| z^r - H x^{j_r} \|^2_{M_z} (j_{r+1} - j_r) \Delta \mathrm{t}, \tag{20}$$

with

$$c_n = card\{j,\ 1 \leq j \leq n,\ \delta_j = 1\}. \tag{21}$$

We expect that the proof that we will present for the nudging observer can be directly adapted to the Kalman approach, hence justifying in the general context of sequential data assimilation methods the choice of intermittently filtering the under-sampled data or continuously filtering a reconstructed data by interpolation.

3 Convergence estimate for the estimation error

3.1 Convergence estimate for the on/off switch

Let us define the corrected estimation error by

$$\widetilde{x}_+^n = x_\bullet(n\Delta \mathrm{t}) - \widehat{x}_+^n, \tag{22}$$

and the corresponding predicted estimation error by

$$\widetilde{x}_-^n = x_\bullet(n\Delta \mathrm{t}) - \widehat{x}_-^n, \tag{23}$$

where $x_\bullet$ is the exact solution of (2) and $\widehat{x}_+^n$ and $\widehat{x}_-^n$ satisfy (14)-(15). We start by giving the dynamical system satisfied by this estimation error in the following proposition.

Proposition 1. *Assuming that* $x_0 \in \mathcal{D}(A_0^2) \times \mathcal{D}(A_0^{\frac{3}{2}})$, *the estimation errors defined by* (22) *and* (23) *satisfy the following discrete dynamical system*

$$\begin{cases} \dfrac{\widetilde{x}_-^{n+1} - \widetilde{x}_+^n}{\Delta \mathrm{t}} = A\dfrac{\widetilde{x}_-^{n+1} + \widetilde{x}_+^n}{2} + \varepsilon^{n+1}, \\[2ex] \dfrac{\widetilde{x}_+^{n+1} - \widetilde{x}_-^{n+1}}{\Delta \mathrm{t}} = -\delta^{n+1}\gamma H^* H \widetilde{x}_+^{n+1} + \nu_{\Delta \mathrm{t}} A^2 \widetilde{x}_+^{n+1} + \varepsilon_\nu^{n+1}, \\[2ex] \widetilde{x}_+^0 = x_0 - \widehat{x}_0, \end{cases} \tag{24}$$

where the consistency terms are

$$\left| \begin{aligned} \varepsilon^{n+1} &= \frac{\Delta \mathrm{t}^2}{2} A^3\Big(\frac{1}{3}x_\bullet(\mathrm{t}_n) - \frac{1}{2}x_\bullet(\mathrm{r}_n)\Big), \qquad \textit{with } \mathrm{t}_n, \mathrm{r}_n \in [n\Delta \mathrm{t}; (n+1)\Delta \mathrm{t}], \\ \varepsilon_\nu^{n+1} &= -\nu_{\Delta \mathrm{t}} A^2 x_\bullet((n+1)\Delta \mathrm{t}). \end{aligned} \right. \tag{25}$$

Proof. Starting from the definition of the predicted estimation error and from the correction phase of the observer (14) we obtain

$$\begin{aligned} \widetilde{x}_-^{n+1} &= x_\bullet((n+1)\Delta \mathrm{t}) - \widehat{x}_+^{n+1} + \delta^{n+1}\Delta \mathrm{t}\gamma H^*(d^{n+1} - H\widehat{x}_+^{n+1}) + \nu_{\Delta \mathrm{t}}\Delta \mathrm{t} A^2 \widehat{x}_+^{n+1} \\ &= (\mathbb{1} + \delta^{n+1}\Delta \mathrm{t}\gamma H^* H)\widetilde{x}_+^{n+1} + \nu_{\Delta \mathrm{t}}\Delta t A^2 \widehat{x}_+^{n+1} \\ &= (\mathbb{1} + \delta^{n+1}\Delta \mathrm{t}\gamma H^* H - \nu_{\Delta \mathrm{t}}\Delta \mathrm{t} A^2)\widetilde{x}_+^{n+1} - \Delta \mathrm{t}\varepsilon_\nu^{n+1}, \end{aligned}$$

which is exactly the second equation in (24). Secondly, to obtain the remaining equation it suffices to notice that

$$\frac{\widetilde{x}_-^{n+1} - \widetilde{x}_+^n}{\Delta \mathrm{t}} = \frac{x_\bullet((n+1)\Delta \mathrm{t}) - x_\bullet(n\Delta \mathrm{t})}{\Delta \mathrm{t}} - \frac{\widehat{x}_-^{n+1} - \widehat{x}_+^n}{\Delta \mathrm{t}}.$$

Hence, using a first-order finite difference approximation of $\dot{x}_\bullet((n+1)\Delta\mathrm{t})$, from the above equality – assuming enough regularity on the initial condition – we can assure that there exist a time t_n and a time $\mathrm{r}_n \in [n\Delta\mathrm{t}; (n+1)\Delta\mathrm{t}]$ such that

$$\frac{\widetilde{x}_-^{n+1} - \widetilde{x}_+^n}{\Delta\mathrm{t}} = \frac{\dot{x}_\bullet((n+1)\Delta\mathrm{t}) + \dot{x}_\bullet(n\Delta\mathrm{t})}{2} - \frac{\widehat{x}_-^{n+1} - \widehat{x}_+^n}{\Delta\mathrm{t}} + \frac{\Delta\mathrm{t}^2}{2}\big(\frac{1}{3}\dddot{x}_\bullet(\mathrm{t}_n) - \frac{1}{2}\dddot{x}(\mathrm{r}_n)\big).$$

Therefore, from (2) and the first equation of (14) we conclude the proof. ■

From this first result we can now give the convergence estimate for the on/off observer.

Theorem 1
Let A be a skew-adjoint operator with compact resolvent and $H \in \mathcal{L}(\mathcal{X}, \mathcal{Z})$ be a bounded linear observation operator such that the observability inequality (4) *holds. Assume that there exists $\rho \in (0,1]$ such that c_n defined by* (21) *satisfies*

$$c_n \geq \rho n, \qquad n > 0. \tag{26}$$

Then, for every $x_0 \in \mathcal{D}(A_0^2) \times \mathcal{D}(A_0^{\frac{3}{2}})$ there exist positive constants M_0, μ_0, C_1 and C_2, independent of $\Delta\mathrm{t} \in (0,1)$ and n, such that $\widetilde{x}_+^n$ solution of (24) *satisfies*

$$\|\widetilde{x}_+^n\|_{\mathcal{X}} \leq M_0 \exp(-\mu_0 c_n \Delta\mathrm{t}) \|\widetilde{x}_0\|_{\mathcal{X}} + \frac{\Delta\mathrm{t}}{1 - \exp(-\mu_0 \rho \Delta t)} \big(\Delta\mathrm{t}^2 C_1 + \nu_{\Delta\mathrm{t}} C_2\big). \tag{27}$$

Proof. From the system (24) we can explicitly compute $\widetilde{x}_+^{n+1}$ function of $\widetilde{x}_+^n$, ε^{n+1} and ε_ν^{n+1} by the following relation

$$\widetilde{x}_+^{n+1} = \mathcal{P}_{n+1}\mathcal{Q}\, \widetilde{x}_+^n + \Delta\mathrm{t}\big(\mathcal{P}_{n+1}\varepsilon^{n+1} + \mathcal{R}_{n+1}\varepsilon_\nu^{n+1}\big), \tag{28}$$

where $\mathcal{P}_n,\ \mathcal{Q},\ \mathcal{R}_n \in \mathcal{L}(\mathcal{X})$ are given by

$$\left|\begin{array}{l} \mathcal{P}_n = \big(\mathbb{1} + \delta^n \gamma \Delta\mathrm{t} H^* H - \Delta\mathrm{t}\nu_{\Delta\mathrm{t}} A^2\big)^{-1} \left(\mathbb{1} - \dfrac{\Delta\mathrm{t}}{2} A\right)^{-1}, \\ \mathcal{Q} = \mathbb{1} + \dfrac{\Delta\mathrm{t}}{2} A, \\ \mathcal{R}_n = \big(\mathbb{1} + \delta^n \gamma \Delta\mathrm{t} H^* H - \Delta\mathrm{t}\nu_{\Delta\mathrm{t}} A^2\big)^{-1}. \end{array}\right.$$

Note that since both semigroups generated by operators $(\Delta\mathrm{t}\nu_{\Delta\mathrm{t}} A^2 - \gamma\Delta\mathrm{t} H^* H)$ and A respectively are semigroups of contraction we have that $\mathcal{P}_n$ and $\mathcal{R}_n$ are well defined and $\|\mathcal{P}_n\|_{\mathcal{L}(\mathcal{X})} < 1$ and $\|\mathcal{R}_n\|_{\mathcal{L}(\mathcal{X})} < 1$ (see, for instance [Tucsnak and Weiss, 2009]). Hence, using this notation we can write (24) as follows

$$\widetilde{x}_+^n = \left(\prod_{j=1}^{n} \mathcal{P}_j \mathcal{Q}\right) \widetilde{x}_+^0 + \Delta\mathrm{t} \sum_{i=0}^{n-1} \left(\prod_{j=1}^{i} \mathcal{P}_j \mathcal{Q}\right) \big(\mathcal{P}_{n-i}\varepsilon^{n-i} + \mathcal{R}_{n-i}\varepsilon_\nu^{n-i}\big). \tag{29}$$

Remark that if $\delta^n = 0$ then $\mathcal{P}_n\mathcal{Q}$ is the operator driving the system

$$\left\{\begin{array}{l} \dfrac{\widetilde{x}_-^{n+1} - \widetilde{x}_+^n}{\Delta\mathrm{t}} = A\dfrac{\widetilde{x}_-^{n+1} + \widetilde{x}_+^n}{2}, \\[2ex] \dfrac{\widetilde{x}_+^{n+1} - \widetilde{x}_-^{n+1}}{\Delta\mathrm{t}} = \nu_{\Delta\mathrm{t}} A^2 \widetilde{x}_+^{n+1}, \\[2ex] \widetilde{x}_+^0 = x_0 - \widehat{x}_0, \end{array}\right. \tag{30}$$

which is a dissipative scheme, thus $\|\mathcal{P}_n\mathcal{Q}\|_{\mathcal{L}(\mathcal{X})} \leq 1$. On the other hand, if $\delta^n = 1$ then $\mathcal{P}_n\mathcal{Q}$ is the operator driving the homogeneous error system (24) which is exponentially stable as long as the observability inequality (4) is satisfied [Ervedoza and Zuazua, 2009]. Hence, there exist two positive constants M_0 and μ_0 such that

$$\left\|\prod_{j=1}^{n}(\mathcal{P}_j\mathcal{Q})\right\|_{\mathcal{L}(\mathcal{X})} \leq M_0 \exp(-\mu_0 c_n \Delta\mathrm{t}), \qquad n \in \mathbb{N}. \tag{31}$$

Combining (29), (31) and the fact that $\|\mathcal{P}_n\|_{\mathcal{L}(\mathcal{X})} < 1$ and $\|\mathcal{R}_n\|_{\mathcal{L}(\mathcal{X})} < 1$ we obtain the following estimate

$$\begin{aligned}\|\widetilde{x}_+^n\|_{\mathcal{X}} &\leq M_0 \exp(-\mu_0 c_n \Delta\mathrm{t})\|\widetilde{x}_+^0\|_{\mathcal{X}} + \Delta\mathrm{t}\sum_{i=0}^{n-1}\exp(-\mu_0 c_i \Delta\mathrm{t})\big(\|\varepsilon^{n-i}\|_{\mathcal{X}} + \|\varepsilon_\nu^{n-i}\|_{\mathcal{X}}\big)\\ &\leq M_0 \exp(-\mu_0 c_n \Delta\mathrm{t})\|\widetilde{x}_+^0\|_{\mathcal{X}} + \frac{\Delta\mathrm{t}}{1-\exp(-\mu_0\rho\Delta\mathrm{t})}\max_{1\leq i\leq n}\big(\|\varepsilon^i\|_{\mathcal{X}} + \|\varepsilon_\nu^i\|_{\mathcal{X}}\big).\end{aligned}$$

Finally, from (25) combined with the conservation of the energy associated with (2), we obtain the final estimate (27) of Theorem 1 with

$$C_1 = \frac{5}{12}\|A^3 x_0\|_{\mathcal{X}} \quad \text{and} \quad C_2 = \|A^2 x_0\|_{\mathcal{X}}. \tag{32}$$

■

The estimate (27) gives the convergence (in the energy norm) of the time semi-discrete observer (14) to the solution of the continuous system (2) when $n \to \infty$ and $\Delta\mathrm{t} \to 0$. Moreover, this estimate provides an explicit dependence between the error and the ratio ρ associated with the sampling frequency. For instance, if the data time-sampling is a constant equal to $\Delta\mathrm{T}$ we have

$$\rho \sim \frac{\Delta\mathrm{t}}{\Delta\mathrm{T}}.$$

Therefore if $\Delta\mathrm{T}$ is large with respect to $\Delta\mathrm{t}$, then ρ is close to zero. Then, in the first term of the estimate (27) right-hand side c_n tends to 0 and the second term is $O(\Delta\mathrm{T}(\Delta\mathrm{t}^2 + \nu_{\Delta\mathrm{t}}))$. Therefore the overall asymptotic estimate reads

$$\|\widetilde{x}_+^n\|_{\mathcal{X}} = O\big(M_0 + \Delta\mathrm{T}(\Delta\mathrm{t} + \frac{\nu_{\Delta\mathrm{t}}}{\Delta t})\big).$$

From this asymptotic estimate, we see in the estimate (27) that the numerical viscosity coefficient appears as a consistency term, which is consistent with the fact that this artificial term is in fact a perturbation of the standard and consistent discretization of (2). For this reason we clearly understand why the viscosity coefficient should be kept $\nu_{\Delta\mathrm{t}} = O(\Delta\mathrm{t}^2)$. Furthermore, the term M_0 indicates that the initial condition error can not be stabilized. Moreover even if $M_0 = 0$ we see that the data time-sampling ΔT controlled the error estimate. If ΔT is typically of the same order of magnitude as T, we retrieve the standard numerical error estimate which deteriorates with the simulation time.

Remark 5

Note that when $\rho = 1$ we retrieve the estimate in [Chapelle et al., 2012b] which first exhibit the gain offered by data assimilation strategies in numerical analysis estimates. More precisely, in this particular case, authors in [Chapelle et al., 2012b] have shown that the numerical error *between the exact solution and the numerical solution is bounded and independent of the total simulation time. The input of data in the observer dynamics balances the accumulation of numerical errors. When $\rho \neq 1$, this remark is still valid but the time-sampling of the data also governed the estimation. We provide in Section 5 a numerical illustration of this phenomenon.*

Remark 6
Theorem 1 can be extended to obtain error estimates for a fully discrete observer, combining (14) *with Galerkin method. The idea is to adapt the proof of Theorem 1 using the method described in [Chapelle et al., 2012b].*

3.2 Convergence estimate using interpolated observations

Similarly to what we have proposed for the on/off strategy we analyze the time-discrete observer that assimilates interpolated data – *i.e.* System (14)-(16). For the sake of clarity we will use the same notation for the estimation error, namely

$$\widetilde{x}^n_+ = x_\bullet(n\Delta\mathrm{t}) - \widehat{x}^n_+ \tag{33}$$

for the corrected estimation error and

$$\widetilde{x}^n_- = x_\bullet(n\Delta\mathrm{t}) - \widehat{x}^n_- \tag{34}$$

for the predicted estimation error.

Proposition 2. *Assuming that* $x_0 \in \mathcal{D}(A_0^2) \times \mathcal{D}(A_0^{\frac{3}{2}})$ *then the estimation error defined by* (33) *and* (34) *satisfies the following discrete dynamical system*

$$\begin{cases} \dfrac{\widetilde{x}^{n+1}_- - \widetilde{x}^n_+}{\Delta\mathrm{t}} = A\dfrac{\widetilde{x}^{n+1}_- + \widetilde{x}^n_+}{2} + \varepsilon^{n+1}, \\[2ex] \dfrac{\widetilde{x}^{n+1}_+ - \widetilde{x}^{n+1}_-}{\Delta\mathrm{t}} = -\gamma H^* H \widetilde{x}^{n+1}_+ + \nu_{\Delta\mathrm{t}} A^2 \widetilde{x}^{n+1}_+ + \varepsilon^{n+1}_\nu + \gamma H^* \varepsilon^{n+1}_d, \\[2ex] \widetilde{x}^0_+ = x_0 - \widehat{x}_0, \end{cases} \tag{35}$$

where ε^{n+1} *and* ε^{n+1}_ν *are given by* (25) *and* ε_d *is the interpolation error, namely*

$$\varepsilon^{n+1}_d = H x_\bullet((n+1)\Delta\mathrm{t}) - d^{n+1}. \tag{36}$$

Proof. From the definition of the predicted estimation error and from the correction phase of the observer (14) we obtain

$$\begin{aligned} \widetilde{x}^{n+1}_- &= x_\bullet((n+1)\Delta\mathrm{t}) - \widehat{x}^{n+1}_+ + \Delta\mathrm{t}\gamma H^*(d^{n+1} - H\widehat{x}^{n+1}_+) + \nu_{\Delta\mathrm{t}}\Delta\mathrm{t}A^2\widehat{x}^{n+1}_+ \\ &= (\mathbb{1} + \Delta\mathrm{t}\gamma H^* H)\widetilde{x}^{n+1}_+ + \nu_{\Delta\mathrm{t}}\Delta\mathrm{t}A^2\widetilde{x}^{n+1}_+ + \Delta\mathrm{t}\gamma H^*(d^{n+1} - Hx_\bullet((n+1)\Delta\mathrm{t})) \\ &= (\mathbb{1} + \Delta\mathrm{t}\gamma H^* H - \nu_{\Delta\mathrm{t}}\Delta\mathrm{t}A^2)\widetilde{x}^{n+1}_+ - \Delta\mathrm{t}\varepsilon^{n+1}_\nu - \Delta\mathrm{t}\gamma H^*\varepsilon^{n+1}_d. \end{aligned}$$

What remains of the proof follows the demonstration of Proposition 1. ∎

We can now give the convergence estimate in the case of interpolated data and, as a first step, we do not make assumptions on the type of interpolation scheme.

Theorem 2
Making the same assumptions on A, H and x_0 than Theorem 1 and denoting by

$$|\varepsilon_d| = \max_{1 \leq i \leq n} \|\varepsilon_d^i\|_{\mathcal{Z}},$$

we can state that there exist positive constants M_0, μ_0, C_1, C_2 and C_3, independent of $\Delta\mathrm{t} \in (0,1)$ and n, such that,

$$\|\widetilde{x}_+^n\|_{\mathcal{X}} \leq M_0 \exp(-\mu_0 n \Delta\mathrm{t}) \|\widetilde{x}_0\|_{\mathcal{X}} + \frac{\Delta\mathrm{t}}{1 - \exp(-\mu_0 \Delta\mathrm{t})} \big(\Delta\mathrm{t}^2 C_1 + \nu_{\Delta\mathrm{t}} C_2 + \gamma C_3 |\varepsilon_d| \big). \tag{37}$$

Proof. From the discrete dynamical system (35) satisfied by the estimation error we can extract the explicit relation

$$\widetilde{x}_+^{n+1} = \mathcal{U}\mathcal{V}\mathcal{W}\widetilde{x}_+^n + \Delta\mathrm{t}\big(\mathcal{U}\mathcal{V}\varepsilon^{n+1} + \mathcal{U}\varepsilon_\nu^{n+1} + \gamma H^* \varepsilon_d^{n+1}\big), \tag{38}$$

where $\mathcal{U}$, $\mathcal{V}$, $\mathcal{W} \in \mathcal{L}(\mathcal{X})$ are given by

$$\left| \begin{aligned} &\mathcal{U} = \big(\mathbb{1} - \Delta\mathrm{t}\, \nu_{\Delta\mathrm{t}} A^2 + \gamma \Delta\mathrm{t} H^* H\big)^{-1}, \\ &\mathcal{V} = \left(\mathbb{1} - \frac{\Delta\mathrm{t}}{2} A\right)^{-1}, \\ &\mathcal{W} = \mathbb{1} + \frac{\Delta\mathrm{t}}{2} A. \end{aligned} \right.$$

Following the same arguments as for Theorem 1

$$\begin{aligned} \|\widetilde{x}_+^n\|_{\mathcal{X}} \leq{} & M_0 \exp(-\mu_0 n \Delta\mathrm{t}) \|\widetilde{x}_+^0\|_{\mathcal{X}} \\ & + \frac{\Delta\mathrm{t}}{1 - \exp(-\mu_0 \Delta\mathrm{t})} \left(\max_{1 \leq i \leq n} \|\varepsilon^i\|_{\mathcal{X}} + \max_{1 \leq i \leq n} \|\varepsilon_\nu^i\|_{\mathcal{X}} + \gamma \|H^*\|_{\mathcal{L}(\mathcal{Z},\mathcal{X})} \max_{1 \leq i \leq n} \|\varepsilon_d^i\|_{\mathcal{Z}} \right). \end{aligned} \tag{39}$$

Hence we obtain the desired results with C_1 and C_2 expressed in (32) and C_3 given by

$$C_3 = \|H^*\|_{\mathcal{L}(\mathcal{Z},\mathcal{X})}. \tag{40}$$

■

It is striking to remark that estimate (37) directly follows intuition since, as we could imagine, when only few data are available the interpolation error naturally increases hence the right-hand side of (37) grows larger. Moreover, the gain γ appears as a coefficient on this part of the upper-bound which clearly implies that the interpolation error enters in the observer dynamical system as some additive noise on the data. To finally illustrate this phenomenon we propose to give an *a priori* bound of the interpolation error in the case of linearly interpolated data.

Proposition 3. *If we associate the sampling time $(t_r)_{r \in \mathbb{N}} \subset \mathbb{N}$ to the sampling time steps $(j_r)_{r \in \mathbb{N}} \subset \mathbb{N}$, by $t_r = j_r \Delta\mathrm{t}$ and if we denote by*

$$\Delta\mathrm{T}_{max} = \max_{r \geq 0} \{t_{r+1} - t_r\},$$

then there exists a constant C_4 depending only on the observation operator H and the initial condition x_0 such that

$$|\varepsilon_d| \leq C_4 \, \Delta\mathrm{T}_{max}^2. \tag{41}$$

Proof. To simplify the presentation we first focus our attention on the interval $[t_0, t_1]$. To start with we remark that d^i in (16) can be written as

$$d^i = H\left(\frac{i\Delta t - t_0}{t_1 - t_0} x_\bullet(t_1) + \frac{t_1 - i\Delta t}{t_1 - t_0} x_\bullet(t_0)\right). \tag{42}$$

Furthermore, there exists $r_0 \in [t_0, i\Delta t]$ and $r_1 \in [i\Delta t, t_1]$ such that

$$\left|\begin{aligned} x_\bullet(t_0) &= x_\bullet(i\Delta t + t_0 - i\Delta t) = x_\bullet(i\Delta t) + (t_0 - i\Delta t)\dot{x}_\bullet(i\Delta t) + \frac{(t_0 - i\Delta t)^2}{2}\ddot{x}_\bullet(r_0), \\ x_\bullet(t_1) &= x_\bullet(i\Delta t + t_1 - i\Delta t) = x_\bullet(i\Delta t) + (t_1 - i\Delta t)\dot{x}_\bullet(i\Delta t) + \frac{(t_1 - i\Delta t)^2}{2}\ddot{x}_\bullet(r_1). \end{aligned}\right.$$

Therefore, replacing $x_\bullet(t_0)$ and $x_\bullet(t_1)$ in (42) we obtain

$$\begin{aligned} d^i =& H\Bigg(x_\bullet(i\Delta t) + \frac{(t_1 - i\Delta t)(t_0 - i\Delta t) + (i\Delta t - t_0)(t_1 - i\Delta t)}{t_1 - t_0}\dot{x}_\bullet(i\Delta t) \\ & \frac{(t_1 - i\Delta t)(t_0 - i\Delta t)^2}{2(t_1 - t_0)}\ddot{x}_\bullet(r_0) + \frac{(i\Delta t - t_0)(t_1 - i\Delta t)^2}{2(t_1 - t_0)}\ddot{x}_\bullet(r_1)\Bigg) \end{aligned}$$

hence

$$d^i - Hx_\bullet(i\Delta t) = H\left(\frac{(t_1 - i\Delta t)(t_0 - i\Delta t)^2}{2(t_1 - t_0)}\ddot{x}_\bullet(r_0) + \frac{(i\Delta t - t_0)(t_1 - i\Delta t)^2}{2(t_1 - t_0)}\ddot{x}_\bullet(r_1)\right).$$

Using now the conservation of the energy associated with (2) this leads to

$$\|\varepsilon_d^i\|_{\mathcal{Z}} \leq \|H\|_{\mathcal{L}(\mathcal{X},\mathcal{Z})} \frac{(i\Delta t - t_0)^2(t_1 - i\Delta t) + (i\Delta t - t_0)(t_1 - i\Delta t)^2}{2(t_1 - t_0)} \|A^2 x_0\|_{\mathcal{X}}$$

and therefore

$$\|\varepsilon_d^i\|_{\mathcal{Z}} \leq \|H\|_{\mathcal{L}(\mathcal{X},\mathcal{Z})} \frac{(t_1 - t_0)^2}{8} \|A^2 x_0\|_{\mathcal{X}}. \tag{43}$$

We conclude the demonstration by giving the expression of the constant, namely

$$C_4 = \frac{1}{8}\|H\|_{\mathcal{L}(\mathcal{X},\mathcal{Z})}\|A^2 x_0\|_{\mathcal{X}}.$$

■

In the light of Theorem 1 and Theorem 2 we understand that the choice of the strategy, namely either interpolated or on/off, relies on a compromise between stability and consistency. On the one hand, the observer with intermittent correction phases bear an exact consistency with respect to the data, however corrections shocks may occur thus leading to potential instabilities. On the other hand, the observer fed with interpolated data admits a correction phase at each model time-step – hence its greater stability – but artificially induces noise in the observer dynamical system due to data interpolation error.

4 Numerical illustrations

We proceed in this section with the illustration of our theoretical results on a simple 1D wave model. Our objective is to show how the two strategies can offer two different alternatives depending on the data sampling. Namely, the on/off time discretization is a consistent formulation with respect to the data sampling whereas the interpolated strategy ensures a stability at every time-step. We will proceed with two classes of numerical results. First we will present a spectrum analysis to numerically demonstrate the stability properties of the proposed feedback laws. This will in particular help us to fix the optimal gains of each method with respect to the other. Secondly, we will present time evolution of the estimation errors for various sources of initial uncertainties in order to show the impact of the data time-sampling in practical data assimilation procedures.

We consider the example of the one-dimensional wave equation

$$\begin{cases} \ddot{w}(x,t) - w_{xx}(x,t) = 0, & (x,t) \in (0,1) \times (0,\infty) \\ w_x(0,t) = w_x(1,t) = 0, & t \in (0,\infty) \\ w(x,0) = w_0(x) + \zeta_0(x), & x \in (0,1) \\ \dot{w}(x,0) = w_1(x) + \zeta_1(x), & x \in (0,1). \end{cases} \tag{44}$$

In this setting we have

$$\left| \begin{array}{l} \mathcal{H} = \mathcal{L}^2(0,1), \\ \mathcal{D}(A_0) = \left\{ w \in \mathcal{H}^1(0,1) \mid w_{xx} \in \mathcal{L}^2(0,1) \right\}, \\ A_0 \varphi = -\varphi_{xx}, \qquad \varphi \in \mathcal{D}(A_0). \end{array} \right.$$

It is easy to see that this particular case fits exactly in the abstract framework described in Section 2. Concerning the observations, we follow the example presented in [Chapelle et al., 2012b] and we assume that

$$z(t) = w(\cdot,t)|_{\omega_0}, \qquad t \in (0,\infty), \tag{45}$$

with $\omega_0 =]0.3, 0.7[\subset (0,1)$ an open and non-empty interval. Hence, the observation space reads

$$\mathcal{Z} = \mathcal{H}^1(\omega_0). \tag{46}$$

Following [Chapelle et al., 2012a] we endow $\mathcal{Z}$ with the inner-product

$$\forall \varphi_1,\ \varphi_2 \in \mathcal{H}^1(\omega_0) \qquad (\varphi_1, \varphi_2)_{\mathcal{Z}} = (\mathrm{Ext}_{\omega_0}(\varphi_1), \mathrm{Ext}_{\omega_0}(\varphi_2))_{\mathcal{H}^1(0,1)}, \tag{47}$$

where the extension operator $\Phi = \mathrm{Ext}_{\omega_0}(\phi) \in \mathcal{H}^1(0,1)$ is defined for all $\phi \in \mathcal{H}^1(\omega_0)$ as the solution of

$$\begin{cases} -\Phi_{xx} = 0, & x \in (0,1) \backslash \omega_0 \\ \Phi = \phi, & x \in \overline{\omega_0} \\ \Phi_x(0) = \Phi_x(1) = 0. \end{cases}$$

For the inner-products $(\cdot,\cdot)_{\mathcal{Z}}$ and $(\cdot,\cdot)_{\mathcal{H}^1(0,1)}$, one can prove [Chapelle et al., 2012a] that the adjoint of the observation operator is

$$H_0^* : \left| \begin{array}{l} \mathcal{Z} \to \mathcal{H}^1(0,1) \\ \varphi \mapsto \mathrm{Ext}_{\omega_0}(\varphi), \end{array} \right.$$

and therefore the observer, decomposed into $\widehat{x} = \begin{pmatrix} \widehat{w} & \widehat{v} \end{pmatrix}^\intercal$, reads

$$\begin{cases} \dot{\widehat{w}} = \widehat{v} + \gamma \mathrm{Ext}_{\omega_0}(z - \widehat{w}|_{\omega_0}), \\ \dot{\widehat{v}} = \widehat{w}_{xx}, \\ \widehat{w}_x|_{x=0} = \widehat{w}_x|_{x=1} = 0, \\ \widehat{w}|_{t=0} = w_0, \\ \widehat{v}|_{t=0} = w_1. \end{cases}$$

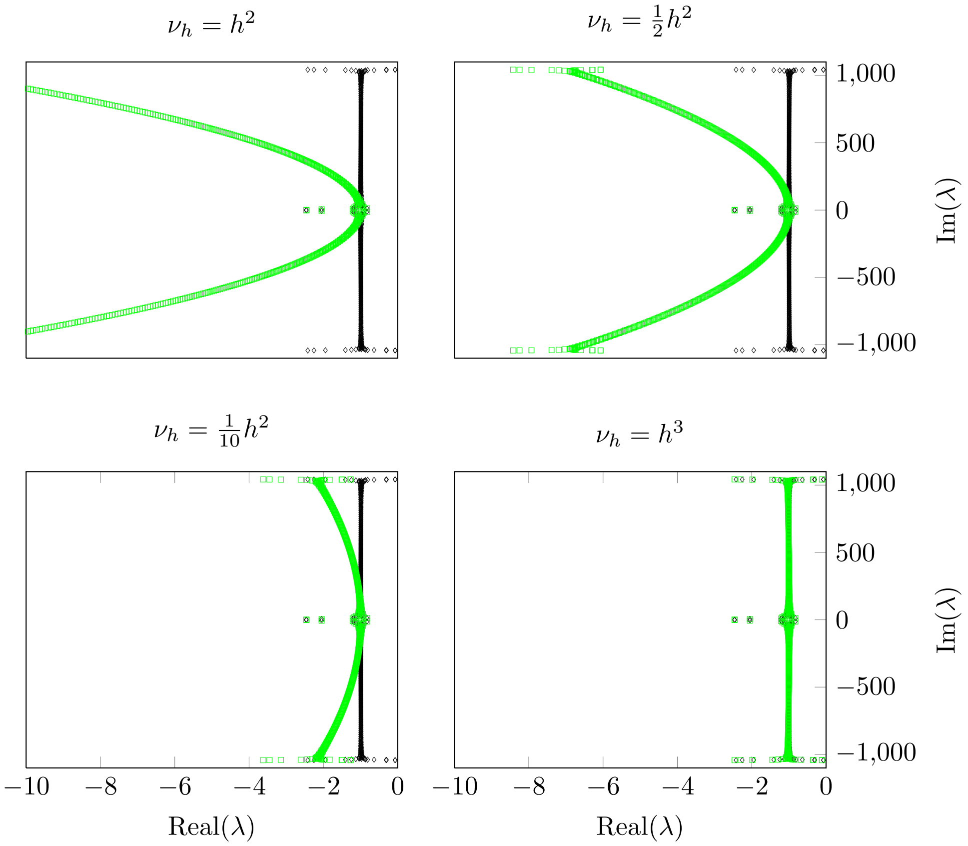

Figure 1: Evolution with respect to the viscous coefficient ν_h of the spectrum of the operator driving the time continuous dynamical system for a fixed value of the gain $\gamma = 5$. In **(black)** the operator without numerical viscosity, and in (green) with numerical viscosity.

4.1 Spectral analysis

As the Luenberger filter aims at stabilizing the estimation error system it is natural to assess the quality of the gain filter by evaluating its damping impact on the otherwise conservative system. Following [Luenberger, 1971], this can be done after full discretization by observing the evolution of the poles of the stabilized operator in both cases, namely using time interpolation or the on/off switch.

To start with, the most natural spectrum to analyze is certainly the spectrum associated with the time-continuous observer formulation, namely with only its spatial discretization. Then, the numerical results can be compared to the existing literature in particular with [Moireau et al., 2009, Chapelle et al., 2012b]. This case is the asymptotic limit of the time discretization and should be considered as our ultimate goal when we expect to produce the most accurate simulations. We will then see the impact of the time discretization in a second set of results. Note that we must proceed with caution here since the on/off time discretization is in essence a time-discrete strategy where we have to compose different operators over the sampling period.

4.1.1 Time continuous spectral analysis

Loss of uniform stability after discretization and numerical viscosity After spatial discretization, the estimation error dynamical system (6) reads

$$\dot{\tilde{x}}_h(t) = \big(A_h - \gamma H_h^* H_h\big)\tilde{x}_h(t), \tag{48}$$

where A_h and H_h are consistent discretization – *w.r.t* a space step h – of the model and the observation operator. Even though the observability inequality (4) is satisfied at a continuous level, this discretization procedure already produces – similarly to what we have mentioned in the case of time discretization – some spurious modes inducing the loss of the exponential stability of (48) – see [Ervedoza and Zuazua, 2009]. To circumvent this difficulty we have introduced some artificial viscosity for the time discretization which should also take into account the spatial discretization. When $\Delta t \to 0$ we obtain the time-continuous error dynamics studied in [Ervedoza and Zuazua, 2009], namely

$$\dot{\tilde{x}}_h(t) = \big(A_h - \gamma H_h^* H_h + \nu_h A_h^2\big)\tilde{x}_h(t). \tag{49}$$

Therefore, we start our numerical investigations with Figure 1 where we plot the evolution of the spectrum of the operator driving the dynamical system (49) *w.r.t.* various values of the artificial viscosity coefficient. These spectra are compared with the spectrum of the operator without numerical viscosity. By these examples we illustrate – in the particular case of the spatial discretization of 1D wave equation using first order finite element method – the creation of spurious high-frequencies that cannot be stabilized by the feedback operator $H_h^* H_h$. Hence, stabilizing the complete frequency range is then performed by decomposing the tasks. The feedback operator manages the low frequencies whereas the high frequencies are controlled by the numerical viscosity.

It should be noted, however, that since this artificial viscosity corresponds to a perturbation of the standard discretization of the problem it should be kept as low as possible. In practice the choice of the coefficient ν_h can be done with an *a priori* knowledge (or estimation) of the frequencies appearing in the specific problem of interest. However, in the rest of our following investigation we will keep a numerical viscosity strong enough to produce unclouded figures.

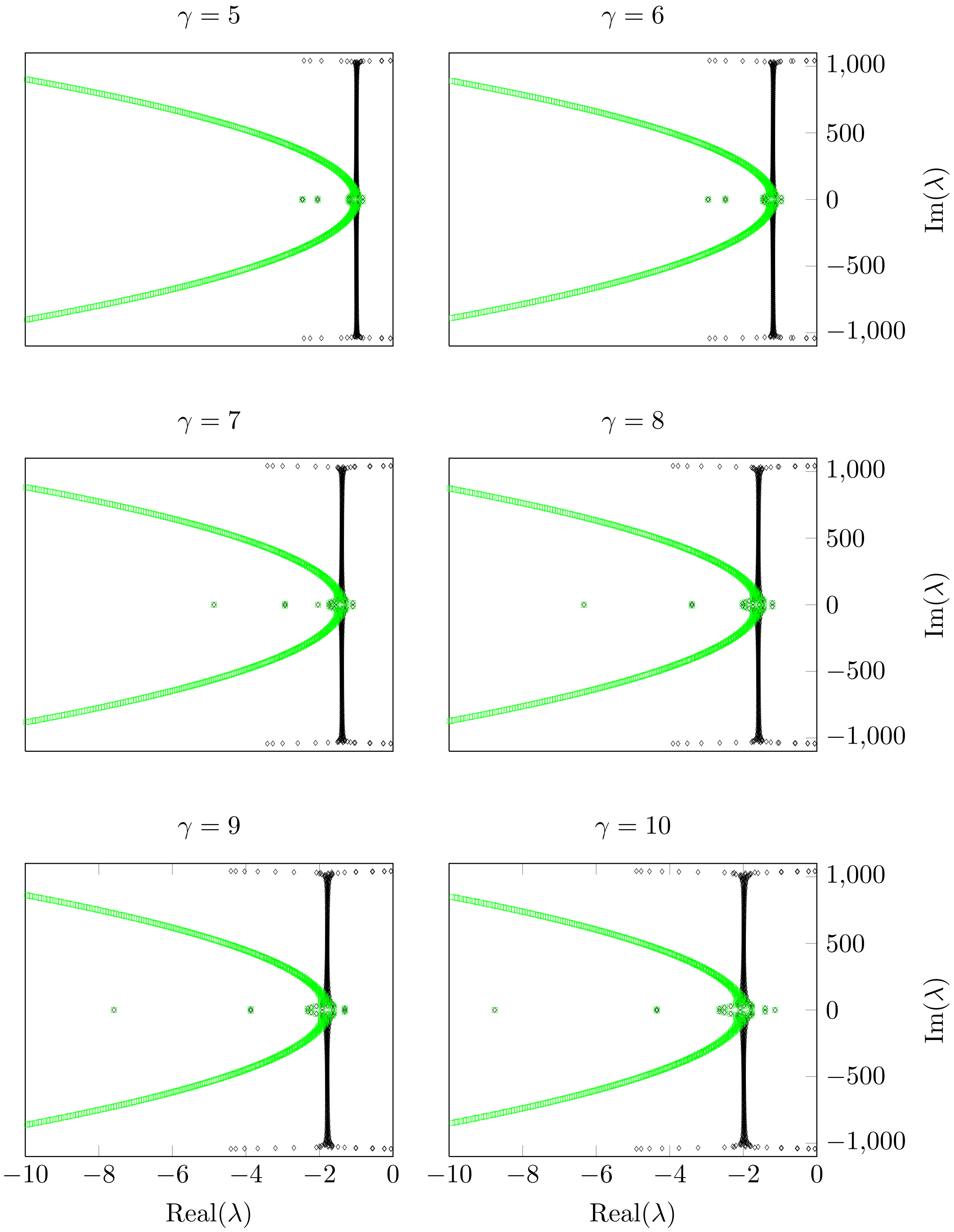

Figure 2: Evolution with respect to the gain γ of the spectrum of the operator driving the time continuous dynamical system. In **(black)** the operator without numerical viscosity, with numerical viscosity in (green).

Overdamping effect and optimal choice of the gain We plot in Figure 2 the spectra for various values of the gain parameter γ – in **(black)** the operator without numerical viscosity and in (green) the operator with numerical viscosity. We fix in these examples $\nu_h = h^2$. These plots enable us to illustrate the classical *overdamping* effect numerically pointed out by authors in [Moireau et al., 2009]. As the gain increases, the frequencies, after being shifted towards the left half plane, start to go back to the imaginary axis. This is particularly critical for the low frequencies. This effect is crucial when choosing an adequate value of the gain with an order of magnitude of

$$\gamma \sim \sqrt{2}\omega_0$$

with ω_0 the lower frequency of the system, see [Moireau et al., 2009]. This indicates that, first, even in the unrealistic case of an outstanding data-to-noise ratio, the gain cannot be chosen “as large as possible”. In other words after some particular value of the gain the ability of the observer to stabilize these low frequency modes looses its efficiency. Hence, the choice of the gain is a compromise between the different range of frequencies we aim at stabilizing. In our work we opt for a sort of “mean” strategy by choosing γ such that a maximum of frequencies are shifted significantly to the left half plane without compromising too much the low frequencies which are more present in the potential errors in practice. As an example in Figure 2 we choose $\gamma = 9$.

4.1.2 Spectral analysis of the time discrete observers

Once we have understood the behavior of the time-continuous observer and choosen a target optimal gain we can now proceed to the numerical study of our different choices of time-discretization.

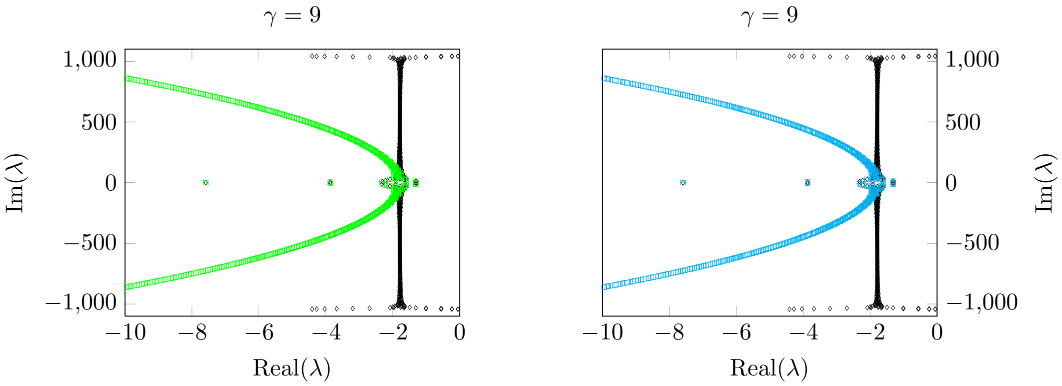

Figure 3: Comparison between the spectra of the time continuous operator (in (green)) and the time-discrete observer using interpolated data (in (cyan)) with time overkill.

Relation between optimal gains and the sampling period In order to study the time discrete observers, we need to define the two *transition* operators driving the homogeneous equivalent of system (35) either with numerical viscosity or not, namely

$$\left|\begin{aligned} A^{\gamma}_{n+1|n} &= \big(\mathbb{1} + \gamma\Delta\mathrm{t}H_h{}^*H_h\big)^{-1}\big(\mathbb{1} - \frac{1}{2}\Delta\mathrm{t}A_h\big)^{-1}\big(\mathbb{1} + \frac{1}{2}\Delta\mathrm{t}A_h\big),\\ A^{\gamma\nu}_{n+1|n} &= \big(\mathbb{1} - \Delta\mathrm{t}\nu A_h^2 + \gamma\Delta\mathrm{t}H_h{}^*H_h\big)^{-1}\big(\mathbb{1} - \frac{1}{2}\Delta\mathrm{t}A_h\big)^{-1}\big(\mathbb{1} + \frac{1}{2}\Delta\mathrm{t}A_h\big),\end{aligned}\right.$$

where, if $\widetilde{x}_+^n$ is the solution of the system (35) with $\varepsilon = \varepsilon_\nu = \varepsilon_d = 0$, then

$$\widetilde{x}_+^{n+1} = A^{\gamma\nu}_{n+1|n}\widetilde{x}_+^n,$$

and, if $\nu_{\Delta t} = 0$ in (35), then

$$\widetilde{x}_+^{n+1} = A^{\gamma}_{n+1|n}\widetilde{x}_+^n.$$

Note that in the definition of $A^{\gamma\nu}_{n+1|n}$, the parameter ν aims at adjusting the amount of numerical viscosity in order to discard spurious modes arising from the time discretization but also the space discretization – see Section 4.1.1. Combining the necessary restrictions arising from both time and space discretization, we understand that we need to choose here the global viscosity coefficient as

$$\nu = O(\max\{\Delta t^2, h^2\}).$$

We now link the eigenvalues α and α_ν of the time discrete observer to the one corresponding to the time continuous observer. Therefore, let us denote by λ an eigenvalue of the operator $A_h - \gamma H_h^* H_h$ to be compared with α. If we initialize the time discrete and time continuous system with the correponding eigenvectors v_λ and u_λ then (from the explicit form of the dynamics) we obtain that, at a given time $n\Delta t$

$$\left| \begin{array}{l} v_\lambda(n\Delta t) = v_\lambda \exp(\lambda n \Delta t) \\ u^n_{\lambda+} = u_\lambda \alpha^n, \end{array} \right.$$

hence seeking $v_\lambda(n\Delta t) \sim u^n_{\lambda+}$ induces $\lambda = \dfrac{\ln(\alpha)}{\Delta t}$. To numerically validate these arguments we plot in Figure 3 the values

$$\frac{\log(\alpha)}{\Delta t}\ \textbf{(black)} \quad \text{and} \quad \frac{\log(\alpha_\nu)}{\Delta t}\ \text{(cyan)}.$$

In order to be able to compare with the time-continous spectrum we set $\Delta t = h^2$ – this configuration can be understood as an *overkill in time* – and we observe a perfect match between the two plots.

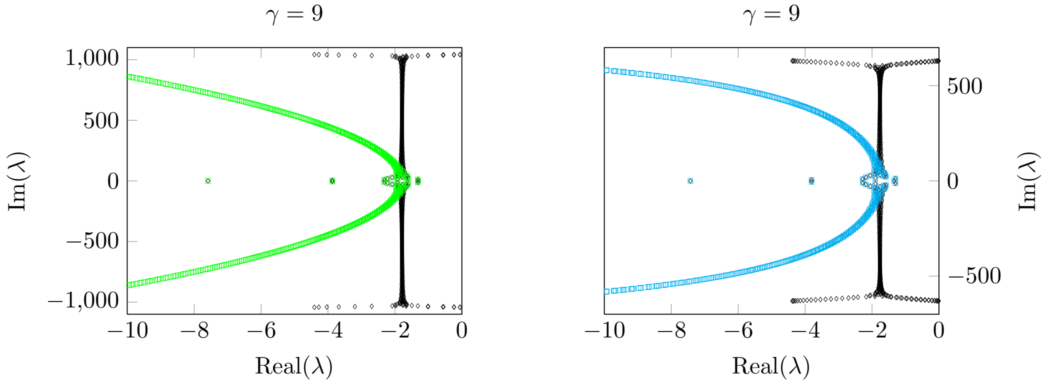

Figure 4: Comparison between the spectra of the time continuous operator (in (green)) and the time-discrete observer using interpolated data (in (cyan)).

In Figure 4 we represent a configuration where $\Delta t = h$. Here the spectrum differs from the time-continuous analysis. We see that additional spurious high frequencies are not controlled by the stabilization operator. This justifies even more the use of numerical viscosity which allows to keep the gain chosen in the time-continuous setting. But ultimately, the choice of the gain made with respect to the time-continuous case is very robust to all time-step discretizations.

We can now move to the analysis of the on/off discrete operator in order to determine the associated optimal gain. In this perspective it is convenient to seek for the time-continuous limit, therefore we consider a time overkill situation by setting $\Delta\mathrm{t} = h^2$. Then, to fix the ideas, we consider the case where $\Delta\mathrm{T} = 5\Delta\mathrm{t}$, namely

$$\forall r \in \mathbb{N} \quad (j_{r+1} - j_r) = 5.$$

We introduce the transition operators from time t_n to t_{n+5} as

$$\left|\begin{aligned} B^{\gamma}_{n+5|n} &= \Big(\big(\mathbb{1} - \frac{1}{2}\Delta\mathrm{t}A_h\big)^{-1}\big(\mathbb{1} + \frac{1}{2}\Delta\mathrm{t}A_h\big)\Big)^4\Big(\big(\mathbb{1} + \gamma\Delta\mathrm{t}{H_h}^*H_h\big)^{-1}\big(\mathbb{1} - \frac{1}{2}\Delta\mathrm{t}A_h\big)^{-1}\big(\mathbb{1} + \frac{1}{2}\Delta\mathrm{t}A_h\big)\Big),\\ B^{\nu\gamma}_{n+5|n} &= \Big(\big(\mathbb{1} - \Delta\mathrm{t}\nu A_h^2\big)^{-1}\big(\mathbb{1} - \frac{1}{2}\Delta\mathrm{t}A_h\big)^{-1}\big(\mathbb{1} + \frac{1}{2}\Delta\mathrm{t}A_h\big)\Big)^4\\ &\qquad\qquad \Big(\big(\mathbb{1} - \Delta\mathrm{t}\nu A_h^2 + \gamma\Delta\mathrm{t}{H_h}^*H_h\big)^{-1}\big(\mathbb{1} - \frac{1}{2}\Delta\mathrm{t}A_h\big)^{-1}\big(\mathbb{1} + \frac{1}{2}\Delta\mathrm{t}A_h\big)\Big), \end{aligned}\right.$$

and we denote by $\widetilde{\beta}$ and $\widetilde{\beta}_\nu$ the corresponding eigenvalues. These operators should be compared to their equivalent transition operators from time t_n to t_{n+5} in the interpolated case, namely the simple composition

$$A^{\gamma}_{n+5|n} = \big(A^{\gamma}_{n+1|n}\big)^5 \quad \text{and} \quad A^{\gamma\nu}_{n+5|n} = \big(A^{\gamma\nu}_{n+1|n}\big)^5,$$

with corresponding eigenvalues $\widetilde{\alpha}$ and $\widetilde{\alpha}_\nu$. Then, in Figure 5 we show

$$\frac{\log(\widetilde{\beta})}{\Delta\mathrm{T}}\ \textbf{(black)} \quad \text{and} \quad \frac{\log(\widetilde{\beta}_\nu)}{\Delta\mathrm{T}}\ \text{(red)},$$

compared with $\widetilde{\alpha}$ and $\widetilde{\alpha}_\nu$ in the time overkill configuration.

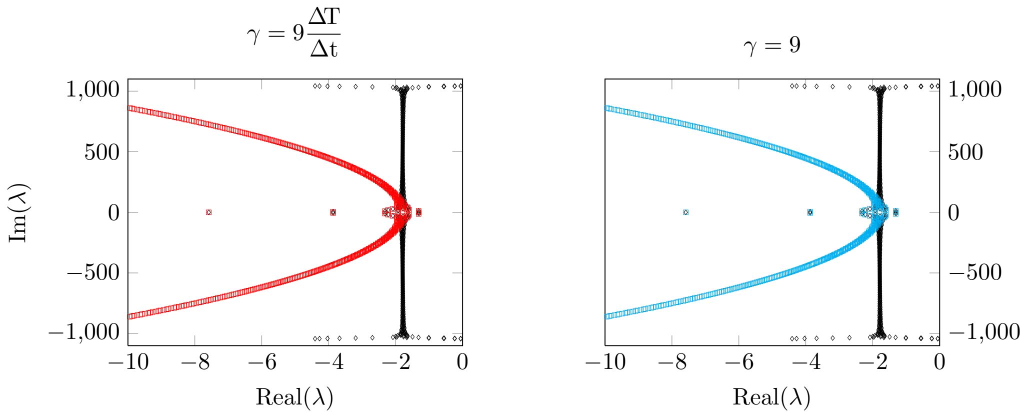

Figure 5: Comparison between the time-discrete on/off observer (in (red)) and the time-discrete observer using interpolated data (in (cyan)) to illustrate the relation between the optimal gains in a time overkill context.

We set the gain value for the on/off observer five times larger than in the interpolated case and we observe a perfect match. Consequently these numerical arguments confirm the intuition that, in order to obtain similar damping rates between the two strategies, the gain value γ_{switch}

for the on/off switch needs to be five times larger than the gain value $\gamma_{\text{int.}}$ for the interpolation strategy. In a general context we can infer the empirical law

$$\frac{\gamma_{\text{switch}}}{\gamma_{\text{int.}}} = \frac{\Delta \mathrm{T}}{\Delta \mathrm{t}} \tag{50}$$

and we point out that we do not face any overdamping phenomena which could have limited the increase of the gain in the on/off switch which is an important contribution of our numerical investigations.

Comparing stabilization properties of the observer We can now analyze a more intricate case where $\Delta\mathrm{t} = h$. We continue to fix the ratio $\Delta\mathrm{T} = 5\Delta\mathrm{t}$ and the spectra of both observers are presented in Figure 6. We observe that additionally to the peculiar form of the spectra more spurious high frequencies appear, validating once again the use of numerical viscosity. Moreover, concerning the on/off observer, we remark some high frequencies that are less stabilized. This can be interpreted as an illustration of the fact that this observer may suffer from a decreased stability on some modes – corresponding to these high frequencies.

Finally in Figure 7 we set $\Delta\mathrm{t} = h^2$ and $\Delta\mathrm{T} = 5h$. This situation is relevant with practical cases where the time-step of the numerical algorithm is much lower than the sampling time-step of the data but more importantly that it is, in essence, meant to reach small values whereas the sampling rate is fixed. The conclusion stated previously remains valid since we still observe a slight deterioration of the damping of some high frequency modes for the on/off estimator.

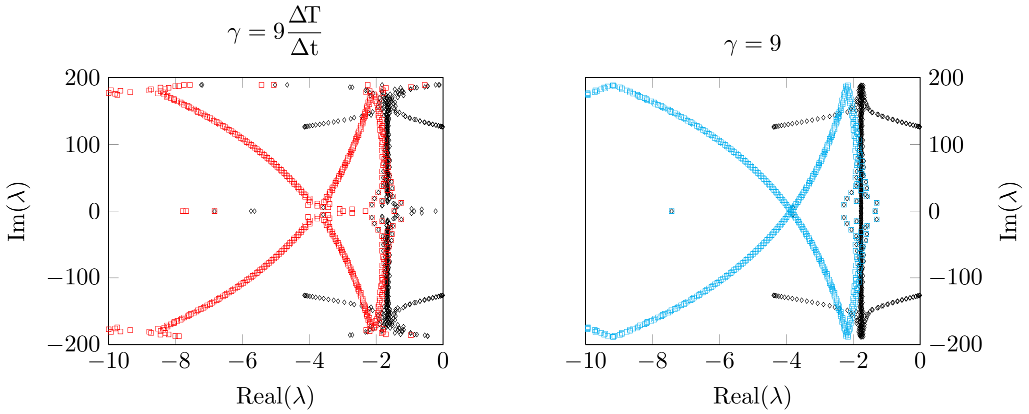

Figure 6: Comparison between the time-discrete on/off observer (in (red)) and the time-discrete observer using interpolated data (in (cyan)) with $\Delta\mathrm{t} = h$ and $\Delta\mathrm{T} = 5h$.

To conclude with this section we can say that the time-continuous spectrum analysis remains a very useful tool to fix the optimal gain. It is obvious for the time-interpolated configuration but in fact it is also the case with the on/off switch. The only modification with the on/off switch configuration is that we have to multiply the gain found during the time-continuous spectrum analysis by the ratio of the data time-step over the model time-step. The stability property is preserved globally and we do not face any overdamping phenomena by increasing the value of the gain in this case.

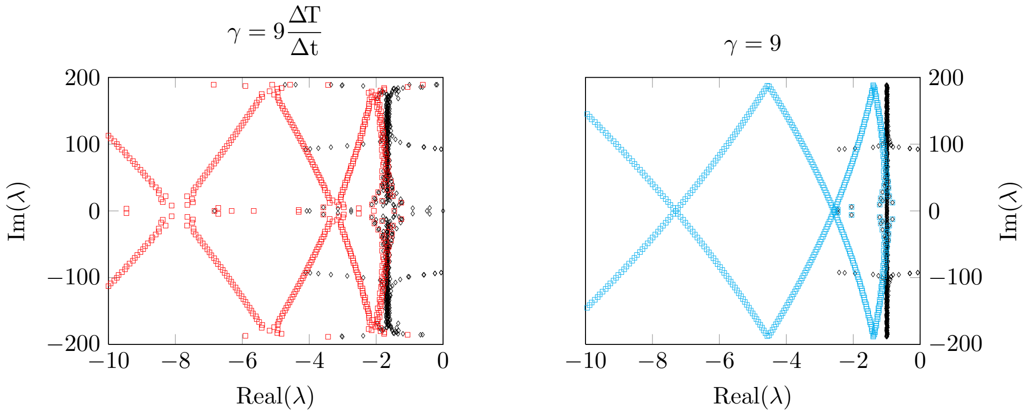

Figure 7: Comparison between the time-discrete on/off observer (in (red)) and the time-discrete observer using interpolated data (in (cyan)) with $\Delta t = h^2$ and $\Delta T = 5h$.

5 Assessing robustness from numerical examples

We propose in this section to assess the effectiveness of the two observers using *synthetic* data. More precisely, we consider the functions

$$\varphi_0(s) = 16s^2(1-s)^2, \qquad \varphi_1(s) = \begin{cases} 3s - 4s^3 & \text{if } s \in (0, 0.5), \\ 4s^3 - 12s^2 + 9s & \text{if } s \in (0.5, 1), \end{cases} \tag{51}$$

that we use to initiate a *direct model* of the form of (44). The solution of this direct model can be computed analytically

$$w(x,t) = \sum_k \sqrt{2}\big(a_k \cos(\pi k t) + b_k \sin(\pi k t)\big) \sin(\pi k x),$$

with

$$a_k = \frac{2\sqrt{2}(\pi^2 - 12)(\cos(\pi k) - 1)}{\pi^5 k^5} \quad \text{and} \quad b_k = \frac{48\sqrt{2}\sin(\frac{\pi k}{2})}{\pi^4 k^4}$$

from which we extract our synthetic observations. Then we simulate the observer where we artificially introduce some errors by setting

$$\widehat{x}_0 = \begin{pmatrix} \varphi_0 - \alpha\delta\varphi \\ \varphi_1 \end{pmatrix},$$

where $\delta\varphi$ is a given perturbation of the initial condition (in displacement) and α is a scalar value representing the perturbation amplitude. Hence, the estimation error dynamical system is initialized with

$$\widetilde{x}_0 = \alpha \begin{pmatrix} \delta\varphi \\ 0 \end{pmatrix}.$$

In our numerical simulation, we set $\gamma_{\text{int.}} = 9$, the optimal value discussed in Section 4 and γ_{switch} is obtained from the ratio (50).

First, we propose to consider the case where $\alpha = 0$, namely we initiate the numerical algorithm with the exact – up to some projection errors – initial condition. It is well-known that standard numerical schemes lead to an accumulation of numerical errors thus entailing a deterioration of the numerical solution as the global simulation time grows larger. This phenomenon is illustrated in Figure 8 where we plot the evolution in time of the estimation errors.

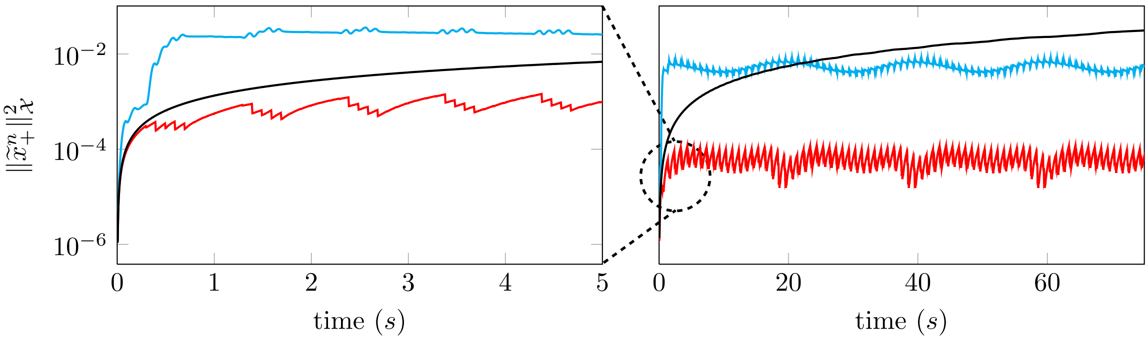

Figure 8: Estimation error with $\frac{\Delta T}{\Delta t} = 20$, $\alpha = 0$. In **(black)** is the simulation without correction, in (cyan) is the observer with linear data interpolation and in (red) is on/off observer

Concerning the observer we set $\frac{\Delta T}{\Delta t} = 20$ and compare the results of both strategies. We observe that the corresponding estimation errors clearly stabilize to a plateau – during the complete time window and even for large total simulation time – which is a particular behavior already obtained in [Chapelle et al., 2012b]. In this configuration we observe that, due to the data interpolation error the on/off strategy provides a better numerical solution than the observer using interpolated data.

Second, we set $\frac{\Delta T}{\Delta t} = 20$, $\alpha = 1$ and $\delta\varphi(x) = \sin(\pi x)$ – the first eigenfunction of the Laplacian operator in the domain. It should be noted that it is not a mode of the stabilized operator driving the dynamics of the estimation error, hence there are multiple excited modes in this dynamical systems. The corresponding results are presented in Figure 9 where we can distinguish several slopes – during early stages of the simulation – in the decay of the estimation error. These slopes correspond to the time constant of stabilization associated with the various modes initially introduced. In the remaining part of the time window we observe that both observers reach a plateau – which is identical to the one observed in Figure 8.

In Figure 10, we increase the magnitude of the perturbation introduced in the system by setting $\alpha = 10^2$. This results in an increase of the potential high frequencies that are initially introduced in the estimation error dynamics. When looking at the snapshots, we see that the on/off observer suffers from high frequency oscillations that do not appear in the observer with the time interpolation scheme. We see here the main advantage of using time interpolation. Namely, since the dissipation brought by the observation operator is present at every time steps, it benefits from a remarkable robustness to noise.

In a forth numerical experiment, we consider in Figure 11 the configuration where less data are available on the system by setting $\frac{\Delta T}{\Delta t} = 200$. It is striking to remark that the on/off observer clearly fulfills its task by assimilating data only where they are available thus leading to a great efficiency in the case of highly coarse time distribution of the observations. On the opposite, the other observer oscillates around a plateau due to large interpolation errors. To underline the impact of interpolation error, we have eventually change the type of interpolation by using a cubic interpolation of the data. The resulting sampling is presented in Figure 12. We understand that when the cubic reconstruction is better than the linear – here at the end

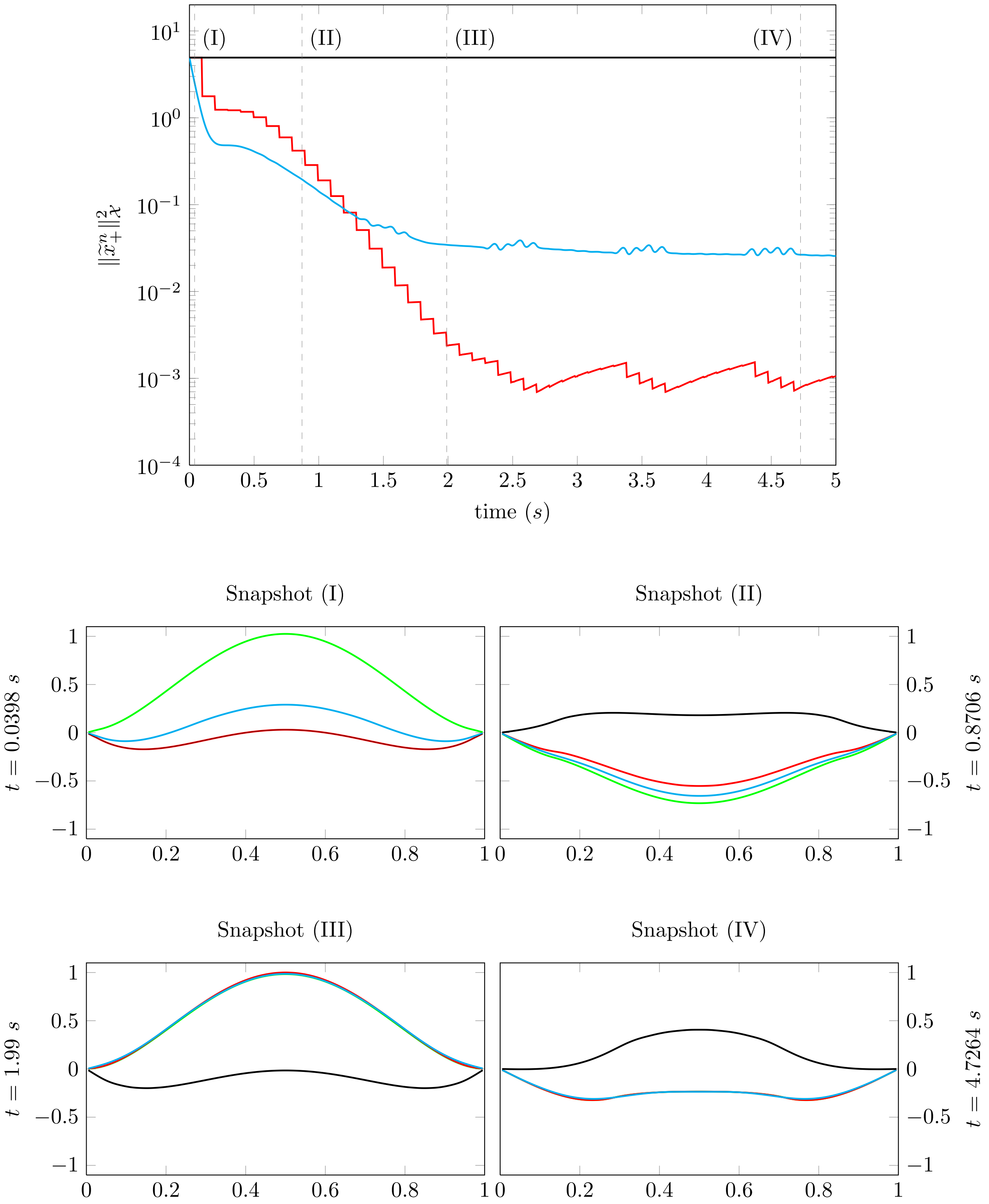

Figure 9: Numerical results with $\frac{\Delta \mathrm{T}}{\Delta \mathrm{t}} = 20$, $\alpha = 1$ and $\delta\varphi(s) = \sin(\pi s)$. In (green) is the exact solution without perturbation, in **(black)** is the simulation without correction, in (cyan) is the observer with linear data interpolation and in (red) is on/off observer.

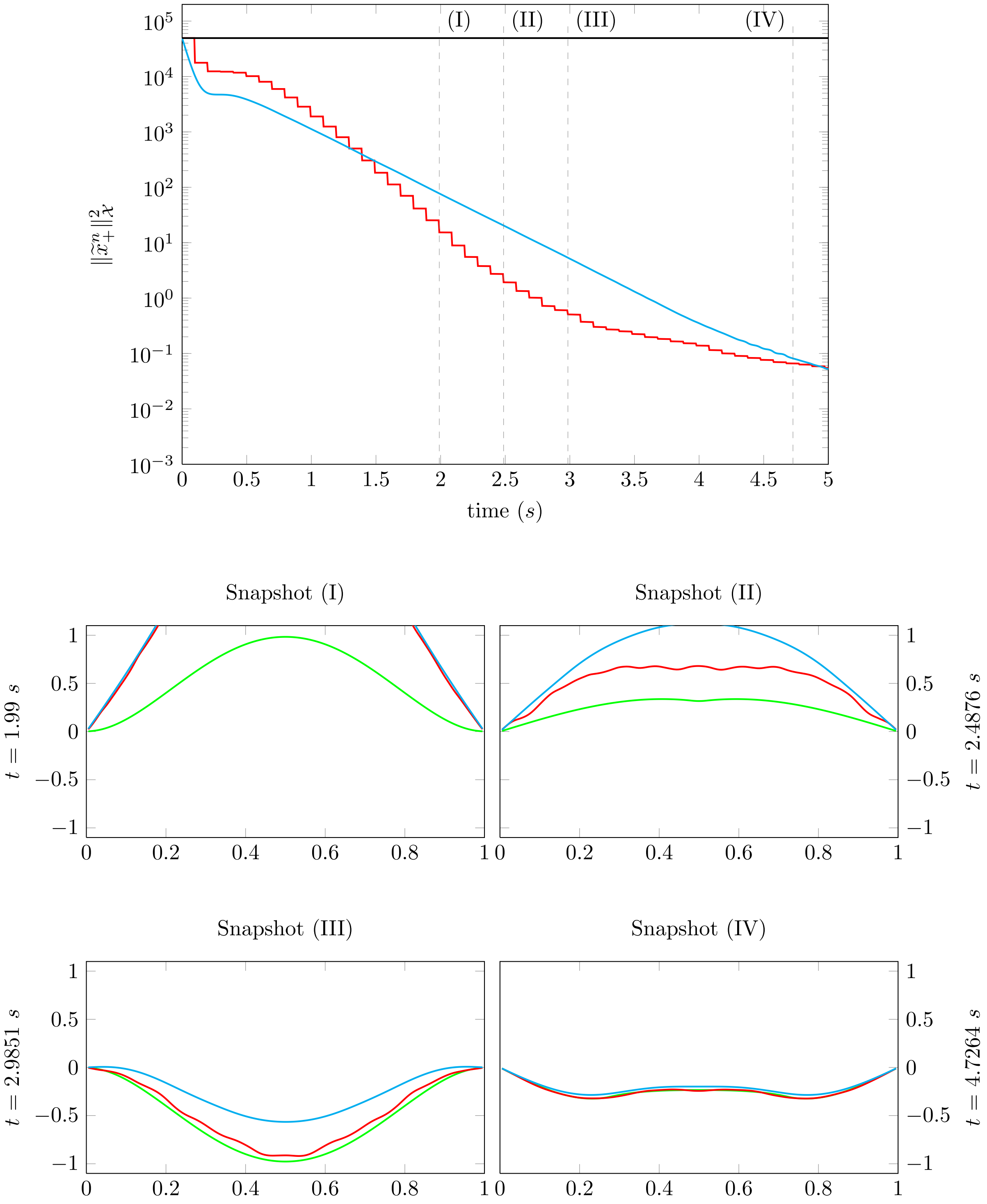

Figure 10: Numerical results with $\frac{\Delta T}{\Delta t} = 20$, $\alpha = 10^2$ and $\delta\varphi(s) = \sin(\pi s)$. In (green) is the exact solution without perturbation, in (cyan) is the observer with linear data interpolation and in (red) is on/off observer.

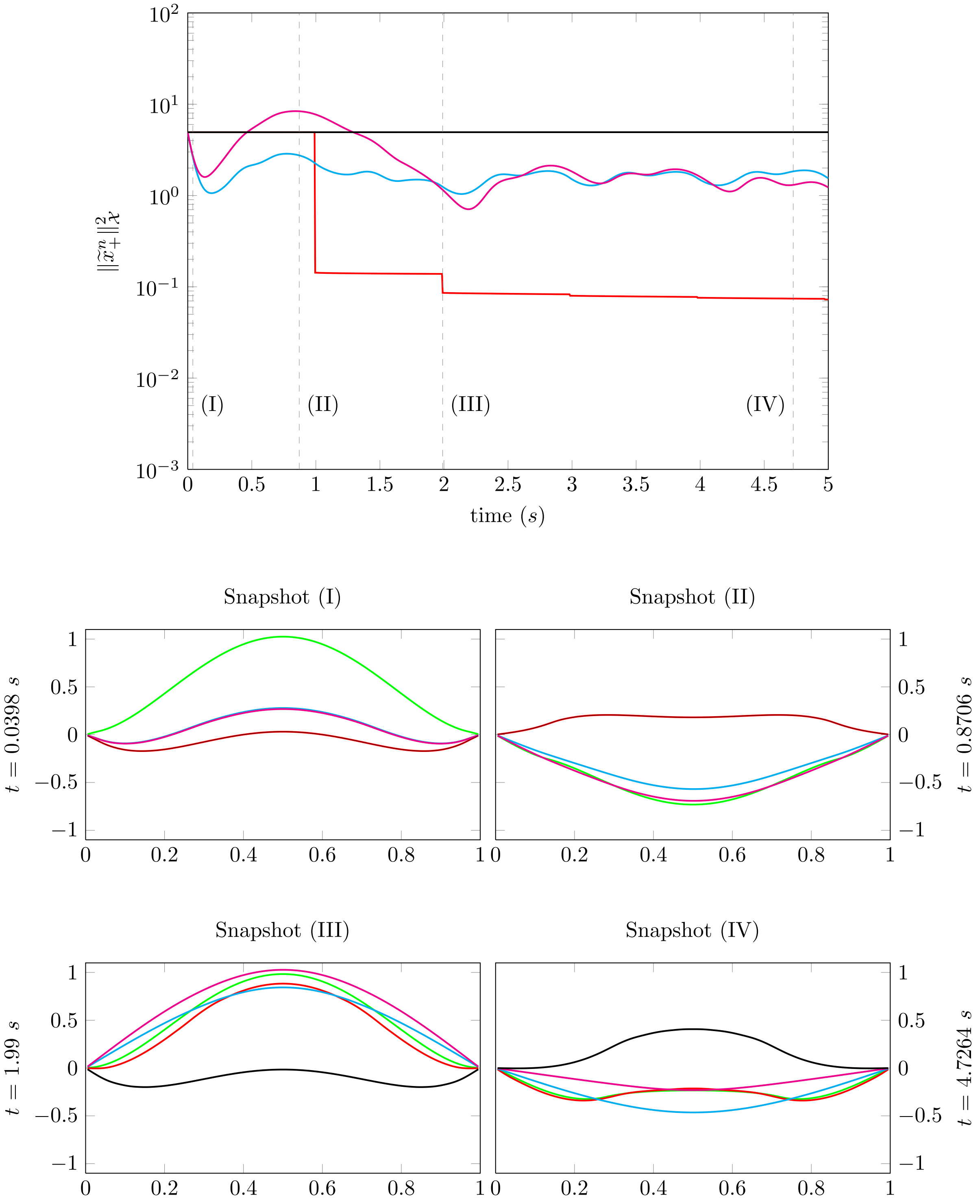

Figure 11: Numerical results with $\frac{\Delta \mathrm{T}}{\Delta \mathrm{t}} = 200$, $\alpha = 1$ and $\delta\varphi(s) = \sin(\pi s)$. In (green) is the exact solution without perturbation, in **(black)** is the simulation without correction, in (cyan) is the observer with linear data, in (purple) is the observer with cubic data interpolation and in (red) is on/off observer.

of the time window – then the final estimation error is lower. However at the beginning of the time window, we see that the cubic interpolation error is larger than with a simple linear interpolation which is of dramatic consequence on the estimation error. This also proves that without any idea on the model generating the data, a simple interpolation scheme is sufficient.

One last result concerns the case where the ratio $\frac{\Delta T}{\Delta t}$ is also set to 200 by decreasing the simulation time-step and using the same sampling period as in Figure 10. This case is representative of the final goal in a numerical procedure, namely for a given configuration we hope to increase the precision by diminishing the model discretization step. In that case, the results are almost exactly similar to the one presented in Figure 9, namely the observer fed with interpolated data is less efficient due to large interpolation error – which is identical to the one introduced in Figure 9 since it only depends on the sampling period as emphasized in Proposition 3. We conclude that (1) the best strategy is always to use the available data, (2) it is in general less risky to use the on/off switch time discretization scheme but (3) we can not expect a precision improvement better than time-discretization step of the data.

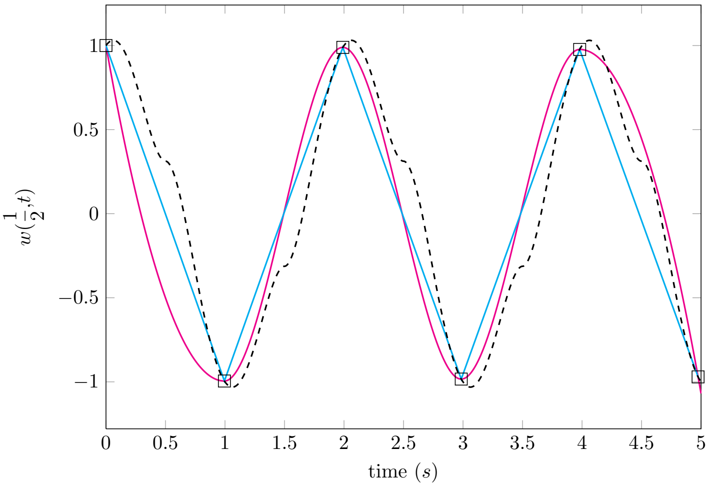

Figure 12: Illustration of the impact of time interpolation. The dashed line is the exact solution at the point $x = \frac{1}{2}$ and the squares are the sampled data. In (cyan) is the time interpolation and in (purple) is the cubic interpolation.

6 Conclusion

In our work we have addressed the issue of designing an observer for vibrating systems that is robust when the data have a coarse distribution in time. To circumvent this difficulty we have proposed an on/off strategy that filters the observation only at times when they are available. This strategy was theoretically and numerically analyzed and compared to the case when the data are reconstructed using an interpolation scheme.

The conclusions are twofold. First we have seen that the interpolation remains valid in the case of reasonable repartition (in time) of the data with potentially high levels of noise. This particularity comes from the presence, at each time step, of the stabilized operator. Secondly, in the case of poor data availability the on/off switch appears to be quite robust since no interpolation error – otherwise entering as a source term in the estimation error dynamical system – is introduced.

Acknowledgment

The authors would like to deeply thanks Dr. Dominique Chapelle for very useful comments on this work.

References

[Auroux and Blum, 2007] Auroux, D. and Blum, J. (2007). A nudging-based data assimilation method: the back and forth nudging (bfn) algorithm. *Nonlin. Processes Geophys.*, 15:305–319.

[Bardos et al., 1992] Bardos, C., Lebeau, G., and Rauch, J. (1992). Sharp sufficient conditions for the observation, control, and stabilization of waves from the boundary. *SIAM J. Control Optim.*, 30(5):1024–1065.

[Bensoussan, 1971] Bensoussan, A. (1971). *Filtrage optimal des systèmes linéaires.* Dunod.

[Bertoglio et al., 2013] Bertoglio, C., Chapelle, D., Fernández, M. A., Gerbeau, J. F., and Moireau, P. (2013). State observers of a vascular fluid–structure interaction model through measurements in the solid. *Comput. Methods Appl. Mech. Engrg.*, 256:149–168.

[Blum et al., 2008] Blum, J., LeDimet, F. X., and Navon, I. N. (2008). Data assimilation for geophysical fluids. *Handbook of Numerical Analysis: Computational Methods for the Atmosphere and the Oceans. Elsevier, Amsterdam*, 14:377–434.

[Chabiniok et al., 2011] Chabiniok, R., Moireau, P., Lesault, P.-F., Rahmouni, A., Deux, J.-F., and Chapelle, D. (2011). Trials on tissue contractility estimation from cardiac cine-MRI using a biomechanical heart model. In *Proceedings of FIMH'11, LNCS 6666*, pages 304–313. Springer.

[Chapelle et al., 2012a] Chapelle, D., Cîndea, N., De Buhan, M., and Moireau, P. (2012a). Exponential convergence of an observer based on partial field measurements for the wave equation. *Math. Probl. Eng.*, 2012:12.

[Chapelle et al., 2012b] Chapelle, D., Cîndea, N., and Moireau, P. (2012b). Improving convergence in numerical analysis using observers. The wave-like equation case. *Math. Models Methods Appl. Sci.*

[Chapelle et al., 2013] Chapelle, D., Fragu, M., Mallet, V., and Moireau, P. (2013). Fundamental principles of data assimilation underlying the Verdandi library: applications to biophysical model personalization within euHeart. *Med. Biol. Eng. Comput.*, 51(11):1221–1233.

[Corpetti et al., 2009] Corpetti, T., Héas, P., Mémin, E., and Papadakis, N. (2009). Pressure image assimilation for atmospheric motion estimation. *Tellus A.*, 61(1):160–178.

[Cox and Zuazua, 1994] Cox, S. and Zuazua, E. (1994). The rate at which energy decays in a damped string. *Comm. Partial Differential Equations*, 19:213–243.

[Daoulatli et al., 2010] Daoulatli, M., Dehman, B., and Khenissi, M. (2010). Local energy decay for the elastic system with nonlinear damping in an exterior domain. *SIAM J. Control Optim.*, 48(8):5254–5275.

[Ervedoza and Zuazua, 2009] Ervedoza, S. and Zuazua, E. (2009). Uniformly exponentially stable approximations for a class of damped systems. *J. Math. Pures Appl.*, 91:20–48.

[Haraux and Zuazua, 1988] Haraux, A. and Zuazua, E. (1988). Decay estimates for some semilinear damped hyperbolic problems. *Arch. Rational Mech. Anal.*, 100(2):191–206.

[Hoke and Anthes, 1976] Hoke, J. and Anthes, R. (1976). The initialization of numerical models by a dynamic-initialization technique(fluid flow models for wind forecasting). *Monthly Weather Review*, 104:1551–1556.

[Imperiale et al., 2011] Imperiale, A., Chabiniok, R., Moireau, P., and Chapelle, D. (2011). Constitutive parameter estimation methodology using Tagged-MRI data. In *Proceedings of FIMH'11, LNCS 6666*, pages 409–417. Springer.

[Kalman and Bucy, 1961] Kalman, R. E. and Bucy, R. S. (1961). New results in linear filtering and prediction theory. *J. Basic Eng.*, 83(3):95–108.

[Li and Xu, 2011] Li, X.-D. and Xu, C.-Z. (2011). Infinite-dimensional Luenberger-like observers for a rotating body-beam system. *Systems & Control Letters*, 60(2):138–145.

[Liu, 1997] Liu, K. (1997). Locally distributed control and damping for the conservative systems. *SIAM J. Control Optim.*, 35(5):1574–1590.

[Luenberger, 1971] Luenberger, D. G. (1971). An introduction to observers. *IEEE T. Automat. Contr.*, 16(6):596–602.

[Moireau et al., 2013] Moireau, P., Bertoglio, C., Xiao, N., Figueroa, C. A., Taylor, C. A., Chapelle, D., and Gerbeau, J. F. (2013). Sequential identification of boundary support parameters in a fluid-structure vascular model using patient image data. *Biomech. Model. Mechanobiol.*, 12:475–496.

[Moireau et al., 2007] Moireau, P., Chapelle, D., and LeTallec, P. (2007). Joint state and parameter estimation for distributed mechanical systems. *Comput. Methods Appl. Mech. Engrg.*, 197:659–677.

[Moireau et al., 2009] Moireau, P., Chapelle, D., and LeTallec, P. (2009). Filtering for distributed mechanical systems using position measurements: Perspectives in medical imaging. *Inverse Probl.*, 25(3):035010.

[Navon, 2008] Navon, I. N. (2008). *Data assimilation for numerical weather prediction: a review.* Springer.

[Nichols, 2010] Nichols, N. (2010). Mathematical concepts of data assimilation. In Lahoz, W., Khattatov, B., and Menard, R., editors, *Data Assimilation*, pages 13–39. Springer Berlin Heidelberg.

[Papadakis and Mémin, 2008] Papadakis, N. and Mémin, E. (2008). Variational assimilation of fluid motion from image sequence. *SIAM J. Imaging Sciences*, 1(4):343–363.

[Ramdani et al., 2012] Ramdani, K., Tucsnak, M., and Weiss, G. (2012). Recovering the initial state of an infinite-dimensional system using observers. *Automatica*, pages 1616–1625.

[Sainte-Marie et al., 2006] Sainte-Marie, J., Chapelle, D., Cimrman, R., and Sorine, M. (2006). Modeling and estimation of the cardiac electromechanical activity. *Comput. Struct.*, 84:1743–1759.

[Simon, 2006] Simon, D. (2006). *Optimal state estimation: Kalman, H_∞ and nonlinear approaches.* Wiley-Interscience.

[Tucsnak and Weiss, 2009] Tucsnak, M. and Weiss, G. (2009). *Observation and control for operator semigroups.* Birkhäuser Basel.

[Zhang et al., 2007] Zhang, X., Zheng, C., and Zuazua, E. (2007). Exact controllability of the time discrete wave equation: a multiplier approach. *Discret. Contin. Dyn. S.*, pages 229–245.

[Zuazua, 2005] Zuazua, E. (2005). Propagation, observation, and control of waves approximated by finite difference methods. *SIAM Review*, 47(2):197–243.

CHAPTER 3

Cardiac estimation from tagged-MR images

This Chapter takes the form of a pre-print article gathering the work carried out in collaboration with D. Chapelle and P. Moireau.

Tagged-MR images are a particular medical image modality of the heart that, by implanting a particular spatial modulation in the magnetization of the tissue, enables to obtain within the image plane a regular pattern – typically of grid-like structure – that deforms with the material. This deforming tag pattern can then be used in clinical routine to assess intra-myocardial deformations.

In our work, we intend to use the valuable information contained in this image modality within a data assimilation context in order to perform joint state and parameter estimation for a complete biomechanical model of the heart. More precisely, we focus our attention on proposing a means of comparison between the model and various types of data sets that could be obtained after a prior step of image processing. This discrepancy measure is then use to feed a sequential data assimilation procedure. Namely, we consider direct observation of the displacement– that we have coined as a limit case when the tag pattern spacial frequency decreases – but also tag planes, tag grids and visible displacements – defined within the image plane. This work comes after a previously published proceeding where we consider – as a proof of concept – the single case of deforming tag planes

Constitutive parameter estimation methodology using tagged-MRI data. *A. Imperiale, R. Chabiniok, P. Moireau and D. Chapelle* – FIMH 2011.

We also provide a new numerical time scheme for the state estimator based on a prediction-correction paradigm. This new algorithm enables us to distinguish the model iteration and the correction phases thus leading to an increased flexibility of the solving process. Typically, this strategy allows the use of iterative solver in order to manage full band observation operators appearing when dealing with data defined in the image domain.

This estimation strategy is performed within a *synthetic data context*. In this context we first run a direct simulation where we set an infarct in the septum of the model geometry – charachterized by an increased stiffness and a reduced contractility. From this *direct* simulation, we extract the tag planes, tag grids and visible displacement in order to feed our data assimilation procedure. From these data we are able to evaluate the location and the intensity of the infarct with a remarkable precision, thus assessing the significant amount of information contained in tagged-MR images and its potential use in clinical routine to propose diagnosis assistance.

Cardiac estimation from tagged-MR images

D. Chapelle, A. Imperiale, P. Moireau†,
†Project-Team MΞDISIM, Inria Saclay-Ile-de-France, Palaiseau, France

Contents

1 Introduction

Cardiac biomechanical modeling has made tremendous progress over the past decades, and some accurate models are now available to represent the complex deformations of the organ – among other quantities of interest – over full heartbeats, frequently based on multi-physics and multi-scale formulations [Nash and Hunter, 2000, Sainte-Marie et al., 2006].

As for all natural systems – as *e.g.* also in geophysics – a great challenge consists in dealing with the many unknown or uncertain quantities that need to be prescribed for running model simulations and that crucially condition, indeed, the results accuracy, hence also the predictive capability of the model in actual applications. These quantities include initial conditions, boundary conditions, and various physical parameters, all of which can hardly – if at all – be directly measured in such natural systems. Nevertheless, other types of measurements are usually available, and thus the problem can be recast in an *estimation* framework, in which these measurements can be used to circumvent – or at least reduce – the uncertainties associated with the dynamical model, thereby providing an estimation of uncertain quantities while allowing predictive simulations. This type of approach is also often referred to as data assimilation.

Concerning the specific problem of estimation in cardiac biomechanical modeling, difficulties arise from both (1) the complexity of the models considered, and (2) the nature of the available measurements, often relying on medical imaging. An effective estimation methodology has been proposed in [Moireau et al., 2009] for this type of model, based on a so-called sequential approach – also known as observer method – by which the dynamical model is corrected at each time using the computed discrepancy between the current simulation and the actual measurements, see also [Chabiniok et al., 2012]. This strategy was designed to be applicable to measurements concerning displacements, whether they be given internally – in a sub-region of the system – or on a boundary or a part thereof, and it was also shown to be extendable to data consisting of segmented surfaces as obtained by processing various types of medical imaging dynamical sequences.

In this paper, we focus on estimation based on data provided by tagged-MR imaging sequences [Zerhouni et al., 1988, Axel and Dougherty, 1989]. Tagged-MR is often considered to be the "gold standard" in cardiac imaging, in particular as regards the assessment of so-called "cardiac mechanical indicators", namely, indicators pertaining to displacements, strains, and volumes [Axel et al., 2005]. As a matter of fact, tagged-MR images visualize the deformations of grids associated with the actual tissues, which is of course most valuable for clinical purposes, both from a qualitative standpoint as assessed by the physician's eye, and with a view to obtaining such quantitative indicators. However, the problem of extracting actual 3D material displacements from a tagged-MR sequence gives rise to serious difficulties [Ryf et al., 2002, Rutz et al., 2008], and in fact in many cases only 2D "apparent" displacements are obtained, which introduces specific inaccuracies in the displacement-based quantitative indicators, in addition to usual inaccuracies pertaining to image processing. Of course these difficulties are also of concern when extracted displacements are to be used in an estimation setup, hence this justifies looking more closely into tagged-MR modalities to devise and analyze strategies to adequately employ them for estimation purposes. Among these strategies, the use of a prior step of processing performed to extract displacements will be considered, albeit other options may prove more effective. Moreover, even when resorting to extracted displacements, as much knowledge as possible should be incorporated into the estimation method as to the precise nature of such measurements, *e.g.* 2D apparent displacements.

The outline of the paper is as follows. In a first section we recall the main principles lying behind the design of observers. From this overview we will understand that they operate on a so-called *discrepancy* measure. Therefore the last part of this first section is dedicated to listing the potential information extracted from tagged-MR images and to proposing – for every type of data – such discrepancy measures. In the following section we carry out a complete analysis of the observer in a simplified but highly relevant linearized configuration. We then address the issue of space and time discretization of the observer in order to perform joint state and parameter estimation. Finally, in the last section we propose several numerical experiments in which we performed parameter identification based on synthetic measurements.

2 Position of the problem

2.1 Principles of observer design

The aim of an observer – also called state estimator – is to approximate a real trajectory, in spite of initial uncertainties, using the knowledge provided by the measurements obtained on this specific real trajectory. Let us consider a real trajectory $\mathrm{x}^{\mathrm{ref}}(t),\ t \in [0, +\infty)$, belonging to the so-called state space $\mathcal{X}$ and solution, in our case, of a – potentially infinite-dimensional – dynamical system summarized in the state form

$$\dot{\mathrm{x}} = \mathrm{A}(\mathrm{x}, t)$$

for a specific initial condition. We assume that this initial condition is uncertain with

$$\mathrm{x}^{\mathrm{ref}}(0) = \mathrm{x}_0 + \zeta_{\mathrm{x}},$$

where x_0 is a known *a priori* and ζ_{x} is the error on the initial condition. Any simulation of x – based on the discretization of the dynamical system – starting only from x_0 will be affected by errors that would in the best case decrease within the time constant of the physics of the problem. To circumvent this difficulty we should try to benefit from the measurements at our disposal on the trajectory. We denote by z these measurements – also called observations and belonging to the observation space $\mathcal{Z}$ – which are assumed to be generated by an observation operator H on the trajectory, up to additional measurements errors

$$\mathrm{z} = \mathrm{H}(\mathrm{x}^{\mathrm{ref}}, t) + \chi.$$

The observer denoted by $\widehat{\mathrm{x}}$ is a system that starts from the only part known in the initial condition – namely x_0 – and uses in time the available measurements z to generate a trajectory $\widehat{\mathrm{x}}(t),\ t \in [0, +\infty)$ that converges to $\mathrm{x}^{\mathrm{ref}}$ as fast as possible. Therefore, simulating $\widehat{\mathrm{x}}$ instead of x from x_0 gives a better approximation of the targeted system.

The main categories of observers we are dealing with here are observers computed by a feedback law based on the measurements

$$\begin{cases} \dot{\widehat{\mathrm{x}}} = \mathrm{A}(\mathrm{x}, t) + \mathrm{G}(\mathrm{z} - \mathrm{H}(\widehat{\mathrm{x}}, t)) \\ \widehat{\mathrm{x}}(0) = \mathrm{x}_0, \end{cases}$$

where G is called the gain operator. The dynamics of $\widehat{\mathrm{x}}$ is corrected when a discrepancy is observed between the actual measurements z and the measurement $\mathrm{H}(\widehat{\mathrm{x}})$ that would have ideally been produced by $\widehat{\mathrm{x}}$. This discrepancy

$$\mathrm{D}(\widehat{\mathrm{x}}, t) = \mathrm{z} - \mathrm{H}(\widehat{\mathrm{x}})$$

is also called innovation since it not only expresses an error of observation but also a source of improvement for the estimator. We point out that with certain types of measurements [Moireau et al., 2009] – as is typically the case with image-based observations – it is sometimes difficult to define an adequate observation operator but easier to directly compute a discrepancy. This is not a problem for the observer definition since only the discrepancy appears.

In a complete linear situation, namely when the dynamics is linear

$$\dot{\mathrm{x}} = \mathrm{A}(t)\mathrm{x} + \mathrm{R},$$

and when the observation operator is also linear

$$\mathrm{z} = \mathrm{H}(t)\mathrm{x}^{\mathrm{ref}} + \chi,$$

the most well-known gain operator is given by the Kalman gain [Bensoussan, 1971]. This operator is expressed as $\mathrm{G}(t) = \mathrm{P}(t)\mathrm{H}(t)^*$ where P is an operator following the Riccati evolution equation

$$\dot{\mathrm{P}} = \mathrm{AP} + \mathrm{PA}^* + \mathrm{PH}^*\mathrm{HP}, \quad \mathrm{P}(0) = \mathrm{P}_0,$$

and H^* is the adjoint of H. However, although P is computable for any dynamics operator A, it leads after spatial discretization to a discrete operator which is intractable in practice. This phenomenon has been known for decades and called “curse of dimensionnality” [Bensoussan, 1971, Simon, 2006]. Therefore, for specific dynamics other types of gains have been investigated as initiated by [Luenberger, 1971]. The idea based on the fact that for

$$\begin{cases} \dot{\widehat{\mathrm{x}}} = \mathrm{A}\widehat{\mathrm{x}} + \mathrm{R} + \mathrm{G}(z - \mathrm{H}\widehat{\mathrm{x}}) \\ \widehat{\mathrm{x}}(0) = \widehat{\mathrm{x}}_0, \end{cases} \tag{1}$$

such that when computing the estimation error

$$\widetilde{\mathrm{x}} = \mathrm{x}^{\mathrm{ref}} - \widehat{\mathrm{x}},$$

we get the following dynamics

$$\begin{cases} \dot{\widetilde{\mathrm{x}}} = (\mathrm{A} - \mathrm{GH})\widetilde{\mathrm{x}} - \mathrm{G}\chi \\ \widetilde{\mathrm{x}}(0) = \zeta_{\mathrm{x}}. \end{cases}$$

In fact, G has to be designed to stabilize the new dynamics operator A − GH so that the homogeneous system tends to 0, namely

$$\widetilde{\mathrm{x}}_{\chi=0} \to 0.$$

This also controls the error dynamics in the presence of noise in the measurements. This strategy is referred to as the Luenberger observer or *nudging*. For second-order hyperbolic systems like the elastodynamics system [Chapelle et al., 2009] have shown that a very simple choice of

$$G = \gamma\mathrm{H}^*, \tag{2}$$

with γ a scalar coefficient can be sufficient as we will recall in the next section. In fact the error dynamics is then given by

$$\begin{cases} \dot{\widetilde{\mathrm{x}}} = (\mathrm{A} - \gamma\mathrm{H}^*\mathrm{H})\widetilde{\mathrm{x}} - \gamma\mathrm{H}^*\chi \\ \widetilde{\mathrm{x}}(0) = \zeta_{\mathrm{x}}, \end{cases}$$

which can be controlled if $\mathrm{A} - \gamma\mathrm{H}^*\mathrm{H}$ is (exponentially) stable. More precisely, we directly have when $\chi = 0$ the following energy estimate on the error, assuming for the sake of simplicity – but useful in the practical cases of the present article – that A is skew-adjoint we get

$$\|\widetilde{\mathrm{x}}(t)\|^2_{\mathcal{X}} - \|\widetilde{\mathrm{x}}(0)\|^2_{\mathcal{X}} \leq -2\gamma \int_0^t \|\mathrm{H}\widetilde{x}(s)\|^2_{\mathcal{Z}} \,\mathrm{d}s$$

showing that the error is at least non-increasing. Moreover we recall the following result when A is a skew adjoint operator and H bounded – also sufficient in the present article.

Theorem 1
Let A be a time-independent skew-adjoint operator generating a group and $\mathrm{H} \in \mathcal{L}(\mathcal{X}, \mathcal{Z})$*. The error system* $\widetilde{\mathrm{x}}$ *of dynamics*

$$\dot{\widetilde{\mathrm{x}}} = (\mathrm{A} - \gamma \mathrm{H}^* \mathrm{H}) \widetilde{\mathrm{x}}$$

is exponentially stable if the following observability condition

$$\exists (C, T) \,|\, \forall \mathrm{x} \textit{ solution of } \dot{\mathrm{x}} = \mathrm{A}\mathrm{x}$$
$$\int_0^T \|\mathrm{H}\mathrm{x}(s)\|_{\mathcal{Z}}^2 \, \mathrm{d}s \geq C \, \|\mathrm{x}(0)\|_{\mathcal{X}}^2 , \tag{3}$$

is satisfied.

Proof. This result is rather classical and can be deduced for example from stabilizability-controllability equivalence [Liu, 1997]. It is also possible to make a direct proof. We recall first the direct energy estimate

$$\forall s, \quad \frac{1}{2} \frac{\mathrm{d}}{\mathrm{d}t} \|\widetilde{\mathrm{x}}(s)\|_{\mathcal{X}}^2 \leq -\gamma \, \|\mathrm{H}\widetilde{\mathrm{x}}(s)\|_{\mathcal{Z}}^2 ,$$

giving

$$\|\widetilde{\mathrm{x}}(t+T)\|_{\mathcal{X}}^2 - \|\widetilde{\mathrm{x}}(t)\|_{\mathcal{X}}^2 \leq -2\gamma \int_t^{t+T} \|\mathrm{H}\widetilde{\mathrm{x}}(s)\|_{\mathcal{Z}}^2 \, \mathrm{d}s.$$

Therefore if we can verify that there exists a time T and a constant C_s such that

$$\|\widetilde{\mathrm{x}}(t)\|_{\mathcal{X}}^2 \leq C_s \int_t^{t+T} \|\mathrm{H}\widetilde{\mathrm{x}}(s)\|_{\mathcal{Z}}^2 \, \mathrm{d}s, \tag{4}$$

we will have

$$\|\widetilde{\mathrm{x}}(t+T)\|_{\mathcal{X}}^2 \leq (1 - \frac{2}{C_s}\gamma) \, \|\widetilde{\mathrm{x}}(t)\|_{\mathcal{X}}^2 ,$$

ensuring the exponential stability. To prove (4), we decompose $\widetilde{\mathrm{x}} = \phi + \eta$ where

$$\begin{cases} \dot{\phi} = \mathrm{A}\phi \\ \phi(t) = \widetilde{\mathrm{x}}(t), \end{cases}$$

and

$$\begin{cases} \dot{\eta} = \mathrm{A}\eta - \mathrm{H}^*\mathrm{H}\widetilde{\mathrm{x}} \\ \eta(t) = 0. \end{cases}$$

The first system satisfies the observability condition (3). This condition can be considered between t and $t+T$ since A is a skew-adjoint operator generating a group. Hence there exists a time T and a constant C_o such that

$$\|\phi(t)\|_{\mathcal{X}}^2 \leq C_o \int_t^{t+T} \|\mathrm{H}\phi(s)\|_{\mathcal{Z}}^2 \, \mathrm{d}s,$$

implying that

$$\|\widetilde{\mathrm{x}}(t)\|_{\mathcal{X}}^2 \leq 2C_o \int_t^{t+T} \|\mathrm{H}\widetilde{\mathrm{x}}(s)\|_{\mathcal{Z}}^2 \, \mathrm{d}s + 2C_o \int_t^{t+T} \|\mathrm{H}\eta(s)\|_{\mathcal{Z}}^2 \, \mathrm{d}s.$$

Concerning now the dynamics of η, we can verify, using Gronwall Lemma that

$$\int_t^{t+T} \|\mathrm{H}\eta(s)\|_{\mathcal{Z}}^2 \, \mathrm{d}s \leq T \, \|\mathrm{H}\|_{\mathcal{L}(\mathcal{Z},\mathcal{X})}^4 \, e^T \int_t^{t+T} \|\mathrm{H}\widetilde{\mathrm{x}}(s)\|_{\mathcal{Z}}^2 \, \mathrm{d}s,$$

as soon as H is bounded. Therefore (4) is satisfied, ensuring the exponential stability of the error system $\widetilde{\mathrm{x}}$. ■

In a nonlinear configuration, fewer theoretical results are available. However, an accepted strategy is to replace in the gain the use of the adjoint of H by the adjoint of the tangent of the observer $\mathrm{dH}(\widehat{\mathrm{x}})^*$ around the estimated trajectory. Therefore for small errors we can expect that the linearized error around the trajectory is stable. In fact we have after linearization of the error

$$\begin{cases} \dot{\widetilde{\delta \mathrm{x}}} = (\mathrm{dA} - \gamma \mathrm{dH}^* \mathrm{dH})\widetilde{\delta \mathrm{x}} - \gamma \mathrm{dH}^* \chi \\ \widetilde{\delta \mathrm{x}}(0) = \zeta_{\mathrm{x}}, \end{cases}$$

of which we could expect a stabilization property [Khalil, 1992, Lohmiller and Slotine, 2005]. In the case where only a discrepancy operator is available, we only have to replace dH by $-\mathrm{dD}$ since $\mathrm{D}(\mathrm{x}, t)$ fundamentally extends the quantity $\mathrm{z} - \mathrm{H}(\mathrm{x}, t)$.

One last fundamental aspect that we need to describe in this introduction to observer design is how parameter estimation – also called identification – can be carried out. Let us denote by θ the uncertain parameter that we have to identify. Note that θ may be a vector of components or even a field. The main idea is to introduce an augmented state vector and dynamics operator

$$^\flat\mathrm{x} = \begin{pmatrix} \mathrm{x} \\ \theta \end{pmatrix}, \quad {}^\flat\mathrm{A} = \begin{pmatrix} \mathrm{A}(\mathrm{x}, \theta) \\ 0 \end{pmatrix},$$

such that we still have ${}^\flat\dot{\mathrm{x}} = {}^\flat\mathrm{A}({}^\flat\mathrm{x})$. Then, a Kalman observer can be directly defined on this augmented model leading to a covariance operator and gain

$$\mathrm{P} = \begin{pmatrix} \mathrm{P}_{\mathrm{xx}} & \mathrm{P}_{\mathrm{x}\theta} \\ \mathrm{P}_{\theta\mathrm{x}} & \mathrm{P}_{\theta\theta} \end{pmatrix}, \quad \mathrm{G} = \begin{pmatrix} \mathrm{G}_{\mathrm{x}} \\ \mathrm{G}_{\theta} \end{pmatrix}.$$

However, it may be more intricate to define a simple Luenberger observer for the augmented system as the observations are frequently linked to the parameters through the state only. Therefore, there is little hope that $\gamma\mathrm{H}^*$ will lead to an efficient gain. An alternative strategy was proposed by [Moireau et al., 2008] as a generalization of the adaptive filtering strategy of [Zhang and Clavel, 2001, Pham, 2001]. The idea is to keep the Luenberger observer on the state while using a Kalman-like gain on the parameters. This strategy can be very effective in practice since it is common to consider a parameter described much more coarsely than the state discretization, thus alleviating the curse of dimensionality associated with optimal filtering. The complete observer reads

$$\begin{cases} \dot{\widehat{\mathrm{x}}} = \mathrm{A}(\widehat{\mathrm{x}}, t) + \gamma \mathrm{H}^*(\mathrm{z} - \mathrm{H}\widehat{\mathrm{x}}) + \mathrm{L}\dot{\theta}, \quad \widehat{\mathrm{x}}(0) = \mathrm{x}_0 \\ \dot{\theta} = \mathrm{U}^{-1}\mathrm{L}^*\mathrm{H}^*(\mathrm{z} - \mathrm{H}\mathrm{x}), \quad \widehat{\theta}(0) = \theta_0 \\ \dot{\mathrm{L}} = \mathrm{d}_{\mathrm{x}}\mathrm{A}\mathrm{L} + \mathrm{d}_{\theta}\mathrm{A}, \quad \mathrm{L}(0) = 0 \\ \dot{\mathrm{U}} = \mathrm{L}^*\mathrm{H}^*\mathrm{H}\mathrm{L}, \quad \mathrm{U}(0) = \mathrm{P}_{\theta\theta}(0), \end{cases} \tag{5}$$

where U is a reduced covariance operator on the parameter space and L is an extension operator from the parameter space to the state space. We see in the dynamics (5) that the state gain is the combination of the Luenberger gain and a gain directly inferred from the parameter filter so that

$$\mathrm{G}_{\mathrm{x}} = (\gamma \mathbb{1} + \mathrm{L}\mathrm{U}^{-1}\mathrm{L}^*)\mathrm{H}^*.$$

In [Moireau et al., 2008], the convergence of the complete observer was also established – at least in linear configuration – based on the idea that the Luenberger state observer reduces the uncertainty to the parameter space where the optimal filter operates. In this sense, this strategy also unified the data assimilation approach [Pham, 2001] and the adaptive filtering strategy [Zhang and Clavel, 2001] as presented in [Moireau et al., 2008]. Moreover, the effectiveness of this approach has already been applied to the biomechanical identification problem in [Moireau et al., 2009, Imperiale et al., 2011, Chabiniok et al., 2012].

2.2 Example of model formulation

We consider here a model of heart contraction involving a large displacement solid formulation coupled to an electrophysiological model. We rely for the structure on the active multi-scale formulation presented in [Sainte-Marie et al., 2006] and summarized by the rheological model presented in Figure 1. We combine an active component inspired from Huxley's crossbridge binding-unbinding model in the fiber direction and a visco-hyperelastic 3D passive model. The active component is then triggered by a command directly linked to the transmembrane potential possibly modeled by an electrophysiological formulation [Sachse, 2004] in the solid domain and assumed as given in the present article. Furthermore, we suppose that the heart wall sustains a uniform intra-cavity pressure given as a function of time or modeled by a lumped parameter system of ordinary differential equations also known as *Windkessel* model.

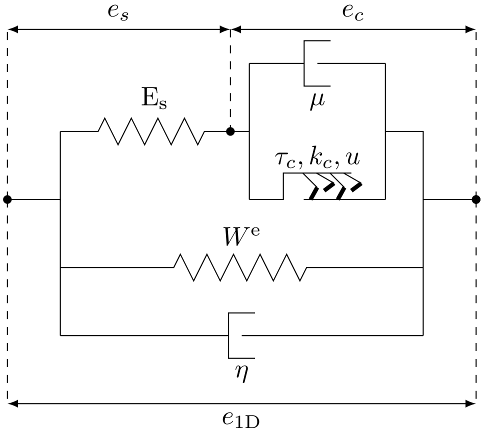

Figure 1: Rheological model of the heart material.

We now introduce some notations in order to summarize the model equations. We denote the heart domain by $\Omega(t)$ at any time t. This domain is the image of a reference configuration Ω_0 through the solid deformation mapping $\underline{\varphi}$

$$\underline{\varphi}\left|\begin{array}{l}\Omega_0\times[0,T]\longrightarrow\Omega(t),\\ \qquad(\underline{\xi},t)\longmapsto\underline{x}=\underline{\varphi}(\underline{\xi},t)=\underline{\xi}+\underline{y}(\underline{\xi},t),\end{array}\right.$$

where $\underline{y}$ denotes the solid displacement, hence the solid velocity is given by $\underline{v}=\underline{\dot{y}}$. We can then define the necessary kinematics quantities. The deformation gradient $\underline{\underline{F}}$ is given by

$$\underline{\underline{F}}(\xi,t)=\underline{\underline{\nabla}}_{\xi}\,\underline{\varphi}=\underline{\underline{\mathbb{1}}}+\underline{\underline{\nabla}}_{\xi}\,\underline{y},$$

such that the deformed volume is given by $J\,\mathrm{d}\Omega$ where $J=\det\underline{\underline{F}}$ and $\mathrm{d}\Omega$ is the volume measure (here in the reference configuration). In the same way, a change of area is given by $J\underline{\underline{F}}^{-\intercal}\cdot\underline{\mathrm{d}\Gamma}$. Furthermore, we introduce the right Cauchy-Green deformation tensor $\underline{\underline{C}}=\underline{\underline{F}}^{\intercal}\cdot\underline{\underline{F}}$, also called "deformed metric tensor". We finally recall that the Green-Lagrange tensor denoted by $\underline{\underline{e}}$ is defined by

$$\underline{\underline{e}}=\frac{1}{2}(\underline{\underline{C}}-\underline{\underline{\mathbb{1}}})=\frac{1}{2}\Big(\underline{\underline{\nabla}}_{\xi}\,\underline{y}+(\underline{\underline{\nabla}}_{\xi}\,\underline{y})^{\intercal}+(\underline{\underline{\nabla}}_{\xi}\,\underline{y})^{\intercal}\cdot\underline{\underline{\nabla}}_{\xi}\,\underline{y}\Big).$$

Regarding the mechanical quantities notation, we denote by ρ the heart mass per unit volume and $\underline{\underline{\sigma}}$ the Cauchy stress tensor associated with the deformed configuration. In the reference configuration, we then define the associated first and second Piola stress tensors $\underline{\underline{T}}=J\underline{\underline{\sigma}}\cdot\underline{\underline{F}}^{-\intercal}$

and $\underline{\underline{\Sigma}} = \underline{\underline{F}}^{-1} \cdot \underline{\underline{T}} = J\underline{\underline{F}}^{-1} \cdot \underline{\underline{\sigma}} \cdot \underline{\underline{F}}^{-\intercal}$. The constitutive law can be considered as a nonlinear rheological combination of a passive part and an active part. The passive part is described by a hyperelastic law of potential $\mathcal{W}$ and a viscous component chosen proportional to the strain rate $\underline{\underline{\dot{e}}}$

$$\underline{\underline{\Sigma}}(\underline{\underline{e}}, \underline{\underline{\dot{e}}}) = \frac{\partial \mathcal{W}}{\partial \underline{\underline{e}}}(\underline{\underline{e}}) + \eta_s \underline{\underline{\dot{e}}}.$$

As far as the expression of the potential $\mathcal{W}$ is concerned, most of the recent developments, see [Dokos et al., 2002, Holzapfel and Ogden, 2009, Göktepe et al., 2011] for example, tend to consider the passive myocardium to be orthotropic – using the fibers and sheets coordinate system. In [Dokos et al., 2002] this statement is based on observing the heart wall response to simple shear experiments on three orthogonal planes, see also [Holzapfel and Ogden, 2009]. Moreover several experiments – see [Nash and Hunter, 2000, Costa et al., 2001, Dokos et al., 2002] or [Holzapfel and Ogden, 2009, Göktepe et al., 2011] – aiming at fitting strain measurements showed that an exponential constitutive law is well-suited to represent the heart material nonlinearities. In our case we choose to define the passive elastic potential as transverse isotropic of exponential type. We justify our approach in two manners: the first one being that even though we do not consider a complete orthotropic model, studies in [Guccione et al., 1995] or in [Vetter and McCulloch, 2000] have shown that a transverse isotropic constitutive law based only on the fiber direction adequately reproduces measured epicardial strain; the second one is that in practice, the characterization of sheets direction can become really complex since very little physiological data are available. Hence, we define the hyperelastic potential as an exponential potential, namely

$$\mathcal{W} = C_0 \exp\big(C_1(J_1 - 3)^2\big) + C_2 \exp\big(C_3(J_4 - 1)^2\big) + \kappa(J - 1) - \kappa \ln(J),$$

where J_1 is the standard first reduced invariant , J_4 is the reduced invariant accounting for the anisotropy of the material in the fiber direction $\underline{\tau}$, namely

$$J_1 = \mathrm{tr}(\underline{\underline{C}}), \quad J_4 = \underline{\tau} \cdot \underline{\underline{C}} \cdot \underline{\tau},$$

and κ is the bulk coefficient.

For the active part we introduce 3 internal variables e_c, k_c, τ_c [Chapelle et al., 2012d], respectively the active strain, the active stiffness and the associated active stress, along the fiber direction. These 3 internal variables rely on a chemically-controlled constitutive law describing myofibre mechanics [Bestel et al., 2001, Huxley, 1957, ?].

$$\begin{cases} \dot{k}_c = -(|u| + \alpha\,|\dot{e}_c|)k_c + n_0 k_0\,|u|_+ & \text{in } \Omega_0 \\ \dot{\tau}_c = -(|u| + \alpha\,|\dot{e}_c|)\tau_c + \dot{e}_c k_c + n_0 \sigma_0\,|u|_+ & \text{in } \Omega_0, \end{cases} \tag{6}$$

where α, k_0, σ_0 are physiological parameters, u is an input term directly related to the calcium concentration *i.e.* to the electrical activity of the heart, while n_0 denotes a prescribed function of e_c – most notably – to represent length-dependence effects and possibly also of other external quantities *e.g.* perfusion related. Then, by rheological rules, we can build

$$\sigma_{\mathrm{1D}} = \frac{1 + 2e_c}{1 + 2\underline{\tau} \cdot \underline{\underline{e}} \cdot \underline{\tau}}(\tau_c + \mu \dot{e}_c),$$

so that

$$\underline{\underline{\Sigma}}(\underline{\underline{e}}, e_c, k_c, \tau_c) = \frac{\partial \mathcal{W}}{\partial \underline{\underline{e}}}(\underline{\underline{e}}) + \eta_s \underline{\underline{\dot{e}}} + \sigma_{\mathrm{1D}}(e_c, k_c, \tau_c)\underline{\tau} \otimes \underline{\tau}.$$

Concerning the boundary conditions, following [Chabiniok et al., 2012] we model the external organs by visco-elastic boundary conditions on a subpart of the boundary which in reference configuration gives

$$\underline{\underline{T}} \cdot \underline{n} = k_s \underline{y} + c_s \underline{v} \text{ on } \Gamma_n(t).$$

Regarding the pressure load, we consider a uniform following pressure on the left and right endocardium easily written in deformed configuration

$$\underline{\underline{\sigma}} \cdot \underline{n}_t = -p_{v,i} \underline{n}_t \text{ on } \Gamma_{n,i}(t), i = \{1, 2\}.$$

Finally the complete mechanical model reads

$$\begin{cases} \dot{\underline{y}} = \underline{v}, & \text{in } \Omega_0 \\ \rho \dot{\underline{v}} - \underline{\operatorname{div}}(\underline{\underline{T}}) = 0, & \text{in } \Omega_0 \\ \underline{\underline{T}} \cdot \underline{n} = k_s \underline{y} + c_s \underline{v} & \text{on } \Gamma_n \\ \underline{\underline{T}} \cdot \underline{n} = -J p_{v,i} \underline{\underline{F}}^{-\intercal} \cdot \underline{n} & \text{on } \Gamma_{c,i} \\ \underline{\underline{T}} \cdot \underline{n} = 0 & \text{on } \partial\Omega_0 \backslash ((\cup_i \Gamma_{c,i}) \cap \Gamma_n) \end{cases} \tag{7}$$

and this, together with the internal variable dynamics (6), constitutes a formal definition of the dynamical operator denoted by A in our above summarized description. A complete mathematical analysis of this type of system contains some open issues – in particular due to the severe nonlinearities considered [Ciarlet, 1988, Le Tallec, 1994]– albeit we will present analyses of simplified versions of the model under various assumptions below, see in particular Section 3.

2.3 Available data from imaging modalities

For the complete understanding of the physiological condition of a patient heart, physicians usually seek for standard characteristics such as the mass, the volume or the ejection fraction. Additionally intra-myocardial deformations are of great importance to assess the cardiac function. Even though the first three features can be obtained using various type of medical image modalities – *e.g.* cine-MRI – the latter is more intricate to capture by non-invasive procedures.

Magnetic resonance imaging with tissue marking – referred to as tagged-MRI – was introduced in the late 80's [Zerhouni et al., 1988]. By non-invasively imprinting a pattern in the acquired images – through specific magnetization of the tissue – this type of modality aims at revealing the myocardial deformations. Various types of tagged image modalities have arisen since its conception. They differ by the orientation, the temporal persistence or even the shape of the pattern. For instance, the SPAcial Modulation of Magnetization (SPAMM) modality – introduced by [Axel and Dougherty, 1989] – generates a grid-like pattern, whereas the first tagging images included a radial pattern – see *e.g.* [Guttman et al., 1994]. The temporal resistance of the pattern in SPAMM images covers the complete heart systole. Figure 2(a) is an example of a SPAMM image (in short axis view) at marking time. We observe the regular pattern within the image domain. Figure 2(b) shows the same image slice obtained during heart contraction. In this last image we observe the deformation of the originally regular pattern subject to the material displacements.

Even though SPAMM images are the most popular tagged-MRI, other modalities exist. For example, we can cite the DANTE sequence – initially introduced by [Mosher and Smith, 1990] – which provides a thinner tag grid pattern. Another example is the so-called CSPAMM modality that aims at decreasing the tag pattern fading using two sequences of SPAMM images – see [Fischer et al., 1993].

Combinations of 2D images are historically the first type of tagged image modalities that were studied. However they naturally suffer from through-the-plane motion. To circumvent this limitation, later works have lead to the production of complete three-dimensional tagged MRI – see [Ryf et al., 2002]. 3D tagging (3D SPAMM) is an imaging modality of major interest since it could provide truly three-dimensional information on the heart strain.

From the most direct type of data to more complex observations, our work is dedicated to the design of observers based on 2D or 3D SPAMM images. Such an endeavor requires – see Section 2.1 – to be able to compute the discrepancies between the potentially pre-processed data and the model. First, we assume that this image processing step leads to the reconstruction of the fully three dimensional deformation of the heart – from 3D SPAMM for instance [Ryf et al., 2002] or from the collection of various 2D SPAMM [Kuijerm et al., 2000]. In this context, following [Moireau et al., 2009] we propose an efficient way to assimilate this direct displacement feedback. However, obtaining these data sets is a demanding process and we further consider three distinct situations aiming at gradually decreasing our demands on this prior processing step. To start with, we propose a discrepancy measure based on the assumption that we are able to reconstruct the tag planes [Kerwin and Prince, 1998, Amini et al., 2001] fitting the tag pattern. In the case of bi-dimensional images, obtaining these surfaces may require a complex interpolation scheme in the image transverse direction. Therefore, in a second step, we consider the case of tag grids [Amini et al., 1998] lying exclusively within the image planes. In a final step we propose means of comparison between the model and 2D apparent displacements [Osman and Prince, 1998, Ledesma-Carbayo et al., 2006] or [Bruurmijn et al., 2013].

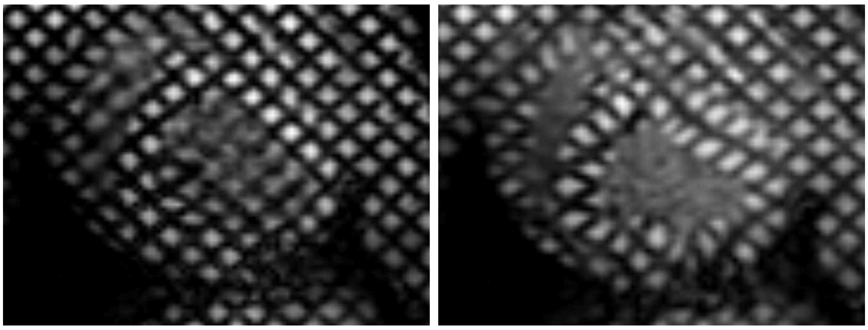

(a) 2D slice at marking time (b) 2D slice during systole

Figure 2: Example of SPAMM images in short axis view.

2.3.1 Extracted 3D displacements from 3D grids

By constructing the tagging pattern in three directions, 3D SPAMM [Ryf et al., 2002] is a powerful image modality that potentially leads to a reconstruction of the complete three dimensional heart motion. For instance authors in [Rutz et al., 2008] propose to adapt the HARmonic Phase (HARP) method – which performs tag patterns tracking by analyzing the frequency contents of the image – to 3D images in order to extract these data. However, even though recent works [Stoeck et al., 2012] have shown that the acquisition time of 3D SPAMM can be reduced – typically by signal under-sampling – this modality suffers from long acquisition time and potentially induces multiple breath-holds. Another technique to extract three dimensional displacements of the heart from SPAMM images is to acquire two orthogonal sets of 2D images in short and long axis – see for instance [O'Dell et al., 1995, Kuijerm et al., 2000] or [Pan et al., 2005]. IT should be noted that this process is likely to suffer from slice misregistration and through-the-plane motion.

Having in mind these image modalities and image processing methods, it seems reasonable to expect that the observations take the form of the complete heart displacement with a resolution corresponding to the tag pattern spacing. In order to obtain a fully (discrete) displacement feedback, the final step is to consider a spatial interpolation scheme between the tag grid and the model mesh. This particular issue will be addressed in Section 4.1.

Nonetheless, in a continuous formalism, we can assume that we have at our disposal some measurements of the displacement in a subdomain ω_0 of the geometry. We introduce the observation operator H such that the measurements are $\mathrm{z} = \mathrm{Hx} + \text{noise}$ with

$$\mathrm{H} : \left| \begin{array}{l} \mathcal{X}^y \to \mathcal{Z} \\ \underline{y} \mapsto \mathbb{1}_{\omega_0} \underline{y}. \end{array} \right.$$

We then need to specify the observation space $\mathcal{Z}$. One possible choice is to consider $\mathcal{L}^2(\omega_0)^3$. However, this space does not characterize the maximum amount of information we have on the system since z comes from a displacement in $\mathcal{H}^1(\Omega_0)^3$. We should rather consider $\mathcal{Z} = \mathcal{H}^1(\omega_0)^3$ and we will see in Section 3 a more complete mathematical justification of this choice. Following [Moireau et al., 2009], we then introduce a convenient way to define a norm in this space. Let us consider the following extension

$$\begin{cases} -\underline{\mathrm{div}}(\underline{\underline{\sigma}}^{\mathrm{lin}}(\underline{\psi})) = 0 & \text{in } \Omega_0 \\ \underline{\psi} = \underline{\varphi} & \text{in } \omega_0 \\ \underline{\underline{\sigma}}^{\mathrm{lin}} \cdot \underline{n} = k_s \underline{\psi} & \text{on } \Gamma_n \\ \underline{\underline{\sigma}}^{\mathrm{lin}} \cdot \underline{n} = 0 & \text{on } \partial\Omega_0 \backslash \cap \Gamma_n, \end{cases} \tag{8}$$

where $\underline{\underline{\sigma}}^{\mathrm{lin}}$ denotes the stress tensor given by linearized isotropic elasticity – see more details in Section 3 below – and with adequate boundary conditions on $\partial\Omega_0$ obtained from (7). We then denote

$$\underline{\psi} = \mathrm{Ext}_{\omega_0}(\underline{\varphi}).$$

Note that an equivalent variational characterization of the extension is given by

$$\forall \underline{v}^\sharp \text{ s.t. } \underline{v}^\sharp_{|\omega_0} = 0, \quad (\mathrm{Ext}_{\omega_0}(\underline{\varphi}), \underline{v}^\sharp)_{\mathcal{E}_0} = 0, \tag{9}$$

where the energy dot-product is here defined by

$$(\underline{y}_1, \underline{y}_2)_{\mathcal{E}_0} = \int_{\Omega_0} \underline{\underline{\sigma}}^{\mathrm{lin}}(\underline{y}_1) : \underline{\underline{\varepsilon}}(\underline{y}_2)\,\mathrm{d}\Omega + \int_{\Gamma_n} k_s\, \underline{y}_1 \cdot \underline{y}_2\,\mathrm{d}\Gamma = \int_{\Omega_0} \underline{\underline{\varepsilon}}(\underline{y}_1) : \underline{\underline{\underline{\underline{A}}}} : \underline{\underline{\varepsilon}}(\underline{y}_2)\,\mathrm{d}\Omega + \int_{\Gamma_n} k_s\, \underline{y}_1 \cdot \underline{y}_2\,\mathrm{d}\Gamma.$$

We can prove – see Section 3 for a similar dot product $(\cdot,\cdot)_{\mathcal{E}_0}$– that $(\mathrm{Ext}_{\omega_0}(\underline{\varphi}), \mathrm{Ext}_{\omega_0}(\underline{\varphi}))^{\frac{1}{2}}_{\mathcal{E}_0}$ is a norm in $\mathcal{Z} = \mathcal{H}^1(\omega_0)^3$. It is now possible to define the adjoint of the observation operator that is needed in (2). We find in [Moireau et al., 2009] and Section 3 that H^* is given by

$$\mathrm{H}^* : \left| \begin{array}{l} \mathcal{Z} \to \mathcal{X} \\ \mathrm{z} \mapsto \mathrm{Ext}_{\omega_0}(\mathrm{z}). \end{array} \right.$$

Therefore we can define in a continuous formalism the observer introduced in [Moireau et al., 2009] corresponding to (2) with $G = \gamma \mathrm{H}^*$. In strong formulation, we have

$$\begin{cases} \dot{\underline{\widehat{y}}} = \underline{\widehat{v}} + \gamma \mathrm{Ext}_{\omega_0}(\mathrm{z} - \mathbb{1}_{\omega_0}\underline{\widehat{y}}), & \text{in } \Omega_0 \\ \rho\dot{\underline{\widehat{v}}} - \underline{\mathrm{div}}(\underline{\underline{\widehat{T}}}) = 0, & \text{in } \Omega_0 \\ \underline{\underline{\widehat{T}}} \cdot \underline{n} = k_s\underline{\widehat{y}} + c_s\underline{\widehat{v}} & \text{on } \Gamma_n \\ \underline{\underline{\widehat{T}}} \cdot \underline{n} = -Jp_{v,i}\underline{\underline{F}}^{-\intercal} \cdot \underline{n} & \text{on } \Gamma_{c,i} \\ \underline{\underline{\widehat{T}}} \cdot \underline{n} = 0 & \text{on } \partial\Omega_0 \backslash ((\cup_i \Gamma_{c,i}) \cap \Gamma_n). \end{cases} \tag{10}$$

As an illustrative example of analysis for this type of strategy, we will establish an energy estimate of the estimation error

$$\widetilde{\mathrm{x}} = \begin{pmatrix} \underline{\widetilde{y}} \\ \\ \underline{\widetilde{v}} \end{pmatrix} = \begin{pmatrix} \underline{y} - \underline{\widehat{y}} \\ \\ \underline{v} - \underline{\widehat{v}} \end{pmatrix}$$

in the simplified case of linearized elasticity and without activation internal variables, namely, with the constitutive law

$$\underline{\underline{\sigma}} = \underline{\underline{\sigma}}^{\mathrm{lin}}(\underline{y}) + \eta_s \underline{\underline{\varepsilon}}(\underline{v}),$$

where $\underline{\underline{\varepsilon}}$ denotes the usual linearized strain tensor. The error then satisfies the following weak formulation

$$\int_{\Omega_0} \rho\, \dot{\underline{\widetilde{v}}} \cdot \underline{v}^\sharp \,\mathrm{d}\Omega + (\underline{\widetilde{y}}, \underline{v}^\sharp)_{\mathcal{E}_0} + \int_{\Omega_0} \eta_s\, \underline{\underline{\varepsilon}}(\underline{\widetilde{v}}) : \underline{\underline{\varepsilon}}(\underline{v}^\sharp) \,\mathrm{d}\Omega + \int_{\Gamma_n} c_s\, \underline{\widetilde{v}} \cdot \underline{v}^\sharp \,\mathrm{d}\Gamma = 0, \quad \forall \underline{v}^\sharp,$$

with the additional observer-based relation

$$\dot{\underline{\widetilde{y}}} = \underline{\widetilde{v}} - \gamma\, \mathrm{Ext}_{\omega_0}(\mathbb{1}_{\omega_0}\underline{\widetilde{y}}),$$

assuming zero measurement error to fix the ideas. Weighing the latter relation by $\underline{\widetilde{y}}$ and using the energy dot-product yields

$$(\underline{\widetilde{v}}, \underline{\widetilde{y}})_{\mathcal{E}_0} = \frac{\mathrm{d}}{\mathrm{d}t}\Big(\frac{1}{2}\left\|\underline{\widetilde{y}}\right\|^2_{\mathcal{E}_0}\Big) + \gamma(\mathrm{Ext}_{\omega_0}(\mathbb{1}_{\omega_0}\underline{\widetilde{y}}), \underline{\widetilde{y}})_{\mathcal{E}_0} = \frac{\mathrm{d}}{\mathrm{d}t}\Big(\frac{1}{2}\left\|\underline{\widetilde{y}}\right\|^2_{\mathcal{E}_0}\Big) + \gamma\left\|\mathrm{Ext}_{\omega_0}(\mathbb{1}_{\omega_0}\underline{\widetilde{y}})\right\|^2_{\mathcal{E}_0},$$

where we have used the orthogonality property (9). We can now substitute this expression in the above variational formulation applied with the test function $\underline{v}^\sharp = \underline{\widetilde{v}}$, which gives

$$\frac{\mathrm{d}}{\mathrm{d}t}\Big(\frac{1}{2}\left\|\underline{\widetilde{v}}\right\|^2_{\mathcal{K}} + \frac{1}{2}\left\|\underline{\widetilde{y}}\right\|^2_{\mathcal{E}_0}\Big) = -\int_{\Omega_0} \eta_s\, \underline{\underline{\varepsilon}}(\underline{\widetilde{v}}) : \underline{\underline{\varepsilon}}(\underline{\widetilde{v}}) \,\mathrm{d}\Omega - \int_{\Gamma_n} c_s\, \underline{\widetilde{v}}^{\,2} \,\mathrm{d}\Gamma - \gamma\left\|\mathrm{Ext}_{\omega_0}(\mathbb{1}_{\omega_0}\underline{\widetilde{y}})\right\|^2_{\mathcal{E}_0}, \tag{11}$$

where

$$\frac{1}{2}\left\|\underline{\widetilde{v}}\right\|^2_{\mathcal{K}} = \frac{1}{2}\int_{\Omega_0} \rho\, \underline{\widetilde{v}}^{\,2} \,\mathrm{d}\Omega,$$

denotes the kinetic energy of the error. We can see that the total energy of the error – namely, elastic energy of the deformation plus kinetic energy of the velocity – decreases at all times, and at a faster rate than with the natural dissipation of the system, due to the observer correction term.

2.3.2 Tagged-MR planes

The limitations of 3D SPAMM that we have mentioned previously make this imaging modality difficult to use in a clinical routine. In most clinical cases only bi-dimensional tagged MRI are available. These data sets can be treated plane by plane to extract apparent displacements. In literature we can distinguish mainly two ways of carrying out this task. A first manner is to track the tag pattern directly in the image plane. For instance authors in [Prince and McVeigh, 1992, Dougherty et al., 1999] consider an optical flow methodology that takes into account the fading of the tag pattern during the acquisition process. Another solution proposed by [Ledesma-Carbayo et al., 2006] is to perform non-rigid image registration. A second family of methods consists in working in the frequency domain. The most popular method is the HARP technique– see [Osman et al., 1999, Osman and Prince, 2000] – which tracks the phase of the tag pattern. Following this trend, recent works proposed by authors in [Garcia-Barnés et al., 2008, Bruurmijn et al., 2013] use the Gabor filter to obtain a better estimation of local deformations in late systole – which appears to be a slight limitation of the HARP methodology.

Prior to proposing a corresponding observer for this type of data, we assume that a first step of image processing leads to the construction of geometrical objects taking the form of tag grids or tag planes and following in time the deformations of the tag patterns – see [Amini et al., 1998, Kerwin and Prince, 1998, Amini et al., 2001] for an example of tag planes construction and [Amini et al., 1992, Radeva et al., 1996, Amini et al., 1998] for tag grids.

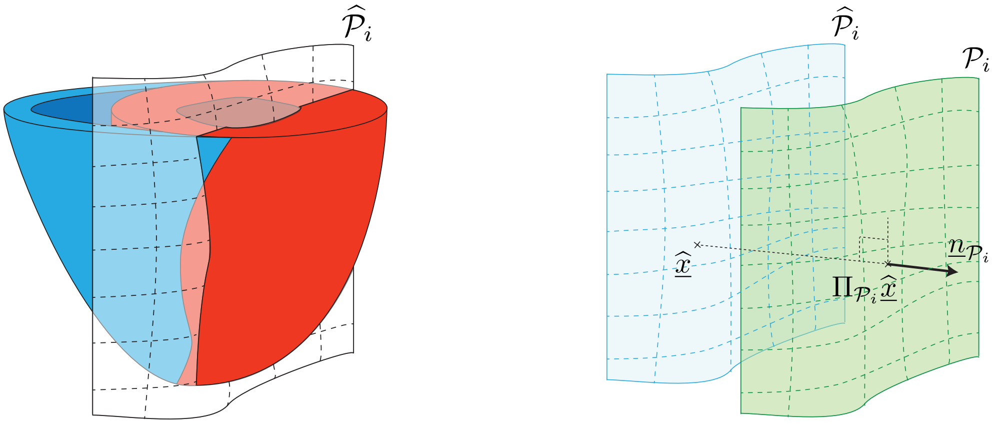

(a) Estimated tag planes

(b) Signed distance between estimated and observed tag planes

Figure 3: Illustration of tag planes discrepancy measure.

For the definition of the spaces and norms associated with the discrepancy measures needed in this section, following [?] we will use an *extension* operator mapping data provided on a surface to the whole solid domain. More precisely, we denote by $\mathcal{S}_0$ a surface embedded in the reference domain Ω_0 and $\underline{e}$ a vector field given on $\mathcal{S}_0$, with $(\underline{e}^1_\perp, \underline{e}^2_\perp)$ defined so that $(\underline{e}^1_\perp, \underline{e}^2_\perp, \underline{e})$ gives an orthonormal basis at any point in $\mathcal{S}_0$. The extension $\underline{\psi} = \mathrm{Ext}_{\mathcal{S}_0}(\underline{e}\ ;\ \varphi)$ from $\mathcal{S}_0$ of the scalar field φ in the direction $\underline{e}$ is defined by

$$\begin{cases} -\underline{\mathrm{div}}(\underline{\underline{\sigma}}^{\mathrm{lin}}(\underline{\psi})) = 0 & \text{in } \Omega_0 \\ \underline{\psi} \cdot \underline{e} = \varphi & \text{on } \mathcal{S}_0 \\ (\underline{\underline{\sigma}}^{\mathrm{lin}} \cdot \underline{n}) \cdot \underline{e}^1_\perp = (\underline{\underline{\sigma}}^{\mathrm{lin}} \cdot \underline{n}) \cdot \underline{e}^2_\perp = 0 & \text{on } \mathcal{S}_0. \end{cases} \tag{12}$$

Note that here the equivalent variational characterization of the extension is given by

$$\forall \underline{v}^\sharp \text{ s.t. } \underline{v}^\sharp\cdot\underline{n}=0 \text{ on } \mathcal{S}_0, \quad (\mathrm{Ext}_{\mathcal{S}_0}(\underline{e}\ ;\ \varphi),\underline{v}^\sharp)_{\mathcal{E}_0}=0. \tag{13}$$

Then we can define a norm on the surface-based data using this extension, namely, $\|\underline{\psi}\|_{\mathcal{E}_0}$. Therefore, considering the linear observation operator providing measurements $\underline{y}\cdot\underline{e}$ on the surface $\mathcal{S}_0$, we can use this norm in the observation space. Accordingly, observer terms in the form $\mathrm{H}^*(\mathrm{z}-\mathrm{H}\,\underline{\widehat{y}})$ will give in a variational setting

$$(\mathrm{Ext}_{\mathcal{S}_0}(\underline{e}\ ;\ \mathrm{z}-\mathrm{H}\,\underline{\widehat{y}}),\mathrm{Ext}_{\mathcal{S}_0}(\underline{e}\ ;\ \mathrm{H}\,\underline{v}^\sharp))_{\mathcal{E}_0}=(\mathrm{Ext}_{\mathcal{S}_0}(\underline{e}\ ;\ \mathrm{z}-\mathrm{H}\,\underline{\widehat{y}}),\underline{v}^\sharp)_{\mathcal{E}_0},$$

where the second expression is obtained by using the characterization (13) when observing that on $\mathcal{S}_0$

$$\mathrm{Ext}_{\mathcal{S}_0}(\underline{e}\ ;\ \mathrm{H}\,\underline{v}^\sharp)\cdot\underline{e}=\underline{v}^\sharp\cdot\underline{e}.$$

Therefore we have in this case

$$\mathrm{H}^*(\mathrm{z}-\mathrm{H}\,\underline{\widehat{y}})=\mathrm{Ext}_{\mathcal{S}_0}(\underline{e}\ ;\ \mathrm{z}-\mathrm{H}\,\underline{\widehat{y}}). \tag{14}$$

Now, when dealing more generally with a discrepancy operator $\mathrm{D}(\underline{\widehat{y}},\mathrm{z})$ pertaining to the displacements on a surface $\mathcal{S}_0$, we will generalize this strategy by using the observer correction given by

$$-\mathrm{Ext}_{\mathcal{S}_0}(\mathrm{d}_y\mathrm{D}(\underline{\widehat{y}},\mathrm{z})\ ;\ \mathrm{D}(\underline{\widehat{y}},\mathrm{z})),$$

obtained by directly substituting in (14) $\mathrm{D}(\underline{\widehat{y}},\mathrm{z})$ for $(\mathrm{z}-\mathrm{H}\,\underline{\widehat{y}})$, and $-\mathrm{d}_y\mathrm{D}(\underline{\widehat{y}},\mathrm{z})$ – associated with a vector field on $\mathcal{S}_0$ – for $\underline{e}$ since in the linear case we have $\mathrm{H}\,\underline{\widehat{y}}=\underline{\widehat{y}}\cdot\underline{e}$ on $\mathcal{S}_0$. Of course, this also easily generalizes to a measurement made of a collection of such surface-based data associated with several surfaces $(\mathcal{S}_0^i)_{i=1}^{N_\mathcal{S}}$ and associated vector fields $\underline{e}^i$, for which the correction will be given (in the linear case) by

$$\mathrm{H}^*(\mathrm{z}-\mathrm{H}\,\underline{\widehat{y}})=\sum_{i=1}^{N_\mathcal{S}}\mathrm{Ext}_{\mathcal{S}_0^i}(\underline{e}^i\ ;\ \mathrm{z}-\mathrm{H}\,\underline{\widehat{y}}). \tag{15}$$

Tag planes We consider data consisting in a set of $N_\mathcal{P}$ tag planes $\mathcal{T}=\bigcup_i^{N_\mathcal{P}}\mathcal{P}^i$ deforming over time. Following the original ideas of [Moireau et al., 2009] – see also [Imperiale et al., 2011] – the discrepancy between the model and the data will be measured using the signed distances between the tag planes and the corresponding synthetic data, namely, deforming surfaces obtained by applying the model displacements to the initial configuration of the tag planes. Let us then denote by $\mathcal{T}_0=\bigcup_i^{N_\mathcal{P}}\mathcal{P}_0^i$ the set of tag planes in the reference configuration, mapped by the estimated trajectory $\underline{\widehat{y}}$ to $\widehat{\mathcal{T}}=\bigcup_i^{N_\mathcal{P}}\widehat{\mathcal{P}}^i$. For any point in a synthetic tag plane $\underline{\widehat{x}}=\underline{\xi}+\underline{\widehat{y}}(\underline{\xi})\in\widehat{\mathcal{P}}^i$ for some $\underline{\xi}\in\mathcal{P}_0^i$, we can compute the signed distance to the corresponding actual tag plane by

$$\mathrm{dist}(\underline{\widehat{x}},\mathcal{P}^i)=(\underline{\widehat{x}}-\Pi_{\mathcal{P}^i}\underline{\widehat{x}})\cdot\underline{n}_{\mathcal{P}^i}\,. \tag{16}$$

The discrepancy operator is then the application mapping the displacement field to this collection of (scalar) distance fields defined over the planes of $\mathcal{T}_0$ – see Figure 3. When differentiating with respect to the displacement field we have

$$\mathrm{d}_y\mathrm{dist}(\underline{\widehat{x}},\mathcal{P}^i)\cdot\underline{v}^\sharp=\underline{n}_{\mathcal{P}^i}\cdot\underline{v}^\sharp,$$

hence, the application of the above-described strategy gives an observer that follows the mechanical system of equations (7), except for the first equation modified into

$$\dot{\underline{\widehat{y}}}=\underline{\widehat{v}}-\gamma\sum_{i=1}^{N_\mathcal{P}}\mathrm{Ext}_{\mathcal{P}_0^i}\big(\underline{n}_{\mathcal{P}^i}(\underline{\widehat{x}})\,;\,\mathrm{dist}(\underline{\widehat{x}},\mathcal{P}^i)\big). \tag{17}$$

Tag grids We now consider the data in the form of a collection of tag lines deforming within a set of (2D) image slices. We thus assume that we have $N_{\mathcal{P}}$ such lines $\big(\mathcal{L}^{ij}\big)_{i=1}^{N_{\mathcal{P}}}$ in each 2D image $\mathcal{I}^j$, with $1 \leq j \leq N_{\mathcal{I}}$. We cannot directly design the discrepancy operator based on the corresponding model lines, since displacement fields are not well-defined along lines in the variational space, hence this would not give a well-posed observer problem. To circumvent this difficulty, we again consider the tag planes in the model and project each point of the planes onto the neighboring image slices – by the Euclidean orthogonal projection denoted by $\Pi_{\mathcal{I}^j}$ for image $\mathcal{I}^j$ – and compute the signed distance of the projected point to the corresponding tag line within each image – see Figure 4 – i.e.

$$\mathrm{dist}(\Pi_{\mathcal{I}^j}\underline{\widehat{x}}, \mathcal{L}^{ij}) = \big(\Pi_{\mathcal{I}^j}\underline{\widehat{x}} - \Pi_{\mathcal{L}^{ij}}\Pi_{\mathcal{I}^j}\underline{\widehat{x}}\big) \cdot \underline{n}_{\mathcal{L}^{ij}}.$$

Then we can interpolate the signed distances thus-obtained in the various images concerned – which provides interpolated distance fields over the model tag planes as a discrepancy operator, namely,

$$\mathrm{D}_i(\underline{\widehat{y}}, \mathrm{z}) = \mathcal{J}_{(j)}\big(\mathrm{dist}(\Pi_{\mathcal{I}^j}\underline{\widehat{x}}, \mathcal{L}^{ij})\big), \tag{18}$$

for each plane $\mathcal{P}_0^i$, where $\mathcal{J}_{(j)}$ denotes the interpolation operator. When differentiating this expression, we have

$$\mathrm{d}_y\mathrm{dist}(\Pi_{\mathcal{I}^j}\underline{\widehat{x}}, \mathcal{L}^{ij}) \cdot \underline{v}^\sharp = \underline{n}_{\mathcal{L}^{ij}} \cdot \underline{v}^\sharp,$$

but we also have a contribution coming from the interpolation operator derivative. Since this interpolation only depends on the coordinate of the point considered along the axis orthogonal to all image slices, denoting by $\mathcal{J}'_{(j)}$ the derivative with respect to this coordinate, a straightforward computation finally yields

$$\mathrm{d}_y\mathrm{D}_i(\underline{\widehat{y}}, \mathrm{z}) = \Big(\mathcal{J}_{(j)}\big(\underline{n}_{\mathcal{L}^{ij}}\big) + \mathcal{J}'_{(j)}\big(\mathrm{dist}(\Pi_{\mathcal{I}^j}\underline{\widehat{x}}, \mathcal{L}^{ij})\big)\underline{n}_{\mathcal{I}}\Big) \cdot \underline{v}^\sharp,$$

where $\underline{n}_{\mathcal{I}}$ denotes the director vector of the orthogonal axis. Note that when considering e.g. linear interpolation the derivative $\mathcal{J}'_{(j)}$ is directly given by the finite difference expression computed between the two adjacent planes. This finally gives for the observer correction equation

$$\dot{\underline{\widehat{y}}} = \underline{\widehat{v}} - \gamma \sum_{i=1}^{N_{\mathcal{P}}} \mathrm{Ext}_{\mathcal{P}_0^i}\Big(\underline{e}^i\,;\, \mathcal{J}_{(j)}\big(\mathrm{dist}(\Pi_{\mathcal{I}^j}\underline{\widehat{x}}, \mathcal{L}^{ij})\big)\Big), \tag{19}$$

with $\underline{e}^i = \mathcal{J}_{(j)}\big(\underline{n}_{\mathcal{L}^{ij}}\big) + \mathcal{J}'_{(j)}\big(\mathrm{dist}(\Pi_{\mathcal{I}^j}\underline{\widehat{x}}, \mathcal{L}^{ij})\big)\underline{\nu}$.

2.3.3 Extracted 2D displacements

Here we will model the measurements corresponding to displacements obtained from the processing of 2D tagged images. We can assume that we are able to track the intersections of material fibers originally orthogonal to image planes throughout the dynamic sequence. This holds e.g. for such fibers corresponding to the intersection of tag planes, but 2D-tag processing techniques generally provide a (2D) displacement field all over the image planes. This displacement corresponds to the shift in the position of the intersection of the deforming material fiber with the image plane between the initial and current configurations. Note that the material point located at the intersection between the fiber and the image changes over time due to through-the-plane motion, hence the measurement is not a material displacement, see Figure 5. This induces serious complications in the exact form of the tangent observation operator dH, but in our case we will use an approximate form based on a small displacements assumption. With this assumption, the observation operator clearly reduces to the components of the material displacements tangential to the image plane. Therefore, in this case the measurement is

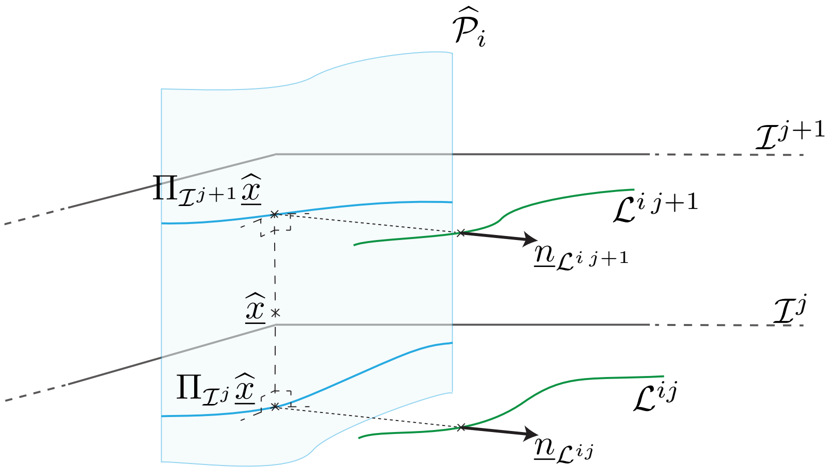

Figure 4: Illustration of tag grids discrepancy measure

a two-component field over a plane – instead of a scalar field for the above distances – hence, we resort to a slightly different extension operator relying on Dirichlet boundary conditions on two conditions, namely, $\underline{\psi} = \mathrm{Ext}'_{\mathcal{S}_0}(\underline{e}\ ;\ \underline{\varphi})$ defined by

$$\begin{cases} -\underline{\mathrm{div}}(\underline{\underline{\sigma}}^{\mathrm{lin}}(\underline{\psi})) = 0 & \text{in } \Omega_0 \\ \Pi_{\underline{e}}\underline{\psi} = \underline{\varphi} & \text{on } \mathcal{S}_0 \\ (\underline{\underline{\sigma}}^{\mathrm{lin}} \cdot \underline{n}) \cdot \underline{e} = 0 & \text{on } \mathcal{S}_0 \end{cases} \tag{20}$$

where $\Pi_{\underline{e}}$ denotes the projection onto the plane orthogonal to $\underline{e}$, plane in which $\underline{\varphi}$ is assumed to lie. Finally, the correction equation for the observer reads

$$\dot{\underline{\widehat{y}}} = \underline{\widehat{v}} + \gamma \sum_{j=1}^{N_{\mathcal{I}}} \mathrm{Ext}'_{\mathcal{I}^j}\big(\underline{n}_{\mathcal{I}}\,;\,\mathrm{z} - \mathrm{H}(\underline{\widehat{y}})\big), \tag{21}$$

where $\underline{n}_{\mathcal{I}}$ denotes the normal to the image planes, and the innovation term $\mathrm{z} - \mathrm{H}(\underline{\widehat{y}})$ will be computed based on the actual tracking of material fibers, i.e. without small displacements assumption.

3 An illuminating example: the linearized configuration

We consider a simplified configuration where the model and the observation operator are linear. As explained in the previous section, this configuration is both an illustrative example where we can handle all the proofs and also a relevant configuration since in nonlinear situations we can analyze convergence for small errors around a trajectory by linearization [Khalil, 1992, Lohmiller and Slotine, 2005].

We consider a linear elastic system in which the Cauchy stress tensor is given by

$$\underline{\underline{\sigma}} = \underline{\underline{\underline{\underline{A}}}} : \underline{\underline{\varepsilon}}(\underline{y}),$$

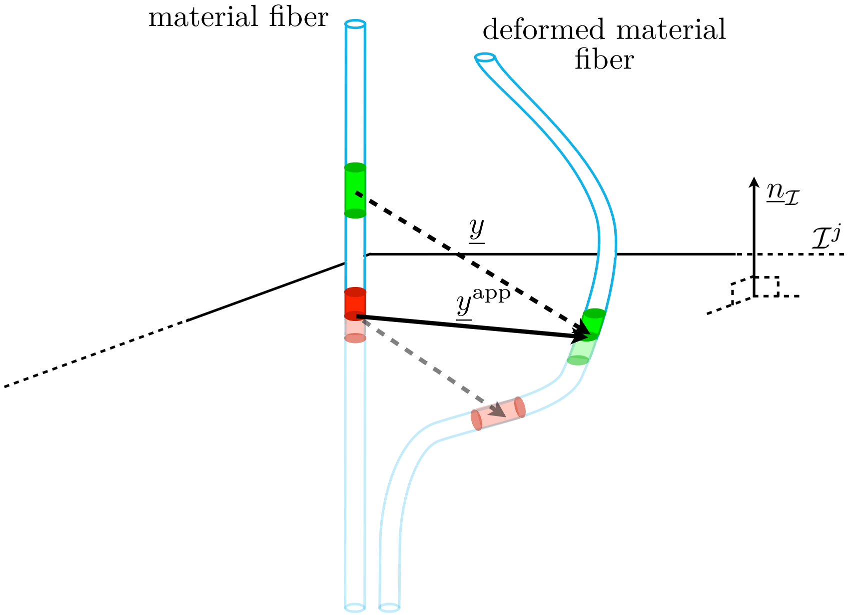

Figure 5: Illustration of apparent displacement in the image plane.

where the linear operator appearing in this (linear) constitutive law is assumed to be constant for the sake of simplicity. We denote $\Delta_e(\cdot) = \underline{\mathrm{div}}(\underline{\underline{\underline{\underline{A}}}} : \underline{\underline{\varepsilon}}(\cdot))$ and define the following model

$$\left\{\begin{aligned} \dot{\underline{y}} &= \underline{v}, && \text{in } \Omega_0 \\ \rho\dot{\underline{v}} - \Delta_e \underline{y} &= \underline{f}, && \text{in } \Omega_0 \\ \underline{y} &= 0 && \text{on } \partial\Omega_0. \end{aligned}\right. \tag{22}$$

The external load is a time-dependent regular function $\underline{f} \in C^1([0,T], \mathcal{L}^2(\Omega_0))$. Let us introduce $\mathcal{X}^v = \mathcal{L}^2(\Omega_0)^3$, the displacement space $\mathcal{X}^y = \mathcal{H}^1_0(\Omega_0)^3$, and $\mathcal{X} = \mathcal{X}^y \times \mathcal{X}^v$. Using the Korn and Poincaré inequalities, $\mathcal{X}^y$ is an Hilbert space with the following scalar product

$$\forall (\underline{y}_1, \underline{y}_2) \in \mathcal{X}^y, \quad (\underline{y}_1, \underline{y}_2)_{\mathcal{E}_0} = \int_{\Omega_0} \underline{\underline{\varepsilon}}(\underline{y}_1) : \underline{\underline{\underline{\underline{A}}}} : \underline{\underline{\varepsilon}}(\underline{y}_2)\, \mathrm{d}\Omega.$$

In a semi-group theory context we introduce the semi-group generator $\mathrm{A} \in \mathcal{L}(\mathcal{D}(A), \mathcal{X})$ with

$$\mathrm{A} = \begin{pmatrix} 0 & \mathbb{1} \\ -\frac{1}{\rho}\Delta_e & 0 \end{pmatrix}$$

and we can prove that (22) admits a classical solution $C^0([0,T], \mathcal{X}^y) \cap C^1([0,T], \mathcal{X}^v)$ for every initial condition in the domain

$$\mathcal{D}(A) = \left\{ (\underline{y}, \underline{v}) \in \mathcal{X}^y \times \mathcal{X}^v, \quad \underline{\mathrm{div}}(\underline{\underline{\underline{\underline{A}}}} : \underline{\underline{\varepsilon}}(\underline{v})) \in \mathcal{X}^v \right\}.$$

On this model we assume to have at our disposal some measurements of the displacement. We introduce the observation operator H such that

$$\mathrm{H} : \left| \begin{aligned} &\mathcal{X}^y \to \mathcal{Z} \\ &\underline{y} \mapsto \mathbb{1}_{\omega_0} \underline{y}, \end{aligned} \right.$$

where $\mathcal{Z} = \mathcal{H}^1(\omega_0)^3$. Using the extension $\underline{\psi} = \mathrm{Ext}_{\omega_0}(\underline{\varphi})$ defined by

$$\begin{cases} -\Delta_e(\underline{\psi}) = 0 & \text{in } \Omega_0 \\ \underline{\psi} = \underline{\varphi} & \text{in } \omega_0 \\ \underline{\psi} = 0 & \text{on } \partial\Omega_0, \end{cases} \tag{23}$$

we can prove the following property.

Proposition 2

$$\forall(\underline{\varphi}_1, \underline{\varphi}_2) \in \mathcal{Z}^2, \quad (\mathrm{Ext}_{\omega_0}(\underline{\varphi}_1), \mathrm{Ext}_{\omega_0}(\underline{\varphi}_2))_{\mathcal{E}_0}, \tag{24}$$

defines a scalar product on $\mathcal{Z} = \mathcal{H}^1(\omega_0)^3$.

Proof. The proof is the simple extension of the results proven in [Chapelle et al., 2012a] for scalar equations. Let $\underline{\varphi}$ be an element of $\mathcal{Z}$. The only difficulty lies in proving the norm equivalence with $\|\underline{\varphi}\|^2_{\mathcal{H}^1(\omega_0)^3}$. First, we have

$$\begin{aligned} \|\underline{\varphi}\|^2_{\mathcal{H}^1(\omega_0)^3} &= \|\underline{\underline{\nabla}}\,\underline{\varphi}\|^2_{\mathcal{L}^2(\omega_0)^3} + \|\underline{\varphi}\|^2_{\mathcal{L}^2(\omega_0)^3} \\ &\leq \|\underline{\underline{\nabla}}\,\mathrm{Ext}_{\omega_0}(\underline{\varphi})\|^2_{\mathcal{L}^2(\Omega_0)^3} + \|\mathrm{Ext}_{\Omega_0}(\underline{\varphi})\|^2_{\mathcal{L}^2(\Omega_0)^3} \\ &\leq (1 + C_p)\,\|\underline{\underline{\nabla}}\,\mathrm{Ext}_{\omega_0}(\underline{\varphi})\|^2_{\mathcal{L}^2(\Omega_0)^3} \\ &\leq C_k(1 + C_p)\,\|\mathrm{Ext}_{\omega_0}(\underline{\varphi})\|^2_{\mathcal{E}_0}, \end{aligned}$$

with C_p given by the Poincaré inequality and C_k given by Korn inequality and a bound C_a on the elasticity tensor. Conversely, by continuity of the extension on $\Omega_0 \backslash \omega_0$ with respect to the data we have for $\underline{\psi} = \mathrm{Ext}_{\omega_0}(\underline{\varphi})$

$$\int_{\Omega_0 \backslash \omega_0} \underline{\underline{\varepsilon}}(\underline{\psi}) : \underline{\underline{\underline{\underline{A}}}} : \underline{\underline{\varepsilon}}(\underline{\psi})\, \mathrm{d}\Omega \leq C_d \|\underline{\varphi}_{|\partial\omega_0}\|^2_{\mathcal{H}^{\frac{1}{2}}(\partial\omega_0)^3}.$$

Hence, denoting by C_t the constant arising from the continuity of the trace operator, we have

$$\begin{aligned} \|\mathrm{Ext}_{\omega_0}(\underline{\varphi})\|^2_{\mathcal{E}_0} &\leq \int_{\omega_0} \underline{\underline{\varepsilon}}(\underline{\psi}) : \underline{\underline{\underline{\underline{A}}}} : \underline{\underline{\varepsilon}}(\underline{\psi})\, \mathrm{d}\Omega + C_d\,\|\underline{\varphi}\|^2_{\mathcal{H}^{\frac{1}{2}}(\partial\omega_0)^3} \\ &\leq C_a\,\|\underline{\underline{\nabla}}\,\underline{\varphi}\|^2_{\mathcal{L}^2(\omega_0)^3} + C_d \|\underline{\varphi}_{|\partial\omega_0}\|^2_{\mathcal{H}^{\frac{1}{2}}(\partial\omega_0)^3} \\ &\leq (C_a + C_d C_t)\|\underline{\varphi}\|^2_{\mathcal{H}^1(\omega_0)^3}, \end{aligned}$$

which completes the proof. ■

It is now possible to define the adjoint of the observation operator.

Proposition 3
The operator H *is bounded from* $\mathcal{X}$ *to* $\mathcal{Z}$ *and* H^* *is given by*

$$\mathrm{H}^* : \left| \begin{array}{l} \mathcal{Z} \to \mathcal{X}^y \\ \underline{\varphi} \mapsto \mathrm{Ext}_{\omega_0}(\underline{\varphi}). \end{array} \right.$$

Proof. Let first prove that H is bounded. We consider $\underline{\psi} \in \mathcal{X}^y$ and $\underline{\varphi}$ such that $\underline{\varphi} = \mathrm{H}\,\underline{\psi}$. We have directly, from norm equivalences,

$$\left\|\underline{\varphi}\right\|_{\mathcal{Z}}^2 = \left\|\mathrm{Ext}_{\omega_0}(\underline{\varphi})\right\|_{\mathcal{E}_0}^2 \leq C_1 \left\|\underline{\varphi}\right\|_{\mathcal{H}^1(\omega_0)^3}^2 \leq C_1 C_2 \left\|\underline{\psi}\right\|_{\mathcal{H}_0^1(\Omega_0)^3}^2 .$$

Then we verify that for all $\underline{\varphi} \in \mathcal{Z}$ and $\underline{v}^\sharp \in \mathcal{X}^y$

$$(\underline{\varphi}, \mathrm{H}\,\underline{v}^\sharp)_{\mathcal{Z}} = \int_{\Omega_0} \underline{\underline{\varepsilon}}(\mathrm{Ext}_{\omega_0}(\underline{\varphi})) : \underline{\underline{\underline{\underline{A}}}} : \underline{\underline{\varepsilon}}(\mathrm{Ext}_{\omega_0}(\underline{v}^\sharp_{|\omega_0}))\, \mathrm{d}\Omega.$$

By the variational characterization of the extension (9) we have

$$\int_{\Omega_0} \underline{\underline{\varepsilon}}(\mathrm{Ext}_{\omega_0}(\underline{\varphi})) : \underline{\underline{\underline{\underline{A}}}} : \underline{\underline{\varepsilon}}(\mathrm{Ext}_{\omega_0}(\underline{v}^\sharp_{|\omega_0}))\, \mathrm{d}\Omega = \int_{\Omega_0} \underline{\underline{\varepsilon}}(\mathrm{Ext}_{\omega_0}(\underline{\varphi})) : \underline{\underline{\underline{\underline{A}}}} : \underline{\underline{\varepsilon}}(\underline{v}^\sharp)\, \mathrm{d}\Omega,$$

since

$$\underline{v}^\sharp_{|\omega_0} - \mathrm{Ext}_{\omega_0}(\underline{v}^\sharp_{|\omega_0}) = 0 \quad \text{on } \omega_0.$$

Therefore

$$(\underline{\varphi}, \mathrm{H}\,\underline{v}^\sharp)_{\mathcal{Z}} = (\mathrm{H}^*\underline{\varphi}, \underline{v}^\sharp)_{\mathcal{E}_0},$$

with H^* given by

$$\mathrm{H}^* : \left|\begin{array}{l} \mathcal{Z} \to \mathcal{X}^y \\ \underline{\varphi} \mapsto \mathrm{Ext}_{\omega_0}(\underline{\varphi}). \end{array}\right.$$

■

We can now define the observer by the dynamics

$$\begin{cases} \dot{\underline{\widehat{y}}} = \underline{\widehat{v}} + \gamma \mathrm{Ext}_{\omega_0}(\mathrm{z} - \mathbb{1}_{\omega_0}\underline{\widehat{y}}), & \text{in } \Omega_0 \\ \rho \dot{\underline{\widehat{v}}} - \Delta_e(\underline{\widehat{y}}) = 0, & \text{in } \Omega_0 \\ \underline{\widehat{y}} = 0, & \text{in } \partial\Omega_0, \end{cases} \tag{25}$$

which converges to the solution of (22) under the observability condition given by the next theorem.

Theorem 4
If there exists a constant C and a time T such that every solution of

$$\begin{cases} \dot{\underline{y}} = \underline{v}, & \textit{in } \Omega_0 \\ \rho \dot{\underline{v}} - \Delta_e \underline{y} = 0, & \textit{in } \Omega_0 \\ \underline{y} = 0 & \textit{on } \partial\Omega_0, \end{cases}$$

satisfies the observability condition

$$\int_0^T \left\|\mathrm{Ext}_{\omega_0}(\mathbb{1}_{\omega_0}\underline{y})\right\|_{\mathcal{E}_0}^2 \,\mathrm{d}t \geq C \left\|\underline{y}\right\|_{\mathcal{E}_0}^2 + \left\|\underline{v}\right\|_{\mathcal{L}^2}^2 , \tag{26}$$

then the observer given by the dynamics (25) *converges to the solution* $\mathrm{x}^{\mathrm{ref}}$ *of* (22) *such that*

$$\mathrm{z} = \mathrm{H}\mathrm{x}^{ref}.$$

Proof. We have defined the reference trajectory as a solution of

$$\dot{\mathrm{x}}^{\mathrm{ref}} = \mathrm{A}\mathrm{x}^{\mathrm{ref}},$$

and the observer as the solution of

$$\dot{\widehat{\mathrm{x}}} = \mathrm{A}\mathrm{x} + \gamma \mathrm{H}^*(\mathrm{z} - \mathrm{H}\mathrm{x}).$$

The error $\widetilde{\mathrm{x}} = \mathrm{x}^{\mathrm{ref}} - \widehat{\mathrm{x}}$ is then solution of

$$\dot{\widetilde{\mathrm{x}}} = (\mathrm{A} - \gamma \mathrm{H}^*\mathrm{H})\widetilde{\mathrm{x}}.$$

which from Theorem 1 converges exponentially to 0 for every initial condition when the observability condition (26) is verified.

■

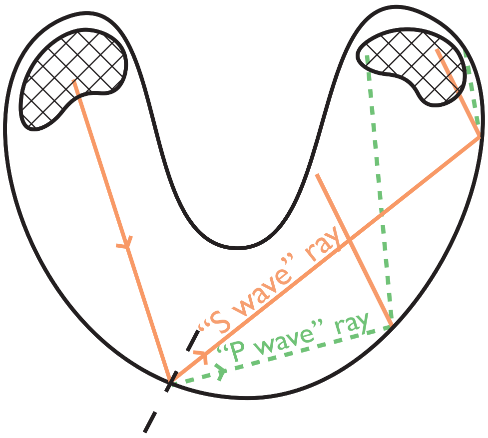

Figure 6: Example of rays associated with the P and W waves. The two types of waves interact at the boundary where each ray generates one P-wave ray and one S wave ray. Each multiple combination of these rays should encounter the domain of observation.

Following [Daoulatli et al., 2010] we define the elastic geometric control condition as the condition that every combination of pressure (P) and shear (S) waves ray should encounter the subdomain of observation – see [Daoulatli et al., 2010] for a complete description of such rays and Figure 6 as an illustrative example. This condition generalizes to the vectorial case the so-called geometric control condition (GCC) introduced by [Bardos et al., 1988], allowing to control any solution of the acoustic wave equation from the observations of the time derivative of the wave in a subdomain.

Theorem 5 (Geometric Control Condition)
The condition of Theorem 4 holds as soon as the elastic geometric control condition is satisfied.

Proof. For technical reasons we assume that the elastic geometric control condition is satisfied for an observation domain $\check{\omega}_0$ slightly smaller than ω_0, namely, with $\check{\omega}_0 \subset \omega_0$ and $\mathrm{dist}(\Omega_0 \setminus \omega_0, \check{\omega}_0) > 0$. We first recall a classical observability result when the velocity is observed. In fact there exists a constant C and a time T such that every solution of (22) satisfies the observability condition

$$\int_0^{\check{T}} \|\underline{v}\|^2_{\mathcal{L}^2(\check{\omega}_0)^3} \,\mathrm{d}t \geq C\Big(\|\underline{y}\|^2_{\mathcal{E}_0} + \|\underline{v}\|^2_{\mathcal{L}^2(\Omega_0)^3}\Big), \tag{27}$$

with $\breve{T} = T - \delta$ for $\delta > 0$ sufficiently small, as soon as the elasticity geometric control condition is verified in the time interval $[0, T[$. Following what was already done for acoustic waves in [Chapelle et al., 2012a] we will use a property of equirepartition (over time) of the total energy localized within the observation subdomain between the kinetic and elastic contributions to infer (26) from (27).

Let $\psi \in C_c^\infty(\overline{\Omega}_0)$ be a cutoff function satisfying

$$\psi(\underline{\xi}) = \begin{cases} 0, & \text{if } \underline{\xi} \in \Omega_0 \backslash \omega_0 \\ 1, & \text{if } \underline{\xi} \in \breve{\omega}_0 \end{cases}$$

and $0 \leq \psi(\underline{\xi}) \leq 1$ for every $\underline{\xi} \in \overline{\Omega}_0$. Denote also $\phi(t) = t^2(\breve{T} - t)^2$. Then, by repeated integrations by parts we obtain

$$\begin{aligned} 0 &= \int_0^{\breve{T}} \int_{\omega_0} \phi\psi(\ddot{\underline{y}} - \Delta_e \underline{y}) \cdot \underline{y} \,\mathrm{d}\Omega\, \mathrm{d}t \\ &= \int_0^{\breve{T}} \int_{\omega_0} \ddot{\phi}\psi \frac{|\underline{y}|^2}{2} \mathrm{d}\Omega \mathrm{d}t - \int_0^{\breve{T}} \int_{\omega_0} \phi\psi |\dot{\underline{y}}|^2 \,\mathrm{d}\Omega\, \mathrm{d}t \\ &\quad - \int_0^{\breve{T}} \int_{\omega_0} \phi\, \underline{\underline{\varepsilon}}(\underline{y}) : \underline{\underline{\underline{\underline{A}}}} : (\underline{\nabla}\psi \otimes \underline{y}) \,\mathrm{d}\Omega\, \mathrm{d}t + \int_0^{\breve{T}} \int_{\omega_0} \phi\psi\, \underline{\underline{\varepsilon}}(\underline{y}) : \underline{\underline{\underline{\underline{A}}}} : \underline{\underline{\varepsilon}}(\underline{y}) \,\mathrm{d}\Omega\, \mathrm{d}t. \end{aligned}$$

Moreover,

$$\begin{aligned} \int_{\omega_0} \underline{\underline{\varepsilon}}(\underline{y}) : \underline{\underline{\underline{\underline{A}}}} : (\underline{\nabla}\psi \otimes \underline{y}) \,\mathrm{d}\Omega &\leq C \left\|\psi\right\|_{\mathcal{W}^{1,\infty}} \left\|\underline{\underline{\varepsilon}}(\underline{y})\right\|_{\mathcal{L}^2(\omega_0)^3} \left\|\underline{y}\right\|_{\mathcal{L}^2(\omega_0)^3} \\ &\leq C \left\|\psi\right\|_{\mathcal{W}^{1,\infty}} \left\|\underline{y}\right\|^2_{\mathcal{H}^1(\omega_0)^3}. \end{aligned}$$

This identity combined with the properties of the cutoff functions ϕ and ψ provides, for any strictly positive ε, the existence of a constant $C > 0$ such that

$$\int_\varepsilon^{\breve{T}-\varepsilon} \int_{\breve{\omega}_0} |\dot{\underline{y}}|^2 \mathrm{d}\Omega\, \mathrm{d}t \leq C \int_0^{\breve{T}} \int_{\omega_0} \|\underline{y}(\cdot, t)\|^2_{\mathcal{H}^1(\omega_0)^3} \,\mathrm{d}t.$$

Substituting $\breve{T} + 2\varepsilon$ for $\breve{T}$ in all the above computations gives

$$\int_\varepsilon^{\breve{T}+\varepsilon} \int_{\breve{\omega}_0} |\dot{\underline{y}}|^2 \,\mathrm{d}\Omega\, \mathrm{d}t \leq C \int_0^{\breve{T}+2\varepsilon} \|\underline{y}(\cdot, t)\|^2_{\mathcal{H}^1(\omega_0)^3} \,\mathrm{d}t.$$

We proceed by making the change of variable $\tau = t - \varepsilon$ in the left-hand side integral, yielding

$$\int_0^{\breve{T}} \int_{\breve{\omega}_0} |\dot{\underline{y}}(\underline{\xi}, \tau + \varepsilon)|^2 \,\mathrm{d}\Omega\, \mathrm{d}\tau \leq C \int_0^{\breve{T}+2\varepsilon} \|\underline{y}\|^2_{\mathcal{H}^1(\omega_0)^3} \,\mathrm{d}t. \tag{28}$$

Noting that $\underline{y}(\underline{\xi}, t + \varepsilon)$ satisfies the elastodynamics system with initial data $(\underline{y}(\underline{\xi}, \varepsilon), \dot{\underline{y}}(\underline{\xi}, \varepsilon))$ and applying (27) with this shifted solution, we obtain that there exists also C such that

$$\int_0^{\breve{T}} \int_{\breve{\omega}_0} |\dot{\underline{y}}(\underline{\xi}, \tau + \varepsilon)|^2 \mathrm{d}\Omega \mathrm{d}\tau \geq C \left(\|\underline{y}(\varepsilon)\|^2_{\mathcal{E}_0} + \|\dot{\underline{y}}(\varepsilon)\|^2_{\mathcal{L}^2(\Omega_0)^3} \right). \tag{29}$$

Combining (28), (29) and the fact that the energy of the solution of the elastodynamics equation is exactly conserved over time, we have our observability inequality (26) upon choosing $\varepsilon = \frac{\delta}{2}$. ■

4 Discretization and analysis

4.1 Spatial discretization and simplified analysis

In this section we discuss the observer built using a set of tag planes that can be decomposed into three distinct families. Each tag plane in a given family shares – at marking time – the same orthogonal direction and, only for clarity purposes, we assume that the three directions, denoted by $(\underline{\mathrm{d}}^1, \underline{\mathrm{d}}^2, \underline{\mathrm{d}}^3)$, are orthogonal. This type of data set may be referred to, in what follows, as (3D) tag planes. We will see how the estimation error dynamical system benefits – at a spatial semi-discrete level – from a stabilization operator acting similarly to a direct volume displacement feedback.

In a nonlinear setting, as we have seen in Section 2.1, the observer is built so that the dynamical system of the linearized estimation error benefits from a stabilization operator of the form $\mathrm{d}_y\mathrm{D}^*(\underline{x},\mathrm{z})\mathrm{d}_y\mathrm{D}(\underline{x},\mathrm{z})$ (where $\underline{x} = \underline{\varphi}(\underline{\xi}, t)$ is the exact trajectory used in the linearization procedure). In the case of tag planes, this operator reads, in a weak formulation,

$$\forall \underline{v}^\sharp,\ \underline{w}^\sharp \in \mathcal{X}^y \quad (\mathrm{d}_y\mathrm{D}^*\mathrm{d}_y\mathrm{D}\ \underline{v}^\sharp, \underline{w}^\sharp)_{\mathcal{E}_0} = \sum_{i=1}^{N_{\mathcal{P}}} (\mathrm{Ext}_{\mathcal{P}_0^i}\big(\underline{n}_{\mathcal{P}^i}\,;\,\underline{n}_{\mathcal{P}^i}\cdot\underline{v}^\sharp\big), \underline{w}^\sharp)_{\mathcal{E}_0},$$

where $\underline{n}_{\mathcal{P}^i}$ is the normal of the tag plane $\mathcal{P}_0^i$ deformed by the transformation $\underline{x} = \underline{\varphi}(\xi, t)$. Therefore, in an energy analysis of the observation error as in Section 2.3.1 we would obtain the dissipation term

$$\sum_{i=1}^{N_{\mathcal{P}}} \Big\| \mathrm{Ext}_{\mathcal{P}_0^i}\big(\underline{n}_{\mathcal{P}^i}\,;\,\underline{n}_{\mathcal{P}^i}\cdot\underline{\widetilde{y}}\big)\Big\|_{\mathcal{E}_0}^2.$$

This is different from the stabilization term considered in Section 2.3.1 based on 3D measurements in a subdomain, but since the normal vectors $\underline{n}_{\mathcal{P}^i}$ span all directions in space – assuming 3D tagging is used – we would expect to obtain comparable stabilization properties, at least provided tag density is sufficient. To substantiate this conjecture without undue technicalities, we consider to fix the ideas a term of the type

$$\|\varphi\|_{\mathcal{Z}}^2 = \sum_{i=1}^{N_{\mathcal{P}}} \Big\| \mathrm{Ext}_{\mathcal{P}_0^i}(\varphi)\Big\|_{\mathcal{H}^1(\Omega_0)}^2,$$

with a scalar field φ and a simple harmonic extension operator. In a first stage of analysis, we consider this expression for a discrete function φ_H constructed based on piecewise-bilinear shape functions associated with the regular tag grid, H denoting the distance between two adjacent planes in any direction. We denote this discrete space by $Q_1^H(\omega_0)$, where ω_0 is the region spanned by the tag grid. Then, straightforward scaling arguments – as is standard in finite element analysis, see *e.g.* [Bathe, 1996] – show that we have the following equivalence of norms for each plane

$$\Big\| \mathrm{Ext}_{\mathcal{P}_0^i}(\varphi_H)\Big\|_{\mathcal{H}^1(\Omega_0)}^2 \sim \|\varphi_H\|_{\mathcal{L}^2(\mathcal{P}_0^i)}^2 + H\,\|\underline{\boldsymbol{\nabla}}_{\mathcal{P}}\,\varphi_H\|_{\mathcal{L}^2(\mathcal{P}_0^i)}^2,$$

where $\underline{\boldsymbol{\nabla}}_{\mathcal{P}}$ denotes the 2D gradient within the plane considered. Therefore, with all the tag planes included we have the equivalence

$$\|\varphi_H\|_{\mathcal{Z}}^2 \sim \sum_{K\subset\omega_0} \big(\|\varphi_H\|_{\mathcal{L}^2(\partial K)}^2 + H\,\|\underline{\boldsymbol{\nabla}}_{\mathcal{P}}\,\varphi_H\|_{\mathcal{L}^2(\partial K)}^2\big),$$

where K denotes a generic (cubic) element within the tag grid mesh. Then, other scaling arguments within these elements give

$$\|\varphi_H\|^2_{\mathcal{L}^2(\partial K)} \sim H^{-1}\,\|\varphi_H\|^2_{\mathcal{L}^2(K)}\,, \quad H\,\|\underline{\boldsymbol{\nabla}}_{\mathcal{P}}\,\varphi_H\|^2_{\mathcal{L}^2(\partial K)} \sim \|\underline{\boldsymbol{\nabla}}\,\varphi_H\|^2_{\mathcal{L}^2(K)}\,,$$

hence, summing all the elements contributions,

$$\|\varphi_H\|^2_{\mathcal{Z}} \geq C\,\|\varphi_H\|^2_{\mathcal{H}^1(\omega_0)}\,,$$

where the constant C is here independent of the tag spacing H, and we see that the "observation norm" effectively controls the $\mathcal{H}^1$-norm within the observation domain, as in the above mathematical analysis, albeit for discrete functions in the tag grid. In numerical simulations of the observer we will instead need to consider $\|\varphi_h\|_{\mathcal{Z}}$ for φ_h fields given by finite element discretizations defined for the model. Nevertheless, in such cases the $\mathcal{Z}$-norm is in essence similar to $\|\mathcal{J}_H(\varphi_h|_{\omega_0})\|_{\mathcal{Z}}$, where $\mathcal{J}_H$ denotes the interpolation operator into the tag grid discrete space, and we have

$$\|\mathcal{J}_H(\varphi_h|_{\omega_0})\|^2_{\mathcal{Z}} \geq C\,\|\mathcal{J}_H(\varphi_h|_{\omega_0})\|^2_{\mathcal{H}^1(\omega_0)} \geq C_{H,h}\,\|\varphi_h\|^2_{\mathcal{H}^1(\omega_0)}\,,$$

where $C_{H,h}$ is strictly positive and adequately controlled – namely, with lower bound independent of both H and h – under compatibility conditions between the tag grid and the finite element mesh, typically requiring that the finite element mesh parameter h and the tag spacing H be of the same order. This may not always be the case in practice, since tag sampling is quite coarse in current MRI modalities, but this provides a reference for the error control in our observer strategy.

4.2 Time discretization

In this section we address the issue of the time discretization of the observer. During this numerical procedure we have focused our effort on ensuring two main properties. The first one is that the dissipative behavior of the (time discrete) estimation error – as emphasized in Theorem 1 – should be preserved, up to some consistency terms inherent to any discretization. Authors in [Moireau et al., 2009] proposed a numerical time scheme for similar observers based on a mid-point scheme. Our approach however differs in the sense that – and this is our second important feature – the time-discrete observer is built on a *prediction-correction* paradigm. Consequently, the prediction part – in practice, iterations of the direct model – and the correction part – *i.e.* the action of filtering the discrepancies between the data and the model – can be managed in separate ways.

4.2.1 Analysis of the time discrete observer

Following the presentation of Section 3 we assume that the dynamical system satisfied by the target trajectory is driven by a linear operator – typically obtained after linearization. Hence, we consider the dynamical system

$$\begin{cases} \dot{\mathrm{x}}(t) = (\mathrm{A} + \eta\mathrm{V})\mathrm{x}(t), \\ \\ \mathrm{x}(0) = \mathrm{x}_0 + \zeta_{\mathrm{x}}, \end{cases} \tag{30}$$

where A is a skew-adjoint operator, V is a self auto-adjoint and semi-negative operator and $\eta \geq 0$ is the viscosity coefficient. A typical example of such dynamics is

$$\mathrm{A} = \begin{pmatrix} 0 & \mathbb{1} \\ \frac{1}{\rho}\Delta_e & 0 \end{pmatrix} \quad \text{and} \quad \eta\mathrm{V} = \begin{pmatrix} 0 & 0 \\ 0 & \eta_s\Delta_e \end{pmatrix}.$$

representative of the systems studied in Section 2 or 3. In a first step, we consider a linear observation operator and we neglect, for simplicity, the observation noise. Hence, denoting by $\Delta \mathrm{t}$ the (constant) time step of the numerical procedure, the time discrete observations read

$$\mathrm{z}^n = \mathrm{H}\mathrm{x}(n\Delta \mathrm{t}).$$

As mentioned in the introduction of this Section we propose a prediction-correction time scheme of the form

$$\begin{cases} \dfrac{\widehat{\mathrm{x}}_-^{n+1} - \widehat{\mathrm{x}}_+^n}{\Delta \mathrm{t}} = (\mathrm{A} + \eta \mathrm{V})\dfrac{\widehat{\mathrm{x}}_-^{n+1} + \widehat{\mathrm{x}}_+^n}{2}, & (31\mathrm{a}) \\[2ex] \dfrac{\widehat{\mathrm{x}}_+^{n+1} - \widehat{\mathrm{x}}_-^{n+1}}{\Delta \mathrm{t}} = \gamma \mathrm{H}^*\big(\mathrm{z}^{n+1} - \mathrm{H}\widehat{\mathrm{x}}_+^{n+1}\big), & (31\mathrm{b}) \\[2ex] \widehat{\mathrm{x}}_+^0 = \mathrm{x}_0. \end{cases}$$

(31a) corresponds to the prediction step since the operators driving the target system appear. (31b) on the other hand corresponds to the correction step. Defining the discrete estimation error from the correction step

$$\widetilde{\mathrm{x}}_+^n = \mathrm{x}(n\Delta \mathrm{t}) - \widehat{\mathrm{x}}_+^n, \tag{32}$$

and associating an error prediction with

$$\widetilde{\mathrm{x}}_-^{n+1} = \mathrm{x}((n+1)\Delta \mathrm{t}) - \widehat{\mathrm{x}}_-^{n+1}, \tag{33}$$

we obtain the following error system after some algebra detailed in Appendix A

$$\begin{cases} \dfrac{\widetilde{\mathrm{x}}_-^{n+1} - \widetilde{\mathrm{x}}_+^n}{\Delta \mathrm{t}} = (\mathrm{A} + \eta \mathrm{V})\dfrac{\widetilde{\mathrm{x}}_-^{n+1} + \widetilde{\mathrm{x}}_+^n}{2} + \varepsilon^n, & (34\mathrm{a}) \\[2ex] \dfrac{\widetilde{\mathrm{x}}_+^{n+1} - \widetilde{\mathrm{x}}_-^{n+1}}{\Delta \mathrm{t}} = -\gamma \mathrm{H}^*\mathrm{H}\widetilde{\mathrm{x}}_+^{n+1}, & (34\mathrm{b}) \\[2ex] \widetilde{\mathrm{x}}_+^0 = \zeta_{\mathrm{x}}. \end{cases}$$

where the error source is given by the order two consistency term

$$\varepsilon^n = \frac{\Delta \mathrm{t}^2}{2}\big(\frac{1}{3}\dddot{\mathrm{x}}(\mathrm{t}_n) - \frac{1}{2}\dddot{\mathrm{x}}(\mathrm{r}_n)\big), \text{ with } \mathrm{t}_n, \mathrm{r}_n \in [n\Delta \mathrm{t}; (n+1)\Delta \mathrm{t}]$$

arising from the mid-point discretization. Denoting the norm of the estimation error

$$\widetilde{\mathcal{E}}_+^{n+1} = \frac{1}{2}\left\|\widetilde{\mathrm{x}}_+^{n+1}\right\|_{\mathcal{X}}^2,$$

we can extract – see Proposition 7 in Appendix A – the energy estimate associated with (34a)-(34b)

$$\begin{aligned} \frac{\widetilde{\mathcal{E}}_+^{n+1} - \widetilde{\mathcal{E}}_+^n}{\Delta \mathrm{t}} = -\eta \left\| \big(\sqrt{-\mathrm{V}}\big)\frac{\widetilde{\mathrm{x}}_-^{n+1} + \widetilde{\mathrm{x}}_+^n}{2} \right\|_{\mathcal{X}}^2 - \gamma \left\|\mathrm{H}\widetilde{\mathrm{x}}_+^{n+1}\right\|_{\mathcal{Z}}^2 \\ - \gamma^2 \frac{\Delta \mathrm{t}}{2}\left\|\mathrm{H}^*\mathrm{H}\widetilde{\mathrm{x}}_+^{n+1}\right\|_{\mathcal{Z}}^2 + (\varepsilon^n, \frac{\widetilde{\mathrm{x}}_-^{n+1} + \widetilde{\mathrm{x}}_+^n}{2})_{\mathcal{X}}. \end{aligned} \tag{35}$$

In (35) we see the effect of the correction step (31b) leading to some dissipation terms brought by the observation operator. The expression is the abstract and discrete version of expression (11), perturbed with natural consistency terms.

As far as the convergence estimate for system (31a)-(31b) is concerned, assuming that the corresponding homogeneous system is exponentially stable and following arguments in [Chapelle et al., 2012b], we can prove – see Proposition 8 – the following estimate

$$\left\|\widetilde{\mathrm{x}}^n_+\right\|_{\mathcal{X}} \leq M \exp(-\mu n \Delta \mathrm{t}) \left\|\widetilde{\mathrm{x}}^0_+\right\|_{\mathcal{X}} + \frac{\Delta \mathrm{t}}{1-\exp(-\mu \Delta \mathrm{t})} \max_{1\leq i \leq n} \left\|\varepsilon^i\right\|_{\mathcal{X}}. \tag{36}$$

The key point of estimate (36) is that the upper bound does not depend on the length of the global time window. This particularity – pointed out by authors in [Chapelle et al., 2012b] in a fully discrete setting and for another type of time scheme – shows how the data assimilation procedure has the additional crucial benefit of improving the discretization error estimation, beyond allowing to circumvent state uncertainties.

The exponential stability of the homogeneous system associated with (34a)-(34b) is however not trivial and depends on the observability of the underlying conservative system and on the amount of damping. Assuming that the observability of the conservative system $\dot{\mathrm{x}} = \mathrm{A}\mathrm{x}$ is verified, the main difficulty – see [Zuazua, 2005, Zhang et al., 2007, Ervedoza and Zuazua, 2009] – is that the process of time discretization of system (30) produces spurious high frequency modes which propagate at an arbitrary low velocity.

In the case of null viscosity, $\eta = 0$, a restriction (of CFL type) on the time step is required so that the observability inequality of the time continuous system can be transmitted to the time discrete system – see [Ervedoza and Zuazua, 2009]. In the case of low viscosity, $\eta = O(\Delta\mathrm{t})$, we can hope that the natural viscosity of the system acts as the *numerical* viscosity introduced by [Ervedoza and Zuazua, 2009] in order to discard the undesired spurious modes. In the case of general viscosity, we enter in another class of problems and can no longer count on the observability inequality – which is based on the analysis of the conservative system.

4.2.2 Non-linear time-scheme

Even though fewer theoretical results can be obtained in the case of nonlinear observation operators, we also provide a time scheme. Following [Moireau et al., 2009], this numerical procedure is based on a linearization scheme which leads, after a local analysis around the trajectory used in the linearization, to a dissipative behavior similar to (35). More precisely, neglecting the observation noise, we assume that the observations are obtained by

$$\mathrm{z}^n = \mathrm{H}(\mathrm{x}(n\Delta\mathrm{t})),$$

where $\mathrm{H}(\cdot)$ is a nonlinear and sufficiently smooth observation operator. Following authors in [Moireau et al., 2009] we propose to define the time discrete observer as

$$\begin{cases} \dfrac{\widehat{\mathrm{x}}^{n+1}_- - \widehat{\mathrm{x}}^n_+}{\Delta\mathrm{t}} = (\mathrm{A} + \eta\mathrm{V}) \dfrac{\widehat{\mathrm{x}}^{n+1}_- + \widehat{\mathrm{x}}^n_+}{2}, & (37\mathrm{a}) \\[2ex] \dfrac{\widehat{\mathrm{x}}^{n+1}_+ - \widehat{\mathrm{x}}^{n+1}_-}{\Delta\mathrm{t}} = \gamma \mathrm{dH}^{e\,*}_+ \big(\mathrm{z}^{n+1} - \mathrm{H}(\widehat{\mathrm{x}}^e_+) - \mathrm{dH}^e_+ (\widehat{\mathrm{x}}^{n+1}_+ - \widehat{\mathrm{x}}^e_+)\big), & (37\mathrm{b}) \\[2ex] \widehat{\mathrm{x}}^0_+ = \mathrm{x}_0, \end{cases}$$

where we denoted by $\widehat{\mathrm{x}}^e_+$ an extrapolated trajectory and dH^e_+ the tangent operator of the observation operator evaluated at $\widehat{\mathrm{x}}^e_+$, *i.e.*

$$\mathrm{dH}^e_+ = \mathrm{dH}(\widehat{\mathrm{x}}^e_+).$$

Proposition 9 in Appendix A shows that the time scheme satisfied by the linearized estimation error reads

$$\begin{cases} \dfrac{\widetilde{\mathrm{x}}_-^{n+1} - \widetilde{\mathrm{x}}_+^{n}}{\Delta \mathrm{t}} = (\mathrm{A} + \eta \mathrm{V}) \dfrac{\widetilde{\mathrm{x}}_-^{n+1} + \widetilde{\mathrm{x}}_+^{n}}{2} + \varepsilon^n, & (38\text{a}) \\[2ex] \dfrac{\widetilde{\mathrm{x}}_+^{n+1} - \widetilde{\mathrm{x}}_-^{n+1}}{\Delta \mathrm{t}} = -\gamma \mathrm{dH}_+^{e\,*} \mathrm{dH}_+^{e} \widetilde{\mathrm{x}}_+^{n+1} + \lambda^n, & (38\text{b}) \\[2ex] \widetilde{\mathrm{x}}_+^{0} = \zeta_{\mathrm{x}}. \end{cases}$$

In equation (38b) the source term is

$$\lambda^n = O(\|\mathrm{x}((n+1)\Delta \mathrm{t}) - \widehat{\mathrm{x}}_+^{e}\|_{\mathcal{X}}^2).$$

We see here the we benefit from the linearization procedure proposed in (37b) – compared with an explicit scheme – since, even though λ^n is, in essence, an error term it is proportional to the square of the estimation error norm. Hence, assuming that the initial condition is reasonably close to the target initial condition, this term will have little influence on the overall stability of the numerical scheme. For this system the energy estimate naturally becomes

$$\begin{aligned} \frac{\widetilde{\mathcal{E}}_+^{n+1} - \widetilde{\mathcal{E}}_+^{n}}{\Delta \mathrm{t}} = -\eta \left\| \left(\sqrt{-\mathrm{V}}\right) \frac{\widetilde{\mathrm{x}}_-^{n+1} + \widetilde{\mathrm{x}}_+^{n}}{2} \right\|_{\mathcal{X}}^2 - \gamma \left\| \mathrm{dH}_+^{e} \widetilde{\mathrm{x}}_+^{n+1} \right\|_{\mathcal{Z}}^2 \\ - \gamma^2 \frac{\Delta \mathrm{t}}{2} \left\| \mathrm{dH}_+^{e\,*} \mathrm{dH}_+^{e} \widetilde{\mathrm{x}}_+^{n+1} \right\|_{\mathcal{Z}}^2 + (\varepsilon^n, \frac{\widetilde{\mathrm{x}}_-^{n+1} + \widetilde{\mathrm{x}}_+^{n}}{2})_{\mathcal{X}} + (\lambda^n, \frac{\widetilde{\mathrm{x}}_+^{n+1} + \widetilde{\mathrm{x}}_-^{n+1}}{2})_{\mathcal{X}}. \end{aligned} \quad (39)$$

Expression (39) is the equivalent of expression (35) in a nonlinear setting using the tangent of the observation operator. Additionally to the consistency terms, we observe that the linearization term appears in the energy estimate. In the case of discrepancy measures, see Section 2.3.2 for practical examples, the observations and the real trajectory are linked through the implicit relation

$$\mathrm{D}(\mathrm{x}, \mathrm{z}) = 0.$$

In this case, the time discrete observer can be directly inferred from system (37a)-(37b)

$$\begin{cases} \dfrac{\widehat{\mathrm{x}}_-^{n+1} - \widehat{\mathrm{x}}_+^{n}}{\Delta \mathrm{t}} = (\mathrm{A} + \eta \mathrm{V}) \dfrac{\widehat{\mathrm{x}}_-^{n+1} + \widehat{\mathrm{x}}_+^{n}}{2}, & (40\text{a}) \\[2ex] \dfrac{\widehat{\mathrm{x}}_+^{n+1} - \widehat{\mathrm{x}}_-^{n+1}}{\Delta \mathrm{t}} = -\gamma \mathrm{dD}_+^{e\,*} \big(\mathrm{D}(\widehat{\mathrm{x}}_+^{e}, \mathrm{z}^{n+1}) + \mathrm{dD}_+^{e} (\widehat{\mathrm{x}}_+^{n+1} - \widehat{\mathrm{x}}_+^{e}) \big), & (40\text{b}) \\[2ex] \widehat{\mathrm{x}}_+^{0} = \mathrm{x}_0. \end{cases}$$

The corresponding estimation error statisfies (38a)-(38b) but the operator $\mathrm{dD}_+^e = \mathrm{dD}(\widehat{\mathrm{x}}_+^e, \mathrm{z})$ appears instead of the tangent of the observation operator. An estimate of the form of (39) can be similarly deduced.

4.2.3 Algorithmic solution process

We now introduce a fully discrete model – solved in practice – by considering the vectors of degrees of freedom associated with the FEM spatial discretization. We denote by capital letters the vectors of degrees of freedom and by italic operators the matrices associated with the functional operators used until then. For example, we define by $Y \in \mathbb{R}^{N_{\mathrm{dof}}}$ the vector of degrees of freedom – of dimension N_{dof} – associated with the function $\underline{y}_h$ defined in the finite-element space $\mathcal{X}_h$. We define by

$$\forall(\underline{y}_{h,1}, \underline{y}_{h,2}), \qquad Y_1^\intercal M Y_2 = (\underline{y}_{h,1}, \underline{y}_{h,2})_{\mathcal{L}^2_\rho(\Omega_0)} = \int_{\Omega_0} \rho \underline{y}_{h,1} \cdot \underline{y}_{h,2} \,\mathrm{d}\Omega,$$

and by

$$\forall(\underline{y}_{h,1}, \underline{y}_{h,2}), \qquad Y_1^\intercal K Y_2 = (\underline{y}_{h,1}, \underline{y}_{h,2})_{\mathcal{E}_0} = \int_{\Omega_0} \underline{\underline{\varepsilon}}(\underline{y}_{h,1}) : \underline{\underline{\underline{\underline{A}}}} : \underline{\underline{\varepsilon}}(\underline{y}_{h,2}) \,\mathrm{d}\Omega + \int_{\Gamma_n} k_s \, \underline{y}_{h,1} \cdot \underline{y}_{h,2} \,\mathrm{d}\Gamma,$$

the mass and stiffness matrix respectively. We then define a state vector as the concatenation of the displacement degrees of freedom plus the velocity degrees of freedom $X = \left(\begin{smallmatrix} Y \\ V \end{smallmatrix}\right)$ and we define the associated norm by

$$N = \begin{pmatrix} K & 0 \\ 0 & M \end{pmatrix}.$$

Concerning the observation space, we define the observation operator after space discretization H. By a slight abuse of notation we keep the same notation H when it applied to Y or to X despite the fact that it corresponds in this latter case to $\left(\begin{smallmatrix} H & 0 \end{smallmatrix}\right)$. Concerning the observation space norm S, we consider the norm computed through the extension operators. For example when considering 3D displacements, H is an interpolator between the mesh and the tag grid whereas S is defined such that

$$\forall(\phi_{H,1}, \phi_{H,2}), \qquad \Phi_{H,1}^\intercal S \Phi_{H,2} = (\phi_{H,1}, \phi_{H,1})_{\mathcal{Z}} = (\mathrm{Ext}(\underline{y}_{h,1}), \mathrm{Ext}(\underline{y}_{h,2}))_{\mathcal{E}_0}$$

where in practice – as extensively detailed in [**?**] – the extension is computed with

$$\mathrm{Ext}(\Phi) = \min_{\Phi = H\Psi} \Psi^\intercal K \Psi. \tag{41}$$

Taking into account this spatial discretization, we can rewrite the correction step (31b) in the form

$$N\Big(\frac{\widehat{X}_+^{n+1} - \widehat{X}_-^{n+1}}{\Delta \mathrm{t}}\Big) = \gamma H^\intercal S\big(Z^{n+1} - H\widehat{X}_+^{n+1}\big).$$

This expression turns into

$$\widehat{X}_+^{n+1} = \widehat{X}_-^{n+1} + \gamma(N + \gamma H^\intercal S_{n+1} H)^{-1} H^\intercal S_{n+1}(Z^{n+1} - H\widehat{X}_-^{n+1}), \tag{42}$$

where $S_{n+1} = \Delta t S$. We remark that the correction (42) corresponds exactly to the Best Linear Unbiased Estimator (BLUE) associated with the observation Z^{n+1}, the observation covariance S_{n+1}^{-1} the *a priori* state $\widehat{X}_-^{n+1}$ and the *a priori* state covariance N^{-1} [Simon, 2006]. If we additionally consider the time discretization of the model by introducing a transition operator $\mathrm{A}_{n+1|n}$ such that (31a) can be rewritten into

$$\widehat{X}_-^{n+1} = A_{n+1|n}(\widehat{X}_+^n)$$

we finally get a time and space discretization of the form

1. Prediction:

$$\widehat{X}_-^{n+1} = A_{n+1|n}(\widehat{X}_+^n), \tag{43a}$$

2. State Correction:

$$\widehat{X}_{+}^{n+1} = \widehat{X}_{-}^{n+1} + \gamma(N + \gamma H^{\intercal} S_{n+1} H)^{-1} H^{\intercal} S_{n+1}(Z^{n+1} - H\widehat{X}_{-}^{n+1}). \tag{43b}$$

System (43a)-(43b) can be seen as a prediction-correction discrete-time sequential estimator as it is the case for the discrete-time Kalman filter [Bensoussan, 1971, Simon, 2006] but here, the *a priori* state covariance remains constant equal to N^{-1}. Therefore whereas the discrete-time Kalman filter is not computable for systems coming from PDEs, our filter is since N is sparse.

Let us now give some additional methodological key points to solve the correction step (43b) in a very effective way. We remark that

$$\mathrm{N} \leq N + \gamma H^{\intercal} S_{n+1} H \leq \mathrm{N}\big(1 + \Delta \mathrm{t}\big),$$

which proves that N^{-1} is a good preconditioner to solve equation (43b) with an iterative solver. This reveals to be very helpful as typically we do not want to store the operator $H^{\intercal} S_{n+1} H$. Indeed, with an iterative solver, we only need to be able to compute for any vector X quantities like $N^{-1}X$ and $(N + \gamma H^{\intercal} S_{n+1} H)X$.

One last difficulty may arise in our specific case where quantities of the form $H^{\intercal} S_{n+1} H X$ can remain difficult to compute because of the choice of the observation norm S computed from the extensions. In [Moireau et al., 2009], authors have demonstrated that a possible approximation of the extension can be to found by replacing the constraint minimization (41) by a penalized minimization

$$\min_{\Psi} \{\epsilon \Psi^{\intercal} K \Psi + (\Phi - H\Psi)^{\intercal} M_{\mathrm{obs}} (\Phi - H\Psi)\} \tag{44}$$

where M_{obs} is the matrix associated with the simple $\mathcal{L}^2$-norm on the observation space. For example, in the simple case of 3D displacement measurements

$$\forall(\phi_{H,1}, \phi_{H,2}), \qquad \Phi_{H,1}^{\intercal} M_{\mathrm{obs}} \Phi_{H,2} = \int_{\omega_0} \underline{y}_{h,1} \underline{y}_{h,2} \, \mathrm{d}\Omega.$$

Therefore we can simply solve this minimization problem with a gradient-based descent algorithm involving only simple computation on the state and on the observation space. This method reveals to be particularly efficient in the case of apparent displacements where the observation space is the concatenation of the set of image planes having a potentially high resolution, hence S corresponds to a very dense operator.

4.3 Joint state and parameter discretization

Once we have defined the discrepancy operator and designed the state observer, we can now consider the additional stage of parameter identification through the state and parameter observer introduced at the end of Section 2.1. We should now define the adequate discretization of the system (5) compatible with the already defined discretization of the state observer itself (40a)-(40b). To that purpose, two discretizations are available in the literature. The first one is based on the fact that (5) corresponds to applying a continuous-time Reduced-Order Extended Kalman Filter (RoEKF) to the parametric space, hence a proper discretization is clearly the prediction-correction scheme defined by the discrete-time RoEKF [Moireau et al., 2008]. The second one [Moireau and Chapelle, 2011] is not directly an exact discretization but more an extension at the discrete-time level. In fact, the parameter dependency makes the joint state and parameter system nonlinear even if the state dynamics is linear. Therefore, the RoEKF filter on the parameters is only an approximate optimal filter. Other choices of approximate reduced order approximate optimal filter can therefore be used when they exist. It is typically the case of the Reduced-Order Unscented Kalman Filter (RoUKF) derived in [Moireau and Chapelle, 2011]. This filter replaces at the discrete-time level the tangent computations in (5) by finite differences computations which appear to be better adapted to large nonlinearities. In addition, there is no need to specifically code the tangent operators but rather introduce some particles that will allow to compute finite difference approximation. This algorithm thus combine efficiency and computational simplicity. Moreover, it reduces to the Reduced-Order Kalman Filter after linearization, which allows to validate its stability with an error linearization study as done in [Moireau and Chapelle, 2011] and reported in the diagram of Figure 7. Indeed, both algorithms reduce to the reduced-order Kalman filter after linearization. For completeness we here recall the complete algorithm in our case, before proceeding to the result section.

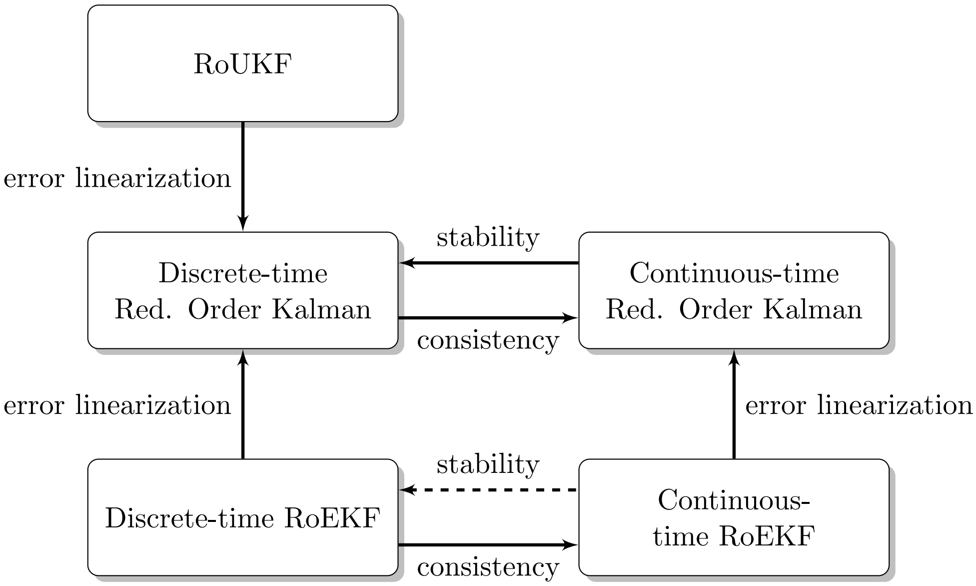

Figure 7: Relations between reduced order filtering procedures

In fact, let us introduce unitary sampling points $I^{[i]}$ and weights α_i with the following rules

$$\sum_{i=1}^{r} \alpha_i I_{[i]} = 0, \quad \sum_{i=1}^{r} \alpha_i I_{[i]} \cdot I_{[i]}^{\intercal} = \mathbb{1} \tag{45}$$

so that, at each time step, the sigma-points can be generated around the estimated values based on the covariance estimation. Given an adequate sampling rule, we store the corresponding weights in the diagonal matrix M_α and precompute the so-called unitary sigma-points (i.e. with zero mean and unit covariance) denoted by $(\vec{I}_{[i]})_{1\leq i \leq r+1}$; we also denote by $[\vec{I}_{[*]}]$ the matrix concatenating the $(\vec{I}_{[i]})$ vectors side by side, and similarly for other matrices aggregating some particle vectors.

we then perform at each time step

1. Sampling:

$$\begin{cases} Q_n & = \sqrt{(U^n)^{-1}} \\ \widehat{X}^n_{[i]+} & = \widehat{X}^+_n + L^n_{\mathrm{x}} \cdot Q_n^{\intercal} \cdot \vec{I}_{[i]}, \quad 1 \leq i \leq r+1 \\ \widehat{\theta}^n_{[i]+} & = \widehat{\theta}^+_n + L^n_{\theta} \cdot Q_n^{\intercal} \cdot \vec{I}_{[i]}, \quad 1 \leq i \leq r+1 \end{cases} \tag{46a}$$

2. State Prediction:

$$\begin{cases} \widehat{X}^{n+1}_{[i]-} & = A_{n+1|n}(\widehat{\mathrm{x}}^{n}_{[i]+}, \widehat{\theta}^{n+1}_{[i]+}), \quad 1 \leq i \leq r+1 \\ \widehat{\theta}^{n+1}_{[i]-} & = \widehat{\theta}^{n}_{[i]+}, \quad 1 \leq i \leq r+1 \\ \widehat{\theta}^{n+1}_{-} & = \sum_{i=1}^{r+1} \alpha_i \widehat{\theta}^{n+1}_{[i]-} = \widehat{\theta}^{n}_{+} \end{cases} \tag{46b}$$

3. State Correction

$$\begin{cases} Z^{n+1}_{[i]-} & = H^{n+1}(\widehat{X}^{n+1}_{[i]-}), \quad 1 \leq i \leq r+1 \\ \widehat{X}^{n+1}_{[i]-+} & = \widehat{X}^{n+1}_{[i]-} + \gamma(N + \gamma H^{\intercal} S_{n+1} H)^{-1} H^{\intercal} S_{n+1} (Z^{n+1}_{[i]-} - H \widehat{X}^{n+1}_{[i]-}), \quad 1 \leq i \leq r+1 \\ \widehat{X}^{n+1}_{-+} & = \sum_{i=1}^{r+1} \alpha_i \widehat{X}^{n+1}_{[i]-} \end{cases} \tag{46c}$$

4. Parametric Correction:

$$\begin{cases} L^{n+1}_{X} & = [\widehat{X}^{n+1}_{[*]-+}] M_{\alpha} [\vec{I}_{[*]}]^{\intercal} \\ Z^{n+1}_{-} & = \sum_{i=1}^{r+1} \alpha_i Z^{n+1}_{[i]-} \\ \Gamma^{n+1} & = [Z^{n+1}_{[*]-}] M_{\alpha} [\vec{I}_{[*]}]^{\intercal} \\ U^{n+1} & = \mathbf{1} + (\Gamma^{n+1})^{\intercal} M^{n+1} \Gamma^{n+1} \\ \widehat{X}^{n+1}_{+} & = \widehat{X}^{n+1}_{-+} - L^{n+1}_{\mathrm{x}} U^{n+1} (\Gamma^{n+1})^{\intercal} M^{n+1} (Z^{n+1} - Z^{n+1}_{-}) \\ \widehat{\theta}^{n+1}_{+} & = \widehat{\theta}^{n+1}_{-} - L^{n+1}_{\theta} U^{n+1} (\Gamma^{n+1})^{\intercal} M^{n+1} (Z^{n+1} - Z^{n+1}_{-}) \end{cases} \tag{46d}$$

5 Results

To illustrate the data assimilation method we propose to perform parameter estimation in a *synthetic data* context. More precisely, in these examples of application we will extract from an infarcted direct simulation the tag planes, tag grids and visible displacements. To do so we set in the septum – see Figure 8 – an infarct represented by an increase in stiffness and a lack of contractility. To represent both effects we define two parameters θ^K and θ such that the constant values C_0 and C_2 appearing in the hyperelastic potential and the contractility of the tissue are transformed into

$$(C_0, C_2) \to 2^{\theta^K}(C_0, C_2) \quad , \; \sigma_0 \to 2^{\theta}\sigma_0.$$

Both considered quantities, namely $\mathcal{W}$ and σ_0, are positive. This prior knowledge is the reason why the parameters appear in an exponential law in the data assimilation strategy. Moreover, this insure stability when the parameters are dynamically evolving during the simulation time window.

Using the calibration strategy of [Caruel et al., 2013] – based on a reduced modelling approach – we propose a complete set of model parameters, see Table 1, leading to a direct model that meets standard values of physiological and mechanical indicators – see Figure 9. For the parameters describing the infarct we choose

$$(\theta^K, \theta) = \begin{cases} (1, -1), & \text{in septum,} \\ \\ (0, 0), & \text{otherwise.} \end{cases}$$

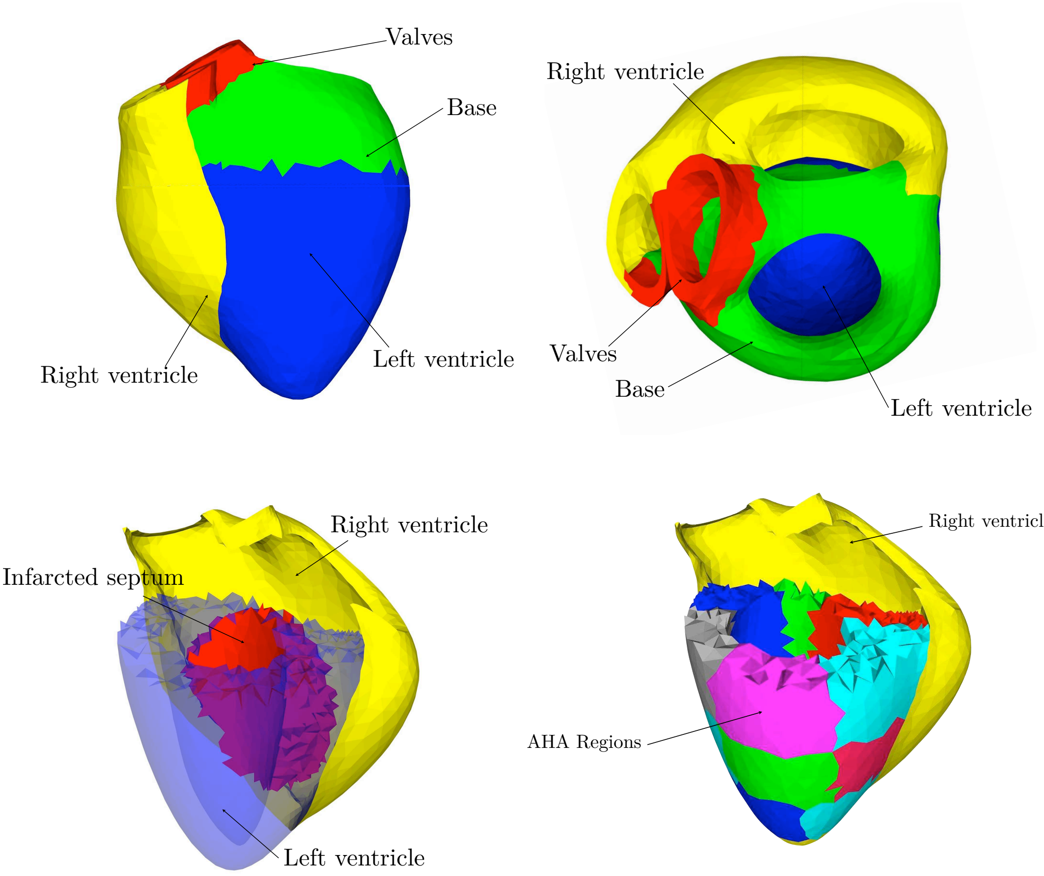

Figure 8: Model geometry, location of the infarct use in direct simulations and in the 2-region estimation case and geometry with AHA-regions in the left ventricle.

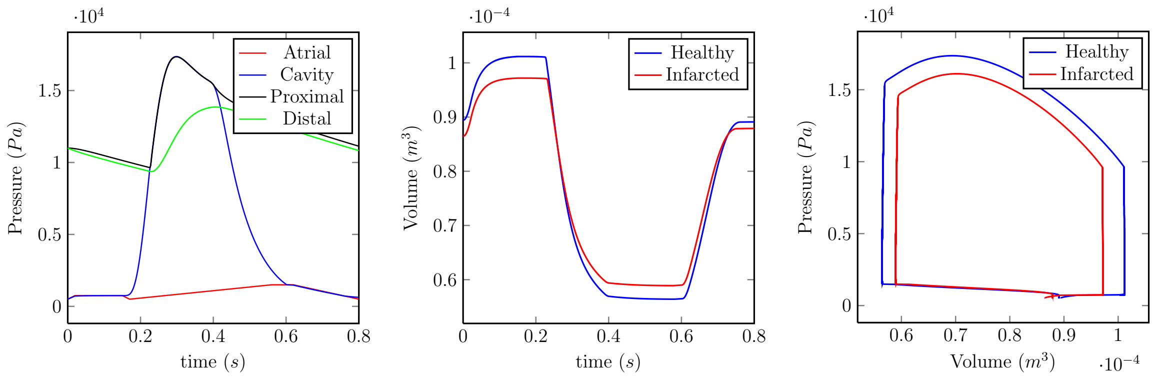

(a) Pressures (healthy heart)

(b) Cavity volumes

(c) P-V loops

Figure 9: Some indicators obtained from direct simulations.

	Valve	Base	Left Vent.	Right Vent		Valve	Base	Left Vent.	Right Vent.
C_0	$85.5 \cdot 10^3$	$28.5 \cdot 10^3$	$5.7 \cdot 10^3$	$5.7 \cdot 10^3$	α	1.5	1.5	1.5	1.5
C_1	$1.1 \cdot 10^{-1}$	$1.1 \cdot 10^{-1}$	$1.1 \cdot 10^{-1}$	$1.1 \cdot 10^{-1}$	σ_0	$6.2 \cdot 10^5$	$6.2 \cdot 10^5$	$6.2 \cdot 10^5$	$7.44 \cdot 10^5$
C_2	$57 \cdot 10^3$	$28.5 \cdot 10^3$	$5.7 \cdot 10^3$	$5.7 \cdot 10^3$	k_0	$1.0 \cdot 10^5$	$1.0 \cdot 10^5$	$1.0 \cdot 10^5$	$1.0 \cdot 10^5$
C_3	$1.1 \cdot 10^{-1}$	$1.1 \cdot 10^{-1}$	$1.1 \cdot 10^{-1}$	$1.1 \cdot 10^{-1}$	μ	$7 \cdot 10^1$	$7 \cdot 10^1$	$7 \cdot 10^1$	$7 \cdot 10^1$
η	$7 \cdot 10^1$	$7 \cdot 10^1$	$7 \cdot 10^1$	$7 \cdot 10^1$	E_s	$3.0 \cdot 10^7$	$3.0 \cdot 10^7$	$3.0 \cdot 10^7$	$3.0 \cdot 10^7$
κ	$2 \cdot 10^5$	$2 \cdot 10^5$	$2 \cdot 10^5$	$2 \cdot 10^5$					

Table 1: Set of model parameters for the heart biomechanical model.

5.1 Synthetic data generation

As we have mentioned in the introduction of this section, we aim at using synthetic data to assess the quality of our proposed tagged-MRI data assimilation strategy. However, generating such synthetic measurements appears to be a very intricate operation also. We provide in the following section the various methodological steps necessary to build, from the biomechanical heart model, the tag planes, the tag grids and the tag apparent displacements.

5.1.1 Generating tag planes and tag grids

A natural idea to build the set of tag planes from a direct simulation is to construct, from the deformed configuration at marking time, a set of bi-dimensional triangular meshes associated with the planes and to consider the nodal interpolation operator between the model tetrahedral mesh and the set of tag meshes. Denoting by $\mathcal{J}_{\mathcal{P}^i_{\mathrm{m}}}$ the interpolation operator of a single tag plane, its displacement $\underline{y}_{\mathcal{P}^i_{\mathrm{m}}}$ is, in this context, given by

$$\underline{y}_{\mathcal{P}^i_{\mathrm{m}}}(\underline{\xi}, t) = \begin{cases} \mathcal{J}_{\mathcal{P}^i_{\mathrm{m}}}(\underline{y}(\underline{\xi}, t) - \underline{y}_{\mathrm{m}}), & \text{if } \underline{\xi} \in \Omega_0 \cap \mathcal{P}^i_{\mathrm{m}}, \\ \\ 0, & \text{otherwise,} \end{cases}$$

where $\underline{y}_{\mathrm{m}}$ is the model displacement at the marking time. This leads [Imperiale et al., 2011] to significantly irregular displacements near the intersections between the model boundary and the tag planes. One way to circumvent this limitation is to consider the tag planes as an elastic material and to regularize the interpolated displacement using an appropriate elastic model. However, as the geometry at hand is bi-dimensional, a shell model would be required. To simplify this task – which is, in essence, an issue of data regularization – we consider a set of elastic (3D) tag layers $\bigcup_i^{N_{\mathcal{P}}} \mathcal{V}^i_{\mathrm{m}}$. In practice each tag layer is built so that $\mathcal{P}^i_{\mathrm{m}} \subset \mathcal{V}^i_{\mathrm{m}}$. Hence, the displacement of a tag plane $\mathcal{P}^i_{\mathrm{m}}$ derives from

$$\underline{y}_{\mathcal{P}^i_{\mathrm{m}}}(\underline{\xi}, t) = \underline{y}_{\mathcal{V}^i_{\mathrm{m}}}(\underline{\xi}, t)|_{\mathcal{P}^i_{\mathrm{m}}}, \tag{47}$$

where $\underline{y}_{\mathcal{V}_{\mathrm{m}} 0^i}$ is the displacement of the tag layer $\mathcal{V}^i_{\mathrm{m}}$, verifying

$$\begin{cases} -\underline{\mathrm{div}}(\underline{\underline{\sigma}}^{\mathcal{V}}(\underline{y}_{\mathcal{V}^i_{\mathrm{m}}})) = 0, & \text{in } \mathcal{V}^i_{\mathrm{m}} \backslash \big(\Omega_0 \cap \mathcal{P}^i_{\mathrm{m}}\big), \\ \\ \underline{y}_{\mathcal{V}^i_{\mathrm{m}}} = \mathcal{J}_{\mathcal{P}^i_{\mathrm{m}}}(\underline{y} - \underline{y}_{\mathrm{m}}), & \text{in } \Omega_0 \cap \mathcal{P}^i_{\mathrm{m}}, \\ \\ \underline{\underline{\sigma}}^{\mathcal{V}}(\underline{y}_{\mathcal{V}^i_{\mathrm{m}}}) \cdot \underline{n} = 0, & \text{on } \partial \mathcal{V}^i_{\mathrm{m}}. \end{cases} \tag{48}$$

The procedure described in (48) is in fact the extension – in the sense of Section 2.3.2 – of the interpolated displacement, namely

$$\underline{y}_{\mathcal{V}^i_{\rm m}} = \mathrm{Ext}_{\Omega_0 \cap \mathcal{P}^i_{\rm m}}\big(\mathcal{J}_{\mathcal{P}^i_{\rm m}}(\underline{y} - \underline{y}_{\rm m})\big).$$

In (48) we denoted by $\underline{\underline{\sigma}}^{\mathcal{V}}$ the Cauchy stress tensor describing the tag layer material. In practice, a relevant choice is a linearization around a given trajectory of the heart material since, within the image, the tag pattern follows the heart material points. As far as the tag grids are concerned, they are obtained by clipping the tag plane meshes with the image planes. Figure 10 illustrates the complete procedure of construction of a tag plane and of several tag lines.

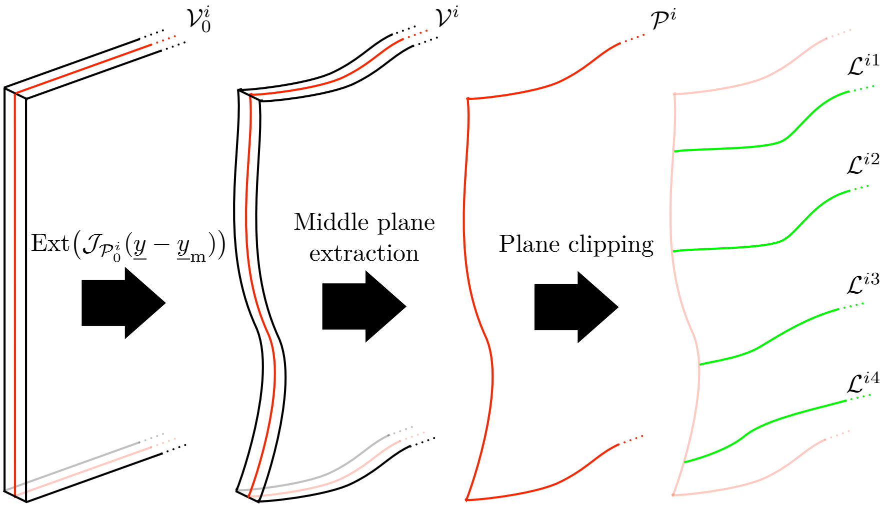

Figure 10: Illustration of synthetic tag plane and tag lines construction.

5.1.2 Generating apparent displacements

Once the tag grids are created, the apparent displacement field can be approximated by tracking the displacement of the tag lines intersection points. More precisely, at marking time, we compute the intersection point of every tag lines ((red) crosses in Figure 11(a)). During the simulation, as the tag lines deform, we track the displacement of the intersection points, leading to the (green) vectors in Figure 11(b). Once the displacements of the intersection points are computed a global apparent displacement on the image plane is obtained ((blue) vectors in Figure 11(c)) by standard interpolation.

It should be noted that the complexity of apparent displacements – discussed in Section 2.3.3 – has already been taken into account during the creation of the tag grids since clipping tag planes is, by nature, an operation of Eulerian type. As a matter of fact, any through-the-plane motion of the tag planes will not reveal on the tag grids and, subsequently, in the synthetic apparent displacements.

5.2 Discrepancy measure in practice

In this section we address a particular issue inherent to the estimation using tagged images – intimately linked to the previously called *marking time*. Addressing this issue will enable us to propose an efficient way to compute in practice the discrepancy measure between the model and the various data type described in this paper.

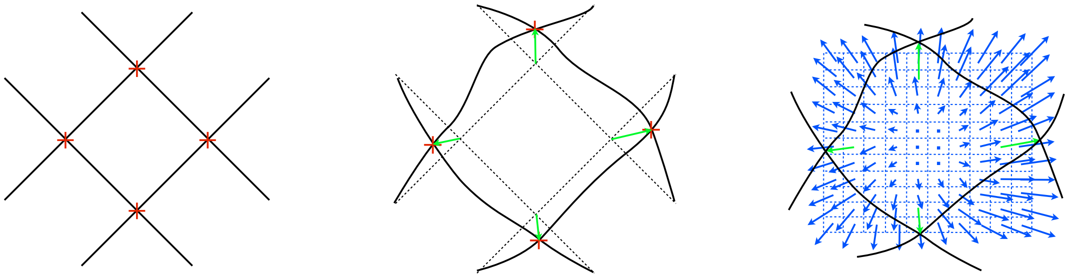

(a) Extracting tag grid intersection points

(b) Tracking intersection points

(c) Interpolation of intersection point displacement in the image plane

Figure 11: Illustration of synthetic apparent displacement computation.

The tagging process is not performed in the reference configuration – never observed in practice. For this reason, the tagging pattern is necessarily built over an already deformed configuration. Hence, any information obtained from a set of tagged-MR images should be considered of Eulerian nature.

However, assuming the displacement at marking time $\underline{y}(\xi, t_{\rm m})$ is known or (at least) estimated, we can circumvent this difficult by introducing this additional information in the filtering procedure.

From an algorithmic stand point, the discrepancy measure is computed as follows:

- 1 **[offline]** Build at marking time – i.e. using the prior on $\underline{y}(\xi, t_{\rm m})$ – the set of tag planes $\bigcup_i^{N_{\mathcal{P}}} \mathcal{P}^i_{\rm m}$.
- 2 **[offline]** Build at marking time the interpolation operator $\{\mathcal{J}_i\}_{i=1}^{N_{\mathcal{P}}}$ from the deformed configuration (by $\underline{y}(\xi, t_{\rm m})$) to the tag planes $\bigcup_i^{N_{\mathcal{P}}} \mathcal{P}^i_{\rm m}$.
- 3 **[online]** From the estimated displacement, deform the tag planes $\bigcup_i^{N_{\mathcal{P}}} \mathcal{P}^i_{\rm m}$ by

$$\forall i = 1, \dots, N_{\mathcal{P}} \quad \underline{\widehat{y}}_{\mathcal{P}^i_{\rm m}}(\underline{\xi}, t) = \mathrm{Ext}_{\Omega_0 \cap \mathcal{P}^i_{\rm m}}(\mathcal{J}_i(\, \underline{\widehat{y}}(\xi, t) - \underline{y}(\xi, t_{\rm m})\,)). \tag{49}$$

- 4 **[online]** From the estimated (deformed) tag planes $\bigcup_i^{N_{\mathcal{P}}} \widehat{\mathcal{P}}^i$ compute the innovation terms appearing in (16) (planes data), in (18) (tag grids) or in (21) (apparent displacement).

In our context of synthetic data assimilation, we directly provided the displacement $\underline{y}(\xi, t_{\rm m})$. In real cases, the task of estimating the displacement at marking time could be carried out using, for instance, the segmentation of the endo- and epicardium of the left ventricle – obtained typically from cine-MR images. In any case it requires another source of information on the system and this points out a certain limitation of the tagged-MRI data set for estimation purposes.

5.3 Spectral analysis

The quality of the state filtering procedure can be assessed by the amount of damping we introduce in the otherwise conservative or weakly damped system. For this reason we propose in this section to analyze the spectra of the operators driving the target dynamical system and the estimation error dynamical system. For simplicity we perform this analysis on the spatial semi-discrete operator and we consider a linear elastic model typically obtained from the linearization around the null trajectory of the actual heart passive model. To facilitate this analysis we also decrease the natural viscosity of the target system. Hence, we consider the solutions of the following spectral problem

$$\begin{pmatrix} 0 & K \\ -K & -C \end{pmatrix} X = \lambda \begin{pmatrix} K & 0 \\ 0 & M \end{pmatrix} X, \tag{50}$$

which corresponds to the operator without filter and where additionally to the stiffness K and mass M matrices, we denote by C the damping matrix obtained after spatial discretization. We also consider the spectral problem

$$\begin{pmatrix} \gamma K(\varepsilon K + H^\intercal M_{\text{obs}} H)^{-1} H^\intercal M_{\text{obs}} H & K \\ -K & -C \end{pmatrix} X = \lambda \begin{pmatrix} K & 0 \\ 0 & M \end{pmatrix} X, \tag{51}$$

where in (51) the form of the stabilization operator in (51) is obtained by solving the optimization problem (44).

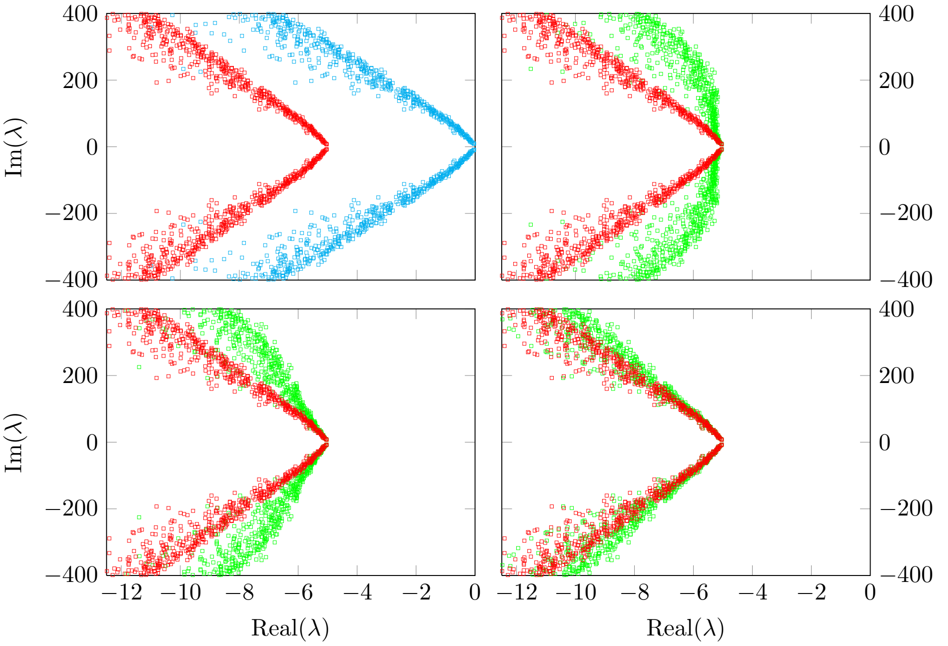

Figure 12: Spectra of the time continuous operators. (Top left) : In (cyan) operators without filter, in (red) complete displacement observer. (Top right): In (green) (3D) tag planes with spacing 8 mm. (Bottom left): In (green) (3D) tag planes with spacing 3.5 mm. (Bottom right): In (green) (3D) tag planes with spacing 0.25 mm

Using the optimal criterion on the gain provided by authors in [Moireau et al., 2009], in Figure 12 we show the spectra obtained for the operators without filter, with complete displacement feedback and with (3D) tag planes. In these plots we also vary the spacing between two consecutive tag planes to 8 mm, 3.5 mm and 0.25 mm.

In the three situations we observe that for low frequencies the observer using tag planes acts as the direct displacement observer – which is consistent with the analysis provided in Section 4.1. For coarse tag patterns we naturally observe that the higher frequencies are less stabilized that with the direct displacement observer. This phenomenon disappears as the tag pattern becomes thinner.

5.4 Estimation results

Since we have evaluated – through spectral analysis – the state estimation capabilities of our proposed observer, we can now assess the joint state and parameter estimator by identification of the infarct location and intensity presented in the beginning of the result section. We distinguish two situations. First we provide the exact location of the infarcted region but not the values of the parameters characterizing the pathology. Hence we have two distinguish regions where we should identify a contractility parameter and the main passive stiffness parameter. This case may be referred to as the 2-Regions case. Second, we use the AHA-Regions to partition the heart left myocardium and retrieve both active contractility and passive stiffness parameters by AHA-Region. That being so, the infarct location will be inferred from the parameters spatial variation through the AHA partition. In all cases, for the sake of simplicity, the reference configuration and the intra-cavity pressures are assumed to be known and the initial condition is defined by solving an equilibrium state with the lowest pressure sustained before the atrial contraction. We point out that, since the stiffness is globally modified between the target system and the observer, an error in the initial condition will be introduced during the estimation.

5.4.1 The 2-Regions case

We start with the simpler 2-Regions case and we only seek to assess the observability potential of the data provided. We assume a fine spatial distribution of the tag planes by setting the space between two consecutive tag planes to 3.5 mm. Denoting by $M_{\mathcal{T}}$ the surface mass matrix computed on the set of tags, we define the measurement observation norm S by setting, in (44)

$$M_{\text{obs}} = \frac{1}{m} M_{\mathcal{T}}.$$

The parameter m represents the square of the standard deviation of the discrepancy measure. In the perspective of only assessing the method capabilities, the observations are extracted from the direct simulations – as explained in Section 5.1 – with a high temporal resolution of 1 output every 25 simulation time step – set in our simulations to $2.5 \cdot 10^{-4}$ – , and no noise is added. Therefore, following [Chabiniok et al., 2012] we rescale

$$m = \frac{\Delta \mathrm{t}_{\text{obs}}}{\Delta \mathrm{t}} m_{\text{obs}} = 25\ m_{\text{obs}}.$$

and set a high confidence in the observations with $m_{\text{obs}} = (0.65\,\text{mm})^2$. The results are presented in Figures 13, 14, 15 and 16. In Figure 13 we consider the most optimistic configuration where three-dimensional tag planes are available whereas in Figure 14 we consider a more realistic configuration where only two directions of tag planes – here a short axis grid only – are available. Then, in Figure 15 we proceed with the corresponding bi-dimensional grid as described in Section 5.1. We thus rely on the grid-based observer discrepancy. Finally we present in Figure 16 the results where extracted 2D apparent displacements are defined as the available measurements. In this particular case, since the innovation corresponds to the comparison of two vector fields defined within the image planes, we take the observation norm as a piecewise constant mass matrix in the image domain. The behavior of the estimation procedure is very similar for all types of processed data considered, and the parameter values are accurately estimated in the two regions, both for the active (contractility) and passive (stiffness) parameters. It should be noted, in particular, that the estimations produced based on 2D tagged data – namely, with tag planes and grids, and apparent displacements – are as effective and accurate as that obtained with 3D tags.

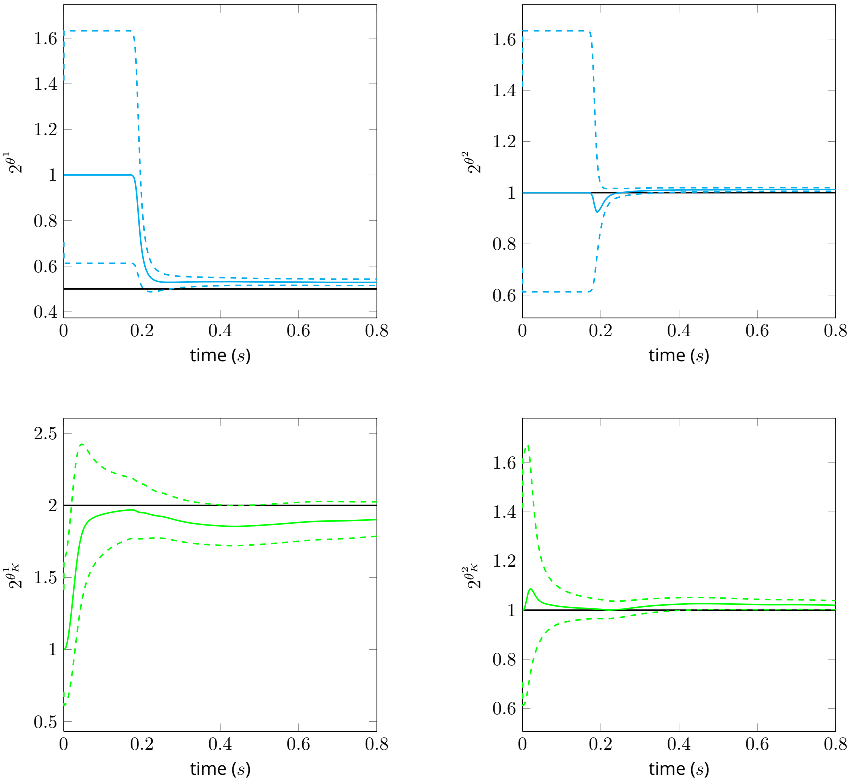

Figure 13: Estimation of passive and active parameters using (3D) tag planes.

5.4.2 The AHA-Regions case

We can now consider a configuration that could be encountered in an actual clinical context. First, we only generate from the direct simulation approximately 20 "synthetic" images in the cardiac cycle from which we extract bi-dimensional tag planes. Then, for the estimation, we set-up an AHA-based partition [Cerqueira et al., 2002] since these regions roughly correspond to the territory of the coronary arteries in the left ventricle. This delimitates 17 regions, namely the 16 AHA regions and the remaining part of the heart.

The evolution of the joint state and parameter is presented in Figure 17 and 18. The state convergence is demonstrated through the evolution of the volume curves and P-V loop plots whereas the evolution of each parameter is presented in Figure 18. The results are divided into 3 groups of parameters associated with the 3 different long axis elevations of the AHA partitions, namely basal (region 1-6), mid (region 7-12) and apical (region 14-16). We can finally produce in Figure 19 the ultimate parameter identification diagram in a bull's eye representation which can be seen as a potential practical presentation in a clinical routine. In addition, we recall the identification that would be obtained with only exploiting cine-MRI segmentation of the endocardium and epicardium as presented in the previous work [Chabiniok et al., 2012]. We directly understand here the identification benefit we have obtained with the tagged-MRI measurements, in particular concerning the passive stiffness parameters.

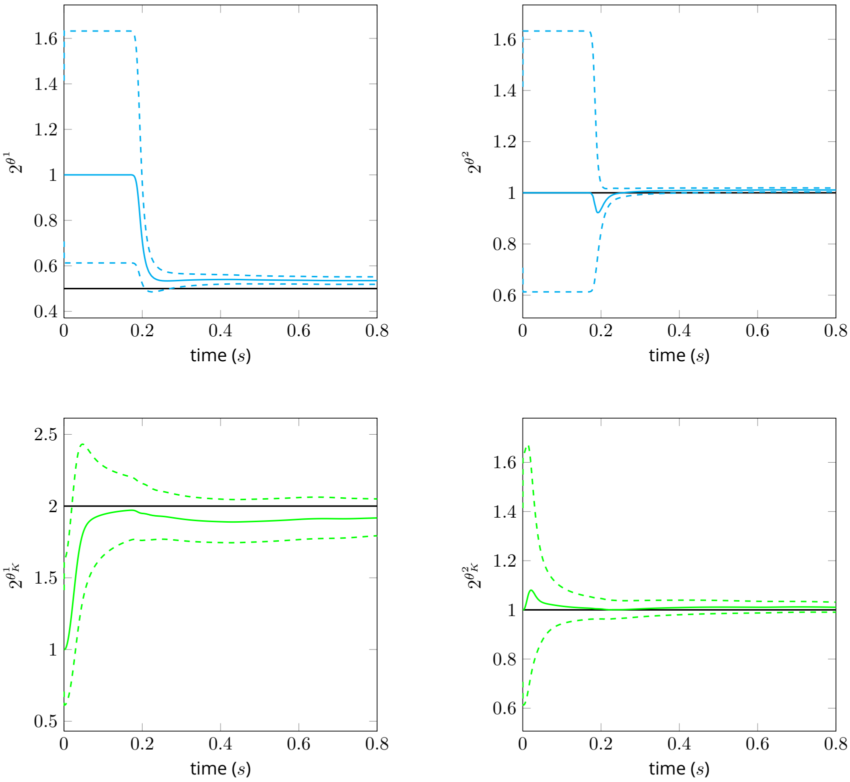

Figure 14: Estimation of passive and active parameters using tag planes.

6 Discussion

First, concerning state estimation, our results confirm the remarkable effectiveness of the previously introduced SDF filter, and the excellent adequacy of both tagged-MR as an imaging modality of choice for estimation purposes, and of our herein-proposed strategies for incorporating such data into the SDF methodology via specifically designed discrepancy operators. Indeed, the above spectral analysis gives a very clear indication as to how fast state estimation errors are being damped when using this estimation chain. The convergence of the spectrum – with respect to tag spacing – towards that of the observer with full 3D observation substantiates our above preliminary mathematical analysis, while the spectrum obtained with coarse tags shows that standard tag spacing is amply sufficient to obtain uniform damping rates. This is also confirmed with the results obtained in the joint state-parameter estimation trials, in which mechanical indicators are effectively and accurately retrieved, recall Fig. 9.

As regards parameter estimation, the additional estimation stage provided by RoUKF filtering – combined with the SDF state observer – also shows very good performance. In the 2-Regions estimation setup, in particular, both active and passive parameters are very accurately estimated, and in a very short time as soon as the parameters concerned become observable in the type of behavior that is encountered along the cardiac cycle. Namely, passive parameters are mostly observable during the – rather short – initial diastolic phase associated with atrial contraction, while of course contractility parameters can only be revealed once the electrical activation actually starts. Note that this 2-Regions setup gives a realistic strategy in clinical perspectives, as cardiac MR performed for infarct diagnosis frequently includes late-enhancement sequences, which can be segmented to provide the desired subdivision into healthy

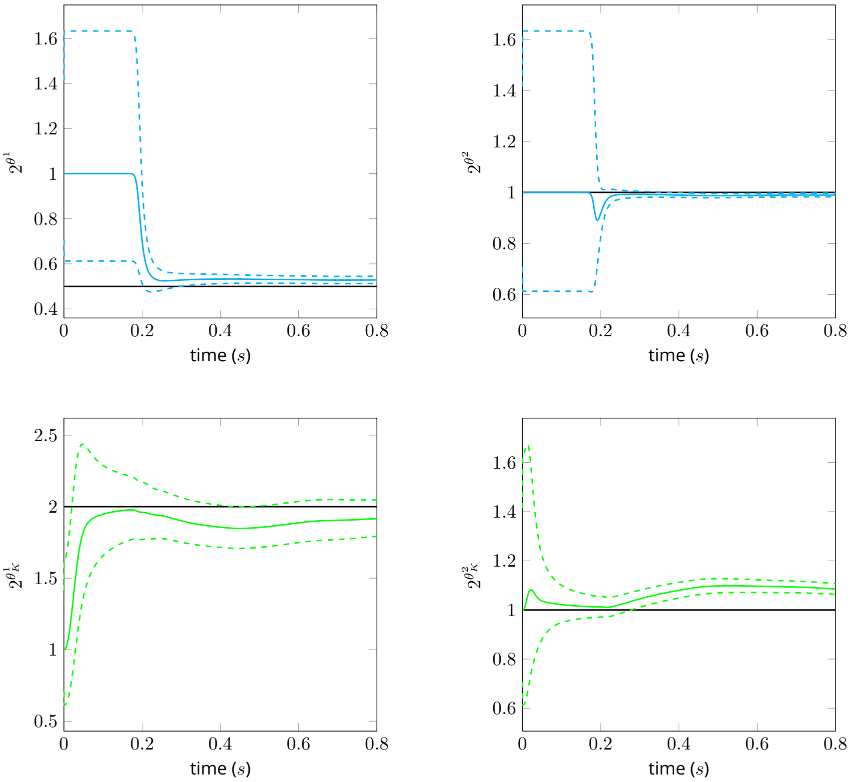

Figure 15: Estimation of passive and active parameters using tag grids.

and diseased regions. In case late-enhancement images (or the associated segmentations) are not available, or when additional concurrent localization information is desired, estimation can be performed based on the AHA subdivision. The corresponding estimation results exhibit the same general features as with two regions – namely, rather fast convergence during diastole and systole for passive and active parameters, respectively – albeit as expected the estimation is less accurate for each individual parameter. Nevertheless, active parameters are still accurately retrieved, and passive parameters are quite discriminately detected within the infarcted region, and much more so than with estimation based on Cine-MR. Of course, fundamental identifiability issues are of concern in this multiple parameter estimation context, and we can expect that identifiability would be improved – hence estimation would be more accurate – when using segmented Cine sequences in addition to tagged images in the estimation procedure.

7 Conclusions

We have proposed specific methods for integrating tagged-MR sequences in a data assimilation framework with a beating heart model. Tagged-MR represent the “gold standard” in cardiac imaging, and great benefits are expected from using the corresponding rich kinematical information for performing the joint estimation of the state of the system, and of various modeling parameters of high potential value in terms of clinical diagnosis assistance.

In this data assimilation framework, a crucial ingredient lies in the adequate formulation of a discrepancy operator to compare the model and the data. We have considered several options, based on: (1) extracted 3D displacements; (2) tag planes in the 3D volume; (3) tag grids in 2D slices; (4) apparent displacements in 2D slices. In practice, the specific choice of discrepancy

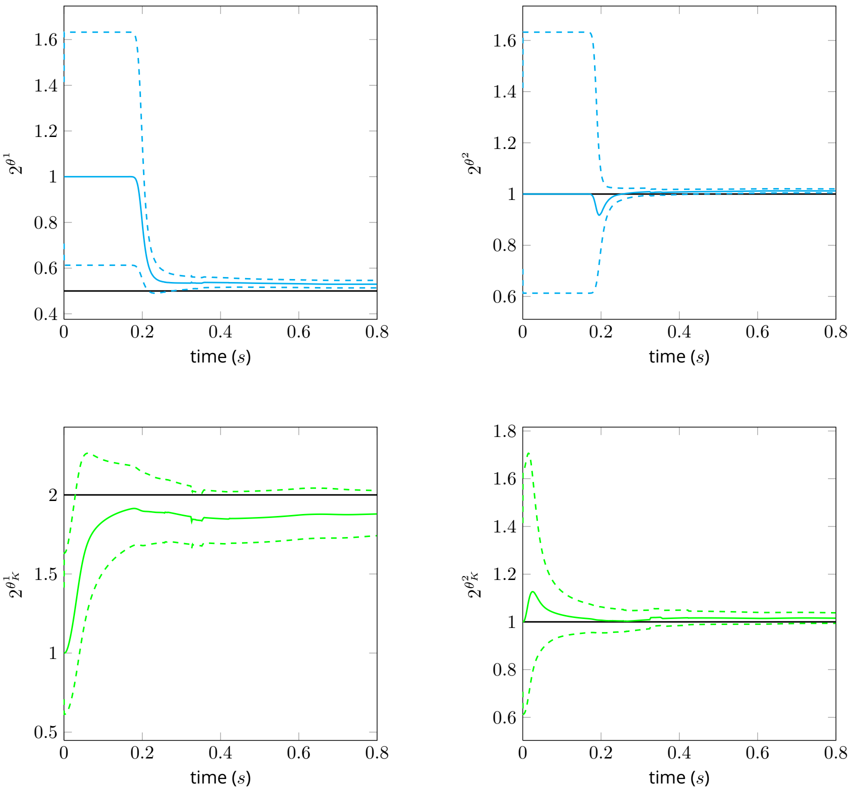

Figure 16: Estimation of passive and active parameters using apparent displacements.

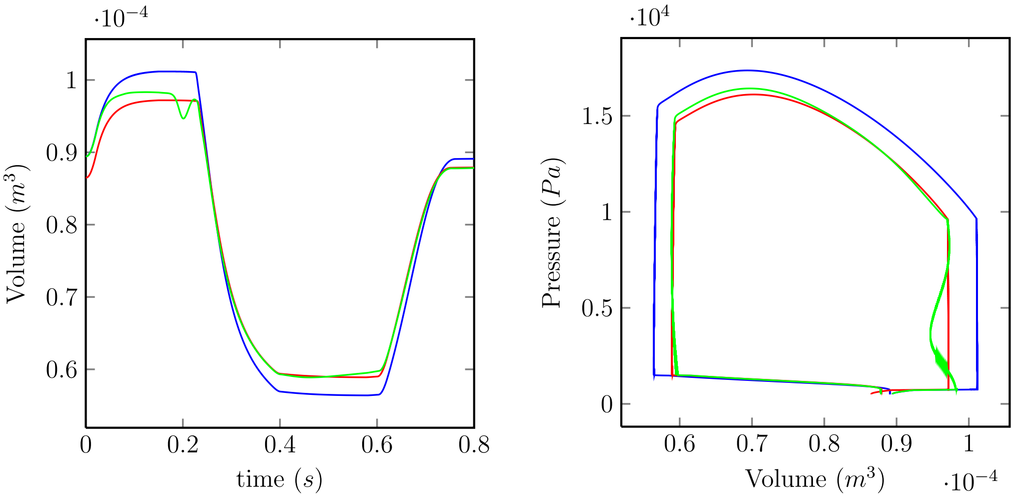

Figure 17: Evolution of the volume (in time) and of the P-V loop for the observer (in (green)) using tag planes with coarse time sampling of the observations and compared to the healthy direct model (in (blue)) and the observed infracted model (in (red)).

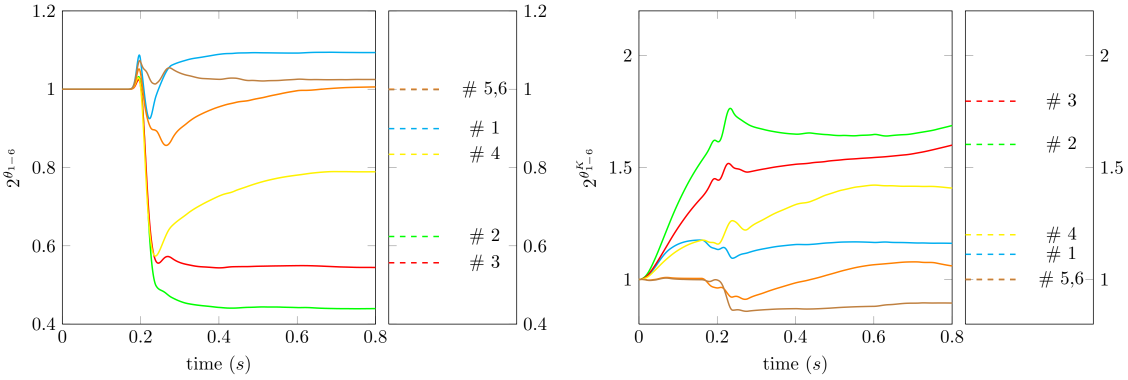

(a) Active #1 - #6

(b) Passive #1 - #6

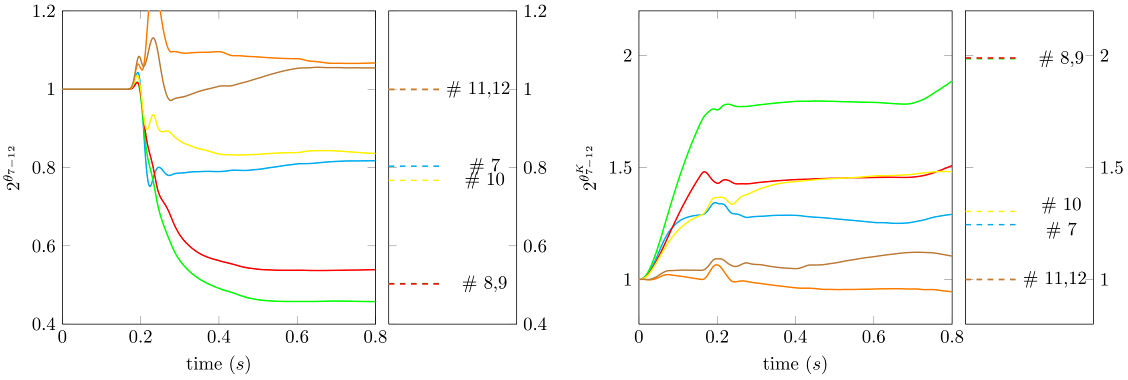

(c) Active #7 - #12

(d) Passive #7 - #12

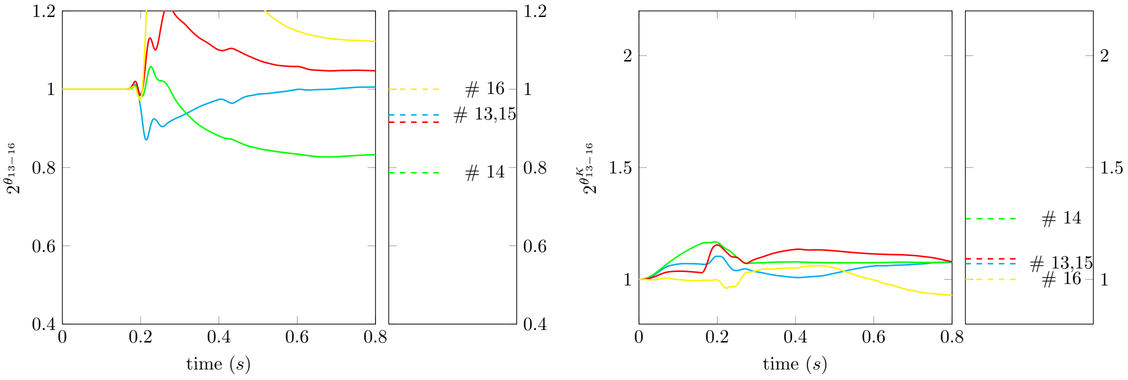

(e) Active #13 - #16

(f) Passive #13 - #16

Figure 18: Time evolution of active (left column) and passive (right column) estimated parameters using tag planes with coarse time sampling of the observations.

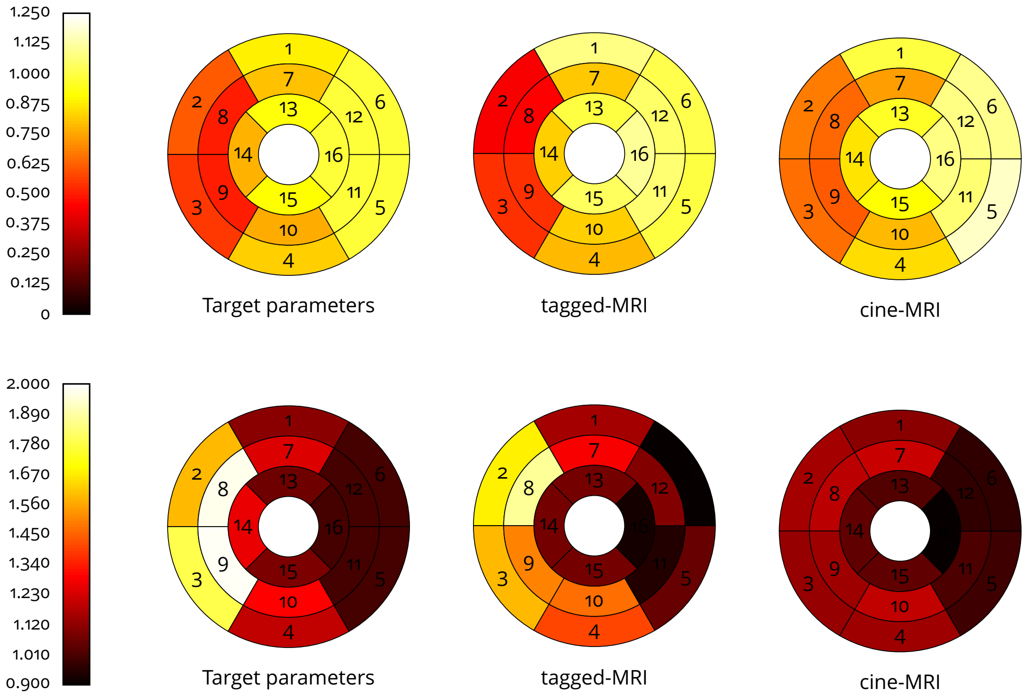

Figure 19: Estimation of active (top row) and passive (bottom row) parameters using tag planes (middle column) and cine surfaces (right column) with coarse time sampling of the observations.

operator could be based on the type of tagged sequence and on the available corresponding post-processing tools, albeit our unified framework also allows detailed comparative assessments. For the purpose of state estimation, each definition of discrepancy operator was accompanied by the formulation of an adapted filtering operator, based on the SDF concept.

We have also proposed well-adapted discretization strategies. As regards time discretization, in particular, a two-step "prediction-correction" type algorithm was designed for the proposed estimation systems, allowing to completely dissociate the operations related to the model and those performed for estimation purposes, e.g. with two different – coupled – software codes. This is very valuable from a software architecture perspective, and in particular makes the estimation strategy compatible with modular concepts such as those underlying the Verdandi assimilation library [Chapelle et al., 2012c].

Mathematical analyses have been provided at the various stages of construction, to substantiate the convergence of the overall observer strategy based on a simplified illuminating example, and also to assess the effects of discretization procedures.

Finally, some detailed numerical assessments of the overall estimation framework have been performed, based on synthetic data produced by a reference cardiac simulation representing the behavior of an infarcted heart in a realistic manner. The assessment results show that state estimation is extremely effective, while the performance of parameter estimation depends on the specific estimation objectives, as can be expected from the point of view of observability. In particular, when the diseased region is pre-determined prior to estimation, active and passive parameters are very accurately and quickly retrieved in the infarcted and healthy regions. When the more challenging objective of estimation in an AHA subdivision is considered without any prior on the diseased region, the convergence of each individual parameter value is less accurate, but the overall distribution of parameters is very adequately retrieved, allowing for effective localization and quantitative assessment of the disease. This provides a great improvement over similar estimation based on using Cine-MR alone, which only gives adequate results for active parameters.

All major ingredients are thus in place for using this methodological framework in a patient-specific context with actual data, which is of course a most natural perspective of this work. Other perspectives concern the consideration of alternative discrepancy operators, such as with the formalism of currents [Vaillant and Glaunès, 2005, Durrleman et al., 2008, Younes, 2010] which would allow to dispense with using sophisticated image post-processing tools on Tagged-MR as a prerequisite for data assimilation.

Appendix A Time discretization analysis

We recall – see (32) and (33) – that the estimation error is defined as

$$\widetilde{\mathrm{x}}_+^n = \mathrm{x}(n\Delta \mathrm{t}) - \widehat{\mathrm{x}}_+^n,$$

and the associatied prediction estimation error as

$$\widetilde{\mathrm{x}}_-^{n+1} = \mathrm{x}((n+1)\Delta \mathrm{t}) - \widehat{\mathrm{x}}_-^{n+1}.$$

The target trajectory x is solution of (30) and the observer $\widehat{\mathrm{x}}$ satisfies (31a)-(31b).

Proposition 6
Assuming that $\mathrm{x} \in C^3([0,T],\mathcal{X})$, *then the estimation error satisfies the following discrete dynamical system*

$$\begin{cases} \dfrac{\widetilde{\mathrm{x}}_-^{n+1} - \widetilde{\mathrm{x}}_+^n}{\Delta \mathrm{t}} = (\mathrm{A} + \eta \mathrm{V}) \dfrac{\widetilde{\mathrm{x}}_-^{n+1} + \widetilde{\mathrm{x}}_+^n}{2} + \varepsilon^n, & (52\mathrm{a}) \\[2ex] \dfrac{\widetilde{\mathrm{x}}_+^{n+1} - \widetilde{\mathrm{x}}_-^{n+1}}{\Delta \mathrm{t}} = -\gamma \mathrm{H}^* \mathrm{H} \widetilde{\mathrm{x}}_+^{n+1}, & (52\mathrm{b}) \\[2ex] \widetilde{\mathrm{x}}_+^0 = \mathrm{x}_0 - \widehat{\mathrm{x}}_0, \end{cases}$$

where the (bounded) source term is

$$\varepsilon^n = \frac{\Delta \mathrm{t}^2}{2} \big(\frac{1}{3} \dddot{\mathrm{x}}(\mathrm{t}_n) - \frac{1}{2} \dddot{\mathrm{x}}(\mathrm{r}_n) \big),$$

with $\mathrm{t}_n, \mathrm{r}_n \in [n\Delta \mathrm{t}; (n+1)\Delta \mathrm{t}]$.

Proof. (52b) is directly infer from the definition of the prediction estimation error and using (31b), namely

$$\begin{aligned} \widetilde{\mathrm{x}}_-^{n+1} &= \mathrm{x}((n+1)\Delta \mathrm{t}) - \widehat{\mathrm{x}}_-^{n+1} = \mathrm{x}((n+1)\Delta \mathrm{t}) - \widehat{\mathrm{x}}_+^{n+1} + \gamma \Delta \mathrm{t} \mathrm{H}^* \mathrm{H} \widetilde{\mathrm{x}}_+^{n+1} \\ &= (\mathbb{1} + \gamma \Delta \mathrm{t} \mathrm{H}^* \mathrm{H}) \widetilde{\mathrm{x}}_+^{n+1}. \end{aligned}$$

We now have to work our way to (52a). First, we remark that

$$\frac{\widetilde{\mathrm{x}}_-^{n+1} - \widetilde{\mathrm{x}}_+^n}{\Delta \mathrm{t}} = \frac{\mathrm{x}((n+1)\Delta \mathrm{t}) - \mathrm{x}(n\Delta \mathrm{t})}{\Delta \mathrm{t}} - \frac{\widehat{\mathrm{x}}_-^{n+1} - \widehat{\mathrm{x}}_+^n}{\Delta \mathrm{t}}. \tag{53}$$

Using a finite difference approximation of $\dot{\mathrm{x}}((n+1)\Delta \mathrm{t})$ and the regularity assumption on the exact trajectory we can insure that there exist some times $\mathrm{t}_n, \mathrm{r}_n \in [n\Delta \mathrm{t}; (n+1)\Delta \mathrm{t}]$ such that

$$\frac{\mathrm{x}((n+1)\Delta \mathrm{t}) - \mathrm{x}(n\Delta \mathrm{t})}{\Delta \mathrm{t}} = (\mathrm{A} + \eta \mathrm{V}) \frac{\mathrm{x}((n+1)\Delta \mathrm{t}) + \mathrm{x}(n\Delta \mathrm{t})}{2} + \frac{\Delta \mathrm{t}^2}{2} \big(\frac{1}{3} \dddot{\mathrm{x}}(\mathrm{t}_n) - \frac{1}{2} \dddot{\mathrm{x}}(\mathrm{r}_n) \big). \tag{54}$$

Therefore, feeding equation (53) with (54) and (31a), we obtain

$$\frac{\widetilde{\mathrm{x}}_-^{n+1} - \widetilde{\mathrm{x}}_+^n}{\Delta \mathrm{t}} = (\mathrm{A} + \eta \mathrm{V}) \frac{\mathrm{x}((n+1)\Delta \mathrm{t}) - \widehat{\mathrm{x}}_-^{n+1} + \mathrm{x}(n\Delta \mathrm{t}) - \widehat{\mathrm{x}}_+^n}{2} + \varepsilon^n. \tag{55}$$

Finally equation (52a) is obtained from the definition of the estimation error and its prediction. ■

Proposition 7
The norm of the estimation error, namely

$$\widetilde{\mathcal{E}}_+^{n+1} = \frac{1}{2}\left\|\widetilde{\mathrm{x}}_+^{n+1}\right\|_{\mathcal{X}}^2,$$

satisfies the following estimate

$$\frac{\widetilde{\mathcal{E}}_+^{n+1}-\widetilde{\mathcal{E}}_+^{n}}{\Delta \mathrm{t}} = -\eta \left\| (\sqrt{-\mathrm{V}})\frac{\widetilde{\mathrm{x}}_-^{n+1}+\widetilde{\mathrm{x}}_+^{n}}{2}\right\|_{\mathcal{X}}^2 - \gamma \left\|\mathrm{H}\widetilde{\mathrm{x}}_+^{n+1}\right\|_{\mathcal{Z}}^2 - \gamma^2\frac{\Delta\mathrm{t}}{2}\left\|\mathrm{H}^*\mathrm{H}\widetilde{\mathrm{x}}_+^{n+1}\right\|_{\mathcal{Z}}^2 + (\varepsilon^n, \frac{\widetilde{\mathrm{x}}_-^{n+1}+\widetilde{\mathrm{x}}_+^{n}}{2})_{\mathcal{X}}. \tag{56}$$

Proof. Denoting by

$$\widetilde{\mathcal{E}}_-^{n+1} = \frac{1}{2}\left\|\widetilde{\mathrm{x}}_-^{n+1}\right\|_{\mathcal{X}}^2,$$

we have, from system (52a)-(52b),

$$\begin{cases} \dfrac{\widetilde{\mathcal{E}}_-^{n+1}-\widetilde{\mathcal{E}}_+^{n+1}}{\Delta \mathrm{t}} = -\eta \left\| (\sqrt{-\mathrm{V}})\dfrac{\widetilde{\mathrm{x}}_-^{n+1}+\widetilde{\mathrm{x}}_+^{n}}{2}\right\|_{\mathcal{X}}^2 + (\varepsilon^n, \dfrac{\widetilde{\mathrm{x}}_-^{n+1}+\widetilde{\mathrm{x}}_+^{n}}{2})_{\mathcal{X}}, \\[2ex] \dfrac{\widetilde{\mathcal{E}}_+^{n+1}-\widetilde{\mathcal{E}}_-^{n+1}}{\Delta \mathrm{t}} = -\gamma(\mathrm{H}^*\mathrm{H}\widetilde{\mathrm{x}}_+^{n+1}, \dfrac{\widetilde{\mathrm{x}}_+^{n+1}+\widetilde{\mathrm{x}}_-^{n+1}}{2})_{\mathcal{X}}. \end{cases} \tag{57}$$

Equation (52b) leads to

$$\frac{\widetilde{\mathcal{E}}_+^{n+1}-\widetilde{\mathcal{E}}_-^{n+1}}{\Delta \mathrm{t}} = -\gamma(\mathrm{H}^*\mathrm{H}\widetilde{\mathrm{x}}_+^{n+1}, \widetilde{\mathrm{x}}_+^{n+1} + \frac{\gamma}{2}\Delta\mathrm{t}\mathrm{H}^*\mathrm{H}\widetilde{\mathrm{x}}_+^{n+1})_{\mathcal{X}} = -\gamma\left\|\mathrm{H}\widetilde{\mathrm{x}}_+^{n+1}\right\|_{\mathcal{Z}}^2 - \gamma^2\frac{\Delta\mathrm{t}}{2}\left\|\mathrm{H}^*\mathrm{H}\widetilde{\mathrm{x}}_+^{n+1}\right\|_{\mathcal{X}}^2,$$

which, by regrouping both equations in (57), entails the desired estimate. ■

Proposition 8
Assuming that the homogenous discrete dynamical system of the error, associated with system (52a)-(52b) *is exponentially stable, then there exists two constants M and μ such that the time discrete estimation error – solution of* (52a)-(52b) *– satisfies*

$$\left\|\widetilde{\mathrm{x}}_+^{n}\right\|_{\mathcal{X}} \leq M\exp(-\mu n\Delta\mathrm{t})\left\|\widetilde{\mathrm{x}}_+^{0}\right\|_{\mathcal{X}} + \frac{\Delta\mathrm{t}}{1-\exp(-\mu\Delta\mathrm{t})}\max_{1\leq i\leq n}\left\|\varepsilon^i\right\|_{\mathcal{X}}. \tag{58}$$

Proof. From (52a) and (52b) we can give the explicit relation

$$\widetilde{\mathrm{x}}_+^{n+1} = \mathcal{P}\mathcal{Q}\widetilde{\mathrm{x}}_+^{n} + \Delta\mathrm{t}\mathcal{P}\varepsilon^n,$$

where

$$\left| \begin{aligned} &\mathcal{P} = \Big(\mathbb{1} + \Delta\mathrm{t}\gamma\mathrm{H}^*\mathrm{H}\Big)^{-1}\Big(\mathbb{1} - \frac{\Delta\mathrm{t}}{2}(\mathrm{A}+\eta\mathrm{V})\Big)^{-1}, \\ &\mathcal{Q} = \Big(\mathbb{1} + \frac{\Delta\mathrm{t}}{2}(\mathrm{A}+\eta\mathrm{V})\Big). \end{aligned} \right.$$

Since both $-\gamma\mathrm{H}^*\mathrm{H}$ and $\big(\mathrm{A}+\eta\mathrm{V}\big)$ are dissipative operators they generate a contraction semigroup and we have that $\mathcal{P}$ and $\|\mathcal{P}\|_{\mathcal{L}(\mathcal{X})} \leq 1$ – see [Tucsnak and Weiss, 2009] and references therein. Using these notations we have

$$\widetilde{\mathrm{x}}_+^{n+1} = \big(\mathcal{P}\mathcal{Q}\big)^n\widetilde{\mathrm{x}}_+^{0} + \Delta\mathrm{t}\sum_{k=0}^{n-1}\big(\mathcal{P}\mathcal{Q}\big)^k\mathcal{P}\varepsilon^{n-k}.$$

The assumption that the homogeneous counterpart of system (52a)-(52b) is exponentially stable is equivalent to

$$\left\| (\mathcal{P}\mathcal{Q})^n \right\|_{\mathcal{L}(\mathcal{X})} \;\leq\; M \exp(-\mu n \Delta \mathrm{t}),$$

thus, we obtain

$$\begin{aligned}\left\|\widetilde{\mathrm{x}}_+^n\right\|_{\mathcal{X}} &\leq M \exp(-\mu n \Delta \mathrm{t}) \left\|\widetilde{\mathrm{x}}_+^0\right\|_{\mathcal{X}} + \Delta \mathrm{t} \max_{1\leq i\leq n} \left\|\varepsilon^i\right\|_{\mathcal{X}} \sum_{k=0}^{n-1} M \exp(-\mu k \Delta \mathrm{t}) \\ &\leq M \Big[\exp(-\mu n \Delta \mathrm{t}) \left\|\widetilde{\mathrm{x}}_+^0\right\|_{\mathcal{X}} + \frac{\Delta \mathrm{t}}{1-\exp(-\mu \Delta \mathrm{t})} \max_{1\leq i\leq n} \left\|\varepsilon^i\right\|_{\mathcal{X}}\Big].\end{aligned}$$

■

Proposition 9
Assuming that $\mathrm{x} \in C^3([0,T],\mathcal{X})$*, then the estimation error satisfies the following discrete dynamical system*

$$\begin{cases} \dfrac{\widetilde{\mathrm{x}}_-^{n+1} - \widetilde{\mathrm{x}}_+^n}{\Delta \mathrm{t}} = (\mathrm{A} + \eta \mathrm{V}) \dfrac{\widetilde{\mathrm{x}}_-^{n+1} + \widetilde{\mathrm{x}}_+^n}{2} + \varepsilon^n, & (59a) \\ \dfrac{\widetilde{\mathrm{x}}_+^{n+1} - \widetilde{\mathrm{x}}_-^{n+1}}{\Delta \mathrm{t}} = -\gamma \mathrm{dH}_+^{e\,*} \mathrm{dH}_+^e \widetilde{\mathrm{x}}_+^{n+1} + \lambda^n, & (59b) \\ \widetilde{\mathrm{x}}_+^0 = \mathrm{x}_0 - \widehat{\mathrm{x}}_0. \end{cases}$$

In equation (59b)*, the source term is*

$$\lambda^n = O(\left\|\mathrm{x}((n+1)\Delta \mathrm{t}) - \widehat{\mathrm{x}}_+^e\right\|_{\mathcal{X}}^2).$$

Proof. Similarly to the linear case, we have defined the prediction estimation error as

$$\widetilde{\mathrm{x}}_-^{n+1} = \mathrm{x}((n+1)\Delta \mathrm{t}) - \widehat{\mathrm{x}}_-^{n+1}.$$

This entails (59b) since from equation (37b) and the linearization of $\mathrm{H}(\mathrm{x}((n+1)\Delta \mathrm{t}))$ around the extrapolated trajectory $\widehat{\mathrm{x}}_+^e$ we have

$$\begin{aligned}\widetilde{\mathrm{x}}_-^{n+1} &= \mathrm{x}((n+1)\Delta \mathrm{t}) - \widehat{\mathrm{x}}_+^{n+1} + \gamma \Delta \mathrm{t} \mathrm{dH}_+^{e\,*}\big(\mathrm{z}^{n+1} - \mathrm{H}(\widehat{\mathrm{x}}_+^e) - \mathrm{dH}_+^e(\widehat{\mathrm{x}}_+^{n+1} - \widehat{\mathrm{x}}_+^e)\big) \\ &= (\mathbb{1} + \gamma \Delta \mathrm{t} \mathrm{dH}_+^{e\,*} \mathrm{dH}_+^e) \widetilde{\mathrm{x}}_+^{n+1} + \Delta \mathrm{t} \lambda^n.\end{aligned}$$

All the other computations previously presented to prove Proposition 6 still hold, so that we obtain the dynamical system (59a)-(59b) satisfied by the estimation error. ■

References

[Amini et al., 1998] Amini, A. A., Chen, Y., Curwen, R. W., Mani, V., and Sun, J. (1998). Coupled B-Snake grids and constrained thin-plate splines for analysis of 2D tissue defomrations from tagged MRI. *IEEE Trans. Med. Imaging.*

[Amini et al., 2001] Amini, A. A., Chen, Y., and Elayyadi., M. (2001). Tag surface reconstruction and tracking of myocardial beads from SPAMM-MRI with parametric B-spline surfaces. *IEEE Trans. Med. Imaging*, pages 94–103.

[Amini et al., 1992] Amini, A. A., Shi, P., and Constable, R. T. (1992). Energy-minimizing deformable grids for tracking tagged MR cardiac images. In *Computers in Cardiology*, pages 651–654.

[Axel and Dougherty, 1989] Axel, L. and Dougherty, L. (1989). MR imaging of motion with spatial modulation of magnetization. *Radiology*, pages 841–845.

[Axel et al., 2005] Axel, L., Montillo, A., and Kim, D. (2005). Tagged magnetic resonance imaging of the heart: a survey. *Medical Image Analysis*, 9(4):376–393.

[Bardos et al., 1988] Bardos, C., Lebeau, G., and Rauch, J. (1988). Un exemple d'utilisation des notions de propagation pour le contrôle et la stabilisation des problèmes hyperboliques. *Rendiconti del Seminario Matematico del Universita Politecnico Torino*, Fascicolo speciale (Hyperbolic Equations (1987)):12–31.

[Bathe, 1996] Bathe, K. (1996). *Finite Element Procedures.* Prentice Hall.

[Bensoussan, 1971] Bensoussan, A. (1971). *Filtrage optimal des systèmes linéaires.* Dunod.

[Bestel et al., 2001] Bestel, J., Clément, F., and Sorine, M. (2001). A biomechanical model of muscle contraction. *M. I. C. C. A. I.*, pages 1159–1161.

[Bruurmijn et al., 2013] Bruurmijn, L., Kause, H. B., Filatova, O. G., Duits, R., Fuster, A., Florack, L. M. J., and van Assen, H. C. (2013). Myocardial deformation from local frequency estimation in tagging MRI. *FIMH 2013.*

[Caruel et al., 2013] Caruel, M., Chabiniok, R., Moireau, P., Lecarpentier, Y., and Chapelle, D. (2013). Dimensional reductions of a cardiac model for effective validation and calibration. *Biomechanics and Modeling in Mechanobiology.* In press.

[Cerqueira et al., 2002] Cerqueira, M. D., Weissman, N. J., Dilsizian, V., Jacobs, A. K., Kaul, S., Laskey, W. K., Pennell, D. J., Rumberger, J. A., Ryan, T., and Verani, M. S. (2002). Standardized myocardial segmentation and nomenclature for tomographic imaging of the heart: A statement for healthcare professionals from the Cardiac Imaging Committee of the Council on Clinical Cardiology of the American Heart Association. *Circulation*, 105(4):539–542.

[Chabiniok et al., 2012] Chabiniok, R., Moireau, P., Lesault, P.-F., Rahmouni, A., Deux, J.-F., and Chapelle, D. (2012). Estimation of tissue contractility from cardiac cine-MRI using a biomechanical heart model. *Biomech. Model. Mechanobiol.*, 11(609-630).

[Chapelle et al., 2012a] Chapelle, D., Cîndea, N., de Buhan, M., and Moireau, P. (2012a). Exponential convergence of an observer based on partial field measurements for the wave equation. *Mathematical Problems in Engineering*, (581053):1–12.

[Chapelle et al., 2012b] Chapelle, D., Cîndea, N., and Moireau, P. (2012b). Improving convergence in numerical analysis using observers. the wave-like equation case. *Math. Models Methods Appl. Sci.*

[Chapelle et al., 2012c] Chapelle, D., Fragu, M., Mallet, V., and Moireau, P. (2012c). Fundamental principles of data assimilation underlying the Verdandi library: applications to biophysical model personalization within euHeart. *Medical & Biological Eng & Computing*, pages 1–13.

[Chapelle et al., 2012d] Chapelle, D., Le Tallec, P., Moireau, P., and Sorine, M. (2012d). Energy-preserving muscle tissue model: formulation and compatible discretizations. *Journal For Multiscale Computational Engineering*, 10(2):189–211.

[Chapelle et al., 2009] Chapelle, D., Moireau, P., and LeTallec, P. (2009). Robust filtering for joint state-parameter estimation in distributed mechanical systems. *Discret. Contin. Dyn. S.*, pages 65–84.

[Ciarlet, 1988] Ciarlet, P. G. (1988). *Mathematical elasticity, Volume I: Three-dimensional elasticity.* Elsevier Science Publishers.

[Costa et al., 2001] Costa, K. D., Holmes, J. W., and McCulloch, A. D. (2001). Modelling cardiac mechanical properties in three dimensions. *Phil. Trans. R. Soc.*, 359:1233–1250.

[Daoulatli et al., 2010] Daoulatli, M., Dehman, B., and Khenissi, M. (2010). Local energy decay for the elastic system with nonlinear damping in an exterior domain. *SIAM J. Control and Optimization*, 48(8):5254–5275.

[Dokos et al., 2002] Dokos, S., Smaill, B. H., Young, A. A., and LeGrice, I. J. (2002). Shear properties of passive ventricular myocardium. *Am. J. Physio. Circ. Physiol.*, 283:2650–2659.

[Dougherty et al., 1999] Dougherty, L., Asmuth, J. C., Blom, A. S., Axel, L., and Kumar, R. (1999). Validation of an optical flow method for tag displacement estimation. *IEEE Trans. Med. Imaging.*

[Durrleman et al., 2008] Durrleman, S., Pennec, X., Trouvé, A., Thompson, P., and Ayache, N. (2008). Inferring brain variability from diffeomorphic deformations of currents: an integrative approach. *Med. Image Anal.*, 12(5):626–37.

[Ervedoza and Zuazua, 2009] Ervedoza, S. and Zuazua, E. (2009). Uniformly exponentially stable approximations for a class of damped systems. *J. Math. Pures Appl.*, 91:20–48.

[Fischer et al., 1993] Fischer, S. E., McKinnon, G. C., Maier, S. E., and Boesiger, P. (1993). Improved myocardial tagging contrast. *Magn. Reson. Med.*, pages 191–200.

[Garcia-Barnés et al., 2008] Garcia-Barnés, J., Gil, D., Pujadas, S., and Carreras, F. (2008). A variational framework for assessment of the left ventricle motion. *Math. Model. Nat. Phenom.*, pages 75–100.

[Göktepe et al., 2011] Göktepe, S., Acharya, S., Wong, J., and Kuhl, E. (2011). Computational modeling of passive myocardium. *Int. J. Numer. Meth. Biomed. Engng.*, 27:1–12.

[Guccione et al., 1995] Guccione, J. M., Costa, K. D., and McCulloch, A. D. (1995). Finite element stress analysis of left ventricular mechanics in the beating dog heart. *J. Biomech.*, 28(10):1167–1177.

[Guttman et al., 1994] Guttman, M., Prince, J. L., and McVeigh, E. R. (1994). Tag and contour detection in tagged MR images of the left ventricle. *IEEE Trans. Med. Imaging*, pages 74–88.

[Holzapfel and Ogden, 2009] Holzapfel, G. A. and Ogden, R. W. (2009). Constitutive modelling of passive myocardium: a structurally based framework for material charcterization. *Phil. Trans. R. Soc*, 367:3445–3475.

[Huxley, 1957] Huxley, A. F. (1957). Muscle structure and theories of contraction. *Prog. Biophys. Mol. Bio.*, 7:258–318.

[Imperiale et al., 2011] Imperiale, A., Chabiniok, R., Moireau, P., and Chapelle, D. (2011). Constitutive parameter estimation methodology using Tagged-MRI data. *FIMH 2011.*

[Kerwin and Prince, 1998] Kerwin, W. S. and Prince, J. L. (1998). MR tag surface tracking using a spatio-temporal filter/interpolator. In *In Proc. ICIP-98*, pages 699–703.

[Khalil, 1992] Khalil, H. K. (1992). *Nonlinear systems.* MacMillan Publishing Company, New York.

[Kuijerm et al., 2000] Kuijerm, J., Marcus, J. T., Götte, J. W., Van Rossum, A. C., and Heethaar, R. M. (2000). Three-dimensional myocardial strain analysis based on short- and long- axis magnetic resonance tagged images using a 1D displacement field. *J. Magn. Reson. Im.*, pages 553–564.

[Le Tallec, 1994] Le Tallec, P. (1994). Numerical methods for nonlinear three-dimensional elasticity. volume 3 of *Handbook of Numerical Analysis*, pages 465 – 622. Elsevier.

[Ledesma-Carbayo et al., 2006] Ledesma-Carbayo, M. J., Bajo, A., Santa Marta, C., E., P.-D., Garcia-Fernandez, M. A., Desco, M., and Santos, A. (2006). Fully automatic cardiac motion estimation fro tagged MRI using non-rigid registration techniques. *IEEE Proceeding Computers in Cardiology*, pages 305–308.

[Liu, 1997] Liu, K. (1997). Locally distributed control and damping for the conservative systems. *SIAM J. Control Optim.*, pages 1574–1590.

[Lohmiller and Slotine, 2005] Lohmiller, W. and Slotine, J. (2005). Contraction analysis of non-linear distributed systems. *International Journal of Control*, 78(9):678–688.

[Luenberger, 1971] Luenberger, D. G. (1971). An introduction to observers. *IEEE T. Automat. Contr.*

[Moireau and Chapelle, 2011] Moireau, P. and Chapelle, D. (2011). Reduced-order unscented kalman filtering with application to parameter identification in large-dimensional systems. *ESAIM: COCV*, 17:380–405.

[Moireau et al., 2008] Moireau, P., Chapelle, D., and Le Tallec, P. (2008). Joint state and parameter estimation for distributed mechanical systems. *Computer Methods in Applied Mechanics and Engineering*, 197:659–677.

[Moireau et al., 2009] Moireau, P., Chapelle, D., and LeTallec, P. (2009). Filtering for distributed mechanical systems using position measurements: Perspectives in medical imaging. *Inverse Problems*, 25.

[Mosher and Smith, 1990] Mosher, T. and Smith, M. (1990). A DANTE tagging sequence for the evaluation of translational simple motion. *Magn. Reson. Med.*, pages 334–339.

[Nash and Hunter, 2000] Nash, M. P. and Hunter, P. J. (2000). Computational mechanics of the heart. *J. Elasticity*, 61:113–141.

[O'Dell et al., 1995] O'Dell, W., Moore, C. C., Hunter, W. C., Zerhouni, E. A., and McVeigh, E. R. (1995). Three-dimensional myocardial deformations: calculation with displacement field fitting to tagged MR images. *Radiology*, pages 829–835.

[Osman et al., 1999] Osman, N. F., Kerwin, W. S., McVeigh, E. R., and Prince, J. L. (1999). Cardiac motion tracking using cine harmonic phase (harp) magnetic resonance imaging. *Magn. Reson. Med.*, pages 1048–1060.

[Osman and Prince, 1998] Osman, N. F. and Prince, J. L. (1998). Direct calculation of 2D components of myocardial strain using sinusoidal MR tagging. In *Proc. SPIE Med. Imag. Conf.*

[Osman and Prince, 2000] Osman, N. F. and Prince, J. L. (2000). Visualizing myocardial function using HARP MRI. *Phys. Med. Biol.*, pages 1665–1682.

[Pan et al., 2005] Pan, L., Prince, J. L., Lima, A. C. J., and Osman, N. F. (2005). Fast tracking of cardiac motion using 3D-HARP. *IEEE Trans. Biomed. Eng.*, pages 1425–1435.

[Pham, 2001] Pham, D. (2001). Stochastic methods for sequential data assimilation in strongly nonlinear systems. *Journal of Marine Systems*, 129:1,194–1,207.

[Prince and McVeigh, 1992] Prince, J. L. and McVeigh, E. R. (1992). Motion estimation from tagged MR image sequences. *IEEE Trans. Med. Imaging.*

[Radeva et al., 1996] Radeva, P., Amini, A. A., and Huang, J. (1996). Deformable B-Solids and implicit snakes for 3D localization and tracking of SPAMM MRI-Data. *Mathematical Methods in Biomedical Image Analysis.*

[Rutz et al., 2008] Rutz, A. K., Ryf, S., Plein, S., Boesiger, P., and Kozerke, S. (2008). Accelerated whole-heart 3D CSPAMM for myocardial motion quantification. *Magn. Reson. Med.*, pages 755–763.

[Ryf et al., 2002] Ryf, S., Spiegel, M. A., Gerber, M., and Boesiger, P. (2002). Myocardial tagging with 3D CSPAMM. *Magn. Reson. Med.*, pages 320–325.

[Sachse, 2004] Sachse, F. (2004). *Computational Cardiology: Modeling of Anatomy, Electrophysiology, and Mechanics.* Springer-Verlag.

[Sainte-Marie et al., 2006] Sainte-Marie, J., Chapelle, D., Cimrman, R., and Sorine, M. (2006). Modeling and estimation of the cardiac electromechanical activity. *Comput. Struct.*, 84:1743–1759.

[Simon, 2006] Simon, D. (2006). *Optimal state estimation: Kalman, H_∞ and nonlinear approaches.* Wiley-Interscience.

[Stoeck et al., 2012] Stoeck, C. T., Manka, R., Boesiger, P., and Kozerke, S. (2012). Undersampled cine 3D tagging for rapid assessment of cardiac motion. *J. Cardiov. Magn. Reson.*

[Tucsnak and Weiss, 2009] Tucsnak, M. and Weiss, G. (2009). *Observation and control for operator semigroups.* Birkhäuser Basel.

[Vaillant and Glaunès, 2005] Vaillant, M. and Glaunès, J. (2005). Surface matching via currents. In *Proceedings of the 19th international conference on Information Processing in Medical Imaging*, volume 3565 of *IPMI'05*, pages 381–392, Berlin, Heidelberg. Springer-Verlag.

[Vetter and McCulloch, 2000] Vetter, F. J. and McCulloch, A. D. (2000). Three-dimensional stress and strain in passive rabbit left ventricl: a model study. *Ann. Biomed. Eng.*, 28:781–792.

[Younes, 2010] Younes, L. (2010). *Shapes and Diffeomorphisms.* Springer.

[Zerhouni et al., 1988] Zerhouni, E. A., Parish, D., Rogers, W., Yang, A., and Shapiro, E. (1988). Human heart : tagging with MR imaging - a method for noninvasive assessment of myocardial motion. *Radiology*, pages 59–63.

[Zhang and Clavel, 2001] Zhang, Q. and Clavel, A. (2001). Adaptive observer with exponential forgetting factor for linear time varying systems. In *Decision and Control, 2001. Proceedings of the 40th IEEE Conference on*, volume 4, pages 3886–3891.

[Zhang et al., 2007] Zhang, X., Zheng, C., and Zuazua, E. (2007). Exact controllability of the time discrete wave equation: a multiplier approach. *Discret. Contin. Dyn. S.*

[Zuazua, 2005] Zuazua, E. (2005). Propagation, observation, and control of waves approximated by finite difference methods. *SIAM Review*, 47(2):197–243.

CHAPTER 4

The formalism of *currents* in a data assimilation context

This Chapter takes the form of a pre-printed article gathering the work carried out in collaboration with A. Routier and P. Moireau.

The main contributions of this article are twofold. First we are able to bring together the concept of *external energy* used in the image processing community – typically used to attract a template object towards a specific region of interest of the gray-level image – and the idea of *discrepancy measure* used in the field of data assimilation. More precisely, we show that the descent methods used to solve *static registration problems* correspond in fact to the correction steps of a dynamical state estimator. This enables us to foresee a sate estimation methodology based on the sophisticate dissimilarity measurements proposed in the image processing field.

As an example – and this is the second contribution of this article – we apply this strategy to the formalism of currents. This formalism aims at representing surfaces as a computational support through their normal vector field. Therefore, any surface can be seen as a linear form on a space of test vector fields, *i.e.* any surface belongs to the dual of this space of test functions. This type of representation was already well-known and in our work we focus our attention on plugging these concepts into a joint state and parameter estimation strategy. The first trials within this context are were published in a proceeding

Improving efficiency of data assimilation procedure for a biomechanical heart model by representing surfaces as currents. *Imperiale, A., Routier, A., Durrleman, S. and Moireau, P.* – FIMH 2013.

Hence, with this new means of comparing the mechanical model and some observations taking the form of surfaces – typically obtained after the segmentation of cine-MRI – we apply a sequential data assimilation procedure to perform parameter identification on a complete biomechanical model. Additionally, we show how this formalism enables us to enlarge the range of data sets that we could filter and we give an example by computing discrepancy measures between the model and level-set functions directly obtained from the raw images – which clearly reduces our demands on a hypothetical prior image processing step.

State estimation of distributed mechanical systems using domain information from current based discrepancy measurements

A. Imperiale†, A. Routier†‡, P. Moireau†,
†Inria, Project-Team MΞDISIM,
‡ICM, Hôpital La Pitié-Salpêtrière, Paris, France

Contents

1 Introduction

Image segmentation is a classical but still active topic with many applications in particular in medical imaging processing in order to extract organs boundaries in static images or in image sequences [Chan and Shen, 2005, Scherzer, 2011]. Among the large variety of image segmentation methods, active contours (in 2D) or surfaces (in 3D), also called deformable objects, are very popular – see for instance [Cohen et al., 1992, Caselles et al., 1997, Aubert et al., 2003, Gout et al., 2005, Sermesant et al., 2003, Li and Acton, 2007, Cohen and Peyré, 2011] and references therein. They traditionally rely on the minimization of a functional [Cohen et al., 1992, Caselles et al., 1997, Aubert et al., 2003, Gout et al., 2005]– also called criterion – involving an image-based computed similarity term and some *a priori* acting as regularization terms. There is a impressive literature on the definition of the image-based similarity term in the image processing community. For instance, distances to contours based similarity have been introduced [Cohen et al., 1992, Sermesant et al., 2003, Peters et al., 2007, Peyré et al., 2012], but also specific fields of contour-nudging such as the gradient vector flow [Xu and Prince, 1998, Li and Acton, 2007, Guillot and Bergounioux, 2009]. In every situation the model-data similarity generates a force that deforms the model object in the direction of the contours of the observed object. Since two shapes are eventually compared, all the methods presented in the image processing context find also an echo in the shape or geometry inference [Younes, 1998, Delfour and Zolésio, 2011, Jones et al., 2006, Chazal et al., 2011, Peyré et al., 2012] where intricate shape distances have been defined. Recently, an original formalism called *currents* has been introduced [Vaillant and Glaunès, 2005, Durrleman et al., 2009, Younes, 2010] in order to define a contour or a surface in a vectorial space by considering by duality their action on a space of vector fields. Once this space is set up the similarity between two contours is directly given by the norm of the difference. In fact, the complexity lies on the shape space definition but then the distances is as simple as a norm. That is why among the rich shape inference methods developed in the literature we have decided to focus on the generic approach offered by the *currents*.

Coming back to the functional definition, we can say that, except in some *a prori*, it does not rely on a strong physical – biophysical in medical imaging – description of the object even in image sequences where a potential full model of the followed object should help a dynamical segmentation. Conversely, data assimilation [Navon, 2008, Blum et al., 2008] – a scientific field initiated in the 70's in environmental sciences which aims at register a physical model on available data – has recently been introduced in life sciences applications as the tool to perform a biophysical personalization of biomechanical model such as the heart [Chapelle et al., 2012b]. In data assimilation, variational methods also rely on a functional minimization with a model-data discrepancy term and some *a priori*. However, whereas the physical models are very detailed, the data at hand are assumed to be available in a form readily exploitable in the data assimilation framework assuming that all the intricate data processing work has been made in a previous step.

We believe that there exists an important benefit in exploiting with the same level of details and the same level of confidence a model and data, in order to provide a unified and rich state estimation of an imaged deformable body. Our strategy is to combine predictive model of motions and state-of-the art similarity measurements in order to propose a unified state estimation of the evolution of a deformable object. In this respect, our methodology is to present how image registration methods defined in a static context where only one image is considered can be translated in the dynamics context in order to correct the model evolution with the data similarity. It will result in a complex dynamic estimator – also called observer in the data assimilation community – which extends the initial strategy presented in [Moireau et al., 2009] by using the *current* formalism to better compare the model and the data. The gain of accuracy obtained by the use of a *current*-based similarity will be assessed by evaluating the capability of the estimator to stabilize efficiently to the target trajectory. As an illustration we specifically have in mind the example of the interpretation of image sequences of the heart contraction, but our methodology is general and can be adapted to various applications. Finally, this work deeply deepens and extends the initial work of [Imperiale et al., 2013], with a computational mechanics point of view allowing also a completely original numerical implementation.

The outline of the paper is as follows. In a first section we develop the formalism of a deformable object submitted to a discrepancy measurement in order to register on a given position. Here we present efficient *Sobolev gradient* descent strategies and show how various extensions can be introduced, for example nonlinearities, rigid body registration etc. Then we show how the formalism of *currents* can be considered in this framework and we derive all the necessary computations for a practical implementation. In the third section, we then consider the dynamical case where a sequence of data is available. We see how the *currents*-based discrepancy defined in the static case can then be directly plugged into a sequential estimator of the motion based on a physically accurate model. We illustrate our strategy with a heart model and even show how some model parameter estimation can be jointly performed in order to increase the prediction capability of the overall data-model interaction system.

2 The static case

In this first section we consider the static registration problem. This problem aims at fitting a *deformable object* – initially in a given reference configuration – to some observations that we have at our disposal. The main difficulty inherent to this type of problem is that the observations are dramatically incomplete and a direct solving is by nature ill-posed. Traditionally, in the most simple cases, a convenient way to propose a solution is to use a Tikhonov regularization process [Henn and Witsch, 2001] in order to invert a generalized inverse of observation operator giving the data to the reference configuration. Instead of explicitly computing some inverse, it is also classical to use descent methods [Neuberger, 1997]. This descent method is built so that, step by step, the obtained solution decreases a similarity measurement between the deforming object and the data. Therefore as an introduction, we gather the key components in a simplified linear setting in order to solve a registration problem using a descent method. This presentation will enable us to propose adequate spaces for the displacements of the deformable object and for the observation. In a second step we then illustrate how this procedure can extend to nonlinear cases.

2.1 A preliminary linear example

2.1.1 The registration problem – abstract formulation

Let Ω_0 be a reference configuration from where we consider a deformation map $\underline{\varphi}$ generating the domain Ω. We have

$$\left|\begin{array}{l}\Omega_0 \to \Omega \\ \underline{\xi} \mapsto \underline{\mathrm{x}} = \underline{\varphi}(\underline{\xi}) = \underline{\xi} + \underline{y}(\underline{\xi}),\end{array}\right.$$

with $\underline{y}$ the displacement vector field. We want to formulate the registration problem as finding a displacement field in a suitable functional space that will deform the reference configuration into the observed configuration. From a notation point of view, we will denote in the sequel the displacement vector field by $\underline{y}$ whereas y will simply denote the displacement as an element of a given functional space denoted $\mathcal{Y}$. This first example is a simplified case in which we assume that we have registered some landmarks, typically on the boundary of the domain as it is often easier in image processing since the boundary of an object present a more textured pattern. Proveided that these landmark are numerous enough, we can expect to have extracted the displacement on a part of the boundary $\Gamma_0^{\text{obs}} \subset \partial\Omega_0$. We can define a so-called *observation operator* as the operator which can generate this type of observations

$$H : \left| \begin{array}{l} \mathcal{Y} \to \mathcal{Z} \\ y \mapsto z, \end{array} \right. \tag{1}$$

where $\mathcal{Y}$ generically represents the chosen displacement space and $\mathcal{Z}$ the observation space. In our work we assume that both $\mathcal{Y}$ and $\mathcal{Z}$ are Hilbert spaces. We refer to the next section for the adequate definition and choice of these spaces. From an abstract standpoint the registration problem consists in solving the following problem

$$\text{Find } y \in \mathcal{Y} \text{ such that } D(y,z) = z - Hy \text{ is as close to 0 as possible.} \tag{$\mathcal{P}$}$$

We will restrict to operator $H \in \mathcal{L}(\mathcal{Y}, \mathcal{Z})$ as it will be mostly the case in the case. Introducing the discrepancy functional – or similarity functional depending of the point of view – as

$$\mathscr{D}(y,z) = \frac{1}{2}\|D(y,z)\|_{\mathcal{Z}}^2 \tag{2}$$

we should find the minima – here 0 if $z \in \operatorname{Ran}(H)$ – of $\mathscr{D}$. In practice, D is not invertible assuming we rely on [Neuberger, 1997] (Chap. 3) to define a solution to our problem expressed as a solution of a descent method.

Theorem 1 ([Neuberger, 1997] Chap. 3)
Let $y_\diamond \in \mathcal{Y}$ and $y(t)$ the function defined on $[0,\infty)$ by

$$\begin{cases} \dot{y}(t) = -\nabla_y \mathscr{D}(y(t), z), & t \geq 0, \\ y(0) = y_\diamond, \end{cases} \tag{3}$$

has a limit $\bar{y} = \lim_{t\to\infty} y(t)$ and

1. *if $\operatorname{Ran}(H) \cap \mathcal{Y} \neq \varnothing$, then $D(\bar{y}) = 0$ and y is the nearest element to $y_\diamond$ which has this property.*
2. *in every case $D(\bar{y}, z) = z - \Pi z$ where Π is the orthogonal projector onto $\operatorname{Ran}(H) = \operatorname{Ker}(H^*)^\perp$.*

Let us recall in what sense the formulation (3) should be understood. First, we should consider a set of admissible displacements $\{y(t)\}_{t\geq 0} \subset \mathcal{Y}$ depending on an artificial time t such that when we evolve along this trajectory the discrepancy functional $\mathscr{D}(y(t), z)$ decreases. Secondly, the functional evaluated on this set of admissible displacements becomes a time-evolutive functional whose time derivative reads

$$\frac{\partial}{\partial t}\mathscr{D}(y(t), z) = \langle \mathrm{d}_y \mathscr{D}(y(t), z), \dot{y}(t)\rangle_{\mathcal{Y}^*, \mathcal{Y}}.$$

Therefore, by setting

$$\forall y^\flat, \quad \langle \mathrm{d}_y \mathscr{D}(y, z), y^\flat \rangle_{\mathcal{Y}^*, \mathcal{Y}} = -(\dot{y}(t), y^\flat)_{\mathcal{Y}},$$

we naturally obtain that

$$\frac{\partial}{\partial t}\mathscr{D}(y(t),z) = -\|\dot{y}\|_{\mathcal{Y}}^2 \leq 0,$$

which is a necessary condition for the discrepancy functional to decrease all along $\{y(t)\}_{t\geq 0}$. Since $\mathcal{Y}$ is assumed to be a Hilbert space, invoking the Riesz representation theorem, we can introduce the gradient of the differential $\mathscr{D}$ as the element of $\mathcal{Y}$ such that

$$\forall y^\flat, \quad (\nabla_y \mathscr{D}(y,z), y^\flat)_{\mathcal{Y}} = \langle \mathrm{d}_y \mathscr{D}(y,z), y^\flat \rangle_{\mathcal{Y}^*,\mathcal{Y}}.$$

Hence, the trajectory $y(t)$ satisfies, in a weak form, the following dynamics

$$\begin{cases} (\dot{y}(t), y^\flat)_{\mathcal{Y}} = -(\nabla_y \mathscr{D}(y(t),z), y^\flat)_{\mathcal{Z}}, \quad \forall y^\flat, \quad t \geq 0, \\ y(0) = y_\diamond, \end{cases} \tag{4}$$

which is the exact weak formulation of (3). Moreover, from the definition (2) of the functional we obtain

$$\forall y^\flat, \quad (\dot{y}, y^\flat)_{\mathcal{Y}} = -\langle \mathrm{d}_y \mathscr{D}(y,z), y^\flat \rangle_{\mathcal{Y}^*,\mathcal{Y}} = (z - Hy, Hy^\flat)_{\mathcal{Y}}.$$

Thus, denoting by $H^* \in \mathcal{L}(\mathcal{Z},\mathcal{Y})$ the adjoint of the observation operator, we get

$$(\dot{y}, y^\flat)_{\mathcal{Y}} = (H^*(z - Hy), y^\flat)_{\mathcal{Y}}.$$

We see that the strong formulation of (3) is given as in [Neuberger, 1997] by

$$\dot{y} = -\nabla_y \mathscr{D}(y,z) = H^*(z - Hy). \tag{5}$$

In fact in [Neuberger, 1997], it is proved that e^{-tH^*H} converges to the projector on $\mathrm{Ker}(H)$. Therefore we understand how (3) eventually filters the potential noise present into the data. More precisely introducing the target solution $y_\bullet$ such that

$$z = Hy_\bullet + \chi$$

with χ some errors, the estimation error $\tilde{y} = y_\bullet - y$ follows the pseudo-dynamics

$$\dot{\tilde{y}} = -H^*H\tilde{y} - H^*\chi.$$

leading to

$$\tilde{y} = e^{-tH^*H}\tilde{y}(0) + \int_0^t e^{-(t-s)H^*H} H^*\chi \, ds.$$

However, since $\mathrm{Ker}(H)$ is rarely reduced to 0, the estimation can not be proved to converge to 0. This is why in practice other sources of information are introduced – typically some *a priori* to generate a unique estimator with exact convergence.

Remark 1 – In the light of Theorem 1, we can understand the descent method (3) as a way to compute the projection onto $\mathrm{Ker}(D^*) \subset \mathcal{Y}$. As it is expected of any projection process, it highly depends on the chosen metrics and this choice will influence both the obtained result and the speed of convergence of (3). In our setting, we need to choose both metrics of the observation space and the displacement space.

2.1.2 Formulation associated with the choice of spaces

In this section we propose to summarize the various possibilities for the metrics on $\mathcal{Z}$ and $\mathcal{Y}$. Moreover, since the adjoint of the observation operator depends on these metrics we will give the expression of H^* in every relevant case, thus entailing the explicit expression of the descent algorithm (3).

Spaces definition A first idea is to define the most simple spaces for the displacements and the observations as $\mathcal{L}^2(\Omega_0, \mathbb{R}^3)$ and $\mathcal{L}^2(\Gamma_0^{\text{obs}}, \mathbb{R}^3)$ respectively. However these spaces are possibly too naive since a displacement $\mathcal{L}^2(\Omega_0, \mathbb{R}^3)$ has no trace on the boundary Γ_0^{obs} and therefore can not lead to an observed displacement in $\mathcal{L}^2(\Gamma_0^{\text{obs}}, \mathbb{R}^3)$. We can then assume that the displacement we are seeking is the resulting displacement of a deformable body. Therefore, we should consider that $y \in \mathcal{H}^1(\Omega_0, \mathbb{R}^3)$ has it is the classical space of definition for an elastic body. Any element of $\mathcal{H}^1(\Omega_0, \mathbb{R}^3)$ has a trace on the boundary Γ_0^{obs} and we can reasonably assume that the observation space is $\mathcal{H}^{\frac{1}{2}}(\Gamma_0^{\text{obs}}, \mathbb{R}^3)$. In order to simplify the presentation of this first example, we suppose that the deformable solid under consideration is fixed on part of its boundary and we will see in the next section how we can relax this assumption. In essence, this means that we have some landmarks where we absolutely trust that the displacement is null. We thus define $\Gamma_0^{\text{D}} \subset \partial\Omega_0$ and exclude Γ_0^{D} from Γ_0^{obs} – namely $\Gamma_0^{\text{obs}} \cap \Gamma_0^{\text{D}} = \varnothing$. Then, our space for the displacement becomes

$$\mathcal{H}^1_{\text{D}}(\Omega_0, \mathbb{R}^3) = \Big\{ y \in \mathcal{H}^1(\Omega_0, \mathbb{R}^3) \,|\, y_{|\Gamma_0^{\text{D}}} = 0 \Big\}.$$

From the previous definition, any combination of displacement and observation space can be considered *a priori*

$$\begin{tikzcd}
 & \mathcal{L}^2(\Omega_0, \mathbb{R}^3) \arrow[rr, leftrightarrow] \arrow[ddrr, leftrightarrow] & & \mathcal{L}^2(\Gamma_0^{\text{obs}}, \mathbb{R}^3) \\
\mathcal{Y} & & \mathcal{Z} & \\
 & \mathcal{H}^1_{\text{D}}(\Omega_0, \mathbb{R}^3) \arrow[rr, leftrightarrow] \arrow[uurr, leftrightarrow] & & \mathcal{H}^{\frac{1}{2}}(\Gamma_0^{\text{obs}}, \mathbb{R}^3).
\end{tikzcd}$$

However, clearly, some spaces seem more adapted to each other. And some combinations seems unadapted since it is impossible to consider in general that a displacement initially in $\mathcal{L}^2(\Omega_0, \mathbb{R}^3)$ where no trace exists on the boundary can generate observations on $\mathcal{L}^2(\Gamma_0^{\text{obs}}, \mathbb{R}^3)$ and even more in $\mathcal{H}^{\frac{1}{2}}(\Gamma_0^{\text{obs}}, \mathbb{R}^3)$. The objective in this first section is to show that these choices – even the non relevant ones – have consequences with respect to our registration objective and the convergence speed of our methodology.

Spaces metrics Before going further, we need to define adequate norms on the different spaces introduced. Concerning $\mathcal{H}^1_{\text{D}}(\Omega_0, \mathbb{R}^3)$, we denote by $\underline{\underline{\sigma}}_\ell$ the corresponding Cauchy stress tensor assumed to be a linear function of the linearized strain tensor

$$\underline{\underline{\varepsilon}} = \frac{1}{2}\Big(\underline{\underline{\nabla}}_{\xi}\underline{y} + (\underline{\underline{\nabla}}_{\xi}\underline{y})^{\intercal}\Big),$$

in the sense that

$$\underline{\underline{\sigma}}_\ell = \underline{\underline{\underline{\underline{A}}}} : \underline{\underline{\varepsilon}}, \tag{6}$$

where the fourth order elasticity tensor is used to characterize the order of magnitude of the deformation stiffness we are seeking. For our application cases, it is assumed to be constant but this can be generalized with a spatially dependency by considering for example

$$\underline{\underline{\underline{\underline{A}}}} \in \mathcal{L}^\infty(\Omega)^6.$$

From Korn and Poincaré inequalities we justify the use of the corresponding norm

$$\forall \underline{y} \in \mathcal{Y}, \quad \|y\|^2_{\mathcal{Y}} = \int_{\Omega_0} \underline{\underline{\varepsilon}}(\underline{y}) : \underline{\underline{\underline{\underline{A}}}} : \underline{\underline{\varepsilon}}(\underline{y}) \, \mathrm{d}\Omega.$$

When $\mathcal{Z}$ is $\mathcal{L}^2(\Gamma_0^{\mathrm{obs}}, \mathbb{R}^3)$, its metrics is given by the standard $\mathcal{L}^2$ inner product. In the case where $\mathcal{Z}$ is not simply of $\mathcal{L}^2$ type, we define a $\mathcal{H}^{\frac{1}{2}}$-norm based on the following extension operator

$$\mathrm{Ext}^{\mathrm{D}}_{\Gamma_0^{\mathrm{obs}}} : \left| \begin{array}{l} \mathcal{Z} \to \mathcal{Y} \\ z \mapsto y \text{ such that } \begin{cases} -\underline{\nabla} \cdot (\underline{\underline{\sigma}}_\ell(\underline{y})) = 0 & \text{in } \Omega_0 \\ \underline{\underline{\sigma}}_\ell(\underline{y}) \cdot \underline{n} = 0 & \text{on } \Gamma_0^{\mathrm{N}} \backslash \Gamma_0^{\mathrm{obs}} \\ \underline{y} = \underline{z} & \text{on } \Gamma_0^{\mathrm{obs}} \\ \underline{y} = 0 & \text{on } \Gamma_0^{\mathrm{D}}. \end{cases} \end{array} \right. \tag{7}$$

Indeed, using this extension operator, we are able to define (see Appendix A) the following norm on $\mathcal{Z}$

$$\|z\|_{\mathcal{Z}} = \|\mathrm{Ext}^{\mathrm{D}}_{\Gamma_0^{\mathrm{obs}}}(z)\|_{\mathcal{Y}} \tag{8}$$

which is equivalent to the usual Sobolev norm $\mathcal{H}^{\frac{1}{2}}(\Gamma_0^{\mathrm{obs}}, \mathbb{R}^3)$. This choice of norm – consistent with our definition of the norm on $\mathcal{Y} = \mathcal{H}^1_{\mathrm{D}}(\Omega_0, \mathbb{R}^3)$ – will reveal to be very helpful in the rest of our computations.

Adjoint definition We can now define the corresponding adjoint of the observation operator, namely $H^* \in \mathcal{L}(\mathcal{Z}, \mathcal{Y})$ such that

$$\forall (y, z), \quad (y, H^* z)_{\mathcal{Y}} = (Hy, z)_{\mathcal{Z}}. \tag{9}$$

We verify by simple computations that

- in the case of $\mathcal{Y} = \mathcal{L}^2(\Omega_0, \mathbb{R}^3)$ and $\mathcal{Z} = \mathcal{L}^2(\Gamma_0^{\mathrm{obs}}, \mathbb{R}^3)$, we immediately see that $H \notin \mathcal{L}(\mathcal{Z}, \mathcal{Y})$ since there is no trace Γ_0^{obs} defined from $\mathcal{Y}$. This space is not adapted but we continue to define a formal adjoint from the simple layer potential

$$H^\delta \left| \begin{array}{r} \mathcal{L}^2(\Gamma_0^{\mathrm{obs}}, \mathbb{R}^3) \to \mathcal{L}^2(\Omega_0, \mathbb{R}^3) \\ z \mapsto \delta_{\Gamma_0^{\mathrm{obs}}} z. \end{array} \right. \tag{10}$$

  in order to provide a comparison element after discretization.

- In the case of $\mathcal{Y} = \mathcal{H}^1_{\mathrm{D}}(\Omega_0, \mathbb{R}^3)$ and $\mathcal{Z} = \mathcal{L}^2(\Gamma_0^{\mathrm{obs}}, \mathbb{R}^3)$, the adjoint $\psi = H^* z$ is then defined as the solution of the weak formulation

$$\forall \underline{y}^\flat, \quad \int_\Omega \underline{\underline{\varepsilon}}(\underline{\psi}) : \underline{\underline{\underline{\underline{A}}}} : \underline{\underline{\varepsilon}}(\underline{y}^\flat) \, \mathrm{d}\Omega = \int_{\Gamma_0^{\mathrm{obs}}} z \cdot \underline{y}^\flat \, \mathrm{d}\Omega,$$

  thus, denoting by

$$\mathrm{Ext}^{\mathrm{N}}_{\Gamma_0^{\mathrm{obs}}} : \left| \begin{array}{l} \mathcal{Z} \to \mathcal{Y} \\ z \mapsto \psi \text{ such that } \begin{cases} -\underline{\nabla} \cdot (\underline{\underline{\sigma}}_\ell(\underline{\psi})) = 0 & \text{in } \Omega_0 \\ \underline{\underline{\sigma}}_\ell(\underline{\psi}) \cdot \underline{n} = 0 & \text{on } \Gamma_0^{\mathrm{N}} \backslash \Gamma_0^{\mathrm{obs}} \\ \underline{\underline{\sigma}}_\ell(\underline{\psi}) \cdot \underline{n} = \underline{z} & \text{on } \Gamma_0^{\mathrm{obs}} \\ \underline{\psi} = 0 & \text{on } \Gamma_0^{\mathrm{D}}. \end{cases} \end{array} \right. \tag{11}$$

  the elastic extension on the domain of the boundary measurements introduced as Neuman boundary conditions, we see that

$$H^* : \left| \begin{array}{r} \mathcal{L}^2(\Gamma_0^{\mathrm{obs}}, \mathbb{R}^3) \to \mathcal{H}^1_{\mathrm{D}}(\Omega_0, \mathbb{R}^3) \\ z \mapsto \mathrm{Ext}^{\mathrm{N}}_{\Gamma_0^{\mathrm{obs}}}(z). \end{array} \right. \tag{12}$$

- By contrast, in the case of $\mathcal{Y} = \mathcal{H}^1_{\mathrm{D}}(\Omega_0, \mathbb{R}^3)$ and $\mathcal{Z} = \mathcal{H}^{\frac{1}{2}}(\Gamma_0^{\mathrm{obs}}, \mathbb{R}^3)$, the adjoint is given as the extension on the domain of the boundary measurements introduced as Dirichlet boundary conditions $\mathrm{Ext}^{\mathrm{D}}_{\Gamma_0^{\mathrm{obs}}}$ introduced in (7).

  $$H^* : \left| \begin{array}{r} \mathcal{H}^{\frac{1}{2}}(\Gamma_0^{\mathrm{obs}}, \mathbb{R}^3) \to \mathcal{H}^1_{\mathrm{D}}(\Omega_0, \mathbb{R}^3) \\ z \mapsto \mathrm{Ext}^{\mathrm{D}}_{\Gamma_0^{\mathrm{obs}}}(z). \end{array} \right. \tag{13}$$

  The demonstration of this result is based on the following Lemma – which can be seen as an orthogonality property.

  Lemma 2
  For all $\psi \in \mathcal{Y}$ such that $\psi_{|\Gamma_0^{obs}} = 0$ we have

  $$\forall \phi \in \mathcal{Z}, \quad (Ext^{\mathrm{D}}_{\Gamma_0^{obs}}(\phi), \psi)_{\mathcal{Y}} = 0.$$

  Proof. From the definition of the extension operator (7), a direct computation entails

  $$\begin{aligned} (\mathrm{Ext}_{\Gamma_0^{\mathrm{obs}}}(\phi), \psi)_{\mathcal{Y}} &= \int_{\Omega_0} \underline{\underline{\varepsilon}}(\underline{\mathrm{Ext}}^{\mathrm{D}}_{\Gamma_0^{\mathrm{obs}}}(\underline{\phi})) : \underline{\underline{\underline{\underline{A}}}} : \underline{\underline{\varepsilon}}(\underline{\psi}) \,\mathrm{d}\Omega \\ &= \int_{\partial\Omega_0} \underbrace{\left(\underline{\underline{\sigma}}_{\ell}(\underline{\mathrm{Ext}}^{\mathrm{D}}_{\Gamma_0^{\mathrm{obs}}}(\underline{\phi})) \cdot \underline{n}\right)}_{0 \text{ on } \Gamma_0^{\mathrm{N}}} \cdot \qquad \underbrace{\underline{\psi}}_{0 \text{ on } \Gamma_0^{\mathrm{D}} \cup \Gamma_0^{\mathrm{obs}}} \qquad \mathrm{d}\Gamma = 0. \end{aligned}$$

  ■

  With this property and the definition (8) of the inner-product we can verify that $\mathrm{Ext}^{\mathrm{D}}_{\Gamma_0^{\mathrm{obs}}}(\cdot)$ is the adjoint of the trace operator on Γ_0^{obs} – in the sense of (9). Indeed, for any $z \in \mathcal{H}^{\frac{1}{2}}(\Gamma_0^{\mathrm{obs}}, \mathbb{R}^3)$ and any $y \in \mathcal{H}^1_{\mathrm{D}}(\Omega_0, \mathbb{R}^3)$

  $$\begin{aligned} (y|_{\Gamma_0^{\mathrm{obs}}}, z)_{\mathcal{Z}} &= (\mathrm{Ext}^{\mathrm{D}}_{\Gamma_0^{\mathrm{obs}}}(y|_{\Gamma_0^{\mathrm{obs}}}), \mathrm{Ext}^{\mathrm{D}}_{\Gamma_0^{\mathrm{obs}}}(z))_{\mathcal{Y}} \\ &= (y, \mathrm{Ext}^{\mathrm{D}}_{\Gamma_0^{\mathrm{obs}}}(z))_{\mathcal{Y}} + (\mathrm{Ext}^{\mathrm{D}}_{\Gamma_0^{\mathrm{obs}}}(y|_{\Gamma_0^{\mathrm{obs}}}) - y, \mathrm{Ext}^{\mathrm{D}}_{\Gamma_0^{\mathrm{obs}}}(z))_{\mathcal{Y}} \\ &= (y, \mathrm{Ext}^{\mathrm{D}}_{\Gamma_0^{\mathrm{obs}}}(z))_{\mathcal{Y}}. \end{aligned}$$

Hence from (3) and the various definitions of the adjoint operator we can infer the different forms that the descent method may take when the metrics on the observation space and the displacement space change.

2.1.3 Numerical discretization

We rely on a numerical investigation here by discretizing the evolution equation (3). We consider a spatial discretization using finite elements – $\mathbb{P}_1$ in this work. We associate with each field – for instance $\underline{y}$ – its corresponding approximation denoted by the subscript h – for example $\underline{y}_h$. Equivalently, this approximation can be represented by its corresponding vector of degrees of freedom written with a vector in uppercase letter – *i.e.* $\vec{Y}$. We then define any linear form with a vector in straight uppercase letter and the finite element matrix operator with a bold uppercase letter. For example, with an adequate choice of integration rules, we define the mass operator by

$$\forall \vec{Y}^{\flat}, \quad \vec{Y}^{\flat\mathsf{T}} \mathbf{M}_{\rho} \vec{Y} = \int_{\Omega_0} \rho \underline{y}_h \cdot \underline{y}^{\flat}_h \,\mathrm{d}\Omega,$$

with ρ is of the order of magnitude of the mass per unit volume of the considered object. To simplify we denote $\mathbf{M} = \mathbf{M}_1$. We also introduce

$$\forall \vec{Y}^\flat, \quad \vec{Y}^{\flat\intercal} \mathbf{M}^{\text{obs}} \vec{Y} = \int_{\Gamma_0^{\text{obs}}} \underline{y}_h \cdot \underline{y}_h^\flat \, \mathrm{d}\Gamma.$$

In the same way, the stiffness operator is defined by

$$\forall \vec{Y}^\flat, \quad \vec{Y}^{\flat\intercal} \mathbf{K} \vec{Y} = \int_{\Omega_0} \underline{\underline{\varepsilon}}(\underline{y}_h) : \underline{\underline{\underline{\underline{A}}}} : \underline{\underline{\varepsilon}}(\underline{y}_h^\flat) \, \mathrm{d}\Omega$$

and for the observations we introduce

$$\forall \vec{Y}^\flat, \quad \vec{Y}^{\flat\intercal} \mathbf{K}^{\text{obs}} Z = \int_{\Omega_0} \underline{\underline{\varepsilon}}(\mathrm{Ext}^{\mathrm{D}}_{\Gamma_0^{\text{obs}}}(\underline{z})) : \underline{\underline{\underline{\underline{A}}}} : \underline{\underline{\varepsilon}}(\underline{y}_h^\flat) \, \mathrm{d}\Omega.$$

To compute $\mathbf{K}^{\text{obs}}$ we refer to [Moireau et al., 2009] where an exact formulation is proposed and an approximation is derived. For the sake of completeness we will recall these computations in the forthcoming section. Finally, using the notation $n + \alpha$ with $\alpha = 1$ or $\frac{1}{2}$ and

$$\vec{Y}^{n+\frac{1}{2}} = \frac{\vec{Y}^{n+1} + \vec{Y}^n}{2},$$

the evolution equation (3) can be time-discretized using either an implicit scheme or a mid-point scheme. We obtain

- in the case of $\mathcal{Y} = \mathcal{L}^2(\Omega_0, \mathbb{R}^3)$ and $\mathcal{Z} = \mathcal{L}^2(\Gamma_0^{\text{obs}}, \mathbb{R}^3)$, in essence we try to solve (and it is not necessarily as remarked before)

  $$\forall y^\flat, \quad \int_{\Omega_0} \underline{\dot{y}} \cdot \underline{y}^\flat \, \mathrm{d}\Omega = \int_{\Gamma_0^{\text{obs}}} (\underline{z} - \underline{y}_{|\Gamma_0^{\text{obs}}}) \cdot \underline{y}^\flat_{|\Gamma_0^{\text{obs}}} \, \mathrm{d}\Gamma,$$

  which reads after time and space discretization

  $$\mathbf{M} \frac{\vec{Y}^{n+1} - \vec{Y}^n}{\Delta t} = \mathbf{H}^\intercal \mathbf{M}^{\text{obs}} (Z - \mathbf{H} \vec{Y}^{n+\alpha}), \tag{14}$$

- in the case of $\mathcal{Y} = \mathcal{H}^1_{\mathrm{D}}(\Omega_0, \mathbb{R}^3)$ and $\mathcal{Z} = \mathcal{L}^2(\Gamma_0^{\text{obs}}, \mathbb{R}^3)$, the weak formulation (4) reads this time

  $$\begin{aligned} \forall y^\flat, \quad \int_{\Omega_0} \underline{\underline{\varepsilon}}(\underline{\dot{y}}) : \underline{\underline{\underline{\underline{A}}}} : \underline{\underline{\varepsilon}}(\underline{y}^\flat) \, \mathrm{d}\Omega &= \int_{\Omega_0} \underline{\underline{\varepsilon}}\big(\mathrm{Ext}^{\mathrm{N}}_{\Gamma_0^{\text{obs}}}(\underline{z} - \underline{y}_{|\Gamma_0^{\text{obs}}})\big) : \underline{\underline{\underline{\underline{A}}}} : \underline{\underline{\varepsilon}}(\underline{y}^\flat) \, \mathrm{d}\Omega \\ &= \int_{\Gamma_0^{\text{obs}}} (\underline{z} - \underline{y}_{|\Gamma_0^{\text{obs}}}) \cdot \underline{y}^\flat \, \mathrm{d}\Omega, \end{aligned}$$

  leading to

  $$\mathbf{K} \frac{\vec{Y}^{n+1} - \vec{Y}^n}{\Delta t} = \mathbf{H}^\intercal \mathbf{M}^{\text{obs}} (Z - \mathbf{H} \vec{Y}^{n+\alpha}), \tag{15}$$

- in the case of $\mathcal{Y} = \mathcal{H}^1_{\mathrm{D}}(\Omega_0, \mathbb{R}^3)$ and $\mathcal{Z} = \mathcal{H}^{\frac{1}{2}}(\Gamma_0^{\text{obs}}, \mathbb{R}^3)$, the weak formulation (4) becomes

  $$\forall y^\flat, \quad \int_{\Omega_0} \underline{\underline{\varepsilon}}(\underline{\dot{y}}) : \underline{\underline{\underline{\underline{A}}}} : \underline{\underline{\varepsilon}}(\underline{y}^\flat) \, \mathrm{d}\Omega = \int_{\Omega_0} \underline{\underline{\varepsilon}}\big(\mathrm{Ext}^{\mathrm{D}}_{\Gamma_0^{\text{obs}}}(\underline{z} - \underline{y}_{|\Gamma_0^{\text{obs}}})\big) : \underline{\underline{\underline{\underline{A}}}} : \underline{\underline{\varepsilon}}(\underline{y}^\flat) \, \mathrm{d}\Omega,$$

  entailing

  $$\mathbf{K} \frac{\vec{Y}^{n+1} - \vec{Y}^n}{\Delta t} = \mathbf{K}^{\text{obs}} (Z - \mathbf{H} \vec{Y}^{n+\alpha}). \tag{16}$$

2.1.4 Numerical comparison in the case of boundary observations

In order to illustrate the differences between the various descent methods presented so far, we propose to reconstruct a given reference displacement $y_\bullet \in \mathcal{H}^1_{\mathrm{D}}(\Omega_0, \mathbb{R}^3)$ observed in a part of the boundary of the geometry – see Figure 2. In Figure 1 we plot the evolution of the logarithm of the error norm, namely

$$\|y_\bullet - y^n\|^2_{\mathcal{L}^2(\Omega_0,\mathbb{R}^3)} \quad \text{and} \quad \|y_\bullet - y^n\|^2_{\mathcal{H}^1_{\mathrm{D}}(\Omega_0,\mathbb{R}^3)}.$$

We also plot the logarithm of the convergence error, *i.e.*

$$\|y^\infty - y^n\|^2_{\mathcal{L}^2(\Omega_0,\mathbb{R}^3)},$$

where y^∞ represents the converged solution of the various algorithms described in (14), (15) and (16). From the first plot of Figure 1 – showing the $\mathcal{L}^2$-norm of the error – we see how the choice of the displacement space to perform the descent method is crucial since the algorithm (14) does not converge towards the targeted displacement. This discrepancy between the algorithm (14) and the algorithms (15) and (16) is clearly visible in Figure 2 where we observe that the obtained displacement from the $\mathcal{L}^2$ descent method (in (green)) is clearly less smooth than the other displacements. Moreover, when analyzing the second plot in Figure (14) we observe that, naturally, the $\mathcal{L}^2$ descent method diverges. Hence, when trying to statically reconstruct a “mechanical” displacement, this illustrative numerical example clearly rules out the descent method (14). Additionally, it shows us that depending on the metrics on the observation space we can obtain an improved precision using the $\mathcal{H}^{\frac{1}{2}}$-norm.

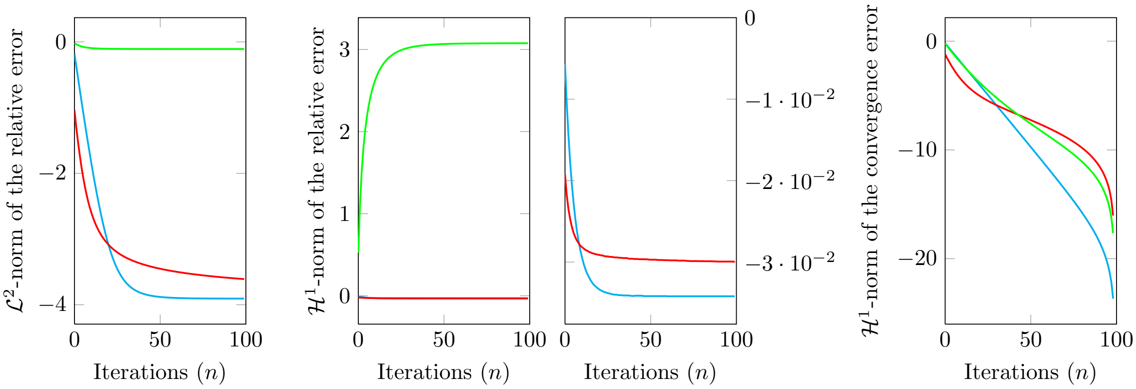

Figure 1: In (green) the solution satisfying (14), in (red) the solution satisfying (15) and in (cyan) the solution satisfying (16).

2.2 Sobolev gradient

The fact that in practice – as illustrated in Section 2.1.3 – the choice of $\mathcal{Y} = \mathcal{H}^1(\Omega_0, \mathbb{R}^3)$ is not only better suited to define a mechanical deformation but also show better converge compared to $\mathcal{Y} = \mathcal{L}^2(\Omega_0, \mathbb{R}^3)$ can typically be justified in the literature through the notion of *Sobolev gradient* [Neuberger, 1997, Karátson and Faragó, 2005], a strategy already well-known in image processing based on functional minimization [Charpiat et al., 2007, Jung et al., 2009, Renka, 2009, Lin et al., 2010]. To facilitate the understanding of this similarity we remain in the case of boundary observations, set $\mathcal{Z} = \mathcal{L}^2(\Gamma_0^{\mathrm{obs}}, \mathbb{R}^3)$ to define at least formally $\mathcal{L}^2$-gradient of $\mathscr{D}$ from the single layer potential

$$\nabla_{\mathcal{L}^2} \mathscr{D}(y, z) = -\delta_{\Gamma_0^{\mathrm{obs}}} \big(z - y|_{\Gamma_0^{\mathrm{obs}}}\big). \tag{17}$$

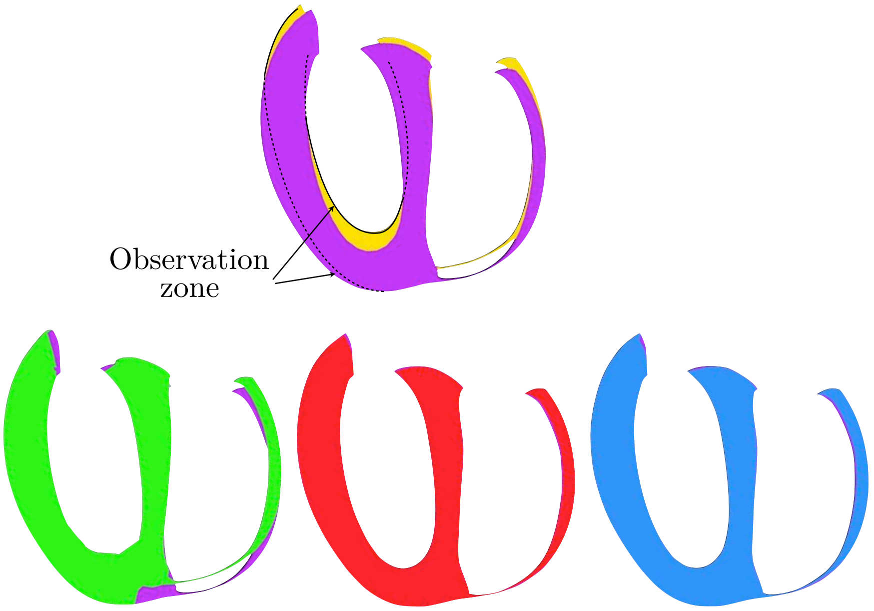

Figure 2: Comparison of the obtained deformed geometry in long axis view. The initial configuration is colored in (yellow) whereas the observed configuration is represented in (purple). In (green) the solution satisfying (14). In (red) the solution satisfying (15). In (cyan) the solution satisfying (16).

On the other hand, the $\mathcal{H}^1$-gradient of $\mathscr{D}$ can be deduced from the expression (12) of the adjoint operator

$$\forall y^\flat, \quad \langle \mathrm{d}_y \mathscr{D}(y,z), y^\flat \rangle_{\mathcal{H}^{1*},\mathcal{H}^1} = (\nabla_{\mathcal{H}^1}\mathscr{D}(y,z), y^\flat)_{\mathcal{H}^1} = -(\mathrm{Ext}^{\mathrm{N}}_{\Gamma_0^{\mathrm{obs}}}(z - y|_{\Gamma_0^{\mathrm{obs}}}), y^\flat)_{\mathcal{H}^1}, \tag{18}$$

more explicitly

$$\nabla_{\mathcal{H}^1}\mathscr{D}(y,z) = -\mathrm{Ext}^{\mathrm{N}}_{\Gamma_0^{\mathrm{obs}}}(z - y|_{\Gamma_0^{\mathrm{obs}}}).$$

From the weak formulation satisfied by the extension operator defined with Neumann boundary conditions (12) we can verify that the following relation – characteristic in the literature of Sobolev gradients – holds

$$\forall y^\flat, \quad (\nabla_{\mathcal{H}^1}\mathscr{D}(y,z), y^\flat)_{\mathcal{H}^1} = (\nabla_{\mathcal{L}^2}\mathscr{D}(y,z), y^\flat)_{\mathcal{L}^2}. \tag{19}$$

Therefore, denoting by, the corresponding strong formulation between the two gradients reads

$$\nabla_{\mathcal{H}^1}\mathscr{D} = \mathrm{Ext}^{\mathrm{N}}_{\Gamma_0^{\mathrm{obs}}}(\nabla_{\mathcal{L}^2}\mathscr{D}),$$

which is exactly the same type of relation obtained in the formalism of Sobolev gradients [Neuberger, 1997, Karátson and Faragó, 2005]. It should be noted that, since we assumed that a part of the boundary is the support of essential boundary conditions, our Sobolev gradient only involves stiffness part of the $\mathcal{H}^1$ norm whereas in [Charpiat et al., 2007, Jung et al., 2009, Renka, 2009, Lin et al., 2010] we see the complete $\mathcal{H}^1$ norm. Fixing some Dirichlet condition was only meant to simplify the presentation. However, if we do not assume any Dirichlet conditions and choose to register a potential rigid motion – as it will be presented in the following Section 2.3.3 – we will also rely on a complete $\mathcal{H}^1$ norm. From a finite element standpoint, the expression (17) reads

$$\forall \vec{Y}^\flat, \quad \vec{Y}^{\flat\intercal}\mathbf{M}\vec{\nabla}_{\mathcal{L}^2}\mathscr{D} = -\vec{Y}^{\flat\intercal}\mathbf{H}^\intercal\mathbf{M}^{\mathrm{obs}}(Z - \mathbf{H}\vec{Y}).$$

Hence, the algorithm (14) can be written as

$$\frac{\vec{Y}^{n+1}-\vec{Y}^{n}}{\Delta t}=-\vec{\nabla}_{\mathcal{L}^2}\mathscr{D}. \tag{20}$$

Additionally, from the weak form of the relation (19) between the two different gradients of the functional, we can see that

$$\forall \vec{Y}^\flat,\quad \vec{Y}^{\flat\intercal}\mathbf{K}\vec{\nabla}_{\mathcal{H}^1}\mathscr{D}=\vec{Y}^{\flat\intercal}\mathbf{M}\vec{\nabla}_{\mathcal{L}^2}\mathscr{D}=-\vec{Y}^{\flat\intercal}\mathbf{H}^\intercal\mathbf{M}^{\mathrm{obs}}(Z-\mathbf{H}\vec{Y}).$$

Thus, the descent method (15) is in fact given by

$$\frac{\vec{Y}^{n+1}-\vec{Y}^{n}}{\Delta t}=-\vec{\nabla}_{\mathcal{H}^1}\mathscr{D}. \tag{21}$$

To summarize, the Sobolev gradient methodology consists in writing the adjoint of an observation operator with respect to an inner-product of $\mathcal{H}^1$ type. We still have to interpret our final – and in fact most effective – choice of gradient descent (16) in the light of Sobolev gradients. In this respect, we first need to derive a penalization form of the adjoint operator given in (7) in order to significantly simplified the expression of the descent method (16). Then the Sobolev gradient associated with (16) should appear more naturally.

2.3 Penalization strategies and applications

In this section we address three problems that can be handled very conveniently using a penalization approach. First, we will start by proposing a penalization form of the adjoint operator given in (7) – already proposed in [Moireau et al., 2009] – which will simplify the descent method (16). Secondly, we propose a way to incorporate in the registration problem some additional *a priori* that we may possess on the targeted solution. Finally, we propose, still through a penalization strategy, to also register potential rigid motion between the target domain and the one to be deformed.

2.3.1 The penalized extension

Let us fix now $\mathcal{Y}=\mathcal{H}^1_{\mathrm{D}}(\Omega_0,\mathbb{R}^3)$ and $\mathcal{Z}=\mathcal{H}^{\frac{1}{2}}_{\mathrm{D}}(\Gamma_0^{\mathrm{obs}},\mathbb{R}^3)$. The first penalization strategy that we want to exploit concerns the definition of the adjoint operator given in Section 2.1.2. With this choice of spaces, the adjoint operator can be written in the following form

$$H^*z=\mathrm{Ext}^{\mathrm{D}}_{\Gamma_0^{\mathrm{obs}}}(z)=\underset{y\,|\,z=Hy}{\operatorname{argmin}}\left(\tfrac{1}{2}\|y\|^2_{\mathcal{H}^1_{\mathrm{D}}(\Omega_0,\mathbb{R}^3)}\right). \tag{22}$$

The disadvantage of this expression is that the data appear as a constraint, thus leading to a mixed formulation which may be inconvenient to solve in practice. Therefore, following the work in [Moireau et al., 2009], we modify this definition of the extension by introducing

$$\mathrm{Ext}^\epsilon(z)=\operatorname{argmin}\left\{\mathscr{J}^\epsilon(y)=\epsilon\frac{1}{2}\|y\|^2_{\mathcal{Y}}+\frac{1}{2}\|z-Hy\|^2_{\mathcal{L}^2(\Gamma_0^{\mathrm{obs}},\mathbb{R}^3)}\right\}. \tag{23}$$

This means that $\psi=\mathrm{Ext}^\epsilon(z)$ is then given by

$$\forall y^\flat,\quad \epsilon(\psi,y^\flat)_{\mathcal{Y}}=(z-H\psi,Hy^\flat)_{\mathcal{L}^2(\Gamma_0^{\mathrm{obs}},\mathbb{R}^3)},$$

leading to the weak formulation

$$\forall y^\flat,\quad a^\epsilon_{\mathrm{Ext}}(\psi,y^\flat)=\ell(y^\flat) \tag{24}$$

where

$$a^{\epsilon}_{\mathrm{Ext}}(\psi, y^{\flat}) = \epsilon(\psi, y^{\flat})_{\mathcal{Y}} + (H\psi, Hy^{\flat})_{\mathcal{L}^2(\Gamma_0^{\mathrm{obs}},\mathbb{R}^3)}$$

is obviously continuous and coercive on $\mathcal{Y}$, and

$$\ell(y^{\flat}) = (z, Hy^{\flat})_{\mathcal{L}^2(\Omega_0^{\mathrm{obs}},\mathbb{R}^3)}$$

is continuous. By the Lax-Milgram Theorem, the weak formulation (24) has a unique solution which is now very easy to compute numerically. In fact after finite element discretization we get

$$\vec{\mathrm{Ext}}^{\epsilon}(Z) = (\epsilon\mathbf{K} + \mathbf{H}^{\intercal}\mathbf{M}^{\mathrm{obs}}\mathbf{H})^{-1}\mathbf{H}^{\intercal}\mathbf{M}^{\mathrm{obs}}Z. \tag{25}$$

We see in (25) that the extension is basically the pseudo-inverse of the observation operator. Hence, our specific choice of equivalent norm on $\mathcal{H}^{\frac{1}{2}}(\Gamma_0^{\mathrm{obs}}, \mathbb{R}^3)$ through the extension shows the direct link between a pseudo-inverse computation and the Sobolev gradient. In fact, rewriting (16) with the penalized extension we obtain

$$\frac{\vec{Y}^{n+1} - \vec{Y}^{n}}{\Delta t} = (\epsilon\mathbf{K} + \mathbf{H}^{\intercal}\mathbf{M}^{\mathrm{obs}}\mathbf{H})^{-1}\mathbf{H}^{\intercal}\mathbf{M}^{\mathrm{obs}}(Z - \mathbf{H}\vec{Y}^{n+\alpha}). \tag{26}$$

In other words, from the comparison with the Sobolev gradient formalism proposed in Section 2.2, we see that the descent algorithm (26) can be expressed as

$$\frac{\vec{Y}^{n+1} - \vec{Y}^{n}}{\Delta t} = -(\epsilon\mathbf{K} + \mathbf{H}^{\intercal}\mathbf{M}^{\mathrm{obs}}\mathbf{H})^{-1}\mathbf{M}\vec{\nabla}_{\mathcal{L}^2}\mathscr{D}. \tag{27}$$

In (26) we directly see the advantage compared to the two previous choices (20) and (21). Indeed here we see that our Sobolev gradient choice introduce a generalized inverse $(\epsilon\mathbf{K}+\mathbf{H}^{\intercal}\mathbf{M}^{\mathrm{obs}}\mathbf{H})^{-1}$ of the operator $\mathbf{H}^{\intercal}\mathbf{M}^{\mathrm{obs}}\mathbf{H}$. Therefore, our gradient choice introduce the steepest descent as $(\epsilon\mathbf{K} + \mathbf{H}^{\intercal}\mathbf{M}^{\mathrm{obs}}\mathbf{H})^{-1}\mathbf{H}^{\intercal}\mathbf{M}^{\mathrm{obs}}\mathbf{H}$ is in essence an operator as close as possible from the identity operator [Neuberger, 1997]. We point out that this strategy can be related to the choice of a preconditioner from Soboloev Gradient strategy[Karátson and Faragó, 2005].

Remark 2 – The extension can be interpreted as a way to go from the initially natural space of observation $\mathcal{L}^2(\Gamma_0^{\mathrm{obs}}, \mathbb{R}^3)$ to, in fact, a most efficient space $\mathcal{H}^1_{\mathrm{D}}(\Omega_0^{\mathrm{obs}}, \mathbb{R}^3)$ or $\mathcal{H}^{\frac{1}{2}}(\Gamma_0^{\mathrm{obs}}, \mathbb{R}^3)$.

2.3.2 From Tikhonov regularization to *a priori* enforcement

We have seen in Theorem 1 that it is possible to build a solution compatible with the measurements in the sense that $z = Hy_{\bullet}$. The second statement of the theorem allows also to take into account some noise in the measurements formally described by the adjunction of function χ so that

$$z = Hy_{\bullet} + \chi.$$

However, in a lot of practical situations, we may also have to take into account a trade-off between two types of information. On the one hand, the measurements available on the system where that we believe up to a certain degree of confidence. On the other hand, some a priori we have on the solution with here also a reasonable level of confidence. In that case we should imagine a functional as the combination of the discrepancy measure and an *a priori* distance

$$\mathscr{J} = \frac{\beta}{2}\|y - y_{\diamond}\|^2_{\mathcal{Y}} + \frac{\gamma}{2}\mathscr{D}(y, z), \tag{28}$$

where β and γ are two weights expressing our respective levels of confidence in the *a priori* or the observations. The evolution equation of Theorem 1 becomes

$$\begin{cases} (\dot{y}, y^\flat)_{\mathcal{Y}} = \beta(y_\diamond - y, y^\flat)_{\mathcal{Y}} + \gamma(H^*(z - Hy), y^\flat)_{\mathcal{Y}}, & t \geq 0 \\ y(0) = y_\diamond. \end{cases} \tag{29}$$

The limit of this problem is then obtained from

$$((\mathbb{1} + \frac{\gamma}{\beta} H^* H) y^\infty, y^\flat)_{\mathcal{Y}} = (y_\diamond + \frac{\gamma}{\beta} H^* z, y^\flat)_{\mathcal{Y}} \tag{30}$$

and logically $Hy^\infty \neq z$.

We can now assume that our *a priori* comes from the modeling of the mechanical behavior of the object, meaning that $y_\diamond$ is the solution of the well-posed problem

$$\begin{cases} -\underline{\nabla} \cdot \underline{\underline{\sigma}}_\ell = \underline{f} & \text{in } \Omega_0 \\ \underline{y} = 0, & \text{on } \Gamma_0^{\mathrm{D}} \\ \underline{\underline{\sigma}}_\ell \cdot \underline{n} = \underline{g}, & \text{on } \Gamma_0^{\mathrm{N}} = \partial\Omega_0 \backslash \Gamma_0^{\mathrm{D}} \end{cases} \tag{31}$$

Considering this model *a priori* and the measurement corresponds typically to the class of overdetermined problem where we have at our disposal – up to a certain level of confidence the – stresses and displacements on the same subdomain or subpart of the boundary. In numerous works [Bonnet and Constantinescu, 2005, Andrieux and Baranger, 2008], this problem was tackled by introducing the notion of *Error in Constitutive Equation (ECE) functional.* To simplify the presentation let us assume that $\underline{f} = 0$ and consider only the case of measurement of the displacement on all the boundary. It means that we have on $\Gamma_0^{\mathrm{obs}} = \Gamma_0^{\mathrm{N}}$ where

$$\begin{cases} \underline{\underline{\sigma}}_\ell \cdot \underline{n} = \underline{g} \\ \underline{y} = z \end{cases}$$

We introduce the notation $\mathrm{Ext}_{\mathrm{D}} = \mathrm{Ext}_{\Gamma_0^{\mathrm{obs}} = \Gamma_0^{\mathrm{N}}}$ for the lifting operator from Dirichlet conditions of all the boundary and $\mathrm{Ext}_{\mathrm{N}}$ the operator solving the model (31). We can rewrite our functional (28) in that case in the form

$$\begin{aligned} \mathscr{J} = \beta \int_{\Omega_0} & \underline{\underline{\varepsilon}}(\underline{y} - \underline{\mathrm{Ext}}_{\mathrm{N}}(g)) : \underline{\underline{\underline{\underline{A}}}} : \underline{\underline{\varepsilon}}(\underline{y} - \underline{\mathrm{Ext}}_{\mathrm{N}}(g)) \, \mathrm{d}\Omega \\ & + \gamma \int_{\Omega_0} \underline{\underline{\varepsilon}}(\underline{\mathrm{Ext}}_{\mathrm{D}}(y|_{\Gamma_0^{\mathrm{obs}}}) - \underline{\mathrm{Ext}}_{\mathrm{D}}(z)) : \underline{\underline{\underline{\underline{A}}}} : \underline{\underline{\varepsilon}}(\underline{\mathrm{Ext}}_{\mathrm{D}}(y|_{\Gamma_0^{\mathrm{obs}}}) - \underline{\mathrm{Ext}}_{\mathrm{D}}(z)) \, \mathrm{d}\Omega \end{aligned} \tag{32}$$

which is definitely similar (and even more general here since we accept specific weights β and γ) to an (ECE) functional where we compare

$$\mathscr{J}_{\mathrm{ECE}} = \int_{\Omega_0} \underline{\underline{\varepsilon}}(\underline{y}_{\mathrm{D}} - \underline{y}_{\mathrm{N}}) : \underline{\underline{\underline{\underline{A}}}} : \underline{\underline{\varepsilon}}(\underline{y}_{\mathrm{D}} - \underline{y}_{\mathrm{N}}) \, \mathrm{d}\Omega$$

whit y_{D} the solution associated with Dirichlet data and y_{N} the solution associated with Neumann data.

2.3.3 Rigid motion registration through penalization

We end this section by considering the case where none of the boundary can be assumed to have Dirichlet boundary conditions, namely $\Gamma_0^{\mathrm{D}} = \varnothing$ which is in fact the most classical situation in registration. In that case it is currently admitted to split the registration into two parts: the rigid registration and the local registration. Concerning the rigid registration, we consider that we have registered the objects such that their center of mass

$$\underline{\xi}_C = \frac{1}{|\Omega_0|}\int_{\Omega_0} \underline{\xi}\,\mathrm{d}\Omega$$

and inertia principal axis, namely the eigenvectors of

$$Q = \frac{1}{|\Omega_0|}\int_{\Omega_0} (\underline{\xi} - \underline{\xi}_C)^2\,\mathrm{d}\Omega$$

– sorted increasingly with respect to their corresponding eigenvalue – are registered on the Euclidian axis $(O, \underline{e}_{\mathrm{x}}, \underline{e}_{\mathrm{y}}, \underline{e}_{\mathrm{z}})$. We finally redefined the reference domain as the resulting domain after this first step of rigid registration.

When no Dirichlet conditions are imposed, the elasticity problem with only Neumann conditions has a kernel which consists of rigid motions of the form

$$\mathcal{K}_{\mathrm{RM}} = \{y \,|\, \underline{y}(\underline{\xi}) = \underline{\tau} + \underline{\omega} \wedge \underline{\xi}\}.$$

It is easy to prove that (see Appendix B) that a supplementary space of $\mathcal{K}_{\mathrm{RM}}$ is given by

$$\mathcal{Y}_{\mathrm{C}} = \left\{ y \,|\, \int_{\Omega_0} \underline{y}(\underline{\xi})\,\mathrm{d}\Omega = 0 \text{ and } \int_{\Omega_0} \underline{y}(\underline{\xi}) \wedge \underline{\xi}\,\mathrm{d}\Omega = 0 \right\}.$$

As a result it is equivalent to minimize the functional (28) on $\mathcal{Y}_{\mathrm{C}}$ or to minimize

$$\mathscr{J}_{\mathrm{RM}} = \beta \left(\int_{\Omega_0} \underline{\underline{\varepsilon}}(\underline{y}) : \underline{\underline{\underline{\underline{A}}}} : \underline{\underline{\varepsilon}}(\underline{y})\ \mathrm{d}\Omega + \left(\int_{\Omega_0} \underline{y}\,\mathrm{d}\Omega \right)^2 + \left(\int_{\Omega_0} \underline{y} \wedge \underline{\xi}\,\mathrm{d}\Omega \right)^2 \right) + \gamma \mathscr{D}(y,z)$$

on $\mathcal{Y}$ equipped with the complete $\mathcal{H}^1$-norm. However, the non-local terms added to the functional leads after spatial discretization to a finite element problem where the matrix has a full band width. A strategy to circumvent this difficulty is therefore to rather minimize

$$\mathscr{J}^{\epsilon}_{\mathrm{RM}} = \beta \int_{\Omega_0} \underline{\underline{\varepsilon}}(\underline{y}) : \underline{\underline{\underline{\underline{A}}}} : \underline{\underline{\varepsilon}}(\underline{y})\ \mathrm{d}\Omega + \beta\epsilon \int_{\Omega_0} \left|\underline{y}\right|^2\ \mathrm{d}\Omega + \gamma \mathscr{D}(y,z)$$

Indeed we can prove (see Appendix B) that if $\underline{\bar{y}}^{\mathrm{RM}}$ minimizes $\mathscr{J}_{\mathrm{RM}}$ and $\underline{\bar{y}}^{\epsilon}$ minimizes $\mathscr{J}^{\epsilon}_{\mathrm{RM}}$, we have

$$\|\underline{\bar{y}}^{\mathrm{RM}} - \underline{\bar{y}}^{\epsilon}\|^2_{\mathcal{Y}} = O(\epsilon).$$

As a result, we rely after rigid motion registration on the same formalism by only defining in the space and the criteria a complete $\mathcal{H}^1$ norm of the type

$$\|y\|^2_{\mathcal{Y}} = \int_{\Omega_0} \underline{\underline{\varepsilon}}(\underline{y}) : \underline{\underline{\underline{\underline{A}}}} : \underline{\underline{\varepsilon}}(\underline{y})\,\mathrm{d}\Omega + \epsilon \int_{\Omega_0} \left|\underline{y}\right|^2\ \mathrm{d}\Omega.$$

In this situation, the penalization strategy introduces enough coercivity to block the rigid modes and leads to a significantly simpler form of the cost functional.

2.4 Non-linearities considerations

2.4.1 Model nonlinearities from large strains consideration

A first generalization of the concepts presented in the previous section is to take into account large strains in the deformations [Lin et al., 2010, Le Guyader and Vese, 2011]. Therefore, we introduce the essentials kinematics description. The deformation gradient $\underline{\underline{F}}$ is given by

$$\underline{\underline{F}}(\xi, t) = \underline{\underline{\nabla}}_{\underline{\xi}}\, \underline{\varphi} = \underline{\underline{\mathbb{1}}} + \underline{\underline{\nabla}}_{\underline{\xi}}\, \underline{y},$$

such that the deformed volume is given by $J\,\mathrm{d}\Omega$ where $J = \det \underline{\underline{F}}$ and $\mathrm{d}\Omega$ is the volume measure (here in the reference configuration), while a change of area is given by $J\underline{\underline{F}}^{-\intercal} \cdot \underline{dS}$. Furthermore, we introduce the right Cauchy-Green deformation tensor $\underline{\underline{C}} = \underline{\underline{F}}^{\intercal} \cdot \underline{\underline{F}}$ which measure the change of orientation of two vectors through the scalar product with

$$\forall(\delta\underline{\xi}_1, \delta\underline{\xi}_2), \quad \underline{\mathrm{x}}_1 \cdot \underline{\mathrm{x}}_2 = \underline{\varphi}(\delta\underline{\xi}_1) \cdot \underline{\varphi}(\delta\underline{\xi}_2) = \delta\underline{\xi}_1 \cdot \underline{\underline{F}}^{\intercal} \cdot \underline{\underline{F}} \cdot \delta\underline{\xi}_2$$

Hence local changes of geometry are described by the nonlinear Green-Lagrange strain tensor

$$\underline{\underline{e}} = \frac{1}{2}(\underline{\underline{C}} - \underline{\underline{\mathbb{1}}}) = \frac{1}{2}\Big(\underline{\underline{\nabla}}_{\underline{\xi}}\, \underline{y} + (\underline{\underline{\nabla}}_{\underline{\xi}}\, \underline{y})^{\intercal} + (\underline{\underline{\nabla}}_{\underline{\xi}}\, \underline{y})^{\intercal} \cdot \underline{\underline{\nabla}}_{\underline{\xi}}\, \underline{y}\Big).$$

with linearized expression $\underline{\underline{\varepsilon}}$.

We characterize the constitutive behavior of the object in large strains using the first Piola-Kirchhoff $\underline{\underline{T}}$ or second Piola-Kirchhoff $\underline{\underline{\Sigma}}$ stress tensors in reference configuration which are related to the Cauchy stress tensor $\underline{\underline{\sigma}}$ on the deformed configuration [Ciarlet, 1988, Le Tallec, 1994, Bathe, 1996] by

$$\underline{\underline{\Sigma}}(\underline{\xi}) = \underline{\underline{F}}(\underline{\xi})^{-1} \cdot \underline{\underline{T}}(\underline{\xi}) = J(\underline{\xi})\underline{\underline{F}}(\underline{\xi})^{-1} \cdot (\underline{\underline{\sigma}}(\underline{\varphi}(\underline{\xi}))) \cdot \underline{\underline{F}}(\underline{\xi})^{-\intercal}$$

We then define a hyperelastic potential W such that

$$\underline{\underline{\Sigma}} = \frac{\partial W}{\partial \underline{\underline{e}}}.$$

Defining the mechanical energy functional as

$$\mathscr{W} = \int_{\Omega_0} W(\underline{\underline{e}})\, \mathrm{d}\Omega$$

we can now modify our minimization functional with

$$\mathscr{J}(y) = \beta\mathscr{W} + \frac{\gamma}{2}\|z - Hy\|^2_{\mathcal{Z}} \tag{33}$$

The minimization then leads to

$$\begin{cases} \Big(\dfrac{y^{n+1} - y^n}{\Delta t}, y^\flat\Big)_{\mathcal{Y}} = -\beta \displaystyle\int_{\Omega_0} \frac{\partial W}{\partial \underline{\underline{e}}} : \mathrm{d}_{\underline{y}}\underline{\underline{e}}(\underline{y})(\underline{y}^\flat)\, \mathrm{d}\Omega + \gamma(Hy^\flat, z - Hy)_{\mathcal{Z}}, \\ y(0) = y_\diamond, \end{cases} \tag{34}$$

where $\mathrm{d}_{\underline{y}}\underline{\underline{e}}(\underline{y})(\underline{y}^\flat)$ is the differential of the Green-Lagrange tensor with respect to the displacement

$$\mathrm{d}_{\underline{y}}\underline{\underline{e}}(\underline{y})(\underline{y}^\flat) = \frac{1}{2}\big(\underline{\underline{F}}^{\intercal} \cdot \nabla y^\flat + (\nabla y^\flat)^{\intercal} \cdot \underline{\underline{F}}\big)$$

Remark 3 – As opposed to what we have seen in Section 2.3.2, the non-linearity of $\mathscr{W}$ impose to define an *a priori* by the introduction of the underlying *a priori* loading, for instance in the case of a model of external force per unit mass f, the formulation can thus become

$$\mathscr{J}(y) = \beta\Big(\mathscr{W} - \langle \underline{f}, \underline{y}\rangle_{\mathcal{V}}\Big) + \frac{\gamma}{2}\|z - Hy\|^2_{\mathcal{Z}} \tag{35}$$

2.4.2 Non-linear observation discrepancies: the distance to surfaces example

As an example of nonlinear discrepancy we consider the simple distance studied by authors in [Moireau et al., 2009]. We consider that the observation is a given surface S_z and define the distance to S_z by

$$\underline{\mathrm{dist}}_\Gamma : \left| \begin{array}{l} \mathbb{R}^3 \mapsto \mathbb{R}^3 \\ \quad \underline{\mathrm{x}} \to \mathrm{dist}_{S_z}(\underline{\mathrm{x}}) = \mathrm{dist}_{S_z}(\underline{\mathrm{x}})\underline{n}_{S_z}(\underline{\mathrm{x}}) \end{array}\right.$$

This distance allows to consider a discrepancy term that generalize the previous $D(y,z) = z - Hy$. In fact we introduce

$$D(y,z) \,:\, y \mapsto \mathrm{dist}_{S_z}(\underline{\varphi}(\underline{\xi})) = \mathrm{dist}_{S_z}(\underline{\xi} + \underline{y}(\underline{\xi}))$$

and, to start with, we simply consider a $\mathcal{L}^2$ discrepancy

$$\mathscr{D}_0(y,z) = \frac{1}{2}\int_{\Gamma_0^{\mathrm{obs}}} \left|\underline{\mathrm{dist}}_{S_z}(\underline{\varphi}(\underline{\xi}))\right|^2 \,\mathrm{d}\Gamma. \tag{36}$$

$\mathcal{L}^2$ discrepancy In order to give the expression of the descent method used to solve the registration problem using this type of similarity measurement we need to differentiate $\mathscr{D}_0$ with respect to a test displacement. In this perspective, we first need to differentiate $\underline{\mathrm{dist}}_{S_z}$ with respect to the space variable $\underline{\mathrm{x}}$. We denote by $\underline{\pi}_{S_z}(\underline{\mathrm{x}})$ the projection of $\underline{\mathrm{x}}$ on the surface S_z. We get

$$\begin{aligned} \underline{\nabla}\,\mathrm{dist}_{S_z}(\underline{\mathrm{x}}) \cdot \underline{\delta \mathrm{x}} &= -\underline{\nabla}\left((\underline{\pi}_{S_z}(\underline{\mathrm{x}}) - \underline{\mathrm{x}}) \cdot \underline{n}_{S_z}\right) \cdot \underline{\delta \mathrm{x}} \\ &= \left(\underline{\underline{\nabla}}\,\underline{\mathrm{x}} \cdot \underline{\delta \mathrm{x}}\right) \cdot \underline{n}_{S_z} - \left(\underline{\underline{\nabla}}\,\underline{\pi}_{S_z}(\underline{\mathrm{x}}) \cdot \underline{\delta \mathrm{x}}\right) \cdot \underline{n}_{S_z} - (\underline{\pi}_{S_z}(\underline{\mathrm{x}}) - \underline{\mathrm{x}}) \cdot \left(\underline{\underline{\nabla}}\,\underline{n}_{S_z} \cdot \underline{\delta \mathrm{x}}\right) \\ &= \underline{\delta \mathrm{x}} \cdot \underline{n}_{S_z}. \end{aligned}$$

Hence, the derivative of the functional reads

$$\begin{aligned} \langle \mathrm{d}_y \mathscr{D}_0(y,z), \delta y\rangle_{\mathcal{Y}^*,\mathcal{Y}} &= \int_{\Gamma_0^{\mathrm{obs}}} \mathrm{dist}_{S_z}(\underline{\xi} + \underline{y}(\underline{\xi}))\underline{n}_{S_z}(\underline{y}(\underline{\xi})) \cdot \underline{\delta y} \,\mathrm{d}\Gamma \\ &= (\mathrm{d}D(y,z)(\delta y), D(y,z))_{\mathcal{L}^2(\Gamma_0^{\mathrm{obs}}, \mathbb{R}^3)}. \end{aligned}$$

As a result, a first descent method would be to consider

$$\langle \dot{y}, y^\flat\rangle_{\mathcal{Y}} = -\langle \mathrm{d}_y \mathscr{D}(y,z), y^\flat\rangle_{\mathcal{Y}^*,\mathcal{Y}} = (\mathrm{d}D(y,z)(y^\flat), D(y,z))_{\mathcal{L}^2(\Gamma_0^{\mathrm{obs}}, \mathbb{R}^3)}. \tag{37}$$

From a numerical point of view, we assume – as in [Moireau et al., 2009] – that surfaces are represented by triangular meshes as it is commonly the case after image segmentation. Hence we numerically compute the distance to a surface – see [Baerentzen and Aanaes, 2005] which allows to compute signed distances on triangular surfaces with an exact change of sign when crossing the surface mesh. We finally get the following descent algorithm

$$\mathbf{M}_\rho \frac{\vec{Y}^{n+1} - \vec{Y}^n}{\Delta t} = -\mathbf{d}\mathbf{D}^{n+\alpha\mathsf{T}}\mathbf{M}^{\mathrm{obs}}\vec{D}(\vec{Y}^{n+\alpha}, Z), \tag{38}$$

or

$$\mathbf{K}\frac{\vec{Y}^{n+1} - \vec{Y}^n}{\Delta t} = -\mathbf{d}\mathbf{D}^{n+\alpha\mathsf{T}}\mathbf{M}^{\mathrm{obs}}\vec{D}(\vec{Y}^{n+\alpha}, Z). \tag{39}$$

with a predilection for the second choice since – as we have seen in Section 2.2 – it corresponds to a $\mathcal{H}^1$ gradient which has been proved in the literature of Sobolev gradients [Neuberger, 1997, Karátson and Faragó, 2005] to lead to better convergence results.

$\mathcal{H}^{\frac{1}{2}}$-like discrepancy An even better gradient descent can be anticipated from (37) and from the definition (26) of the adjoint operator in the case of $\mathcal{H}^{\frac{1}{2}}$-like observation space. This leads, at the discretized level, to

$$\frac{\vec{Y}^{n+1}-\vec{Y}^{n}}{\Delta t} = -(\epsilon\mathbf{K} + \mathbf{dD}^{\intercal}\mathbf{M}^{\mathrm{obs}}\mathbf{dD})^{-1}\mathbf{dD}^{\intercal}\mathbf{M}^{\mathrm{obs}}\vec{D}(\vec{Y}^{n+\alpha}, Z), \tag{40}$$

where the bilinear form $\mathbf{dD}^{\intercal}\mathbf{M}^{\mathrm{obs}}\mathbf{dD}$ is defined as

$$\begin{aligned}\delta\vec{Y}\mathbf{dD}^{\intercal}\mathbf{M}^{\mathrm{obs}}\mathbf{dD}\vec{Y}^{\flat} &= (\mathrm{d}D(y,z)(\delta y), \mathrm{d}D(y,z)(y^{\flat}))_{\mathcal{L}^2(\Gamma_0^{\mathrm{obs}},\mathbb{R}^3)}\\ &= \int_{\Gamma_0^{\mathrm{obs}}} (\underline{n}_{S_z}\cdot\underline{\delta y})(\underline{n}_{S_z}\cdot\underline{y}^{\flat})\,\mathrm{d}\Gamma.\end{aligned}$$

We have equivalently

$$\mathbf{K}\frac{\vec{Y}^{n+1}-\vec{Y}^{n}}{\Delta t} = -\mathbf{K}(\epsilon\mathbf{K} + \mathbf{dD}^{\intercal}\mathbf{M}^{\mathrm{obs}}\mathbf{dD})^{-1}\mathbf{dD}^{\intercal}\mathbf{M}^{\mathrm{obs}}\vec{D}(\vec{Y}^{n+\alpha}, Z),$$

which when $\epsilon \to 0$ is the discretization of the following weak form

$$(\dot{y}, y^{\flat})_{\mathcal{Y}} = -(\mathrm{Ext}^{\mathrm{D}}_{\Gamma_0^{\mathrm{obs}};\underline{n}_{S_z}}(\mathrm{dist}_{S_z}), y^{\flat})_{\mathcal{Y}}. \tag{41}$$

with

$$\mathrm{Ext}^{\mathrm{D}}_{\Gamma_0^{\mathrm{obs}};\underline{n}_{S_z}} : \left|\begin{array}{l} \mathcal{Z} \to \mathcal{Y} \\ z \mapsto y \text{ such that } \begin{cases} -\underline{\nabla}\cdot(\underline{\underline{\sigma}}_{\ell}(\underline{y})) = 0 & \text{in } \Omega_0 \\ \underline{\underline{\sigma}}_{\ell}(\underline{y})\cdot\underline{n} = 0 & \text{on } \Gamma_0^{\mathrm{N}}\backslash\Gamma_0^{\mathrm{obs}} \\ \underline{\underline{\sigma}}_{\ell}(\underline{y})\cdot e^{(j)}_{S_z,\perp} = 0,\ j=1,2 & \text{on } \Gamma_0^{\mathrm{obs}} \\ \underline{y}\cdot\underline{n}_{S_z} = \underline{z} & \text{on } \Gamma_0^{\mathrm{obs}} \\ \underline{y} = 0 & \text{on } \Gamma_0^{\mathrm{D}} \end{cases}\end{array}\right. \tag{42}$$

In the linear case, we have seen that descent strategies like (41) can be deduced from a $\mathcal{H}^{\frac{1}{2}}$ discrepancy, here typically of the form

$$\mathscr{D}_1(y) = \frac{1}{2}\int_{\Omega_0} \mathrm{Ext}^{\mathrm{D}}_{S_z;\underline{n}}(\mathrm{dist}_{S_z}) : \underline{\underline{\underline{\underline{A}}}} : \mathrm{Ext}^{\mathrm{D}}_{S_z;\underline{n}}(\mathrm{dist}_{S_z})\,\mathrm{d}\Omega.$$

However here this is not exactly the case. In fact, to retrieve this property we should have defined the extension by

$$\mathrm{Ext}^{\flat}_{\Gamma_0^{\mathrm{obs}}}(\mathrm{dist}_{S_z}) = \underset{y\,|\,y\cdot\underline{n}_{S_z}=\mathrm{dist}_{S_z}}{\mathrm{argmin}} \left(\tfrac{1}{2}\|y\|^2_{\mathcal{H}^1_{\mathrm{D}}(\Gamma_0^{\mathrm{obs}},\mathbb{R}^3)}\right). \tag{43}$$

which is not equivalent to $\mathrm{Ext}^{\mathrm{D}}_{S_z;\underline{n}}(\mathrm{dist}_{S_z})$ because dist_{S_z} depends of the y. Some further computations show that the difference between the two extension definitions include additives surface curvature terms of second order with respect to the distances. curvature terms can be intricate to compute in practice, in particular with triangular meshes. We thus believe that with $\mathrm{Ext}^{\mathrm{D}}_{S_z;\underline{n}}(\mathrm{dist}_{S_z})$, we have an adequate compromise between efficiency and simplicity.

Moreover, even if the minimization principle is not exactly ensured anymore we can still show that our methods converge for small initial errors in term of distances. In fact, introducing again a target solution $y_{\bullet}$ we can prove that the error $\tilde{y} = y_{\bullet} - y$ follows after linearization the linearized error dynamics associated with $\delta\tilde{y}$

$$\epsilon(\dot{\delta\tilde{y}}, y^{\flat})_{\mathcal{Y}} + \langle \mathrm{d}_y\mathscr{D}(y_{\bullet}, z)(\dot{\delta\tilde{y}}), \mathrm{d}_y\mathscr{D}(y_{\bullet}, z)(y^{\flat})\rangle = -\langle \mathrm{d}_y\mathscr{D}(y_{\bullet}, z)(\delta\tilde{y}), \mathrm{d}_y\mathscr{D}(y_{\bullet}, z)(y^{\flat})\rangle$$

leading to the decrease of $\|\delta\tilde{y}\|_{\mathcal{Y}}$. To summarize, we have presented a efficient strategy which take us away from exact minimization principles but ensures a similar objective to what is presented in [Neuberger, 1997], namely an effective descent procedure in order to make the estimation error as small as possible.

A time-discretization scheme based on linearization for nonlinear observation discrepancies In practice, the resolution of (40) offer some technical difficulty as soon as $\alpha > 0$. In fact when the time-scheme is implicit we have a non-linear definition of $\vec{Y}^{n+1}$ which require typically a Newton based method. However, an implicit time-scheme avoid any *CFL* condition and allows to select any time-step. Following [Moireau et al., 2009] we show it is in fact possible to replace (40) by a first order approximation-based time-scheme of the form

$$\frac{\vec{Y}^{n+1}-\vec{Y}^{n}}{\Delta t} = -(\epsilon \mathbf{K} + \mathbf{dD}^{e\intercal}\mathbf{M}^{\mathrm{obs}}\mathbf{dD}^{e})^{-1}\mathbf{dD}^{e\intercal}\mathbf{M}^{\mathrm{obs}}\Big(\vec{D}(\vec{Y}^{e}, Z) + \mathbf{dD}^{e}(\vec{Y}^{n+\alpha} - \vec{Y}^{e})\Big) \tag{44}$$

where y^e is an adequate extrapolated trajectory, typically

$$\vec{Y}^{e} = \frac{3\vec{Y}^{n} - \vec{Y}^{n-1}}{2}$$

or simply $\vec{Y}^e = \vec{Y}^n$. In a similar context, this time scheme was proved in [Moireau et al., 2009] to be consistent with (40) up to a second order of the time-step – when the extrapolation $\vec{Y}^e$ is chosen carefully – and unconditionally stable also up to a second order of the time-step. Moreover our Sobolev-gradient already necessitate the computation of operator of the form $\mathbf{dD}^{e\intercal}\mathbf{M}^{\mathrm{obs}}\mathbf{dD}^{e}$, hence the linearization do not introduce further intricate operator to be computed.

2.4.3 Illustrative example of registration from signed distance

To numerically assess the various registration methodology that we have described we present two types of results. First we consider same example as the one proposed in Section **??** with a linear observation operator. Here however we proceed to the registration using the distance-to-surface discrepancy. The convergence profiles and the resulting solution are very similar to those obtained with a linear observation operator, hence justifying our strategy to first derive our algorithm in a linear framework.

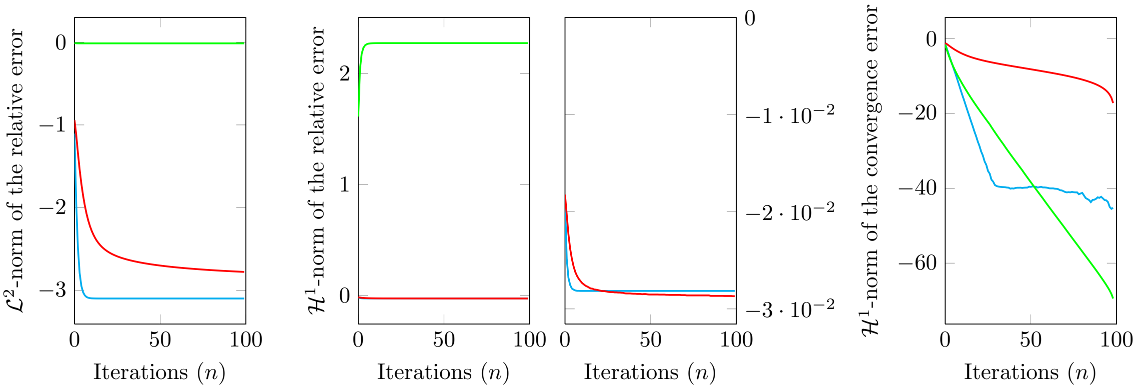

Figure 3: In (green) the solution associated with (38) with the time discretization based on the linearization of the distance operator. Equivalently, in (red) the solution associated with (39) and in (cyan) the solution associated with (40).

We then proceed to a more realistic case were we want to register an initial geometry on the result of a segmentation. The segmentaed object is a pig heart manually segmented as described in [Chabiniok et al., 2011]. The segmentation corresponds to two triangular surfaces representing the left and right endocardium. Each one are closed at the base due to software constraints.

The initial geometry is a computational tetrahedral mesh used in [Chabiniok et al., 2011] for mechanical simulations. We decide to register the initial geometry corresponding to to the end diastolic phase on the image corresponding to the end systolic phase. No boundary conditions is imposed and we therefore rely on the rigid motion filtering extension. Moreover, we adopt a linear elasticity *a priori*. The results are presented in Figure 4 with the geometry before and after the registration.

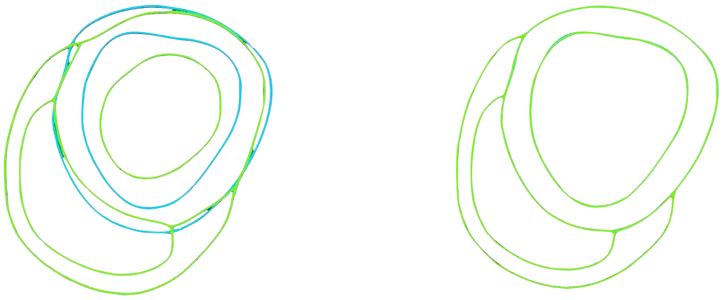

(a) Initial geometry (SAX-view) (b) Registered geometry (SAX-view)

(c) Initial geometry (LAX-view) (d) Registered geometry (LAX-view)

Figure 4: Solving a registration problem using the signed distance function. The model geometry contours are in (green) and the target surface contours are in (cyan). First row: Short-axis view (SAX) and Second row: long-axis view (LAX)

2.5 Integration of the formalism of *Currents*

In the previous section we have considered the signed distance operator, a first type of nonlinear discrepancy measure well-suited to data type such as surfaces. However, as we mentioned, this operator suffers from standard disadvantages that may deteriorate the efficiency of the registration procedure. These drawbacks are in fact the main motivation to look for more sophisticated fidelity-to-data terms. In this respect we focus here on the formalism of *currents* which has been successfully used in the field of medical image analysis – see [Vaillant and Glaunès, 2005, Durrleman et al., 2009, Younes, 2010]. The price to pay is that this formalism clearly induces much more involved computation and derivation than a simple distance. However, our objective is to show how the strategy presented in the previous sections – and in particular in Section 2.4.2 – easily extends to this new and more intricate discrepancy. In particular our Sobolev gradient based descent method allows to propose an effective strategy which in the first step standard "$\mathcal{L}^2$"-based computations before introducing in a last step an extension operator to accelerate the convergence. We point out that using a minimization criterion involving directly the extension will lead to almost intractable terms in the formalism of *currents.*

2.5.1 The formalism of Currents

This formalism is based on the idea that, through its normal vector field, any surface can be represented as a computational support. More precisely, if we consider a test vector field $\underline{w}$ defined in the ambient space and a surface S admitting $\underline{n}$ as its normal then one can consider the following operation resulting in the scalar value:

$$S(w) = \int_S \underline{w} \cdot \underline{n} \, \mathrm{d}\Gamma. \tag{45}$$

The validity of this expression is entirely conditioned by the regularity of the involved vector fields and the relationship between $\mathcal{W}$ the space of test vector fields and $\mathcal{N}$, the space of admissible normal vector fields is a recurrent topic when dealing with currents. As an extreme example where the least regularity is assumed on the normal vector field, equation (45) is defined for $w \in \mathcal{W} \subset \mathcal{C}^0(\mathbb{R}^3, \mathbb{R}^3)$ and $n \in \mathcal{N} \subset \mathcal{L}^1(S, \mathbb{R}^3)$. Another appealing example is when we expect the least regularity on $\mathcal{W}$, that is to say the trace of any test vector field is defined allowing (45) to make sense. This leads to $w \in \mathcal{W} = \mathcal{H}^1(\mathbb{R}^3, \mathbb{R}^3)$ and $n \in \mathcal{N} \subset \mathcal{L}^2(S, \mathbb{R}^3)$. In the following we will say that a surface S is *represented as a current* if its normal n belongs to $\mathcal{N}$ and if the couple $(\mathcal{W}, \mathcal{N})$ is such that S belongs to $\mathcal{W}^*$, the dual of the space of test vector fields. Additionally, if $\mathcal{W}$ is a Hilbert space then for any surface S represented as a current we can define its Riesz representation $s \in \mathcal{W}$ such that

$$\forall w \in \mathcal{W} \quad \langle S, w \rangle_{\mathcal{W}^*, \mathcal{W}} = (s, w)_{\mathcal{W}} = \int_S \underline{w} \cdot \underline{n} \, \mathrm{d}\Gamma. \tag{46}$$

At this early stage, we can see how this point of view can help us to introduce a fidelity-to-data term since we can define the norm on the space of admissible surfaces by

$$\forall S \in \mathcal{W}^* \quad \|S\|^2_{\mathcal{W}^*} = \langle S, s \rangle_{\mathcal{W}^*, \mathcal{W}} = \int_S \underline{s} \cdot \underline{n} \, \mathrm{d}\Gamma. \tag{47}$$

In the sequel we will see how we can use this formalism to provide numerically tractable expressions of the terms appearing in the descent method. More precisely, going back to our original registration problem, we consider S_z the given surface and $S_y = H(y)$ the corresponding model surface, subject to the solid displacement y. Consequently the discrepancy measure that we aim at minimizing reads

$$\mathscr{D}(y, z) = \frac{1}{2} \|S_z - S_y\|^2_{\mathcal{W}^*}. \tag{48}$$

In the following, for the sake of simplicity, we will assume that the deformation φ of the solid is smooth enough so that de deformed surface S can still be represented as a current. More precisely, denoted by S_0 the surface in the reference configuration, we assume that the operator

$$\forall \underline{w} \in \mathcal{W} \quad S(\underline{w}) = \int_{S_0} \underline{w}(\underline{\xi} + \underline{y}(\underline{\xi})) \cdot J \underline{\underline{F}}^{-\intercal} \underline{n}_0(\underline{\xi}) \, \mathrm{d}\Gamma,$$

remains a continuous linear form on $\mathcal{W}$ for any displacement $y \in \mathcal{Y}$. Note that this hypothesis may be strong but is a necessary step to derive the formalism in a first step.

2.5.2 Differentiation of the discrepancy measure & tangent current

In Section 2.4 we defined a steepest descent method employing the differential of $\mathscr{D}$. We proceeded in two steps. First we compute a direct differentiate and then we use an extension operator in order to define a Sobolev gradient and accelerate the convergence of the descent method.

In the case of *currents*, the simple differentiation formally reads

$$-\langle \mathrm{d}_y\mathscr{D}, \delta y\rangle_{\mathcal{Y}^*,\mathcal{Y}} = (\mathrm{d}S(\delta y), S_z - S)_{\mathcal{W}^*} = \langle \mathrm{d}S(\delta y), s_z - s\rangle_{\mathcal{W}^*,\mathcal{W}}. \tag{49}$$

From (49) we understand that the first major difficulty that we are facing is the definition of the Gâteaux derivative of the current $S = H(y)$ around a displacement y and in the direction δy – denoted by $\mathrm{d}S(\delta y)$ and referred to as the *tangent current* of S. As both integrands appearing in (45) depend on the displacement, the expression of the tangent current is obtained by

$$\forall w \in \mathcal{W} \quad \langle \mathrm{d}S(\delta y), w\rangle_{\mathcal{W}^*,\mathcal{W}} = \int_S \left(\underline{\underline{\nabla}}_{\underline{x}}\underline{w}\cdot\underline{\delta y}\right)\cdot\underline{\mathrm{d}\Gamma} + \int_S \underline{w}\cdot\left(\mathrm{d}\,\underline{\mathrm{d}\Gamma}(\underline{\delta y})\right). \tag{50}$$

where we use the compact notation of the surface element $\underline{\mathrm{d}\Gamma} = \underline{n}\,\mathrm{d}\Gamma$ – n being the normal vector field of the model surface. Hence the terms appearing in the descent method algorithm take the following form :

$$-\langle \mathrm{d}_y\mathscr{D}, \delta y\rangle_{\mathcal{Y}^*,\mathcal{Y}} = \int_S \left(\underline{\underline{\nabla}}_{\underline{x}}(\underline{s}_z - \underline{s})\cdot\underline{\delta y}\right)\cdot\underline{n}\,\mathrm{d}\Gamma + \int_S (\underline{s}_z - \underline{s})\cdot\left(\mathrm{d}\,\underline{\mathrm{d}\Gamma}(\underline{\delta y})\right). \tag{51}$$

From the first term of (50) we understand that the trace of the spatial derivative of any test vector field in $\mathcal{W}$ needs to be at least square integrable on any surfaces embedded in $\mathbb{R}^3$, in order to define $\mathrm{d}S(\delta y)$ as an element of $\mathcal{W}^*$. The second term of (50) is the derivative of the surface element around a displacement y in the direction δy. This derivative is expressed by differentiating successively the normal vector field and the surface measure, namely

$$\mathrm{d}\,\underline{\mathrm{d}\Gamma}(\underline{\delta y}) = \left(\mathrm{d}\underline{n}(\underline{\delta y})\right)\mathrm{d}\Gamma + \underline{n}\left(\mathrm{d}\,\mathrm{d}\Gamma(\underline{\delta y})\right). \tag{52}$$

There exist intrinsic forms of this differential which are well-known in the shape optimization community [Delfour and Zolésio, 2011]. Here we propose a form which depends of a parameterization of the surface which will reveal to be of direct use in finite element procedures [Chapelle and Bathe, 2011] as these terms also appear in shell formulations and their discretizations. Indeed, let us define $\phi_0(\xi^1,\xi^2)$ a parametrization of the model surface in the reference configuration, admitting

$$i = 1, 2 \quad \underline{\alpha}_i = \frac{\partial\phi_0}{\partial\xi^i}(\xi^1,\xi^2)$$

as a basis of the tangent plane. Let $\phi(\xi^1,\xi^2)$ be the paramatrization of the deformed model surface defined by $\phi = \varphi\circ\phi_0$. The basis of the its tangent plane is expressed by

$$\begin{aligned} i = 1, 2 \quad \underline{a}_i &= \frac{\partial\phi}{\partial\xi^i}(\xi^1,\xi^2) \\ &= \frac{\partial\phi_0}{\partial\xi^i}(\xi^1,\xi^2) + \frac{\partial}{\partial\xi^i}\underline{y}(\phi_0(\xi^1,\xi^2)) \\ &= \underline{\alpha}_i + \underline{\underline{\nabla}}_{\underline{\xi}}\,\underline{y}^\intercal\cdot\underline{\alpha}_i = \underline{\alpha}_i + \underline{y}_{\,,i}. \end{aligned}$$

In the previous expression we use the compact notation $\underline{y}_{\,,i} = \underline{\underline{\nabla}}_{\underline{\xi}}\,\underline{y}^\intercal\cdot\underline{\alpha}_i$. Remarking that

$$\left|\begin{aligned} &\mathrm{d}\underline{n}(\underline{\delta y})\cdot\underline{n} = 0, \\ \\ &\mathrm{d}\underline{n}(\underline{\delta y})\cdot\underline{a}_i = -\underline{n}\cdot\mathrm{d}\underline{a}_i(\underline{\delta y}) = -\underline{n}\cdot\underline{\delta y}_{\,,i}, \end{aligned}\right.$$

we can give the expression of the first term appearing in (52)

$$\mathrm{d}\underline{n}(\underline{\delta y}) = -\sum_{i=1,2} \big(\underline{n}\cdot\underline{\delta y}_{,i}\big)\,\underline{a}^i = \underline{\mathrm{d}\tau}(\underline{\delta y}), \tag{53}$$

with $(\underline{a}^1, \underline{a}^2)$ the contravariant basis of the tangent plane verifying $\underline{a}^i \cdot \underline{a}_j = \delta^i_j$ – where δ is the Kronecker delta [Chapelle and Bathe, 2011]. This derivative is necessarily orthogonal to the normal vector field – hence the notation $\mathrm{d}\tau$ – and its components in the tangent plane are expressed using the spatial derivative of the test displacement δy in the corresponding model surface. Once again we assume enough regularity on the displacements for this term to be well defined. Remarking that for any vectors $\underline{u}$, $\underline{v}$ and $\underline{w}$ in $\mathbb{R}^3$ we have

$$\big(\underline{u}\cdot\underline{v}\big)\underline{w} = \underline{w}\otimes\underline{v}\cdot\underline{u}, \tag{54}$$

expression (53) can also be understood as

$$\underline{\mathrm{d}\tau}(\underline{\delta y}) = -\underline{a}_1\otimes\underline{n}\cdot\underline{\delta y}_{,1} - \underline{a}_2\otimes\underline{n}\cdot\underline{\delta y}_{,2}, \tag{55}$$

which emphasizes the fact that $\mathrm{d}\tau(\cdot)$ is a linear operator on the space of admissible displacement. Moving on to the second term in (52), we rewrite the surface measure as

$$\mathrm{d}\Gamma = \|\underline{a}_1\wedge\underline{a}_2\|\;\mathrm{d}\xi^1\mathrm{d}\xi^2 = \sqrt{a}\;\mathrm{d}\xi^1\mathrm{d}\xi^2.$$

The scalar value a appearing in the previous expression can be differentiated to obtain

$$\begin{aligned}\mathrm{d}\sqrt{a}(\underline{\delta y}) &= \frac{1}{2}\frac{\mathrm{d}a(\underline{\delta y})}{\sqrt{a}} = \frac{\underline{a}_1\wedge\underline{a}_2}{\sqrt{a}}\cdot\Big(\mathrm{d}\underline{a}_1(\underline{\delta y})\wedge\underline{a}_2 + \underline{a}_1\wedge\mathrm{d}\underline{a}_2(\underline{\delta y})\Big)\\ &= \underline{n}\cdot\Big(\underline{\delta y}_{,1}\wedge\underline{a}_2 + \underline{a}_1\wedge\underline{\delta y}_{,2}\Big) = \underline{\delta y}_{,1}\cdot\Big(\underline{a}_2\wedge\underline{n}\Big) + \underline{\delta y}_{,2}\cdot\Big(\underline{a}_1\wedge\underline{n}\Big).\end{aligned}$$

We thus observe that there exists a real value c such that

$$\underline{a}_2\wedge\underline{n} = c\;\underline{a}^1 \quad \text{with} \quad c = -(\underline{a}_2\wedge\underline{a}_1)\cdot\underline{n} = -\|\underline{a}_2\wedge\underline{a}_1\|.$$

Using the same arguments for $\underline{a}_1\wedge\underline{n}$ we obtain

$$\begin{aligned}\underline{n}\;\Big(\mathrm{d}\,\mathrm{d}\Gamma(\underline{\delta y})\Big) &= -\Big(\underline{\delta y}_{,1}\cdot\underline{a}^1 + \underline{\delta y}_{,2}\cdot\underline{a}^2\Big)\underline{n}\,\mathrm{d}\Gamma\\ &= -\Big(\underline{n}\otimes\underline{a}^1\cdot\underline{\delta y}_{,1} + \underline{n}\otimes\underline{a}^2\cdot\underline{\delta y}_{,2}\Big)\,\mathrm{d}\Gamma\\ &= \underline{\mathrm{d}\nu}(\underline{\delta y})\,\mathrm{d}\Gamma.\end{aligned} \tag{56}$$

The obtained vector field is in the normal direction – justifying the notation $\mathrm{d}\nu$ – and also uses the trace of the spatial derivative of the displacement on the model surface. Regrouping equations (55) and (56) we will denote the derivative of a surface element by

$$\mathrm{d}\,\underline{\mathrm{d}\Gamma}(\underline{\delta y}) = \Big(\underline{\mathrm{d}\tau}(\underline{\delta y}) + \underline{\mathrm{d}\nu}(\underline{\delta y})\Big)\,\mathrm{d}\Gamma. \tag{57}$$

We understand here that we need a strong regularity on the displacement in order to define (57). This means that the classical spaces $\mathcal{H}^1(\Omega_0, \mathbb{R}^3)$ is not sufficient to consider this type of terms. We should rely for example on a more regular space, for instance we could imagine the displacements belong to $\mathcal{H}^s(\Omega_0, \mathbb{R}^3)$ with $s \geq 2$. Here we then remain formal on the derivation of the observer and leave the necessary regularity conditions to a future work.

2.5.3 Reproducing Kernel Hilbert Spaces.

In order to provide a numerically tractable form of the vector fields appearing in (51) we follow [Vaillant and Glaunès, 2005, Durrleman et al., 2009, Younes, 2010] and define $\mathcal{W}$ as a Reproducing Kernel Hilbert Space (RKHS). Clearly the choice of this RKHS should be consistent with the space of admissible displacements since an admissible displacement has generated the target surfaces. We believe here also that a $\mathcal{H}^s(\Omega_0, \mathbb{R}^3)$ with $s \geq 2$ could be a good candidate for the admissible displacements space in order to be compatible with the use of RKHS spaces but the study of this question will remain beyond the scope of this article.

To start with RKHS spaces, we refer to [Aronszajn, 1950] and recall some standard properties of these spaces

Definition 3
The Hilbert space $\mathcal{W}$ is said to be a RKHS if the evaluation functions

$$\forall \underline{x} \in \mathbb{R}^3,\ \forall \underline{\alpha} \in \mathbb{R}^3 \quad \delta_x^\alpha \left| \begin{array}{l} \mathcal{W} \to \mathbb{R} \\ w \mapsto \delta_x^\alpha(w) = \underline{\alpha} \cdot \underline{w}(\underline{x}), \end{array} \right. \tag{58}$$

are continuous linear forms, namely $\delta_x^\alpha \in \mathcal{W}^*$.

We can remark that any Hilbert space that verifies $\mathcal{W} \subset \mathcal{C}^0(\mathbb{R}^3, \mathbb{R}^3)$ is necessarily a RKHS. Moreover, using the Riesz representation theorem we can ensure that for a given functional δ_x^α there exists a unique function k_x^α such that

$$\forall w \in \mathcal{W} \quad \langle \delta_x^\alpha, w \rangle_{\mathcal{W}^*,\mathcal{W}} = (\mathrm{k}_x^\alpha, w)_{\mathcal{W}} = \underline{\alpha} \cdot \underline{w}(\underline{x}).$$

Remarking the linearity with respect to α of the last term we can state that there exists a unique two-arguments function $\mathrm{k}(\cdot,\cdot)$ – called the *kernel* of $\mathcal{W}$ – verifying the so-called *reproducing property*

$$\forall \underline{x} \in \mathbb{R}^3,\ \forall \underline{\alpha} \in \mathbb{R}^3,\ \forall w \in \mathcal{W} \quad \underline{\alpha} \cdot \underline{w}(\underline{x}) = (\mathrm{k}(\underline{x}, \cdot)\underline{\alpha}, w)_{\mathcal{W}}. \tag{59}$$

As a matter of fact, we will extract from this reproducing property most of the results that are needed to solve the registration problem using the formalism of currents.

Proposition 4
Let S be a surface represented as a current and admitting $n \in \mathcal{N}$ as its normal vector field. If $\mathcal{W}$ is a RKHS then the Riesz representation of S is given by

$$\underline{s}(\underline{x}) = \int_S \mathrm{k}(\underline{\widetilde{x}}, \underline{x}) \underline{n}(\underline{\widetilde{x}})\, \mathrm{d}\Gamma. \tag{60}$$

Proof. Applying the reproducing property in the definition of the operator S we obtain for any test vector field $w \in \mathcal{W}$

$$\langle S, w \rangle_{\mathcal{W}^*,\mathcal{W}} = \int_S \underline{w} \cdot \underline{n}\, \mathrm{d}\Gamma = \int_S (\mathrm{k}(\underline{\widetilde{x}}, \cdot)\underline{n}, w)_{\mathcal{W}}\, \mathrm{d}\Gamma = (s, w)_{\mathcal{W}}.$$

■

If S_1 and S_2 are two surfaces represented as currents, then, using the expression of their Riesz, we have

$$\begin{aligned} (S_1, S_2)_{\mathcal{W}^*} &= (s_1, s_2)_{\mathcal{W}^*} = \langle S_1, s_2 \rangle = \langle S_2, s_1 \rangle \\ &= \int_{S_1} \int_{S_2} \underline{n}_1(\underline{x}) \cdot \mathrm{k}(\underline{\widetilde{x}}, \underline{x}) \underline{n}_2(\underline{\widetilde{x}})\, \mathrm{d}\Gamma\, \mathrm{d}\Gamma, \end{aligned}$$

and the norm between these objects can be computed by

$$
\begin{aligned}
\|S_1 - S_2\|^2_{\mathcal{W}^*} &= \|S_1\|^2_{\mathcal{W}^*} - 2\langle S_1, S_2\rangle_{\mathcal{W}^*} + \|S_2\|^2_{\mathcal{W}^*} \\
&= \iint_{S_1} \underline{n}_1(\underline{x}) \cdot \mathrm{k}(\underline{\widetilde{x}}, \underline{x})\underline{n}_1(\underline{\widetilde{x}})\,\mathrm{d}\Gamma\,\mathrm{d}\Gamma + \iint_{S_2} \underline{n}_2(\underline{x}) \cdot \mathrm{k}(\underline{\widetilde{x}}, \underline{x})\underline{n}_2(\underline{\widetilde{x}})\,\mathrm{d}\Gamma\,\mathrm{d}\Gamma \\
&\qquad - 2\int_{S_1}\int_{S_2} \underline{n}_1(\underline{x}) \cdot \mathrm{k}(\underline{\widetilde{x}}, \underline{x})\underline{n}_2(\underline{\widetilde{x}})\,\mathrm{d}\Gamma\,\mathrm{d}\Gamma.
\end{aligned}
\tag{61}
$$

Choosing a kernel In practice, it is much more convenient to rather choose only the kernel k than the space $\mathcal{W}$. However, we need to choose this two-argument function such that we can ensure that there exists a unique RKHS admitting this function as its kernel and secondly such that the regularity of $\mathcal{W}$ can be controlled. These questions have been extensively detailed in [Vaillant and Glaunès, 2005, Glaunès et al., 2008, Durrleman et al., 2009] and we will just gather the necessary results that we need for solving our particular registration problem.

For the sake of simplicity we will only consider real valued kernel. It is not a large restriction since every key concept explained below can be extended when k is a tensor of order two. To start with, we cite a first result which is a sufficient condition for the existence of a unique RKHS from the choice of the kernel [Aronszajn, 1950]:

Lemma 5
If k *is symmetric positive semi-definite scalar function, that is to say*

$$
\left|
\begin{array}{l}
\forall(\underline{\mathrm{x}}_i, \underline{\mathrm{x}}_j) \in \mathbb{R}^3 \times \mathbb{R}^3, \quad \mathrm{k}(\underline{\mathrm{x}}_i, \underline{\mathrm{x}}_j) = \mathrm{k}(\underline{\mathrm{x}}_j, \underline{\mathrm{x}}_i), \\
\\
\forall\{\underline{\mathrm{x}}_i\}_{i=1}^N \subset \mathbb{R}^3 \text{ and } \{\underline{\alpha}_i\}_{i=1}^N \subset \mathbb{R}^3 \quad , \displaystyle\sum_{i,j=1}^n \underline{\alpha}_i \cdot \mathrm{k}(\underline{\mathrm{x}}_i, \underline{\mathrm{x}}_j)\underline{\alpha}_j \ \geq \ 0,
\end{array}
\right.
\tag{62}
$$

then there exists a unique RKHS such that k *is its kernel.*

The demonstration of this theorem mainly uses a density argument by proving that the closure of the finite dimensional space spanned by the function of the form $K(\cdot, \underline{x}_i)\underline{\alpha}_i$ is in fact a Hilbert space that necessarily admits k as its kernel and is unique. Another important result that we consider concerns the regularity of the spaces created from a kernel.

Lemma 6
If, for an integer $p \geq 0$, k *is symmetric positive semi-definite scalar function such that its derivatives of order $2p$ are continuous, bounded in $\mathbb{R}^3$ and such that $\forall \underline{x} \in \mathbb{R}^3$, $\mathrm{k}(\underline{x}, \cdot)$ and its derivative of order p at least vanish at infinity then the unique RKHS associated with* k *is continuously embedded in $\mathcal{C}^p(\mathbb{R}^3, \mathbb{R}^3)$.*

This regularity property is also proved using the same density argument. The choice of the kernel is crucial since, has we have seen in equation (61), it rules the metric on the space of currents. As an example, numerical experiments were successfully carried out in [Glaunès et al., 2008] using a Gaussian kernel of the form

$$
\forall \underline{x},\ \underline{\widetilde{x}} \in \mathbb{R}^3 \quad \mathrm{k}(\underline{x}, \underline{\widetilde{x}}) = \exp\Big(-\frac{\|\underline{x} - \underline{\widetilde{x}}\|^2}{\mu^2}\Big).
\tag{63}
$$

Other types of kernel may be consider – see [Glaunès et al., 2008] for numerous examples. From Lemma 5 and Lemma 6, the RKHS built form this kernel is continuously embedded in $\mathcal{C}^\infty(\mathbb{R}^3, \mathbb{R}^3)$.

2.5.4 Time discretization

From the expression (49) of the first derivative of the fidelity-to-data term, the time discrete descent method reads

$$\begin{cases} \Big(\dfrac{y^{n+1}-y^n}{\Delta t}, y^\flat\Big)_{\mathcal{Y}} = (\mathrm{d}S^{n+\alpha}(y^\flat), S_z - S^{n+\alpha})_{\mathcal{W}^*}, \\ y^0 = y_\diamond, \end{cases} \tag{64}$$

where we use, for now at least, the natural gradient of the discrepancy measure. In (64) we denote by $S^{n+\alpha} = H(y^{n+\alpha})$ the model surface subject to the displacement $y^{n+\alpha}$ and by $\mathrm{d}S^{n+\alpha}(y^\flat)$ the tangent current around the displacement $y^{n+\alpha}$ in the direction $y^\flat$. This system is non linear and as previously we consider an extrapolated displacement y^e and propose the following linearization scheme:

$$\begin{cases} (\dfrac{y^{n+1}-y^n}{\Delta t}, y^\flat)_{\mathcal{Y}} = (\mathrm{d}S^e(y^\flat), S_z - S^e - \mathrm{d}S^e(y^{n+\alpha}-y^e))_{\mathcal{W}^*}, \\ y^0 = y_\diamond. \end{cases} \tag{65}$$

In practice, the explicit part of the numerical scheme proposed in (65) is computed using (51) applied to $y^\flat$. However, the other terms obtained after linearization employ the bilinear form $(\mathrm{d}S(y^\flat), \mathrm{d}S(y^\sharp))_{\mathcal{W}^*}$, where $y^\sharp$ is another test displacement. To deal with this new term we will give an expression of the Riesz representation of the tangent current – denoted by ds – and use the identity

$$(\mathrm{d}S(y^\flat), \mathrm{d}S(y^\sharp))_{\mathcal{W}^*} = \langle \mathrm{d}S(y^\flat), \mathrm{d}s(y^\sharp)\rangle_{\mathcal{W},\mathcal{W}^*}.$$

Proposition 7
Let us consider S – with normal vector field $\underline{n}$ – the deformed surface by a smooth displacement y and represented as a current. If the space of test vector fields is a RKHS embedded in $\mathcal{C}^1(\mathbb{R}^3,\mathbb{R}^3)$ then the tangent current around y and in the direction δy exists and its Riesz representation is given by

$$\underline{\mathrm{d}s}(\delta y)\Big|_{\underline{x}} = \int_S \Big(\underline{\nabla}_1 \mathrm{k}(\underline{\widetilde{x}}, \underline{x}) \cdot \underline{\delta y}(\underline{\widetilde{x}})\Big)\underline{n}(\underline{\widetilde{x}})\,\mathrm{d}\Gamma + \int_S \mathrm{k}(\underline{\widetilde{x}}, \underline{x})\ \Big(\underline{\mathrm{d}\tau}(\underline{\delta y}) + \underline{\mathrm{d}\nu}(\underline{\delta y})\Big)\Big|_{\underline{\widetilde{x}}}\,\mathrm{d}\Gamma. \tag{66}$$

Proof. Assuming that $\mathcal{W}$ is a RKHS embedded in $\mathcal{C}^1(\mathbb{R}^3,\mathbb{R}^3)$ implies the existence of the tangent current $\mathrm{d}S(\delta y)$ as an element of $\mathcal{W}^*$. Moreover, let h be a strictly positive scalar value, from the reproducing property (59) we have for any $\underline{\alpha} \in \mathbb{R}^3$ and $w \in \mathcal{W}$:

$$\frac{1}{h}\Big(\underline{w}(\underline{x}+h\underline{\delta x}) - \underline{w}(\underline{x})\Big)\cdot\underline{\alpha} = \Big(\frac{1}{h}\Big(\mathrm{k}(\underline{x}+h\underline{\delta x},\cdot) - \mathrm{k}(\underline{x},\cdot)\Big)\underline{\alpha},\ w\Big)_{\mathcal{W}}.$$

Hence, as h tends to zeros we can understand how the reproducing property also exists for the derivatives of the test vector field, namely:

$$\Big(\underline{\underline{\nabla}}_{\underline{x}}\underline{w}\cdot\underline{\delta x}\Big)\cdot\underline{\alpha} = \Big(\ (\underline{\nabla}_1\mathrm{k}(\underline{x},\cdot)\cdot\underline{\delta x})\underline{\alpha}\ ,\ w\ \Big)_{\mathcal{W}}, \tag{67}$$

where $\underline{\nabla}_1\mathrm{k}$ is the gradient of the kernel with respect to the first variable. Applying the reproducing properties (59) and (67) to the definition of the tangent current (50) leads to the expression of its Riesz representation. ■

Remark 4 – The differentiation operator and the Riesz identification are commutative since, by differentiating the Riesz representation of S – defined in (60) – around y and in the direction δy, we obtain

$$\begin{aligned}
\mathrm{d}\underline{s}(\delta y) &= \mathrm{d}\Big(\int_S \mathrm{k}(\underline{\widetilde{x}},\underline{x})\ \underline{n}(\underline{\widetilde{x}})\,\mathrm{d}\Gamma\Big)(\delta y)\\
&= \int_S \Big(\underline{\nabla}_1\mathrm{k}(\underline{\widetilde{x}},\underline{x})\cdot\underline{\delta y}(\underline{\widetilde{x}})\Big)\underline{n}(\underline{\widetilde{x}})\,\mathrm{d}\Gamma + \int_S \mathrm{k}(\underline{\widetilde{x}},\underline{x})\ \Big(\underline{\mathrm{d}\tau}(\underline{\delta y})+\underline{\mathrm{d}\nu}(\underline{\delta y})\Big)\Big|_{\underline{\widetilde{x}}}\,\mathrm{d}\Gamma\\
&= \underline{\delta s}(\delta y).
\end{aligned}$$

Proposition 8
Assuming that the space of test vector field is a RKHS embedded in $\mathcal{C}^2(\mathbb{R}^3,\mathbb{R}^3)$, the bilinear form appearing in the algorithm (64) is defined, around a displacement y and for any $y^\flat$ and $y^\sharp$ in $\mathcal{Y}$, by :

$$\begin{aligned}
(\mathrm{d}S(y^\flat),\mathrm{d}S(y^\sharp))_{\mathcal{W}^*} &= \int_S\int_S \Big(\underline{\nabla}_2\mathrm{k}(\underline{\widetilde{x}},\underline{x})\Big)\cdot\underline{y}^\flat(\underline{x})\underline{n}(\underline{x})\cdot\Big(\underline{\mathrm{d}\tau}(\underline{y}^\sharp)+\underline{\mathrm{d}\nu}(\underline{y}^\sharp)\Big)\Big|_{\underline{\widetilde{x}}}\,\mathrm{d}\Gamma\,\mathrm{d}\Gamma\\
&+\int_S\int_S \Big(\underline{\nabla}_1\mathrm{k}(\underline{\widetilde{x}},\underline{x})\cdot\underline{y}^\sharp(\underline{\widetilde{x}})\Big)\underline{n}(\underline{\widetilde{x}})\cdot\Big(\underline{\mathrm{d}\tau}(\underline{y}^\flat)+\underline{\mathrm{d}\nu}(\underline{y}^\flat)\Big)\Big|_{\underline{x}}\,\mathrm{d}\Gamma\,\mathrm{d}\Gamma\\
&+\int_S\int_S \Big(\underline{\underline{\nabla}}{}^2_{12}\mathrm{k}(\underline{\widetilde{x}},\underline{x}) : \big(\underline{y}^\flat(\underline{x})\otimes\underline{y}^\sharp(\underline{\widetilde{x}})\big)\Big)\underline{n}(\underline{\widetilde{x}})\cdot\underline{n}(\underline{x})\,\mathrm{d}\Gamma\,\mathrm{d}\Gamma\\
&+\int_S\int_S \mathrm{k}(\underline{\widetilde{x}},\underline{x})\Big(\underline{\mathrm{d}\tau}(\underline{y}^\sharp)+\underline{\mathrm{d}\nu}(\underline{y}^\sharp)\Big)\Big|_{\underline{\widetilde{x}}}\cdot\Big(\underline{\mathrm{d}\tau}(\underline{y}^\flat)+\underline{\mathrm{d}\nu}(\underline{y}^\flat)\Big)\Big|_{\underline{x}}\,\mathrm{d}\Gamma\,\mathrm{d}\Gamma.
\end{aligned}\tag{68}$$

Where, we denoted by $\underline{\underline{\nabla}}{}^2_{12}\mathrm{k}$ the Hessian cross matrix of k, $\underline{\underline{\nabla}}{}^2_{12}\mathrm{k} = \underline{\underline{\nabla}}_2\Big(\underline{\nabla}_1\mathrm{k}\Big)$.

Proof. As mentioned previously we will use the expression (66) of the Riesz representation of the tangent current. To begin with, from (50), we have

$$\begin{aligned}
(\mathrm{d}S(y^\flat),\mathrm{d}S(y^\sharp))_{\mathcal{W}^*} = \int_S \Big(\underline{\underline{\nabla}}_x\underline{\mathrm{d}s}(y^\sharp)\Big|_{\underline{x}}\cdot\underline{y}^\flat(\underline{x})\Big)\cdot\underline{n}(\underline{x})\,\mathrm{d}\Gamma&\\
+\int_S \underline{\mathrm{d}s}(y^\sharp)\Big|_{\underline{x}}\cdot\Big(\underline{\mathrm{d}\tau}(\underline{y}^\flat)+\underline{\mathrm{d}\nu}(\underline{y}^\flat)\Big)\Big|_{\underline{x}}\,\mathrm{d}\Gamma.&
\end{aligned}\tag{69}$$

The regularity of $\underline{\mathrm{d}s}(y^\sharp)\in\mathcal{W}$ – which is, by assumption, embedded in $\mathcal{C}^2(\mathbb{R}^3,\mathbb{R}^3)$ – ensures that the previous expression is well defined. From (66), we have, for any $\underline{x}\in\mathbb{R}^3$

$$\underline{\mathrm{d}s}(y^\sharp)\Big|_{\underline{x}} = \int_S \Big(\underline{\nabla}_1\mathrm{k}(\underline{\widetilde{x}},\underline{x})\cdot\underline{y}^\sharp(\underline{\widetilde{x}})\Big)\underline{n}(\underline{\widetilde{x}})\,\mathrm{d}\Gamma + \int_S \mathrm{k}(\underline{\widetilde{x}},\underline{x})\ \Big(\underline{\mathrm{d}\tau}(\underline{y}^\sharp)+\underline{\mathrm{d}\nu}(\underline{y}^\sharp)\Big)\Big|_{\underline{\widetilde{x}}}\,\mathrm{d}\Gamma.\tag{70}$$

In the following we concentrate our effort in giving the expression of the spatial derivative of $\underline{\mathrm{d}s}(y^\sharp)$. To start with, the second term appearing in (70) is easily differentiated into

$$\underline{\underline{\nabla}}_x\Big(\int_S \mathrm{k}(\underline{\widetilde{x}},\underline{x})\ \Big(\underline{\mathrm{d}\tau}(\underline{y}^\sharp)+\underline{\mathrm{d}\nu}(\underline{y}^\sharp)\Big)\Big|_{\underline{\widetilde{x}}}\,\mathrm{d}\Gamma\Big)\cdot\underline{y}^\flat(\underline{x}) = \int_S \underline{\nabla}_2\mathrm{k}(\underline{\widetilde{x}},\underline{x})\cdot\underline{y}^\flat(\underline{x})\ \Big(\underline{\mathrm{d}\tau}(\underline{y}^\sharp)+\underline{\mathrm{d}\nu}(\underline{y}^\sharp)\Big)\Big|_{\underline{\widetilde{x}}}\,\mathrm{d}\Gamma,$$

where $\underline{\nabla}_2\mathrm{k}(\underline{\widetilde{x}},\underline{x})$ stands for the derivative of the kernel with respect to the second spatial variable.

Concerning the first term in (70), we apply (54) to obtain

$$\int_S (\underline{\nabla}_1\mathrm{k}(\underline{\widetilde{x}},\underline{x})\cdot\underline{y}^\sharp(\underline{\widetilde{x}}))\underline{n}(\underline{\widetilde{x}})\,\mathrm{d}\Gamma = \int_S \underline{n}(\underline{\widetilde{x}})\otimes\underline{y}^\sharp(\underline{\widetilde{x}})\cdot\underline{\nabla}_1\mathrm{k}(\underline{\widetilde{x}},\underline{x})\,\mathrm{d}\Gamma,$$

which, after spatial differentiation, leads to

$$\underline{\underline{\nabla}}_{\underline{x}}\Big(\int_S \underline{n}(\widetilde{\underline{x}}) \otimes \underline{y}^\sharp(\widetilde{\underline{x}}) \cdot \underline{\nabla}_1 \mathrm{k}(\widetilde{\underline{x}},\underline{x})\,\mathrm{d}\Gamma\Big)\cdot \underline{y}^\flat(\underline{x}) = \int_S \underline{n}(\widetilde{\underline{x}}) \otimes \underline{y}^\sharp(\widetilde{\underline{x}})\cdot\Big(\underline{\underline{\nabla}}^2_{12}\mathrm{k}(\widetilde{\underline{x}},\underline{x})\cdot\underline{y}^\flat(\underline{x})\Big)\,\mathrm{d}\Gamma.$$

Now, applying once more (54), where $\underline{u}$ is replaced by $\underline{\underline{\nabla}}^2_{12}\mathrm{k}(\widetilde{\underline{x}},\underline{x})\cdot\underline{y}^\flat(\underline{x})$, we obtain

$$\underline{\underline{\nabla}}_{\underline{x}}\Big(\int_S \Big(\underline{\nabla}_1 \mathrm{k}(\widetilde{\underline{x}},\underline{x})\cdot\underline{y}^\sharp(\widetilde{\underline{x}})\Big)\underline{n}(\widetilde{\underline{x}})\,\mathrm{d}\Gamma\Big)\cdot\underline{y}^\flat(\underline{x}) = \int_S \Big(\underline{\underline{\nabla}}^2_{12}\mathrm{k}(\widetilde{\underline{x}},\underline{x}) : \big(\underline{y}^\flat(\underline{x})\big)\otimes\underline{y}^\sharp(\widetilde{\underline{x}})\big)\Big)\underline{n}(\widetilde{\underline{x}})\,\mathrm{d}\Gamma.$$

Regrouping the previous computation, the spatial derivative of the Riesz representation of the tangent current is then given by

$$\begin{aligned}\underline{\underline{\nabla}}_{\underline{x}}\underline{\mathrm{d}s}(y^\sharp)\Big|_{\underline{x}}\cdot\underline{y}^\flat(\underline{x}) = &\int_S \underline{\nabla}_2\mathrm{k}(\widetilde{\underline{x}},\underline{x})\cdot\underline{y}^\flat(\underline{x})\ \Big(\underline{\mathrm{d}\tau}(\underline{y}^\sharp)+\underline{\mathrm{d}\nu}(\underline{y}^\sharp)\Big)\Big|_{\widetilde{\underline{x}}}\,\mathrm{d}\Gamma\\ &+\int_S\Big(\underline{\underline{\nabla}}^2_{12}\mathrm{k}(\widetilde{\underline{x}},\underline{x}) : \big(\underline{y}^\flat(\underline{x})\big)\otimes\underline{y}^\sharp(\widetilde{\underline{x}})\big)\Big)\underline{n}(\widetilde{\underline{x}})\,\mathrm{d}\Gamma. \quad (71)\end{aligned}$$

Replacing the expression (71) of the spatial derivative of the Riesz representation and the expression (70) of the tangent current in the expression (69) of the bilinear form we obtain the desired result (68). ■

Remark 5 – In our numerical experiments we used a Gaussian kernel whose successive derivatives are expressed as follows,

$$\left|\begin{aligned}&\mathrm{k}(\widetilde{\underline{x}},\underline{x}) = \exp\Big(-\frac{\|\underline{x}-\widetilde{\underline{x}}\|^2}{\mu^2}\Big),\\ &\underline{\nabla}_1\mathrm{k}(\widetilde{\underline{x}},\underline{x}) = -\frac{2}{\mu^2}(\widetilde{\underline{x}}-\underline{x})\ \mathrm{k}(\widetilde{\underline{x}},\underline{x}),\\ &\underline{\nabla}_2\mathrm{k}(\widetilde{\underline{x}},\underline{x}) = \frac{2}{\mu^2}(\widetilde{\underline{x}}-\underline{x})\ \mathrm{k}(\widetilde{\underline{x}},\underline{x}),\\ &\underline{\underline{\nabla}}^2_{12}\mathrm{k}(\widetilde{\underline{x}},\underline{x}) = \Big(\frac{2}{\mu^2}\mathbb{1}-\frac{4}{\mu^4}(\widetilde{\underline{x}}-\underline{x})\otimes(\widetilde{\underline{x}}-\underline{x})\Big)\mathrm{k}(\widetilde{\underline{x}},\underline{x}).\end{aligned}\right. \quad (72)$$

We will discuss later the influence of the real value μ, referred to as the kernel width, in our procedure.

Remark 6 – It is important to notice that, in essence, the bilinear form previously described is necessarily symmetric and positive semi-definite. The symmetry property is self-evident and the positivity comes from the fact for any admissible displacement y we have

$$(\mathrm{d}S(y),\mathrm{d}S(y))_{\mathcal{W}^*} = \|\mathrm{d}S(y)\|^2_{\mathcal{W}^*} \geq 0. \quad (73)$$

2.5.5 Space discretization and assembling procedure

In this paragraph we deal with the numerical aspects of the previously described algorithm, equations (65). More precisely, from a finite element standpoint, we investigate the expression of the matrix $\mathbf{dS}^e|\mathbf{dS}^e$ and the vector $\vec{\Lambda}^e$ – potentially referred to as the innovation term – such that

$$(\mathrm{d}S^e(y_h^\flat), S_z - S^e - \mathrm{d}S^e(y_h^{n+\alpha} - y_h^e))_{\mathcal{W}^*} = \vec{Y}^{\flat\mathsf{T}}\vec{\Lambda}^e - \vec{Y}^{\flat\mathsf{T}}\mathbf{dS}^e|\mathbf{dS}^e\Big(\vec{Y}^{n+\alpha} - \vec{Y}^e\Big),$$

where $y_h^\flat$ is a finite element test function. Starting with $\vec{\Lambda}^e$, we have from (50) and (54) that

$$\begin{aligned}\vec{Y}^{\flat\mathsf{T}}\vec{\Lambda}^e &= \vec{Y}^{\flat\mathsf{T}}\vec{\Lambda}_1^e + \vec{Y}^{\flat\mathsf{T}}\vec{\Lambda}_2^e \\ &= \int_{S^e}\Big(\underline{\underline{\nabla}}_{\underline{x}}(\underline{s}_z - \underline{s}^e)\cdot\underline{y}_h^\flat\Big)\cdot\underline{n}^e\,\mathrm{d}\Gamma + \int_{S^e}(\underline{s}_z - \underline{s}^e)\cdot\Big(\underline{\mathrm{d}\tau}(\underline{y}_h^\flat) + \underline{\mathrm{d}\nu}(\underline{y}_h^\flat)\Big)\,\mathrm{d}\Gamma.\end{aligned} \tag{74}$$

Denoting by n_z the normal vector field of the observed surface and n^e the normal vector field of the model surface subject to the extrapolated displacement y^e, both Riesz representation of the two surfaces appearing in the previous expression are given by

$$\underline{s}_z(\underline{x}) = \int_{S_z}\mathrm{k}(\underline{\widetilde{x}},\underline{x})\underline{n}_z(\underline{\widetilde{x}})\,\mathrm{d}\Gamma \quad \text{and} \quad \underline{s}^e(\underline{x}) = \int_{S^e}\mathrm{k}(\underline{\widetilde{x}},\underline{x})\underline{n}^e(\underline{\widetilde{x}})\,\mathrm{d}\Gamma.$$

Remarking that

$$\begin{aligned}\underline{\underline{\nabla}}_{\underline{x}}\underline{s}_z(\underline{x})\cdot\underline{y}_h^\flat(\underline{x}) &= \int_{S_z}\Big(\underline{\nabla}_2\mathrm{k}(\underline{\widetilde{x}},\underline{x})\cdot\underline{y}_h^\flat(\underline{x})\Big)\underline{n}_z(\underline{\widetilde{x}})\,\mathrm{d}\Gamma \\ &= \Big(\int_{S_z}\underline{n}_z(\underline{\widetilde{x}})\otimes\underline{\nabla}_2\mathrm{k}(\underline{\widetilde{x}},\underline{x})\,\mathrm{d}\Gamma\Big)\cdot\underline{y}_h^\flat(\underline{x}),\end{aligned}$$

the first term of the innovation is expressed as follows

$$\vec{Y}^{\flat\mathsf{T}}\vec{\Lambda}_1^e = \int_{S^e}\underline{n}^e(\underline{x})\cdot\Big(\int_{S_z}\underline{n}_z(\underline{\widetilde{x}})\otimes\underline{\nabla}_2\mathrm{k}(\underline{\widetilde{x}},\underline{x})\,\mathrm{d}\Gamma - \int_{S^e}\underline{n}^e(\underline{\widetilde{x}})\otimes\underline{\nabla}_2\mathrm{k}(\underline{\widetilde{x}},\underline{x})\,\mathrm{d}\Gamma\Big)\cdot\underline{y}_h^\flat(\underline{x})\,\mathrm{d}\Gamma. \tag{75}$$

Concerning the numerical integration of these terms, for the sake of simplicity and following [Glaunès et al., 2008], we have chosen a one-point integration rule at the center of each triangle, however our assembling strategy differs from [Imperiale et al., 2013]. We denote by $\mathcal{T}^e = \{T_i\}_{i=1}^{N_T}$ the set of triangles of the model surface and $\{\underline{c}_i\}_{i=1}^{N_T}$ the set composed by the center of every triangles. In the same manner we denote by

$$\mathcal{T}_z = \{T_i^z\}_{i=1}^{N_T^z} \quad \text{and} \quad \{\underline{c}_i^z\}_{i=1}^{N_T^z},$$

the triangles and their centers of the observed surface. In order to lighten the expressions, we consider a triangle $T \in \mathcal{T}^e$ of the deformed model surface and denote by $\underline{n}$ its normal unit vector, $|T|$ its surface area and $\underline{c}$ its center. With these notations and our choice of integration rule, the contribution of a triangle in $\mathcal{T}^e$ for $\vec{\Lambda}_1^e$ is computed by

$$\begin{aligned}&\int_T\Big(\underline{\underline{\nabla}}_{\underline{x}}(\underline{s}_z - \underline{s}^e)\cdot\underline{\delta y}\Big)\cdot\underline{n}^e\,\mathrm{d}\Gamma \approx \\ &\underline{n}\,|T|\cdot\Big(\sum_{j=1}^{N_T^z}\underline{n}_z(\underline{c}_j^z)\otimes\underline{\nabla}_2\mathrm{k}(\underline{c}_j^z,\underline{c})\,|T_j^z| - \sum_{j=1}^{N_T}\underline{n}^e(\underline{c}_j)\otimes\underline{\nabla}_2\mathrm{k}(\underline{c}_j,\underline{c})\,|T_j|\Big)\cdot\frac{1}{3}\Big(\underline{\delta y}^{(1)} + \underline{\delta y}^{(2)} + \underline{\delta y}^{(3)}\Big),\end{aligned} \tag{76}$$

where in (76) we consider δy a local finite element function on the triangle T, with components at the $\mathbb{P}_1$ degrees of freedom denoted by $\underline{\delta y}^{(1)}$, $\underline{\delta y}^{(2)}$ and $\underline{\delta y}^{(3)}$. We denote by $\mathbf{I}_c$ the 3×9 local matrix responsible for the numerical integration using the one-point rule, namely

$$
\begin{aligned}
\frac{1}{3}\Big(\underline{\delta y}^{(1)} + \underline{\delta y}^{(2)} + \underline{\delta y}^{(3)}\Big) &= \mathbf{I}_c \cdot \begin{pmatrix} \underline{\delta y}^{(1)} \\ \underline{\delta y}^{(2)} \\ \underline{\delta y}^{(3)} \end{pmatrix} \\
&= \begin{pmatrix} 1/3 & & & 1/3 & & & 1/3 & & \\ & 1/3 & & & 1/3 & & & 1/3 & \\ & & 1/3 & & & 1/3 & & & 1/3 \end{pmatrix} \cdot \begin{pmatrix} \underline{\delta y}^{(1)} \\ \underline{\delta y}^{(2)} \\ \underline{\delta y}^{(3)} \end{pmatrix}.
\end{aligned}
$$

In an assembling procedure the local term $\vec{\Lambda}_1^e$ at a triangle level is given by

$$
\mathbf{I}_c^\intercal \cdot \Big(\sum_{j=1}^{N_T^z} \underline{n}_z(\underline{c}_j^z) \otimes \underline{\nabla}_2 \mathrm{k}(\underline{c}_j^z, \underline{c}) \, |T_j^z| - \sum_{j=1}^{N_T} \underline{n}^e(\underline{c}_j) \otimes \underline{\nabla}_2 \mathrm{k}(\underline{c}_j, \underline{c}) \, |T_j| \Big) \cdot \underline{n} \, |T| \,. \tag{77}
$$

The second term of the innovation can be computed classically using the local barycentric coordinate system. On the considered triangle $T \in \mathcal{T}^e$, the spatial coordinate is uniquely expressed in the local barycentric coordinate system by

$$
\underline{x} = \underline{x}(r,s) = \sum_{i=1}^{3} \lambda_k(r,s)\underline{x}^{(k)},
$$

where $\{\lambda_i(r,s)\}_{i=1}^3$ are the two dimensional linear shape functions

$$
\begin{cases} \lambda_1(r,s) = r \\ \lambda_2(r,s) = s \\ \lambda_3(r,s) = 1 - r - s, \end{cases}
$$

and $\{\underline{x}^{(k)}\}_{k=1}^3$ are the summits of the deformed triangle under consideration. With these notations, the surface element of the triangle is constant and given by

$$
\underline{n}\,\mathrm{d}\Gamma = \frac{\partial \underline{x}}{\partial r} \wedge \frac{\partial \underline{x}}{\partial s} \mathrm{d}r\mathrm{d}s
$$

One can easily verify that

$$
\begin{cases}
\dfrac{\partial \lambda_1}{\partial r}(r,s) = 1, \quad \dfrac{\partial \lambda_1}{\partial s}(r,s) = 0, \\[2ex]
\dfrac{\partial \lambda_2}{\partial r}(r,s) = 0, \quad \dfrac{\partial \lambda_2}{\partial s}(r,s) = 1, \\[2ex]
\dfrac{\partial \lambda_3}{\partial r}(r,s) = -1, \quad \dfrac{\partial \lambda_3}{\partial s}(r,s) = -1,
\end{cases}
$$

so that

$$
\frac{\partial \underline{x}}{\partial r} = \underline{x}^{(1)} - \underline{x}^{(3)} = \underline{e}^{(2)}, \quad \frac{\partial \underline{x}}{\partial s} = \underline{x}^{(2)} - \underline{x}^{(3)} = \underline{e}^{(1)}.
$$

We consider δy a local finite element function on the triangle T expressed in the local barycentric coordinates as

$$
\underline{\delta y}(r,s) = \sum_{i=1}^{3} \lambda_k(r,s)\underline{\delta y}^{(k)},
$$

and verifying

$$\frac{\partial}{\partial r}\underline{\delta y} = \underline{\delta y}^{(1)} - \underline{\delta y}^{(3)} \quad \text{and} \quad \frac{\partial}{\partial s}\underline{\delta y} = \underline{\delta y}^{(2)} - \underline{\delta y}^{(3)}.$$

The derivative of a surface element with respect to a test displacement is then given by

$$\Big(\underline{\mathrm{d}\tau}(\underline{\delta y}) + \underline{\mathrm{d}\nu}(\underline{\delta y})\Big)\,\mathrm{d}\Gamma = \frac{\partial \underline{x}}{\partial r} \wedge \frac{\partial}{\partial s}\underline{\delta y} + \frac{\partial}{\partial r}\underline{\delta y} \wedge \frac{\partial \underline{x}}{\partial s}\;\mathrm{d}r\mathrm{d}s$$

$$= \underline{e}^{(2)} \wedge (\underline{\delta y}^{(2)} - \underline{\delta y}^{(3)}) + (\underline{\delta y}^{(1)} - \underline{\delta y}^{(3)}) \wedge \underline{e}^{(1)}\;\mathrm{d}r\mathrm{d}s.$$

Denoting by

$$\Big[\frac{\partial \underline{x}}{\partial s} \wedge\ \Big] = \begin{pmatrix} 0 & -e_3^{(1)} & e_2^{(1)} \\ e_3^{(1)} & 0 & -e_1^{(1)} \\ -e_2^{(1)} & e_1^{(1)} & 0 \end{pmatrix} \quad \text{and} \quad \Big[\frac{\partial \underline{x}}{\partial r} \wedge\ \Big] = \begin{pmatrix} 0 & -e_3^{(2)} & e_2^{(2)} \\ e_3^{(2)} & 0 & -e_1^{(2)} \\ -e_2^{(2)} & e_1^{(2)} & 0 \end{pmatrix},$$

we can define $\mathbf{Q}$, a 3×9 local matrix, such that

$$\Big(\underline{\mathrm{d}\tau}(\underline{\delta y}) + \underline{\mathrm{d}\nu}(\underline{\delta y})\Big)\,\mathrm{d}\Gamma = \mathbf{Q} \cdot \begin{pmatrix} \underline{\delta y}^{(1)} \\ \underline{\delta y}^{(2)} \\ \underline{\delta y}^{(3)} \end{pmatrix}\;\mathrm{d}r\mathrm{d}s,$$

where

$$\mathbf{Q} = \begin{pmatrix} \mathbf{O}_{3\times 3} & \Big[\frac{\partial \underline{x}}{\partial r} \wedge\ \Big] & -\Big[\frac{\partial \underline{x}}{\partial r} \wedge\ \Big] \end{pmatrix} + \begin{pmatrix} -\Big[\frac{\partial \underline{x}}{\partial s} \wedge\ \Big] & \mathbf{O}_{3\times 3} & \Big[\frac{\partial \underline{x}}{\partial s} \wedge\ \Big] \end{pmatrix}. \tag{78}$$

With these notations and the choice of integration rule, the contribution of a triangle in $\mathcal{T}^e$ for $\vec{\Lambda}_2^e$ is computed by

$$\int_T (\underline{s}_z - \underline{s}^e) \cdot \Big(\underline{\mathrm{d}\tau}(\underline{\delta y}) + \underline{\mathrm{d}\nu}(\underline{\delta y})\Big)\,\mathrm{d}\Gamma$$

$$\approx \Big(\sum_{j=1}^{N_T^z} \mathrm{k}(\underline{c}_j^z, \underline{c})\underline{n}_z(\underline{c}_j^z)\,|T_j^z| - \sum_{j=1}^{N_T} \mathrm{k}(\underline{c}_j, \underline{c})\underline{n}^e(\underline{c}_j)\,|T_j|\Big) \cdot \mathbf{Q} \cdot \begin{pmatrix} \underline{\delta y}^{(1)} \\ \underline{\delta y}^{(2)} \\ \underline{\delta y}^{(3)} \end{pmatrix} \int_{r,s} \mathrm{d}r\mathrm{d}s$$

$$= \frac{1}{2}\Big(\sum_{j=1}^{N_T^z} \mathrm{k}(\underline{c}_j^z, \underline{c})\underline{n}_z(\underline{c}_j^z)\,|T_j^z| - \sum_{j=1}^{N_T} \mathrm{k}(\underline{c}_j, \underline{c})\underline{n}^e(\underline{c}_j)\,|T_j|\Big) \cdot \mathbf{Q} \cdot \begin{pmatrix} \underline{\delta y}^{(1)} \\ \underline{\delta y}^{(2)} \\ \underline{\delta y}^{(3)} \end{pmatrix}.$$

Hence, in an assembling procedure the local term $\vec{\Lambda}_2^e$ at a triangle level is given by

$$\frac{1}{2}\mathbf{Q}^\intercal \cdot \Big(\sum_{j=1}^{N_T^z} \mathrm{k}(\underline{c}_j^z, \underline{c})\underline{n}_z(\underline{c}_j^z)\,|T_j^z| - \sum_{j=1}^{N_T} \mathrm{k}(\underline{c}_j, \underline{c})\underline{n}^e(\underline{c}_j)\,|T_j|\Big). \tag{79}$$

From the different operators that we need for the innovation term and from the expression (68) of the bilinear form, we can directly give the local expression of $\mathbf{dS}^e|\mathbf{dS}^e$:

$$\frac{|T_i|}{2}\mathbf{I}_c^\intercal \cdot \Big(\underline{n}(\underline{c}_i) \otimes \underline{\nabla}_2 \mathrm{k}(\underline{c}_j, \underline{c}_i)\Big)^\intercal \cdot \mathbf{Q}_j + \frac{|T_j|}{2}\mathbf{Q}_i^\intercal \cdot \Big(\underline{n}(\underline{c}_j) \otimes \underline{\nabla}_1 \mathrm{k}(\underline{c}_j, \underline{c}_i)\Big) \cdot \mathbf{I}_c$$

$$+ \Big(\underline{n}(\underline{c}_i)\,|T_i| \cdot \underline{n}(\underline{c}_j)\,|T_j|\Big)\mathbf{I}_c^\intercal \cdot \underline{\underline{\nabla}}_{12}^2 \mathrm{k}(\underline{c}_j, \underline{c}_i) \cdot \mathbf{I}_c + \frac{\mathrm{k}(\underline{c}_j, \underline{c}_i)}{4}\mathbf{Q}_i^\intercal \cdot \mathbf{Q}_j. \tag{80}$$

To conclude the presentation of the discretization procedure for the *current*-based descent method, we infer – from the spatial discretization of the terms described in this section – the form of the various algorithm depending on the type of gradient that we consider. Namely,

- in the direct application of the norm in $\mathcal{W}^*$

$$\mathbf{M}_\rho \frac{\vec{Y}^{n+1}-\vec{Y}^{n}}{\Delta t} = \vec{\Lambda}^e - \mathbf{dS}^e|\mathbf{dS}^e(\vec{Y}^{n+\alpha}-\vec{Y}^e), \tag{81}$$

- in the case of $\mathcal{H}^1$-type Sobolev-gradient

$$\mathbf{K}\frac{\vec{Y}^{n+1}-\vec{Y}^{n}}{\Delta t} = \vec{\Lambda}^e - \mathbf{dS}^e|\mathbf{dS}^e(\vec{Y}^{n+\alpha}-\vec{Y}^e), \tag{82}$$

- in the case of our best choice of Sobolev-gradient based on the generalized inverse of the tangent

$$\frac{\vec{Y}^{n+1}-\vec{Y}^{n}}{\Delta t} = (\epsilon\mathbf{K} + \mathbf{dS}^e|\mathbf{dS}^e)^{-1}\big(\vec{\Lambda}^e - \mathbf{dS}^e|\mathbf{dS}^e(\vec{Y}^{n+\alpha}-\vec{Y}^e)\big). \tag{83}$$

where in all cases we have used the time-scheme obtained by linearization of the discrepancy.

Approximating Gâteaux derivative for operators cross-checking The complexity of the operator explicitly expressed in (80) naturally calls for means of cross-checking. A natural way to do so is to use an approximation of the Gâteaux derivative of a current. More precisely, defining by S_0 a part of the deformable object surface in the reference configuration and $S(y^\flat)$ the corresponding surface deformed by any admissible displacement $y^\flat$, then the tangent current around the reference configuration can be approximated by

$$\forall y^\flat, \quad \mathrm{d}S_0(y^\flat) = \lim_{\tau\to 0}\frac{1}{\tau}\big(S(\tau y^\flat) - S_0\big) \sim \frac{1}{\tau}\big(S(\tau y^\flat) - S_0\big),$$

for a small scalar value $\tau > 0$.

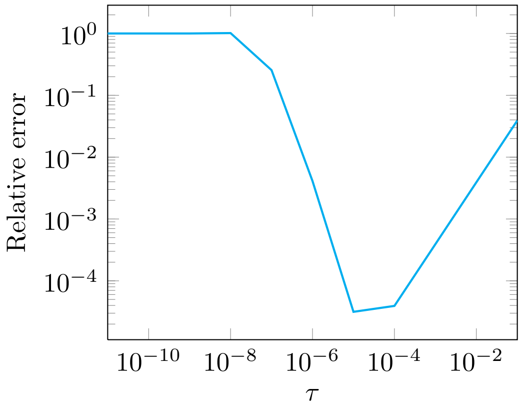

Figure 5: Evolution of the relative error between the assambled operator and the operator approximated by in (84) with respect to the parameter τ.

Now, since we already set a finite element space that, by definition, approximate the space of admissible displacement, the operator $(\mathrm{d}S(y^\flat), \mathrm{d}S(y^\sharp))_{\mathcal{W}^*}$ can therefore be approximated by

$$\forall y^\flat, \quad \forall y^\sharp, \quad (\mathrm{d}S(y^\flat), \mathrm{d}S(y^\sharp))_{\mathcal{W}^*} \sim \sum_{i,j}^{N}\Big(\frac{1}{\tau}\big(S(\tau\varphi_i) - S_0\big), \frac{1}{\tau}\big(S(\tau\varphi_j) - S_0\big)\Big)_{\mathcal{W}^*}, \tag{84}$$

where $\{\varphi_i\}_{i=1}^N$ are the finite element basis functions. In Figure 5 we plot the evolution of the relative error between the operator assembled using (80) and its approximation (84). We observe a first appropriate behavior when τ decreases – which indicates a correct assembling procedure – rapidly deteriorated for smaller values, characteristic of numerical errors inherent of this type of approximation.

Domain decomposition The algorithms (81), (82) and (83) can be expressed as

$$\mathbf{A}(\vec{Y}^e)\vec{Y}^{n+1} = F(\vec{Y}^e, \vec{Y}^n), \tag{85}$$

where the matrix $\mathbf{A}$ and right-hand side term F appearing in the linear problem depends on the type of gradient that we consider, namely

$$\mathbf{A} = \left| \begin{array}{l} \frac{1}{\Delta t}\mathbf{M} + \alpha \mathbf{dS}^e|\mathbf{dS}^e, \\ \\ \frac{\epsilon}{\Delta t}\mathbf{K} + (\frac{1}{\Delta t} + \alpha)\mathbf{dS}^e|\mathbf{dS}^e, \end{array} \right.$$

and

$$F = \left| \begin{array}{l} \vec{\Lambda}^e + \mathbf{dS}^e|\mathbf{dS}^e\vec{Y}^e + \frac{1}{\Delta t}\mathbf{M}\vec{Y}^n + (1-\alpha)\mathbf{dS}^e|\mathbf{dS}^e\vec{Y}^n, \\ \\ \vec{\Lambda}^e + \mathbf{dS}^e|\mathbf{dS}^e\vec{Y}^e + \frac{1}{\Delta t}\big(\epsilon\mathbf{K} + \mathbf{dS}^e|\mathbf{dS}^e\big)\vec{Y}^n + (1-\alpha)\mathbf{dS}^e|\mathbf{dS}^e\vec{Y}^n. \end{array} \right.$$

From the expression of the bilinear form (68), we can understand that the matrix $\mathbf{dS}^e|\mathbf{dS}^e$ obtained after discretization is potentially full. The band width depends however on the kernel width μ since it regulates the decrease of the Gaussian kernel. Figure 6 shows an example of the evolution of the matrix pattern with respect to different values of the kernel width μ illustrating the filling phenomenon – values lower than the computer precision fixed to 1e-17 are set to 0.

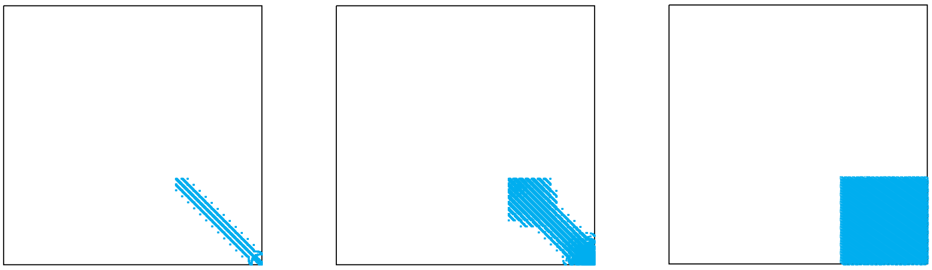
(a) $\mu = 10^{-1}$ (b) $\mu = 1$ (c) $\mu = 10^1$

Figure 6: Sparse pattern of the matrix $\mathbf{dS}^e|\mathbf{dS}^e$ for a toy geometry example (with 1548 degress of freedom) for different values of the kernel width μ – values lower than the computer precision fixed to 1e-17 are set to 0

In the perspective of a direct solver (commonly used in the context of non linear mechanics) this feature may lead to a dramatic increase of the total computational time needed to solve the linear problem. In order to circumvent this difficulty we propose to perform a domain decomposition strategy to separate the degrees of freedom on the part of the surface concerned by the current observation operator and the remaining degrees of freedom. Considering Γ the indexes of the degrees of freedom that belong to the surface under consideration and I the remaining indexes, then the linear system (85) is decomposed block-wise into

$$\begin{pmatrix} \mathbf{A}_{\mathrm{II}} & \mathbf{A}_{\mathrm{I}\Gamma} \\ \\ \mathbf{A}_{\Gamma\mathrm{I}} & \mathbf{A}_{\Gamma\Gamma} \end{pmatrix} \begin{pmatrix} \vec{Y}_{\mathrm{I}} \\ \\ \vec{Y}_{\Gamma} \end{pmatrix}^{n+1} = \begin{pmatrix} F_{\mathrm{I}} \\ \\ F_{\Gamma} \end{pmatrix},$$

where the block $\mathbf{A}_{\Gamma\Gamma}$ is potentially full. As an example of possible choices, in order to obtain the solution of (85) we can choose a Gauss-Seidel iterative algorithm

$$\begin{cases} \mathbf{A}_{\mathrm{II}}\vec{Y}_{\mathrm{I}}^{(k+1)} + \mathbf{A}_{\mathrm{I}\Gamma}\vec{Y}_{\Gamma}^{(k+1)} = F_{\mathrm{I}}, \\ \\ \mathbf{A}_{\Gamma\Gamma}\vec{Y}_{\Gamma}^{(k+1)} + \mathbf{A}_{\Gamma\mathrm{I}}\vec{Y}_{\Gamma}^{(k)} = F_{\Gamma}. \end{cases} \tag{86}$$

Indeed in (86) we isolate the inversion of the block $\mathbf{A}_{\Gamma\Gamma}$, which is full but of the size of the number of degrees of freedom on the surface. Then we proceed to the inversion of $\mathbf{A}$ where the band width corresponds to classical finite element operator. In practice this algorithm converges typically in less than 10 iterations.

2.5.6 Image based registration

In this section, we want to benefit from the formalism of currents to solve goes a step further in the unification of the registration problems and formalism. Here our objective is to consider a lower level type of data, namely a level set segmentation of the image instead of a triangulated surface – as required in the case of the signed distance operator. More precisely, we assume that the observations on the target takes the form of an image where the boundary – or a part of the boundary – represents significant changes in the image intensity. In this context we then assume that a segmentation procedure is performed on the image in order to obtain a level-set function whose zero-value isosurface corresponds to the segmentation of the target surface boundary. Readers may refer to [Oster and Fedkiw, 2009, Paragios, 2003, Chan and Shen, 2005, Scherzer, 2011] for an extensive presentation of level sets with application to segmentation procedures.

From equations (77) and (79) of the innovation term appearing in the *currents*-based discrepancy, we understand that the registration procedure requires (1) the centers of the triangles $\underline{c}^z$, (2) their normal unit $\underline{n}_z$ vectors and (3) their surface area $|T^z|$. Computing the isosurface of ϕ directly leads to an estimation of the centers of every triangles by using the center of the set of voxels defining the isosurface. In theses voxels, the normal unit vector is classically estimated through the spatial gradient of the level-set function,

$$\underline{n}_{zi} = \frac{\underline{\nabla}\,\phi(\underline{c}_i^z)}{|\underline{\nabla}\,\phi(\underline{c}_i^z)|}. \tag{87}$$

Focusing on the definition of the surface area we have to deal with, we should want to estimate it by considering the surface of the plane defined by the estimated normal vector field, passing by the center of each voxel and clipping the voxel. Taking into account all the different cases occurring when clipping a voxel with this plane may lead to unnecessary technicalities, therefore we rather simplify the approach by replacing the voxel by an ellipsoid defined within the voxel, see Figure 7. The intersection is then straightforward to compute. Let $\mathbf{O}$ be the image orientation defined through three orthogonal unit vectors $(\underline{i}, \underline{j}, \underline{k})$. In the canonical coordinate system, i.e. after applying $\mathbf{O}^{-1}$, the ellipsoid is given by

$$\frac{1}{\delta x_1^2}x_1^2 + \frac{1}{\delta x_2^2}x_2^2 + \frac{1}{\delta x_3^2}x_3^2 = 1, \tag{88}$$

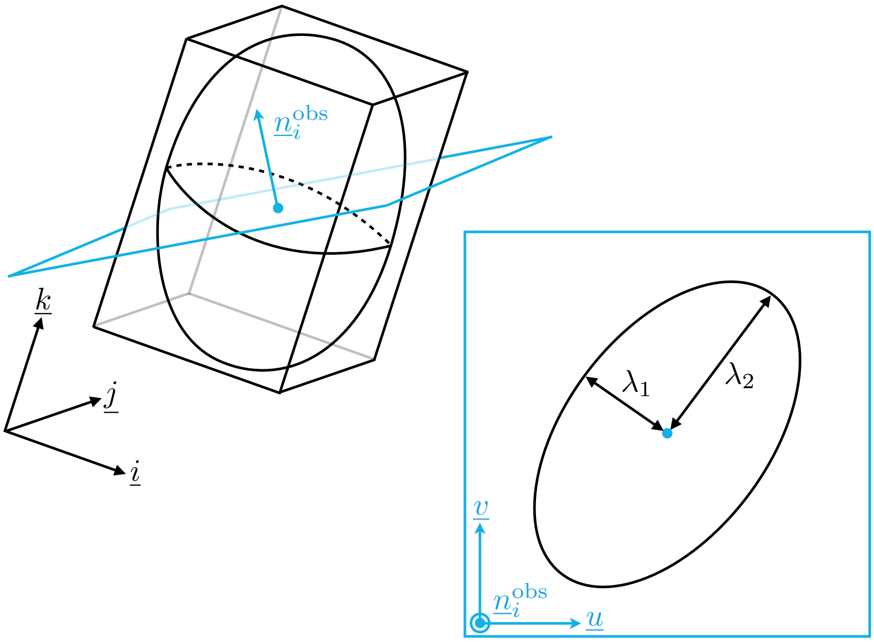

Figure 7: Estimation of a triangle surface area through the normal vector field defined within a voxel.

where $\delta x_1 \times \delta x_2 \times \delta x_3$ is the voxel volume. Lying in the canonical coordinate system, we can define the plane coordinate system using $\mathbf{O}^{-1}\underline{n}_{zi}$ and complete the basis with two orthogonal unit vectors $\underline{u}$ and $\underline{v}$. Denoting by η_1, η_2 and η_3 the spatial coordinates in this coordinate system, the ellipse is defined by three parameters a, b, c such that

$$\begin{cases} \eta_3 = 0, \\ a\eta_1^2 + b\eta_2^2 + 2c\eta_1\eta_2 = 1. \end{cases} \tag{89}$$

Remarking that

$$\begin{pmatrix} x_1 \\ x_2 \\ x_3 \end{pmatrix} = \begin{pmatrix} \underline{u} & \underline{v} & \mathbf{O}^{-1}\underline{n}_{zi} \end{pmatrix} \cdot \begin{pmatrix} \eta_1 \\ \eta_2 \\ \eta_3 \end{pmatrix},$$

and replacing (x_1, x_2, x_3) in (88), we infer the values of the coefficients

$$\left| \begin{aligned} a &= \frac{1}{\delta x_1^2} u_1^2 + \frac{1}{\delta x_2^2} u_2^2 + \frac{1}{\delta x_3^2} u_3^2 \\ b &= \frac{1}{\delta x_1^2} v_1^2 + \frac{1}{\delta x_2^2} v_2^2 + \frac{1}{\delta x_3^2} v_3^2 \\ c &= \frac{1}{\delta x_1^2} u_1 v_1 + \frac{1}{\delta x_2^2} u_2 v_2 + \frac{1}{\delta x_3^2} u_3 v_3. \end{aligned} \right.$$

Eventually the triangle surface area is thus estimated by

$$|T_i^z| = 2\pi\lambda_1\lambda_2, \tag{90}$$

where λ_1 and λ_2 are the eigenvalues of the symmetric positive definite matrix $\begin{pmatrix} a & c \\ c & b \end{pmatrix}$.

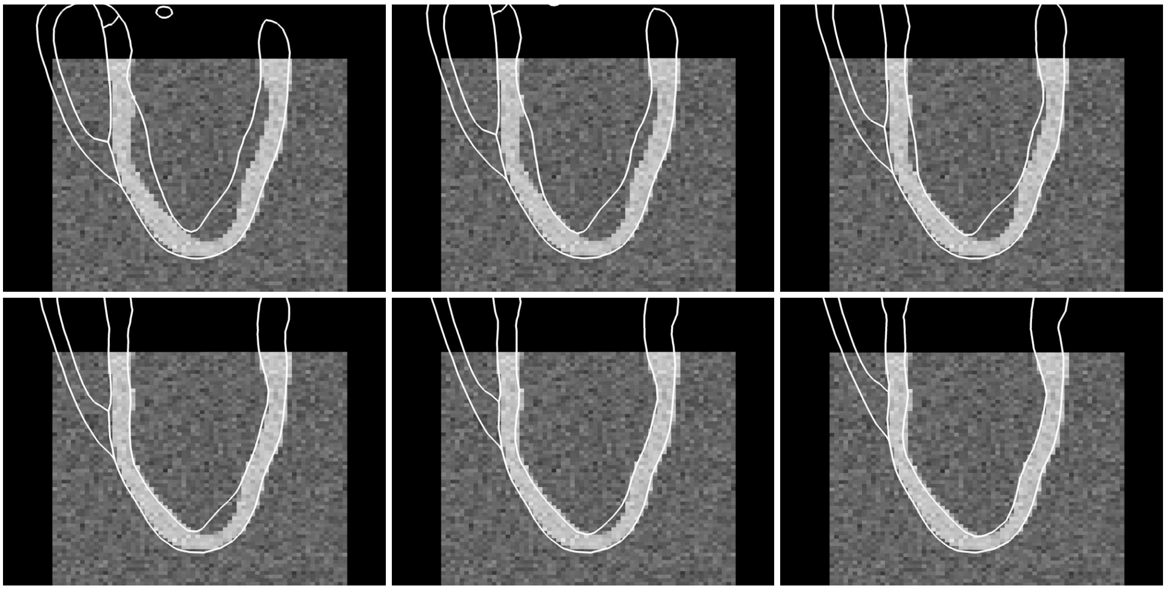

Figure 8: Solving the registration problem using a level-set segmentation *current*. Evolution of the deformable object during various of the descent method, in long axis view.

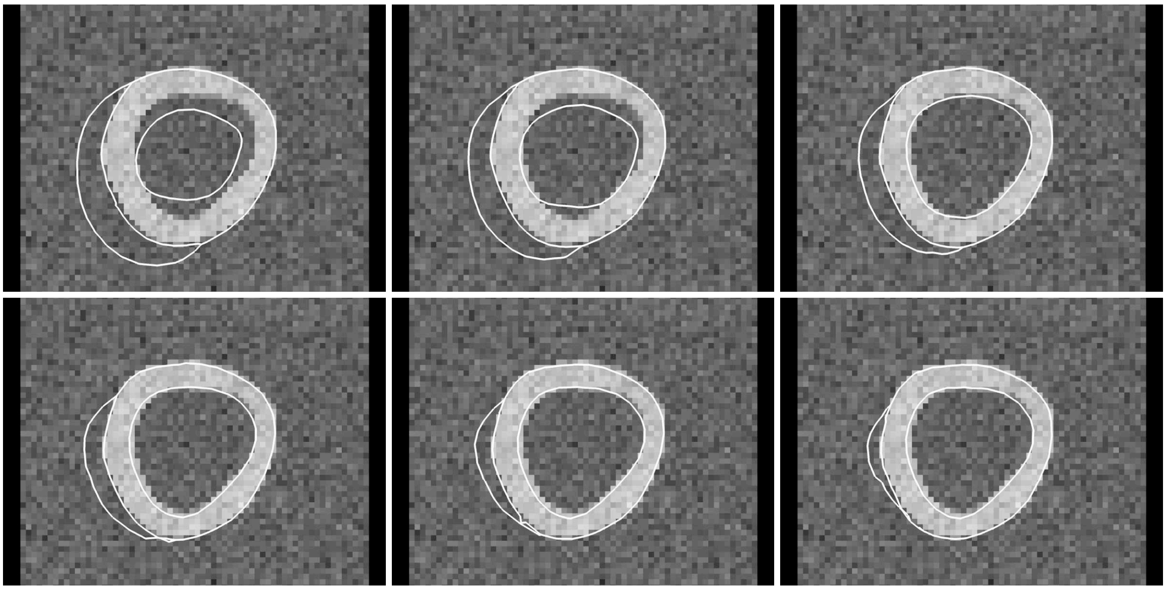

Figure 9: Solving the registration problem using a level-set segmentation *current*. Evolution of the deformable object during various of the descent method, in short axis view.

Examples of application with synthetic data. First we consider the same numerical experience in which we evaluate our norm choices and Sobolev-gradient corresponding to (81), (82) and (83). The results are presented in Figure 10 and we also understand the interest of our particular choice of Sobolev-gradient of (83).

Then, we consider again the realistic registration problem defined in Section 2.4.3 from the Pig data of [Chabiniok et al., 2011]. Since finding adequate level-set strategies for actual heart MR-images [Paragios, 2003] is beyond the purpose of this methodological article, we decide to not rely on the original MR-images of [Chabiniok et al., 2011]. Instead, we generate a synthetic image by rasterizing [Bresenham, 1965] the manual segmentation of the pig heart. After adding some white noise on the image, we perform a level-set segmentation based on [Chan and Vese, 2001] using Yan Zhang's *2D-3D image segmentation Matlab toolbox*[1]. We then use the level set to define the *current* and register our computational mesh. The results are presented in Figure 8 and 9.

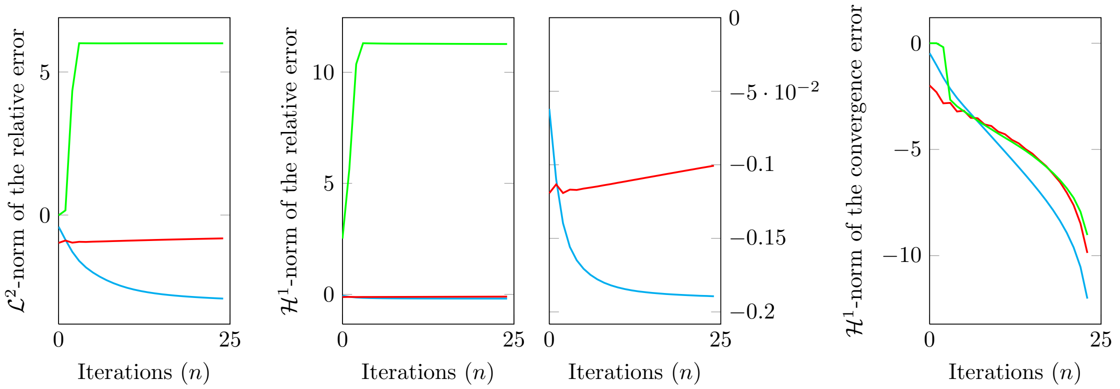

Figure 10: In (green) the solution associated with (81), in (red) the solution associated with (82) and in (cyan) the solution associated with (83).

2.5.7 Similarity with active surfaces, Gradient Vector Flow (GFV) and Vector Filed Convolution (VFC)

In the classical formalism of active contours or their three-dimensional equivalent, active surfaces [Cohen et al., 1992, Caselles et al., 1997, Aubert et al., 2003, Gout et al., 2005, Sermesant et al., 2003, Li and Acton, 2007, Cohen and Peyré, 2011], we consider a parametric surface $S(t, r, s)$, where t represents an artificial time variable and (r, s) are the spatial parametrization of the surface embedded in $\mathbb{R}^3$. The dynamics of this (active) surfaces is then ruled by a descent method

$$\begin{cases} \dot{S}(t) = -\big(\nabla\mathcal{E}^{\text{int}} + \nabla\mathcal{E}^{\text{ext}}\big)(S(t)), \quad t \geq 0 \\ S(0) = S_\diamond, \end{cases} \tag{91}$$

where $S_\diamond$ is a given prior on the surface. The formalism (91) should be compared to our formalism where we defined the object deformation through its displacement with

$$\begin{cases} \Big(\dfrac{y^{n+1} - y^n}{\Delta t}, y^\flat\Big)_{\mathcal{Y}} = \beta \displaystyle\int_{\Omega_0} \frac{\partial W}{\partial \underline{\underline{e}}} : \mathrm{d}_{\underline{y}}\underline{\underline{e}}(\underline{y})(\underline{y}^\flat)\,\mathrm{d}\Omega + \gamma(\mathrm{d}S(y^\flat), S_z - S(\underline{y}))_{\mathcal{W}^*}, \\ y(0) = y_\diamond, \end{cases} \tag{92}$$

---

[1] http://www.mathworks.com/matlabcentral/fileexchange/24998-2d3d-image-segmentation-toolbox

In (91), $\mathcal{E}^{\mathrm{int}}$ is the so-called *internal energy* used in this formalism to favor smooth deformation which is thus directly comparable to the linear or non-linear elasticity penalization presented in our formalism. Besides, $\mathcal{E}^{\mathrm{ext}}$ is an external energy typically computed from the image. This external energy is typically designed so that its gradient leads to a vector field embedded in the image domain to attract the active surface towards the so-called Region Of Interests (ROIs) of the image. The term $\mathcal{E}^{\mathrm{ext}}$ is then directly comparable our discrepancy term. In the literature however, it was accepted to circumvent the formal definition of this external energy by by directly prescribing an *external force* f^{ext} so that the dynamics of the active surface reads

$$\begin{cases} \dot{S}(t) = -\nabla\mathcal{E}^{\mathrm{int}}(S(t)) + f^{\mathrm{ext}}(S(t)), \quad t \geq 0 \\ S(0) = S_0, \end{cases} \tag{93}$$

Popular examples of such external force are the so-called Gradient Vector Field (GVF) – see for instance [Xu and Prince, 1998, Guillot and Bergounioux, 2009] – or the Vector Field Convolution (VFC) [Li and Acton, 2007] obtained through vectorial convolution of an *edge map* that we denote by e – with $\mathcal{I}$ representing the grey-level intensity of the image. There exist various ways to define an edge-map, a typical example is

$$e(\underline{x}) = -\|\nabla\mathcal{I}(\underline{x})\|^2.$$

In this context we have

$$\underline{f}^{\mathrm{ext}}(\underline{x}) = \int_{\mathcal{I}} \mathrm{k}^{\mathrm{vfc}}(\underline{x}, \underline{\widetilde{x}})\underline{m}(\underline{x}, \underline{\widetilde{x}})e(\underline{\widetilde{x}})\mathrm{d}\mathcal{I}, \tag{94}$$

where $\underline{m}$ is defined as a unit vector pointing to the kernel origin [Li and Acton, 2007]. This definition of the external force should be compared to the definition of the Riesz representation of a current (60). This important similarity goes as far as defining the convolution kernel $\mathrm{k}^{\mathrm{vfc}}$ as a Gaussian kernel.

3 Dynamical case

In the first part of this work we have examined various strategies of static registration of a deformable model on some given data. We can now move to the case where we have a time-sequence of data. We focus here on the most relevant case of available surfaces segmented from a 3D+t image sequence and we expect to apply the formalism of *currents*. In this context, we assume to have modeled the motion – namely the time-deformation – on the deformable object considered and we expect to benefit from it. This configuration enters in the context of data assimilation [Blum et al., 2008, Navon, 2008, Chapelle et al., 2012b] and we specifically have in mind cardiac applications where various models of the heart contraction exist. In the sequel we show how this class of "dynamics registration" can benefit from the static case. In this respect we intend to mainly follow the work of [Moireau et al., 2009] and propose to embed it in the context of the the formalism of *currents*.

3.1 A sequential state estimator using distances

From a general standpoint, data assimilation aims at providing a reconstruction of a real system using the two complementary sources of information namely a model representing the physical process under study and some specific observations on the target system. In the community of data assimilation, the model is generally a dynamical system taking the form of potentially nonlinear partial differential equations. In most cases, it gathers some information on the physics lying behind the observed phenomenon and encapsulated in a mathematical formalism. Notwithstanding its ability to represent any possible trajectory – with a variable precision – a model often contains a various range of potential errors, *e.g.* on the operator driving the dynamical system, on the initial conditions or on some parameters. By extracting the valuable information contained in the observations, data assimilation procedure aims at correcting these errors and, by doing so, providing a more precise simulation of the real system. Formally in data assimilation we have to define a model – written in first order form – modeling the physical phenomena, in our case the deformation evolution. This model formally reads

$$\dot{x}(t) = A(x(t)).$$

In order to rewrite a mechanical system – with inertia – in a first order form, we should concatenate the displacement and the velocity in the state vector in order to define $x = \begin{pmatrix} y & v \end{pmatrix}^\intercal$. On this class of system we consider a target trajectory denoted by $x_\bullet$, which follows

$$\begin{cases} \dot{x}_\bullet(t) = A(x_\bullet(t)) + \omega_\bullet, \\ \\ x_\bullet(0) = x_\diamond + \zeta_\bullet, \end{cases}$$

where $x_\diamond$ is some *a priori* on the initial conditions and $\zeta_\bullet$ and $\omega_\bullet$ are potential uncertainties. Along with this target trajectory we associate some observations of the form

$$z(t) = H(x_\bullet(t)) + \chi(t).$$

In the spirit of the first part of this work, the observation operator only applies to the displacement part of the state therefore $H(x)$ is in fact $H(y)$ and the tangent operator is then $\mathrm{d}_x H = (\mathrm{d}_y H \quad 0)$. In this context, the principle of data assimilation is to retrieve the trajectory $x_\bullet$ with the combined help of the model A, the observations z and a method to compute the discrepancy $D(z, x)$ for any computed state x.

We distinguish two different categories of data assimilation methods. The first one, referred to as the family of variational methods [Navon, 2008], is based on minimizing a functional which balances the confidence we have on the *a priori* knowledge of the target system and the confidence on the observations. Typically we define on a time window $[0, T]$

$$\mathscr{J}_T(\zeta, \omega) = \frac{1}{2} \|\zeta\|_{\mathcal{X}} \frac{1}{2} + \int_0^T (\|D(z, \underline{y})\|^2_{\mathcal{Z}} + \|\omega\|^2_{\mathcal{X}})\, \mathrm{d}t \tag{95}$$

for any trajectory

$$\begin{cases} \dot{x}(t) = A(x(t)) + \omega, \\ \\ x(0) = x_\diamond + \zeta. \end{cases}$$

The second category – which we will be focusing on – gather the so-called sequential data assimilation methods. They aim at proposing an observer $\hat{x}$ – also referred to as an estimator – of the exact trajectory $x_\bullet$ by filtering in time the discrepancy between the model and the observation z. The observer dynamics is generally built under a feedback law based on the discrepancy with the data which takes the form of

$$\begin{cases} \dot{\hat{x}}(t) = A\hat{x}(t) + G(t)\big(z(t) - H(\hat{x}(t))\big), \\ \\ \hat{x}(0) = x_\diamond, \end{cases}$$

where G is the so-called *gain operator* also called *filter operator* since it allows to filter the data noise through the use of the model. There exists various possible definitions of the gain operator, a typical example being is the popular Extended Kalman Filter (EKF) [Simon, 2006, Chapelle et al., 2012b] defined as $G(t) = P(t)\mathrm{d}H^*$, where P is an operator – corresponding to a covariance matrix in a stochastic standpoint – following the Riccati dynamical equation

$$\dot{P} = \mathrm{d}AP + P\mathrm{d}A^* + P\mathrm{d}H^*\mathrm{d}HP, \quad P(0) = P_0.$$

This gain operator has the advantage of proposing an observer for any model operator A. In fact in the context of linear operators, this gain derives exactly from the minimization functional (95) in the sense that

$$\forall t, \quad \hat{x}_{\mathrm{Kal}}(t) = x[\operatorname{argmin}(\mathscr{J}_t(\zeta, \omega)))](t).$$

For nonlinear operators however, EKF represents only an approximation of the "optimal" gain [Chapelle et al., 2012b]. At any rate, optimal filters suffer from the fact that the operator P leads to a full matrix after spatial discretization – which represents a prohibitive cost in the perspective of manipulating finite element variables. To circumvent this "curse of dimensionality" and following [Luenberger, 1971], simpler alternative based on the specific model dynamics. This idea is referred to as the nudging approach in the data assimilation community [Hoke and Anthes, 1976, Auroux and Blum, 2008] and the resulting estimator is called Luenberger observer. There is no more equivalence with a minization criterion and the only objective is then to make the estimation error $\tilde{x} = x_\bullet - \hat{x}$ as small as possible. Here we recognize the same type of arguments as those encountered in the static case. Following this path, authors in [Moireau et al., 2009, Chapelle et al., 2012a, Chapelle et al.,] have demonstrated in the context of linear elastodynamics systems with linear observation operators the effectiveness of a simple gain operator of the form $G = \gamma H^*$. They define the observer as the solution of the dynamics

$$\begin{cases} \dot{\hat{x}}(t) = A(\hat{x}(t)) - \gamma H^*\big(z(t) - H\hat{x}(t)\big), \\ \\ \hat{x}(0) = x_\diamond, \end{cases}$$

where we clearly recognize the derivative of the discrepancy functional defined in (2) in the context of the static registration problem addressed in Section 2. The error dynamics is then given by

$$\begin{cases} \dot{\tilde{x}}(t) = \big(A - G(t)H\big)\tilde{x}(t) + G(t)\chi(t), \\ \\ \tilde{x}(0) = \zeta_\bullet. \end{cases}$$

For elastodynamics systems, A is a skew-adjoint operator allowing the energy conservation of the initial system

$$\frac{1}{2}\frac{\mathrm{d}}{\mathrm{d}t}\|x_\bullet\|^2_{\mathcal{X}} = 0.$$

where $\mathcal{X}$ is a Hilbert space endowed with the norm $\|\cdot\|_{\mathcal{X}}$ gathering the admissible state. Besides, the energy of the estimation error reads

$$\frac{1}{2}\frac{\mathrm{d}}{\mathrm{d}t}\|\tilde{x}\|^2_{\mathcal{X}} = -\gamma\|H\tilde{x}\|^2_{\mathcal{Z}} + g(\omega_*(t), \chi(t)), \tag{96}$$

which is dissipative – up to the noise terms – and involves the observation operator. Even more importantly, in data assimilation the error can be proved to converged to 0 at least when ω_* and χ are null– see [Moireau et al., 2009] in the elastodynamics case – whereas in the static case it was only possible to make the observed part of the error going to 0. This can be explained by the presence of the strong *a priori* represented by the model.

When dealing with nonlinear operators, authors in [Moireau et al., 2009] propose the following extension which are directly written after spatial discretization

$$\mathbf{M}_\rho \ddot{\vec{Y}} + \vec{K}(\vec{Y}, \dot{\vec{Y}}) = \vec{F}, \tag{97}$$

where $\mathbf{M}_\rho$ is the mass matrix, $\vec{K}$ is the residual associated with the power of internal forces and $\vec{F}$ is the residual associated with the power of external forces. For instance, in linear viscoelasticity we have

$$\vec{K}(\vec{Y}, \dot{\vec{Y}}) = \mathbf{K}\vec{Y} + \mathbf{C}\dot{\vec{Y}}$$

where $\mathbf{K}$ is the stiffness matrix and $\mathbf{C}$ account for some natural damping in the system, typically of the form of a Rayleigh damping $\mathbf{C} = \alpha \mathbf{M}_\rho + \beta \mathbf{K}$ with α and β two parameters. Then – still in [Moireau et al., 2009] – the authors propose and fully analyze the following observer

$$\begin{cases} \dot{\hat{\vec{Y}}} = \hat{\vec{V}} - \gamma(\epsilon \mathbf{K} + \mathbf{dD}^\intercal \mathbf{M}^{\mathrm{obs}} \mathbf{dD})^{-1} \mathbf{dD}^\intercal \mathbf{M}^{\mathrm{obs}} \vec{D}(\hat{\vec{Y}}, Z), \\ \\ \mathbf{M}_\rho \dot{\hat{\vec{V}}} + \vec{K}(\hat{\vec{Y}}, \hat{\vec{V}}) = \vec{F}, \\ \\ \hat{\vec{Y}}(0) = \vec{Y}_\diamond, \quad \hat{\vec{V}}(0) = \vec{V}_\diamond. \end{cases} \tag{98}$$

where the identity between the displacement and the velocity is perturbed with the specific Sobolev-gradient associated with a $\mathcal{L}^2$ discrepancy norm. Therefore our strategy is to extend the formulation (98) within the formalism of *currents*.

3.2 Formulation with a *current*-based discrepancy

Our idea is thus to extend the observer defined in [Moireau et al., 2009] which was limited to a simple distance-to-surfaces discrepancy operator – as presented in (98) – to a *current*-based discrepancy. As we have justified in the previous sections, we can directly infer the dynamics of the estimator by merging the model dynamics with the *current*-based discrepancy defined in the static case with the Sobolev gradient. To start with – similarly to Section 2.5.5 – we define

$$\left| \begin{aligned} &(\mathrm{d}S(y_h^\flat), \mathrm{d}S(y_h^\sharp))_{\mathcal{W}^*} = \vec{Y}^{\flat\mathsf{T}} \mathbf{dS}|\mathbf{dS} \vec{Y}^\sharp, \\ \\ &(\mathrm{d}S(y_h^\flat), S_z - S)_{\mathcal{W}^*} = \vec{Y}^{\flat\mathsf{T}} \vec{\Lambda}. \end{aligned} \right. \tag{99}$$

In this formulation both $\mathbf{dS}|\mathbf{dS}$ and $\vec{\Lambda}$ depend nonlinearly on the displacements since both terms $\mathrm{d}S$ and S – referred to as the tangent current and the current – are defined on the deformed model surface. Hence, identifying with the terms appearing in (98), the spatial discretization of the state observer for elastodynamics system using the formalism of currents reads

$$\begin{cases} \dot{\hat{\vec{Y}}} = \hat{\vec{V}} - \gamma(\epsilon \mathbf{K} + \mathbf{dS}|\mathbf{dS})^{-1} \vec{\Lambda}, \\ \\ \mathbf{M}_\rho \dot{\hat{\vec{V}}} + \vec{K}(\hat{\vec{Y}}, \hat{\vec{V}}) = \vec{F}, \\ \\ \hat{\vec{Y}}(0) = \vec{Y}_\diamond, \quad \hat{\vec{V}}(0) = \vec{V}_\diamond. \end{cases} \tag{100}$$

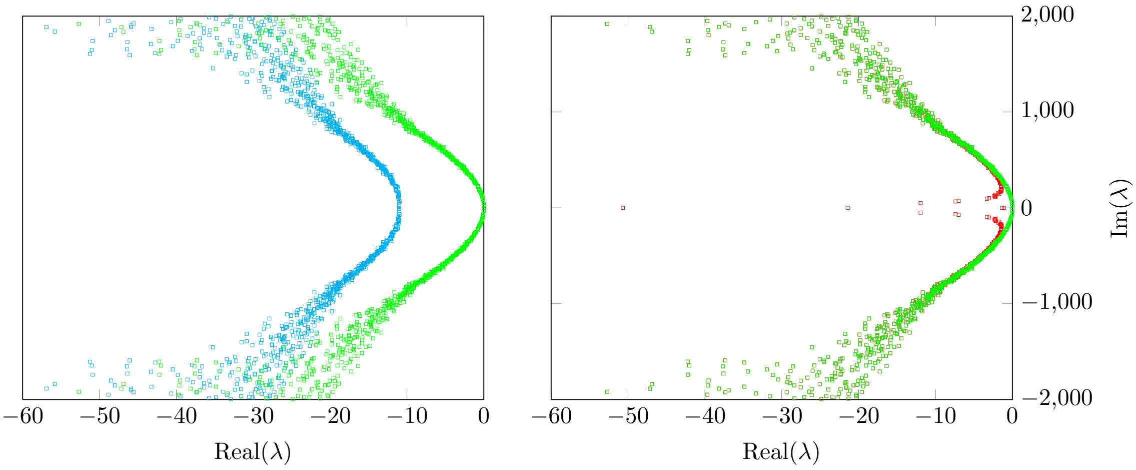

Figure 11: Spectrum of the stabilized operator using either the $\mathcal{H}^{\frac{1}{2}}$-norm (in (cyan)) and the $\mathcal{L}^2$-norm (in (red)). In (green) are the modes of the original operator, *i.e.* without stabilization.

3.2.1 Stabilization property of the state estimator

As we have mentioned in the Section 3.1 the main goal of the Luenberger filter is to stabilize the dynamics of the estimation error. Hence, in mechanical systems the principle is to add some dissipative terms in the system dynamics. The idea was already developed in great detail in [Moireau et al., 2009] so we limit ourselves to recalling briefly how the dissipative term is assessed. To simplify, from (100) we derive the dynamics of the estimation error around the null trajectory

$$\begin{cases} \dot{\tilde{\vec{Y}}} = \tilde{\vec{V}} + \gamma(\epsilon\mathbf{K} + \mathbf{dS}_0|\mathbf{dS}_0)^{-1}\mathbf{dS}_0|\mathbf{dS}_0\tilde{\vec{Y}}, \\ \\ \mathbf{M}_\rho\dot{\tilde{\vec{V}}} + \mathbf{C}\tilde{\vec{V}} + \mathbf{K}\tilde{\vec{Y}} = 0, \\ \\ \tilde{\vec{Y}}(0) = \vec{\zeta}^Y, \quad \tilde{\vec{V}}(0) = \vec{\zeta}^V. \end{cases} \tag{101}$$

where $\vec{\zeta}_\bullet = \begin{pmatrix} \vec{\zeta}^Y & \vec{\zeta}^V \end{pmatrix}^\intercal$, $\mathbf{dS}_0|\mathbf{dS}_0$ is the operator defined by (99) with a tangent current evaluated at a null displacement and $\mathbf{K}$ is the linearized elasticity matrix. We then obtain – following [Moireau et al., 2009] – the energy balance

$$\frac{1}{2}\frac{\mathrm{d}}{\mathrm{dt}}\left(\tilde{\vec{V}}^\intercal\mathbf{M}_\rho\tilde{\vec{V}} + \tilde{\vec{Y}}^\intercal\mathbf{K}\tilde{\vec{Y}}\right) = -\tilde{\vec{V}}^\intercal\mathbf{C}\tilde{\vec{V}} - \tilde{\vec{Y}}\mathbf{K}(\epsilon\mathbf{K} + \mathbf{dS}_0|\mathbf{dS}_0)^{-1}\mathbf{dS}_0|\mathbf{dS}_0\tilde{\vec{Y}},$$

which is, after linearization, a spatial discretized counterpart of the energy balance mentioned in (96). As already proved in [Moireau et al., 2009], the operator $\mathbf{K}(\epsilon\mathbf{K} + \mathbf{dS}_0|\mathbf{dS}_0)^{-1}\mathbf{dS}_0|\mathbf{dS}_0$ is symmetric positive since

$$\mathbf{K}(\epsilon\mathbf{K} + \mathbf{dS}_0|\mathbf{dS}_0)^{-1}\mathbf{dS}_0|\mathbf{dS}_0 = \mathbf{K} - \epsilon\mathbf{K}(\epsilon\mathbf{K} + \mathbf{dS}_0|\mathbf{dS}_0)^{-1}\mathbf{K}.$$

Therefore, the additional damping term in the energy balance of the error is given by $\tilde{\vec{Y}}^\intercal\mathbf{K}(\epsilon\mathbf{K} + \mathbf{dS}_0|\mathbf{dS}_0)^{-1}\mathbf{K}\tilde{\vec{Y}}$. By contrast when the Sobolev-gradient is not used the energy balance exists, but in the form

$$\frac{\mathrm{d}}{\mathrm{dt}}\left(\frac{1}{2}\tilde{\vec{V}}^\intercal\mathbf{M}_\rho\tilde{\vec{V}} + \frac{1}{2}\tilde{\vec{Y}}^\intercal\mathbf{K}\tilde{\vec{Y}}\right) = -\tilde{\vec{V}}^\intercal\mathbf{C}\tilde{\vec{V}} - \tilde{\vec{Y}}^\intercal\mathbf{dS}_0|\mathbf{dS}_0\tilde{\vec{Y}}.$$

Thus the amount of damping added in the energy balance is this time $\tilde{\vec{Y}}^\intercal \mathbf{dS}_0|\mathbf{dS}_0\tilde{\vec{Y}}$ and in the following we numerically show that it is less effective than $\mathbf{K}(\epsilon\mathbf{K} + \mathbf{dS}_0|\mathbf{dS}_0)^{-1}\mathbf{dS}_0|\mathbf{dS}_0$.

In this respect, we continue to rely on [Moireau et al., 2009] where they solve a spectral problem to characterize the amount of dissipation added by the data-discrepancy term to each mode of the linearized error system. Consequently we find the family of (λ, Φ) such that

$$\begin{pmatrix} \gamma\mathbf{K}(\epsilon\mathbf{K} + \mathbf{dS}_0|\mathbf{dS}_0)^{-1}\mathbf{dS}_0|\mathbf{dS}_0 & \mathbf{K} \\ -\mathbf{K} & -\mathbf{C} \end{pmatrix} \Phi = \lambda \begin{pmatrix} \mathbf{K} & 0 \\ 0 & \mathbf{M}_\rho \end{pmatrix} \Phi, \tag{102}$$

as opposed to

$$\begin{pmatrix} \gamma\mathbf{dS}_0|\mathbf{dS}_0 & \mathbf{K} \\ -\mathbf{K} & -\mathbf{C} \end{pmatrix} \Phi = \lambda \begin{pmatrix} \mathbf{K} & 0 \\ 0 & \mathbf{M}_\rho \end{pmatrix} \Phi. \tag{103}$$

Note that these computations are performed here within the formalism of *current* as an extension of the computations performed in [Moireau et al., 2009] for linear observation operators or distance operators. In Figure 11 we plot the spectra corresponding to both cases with a rigidity matrix obtained from the standard Hook's law and with low viscosity. The gain value is defined by the criterion proposed by authors in [Moireau et al., 2009]. The left plot represents the poles of the stabilized operator in (cyan) and the poles of the without stabilization in (green). We clearly observe the shifting of the poles towards the left-half plane. We remark that this shift concerns the complete frequency range which is a clear sign of efficiency. In the contrary, the right plot of Figure 11 concerns the $\mathcal{L}^2$ case and we observe that even though some poles – corresponding to the lowest frequencies – are stabilized, it appears that this formulation is inefficient when looking at the overall amount of damping brought into the dynamics. These numerical illustrations confirm this methodology inspired from the Sobolev gradient paradigm is necessary to provide an efficient state estimator and proves that the choice of the adequate observation norm is indeed crucial.

We now propose a second numerical assessment – through spectral analysis – of the *current*-based observer. We propose to (1) compare with relevant other choices of observers and (2) assess the sensibility of the observer with respect to the kernel width μ. More precisely, the "$\mathcal{L}^2$" stabilization term of the other observers that we consider are built from observation operators corresponding to

- the surface displacement feedback

$$\tilde{\vec{Y}}^\intercal \mathbf{H}^\intercal \mathbf{M}^{\mathrm{obs}} \mathbf{H} \tilde{\vec{Y}} = \int_{S_0} \|\tilde{y}_h\|^2 \,\mathrm{d}\Gamma, \tag{104}$$

- the normal displacement feedback

$$\tilde{\vec{Y}}^\intercal \mathbf{H}^\intercal \mathbf{M}^{\mathrm{obs}} \mathbf{H} \tilde{\vec{Y}} = \int_{S_0} (\tilde{y}_h \cdot \underline{n}_0)^2 \,\mathrm{d}\Gamma, \tag{105}$$

- the linearization of the signed distance function around the null trajectory, which also reads

$$\tilde{\vec{Y}}^\intercal \mathbf{dD}_0^\intercal \mathbf{M}^{\mathrm{obs}} \mathbf{dD}_0 \tilde{\vec{Y}} = \int_{S_0} (\tilde{y}_h \cdot \underline{n}_0)^2 \,\mathrm{d}\Gamma. \tag{106}$$

We compare these operators to the one extracted from the *current*-based discrepancy which reads in a weak formulation

$$\tilde{\vec{Y}}^\intercal \mathbf{dS}_0|\mathbf{dS}_0 \tilde{\vec{Y}} = (\mathrm{d}S_0(\tilde{y}_h), \mathrm{d}S_0(\tilde{y}_h))_{\mathcal{W}^*},$$

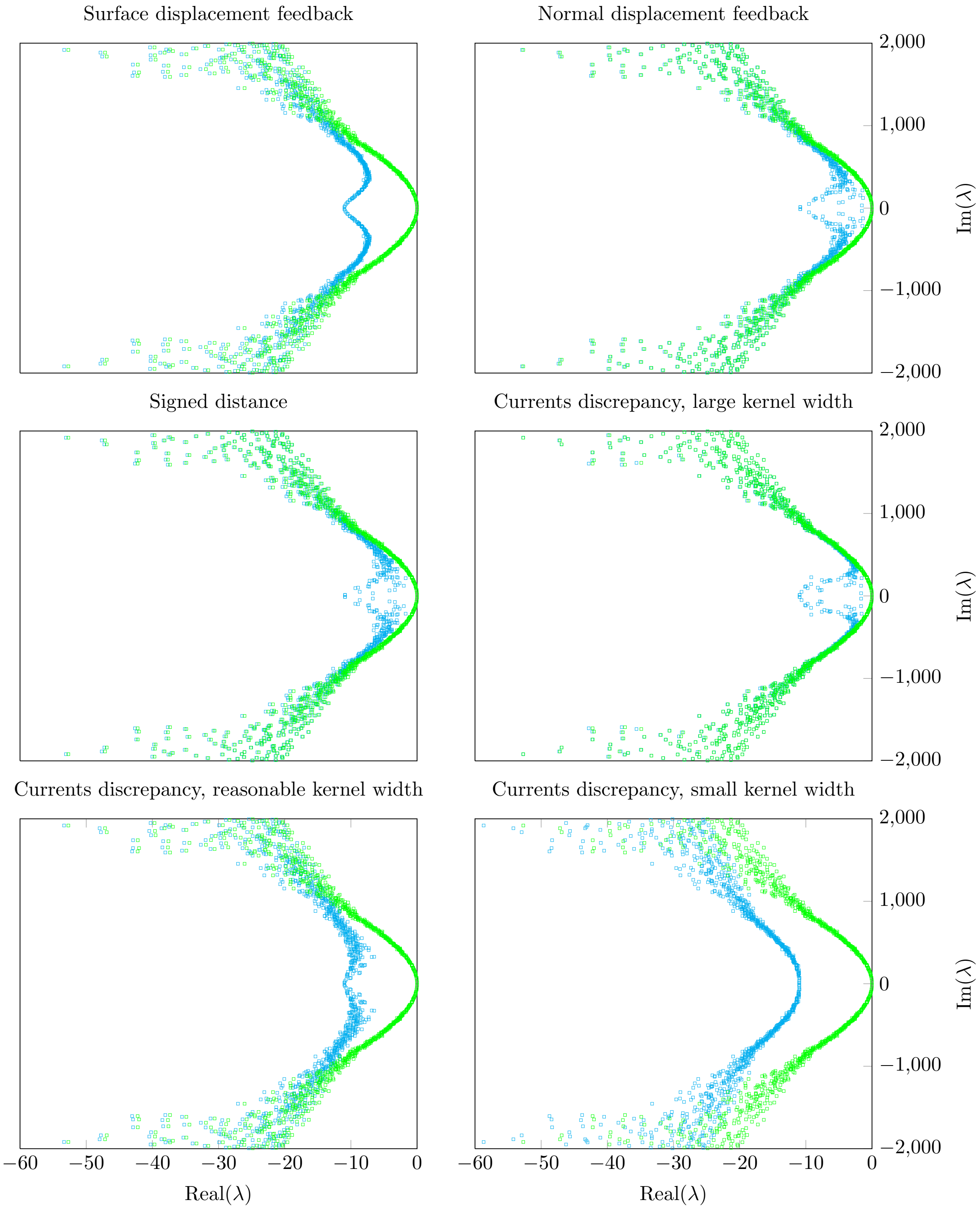

Figure 12: Spectral analysis and comparison of the various observers.

where the expression of the right hand side is given by (68). These stabilization operators need to be understand in a Sobolev-gradient strategies in the sense of (102). We show in Figure 12 the obtained spectra. The first plot in Figure 12 corresponds to the surface displacement feedback (104). The next two plots concern the feedback of the normal component displacement (105) and the linearized signed distance operator (106). We clearly demonstrate here the loss of observability induced by such observation operators compared to the complete displacement feedback on the boundary.

The last three plots concerns the observer based on the *current* formalism. The difference between the three plots is that we start from a large value of the kernel width – in the first plot $\mu = 50$ – and we evolve towards smaller values, namely $\mu = 10$ and $\mu = 0.1$. These plots illustrate a crucial concept of the discrepancy measure based on currents. Namely, as the kernel width decreases the stabilization property appears to significantly improve. This is due to the fact that – as mentioned in [Durrleman et al., 2009, Durrleman et al., 2011] – the kernel width directly controls the sensitivity of the metrics to shape variations and any shape dissimilarities of characteristic length below μ will not be perceived by the discrepancy measure.

For a reasonable value of the band width we observe however a significantly improved damping of the system – compared with the distance-based observer. Moreover, in light of these plots we could imagine that, to obtain the best behavior of the observer, we need to choose the lowest kernel width. However this not possible in practice for several reasons. A first one would be that the metrics would become sensitive to – otherwise smoothed – data noise. More importantly, when $\mu \to 0$, the kernel acts as a Dirac delta function. Hence the Riesz representation of the data surface can be assimilated to

$$s_z \underset{\mu\to 0}{\sim} \delta_{S_z} \underline{n}_z,$$

entailing

$$S_z - S \underset{\mu\to 0}{\to} 0, \tag{107}$$

which could be interpreted as a non-visibility of the data from the model standpoint. To conclude these spectral analysis show that the choice of the kernel width is of prime importance and correspond to a compromise between shape sensitivity and observability.

3.2.2 Time discretization issues

We are now able to propose a complete discrete version of the Luenberger filter, and several possibilities may be considered. The first approach – also proposed in [Moireau et al., 2009] – consists in a midpoint time discretization coupled with the linearization procedure detailed in Section 2.5.4 for the correction term derived from currents. This time discrete formulation of the observer (100) reads

$$\begin{cases} \dfrac{\hat{\vec{Y}}^{n+1} - \hat{\vec{Y}}^{n}}{\Delta t} = \hat{\vec{V}}^{n+\frac{1}{2}} - \gamma(\epsilon \mathbf{K} + \mathbf{dS}^e | \mathbf{dS}^e)^{-1} \big(\vec{\Lambda}^e + \mathbf{dS}^e | \mathbf{dS}^e (\hat{\vec{Y}}^{n+1} - \hat{\vec{Y}}^e) \big), \\[2ex] \mathbf{M}_\rho \dfrac{\hat{\vec{V}}^{n+1} - \hat{\vec{V}}^{n}}{\Delta t} + \vec{K}(\hat{\vec{Y}}^{n+\frac{1}{2}}, \hat{\vec{V}}^{n+\frac{1}{2}}) = \vec{F}^{n+\frac{1}{2}}, \\[2ex] \hat{\vec{Y}}^0 = \vec{Y}_\diamond, \quad \hat{\vec{V}}^0 = \vec{V}_\diamond. \end{cases} \tag{108}$$

Another choice is to consider the prediction-correction algorithm proposed in [Chapelle et al.,]. The primary goal of this time scheme is to separate the model iterations from the correction phases in order to enable a different treatment for those two computational steps. More precisely in [Chapelle et al.,] this algorithm is used to solve – in one hand – the linear system inherited from the mechanical model using a direct solver and to manage – on the other hand – the observation operators – entailing a matrix with a wide band width in the application cases of [Chapelle et al.,] – through an iterative solver. Denoting by

$$\hat{\vec{Y}}^n_-,\ \hat{\vec{Y}}^n_+ \text{ and } \hat{\vec{V}}^n_-,\ \hat{\vec{V}}^n_+$$

the predicted and corrected discrete unknowns of our problem, this algorithm reads

1. Prediction:

$$\begin{cases} \dfrac{\hat{\vec{Y}}^{n+1}_- - \hat{\vec{Y}}^n_+}{\Delta t} = \dfrac{\hat{\vec{V}}^{n+1}_- + \hat{\vec{V}}^{n+1}_+}{2}, \\ \\ \mathbf{M}_\rho \dfrac{\hat{\vec{V}}^{n+1} - \hat{\vec{V}}^n}{\Delta t} + \vec{K}(\hat{\vec{Y}}^{n+\frac{1}{2}}, \hat{\vec{V}}^{n+\frac{1}{2}}) = \vec{F}^{n+\frac{1}{2}}, \end{cases} \tag{109a}$$

2. Correction

$$\frac{\hat{\vec{Y}}^{n+1}_+ - \hat{\vec{Y}}^{n+1}_-}{\Delta t} = -\gamma(\epsilon \mathbf{K} + \mathbf{dS}^e_+ | \mathbf{dS}^e_+)^{-1} \big(\vec{\Lambda}^e + \mathbf{dS}^e_+ | \mathbf{dS}^e_+ (\hat{\vec{Y}}^{n+1}_+ - \hat{\vec{Y}}^e_+)\big), \tag{109b}$$

It is striking to remark that in this prediction-correction paradigm the correction phase correspond exactly to one iteration of the descent method used to solve the static registration problem. Additionally it has been demonstrated that in this time scheme the correction can constructed by interpolating the discrepancy – see [Moireau et al., 2009] and also below – or only when the data are available [Cîndea et al.,].

Stabilization example To illustrate this state estimation procedure we place our work in the context of *synthetic data assimilation*. In this context we consider a first elastodynamics direct model where the initial condition – in displacement – is obtained by solving an equilibrium state of a simple *one-cavity* geometry – as illustrated in Figure 13(a) – subject to an internal pressure. While the system vibrates – due to its low viscosity – we extract the internal and external surfaces of the deforming object, corresponding to potential segmentations of the left endo- and epicardium of the heart. Then, we artificially introduce an error in the initial condition by increasing the initial pressure load and we use this data set in the estimator (100) in order to retrieve the state of the direct model. In Figure 13(b) we plot the evolution of the cavity volume for the direct model with a low initial pressure load (in (blue)) – from which we extracted the data – and the direct model resulting from an increased pressure load (in (red)). We also plot the state estimator in (green) fed with the synthetic surfaces represented as currents. While the direct model naturally vibrates during the time window, the state estimator rapidly converge towards the targeted trajectory.

3.2.3 Extension to nonlinear models: the cardiac mechanics example

To finally illustrate the data assimilation methodology described in this paper we address the issue of parameter identification on a complete cardiac model extensively detailed in [Sainte-Marie et al., 2006, Chapelle et al., 2012c]. In this model, the constitutive law corresponding to the cardiac material is made of two additive components corresponding to the underlying visco-elasticity of the heart – referred to as the passive part of the material – and its

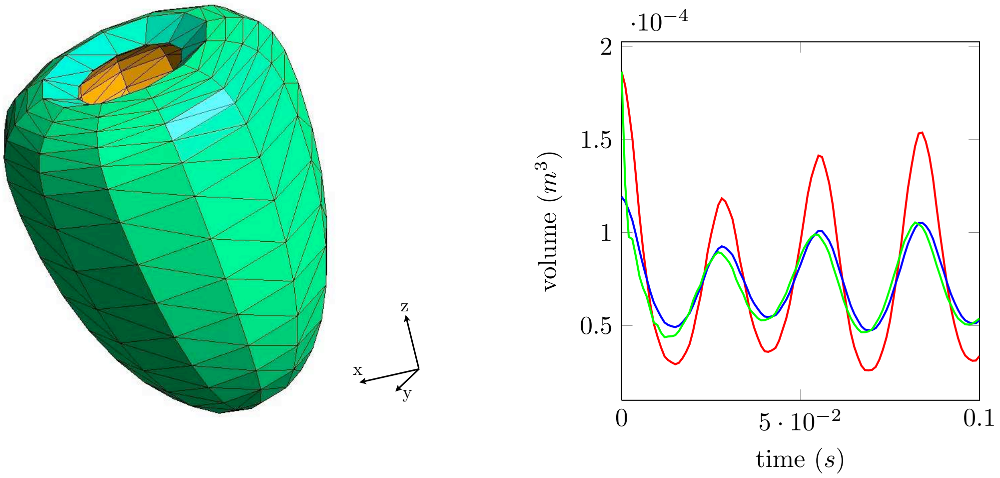

(a) Simple one-cavity geometry

(b) Illustration of state estimation through the evolution of the cavity volume.

Figure 13: In (red) and (blue) are the direct models with high and low pressure respectively where as the observer is the (green) line.

sensitivity to electrical activation – the active part. As regards the passive part, it is classical to consider a hyperelastic potential of the exponential type [Holzapfel and Ogden, 2009], namely

$$W = C_0 \exp\left(C_1(J_1 - 3)^2\right) + C_2 \exp\left(C_3(J_4 - 1)^2\right) + \kappa(J - 1) - \kappa \ln(J),$$

where $J_1 = \mathrm{tr}(\underline{\underline{C}}) \det(\underline{\underline{C}})^{-\frac{1}{3}}$ is the first reduced invariant, $J_4 = \left(\underline{\tau} \cdot \underline{\underline{C}} \cdot \underline{\tau}\right) \det(\underline{\underline{C}})^{-\frac{1}{3}}$ is the reduced invariant accounting for the anisotropy of the material in the fiber direction $\underline{\tau}$ and κ is the bulk coefficient with $J = \det(\underline{\underline{C}})^{-\frac{1}{2}}$. The constant values C_0, C_1, C_2 and C_3 are model parameters potentially subject to parameter identification. We point out that in the end W is in fact a function of the Green-Lagrance dedormation tensor $\underline{\underline{e}}$.

For the active part we define 3 variables: the active strain e_c, the active stiffness k_c and the corresponding stress τ_c in the fiber direction [Chapelle et al., 2012c]. The dynamics of these variables is defined by a model of the chemical mechanism taking place at a myofiber scale

$$\begin{cases} \dot{k}_c = -(|u| + \alpha\, |\dot{e}_c|)k_c + n_0 k_0\, |u|_+ & \text{in } \Omega_0 \\ \dot{\tau}_c = -(|u| + \alpha\, |\dot{e}_c|)\tau_c + \dot{e}_c k_c + n_0 \sigma_0\, |u|_+ & \text{in } \Omega_0, \end{cases} \tag{110}$$

where α, n_0, k_0, σ_0 are physiological parameters and u is an input term directly related to the electrical activity of the heart. Applying the combination rules of a reological system we can define a one-dimensional stress [Chapelle et al., 2012c]

$$\sigma_{1\mathrm{D}} = \frac{1 + 2e_c}{1 + 2\underline{\tau} \cdot \underline{\underline{e}} \cdot \underline{\tau}}(\tau_c + \mu \dot{e}_c),$$

so that

$$\underline{\underline{\Sigma}} = \frac{\partial W}{\partial \underline{\underline{e}}} + \sigma_{1\mathrm{D}} \underline{\tau} \otimes \underline{\tau} + \eta \underline{\underline{\dot{e}}}.$$

Concerning the boundary conditions, following [Chabiniok et al., 2011] we model the interactions between the heart and the external organs by visco-elastic boundary conditions on a the epicardium of the model geometry. This leads, in reference configuration, to

$$\underline{\underline{T}} \cdot \underline{n} = k_s \underline{y} + c_s \underline{v} \text{ on } \Gamma_n(t).$$

Moreover, we simplify the blood pressure insight the cavities of the model geometry using a uniform following pressure – as proposed in [Chabiniok et al., 2011] – which is easily written in deformed configuration

$$\underline{\underline{\sigma}} \cdot \underline{n}_t = -p_{v,i} \underline{n}_t \text{ on } \Gamma_{n,i}(t), i = \{1, 2\}.$$

Finally the complete mechanical model reads

$$\begin{cases} \dot{\underline{y}} = \underline{v}, & \text{in } \Omega_0 \\ \rho \dot{\underline{v}} - \underline{\nabla} \cdot (\underline{\underline{T}}) = 0, & \text{in } \Omega_0 \\ \underline{\underline{T}} \cdot \underline{n} = k_s \underline{y} + c_s \underline{v} & \text{on } \Gamma_n \\ \underline{\underline{T}} \cdot \underline{n} = -J p_{v,i} \underline{\underline{F}}^{-\intercal} \cdot \underline{n} & \text{on } \Gamma_{c,i} \\ \underline{\underline{T}} \cdot \underline{n} = 0 & \text{on } \partial\Omega_0 \backslash ((\cup_i \Gamma_{c,i}) \cap \Gamma_n) \end{cases} \tag{111}$$

and this, together with the internal variable dynamics (110), constitutes a formal definition of the dynamical operator denoted by A in our above summarized description. After spatial discretization, this model directly enter in the formalism proposed in (97) with only additional internal variable computed at each point of integration [Sainte-Marie et al., 2006].

3.2.4 Extension to a joint parameter estimation strategy

So far we have mentioned the capability of filtering a *current*-based discrepancy measure in a state observer methodology. However, one very interesting aspect in data assimilation procedures is to simultaneously reduce the uncertainties on the state and jointly identify some constitutive parameters. This can typically be used to better personalized the model on the specific system that is observed. Considering the cardiac medical applications we presented, it allows to create a patient-specific model that can correspond to the specific state of the patient – possibly associated with a pathology.

In this respect, we rely on the joint state and parameter strategy proposed by authors in [Moireau et al., 2008, Moireau and Chapelle, 2011] which has been successfully applied in the field of data assimilation for biomechanical models. Readers may refer to [Chabiniok et al., 2011, Chapelle et al., 2012b] for a presentation of this data assimilation procedure in practical situations. This data assimilation methodology is basically built under the idea that performing a joint state and parameter estimation can be carried out by separating the task using two different types of filter. The uncertainties on the state space are handled using a Luenberger filter – as described in Section 3.1. Once the state uncertainties are controlled, a reduced-order Unscented Kalman filter (RoUKF) [Moireau and Chapelle, 2011] is added in order to manage the uncertainties on the remaining parameter space. In a nutshell, the RoUKF algorithm aims at approximating - using appropriate sampling points – the operators accounting for the model sensitivity with respect to the parameters. Using a Kalman-like method for the parameter is possible since, in a lot of practical situations the parameters variations are smooth, hence allowing to discretized them in a space of much smaller dimension than the state space dimension.

This approach is completely compatible with all the observation operators or discrepancy operators presented before. In particular, it is fully compatible with the current formalism associated with shape data. In this section we propose to rapidly summarize the main concepts of this method before applying it using *current*-based discrepancy measure. For the sake of simplicity we consider the model after time and space discretization, namely

$$X^{n+1} = \mathbf{A}^{n+1|n}(X_n) \tag{112}$$

and with the state estimator it reads

$$X^{n+1} = \mathbf{A}_\ell^{n+1|n}(X^n, Z^n) = \mathbf{A}^{n+1|n}(X^n) + G_\ell \mathbf{D}(X^n, Z^n) \tag{113}$$

where G_ℓ is the Luenberger observer defined either from (108) or from (109). Moreover, we introduce the unitary sampling points $I^{[i]}$ and weights α_i with the following rules

$$\sum_{i=1}^{p} \alpha_i I_{[i]} = 0, \quad \sum_{i=1}^{p} \alpha_i I_{[i]} \cdot I_{[i]}{}^{\intercal} = \mathbb{1}, \tag{114}$$

so that, at each time step, the sigma-points can be generated around the estimated values based on the covariance estimation. Given an adequate sampling rule, we store the corresponding weights in the diagonal matrix M_α and precompute the so-called unitary sigma-points (i.e. with zero mean and unit covariance) denoted by $(\vec{I}_{[i]})_{1\leq i\leq r+1}$. We also denote by $[\vec{I}_{[*]}]$ the matrix concatenating the $(\vec{I}_{[i]})$ vectors side by side, and similarly for other matrices aggregating some particle vectors. We then perform at each time step the following algorithm

1. Sampling:

$$\begin{cases} Q^n & = \sqrt{(U^n)^{-1}} \\ \hat{X}^n_{[i]+} & = \hat{X}^+_n + L^n_{\mathrm{x}} \cdot Q^{n\intercal} \cdot \vec{I}_{[i]}, \quad 1 \leq i \leq r+1 \\ \hat{\theta}^n_{[i]+} & = \hat{\theta}^+_n + L^n_\theta \cdot Q^{n\intercal} \cdot \vec{I}_{[i]}, \quad 1 \leq i \leq r+1 \end{cases} \tag{115a}$$

2. State Prediction:

$$\begin{cases} \hat{X}^{n+1}_{[i]-} & = \mathbf{A}_\ell^{n+1|n}(\hat{x}^n_{[i]+}, \hat{\theta}^{n+1}_{[i]+}), \quad 1 \leq i \leq r+1 \\ \hat{\theta}^{n+1}_{[i]-} & = \hat{\theta}^n_{[i]+}, \quad 1 \leq i \leq r+1 \\ \hat{\theta}^{n+1}_{-} & = \sum_{i=1}^{r+1} \alpha_i \hat{\theta}^{n+1}_{[i]-} = \hat{\theta}^n_+ \end{cases} \tag{115b}$$

3. Parametric Correction:

$$\begin{cases} L^{n+1}_{\mathrm{x}} & = [\hat{X}^{n+1}_{[*]-+}] M_\alpha [\vec{I}_{[*]}]^\intercal \\ \mathbf{D}^{n+1}_{[i]-} & = \mathbf{D}(\hat{X}^{n+1}_{[i]-}, \hat{\theta}^{n+1}_{[i]+}) \\ \mathbf{D}^{n+1}_{-} & = \sum_{i=1}^{r+1} \alpha_i \mathbf{D}^{n+1}_{[i]-} \\ \Gamma^{n+1} & = [\mathbf{D}^{n+1}_{[*]-}] M_\alpha [\vec{I}_{[*]}]^\intercal \\ U^{n+1} & = \mathbf{1} + \Delta t (\Gamma^{n+1})^\intercal \mathrm{M}_+ \Gamma^{n+1} \\ \hat{X}^{n+1}_{+} & = \hat{X}^{n+1}_{-} - \Delta t L^{n+1}_{\mathrm{x}} U^{n+1} (\Gamma^{n+1})^\intercal \mathrm{M}_+ \mathbf{D}^{n+1}_{-} \\ \hat{\theta}^{n+1}_{+} & = \hat{\theta}^{n+1}_{-} - \Delta t L^{n+1}_{\theta} U^{n+1} (\Gamma^{n+1})^\intercal \mathrm{M}_+ \mathbf{D}^{n+1}_{-} \end{cases} \tag{115c}$$

where M_+ is a norm associated with the discrepancy computation as described below. The advantage of this algorithm is that it can be implemented independently of the model as in the data assimilation library Verdandi [Chapelle et al., 2012b]. However, it is in essence based on the fact that the discrepancy tangent can be computed with the form $\sum_i (\mathbf{D}^{n+1}_{[i]-})^\intercal \mathrm{M}_+ (\mathbf{D}^{n+1}_{[i]-})$ which can generate some technical difficulties when applied to the formalism of *currents* where the duality is not represented by the transposition.

The innovation and the formalism of currents In (115c) we denoted by $\mathbf{D}(Z_{n+1}, \hat{X}_{n+1}^{[i]-})$ the discrepancy between the data given and a sampled model trajectory. This term corresponds – in the data assimilation community – to the so-called *innovation*. Hence, in the context of *currents*, the innovation reads

$$\mathbf{D}_{[i]-}^{n+1} \leftarrow S_z - S^{[i]-}, \tag{116}$$

where $S^{[i]-}$ correspond to the model surface deformed by the displacement of the particle i. This term has to be computed at each time step and it should be noted that it differs from those treated in Section 2.5 since, in essence, (116) should be understood in $\mathcal{W}^*$. As a possible remedy, it was proposed in [Durrleman et al., 2009] a discretization of $\mathcal{W}^*$ that is computationally tractable. This method is based on the projection of the discrete momenta of a surface – namely for a triangulated surface the center of each face and the corresponing normal – into a fixed three-dimensional regular grid. From this projected momenta the Riesz representation of the surface can be efficiently computed using a discrete fast Fourier transform. If we imagine to use this technique, the dimension of the innovation vector will be that of the (3D) grid. More precisely, if we denote by $\{\underline{\alpha}_i\}_{i=1}^{N_\mathrm{G}}$ the set of points defining the grid, then the innovation will be

$$\mathbf{D}_{[i]-}^{n+1} \leftarrow \underline{s}_z(\underline{\alpha}_i) - \underline{s}^{[i]-}(\underline{\alpha}_i) \quad \forall i = 1, \cdots, N_\mathrm{G}. \tag{117}$$

We recall that, the expression (117) is given using the Riesz representation of both surfaces given by (60). The norm on the observation space M_+ could be typically defined as a 3×3-block diagonal matrix, each block having $(\delta x_1, \delta x_2, \delta x_3)$ as its diagonal – δx_1, δx_2 and δx_2 being the dimensions of the (regular) grid. This definition of the observation norm is a relevant choice since the grid is similar to the image domain – which, by nature, is a piece-wise constant object – wherein the data are defined.

Even though this procedure has the advantage to combine precision – since it is a consistent discretization of $\mathcal{W}^*$, see [Durrleman et al., 2009] – and numerical tractability, it is a heavy procedure to set up – from an algorithmic point of view. Hence, in our numerical simulations we restrict ourselves to a simpler form of the innovation term (116). More precisely, we propose to define the innovation by considering the action of the bilinear form $S_z - S^{[i]-}$ on every triangles of the deformed model geometry, namely

$$\mathbf{D}_{[i]-}^{n+1} \leftarrow (T_i, S_z - S^{[i]-})_{\mathcal{W}^*}, \quad \forall i = 1, \cdots, N_T. \tag{118}$$

With this simpler form, denoting by $\{\underline{c}_i\}_{i=1}^{N_T}$ the center of the triangles $\{T_i\}_{i=1}^{N_T}$, the innovation vector will be the concatenation of

$$\mathbf{D}_{[i]-}^{n+1} \leftarrow \underline{s}_z(\underline{c}_i) - \underline{s}^{[i]-}(\underline{c}_i) \quad \forall i = 1, \cdots, N_T,$$

and the norm on the observation space reads

$$\mathrm{M}_+ = \begin{pmatrix} |T_1^z|\,\underline{n}_1 & & \\ & \ddots & \\ & & \left|T_{N_T}^z\right|\underline{n}_{N_T} \end{pmatrix}.$$

We still point out that, fundamentally the question of introducing the currents in the RoUKF algorithm without modifying the scalar product is thus an intricate problem that should be further address in future work. In our work we choose the second and simpler approach since our purpose here is only to illustrate the potential capability to jointly identify some parameters from data in the form of *currents*.

Time interpolation of the innovation In most practical cases the data sampling step and the numerical time step differ. A first idea is to consider the data only when they are available as it it commonly the case in the data assimilation community [Chapelle et al., 2012b] and recently justified for some data assimilation procedures [Cîndea et al.,]. We have also mentioned the solution proposed in [Moireau et al., 2009] with a linear interpolation scheme on the innovation in order to reconstruct a time continuous innovation term so that we can apply the correction at any time step. Namely, let us denote by $\{t^k\}_k$ the set of sampling time when the data $S_z(t^k)$ are available, then a time distributed innovation of a particle would read

$$\alpha^k(S_z(t^{k+1}) - S^{[i]-}(t)) + (1-\alpha^k)(S_z(t^k) - S^{[i]-}(t)), \tag{119}$$

with $\alpha^k = (\frac{t-t^k}{t^{k+1}-t^k})$. It should be noted that, since the formalism of currents leads to algebraic operations between surfaces we could recast the previous expression into

$$\big(\alpha^k S_z(t^{k+1}) + (1-\alpha^k)S_z(t^k)\big) - S(t). \tag{120}$$

However, (120) provides little improvement since – due to the nonlinearities introduced by the kernel – the interpolated observed currents is not equivalent to the currents defined by the interpolated momenta, expressed as

$$\sum_{j=1}^{N_T^z} \mathrm{k}\Big(\alpha^k \underline{c}_j^z(t^{k+1}) + (1-\alpha^k)\underline{c}_j^z(t^k), \underline{x}\Big)\ \Big(\alpha^k \underline{n}_z \left|T_j^z\right|_{\big|t^{k+1}} + (1-\alpha^k)\underline{n}_z \left|T_j^z\right|_{\big|t^k}\Big).$$

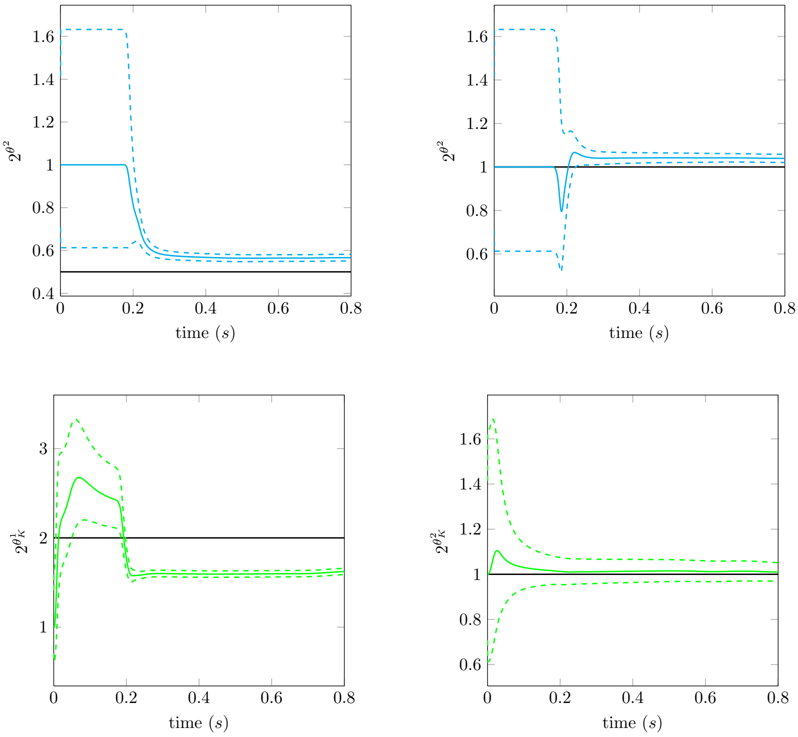

Figure 14: Estimation of passive and active parameters from endo- and epicardium synthetic segmentation using currents formalism.

Applications and results Similarly to what we have proposed in the case of state estimation we propose to embed our illustration in a synthetic data context. To do so we we start by proposing a direct model that represent an infarcted heart and we set in the septum of the model geometry an infarct represented by an increase in stiffness and a lack of contractility. This illustration is exactly similar to [Chapelle et al.,] which follows [Imperiale et al., 2011, Chabiniok et al., 2011, Imperiale et al., 2013]. To summarize the infarct is characterized by two parameters θ^K and θ such that the parameters C_0 and C_2 appearing in the hyperelastic potential and the contractility of the tissue are transformed into

$$(C_0, C_2) \to 2^{\theta^K}(C_0, C_2) \quad , \; \sigma_0 \to 2^{\theta}\sigma_0.$$

As an example, a possible way of describing the infarct is to set

$$(\theta^K, \theta) = \begin{cases} (1, -1), & \text{in the septum,} \\ \\ (0, 0), & \text{otherwise.} \end{cases}$$

From this direct model we extract the endo- and epicardium surfaces of the left ventricle. Using the filtering algorithm described in Section 3.2.4 and representing these surfaces as *currents* we retrieve the values of the parameters in on cardiac cycle – see Figure 14. The dashed lines corresponds to the standard deviation of each parameters, thus representing the confidence we can have on the estimation provided by the data assimilation procedure.

Conlusion

In this article we have presented a unified formalism to register a deformable model on data extracted from medical imaging. Our main idea is to base our formalism on the classical description of mechanical deformation and kinematics. Then, we derive classical discrepancy terms associated with the deformation definition. Furthermore, we extend these discrepancies to state-of-the-art dissimilarities measurement based on the formalism of *currents* allowing to efficiency defined surfaces data even when the segmentation is associated with a level-set. This formalism defined in a static context allows typically to register a geometric mesh on data. We then show how the static formalism directly extend to the dynamics context where we have at our disposal a model of the deformation evolution and data, namely a data assimilation context. We then see how the improvement offered by the formalism of *currents* in the static configuration is also significant in the reduction of the estimation error in dynamical cases. Combined to known joint state and parameter estimation strategies it allows us to register a model on data and concurrently personalize the biophysical parameters of the model. In particular we illustrate this unified strategy in cardiac mechanics in order to show how sophisticated geometric inference have a great potential in the popular topic of patient-specific geometric and biophysics personalization in cardiac-mechanics [Smith and al, 2011, Chapelle et al., 2012b].

A Equivalent norms on the observation space

We have the following lemma

Lemma 9
The bilinear form associated with

$$\forall (z_1, z_2) \in \mathscr{Z}^2, \quad (z_1, z_2)_{\mathscr{Z}} = (Ext^{\mathrm{D}}_{\Gamma_0^{obs}}(z_1), Ext^{\mathrm{D}}_{\Gamma_0^{obs}}(z_2))_{\mathcal{Y}}$$

defined respectively a scalar product and a corresponding norm on $\mathcal{H}^{\frac{1}{2}}(\Gamma_0^{obs}, \mathbb{R}^3)$ *respectively equivalent to their usual norms.*

Proof. Concerning $y = \mathrm{Ext}^{\mathrm{D}}_{\Gamma_0^{\mathrm{obs}}}(z)$, the continuity of the Dirichlet problem with respect to the data gives

$$\forall y, \quad \int_{\Omega_0} \underline{\underline{\varepsilon}}(\underline{y}) : \underline{\underline{\underline{\underline{A}}}} : \underline{\underline{\varepsilon}}(\underline{y}) \, \mathrm{d}\Omega \leq C \|z\|^2_{\mathcal{H}^{\frac{1}{2}}(\Gamma_0^{\mathrm{obs}}, \mathbb{R}^3)}.$$

Furthermore by continuity of the trace operator

$$\exists C_t, \quad \|z\|_{\mathcal{H}^{\frac{1}{2}}(\Gamma_0^{\mathrm{obs}}, \mathbb{R}^3)} \leq C_t \|y\|_{\mathcal{H}^1(\Omega_0, \mathbb{R}^3)}$$

and using Korn inequality we have

$$\exists (c, C) \,|\, \forall z \in \mathcal{H}^{\frac{1}{2}}(\Gamma_0^{\mathrm{obs}}, \mathbb{R}^3)$$

$$c\|z\|^2_{\mathcal{H}^{\frac{1}{2}}(\Gamma_0^{\mathrm{obs}}, \mathbb{R}^3)} \leq \int_{\Omega_0} \underline{\underline{\varepsilon}}(\underline{\mathrm{Ext}}^{\mathrm{D}}_{\Gamma_0^{\mathrm{obs}}}(z)) : \underline{\underline{\underline{\underline{A}}}} : \underline{\underline{\varepsilon}}(\underline{\mathrm{Ext}}^{\mathrm{D}}_{\Gamma_0^{\mathrm{obs}}}(z)) \, \mathrm{d}\Omega \leq C\|z\|^2_{\mathcal{H}^{\frac{1}{2}}(\Gamma_0^{\mathrm{obs}}, \mathbb{R}^3)}$$

which achieves the proof. ■

B Rigid motion filtering

We consider the minimization of the quadratic functional

$$\forall y \in \mathcal{Y} \mathscr{J}(y) = \frac{1}{2} a(y, y) - f(y)$$

where a is a bilinear symmetric form where we want to filter the potential rigid body displacements. More precisely introduce the space of rigid body displacements

$$\mathcal{Y}_0 = \Big\{ y \in \mathcal{Y} \text{ s.t. } \exists (\underline{\tau}, \underline{\omega}) \in \mathbb{R}^6 \,|\, \underline{y}(\underline{\mathrm{x}}) = \underline{\tau} + \underline{\omega} \wedge \underline{\mathrm{x}} \Big\}$$

and we assume that $\mathscr{J} = 0$ on $\mathcal{Y}_0$

Hence, after differentiating the criterion, we have to solve

$$\forall y^\flat \in \mathcal{Y}_0^\perp, \quad a(y, y^\flat) = f(y^\flat), \tag{121}$$

whereas

$$\forall y^\flat \in \mathcal{Y}_0, \quad a(y, y^\flat) = 0 = f(y^\flat).$$

To do so, we first characterize the space

$$\mathcal{Y}_0^\perp = \Big\{ y \in \mathcal{Y} \text{ s.t. } \forall y^\flat \in \mathcal{Y}_0, \quad (y, y^\flat)_{\mathcal{L}^2(\Omega)} = 0 \Big\}$$

Proposition 10
The space $\mathcal{Y}_0^{\perp}$ is characterized by

$$\Big\{ y \in \mathcal{Y} \text{ s.t. } \int_\Omega \underline{y}(\underline{\mathrm{x}})\,\mathrm{d}\Omega = 0 \text{ and } \int_\Omega (\underline{\mathrm{x}} \wedge \underline{y})\,\mathrm{d}\Omega = 0 \Big\}$$

Proof. First, the space $\mathcal{Y}_0^{\perp}$ is of codimension 6 so its characterized by only 6 independent linear relations. Let us consider $\underline{y} \in \mathcal{Y}_0^{\perp}$. Since

$$\forall y^\flat \in \mathcal{Y}_0, \quad (y, y^\flat)_{\mathcal{L}^2(\Omega,\mathbb{R}^3)} = 0,$$

we have in particular that

$$\forall \underline{\tau} \in \mathbb{R}^3, \quad \int_\Omega \underline{y}(\underline{\mathrm{x}}) \cdot \underline{\tau}\,\mathrm{d}\Omega = 0.$$

Moreover, we also have

$$\forall \underline{\omega} \in \mathbb{R}^3, \quad \int_\Omega \underline{y}(\underline{\mathrm{x}}) \cdot (\underline{\omega} \wedge \underline{\mathrm{x}})\,\mathrm{d}\Omega = 0.$$

which implies that

$$\int_\Omega \underline{\omega} \cdot (\underline{\mathrm{x}} \wedge \underline{y})\,\mathrm{d}\Omega = 0.$$

Therefore the space $\mathcal{Y}_0^{\perp}$ is characterized by

$$\Big\{ y \in \mathcal{Y} \text{ s.t. } \forall(\underline{\tau}, \underline{\omega}) \in \mathbb{R}^6 \mid \int_\Omega \underline{y}(\underline{\mathrm{x}}) \cdot \underline{\tau}\,\mathrm{d}\Omega = 0 \text{ and } \int_\Omega (\underline{\mathrm{x}} \wedge \underline{y}) \cdot \underline{\omega}\,\mathrm{d}\Omega = 0 \Big\}$$

which conclude the proof. ■

Therefore solving (121) is equivalent to solve

$$\forall y^\flat \in \mathcal{Y} \quad a(y, y^\flat) + \kappa \bigg(\Big(\int_\Omega \underline{y}(\underline{\mathrm{x}})\,\mathrm{d}\Omega \Big) \Big(\int_\Omega \underline{y}^\flat(\underline{\mathrm{x}})\,\mathrm{d}\Omega \Big) + \Big(\int_\Omega \underline{y}(\underline{\mathrm{x}}) \wedge \underline{\mathrm{x}}\,\mathrm{d}\Omega \Big) \Big(\int_\Omega \underline{y}^\flat(\underline{\mathrm{x}}) \wedge \underline{\mathrm{x}}\,\mathrm{d}\Omega \Big) \bigg) = f(y^\flat)$$

for any parameter κ. Indeed the additional term has no contribution on $\mathcal{Y}_0^{\perp}$. We point out that this variational problem corresponds to the functional

$$\mathscr{J}_\kappa(y) = \frac{1}{2} a(y, y) + \frac{\kappa}{2} \bigg(\Big(\int_\Omega \underline{y}(\underline{\mathrm{x}})\,d\Omega \Big)^2 + \Big(\int_\Omega \underline{y}(\underline{\mathrm{x}}) \wedge \underline{\mathrm{x}}\,\mathrm{d}\Omega \Big)^2 \bigg) - f(y)$$

but minimized without constraint. However this variational problem require to compute a non-local term which are not very convenient. Therefore we replace it a the simpler formulation which is find y_ϵ such that

$$\forall y^\flat \in \mathcal{Y} \quad a(y_\epsilon, y^\flat) + \epsilon (y_\epsilon, y^\flat)_{\mathcal{L}^2(\Omega,\mathbb{R}^3)} = f(y^\flat). \tag{122}$$

Using this simplified variational formulation will be justified when we prove that the solution y_ϵ is close to y in a given norm. We have that

$$\forall y^\flat \in \mathcal{Y}_0^{\perp}, \quad \left| \begin{aligned} a(y_\epsilon, y^\flat) + \epsilon (y_\epsilon, y^\flat) &= f(y^\flat) \\ a(y, y^\flat) &= f(y^\flat) \end{aligned} \right.$$

therefore we have a

$$a(y_\epsilon - y, y^\flat) = -\epsilon (y_\epsilon, y^\flat)$$

leading to a constant C such that

$$|(y_\epsilon - y)|^2_{\mathcal{H}^1_0(\Omega,\mathbb{R}^3)} \leq C\epsilon \|y_\epsilon\|^2_{\mathcal{L}^2(\Omega,\mathbb{R}^3)} \|(y_\epsilon - y)\|^2_{\mathcal{L}^2(\Omega,\mathbb{R}^3)}$$

Moreover y_ϵ and y are in $\mathcal{Y}_0^\perp$. On $\mathcal{Y}_0^\perp$ by Korn and Poincaré inequality we can ensure that there exists a constant C_2 such that

$$\|(y_\epsilon - y)\|_{\mathcal{H}^1(\Omega,\mathbb{R}^3)} \leq C_2 |(y_\epsilon - y)|_{\mathcal{H}^1_0(\Omega,\mathbb{R}^3)},$$

which means that finally

$$\|(y_\epsilon - y)\|_{\mathcal{H}^1(\Omega,\mathbb{R}^3)} \leq C C_2 \epsilon \|y_\epsilon\|.$$

Therefore

$$\|(y_\epsilon - y)\|_{\mathcal{H}^1(\Omega,\mathbb{R}^3)} = O(\epsilon)$$

which justifies to choose the variational formulation (122). This variational formulation is directly associated with the penalized criterion

$$\mathscr{J}_\epsilon(y) = \frac{1}{2}a(y,y) + \frac{\epsilon}{2}\|y\|^2_{\mathcal{L}^2(\Omega,\mathbb{R}^3)} - f(y)$$

References

[Andrieux and Baranger, 2008] Andrieux, S. and Baranger, T. (2008). An energy error-based method for the resolution of the Cauchy problem in 3D linear elasticity. *Comput Method Appl M*, 197(9-12):902–920.

[Aronszajn, 1950] Aronszajn, N. (1950). Theory of Reproducing Kernels. *Transactions of the American Mathematical Society*, 68(3):337–404.

[Aubert et al., 2003] Aubert, G., Barlaud, M., Faugeras, O., and Jehan-Besson, S. (2003). Image segmentation using active contours: Calculus of variations or shape gradients? *Siam J Appl Math*, 63(6):2128–2154.

[Auroux and Blum, 2008] Auroux, D. and Blum, J. (2008). A nudging-based data assimilation method: the back and forth nudging (bfn) algorithm. *Nonlinear Processes in Geophysics*, 15:305–319.

[Baerentzen and Aanaes, 2005] Baerentzen, J. and Aanaes, H. (2005). Signed distance computation using the angle weighted pseudo-normal. *IEEE Transactions on Visualization and Computer Graphics*, 11(3):243–253.

[Bathe, 1996] Bathe, K.-J. (1996). *Finite element procedures.*

[Blum et al., 2008] Blum, J., LeDimet, F. X., and Navon, I. N. (2008). Data assimilation for geophysical fluids. *Computational Methods for the Atmosphere and the Oceans*, 14:377–434.

[Bonnet and Constantinescu, 2005] Bonnet, M. and Constantinescu, A. (2005). Inverse problems in elasticity. *Inverse Problems*, 21(2):R1–R50.

[Bresenham, 1965] Bresenham, V. (1965). Algorithm for computer control of a digital plotter. *IBM Systems Journal*, 4(1):25—30.

[Caselles et al., 1997] Caselles, V., Kimmel, R., and Sapiro, G. (1997). Geodesic active contours. *International journal of computer vision*, 22(1):61–79.

[Chabiniok et al., 2011] Chabiniok, R., Moireau, P., Lesault, P.-F.and Rahmouni, A., Deux, J.-F., and Chapelle, D. (2011). Estimation of tissue contractility from cardiac cine-mri using a biomechanical heart model. *Biomechanics and modeling in mechanobiology.*

[Chan and Shen, 2005] Chan, T. and Shen, J. (2005). *Image processing and analysis: variational, PDE, wavelet and stochastic methods.* Siam.

[Chan and Vese, 2001] Chan, T. F. and Vese, L. A. (2001). Active contours without edges. *Image Processing, IEEE Transactions on*, 10(2):266–277.

[Chapelle and Bathe, 2011] Chapelle, D. and Bathe, K. (2011). *The Finite Element Analysis of Shells - Fundamentals - Second Edition.* Computational Fluid and Solid Mechanics. Springer.

[Chapelle et al., 2012a] Chapelle, D., Cîndea, N., de Buhan, M., and Moireau, P. (2012a). Exponential convergence of an observer based on partial field measurements for the wave equation. *Mathematical Problems in Engineering*, (581053):1–12.

[Chapelle et al., 2012b] Chapelle, D., Fragu, M., Mallet, V., and Moireau, P. (2012b). Fundamental principles of data assimilation underlying the verdandi library: applications to biophysical model personalization within euheart. *Medical & Biological Eng & Computing*, pages 1–13.

[Chapelle et al.,] Chapelle, D., Imperiale, A., and Moireau, P. Cardiac estimation from tagged-mr images. To be submitted.

[Chapelle et al., 2012c] Chapelle, D., Le Tallec, P., Moireau, P., and Sorine, M. (2012c). Energy-preserving muscle tissue model: formulation and compatible discretizations. *Journal For Multiscale Computational Engineering*, 10(2):189–211.

[Charpiat et al., 2007] Charpiat, G., Maurel, P., Pons, J., Keriven, R., and Faugeras, O. (2007). Generalized gradients: Priors on minimization flows. *International journal of computer vision*, 73(3):325–344.

[Chazal et al., 2011] Chazal, F., Cohen-Steiner, D., and Mérigot, Q. (2011). Geometric Inference for Probability Measures. *Found Comput Math*, 11(6):733–751.

[Ciarlet, 1988] Ciarlet, P. G. (1988). *Mathematical Elasticity, Vol. I : Three-Dimensional Elasticity.* Studies in Mathematics and its Applications. North Holland.

[Cîndea et al.,] Cîndea, N., Imperiale, A., and Moireau, P. Data assimilation of time under-sampled measurements using observers, application to wave-like equations. To be submitted.

[Cohen et al., 1992] Cohen, I., Cohen, L. D., and Ayache, N. (1992). Using Deformable Surfaces to Segment 3-D Images and Infer Differential Structures. *Cvgip-Imag Understan*, 56(2):242–263.

[Cohen and Peyré, 2011] Cohen, L. and Peyré, G. (2011). Non-local Active Contours. In *SSVM'11: 3rd International Conference on Scale Space and Variational Methods in Computer Vision.*

[Delfour and Zolésio, 2011] Delfour, M. C. and Zolésio, J.-P. (2011). *Shapes and geometries: metrics, analysis, differential calculs, and optimization.* Advances in design and control. Society for Industrial and Applied Mathematics.

[Durrleman et al., 2011] Durrleman, S., Fillard, P., Pennec, X., Trouvé, A., and Ayache, A. (2011). Registration, atlas estimation and variability analysis of white matter fiber boundles modeled as currents. *NeuroImage*, 55(3):1073.

[Durrleman et al., 2009] Durrleman, S., Pennec, X., Trouvé, A., and Ayache, A. (2009). Statistical models on sets of curves and surfaces based on currents. *Medical Image Analysis*, 13(5):793–808.

[Glaunès et al., 2008] Glaunès, J., Qui, J., M., I., M., and Younes, L. (2008). Large deformation diffeomorhpic metric curve mapping. *International Journal of Computer Vision*, 80(3):317–336.

[Gout et al., 2005] Gout, C., Le Guyader, C., and Vese, L. (2005). Segmentation under geometrical conditions using geodesic active contours and interpolation using level set methods. *Numerical algorithms*, 39(1):155–173.

[Guillot and Bergounioux, 2009] Guillot, L. and Bergounioux, M. (2009). Existence and Uniqueness Results for the Gradient Vector Flow and Geodesic Active Contours Mixed Model. *Commun Pur Appl Anal*, 8(4):1333–1349.

[Henn and Witsch, 2001] Henn, S. and Witsch, K. (2001). Iterative multigrid regularization techniques for image matching. *Siam J Sci Comput*, 23(4):1077–1093.

[Hoke and Anthes, 1976] Hoke, J. and Anthes, R. (1976). The initialization of numerical models by a dynamic-initialization technique(fluid flow models for wind forecasting). *Monthly Weather Review*, 104:1551–1556.

[Holzapfel and Ogden, 2009] Holzapfel, G. and Ogden, R. (2009). Constitutive modelling of passive myocardium: a structurally based framework for material characterization. *Phil. Trans. R. Soc. A*, 367:3445—3475.

[Imperiale et al., 2011] Imperiale, A., Chabiniok, R., Moireau, P., and Chapelle, D. (2011). Constitutive Parameter Estimation Using Tagged-MRI Data. In Metaxas, D. N. and Axel, L., editors, *FIMH'11 - Sixth International Conference on Functional Imaging and Modeling of the Heart*, volume 6666, pages 409–417, New York, United States. Springer.

[Imperiale et al., 2013] Imperiale, A., Routier, A., Durrleman, S., and Moireau, P. (2013). Improving Efficiency of Data Assimilation Procedure for a Biomechanical Heart Model by Representing Surfaces as Currents. In S. Ourselin, D. R. and Smith, N., editors, *FIMH - 7th International Conference on Functional Imaging and Modeling of the Heart - 2013*, volume 7945, pages 342–351.

[Jones et al., 2006] Jones, M., Baerentzen, J., and Sramek, M. (2006). 3D distance fields: A survey of techniques and applications. *Visualization and Computer Graphics, IEEE Transactions on DOI - 10.1109/TVCG.2005.49*, 12(4):581–599.

[Jung et al., 2009] Jung, M., Chung, G., Sundaramoorthi, G., Vese, L., and Yuille, A. (2009). Sobolev gradients and joint variational image segmentation, denoising and deblurring. In *Computational Imaging VII, SPIE*, pages 01–13.

[Karátson and Faragó, 2005] Karátson, J. and Faragó, I. (2005). Preconditioning operators and Sobolev gradients for nonlinear elliptic problems. *Computers & Mathematics with Applications*, 50(7):1077–1092.

[Le Guyader and Vese, 2011] Le Guyader, C. and Vese, L. (2011). A combined segmentation and registration framework with a nonlinear elasticity smoother. *Comput Vis Image Und*, 115(12):1689–1709.

[Le Tallec, 1994] Le Tallec, P. (1994). Numerical methods for nonlinear three-dimensional elasticity. In Ciarlet, P. G. and Lions, J.-L., editors, *Handbook of Numerical Analysis*, volume 3. Elsevier.

[Li and Acton, 2007] Li, B. and Acton, S. (2007). Active contour external force using vector field convolution for image segmentation. *Ieee T Image Process*, 16(8):2096–2106.

[Lin et al., 2010] Lin, T., Dinov, I., Toga, A., and Vese, L. (2010). Nonlinear elasticity registration and sobolev gradients. *Biomedical Image Registration*, pages 269–280.

[Luenberger, 1971] Luenberger, D. G. (1971). An introduction to observers. *IEEE T. Automat. Contr.*

[Moireau and Chapelle, 2011] Moireau, P. and Chapelle, D. (2011). Reduced-order unscented kalman filtering with application to parameter identification in large-dimensional systems. *Control, Optimisation and Calculus of Variations*, 17:380–405.

[Moireau et al., 2008] Moireau, P., Chapelle, D., and Le Tallec, P. (2008). Joint state and parameter estimation for distributed mechanical systems. *Computer Methods in Applied Mechanics and Engineering*, pages 659–677.

[Moireau et al., 2009] Moireau, P., Chapelle, D., and Le Tallec, P. (2009). Filtering for distributed mechanical dystems using position measurements: perspectives in medical imaging. *Inverse Problems*, 25.

[Navon, 2008] Navon, I. N. (2008). *Data assimilation for numerical weather prediction: a review.* Springer.

[Neuberger, 1997] Neuberger, J. (1997). *Sobolev Gradients and Differential Equations.* Springer.

[Oster and Fedkiw, 2009] Oster, S. and Fedkiw, R. (2009). *Level Set Methods and Dynamic Implicit Surfaces.* Springer.

[Paragios, 2003] Paragios, N. (2003). A level set approach for shape-driven segmentation and tracking of the left ventricle. *Ieee T Med Imaging*, 22(6):773–776.

[Peters et al., 2007] Peters, J., Ecabert, O., Meyer, C., Schramm, H., Kneser, R., Groth, A., and Weese, J. (2007). Automatic whole segmentation in static magnetic resonance image volumes. In *Proc. MICCAI 2007.*

[Peyré et al., 2012] Peyré, G., Fadili, J., and Rabin, J. (2012). Wasserstein active contours. In *Image Processing (ICIP), 2012 19th IEEE International Conference on*, pages 2541–2544.

[Renka, 2009] Renka, R. (2009). Image segmentation with a Sobolev gradient method. *Nonlinear Analysis*, 71(12):e774–e780.

[Sainte-Marie et al., 2006] Sainte-Marie, J., Chapelle, D., Cimrman, R., and Sorine, M. (2006). Modeling and estimation of the cardiac electromechanical activity. *Comput. Struct.*, 84:1743–1759.

[Scherzer, 2011] Scherzer, O., editor (2011). *Handbook of Mathematical Methods in Imaging*. Springer.

[Sermesant et al., 2003] Sermesant, M., Forest, C., Pennec, X., Delingette, H., and Ayache, N. (2003). Deformable biomechanical models: Application to 4D cardiac image analysis. *Medical Image Analysis*, 7(4):475–488.

[Simon, 2006] Simon, D. (2006). *Optimal state estimation: Kalman, H_∞ and nonlinear approaches*. Wiley-Interscience.

[Smith and al, 2011] Smith, N. and al (2011). euHeart: Personalized and integrated cardiac care using patient-specific cardiovascular modelling. *Journal of the Royal Society Interface Focus*, 1(3):349–364.

[Vaillant and Glaunès, 2005] Vaillant, M. and Glaunès, J. (2005). Surface matching via currents. In *Proceedings of the 19th international conference on Information Processing in Medical Imaging*, volume 3565 of *IPMI'05*, pages 381–392, Berlin, Heidelberg. Springer-Verlag.

[Xu and Prince, 1998] Xu, C. and Prince, J. L. (1998). Snakes, shapes, and gradient vector flow. *Image Processing, IEEE Transactions on*, 7(3):359–369.

[Younes, 1998] Younes, L. (1998). Computable elastic distances between shapes. *Siam J Appl Math*, 58(2):565–586.

[Younes, 2010] Younes, L. (2010). *Shapes and diffeomorphisms*. Springer.

Towards applications to real cases and perspectives

In this final chapter we propose to gather most of the methodological key points in order to apply the data assimilation procedure extensively detailed in the Chapter 3. This procedure aims at using the tagged-MR images to perform parameter identification of a complete cardiac biomechanical model – see Chapter 1 for a presentation of such a model. In order to feed this data assimilation method, we have assumed in Chapter 3 that a prior image processing step led to the construction of various data type, such as deforming tag planes, deforming tag grids and apparent displacements – defined within the image plane. Therefore, as a first step to apply, we will discuss the creation of these data types – mainly based on the assumption that we were able to reconstruct, typically using an image processing software – the apparent displacement. Furthermore, additionally to the tagged-MRI, we will assume that we possess also the cine-MR images, which is not a restrictive assumption since these data are much more common in clinical routine. We will see that, since these images provide precised information on the contours of the specific observed organ, they bring complementary informations that we will use mostly to adjust some key features of the geometry used in practice to bear the various computations. After the description of the available data, we will address the various issues that necessarily arise if we want to perform a direct model that corresponds – with some natural errors of course – to the specific case at hand. Finally, we present the last adjustments needed to use the data assimilation methodology.

Extracting data from raw images

The data we are considering are cine- and tagged-MR images. Figures 4.1 and 4.2 show an example of 2D image slices of both modalities during diastole and systole. We will see that the complementary information encapsulated in both images will help us to circumvent various difficulties. On the one hand, the cine-MR images provide – with a quite spectacular precision – some information on the internal and external surfaces of the heart. Moreover, compared to the tagged-MRI, they are very much persistent in time, thus leading to a constant signal-to-noise ratio over the heat beat. On the other hand, tagged-MR images do not directly give insight on the contour of the organ but provide extremely valuable information on intra-myocardial deformations. Figures 4.1 and 4.2 show a sample of both modalities in diastole and systole. In this section we discuss the various data sets that can be obtained – with reasonable assumptions on the prior image precessing step – from these images.

Processing cine-MR images Thanks to their time persistence and their ability to delimitate the heart external surface, cine-MR images can be used to extract the surfaces repre-

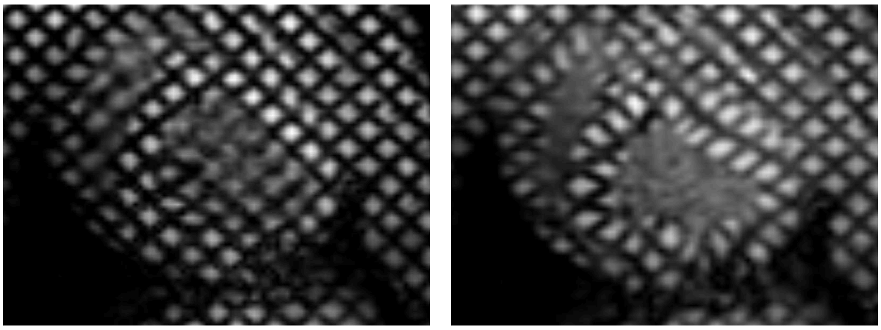

(a) 2D slice at marking time (b) 2D slice during systole

Figure 4.1: Example of SPAMM images in short axis view, acquired at T_0.

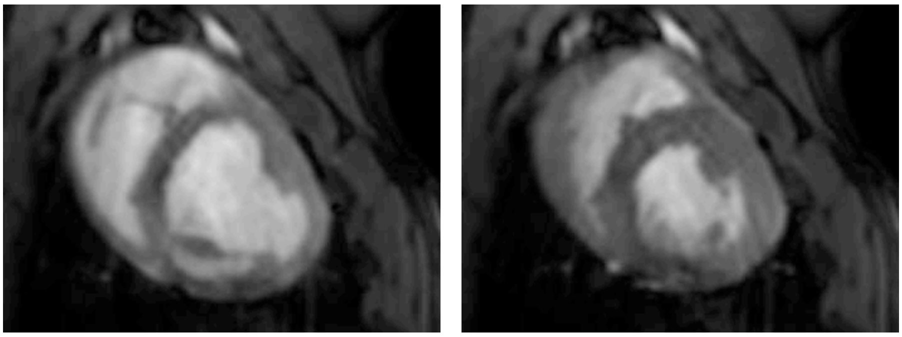

(a) 2D slice during diastole (b) 2D slice during systole

Figure 4.2: Example of cine-MR images in short axis view, acquired at T_0.

senting the left endo- and epicardium. In most practical cases, the right ventricle is likely to be difficult to capture in cine-MR images. Figure 4.3(a) shows an example of left ventricle segmentation in short-axis view. The segmentation of such images can be performed either manually or with semi-automatic methods [Bister et al., 1989, Goshtasby and Turner, 1995, Cocosco et al., 2008]. Moreover, from these images one can build the surface of the computational mesh needed to numerically solve the model dynamical system – see Figure (4.3(b)). The construction of such computational meshes is much more complex, but in our work we only assume that we have a reasonable template of the geometry. We will see in the next section that this template can be adjusted *a posteriori* using the segmentation of the left ventricle by solving a static registration problem – readers may refer to Chapter 4 for a detailed presentation of such problems.

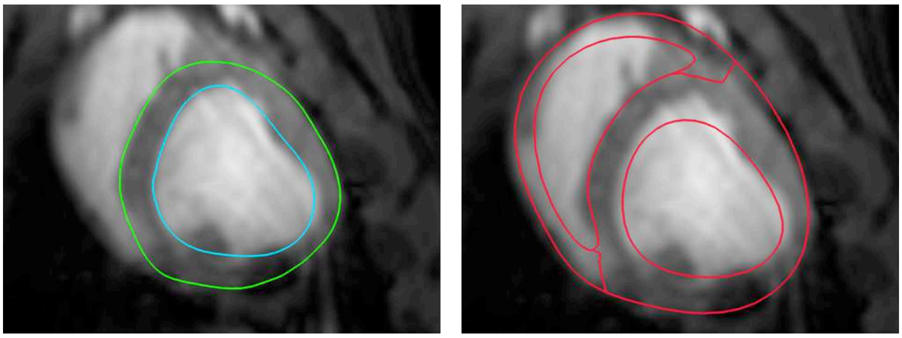
(a) Segmentation of the LV endo- and epicardium (in (cyan) and (green))

(b) Computational mesh (in (red))

Figure 4.3: Cine-MRI process, in SAX view – *Manual segmentation of cine-MRI performed by Radomir Chabiniok, King's College London, UK.*

Processing tagged-MR images Since they are more common in clinical routine, the processing of cine-MR images is nowadays a well managed problem [Bister et al., 1989, Goshtasby and Turner, 1995, Cocosco et al., 2008]. Concerning the tagged-MR images we assume that a prior step of image processing led to the extraction of apparent displacements defined within the image plane. In the literature, this data type appears to be the most common type of output of tagged-MRI processing. In practice, carrying out this task can be done in several ways.

A first way is to use an optical flow methodology to track the deforming tag pattern directly in the image plane – [Prince and McVeigh, 1992, Dougherty et al., 1999] for instance. Another possibility proposed by [Ledesma-Carbayo et al., 2006] is to perform non-rigid image registration. Moreover, some methodologies are based on a frequency representation of the image. The most popular method is the HARP technique which aims at tracking the phase of the tag pattern– see [Osman et al., 1999, Osman and Prince, 2000].

Figure 4.4(a) illustrates a typical output of a tagged-MRI processing software based on the work of [Clarysse et al., 2000]. Once the apparent displacements are acquired, we can build the corresponding deforming tag planes and tag grids, and in what follows we propose a methodology to perform this task.

---

[0] Obtained using the *inTag* plugin of the *OsiriX* software – `http://www.creatis.insa-lyon.fr/inTag/`.

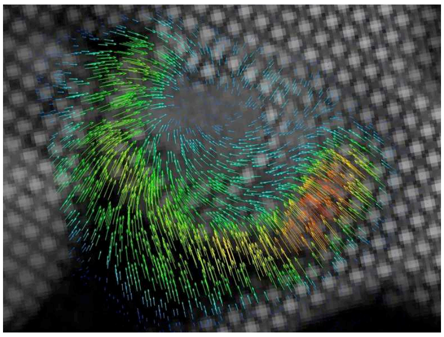

(a) Extraction of tag apparent displacement from *inTag* plugin of the *OsiriX* software

Figure 4.4: tagged-MRI process, in SAX view.

To start with, we consider the issue of generating the tag planes. The method that we propose is highly related to the one described in the Chapter 3 of this thesis used to build synthetic tag planes from a direct simulation of a model of the heart. The first step is to built a set of template tag layers – denoted by $\{\mathcal{V}_0^i\}_{i=1}^{N_\mathcal{T}}$ in Chapter 3 – and to perform a rigid transformation of these templates into the image plane. It should be noted that in modern meta-data – such as Dicom images, a popular standard for medical image storing – the orientation and origin of the image planes are usually provided. Once the tag layers are transformed into the image orientation some adjustment may be required so that the complete set of tag layers match the image tag pattern. In practice, it may happen that we can observe some irregularities in the image tag pattern – mainly close to the external surface of the organ – which may compromise the complete matching between the tag layers and the tag pattern. In this situation, it is important to notice that the valuable informations in tagged-MR images are spatially located within the heart wall, hence it is sufficient to require that the tag layers fit the image tag pattern only in this area. Once the tag layers fit the tag pattern, we have the linear interpolation operator from the image plane to the volume mesh of each tag layer – ass illustrated in Figure 4.5. This step is classically done by computing the barycentric coordinate of each pixel – localized by its center – within the tetrahedra of the tag layer. Denoting by $\mathbf{I}_{\mathcal{I}\cap\mathcal{V}}$ this operator and by $\vec{Y}^{app}$ – as in Chapter 3 – the apparent displacement in the image plane – then the displacement of the complete tag layer can be obtained by solving the minization problem

$$\min_{\vec{Y}} \frac{\varepsilon}{2}\vec{Y}^\intercal\mathbf{K}\vec{Y} + \frac{1}{2}\big(\mathbf{I}_{\mathcal{I}\cap\mathcal{V}}^\intercal\vec{Y}^{app} - \vec{Y}\big)^\intercal\mathbf{M}\big(\mathbf{I}_{\mathcal{I}\cap\mathcal{V}}^\intercal\vec{Y}^{app} - \vec{Y}\big), \tag{4.1}$$

where $\mathbf{K}$ is a stiffness matrix built on a tag layer and $\mathbf{M}_{\mathcal{I}\cap\mathcal{V}}$ correspond to a mass matrix. The strategy (4.1) is in fact a Tikhonov regularization of the apparent displacement projected in the tag layer. The solution of (4.1) is obtained through

$$\vec{Y} = \big(\varepsilon\mathbf{K} + \mathbf{I}_{\mathcal{I}\cap\mathcal{V}}\mathbf{M}\mathbf{I}_{\mathcal{I}\cap\mathcal{V}}^\intercal\big)^{-1}\mathbf{M}\mathbf{I}_{\mathcal{I}\cap\mathcal{V}}^\intercal\vec{Y}^{app}.$$

Once the tag layers are deformed we can extract the middle plane and repeat this procedure at each image sampling step in order to obtain a set of deforming tag planes.

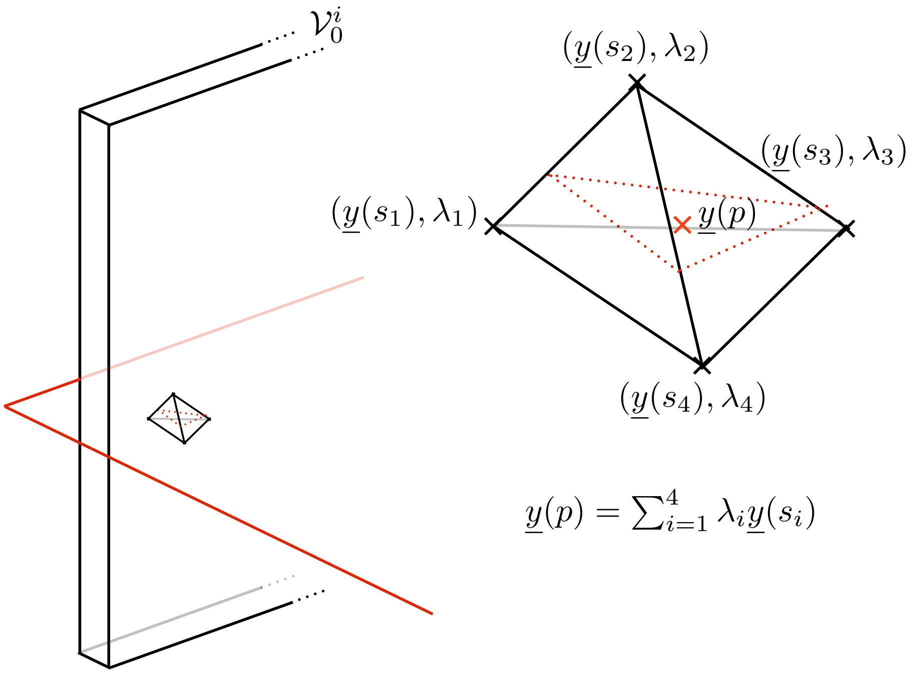

Figure 4.5: Illustration of image plane-to-tag layer interpolation process.

In order to obtain the corresponding tag grids, a possibility is to clip the previously obtained tag planes. However, the process of clipping geometries is – from an algorithmic point of view – quite heavy and may lead to irregular one-dimensional line meshes. Therefore a more suitable way is to adapt the previously stated methodology to a set of tag grids. Let $\{\mathcal{L}^j\}_j \subset \mathcal{I}$ be the set of template tag lines that, after a rigid transformation, are embedded in the image slice $\mathcal{I}$ and match the tag pattern at least in the region where the heart appears. Let Ω be the computational mesh obtained from cine-MRI – see Figure 4.3(b). The displacement of a tag line $\mathcal{L}^i$ is defined as the solution of

$$\min_{\vec{Y}} \frac{\varepsilon}{2}\vec{Y}^\top \mathbf{K}^{1\mathrm{D}}\vec{Y} + \frac{1}{2}\left(\vec{Y}^{app} - \vec{Y}|_{\mathcal{L}^i\cap\Omega}\right)^\top \mathbf{M}\left(\vec{Y}^{app} - \vec{Y}|_{\mathcal{L}^i\cap\Omega}\right), \tag{4.2}$$

where we denoted by $\mathbf{K}^{1\mathrm{D}}$ a stiffness matrix corresponding to a one-dimensional elastic energy, typically the Timoshenko's beam model [Thomson, 1993]. Figure 4.6(a) illustrates how the the apparent displacement is interpolated onto the tag line and Figure 4.6(b) shows an example of tag grid reconstruction.

Methodological key point

Extracting data

- Extract from cine-MR images left endo- and epicardium surfaces at each image sampling time step and at least on computational mesh from the image sequence.

- From the tagged-MR images extract the apparent displacement defined within the image plane. Build tag planes from apparent displacement interpolation and regularization. Build tag grids from tag planes clipping or apparent displacement interpolation and regularization.

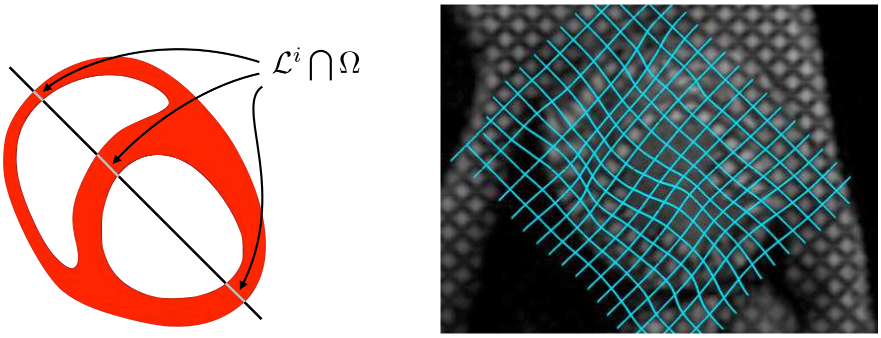

(a) Tag line displacement interpolation (b) Reconstruction of deforming tag grids (in (cyan))

Figure 4.6: Reconstruction of tag line deformation from apparent displacement.

Preparing the direct model

In the previous section we have described how we can build the various data types that could potentially be used in a data assimilation procedure – typically using the observer-based methodology described in [Moireau et al., 2009, Chabiniok et al., 2012] and recalled in the Chapter 2 and Chapter 3 of this thesis. In this section we address some potential issues that may arise when trying to perform a direct simulation based on a cardiac model. To start with we will see how the computational geometry can be adjusted to the specifics of the geometry appearing in the images using a static registration problem – as presented in Chapter 4. Using a similar method, we also provide a way to automatically build the contact surface used in the direct model given in Chapter 1 to represent the interaction between the heart external surface and the pericardium. These first two adjustments are mainly built using the cine-MRI segmentations – which shows at least once again that cine-MR images are of utmost importance. We will finally see how these segmentations can also be used to provide an estimation of the initial condition of the problem dynamics.

Adjusting computational meshes In practical cases, the segmented endo- and epicardium and the corresponding surfaces in the segmented computational mesh are likely to have discrepancies. These discrepancies come from the fact that the latter is much more intricate to obtain since it needs to satisfy some requirements in order to bear the forthcoming numerical computations – such as smoothness, non-overlapping of elements and so on. Therefore the computational geometry is in practice segmented independently from the endo- and epicardium surfaces and potentially subject to post-processing – typically algorithm for surface fairing – see for example [Welch and Witkin, 1994, Desbrun et al., 1999] – or volume adjustment. In the perspective of applying data assimilation methods, these discrepancies will directly enter as some noise that may deteriorate the estimation quality. To circumvent this difficulty one solution is to perform a prior run of state observer fed with the segmentations of the left ventricle and then to extract from the simulations the dynamically registered mesh. Even though this method is valid in practice, another possible solution is to statically deform the computational mesh towards the segmented surfaces using a descent method – as described in Chapter 4. Figure 4.7 represents the model geometry fitted to the segmentation in Tele-Systole (TS). Denoting by $\mathcal{S}$ both the endo- and epicardium surfaces – the target surfaces – then this regristration problem can be solved by seeking the deformation $\underline{\varphi}$ of the computational mesh Ω solution of

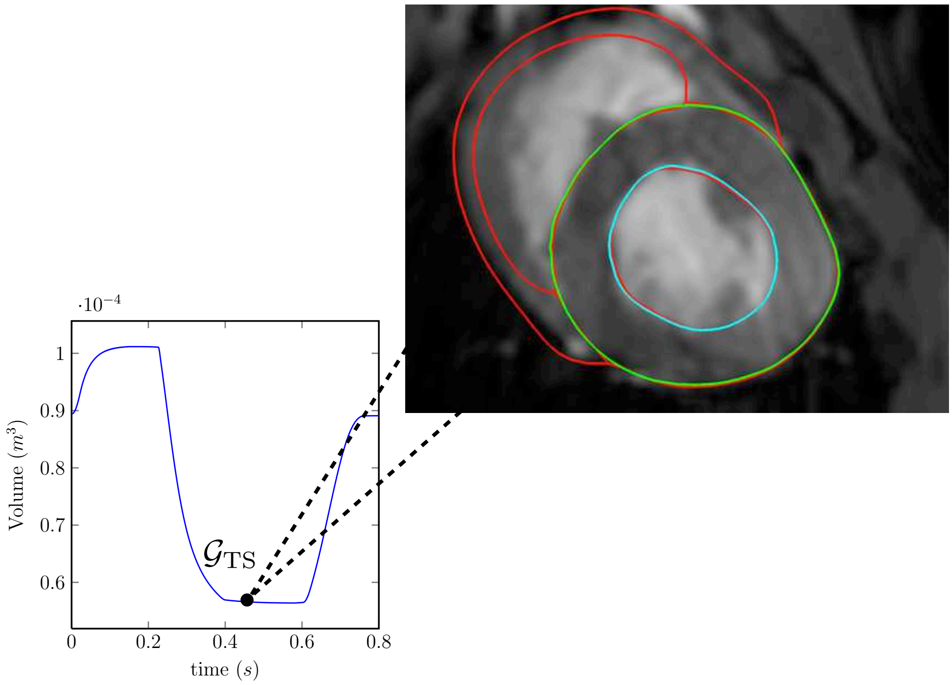

Figure 4.7: Adjusting computational mesh (in (red)) to fit end systole data set (in (cyan) and (green)).

$$\min_{\underline{\varphi}} \frac{1}{2}\mathcal{E}_{\mathrm{e}}(\underline{\underline{e}}) + \frac{1}{2}\|\mathrm{dist}(\underline{\varphi}(\Omega),\mathcal{S})\|^2 . \tag{4.3}$$

In (4.3) we denoted by $\mathcal{E}_{\mathrm{e}}$ the elastic energy corresponding to the deformation $\underline{\varphi}$ and $\underline{\underline{e}}$ the Green-Lagrange tensor associated to $\underline{\varphi}$. This elastic energy typically derives from an elastic potential W^{e}

$$\mathcal{E}_{\mathrm{e}} = \int_{\Omega} W^{\mathrm{e}} \, \mathrm{d}\Omega . \tag{4.4}$$

Inspired from [Moireau et al., 2009] and what we have mentioned in the Chapter 4 of this thesis, we measure the discrepancy between the target surfaces and the geometry surface using the signed distance function $\mathrm{dist}(\cdot,\mathcal{S})$. Depending on the intensity of the distance between the target surfaces and the priori computational mesh, the deformation may become significant. To avoid critical alterations of the tetrahedra constituting the geometry, the elastic potential W^{e} should at least contain some terms penalizing the local volume measure $\det(\underline{\underline{\nabla}}\underline{\varphi})$ – *i.e.* it is advised to consider in this registration problem the computational mesh as a nearly incompressible material.

As another advantage of this methodology, it should be noted that – as a result – we have smoothed the internal surface of the heart geometry, delimiting the left and right ventricle. This delineation has its importance during identification of constitutive parameters restricted to the left ventricle.

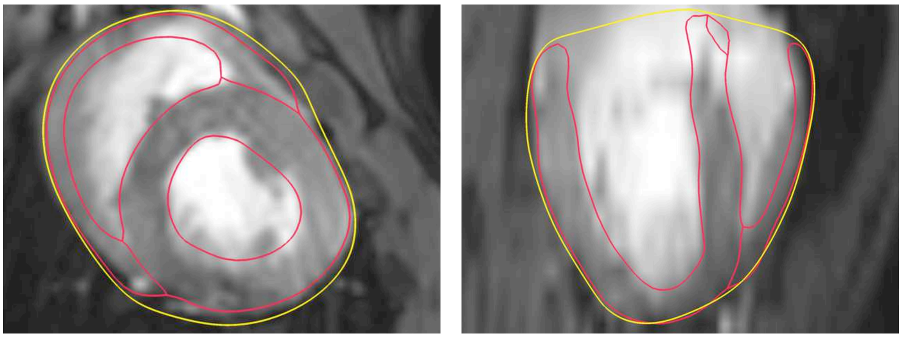

(a) SAX-view

(b) LAX-view

Figure 4.8: Contact surface (in (yellow)) for the direct model.

Building of contact surface Once the model geometry is adjusted we also need to build the contact surface necessary to represent the interactions between the heart and its surroundings. The difficulty here is that this contact surface should encompass the geometry in a smooth way so as not to block the sliding movements of the heart during systole. To do so we consider a template $\mathcal{T}$ – in practice a sphere with a given thickness – built around the computational mesh that we deform in the same manner as previously discribed in (4.3). In this simpler registration problem – we are only interested in the resulting internal surface of the deformed template – we can consider $\mathcal{E}_{\mathrm{e}}^{\mathrm{lin}}$ an elastic energy that derives from a linear constitutive law. Hence the deformation $\underline{\varphi}$ is the solution of

$$\min_{\underline{\varphi}} \frac{1}{2}\mathcal{E}_{\mathrm{e}}^{\mathrm{lin}}(\underline{\underline{e}}) + \frac{1}{2}\|\mathrm{dist}(\underline{\varphi}(\mathcal{T}),\Omega)\|^2 \,. \tag{4.5}$$

Estimation of the reference configuration As we have mentioned several times throughout this thesis, the reference configuration of the heart is never observed. In a synthetic context this was not an issue since it could be directly prescribed as the geometry obtained after tele-systole – as shown in Figure 4.9. This configuration, situated at the end of the isovolumetric relaxation, represents the configuration in the heart cycle that sustains the smallest amount of internal stresses, justifying its choice as the closest configuration to the reference.

In a real context however, if we want to minimize the amount of initial errors introduced in the system, we cannot restrict ourselves to define the geometry at the end of the isovolumetric relaxation as the reference configuration since – in the perspective of data assimilation – it will introduce significant errors on the initial conditions. Therefore we have to

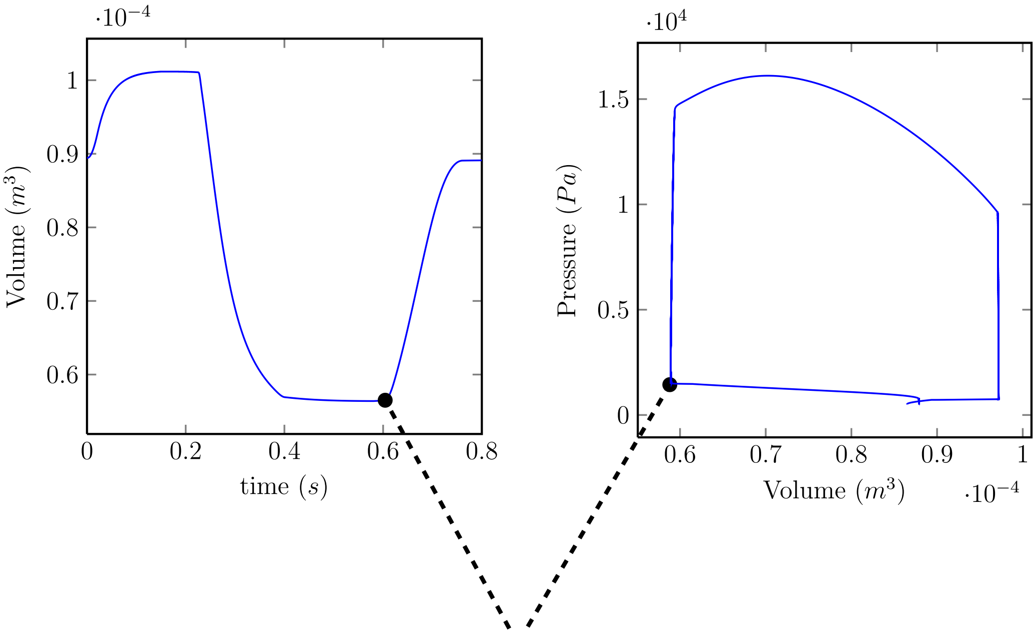

Config. with smallest stress & strain

Figure 4.9: Position in the heart cycle of the configuration closest to the reference configuration

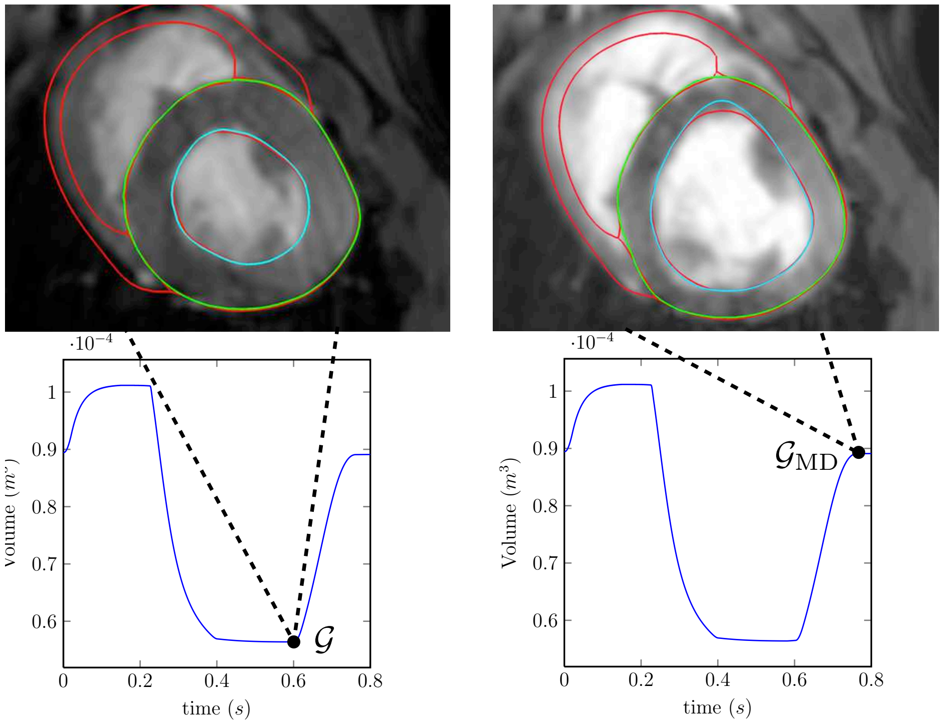

Figure 4.10: Various fitted geometries used to solve the inverse problem.

provide at least an *a priori* estimation of the reference configuration. To do so we will assume that at least some information on the pressure sustained by the cavity are available on the system. Let us denote by P_{MD} the homogeneous pressure inside the left-ventricle in Mid-Diastole. The problem of estimating the reference configuration Ω_0 can be expressed as

$$\text{Find } \Omega_0 \text{ such that internal stresses in } \underline{\varphi}(\Omega_0, t_{\mathrm{MD}}) \text{ balances the pressure } P_{\mathrm{MD}}. \tag{4.6}$$

To solve this problem we propose the following iterative process.

$$\left|\begin{array}{l} \text{From a first guess } \underline{y}^0_{\mathrm{MD}}, \\ \\ \text{do} \begin{cases} \Omega_0^{n+1} = \Omega_0^n - \underline{y}^n_{\mathrm{MD}} \\ \underline{y}^{n+1}_{\mathrm{MD}} \text{ solution of } \displaystyle\int_{\Omega_0} \underline{\underline{\Sigma}}(\underline{y}^{n+1}_{\mathrm{MD}}) : \mathrm{d}_{\underline{y}}\underline{\underline{e}} \cdot \underline{v}^\flat \, \mathrm{d}\Omega_0 = -P_{\mathrm{MD}} \int_{\mathcal{E}n_{\mathrm{L}}} \underline{n}_{\mathrm{L}} \cdot \underline{v}^\flat \mathrm{d}\sigma \end{cases} \\ \\ \text{until } \|\Omega_0^{n+1} - \Omega_0^n\| \leq \varepsilon. \end{array}\right. \tag{4.7}$$

To have a good chance for the algorithm (4.7) to converge, one needs to prescribe a reasonable first guess $\underline{y}^0_{\mathrm{MD}}$. Since solving registration problems of the form of (4.3) is reasonably cheap and automatic, we solve (4.3) with the segmentations obtained at the end of the isovolumetric relaxation and in Mid-Diastole. Thus we obtain two geometries $\mathcal{G}$ and $\mathcal{G}_{\mathrm{MD}}$ (see Figure 4.10). Hence we define the first guess of the iterative process (4.7) as

$$\underline{y}^0_{\mathrm{MD}} = \mathcal{G}_{\mathrm{MD}} - \mathcal{G}.$$

Methodological key point

Preparing direct model

- Adjust the computational mesh through solving a registration problem on the corresponding left ventricle segmentation using a nonlinear hyperelastic model.
- Build contact surface.
- Compute first guess of displacement from reference configuration in order to solve the inverse problem for estimating the reference configuration.

Anticipating estimation difficulties

So far we have described the various types of data sets that could feed our data assimilation procedure. In the particular case of tagged-MRI they take the form or either apparent displacements in the image plane, deforming tag grids or deforming tag planes. We also have detailed some key components of the direct model that need to be adjusted prior to be able to run realistic direct simulations. In this third section we finally discuss some difficulties that may arise when applying the data assimilation procedure – detailed at length in [Moireau et al., 2009] and recall in Chapter 2.

Kalman filtering and contact constraint In a nutshell the data assimilation that we aim at using propose to jointly perform parameter and state estimation. On the one hand the potential state uncertainties are controlled using a Luenberger type filter [Luenberger, 1971, Auroux and Blum, 2007, Ramdani et al., 2012] which, in essence, aims at adding some dissipative components in the state error estimation dynamics so that it would benefit from an improved stabilized behavior – compared to the natural damping present in the system. On the other hand, the remaining parameter errors are tackled using a Reduced-order Unscented Kalman Filter (RoUKF) [Julier et al., 1995, Julier, 2002, Moireau and Chapelle, 2011] that proposes to use adequate sampling points to approximate the propagation – through the nonlinear dynamics – of the predicted and corrected mean and covariance of the system. These sampling points are referred to *particles*. These particles are computed around the estimated trajectory based on the covariance estimation.

However, this way of creating particles is blind to the contact constraint we propose to impose in order to represent the peculiar relation between the outer surface of the heart and the pericardium. Therefore once the particle are created, some of them may not respect this constraint thus leading to a dramatic increase of the external forces resulting in the representation of the contact using distances – as presented in Chapter 1. Hence we face two problems, the first being that, in order to fairly approximate the model sensitivity of the model with respect to the parameters the particles have to respect the contact constraint. We thus need to refer to the work around Kalman filtering with nonlinear constraints – see *e. g.* [Simon and Li Chia, 2002, Ungarala et al., 2007, Kandepu et al., 2008] – which, in essence, can be summarize at a fully-discrete level and from an algorithmic standpoint to statically solving the contact constraint right after the particles are created. The second problem that we face when introducing the contact constraint is that the Newton's method may diverge during the computation of the model iteration – typically during systole where the heart tends to press onto the pericardium, downwards in the direction of the long axis. To circumvent this difficulty each particle requires a time-step adaptation algorithm to enable time-step reduction. However doing this impose an intricate timeline management since each particle has to converge prior to gather them in order to retrieve the estimated trajectory. The complete algorithm is illustrated in Figure 4.11.

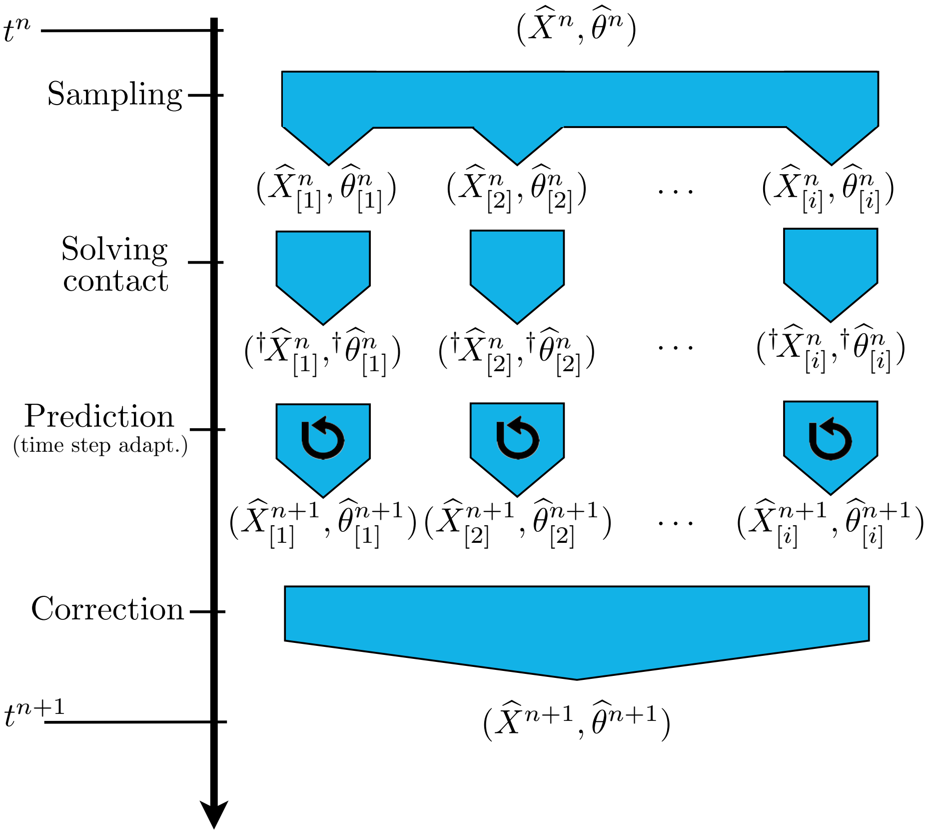

Figure 4.11: Scheme of the unscented Kalman filter adapted for solving the contact constraint.

Estimating displacement at tagging marking time Additionally, as we have understood from Chapter 3, assimilating the (rich) information contained in the tagged-MR images requires to have an estimation of the displacements at the marking time. We recall that this is due to the Eulerian nature of the process of tagging. More precisely since the tag pattern is imprinted in an already deformed configuration, typically during diastole, the deformation of the tag grid follows – instead of a displacement from the reference configuration – the deformation from this tagged configuration. To circumvent this difficulty, in Chapter 3, we have propose a methodology based on the assumption that we were able to provide an estimation of the displacement at marking time. In the context of real observations, this estimation can be obtained typically by statically registering the computational mesh defined at the end of the isovolumetric relaxation to the cine-MR segmentations that are as close as possible of the marking time. This fact reflects once again that the cine-MR modalities gather necessary information in order to apply data assimilation methods using tagged-MRI. As a matter of fact it appears that, in the perspective of clinical applications, the couple tagged- and cine-MR images should be considered as an invaluable joint source of information.

Methodological key point

Preparing direct model

- Adapt RoUKF to solve the contact constraint after particle creation.
- Enable separate timelines for each particle to allow time adaptation at a particle level.
- Estimate displacement at marking time using cine-MR segmentations.

Perspectives

Data assimilation is the pathway to combine the valuable information contained in mathematical models with the potential information on the observed phenomena. In the context of cardiac modelling, recent works [Moireau et al., 2009, Chabiniok et al., 2012, Moireau et al., 2013] in this respect have shown that the audacious objective of proposing a complete package of methodological tools in order to provide diagnosis assistance in a clinical routine is achievable. However, in this perspective, applying state-of-the-art data assimilation methods requires to be able to compute a means of comparison between the biomechanical model – on the one hand – and the observations – on the other hand. In practical cases, the model and the data are of very different nature, thus the task of comparing them becomes significantly intricate. As a matter of fact, since any data assimilation method is based on such discrepancy measure, the complete structure of any endeavours aiming at personalizing a mathematical model from realistic data sets necessarily incorporates such complex dissimilarity measure. It is in this context that the main contributions of this thesis take shape. We have provided a realistic example of applications of complete data assimilation methods using a biomechanical model of the heart and observations obtained from pre-precessed tagged-MR images – a rich image modality potentially leading in clinical routine to a highly precise assessment of the patient heart function. Moreover, we were able to derive a new discrepancy measure – based on the formalism of *currents* and related to shape sensitivity analysis – in order to compare mechanical systems with level-set segmentations of images. These contributions were illustrated on synthetic but realistic examples of parameter identification. From this work we can extract several potential perspectives

- As we have partially detailed in this final chapter, the closest perspective is to apply the discrepancy operators built in our work from pre-processed tagged-MR images within a real data context as it was done in [Chabiniok et al., 2012] for the distances operator to surfaces – segmented from cine-MR modalities.

- In Chapter 4 we have derived a means of coupling elasticity systems and the formalism of currents. However, for simplicity, we have put aside some technicalities concerning the required regularity of the various spaces appearing in this methodology. Indeed, we have shown that the tangent current of the model surface is defined through the surface gradient of the deformation – which is not defined from standard regularity assumptions. However, since there is a dual relation between the space of currents and the space of test functions that belongs to the R.K.H.S. we could imagine to still rigorously prove the well-posedness of these terms by imposing some regularities on the space of test functions.

- From a data assimilation standpoint, we have seen that when the adjoint of the tangent operator is not directly accessible the standard algorithms fail to propose an equivalent alternative to enable data assimilation procedure written in a weak form. For example in Chapter 4, the adjoint of a tangent current could not be derived thus prohibiting the use of external data assimilation library such as Verdandi [Chapelle et al., 2012].

- Another perspective would be do get even closer to the raw image data than what we have proposed in the Chapter 4. Indeed, in this context we have proven that the formalism of currents enables us to represent a surface from a pre-computed level-set. However it would be an interesting perspective to be able to completely fill the gap between the mechanical model and the raw images by proposing a surface representation directly from the gradient of the grey-level image.

- Long term perspectives could also be imagined from this novel *current*-based discrepancy measure. Indeed, in a large amount of applications of data assimilation methods the data take the form of evolving geometrical objects or shapes. We could cite the example of data assimilation methods in the context of electro-phyiological models [Konukoglu et al., 2011] where the data could potentially be the front propagation of the transmembrane potential. Another possible example lies in the construction of predictive model for fire propagation [Rochoux et al., 2013] where the observations take the form of the flame fronts or even in the field of data assimilation for meteorology [Corpetti et al., 2009, Titaud et al., 2010] where typically the clouds contours would be represented as currents.

Bibliography of the fifth Chapter

[Auroux and Blum, 2007] Auroux, D. and Blum, J. (2007). A nudging-based data assimilation method: the back and forth nudging (bfn) algorithm. *Nonlin. Processes Geophys.*

[Bister et al., 1989] Bister, M., Taeymans, Y., and Cornelis, J. (1989). Automated segmentation of cardiac mr images. In *Computers in Cardiology 1989, Proceedings.*, pages 215–218. IEEE.

[Chabiniok et al., 2012] Chabiniok, R., Moireau, P., Lesault, P.-F., Rahmouni, A., Deux, J.-F., and Chapelle, D. (2012). Estimation of tissue contractility from cardiac cine-mri using a biomechanical heart model. *Biomech. Model. Mechanobiol.*, 11(609-630).

[Chapelle et al., 2012] Chapelle, D., Fragu, M., Mallet, V., and Moireau, P. (2012). Fundamental principles of data assimilation underlying the verdandi library: applications to biophysical model personalization within euheart. *Medical & Biological Eng & Computing*, pages 1–13.

[Clarysse et al., 2000] Clarysse, P., Basset, C., Khouas, L., Croisille, P., Friboulet, D., Odet, C., and Magnin, I. (2000). Two-dimensional spatial and temporal displacement and deformation field fitting from cardiac magnetic resonance tagging. *Med. Image. Anal.*

[Cocosco et al., 2008] Cocosco, C. A., Niessen, W. J., Netsch, T., Vonken, E.-j. P., Lund, G., Stork, A., and Viergever, M. A. (2008). Automatic image-driven segmentation of the ventricles in cardiac cine mri. *Journal of Magnetic Resonance Imaging*, 28(2):366–374.

[Corpetti et al., 2009] Corpetti, T., Héas, P., Mémin, E., and Papadakis, N. (2009). Pressure image assimilation for atmospheric motion estimation. *Tellus A.*, 61(1):160–178.

[Desbrun et al., 1999] Desbrun, M., Meyer, M., Schröder, P., and Barr, A. H. (1999). Implicit fairing of irregular meshes using diffusion and curvature flow. *AMT SUGGRAPH*.

[Dougherty et al., 1999] Dougherty, L., Asmuth, J. C., Blom, A. S., Axel, L., and Kumar, R. (1999). Validation of an optical flow method for tag displacement estimation. *IEEE Trans. Med. Imaging*.

[Goshtasby and Turner, 1995] Goshtasby, A. and Turner, D. A. (1995). Segmentation of cardiac cine mr images for extraction of right and left ventricular chambers. *Medical Imaging, IEEE Transactions on*, 14(1):56–64.

[Julier, 2002] Julier, S. J. (2002). The scaled unscented transformation. *Proceedings of the American Control Conference*.

[Julier et al., 1995] Julier, S. J., Uhlmann, J. K., and Durrant-Whyte, H. F. (1995). A new approach for filtering non linear systems. *Proceedings of the American Control Conference*, pages 1628–1632.

[Kandepu et al., 2008] Kandepu, R., Imsland, L., and Foss, B. A. (2008). Constrained state estimation using the unscented kalman filter. *16th Mediterranean Conference on Control and Automation*.

[Konukoglu et al., 2011] Konukoglu, E., Relan, J., Cilingir, U., Menze, B. H., Chinchapatnam, P., Jadidi, A., Cochet, H., Hocini, M., Delingette, H., Jaïs, P., et al. (2011). Efficient probabilistic model personalization integrating uncertainty on data and parameters: Application to eikonal-diffusion models in cardiac electrophysiology. *Progress in Biophysics and Molecular Biology*, 107(1):134–146.

[Ledesma-Carbayo et al., 2006] Ledesma-Carbayo, M. J., Bajo, A., Santa Marta, C., E., P.-D., Garcia-Fernandez, M. A., Desco, M., and Santos, A. (2006). Fully automatic cardiac motion estimation fro tagged mri using non-rigid registration techniques. *IEEE Proceeding Computers in Cardiology*, pages 305–308.

[Luenberger, 1971] Luenberger, D. G. (1971). An introduction to observers. *IEEE T. Automat. Contr.*

[Moireau et al., 2013] Moireau, P., Bertoglio, C., Xiao, N., Figueroa, C. A., Taylor, C. A., Chapelle, D., and Gerbeau, J. F. (2013). Sequential identification of boundary support parameters in a fluid-structure vascular model using patient image data. *Biomech. Model. Mechanobiol.*, 12:475–496.

[Moireau and Chapelle, 2011] Moireau, P. and Chapelle, D. (2011). Reduced-order unscented kalman filtering with application to parameter identification in large-dimensional systems. *ESAIM: COCV*, 17:380–405.

[Moireau et al., 2009] Moireau, P., Chapelle, D., and LeTallec, P. (2009). Filtering for distributed mechanical systems using position measurements: Perspectives in medical imaging. *Inverse Problems*, 25.

[Osman et al., 1999] Osman, N. F., Kerwin, W. S., McVeigh, E. R., and Prince, J. L. (1999). Cardiac motion tracking using cine harmonic phase (harp) magnetic resonance imaging. *Magn. Reson. Med.*, pages 1048–1060.

[Osman and Prince, 2000] Osman, N. F. and Prince, J. L. (2000). Visualizing myocardial function using harp mri. *Phys. Med. Biol.*, pages 1665–1682.

[Prince and McVeigh, 1992] Prince, J. L. and McVeigh, E. R. (1992). Motion estimation from tagged mr image sequences. *IEEE Trans. Med. Imaging*.

[Ramdani et al., 2012] Ramdani, K., Tucsnak, M., and Weiss, G. (2012). Recovering the initial state of an infinite-dimensional system using observers. *Automatica*, pages 1616–1625.

[Rochoux et al., 2013] Rochoux, M. C., Cuenot, B., Ricci, S., Trouvé, A., Delmotte, B., Massart, S., Paoli, R., and Paugam, R. (2013). Data assimilation applied to combustion. *Comptes Rendus Mécanique*, 341(1):266–276.

[Simon and Li Chia, 2002] Simon, D. and Li Chia, T. (2002). Kalman filtering with state equality constraints. *IEEE T. Aearo. Elec. Sys.*

[Thomson, 1993] Thomson, W. T. (1993). *Theory of vibration with applications*. Taylor & Francis.

[Titaud et al., 2010] Titaud, O., Vidard, A., Souopgui, I., and LeDimet, F. X. (2010). Assimilation of image sequences in numerical models. *Tellus A*, 62(1):30–47.

[Ungarala et al., 2007] Ungarala, S., Dolence, E., and Li, K. (2007). Constrained extended kalman filter for nonlinear state estimation. *8th International IFAC Symposium on Dynamics and Control of Process Systems*, pages 63–68.

[Welch and Witkin, 1994] Welch, W. and Witkin, W. (1994). Free-form shape design using triangulated surfaces. *SIGGRAPH'94 Conference Proceedings*, pages 247–256w.

Alexandre IMPERIALE

Méthodes d'assimilation de la donnée image pour la personnalisation de modèles mécaniques

Application à la mécanique cardiaque et aux images de marquage tissulaire

Cette thèse est dédiée à l'intégration de données complexes issues de l'imagerie dans une stratégie d'assimilation de données pour des modèles mécaniques. Notre stratégie s'appuie sur des travaux récents proposant une méthode séquentielle d'assimilation de données qui se décompose en un filtre de Luenberger pour l'espace d'état et un filtre optimal réduit à l'espace des paramètres. Nous l'appliquons à l'identification de paramètres pour un modèle biomécanique du cœur et, dans ce cadre, nous formalisons la construction de comparateurs de formes évolués pour deux types de données : d'une part des données extraites d'un traitement de l'Imagerie par Résonance Magnétique (IRM) de marquage tissulaire et, d'autre part, des données plus classiques de type contours de l'objet. D'abord fondés sur des simples distances nous enrichissons ces comparateurs grâce au formalisme des courants permettant d'inscrire le contour de l'objet dans le dual d'un espace de fonctions-test appropriées. Pour chacun des comparateurs nous analysons son impact sur l'observabilité du système et, pour le cas de l'imagerie de marquage tissulaire, nous prouvons qu'ils sont équivalents à une mesure directe du déplacement. D'un point de vue numérique, la prise en compte de ces mesures complexes présente d'importantes difficultées nous poussant à mettre en place des schémas numériques originaux permettant une manipulation plus flexible des différents opérateurs d'observation. Nous profitons de ces nouveaux moyens d'extraction de l'information contenue dans les données d'imagerie pour permettre, dans des cas réalistes, l'identification de la position et de l'intensité d'un infarctus du myocarde.

Mots-clés : Assimilation de données, Comparateurs de formes, Mécanique cardiaque, IRM de marquage tissulaire, Courants.

Image-based data assimilation methods for the personalization of mechanical models

Application to cardiac mechanics and tagged-MRI

This thesis aims at incorporating complex data derived from images into a data assimilation strategy available for mechanical systems. Our work relies on some recent developments that propose a sequential data assimilation method made of a Luenberger filter for the state space and an optimal filter reduced to the remaining parameter space. We aim at performing parameter identification for a biomechanical model of the heart and, within the scope of this application, we formalize the construction of shape discrepancy measurements for two types of data sets: first, the data expected of a processing step of tagged Magnetic Resonance Imaging (tagged-MRI) and, second, more standard data composed by the contours of the object. Initially based on simple distance measurements we enrich these discrepancy measures by incorporating the formalism of currents which enables to embed the contours of the object within the dual of an appropriate space of test functions. For each discrepancy operators we analyze its impact on the observability of the system and, in the case of tagged-MRI, we prove that they are equivalent to a direct measurement of the displacement. From a numerical standpoint, taking into account these complex data sets is a great challenge that motivates the creation of new numerical schemes that provide a more flexible management of the various observation operators. We assess these new means of extracting the rich information contained in the image by identifying in realistic cases the position and the intensity of an infarct in the heart tissue.

Keywords: Data assimilation, Shape discrepancy measure, Cardiac mechanics, Tagged-MRI, Currents.